

Research in Optoelectronics (A)

Reprints published in 2004

by

Professor Larry A. Coldren

and Collaborators

Published as

Technical Report # ECE 05-01

of

The Department of Electrical & Computer Engineering

The University of California

Santa Barbara, CA 93106

Phone: (805) 893-4486

Fax: (805) 893-4500

E-mail: coldren@ece.ucsb.edu

www.ece.ucsb.edu/Faculty/Coldren

Introduction:

This edition of Prof. Coldren's reprint book chronicles conference and journal articles published in 2004. These generally focus on III-V semiconductor lasers and related photonic integrated circuits. The work spans efforts from basic materials and processing technology, through device physics and design, to device formation, characterization, and insertion into systems demonstrations.

The reprints have been grouped into four areas: **I. Photonic Integrated Circuits and Related Technology; II. InP-based Vertical-Cavity Lasers; III. Photodetectors and Receivers; and IV. Terahertz Technology.** By far the majority of the work is in the first area, which has been further subdivided into *A. Widely-Tunable Monolithic Transmitters; B. Widely-Tunable Wavelength Converters; C. Quantum-Well Intermixing Technology; D. Sensors; and E. Materials Technology.* All of the work except the Terahertz devices and some of the sensor effort is based upon an InP platform, either via MOCVD or MBE. The epitaxial growth activity is strongly supported by Prof. DenBaars (MOCVD) and Prof. Gossard (MBE), who co-advise the students involved in these areas. Thus, their contributions have been invaluable to the research, even when they do not appear as co-authors on the device oriented papers.

The work was performed under the support of several grants from industry and government, some gift funds from industry, and support from the Kavli Endowed Chair in Optoelectronics and Sensors. Specific projects included one on RF-Photonics under the DARPA R-FLICS program; work on photocurrent-driven widely-tunable wavelength converters supported by the Intel Corp as well as DARPA via the CSWDM program; efforts to create high-bit-rate wavelength converters and buffers under the DARPA DoDN program; two projects to create very high-efficiency optical interconnects for ICs using either edge-emitting short-cavity laser-modulators (supported by the DARPA C2OI program) or directly-modulated vertical-cavity surface-emitting lasers (supported by MARCO as part of the Interconnect Focus Center); and a bio-chemical sensor project under the support of the Army via the Institute for Collaborative Biotechnologies. Two UC-MICRO projects were also supported with leveraging funding from Intel (more work on Photonic ICs) and Agilent (1300 nm laser-modulators).

The first general research area documented in the enclosed reprints is on Photonic Integrated Circuits and Related Technology. The work continues to extend the sampled-grating distributed Bragg reflector (SGDBR) laser platform to include more and more active and passive components for greater functionality. This research has been led by investigators at both UCSB and Agility Communications, Inc. Since its founding by Prof. Coldren and two of his graduate students in 1998, Agility has been successful in commercializing the tunable transmitter technology, and it continues to pursue research, sometimes in collaboration with UCSB, to create new components for future lightwave systems.

The first two groups of reprints (*IA. Widely-Tunable Monolithic Transmitters & IB. Widely-Tunable Wavelength Converters*) give numerous examples of work that expands

the basic ‘off-set gain-region’ integration platform, combining the widely-tunable Sampled-Grating Distributed-Bragg-Reflector (SGDBR) laser with monolithically integrated amplifiers (SOAs), modulators (both EA and MZ), waveguide splitters (MMIs), and photodetectors. A representative highlight of this work is shown in Fig. 1. This depicts an SGDBR integrated with a backside detector, an SOA post-amp, and a Mach-Zehnder modulator (MZM). In this case the electrodes of the MZM are formed with ‘T-coplanar’ series-connected traveling-wave transmission lines. Also, a separate phase section is included in the MZM to establish the zero-bias set point, and a curved output guide suppresses facet reflections. As can be seen the frequency can extend to nearly 40GHz with proper choice of load resistor. Digital data up to 40 Gb/s has been transmitted with such a device along short distances of fiber.

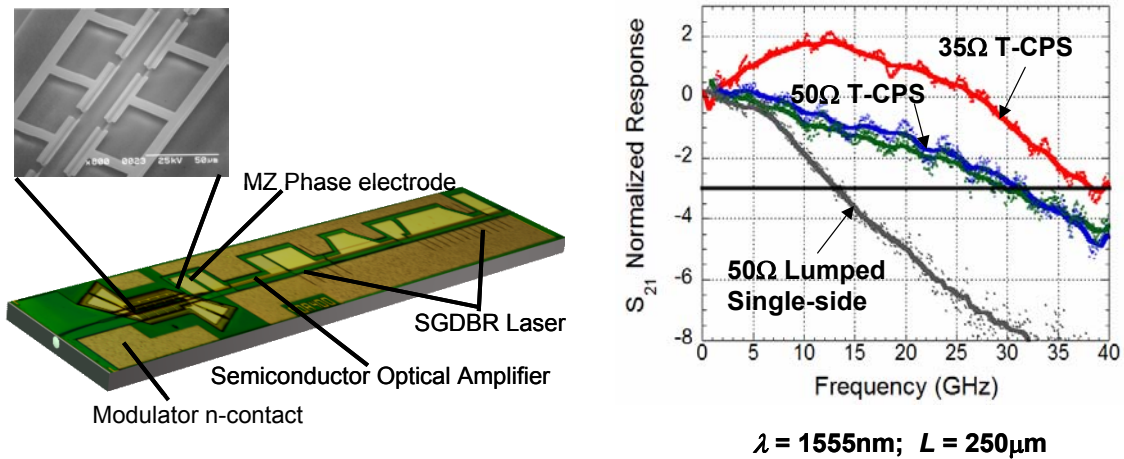
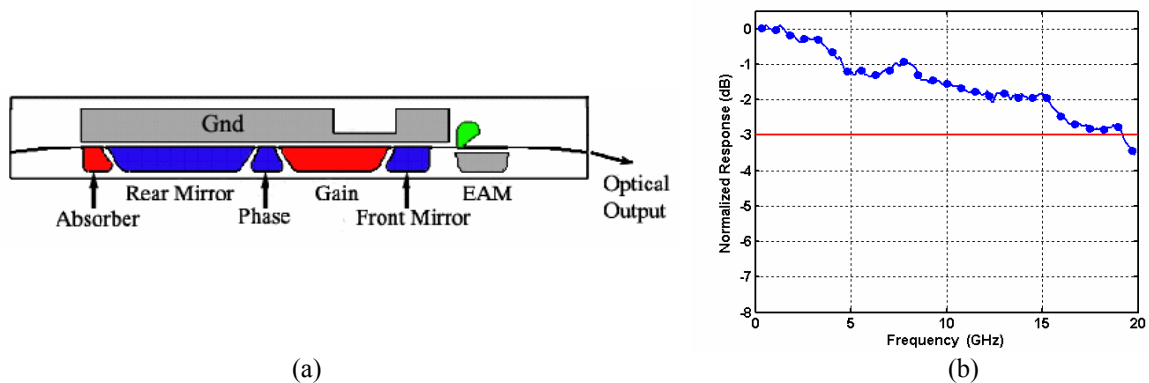


Figure 1. Integrated SGDBR-MZM schematic, inset SEM of T-CPS transmission line, and experimental small-signal modulation response.

As will be shown below, analogous SGDBR-MZMs or SGDBR-EAMs have also been incorporated into wavelength converters. In fact, the majority of our work has involved the integration of EAMs (Electro-Absorption Modulators) with the widely-tunable SGDBR. Both the standard offset-gain region technology as well as the novel quantum-well intermixing (QWI) technology covered in Section 1C has been used. Figure 2 illustrates results from a single-chip transmitter that incorporates an SGDBR with an EAM using the QWI technology platform.



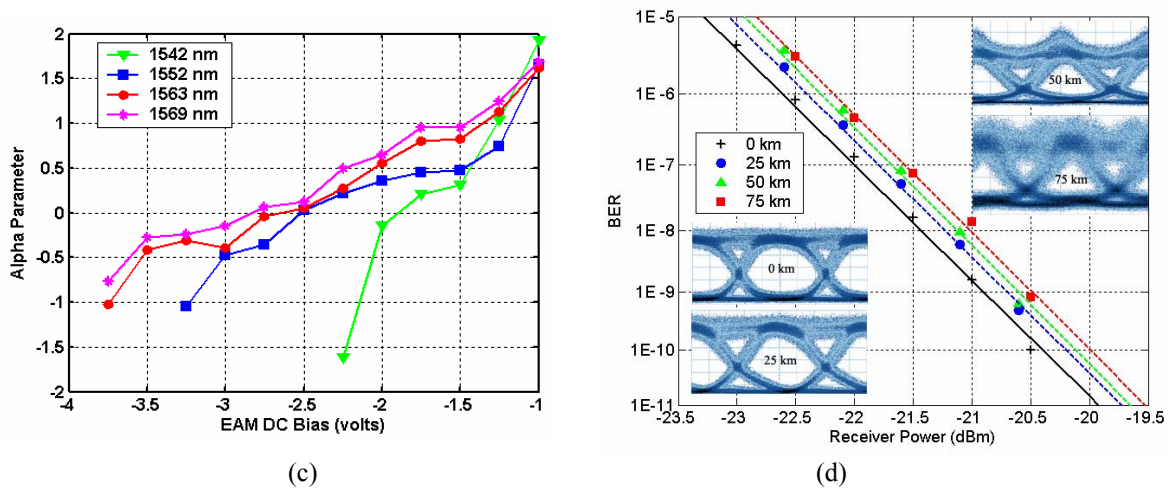


Figure 2. (a) Schematic of QWI-SGDBR-EAM; (b) small signal frequency response; (c) large-signal chirp parameter for several wavelengths across the band; and (d) Bit-error-rate vs. distance at one wavelength.

As discussed previously, the QWI process only involves a single growth and ion implant. The multiple bandgaps are provided by multiple anneals interspersed with chemical etching steps to remove the vacancy source from areas where the bandgap is to be frozen. The above result is significant, because typical EAMs that can operate over wide wavelength ranges will not provide a negative chirp parameter unless the insertion loss is quite high. In this case we found that the zero chirp point could be crossed with only 2 dB of excess loss at all wavelengths across the C-band. The transmission results confirm transmitter operation with a negative EAM chirp parameter.

For optical interconnect applications, in which signals from one IC are to be transferred to another within a computer, very efficient transmitters and receivers are required. Although VCSELs would seem to be the obvious choice for the transmitter end, and we are indeed pursuing this path, VCSELs have trouble providing the power levels and modulation bandwidths that will soon be required in these applications. Figure 3 illustrates preliminary results for a laser-EAM design formed with the same QWI technology platform as used in Fig. 2. The longer-term objective is to create these devices at 980 nm on GaAs. In fact, we have already obtained preliminary results there, but they were not published in 2004.

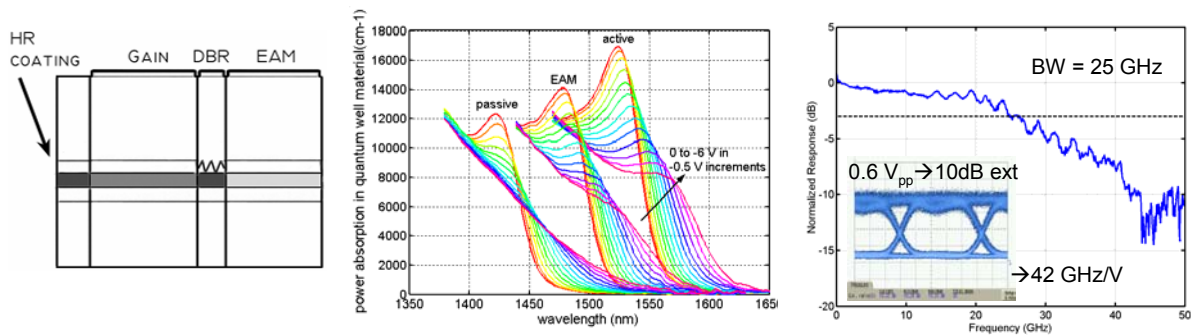


Figure 3. Short-cavity laser-EAM formed with QWI technology at 1550nm and results.

For the case of Fig. 3, the EAM could be better optimized for the wavelength being used, so very low voltage swing (0.6 V) for 10 dB extinction was observed. The high 3 dB bandwidth (~25GHz) obtained without any traveling-wave structures suggests that 40Gb/s operation should soon be possible with less than 10 mW of power dissipated in the EAM.

One of the key targets of our research is to make very efficient, high-speed widely-tunable wavelength converters. Figures 4 and 5 illustrate the use of the SGDBR-EAM and SGDBR-MZM transmitter stages within wavelength converters, which also incorporate a receiver stage consisting of an SOA-PIN integration that is interconnected to the transmitter on the same chip. These might be more appropriately referred to as transceivers on a chip, since the received signal is available electrically for monitoring. However, a key point is that only dc biases need be supplied to the chips. A related effort that is not fully documented in the 2004 reprints is the SOA-PIN receivers. These must be high-gain and high-saturation power in order to provide the voltage swings necessary to drive the modulators. Of course, developing lower voltage modulators greatly helps in this endeavor.

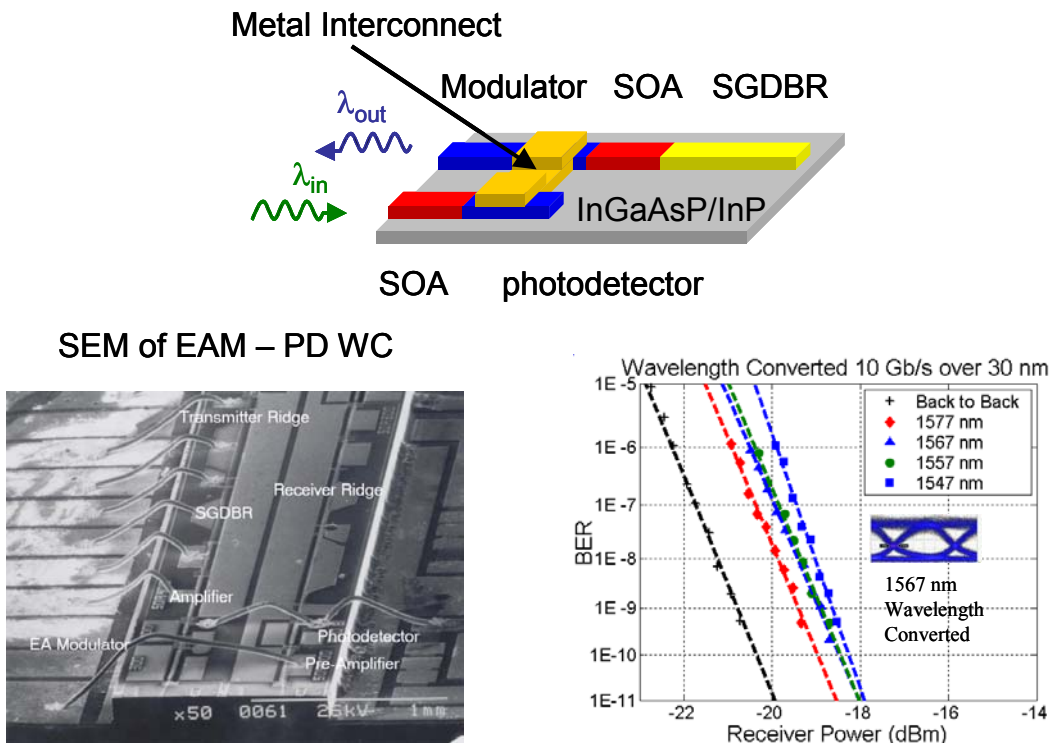


Figure 4. Widely-tunable EAM-based photocurrent driven wavelength converter and results at 10Gb/s.

Figure 5 shows analogous results for a widely-tunable MZM-based wavelength converter. In this case transmission down some length of fiber is illustrated. The fact that the initial power penalty is reduced with distance is again indicative of negative chirp on the converted output lightwave. Good performance is observed over much of the C-band.

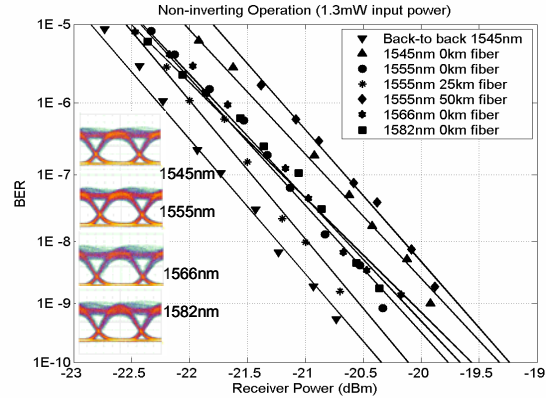
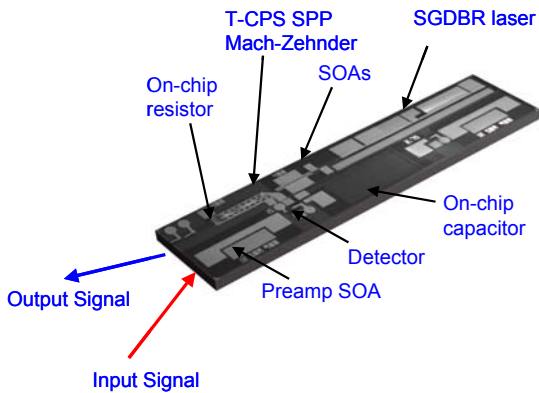


Figure 5. Widely-tunable MZM-based wavelength converter and results.

Another effort involves ‘all-optical’ wavelength converter designs, in which the input signal is coupled directly into an SOA in one arm of a Mach-Zehnder that modulates the output of the cw SGDBR. Although Prof. Coldren’s group was heavily involved in the development of this technology, it is now a main focus of Prof. Blumenthal’s group, and thus will not be detailed as much in this introduction.

Section 1D includes some of the work on bio-chemical sensors carried out in Prof. Coldren’s group. Figure 6 outlines one experiment that uses an oxidized layer beneath the optical waveguide to enhance the extension of the fields into the aqueous solution above it. This design increased the sensitivity by almost two orders of magnitude compared to prior designs with no oxide layer.

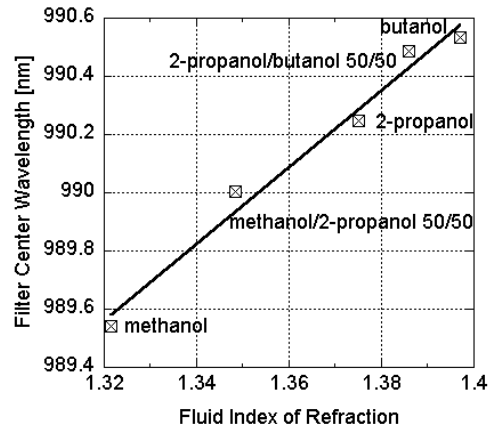
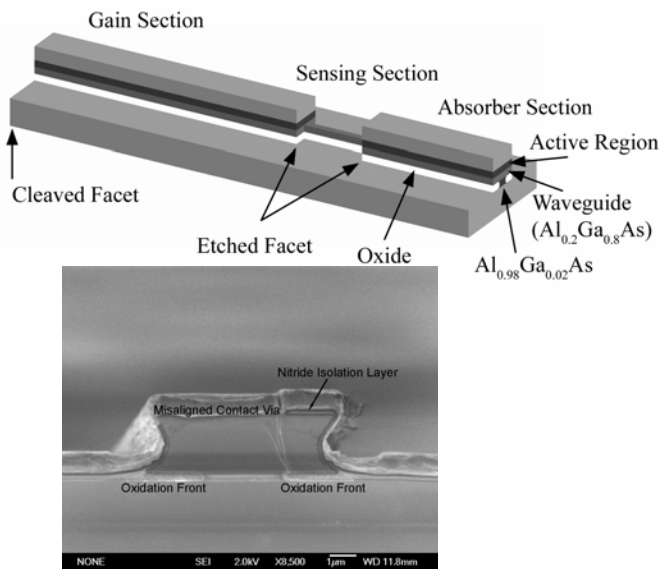


Figure 6. Schematic of GaAs-based sensor; cross-sectional SEM showing the buried oxide layer; and a plot of the etalon sensing section center wavelength vs. fluid index.

Other work in the sensor area included in this reprint book summarizes results from other chip designs. In one case, two tunable lasers are heterodyned into an on-chip detector. A region of sensor laser is exposed to the analyte, altering the cavity effective index, and thereby its output frequency. The other acts as a local oscillator to down-convert the output of the sensor laser to the VHF region after combining in the detector. This is an attractive approach because the light is generated, it senses the surface adsorbed analyte, and it is detected on a single chip. No light has to be coupled onto or off of the chip.

The materials technology area, Section 1E, contains a collection of papers focused on advancing the state-of-the-art of the materials and processes used in much of our III-V device work. As mentioned above, the quantum-well-intermixing work is covered in Section 1C, so here are included other efforts that primarily involve combining materials with different properties, either by wafer fusion or epitaxial growth.

The second general area of research has been a continued effort to make high-performance 1300 – 1550 nm InP-based Vertical-Cavity Surface-Emitting Lasers (VCSELs): **II. InP-based VCSELs**. In this calendar year only one paper has been published, although a significant effort continues. We anticipate a wealth of results to be published within the next year. The focus of the effort is to create all-epitaxial VCSELs in a single MBE growth using AlGaAsSb alloys for the mirrors and InGaAlAs MQW active regions. Both 1310 and 1550 nm VCSELs with good characteristics have already been demonstrated.

The third general area of work contained herein is in **III. Photodetectors and Receivers**. In fact, all of the reprints in this section are from the group of Prof. Joseph C. Campbell of the University of Texas at Austin. Prof. Coldren's effort has been in growing the materials used. It might also be mentioned, however, that the receivers for the wavelength converters discussed above are being developed at UCSB, and we also anticipate a number of publications on this work within the next year.

The final group of papers is **IV. Terahertz Technology**. As in the previous section the work reported here was led by other investigators, so it will not be emphasized here. Our contribution has been to create novel epitaxial structures via MBE, and these have enabled new advances in the detection of electromagnetic energy in the tera-Hertz regime.

Professor Coldren's Group



Back Row (from left):

Jon Klamkin, Chad Wang, Leif Johansson, James Raring, Milan Mašanović, Gordon Morrison, Geir Myrvaagnes, Matt Sysak, Danny Feezell, David Buell

Front Row:

Uppili Krishnamachari, Nick Stoltz, Joseph Chang, John Hutchinson, Daniel Cohen, Professor Coldren, Jon Barton, Abbey Keck, Janet Chen, Jill Nolde, Bjorn-Øve Finland, Matt Dummer, Anna Tauke-Pedretti

Kneeling: Jon Getty

Not Pictured: Erik Skogen, Dan Lofgreen, Rintaro Koda

Professor Coldren's Group

I. Visiting Researchers

J. Getty	Post Doctoral Researcher, UCSB
J. Hutchinson	Visiting Researcher, Intel Corporation
L. Johansson	Post Doctoral Researcher, UCSB
G. Morrison	Post Doctoral Researcher, UCSB
M. Reddy	Post Doctoral Researcher, UCSB, now at Univ. of Iowa
E. Skogen	Post Doctoral Researcher, UCSB, now at Sandia

II. Students

J. Barton	Ph.D. Program
D. Buell	Ph.D. Program
Y. Chang	Ph.D. Program
C. Chen	Ph.D. Program
M. Dummer	Ph.D. Program
D. Feezell	Ph.D. Program
J. Henness	M.S. Program, now at Inovati
A. Huntington	Ph.D. Program, now at Voxel
R. Koda	Ph.D. Program, now at Sony
J. Klamkin	Ph.D. Program
U. Krishnamachari	Ph.D. Program
D. Lofgreen	Ph.D. Program, now at Raytheon
M. Mašanović	Ph.D. Program
J. Nolde	Ph.D. Program
J. Raring	Ph.D. Program
N. Stoltz	Ph.D. Program
M. Sysak	Ph.D. Program
A. Tauke Pedretti	Ph.D. Program
C. Wang	Ph.D. Program

III. Staff

D. Cohen	Principal Development Engineer
M. Englander	Project Manager, OTC

Collaborators

I. Faculty

D. Blumenthal	UCSB
J. Campbell	University of Texas, Austin
S. DenBaars	UCSB
A. Gossard	UCSB
J. Harris	Stanford
A. Holmes Jr.	University of Texas, Austin
E. Hu	UCSB
D. Miller	Stanford
U. Mishra	UCSB
J. Piprek	UCSB
M. Sherwin	UCSB

II. Researchers

P. Abraham	Agility Communications, Inc.
Y.A. Akulova	Agility Communications, Inc.
T. Asano	Sony Corporation
J. Beck	DRS Infrared Technologies, LP, Dallas
C. Coldren	Agility Communications, Inc.
J. Decobert	Alcatel R&L
G.A. Fish	Agility Communications, Inc.

E. Hall	Agility Communications, Inc
M. Kinch	DRS Infrared Technologies, LP, Dallas
P. Koh	Agility Communications, Inc.
P. Kozodoy	Agility Communications, Inc.
M. Larson	Agility Communications, Inc.
H. Marchand	Agility Communications, Inc.
A. Rivlin	BioCentrix
C. Schow	Agility Communications, Inc.
N. Trenado	Post Doctoral Researcher, UCSB (Bowers)
N. Tscherptner	Alcatel R&L
J. Zheng	Intel

Collaborating Students

A. Beck	University of Texas, Austin (Campbell)
S. Carter	UCSB (Sherwin)
J. Champlain	UCSB (Mishra)
V. Ciulin	UCSB (Sherwin)
S. Demiguel	University of Texas, Austin (Campbell)
H. Demir	Stanford (Miller)
S. Estrada	UCSB (Hu)
O. Fidaner	Stanford (Harris)
X. Guo	University of Texas, Austin (Campbell)
J. Hader	UCSB (Piprek)
M. Hanson	UCSB (Gossard)
J. Hsu	University of Texas, Austin (Holmes)
Z. Hu	UCSB (Blumenthal)
J. Hurst	University of Texas, Austin (Campbell)
V. Lal	UCSB (Blumenthal)
X. Li	University of Texas, Austin (Campbell)

F. Ma	University of Texas, Austin (Campbell)
V. Sabnis	Stanford (Miller)
A. Stonas	UCSB (Hu)
J. Summers	UCSB (Blumenthal)
X. Sun	University of Texas, Austin (Campbell)
S. Wang	University of Texas, Austin (Campbell)
X. Zheng	University of Texas, Austin (Campbell)

Table of Contents:

<u>I. Photonic Integrated Circuits and Related Technology</u>	Page
<i>IA. Widely Tunable Monolithic Transmitters</i>	
L.A. Coldren, G.A. Fish, Y.A. Akulova, J.S. Barton, L.A. Johansson, and C.W. Coldren, "Tunable Semiconductor Lasers: A Tutorial," <i>Journal of Lightwave Technology</i> , 22 , (1), pp. 193-202 (January 2004) INVITED PAPER	
L.A. Coldren, "Scalable and Reliable Photonic Integrated Circuits for Scalable and Reliable WDM Networks," <i>Proc. Contemporary Photonics Technology Conference</i> , paper no. A1, Tokyo, Japan (January 2004) INVITED PAPER	
L.A. Johansson, Y.A. Akulova, G.A. Fish, and L.A. Coldren, "Sampled-Grating DBR Laser Integrated with SOA and Tandem Electroabsorption Modulator for Chirp-Control," <i>Electronics Letters</i> , 40 , pp. 70-71 (January 2004)	
L.A. Johansson, J.S. Barton, L.A. Coldren, and G.A. Fish, "High-Speed Optical Frequency Modulation in a Monolithically Integrated Widely-Tunable Laser - Phase Modulator," <i>Proc. OFC 2004</i> , paper no. FL2, Los Angeles, CA (February 22-27, 2004)	
Y.A. Akulova, G.A. Fish, P. Koh, P. Kozodoy, M. Larson, C. Schow, E. Hall, H. Marchand, P. Abraham, and L.A. Coldren, "10 Gb/s Mach-Zehnder Modulator Integrated with Widely-Tunable Sampled Grating DBR Laser," <i>Proc. OFC 2004</i> , paper no. TuE4, Los Angeles, CA (February 22-27, 2004)	
G.A. Fish, Y.A. Akulova, L.A. Johansson, and L.A. Coldren, "Wavelength Agile, Integrated Analog Optical Transmitters," <i>Proc. GOMAC Tech</i> , pp. 225-228, Monterey, CA (March 15-18, 2004)	
L.A. Coldren, and J.C. Campbell, "High-Efficiency 'Receiverless' Optical Interconnects," <i>Proc. GOMAC Tech</i> , paper no. 9.4, Monterey, CA (March 15-18, 2004) (Abstract Only)	
C.S. Wang, E.J. Skogen, G.B. Morrison, J.W. Raring, and L.A. Coldren, "Efficient, Integrated Optical Transmitters for High-Speed Optical Interconnect Applications," <i>Proc. IEEE/LEOS Workshop on Interconnections Within High Speed Digital Systems</i> , Santa Fe, NM (May 2-5, 2004)	

L.A. Johansson, Z. Hu, D.J. Blumenthal, L.A. Coldren, Y.A. Akulova, and G.A. Fish, "Monolithically Integrated 40 GHz Pulse Source with >40 nm Wavelength Tuning Range," *Proc. Integrated Photonics Research*, paper no. IPD4, San Francisco, CA (June 2004)

E.J. Skogen, C.S. Wang, J.W. Raring, G.B. Morrison, and L.A. Coldren, "Small-Footprint, High-Efficiency, Integrated Transmitters for High-Speed Optical Interconnect Applications," *Proc. Integrated Photonics Research*, paper no. IThD2, San Francisco, CA (June 2004)

C.S. Wang, E.J. Skogen, J.W. Raring, G.B. Morrison, and L.A. Coldren, "Short-Cavity 1.55 μ m DBR Lasers Integrated with High-Speed EAM Modulators," *Proc. International Semiconductor Lasers Conference*, paper no. WB1, Matsue, Japan (September 21-25, 2004)

J.M. Hutchinson, L.A. Johansson, J.T. Getty, J.A. Hennes, and L.A. Coldren, "InGaAsP/InP Gain-Levered Tunable Lasers," *Proc. International Semiconductor Lasers Conference*, paper no. SaA4, Matsue, Japan (September 21-25, 2004)

J. Klamkin, J.T. Getty, J.M. Hutchinson, L.A. Johansson, E.J. Skogen, and L.A. Coldren, "Widely-Tunable Single-Mode Bipolar Cascade SGDBR Lasers," *Proc. International Semiconductor Lasers Conference*, paper no. WC2, Matsue, Japan (September 21-25, 2004)

L.A. Johansson, J.S. Barton, and L.A. Coldren, "Analog Performance of an InP Mach-Zehnder Modulator Integrated with a Widely Tunable Laser," *Proc. Microwave Photonics 2004*, paper no. WB.2, Ogunquit, ME (October 4-6, 2004)

L.A. Johansson, Y.A. Akulova, G.A. Fish, and L.A. Coldren, "Linearized Modulator for Monolithically Integrated Photonic Devices," *Proc. Microwave Photonics 2004*, paper no. TE-3, Ogunquit, ME (October 4-6, 2004)

J.S. Barton, M. Dummer, A. Tauke-Pedretti, E.J. Skogen, J.W. Raring, M.N. Sysak, M.L. Mašanović, L.A. Johansson, and L.A. Coldren, "InP-Based Active Photonic Integrated Circuits," *Proc. LEOS 2004 Annual Meeting*, paper no. TuA5, pp. 169-170, Puerto Rico (November 7-11, 2004) INVITED PAPER

J.W. Raring, E.J. Skogen, S.P. DenBaars, and L.A. Coldren, "Demonstration of Negative Chirp Characteristics Over Wide Wavelength Range Using Monolithically Integrated SG-DBR Laser/Electroabsorption Modulator," *Electronics Letters*, **40**, (25), pp. 1599-1600 (December 2004)

IB. Widely-Tunable Wavelength Converters

J. Piprek, N. Trenado, J.M. Hutchinson, J.A. Hennes, and L.A. Coldren, "Three-Dimensional Simulation of an Integrated Wavelength Converter," *Proc. SPIE Photonics West Conference*, paper no. 5349-26, San Jose, CA (January 24-29, 2004)

J.M. Hutchinson, J.S. Barton, M.L. Mašanović, M.N. Sysak, J.A. Hennes, L.A. Johansson, D.J. Blumenthal, and L.A. Coldren, "Monolithically Integrated InP-Based Tunable Wavelength Conversion," *Proc. SPIE Photonics West Conference*, paper no. 5349-25, San Jose, CA (January 24-29, 2004)

M.L. Mašanović, V. Lal, J.A. Summers, J.S. Barton, E.J. Skogen, L.A. Coldren, and D.J. Blumenthal, "10 Gbps and 2.5 Gbps Error-Free Operation of a Monolithically Integrated Widely-Tunable All-Optical Wavelength Converter with Independent Phase Control and Output 35nm Tuning Range," *Proc. OFC 2004*, paper no. ThS5, Los Angeles, CA (February 22-27, 2004)

J.M. Hutchinson, J. Zheng, J.S. Barton, J.A. Hennes, M.L. Mašanović, M.N. Sysak, L.A. Johansson, D.J. Blumenthal, L.A. Coldren, H.V. Demir, V.A. Sabnis, O. Fidaner, J.S. Harris, and D.A.B. Miller, "Indium Phosphide-Based Optoelectronic Wavelength Conversion for High-Speed Optical Networks," *Intel Technology Journal*, **8**, (2), pp. 161-171 (May 2004)

L.A. Johansson, Y.A. Akulova, G.A. Fish, and L.A. Coldren, "Widely-Tunable, Photocurrent-Driven Wavelength Converter for Narrowband Analog Applications," *Proc. CLEO*, paper no. CWQ2, San Francisco, CA (May 2004)

J.S. Barton, M.L. Mašanović, M.N. Sysak, J.M. Hutchinson, E.J. Skogen, D.J. Blumenthal, and L.A. Coldren, "2.5Gbit/s Error Free Wavelength Conversion Using a Monolithically-Integrated Widely-Tunable SGDBR-SOA-MZ Transmitter and Integrated Photodetector," *Photonic Technology Letters*, **16**, (6), pp. 1531-1533 (June 2004)

J. Piprek, J.M. Hutchinson, J.A. Hennes, L.A. Coldren, and J. Hader, "Many-Body Effects on InP-Based Optoelectronic Wavelength Converters for WDM Applications," *Proc. 4th Intl. Conf. Numerical Simulation of Optoelectronic Devices*, paper no. ThP2, Santa Barbara, CA (August 2004)

M.N. Sysak, J.S. Barton, L.A. Johansson, J.W. Raring, E.J. Skogen, M.L. Mašanović, D.J. Blumenthal, and L.A. Coldren, "Single-Chip Wavelength Conversion Using a Photocurrent-Driven EAM Integrated With a Widely Tunable Sampled-Grating DBR Laser," *Photonic Technology Letters*, **16**, (9), pp. 2093-2095 (September 2004)

M.L. Mašanović, V. Lal, J.A. Summers, J.S. Barton, E.J. Skogen, L.A. Coldren, and D.J. Blumenthal, "Design and Performance of a Monolithically Integrated Widely Tunable All-Optical Wavelength Converter with Independent Phase Control," *Photonic Technology Letters*, **16**, (10), pp. 2299-2301 (October 2004)

J. Piprek, J.M. Hutchinson, J.A. Henness, M.L. Mašanović, and L.A. Coldren, "Saturation Analysis of a Monolithic Wavelength Converter," *Proc. SPIE: Physics and Applications of Optoelectronic Devices*, **5594**, pp. 102-109, Philadelphia, PA (October 25, 2004)

J. Klamkin, L.A. Johansson, J.T. Getty, J.M. Hutchinson, E.J. Skogen, and L.A. Coldren, "Photocurrent Driven Widely-Tunable Wavelength Converter Based on a Directly Modulated Bipolar Cascade SGDBR Laser," *Proc. LEOS 2004 Annual Meeting*, paper no. MK4, pp. 98-99, Puerto Rico (November 7-11, 2004)

IC. Quantum-Well Intermixing Technology

J.W. Raring, E.J. Skogen, L.A. Johansson, M.N. Sysak, and L.A. Coldren, "Low Dispersion Penalty at 10 Gb/s, Over 75km, Using a Quantum-Well-Intermixed Electroabsorption-Modulator/Widely-Tunable Laser Transmitter," *Proc. OFC 2004*, paper no. PDP13, Los Angeles, CA (February 22-27, 2004)

J.W. Raring, E.J. Skogen, L.A. Johansson, and L.A. Coldren, "Enhanced Frequency Response in Buried Ridge Quantum Well Intermixed SGDBR Laser Modulators," *Proc. CLEO*, paper no. CWC1, San Francisco, CA (May 2004)

J.W. Raring, E.J. Skogen, L.A. Johansson, M.N. Sysak, J.S. Barton, M.L. Masanovic, and L.A. Coldren, "Quantum Well Intermixing for Monolithic Integration: A Demonstration of Novel Widely-Tunable 10Gb/s Transmitters and Wavelength Converters," *Proc. Integrated Photonics Research*, paper no. IWC3, San Francisco, CA (June 2004)

J.W. Raring, E.J. Skogen, L.A. Johansson, M.N. Sysak, J.S. Barton, M.L. Mašanović, and L.A. Coldren, "Demonstration of Widely-Tunable Single-Chip 10 Gb/s Laser-Modulators Using Multiple-Bandgap InGaAsP Quantum-Well Intermixing," *Photonic Technology Letters*, **16**, (7), pp. 1613-1615 (July 2004)

J.T. Getty, E.J. Skogen, and L.A. Coldren, "Improved Ridge Lasers Utilizing Laterally-Intermixed Active Regions," *LEOS 2004 Annual Meeting*, paper no. TuW6, Puerto Rico (November 7-11, 2004)

ID. Sensors

D.A. Cohen, C.S. Wang, J.A. Nolde, D.D. Lofgreen, and L.A. Coldren, "A Monolithic Evanescent Field Spore Detector," *Proc. Integrated Photonics Research*, paper no. IThB3, San Francisco, CA (June 2004).

C.S. Wang, J.A. Nolde, D.A. Cohen, D.D. Lofgreen, and L.A. Coldren, "A Monolithic Diode Laser Chemical Sensor with a Quasi-Symmetrical Sensing Waveguide for Improved Sensitivity," *Applied Physics Letters*, **85**, (2), pp. 320-322 (July 2004)

D.A. Cohen, J.A. Nolde, C.S. Wang, E.J. Skogen, A. Rivlin, and L.A. Coldren, "Biophotonic Integrated Circuits," *Proc. SPIE Physics and Applications of Optoelectronic Devices*, paper no. 5594-12, Philadelphia, PA (October 25, 2004)

IE. Materials Technology

S. Estrada, J. Champlain, C.S. Wang, A. Stonas, L.A. Coldren, S.P. DenBaars, U. Mishra, and E. Hu, "Wafer-Fused n-AlGaAs/p-GaAs/n-GaN Heterojunction Bipolar Transistor with uid-GaAs Base-Collector Setback," *Proc. Materials Research Society Symposium*, **798**, paper no. Y10.2 (December 2003 – mistakenly omitted from 2003 reprint)

J.W. Raring, E.J. Skogen, L.A. Coldren, and S.P. DenBaars, "A Study of Regrowth Interface and Material Quality for a Novel InP Based Architecture," *Proc. 12th Intl. Conf. on Metal Organic Vapor Phase Epitaxy (ICMOVPE)*, Maui, HI (May 30-June 4, 2004)

E.J. Skogen, J.S. Barton, L.A. Coldren, and S.P. DenBaars, "High-Quality Grating Regrowth Interface in the InP/InGaAsP Material System Using TBA and TBP," *Proc. 12th Intl. Conf. on Metal Organic Vapor Phase Epitaxy (ICMOVPE)*, Maui, HI (May 30-June 4, 2004)

J.W. Raring, E.J. Skogen, S.P. DenBaars, and L.A. Coldren, "A Study of Regrowth Interface and Material Quality for a Novel InP-Based Architecture," *Journal of Crystal Growth*, **273**, (1-2), pp. 26-37 (December 2004)

E.J. Skogen, J.S. Barton, J.W. Raring, L.A. Coldren, and S.P. DenBaars, "High Contrast InP/InGaAsP Grating MOCVD Regrowth Using TBA and TBP," *Journal of Crystal Growth*, **272**, pp. 564-569 (December 2004)

II. InP-Based Vertical Cavity Laser

M.H.M. Reddy, T. Asano, D. Feezell, D.A. Buell, A.S. Huntington, R. Koda, and L.A. Coldren, "Selectively Etched Tunnel Junction for Lateral Current and Optical Confinement in InP-Based Vertical Cavity Lasers," *Journal of Electronic Materials*, **33**, (2), pp. 118-122 (February 2004)

III. Photodetectors and Receivers

J.C. Campbell, S. Demiguel, F. Ma, A. Beck, X. Guo, S. Wang, X.G. Zheng, X. Li, J.D. Beck, M.A. Kinch, A.S. Huntington, L.A. Coldren, J. Decobert, and N. Tschertner, "Recent Advances in Avalanche Photodiodes," *IEEE/Journal of Special Topics in Quantum Electronics*, **10**, (4), pp. 777-787 (July-Aug 2004)

A.S. Huntington, C.S. Wang, X.G. Zheng, J.C. Campbell, and L.A. Coldren, "Relationship of Growth Mode to Surface Morphology and Dark Current in InAlAs/InGaAs Avalanche Photodiodes Grown by MBE on InP," *Journal of Crystal Growth*, **267**,(3-4), pp. 458-465 (July 2004)

X.G. Zheng, J. Hsu, J.B. Hurst, X. Li, S. Wang, X. Sun, A.L. Holmes, Jr., J.C. Campbell, A.S. Huntington, and L.A. Coldren, "Long-Wavelength In_{0.53}Ga_{0.47}As-In_{0.52}Al_{0.48}As Large-Area Avalanche Photodiodes and Arrays," *IEEE/Journal of Quantum Electronics*, **40**, (8), pp. 1068-1073 (August 2004)

IV. Terahertz Technology

S.G. Carter, V. Ciulin, M.S. Sherwin, M. Hanson, A.S. Huntington, L.A. Coldren, and A.C. Gossard, "Terahertz Electro-Optic Wavelength Conversion in GaAs Quantum Wells: Improved Efficiency and Room-Temperature Operation," *Applied Physics Letters*, **84**, (6), pp. 840 (February 2004)

S.G. Carter, V. Ciulin, M.S. Sherwin, C.S. Wang, A.S. Huntington, and L.A. Coldren, "Terahertz-Optical Mixing in *n*-Doped GaAs Quantum Wells," *Proc. CLEO*, paper no. IMD1, San Francisco, CA (May 2004)

V. Ciulin, S.G. Carter, M.S. Sherwin, A.S. Huntington, and L.A. Coldren, "Terahertz Optical Mixing in Biased GaAs Single Quantum Wells," *Physical Review B*, **70**, article no. 115312 (September 2004)

I. Photonic Integrated Circuits and Related Technology

A. Widely Tunable Monolithic Transmitters

Tunable Semiconductor Lasers: A Tutorial

Larry A. Coldren, *Fellow, IEEE*, G. A. Fish, Y. Akulova, J. S. Barton, L. Johansson, and C. W. Coldren, *Member, IEEE*

Tutorial Paper

Abstract—Tunable semiconductor lasers have been listed in numerous critical technology lists for future optical communication and sensing systems. This paper summarizes a tutorial that was given at OFC '03. It includes some discussion of why tunable lasers might be beneficial, an outline of basic tuning mechanisms, some examples of tunable lasers that have been commercialized, and a discussion of control techniques. More extensive data is given for the widely-tunable sampled-grating distributed-Bragg-reflector (SGDBR) type of laser, including data for such lasers integrated monolithically with modulators to form complete transmitter front ends. A summary of reliability data for the SGDBR laser is also given. It is concluded that tunable lasers can reduce operational costs, that full-band tunability is desirable for many applications, that monolithic integration offers the most potential for reducing size, weight, power and cost, and that sufficient reliability for system insertion has been demonstrated.

Index Terms—Photonic integrated circuits, semiconductor lasers, tunable lasers.

I. INTRODUCTION

TUNABLE lasers have been of interest for some time [1]. Applications range from sources for fiber optic telecommunication systems to broadband sensors. About three or four years ago, the telecom application began to drive significant investments into this field to support the perceived need for dynamic networks and wavelength reconfigurability in wavelength division multiplexing (WDM) systems. Vast reductions in operational costs were predicted for such flexible fiber-optic networks that were thought to be necessary for the rapidly expanding demand for bandwidth. However, as many new companies joined this effort, there was a large overbuild of capacity, and the need for the new networks vanished, or more accurately, was pushed back to at least the present time. The good news for the industry is that the demand for bandwidth continues to nearly double each year.

Although the potential to reduce operational costs with more dynamical networks still exists, the delay in significant network expansion has led to a reappraisal of the value proposition for tunable lasers. Today, the main value for telecom networks appears to be in the areas of inventory reduction, both in the manufacture and operation of WDM systems. With fixed frequency

distributed-feedback (DFB) lasers, dozens of different wavelength codes must be manufactured and inventoried, and perhaps more importantly, dozens of different wavelength-specific line cards must be manufactured and inventoried. Since the cost of line cards is measured in multiples of \$10 k, this can be a significant overhead. Thus, even for this less glamorous application, the savings are finite, but as a result, today's tunable laser solutions are compared to fixed-frequency DFBs for both cost and performance.

Bearing all of this in mind, it is generally agreed that if tunable lasers with the same performance specs as DFBs were available, most systems companies would select them over DFBs for a small price premium. As we will show in this report, some tunable embodiments appear to have reached specification parity with DFBs, so the situation may indeed be favorable for tunables in future WDM networks. By the time one considers the price of a line card, the increased cost of incorporating the tunable laser can be quite small, relatively speaking, and one can gain the functionality of a "universal" line card, which can be programmed to function at any wavelength over the tuning range of the laser [2]. Of course, this is a strong argument for full-band tunability in the laser, because only one part would then be necessary for any slot. Finally, there is still the compelling argument that the line card can be re-provisioned at some later point in time, should the network architecture evolve to accommodate this, and again, full-band tunability would be desired.

The situation in the sensor area is perhaps even more attractive for tunable lasers. Here many sensor types rely upon the ability to sweep the laser frequency over a wide range for their basic functionality, so they are essential. This, perhaps, is a subject for a different audience than those attending the Optical Fiber Communication conference, the audience for which this tutorial was designed.

II. WHY TUNABLE LASERS?

Although we have already stated that the current justification for wanting tunable laser solutions is in reduced manufacturing and operational costs deriving from inventory reduction, there are still a number of potential applications in the telecom area that might be important in the near future [3]. The first to be mentioned is in reconfigurable optical-add-drop multiplexers (ROADMs). As illustrated in Fig. 1 these allow single (or multiple) optical channels to be removed and replaced on a fiber without de-multiplexing, regenerating, and re-multiplexing the entire array of wavelengths contained in the fiber. In applications where this functionality is desired, the ROADM can vastly reduce the cost of dropping and/or adding a relatively small amount of information from or to the fiber.

Manuscript received July 2, 2003; revised October 10, 2003.

L. A. Coldren is with the Departments of Materials and Electrical & Computer Engineering, University California, Santa Barbara, CA 93106 USA, and is also with the Agility Communications, Incorporated, Santa Barbara, CA 93117 USA.

G. A. Fish, Y. Akulova, and C. W. Coldren are with the Agility Communications, Incorporated, Santa Barbara, CA 93117 USA.

J. S. Barton and L. Johansson are with the Departments of Materials and Electrical & Computer Engineering, University California, Santa Barbara, CA 93106 USA.

Digital Object Identifier 10.1109/JLT.2003.822207

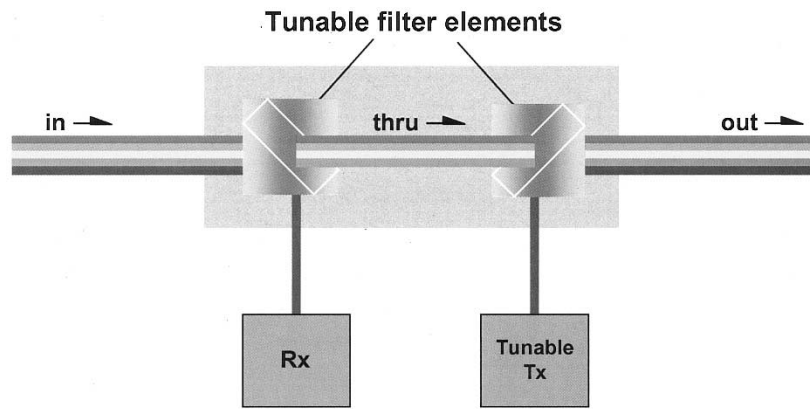


Fig. 1. Reconfigurable optical add/drop port. A tunable filter selectively removes (or adds) a single (or several) optical WDM channel from the fiber. A tunable transmitter is needed to insert any desired channel at the add port.

Tunable lasers are also natural complementary components in optical switches of various kinds. Here they generally are used for the function of wavelength switching or “wavelength conversion,” in which an incoming signal on one wavelength is re-modulated onto another wavelength on the output [4]. This can be accomplished in numerous ways, the most straightforward of which is to incorporate a tunable laser within a line card or transponder, so that the output can be set to any wavelength value. These “optical-electronic-optical” (OEO) components include 3R regeneration to reconstitute the signal to its original form. One can also make “all optical” wavelength converters that use the incoming signal on one wavelength to drive a modulator that applies the signal directly to a second selectable output wavelength generated by a tunable laser. Recently, this function has been demonstrated with a single monolithic chip [5], [6]. However, in these “all-optical” approaches 3R or even 2R regeneration of the signal is generally not provided, so that these elements can only work with relatively clean data, and they can only be cascaded a few times before a 3R regeneration is necessary.

Fig. 2 shows an all-optical space switch that uses wavelength converters at the input and a passive optical router switching fabric to provide space switching. In this case the input signal is placed on the wavelength that the passive “lambda router” will route to the desired output port. If the signal is to be re-multiplexed, it would then have to be again converted to the desired wavelength to enter the optical multiplexer. This sort of switching architecture is also currently being investigated by several groups for all-optical packet switching [7], [8]. In this case, the tunable lasers in the front-end wavelength converters (shown as line cards with tunable lasers in Fig. 2) must switch wavelengths very fast—typically in the nanosecond range. Such a criterion will favor the tunable laser types that are controlled electronically versus the ones that have thermal or mechanical tuning elements.

Again, the sensor application area has already been mentioned, so it shall not be discussed further here.

III. BASIC TUNING MECHANISMS

Fig. 3 gives a schematic of a generic tunable laser together with the relative spectra of the necessary filter and gain elements as well as the location of the various cavity modes that all must be properly aligned and translated to create a tunable, single-frequency laser. Of course, in most practical embodiments, the

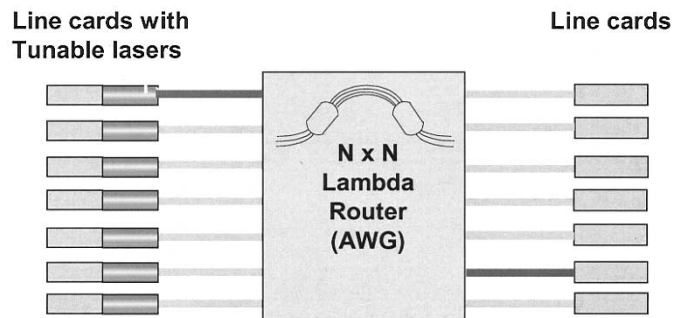


Fig. 2. Transparent optical space switch composed of a wavelength converter array and a passive router such as an arrayed-waveguide-router (AWG). Line cards with tunable lasers can more generally be replaced by wavelength converters.

filter, mirror and phase-shifting elements are combined in some way to create a unique physical structure for the different kinds of tunable lasers. Fig. 3 can be used to see how a tunable semiconductor laser evolves from the most basic “Fabry-Perot” laser, which has just the gain and the two simple mirror elements, to a “single-frequency” laser, which adds the mode-selection filter, to a “tunable single-frequency” laser, which adds possible adjustment of the mirror position and the center frequency of the mode-selection filter, as well as adding a new adjustable cavity phase element. For more analytical discussion, the reader is referred to [9], [10].

The most common Fabry-Perot laser is composed of a uniform cleaved semiconductor chip that is structured to provide gain for a guided optical mode with the cleaves functioning as the mirrors. The most common single-frequency laser is probably the DFB laser, illustrated in Fig. 4(a), in which an index grating is formed near the optical waveguide to provide a continuous reflection that gives both the mirror functionality as well as the mode selection filter. The vertical-cavity surface-emitting laser (VCSEL) as illustrated in Fig. 4(b), is also a single-frequency laser, but in this case the cavity is vertical and the grating mirrors sandwich the gain region. Although the distributed-Bragg-reflector (DBR) mirrors are frequency selective, the primary mode selection is done by the finite width of the gain spectrum in this case, because both the mirror spectrum and the mode spacing are made large by the short cavity length—a somewhat different case than that suggested in Fig. 3.

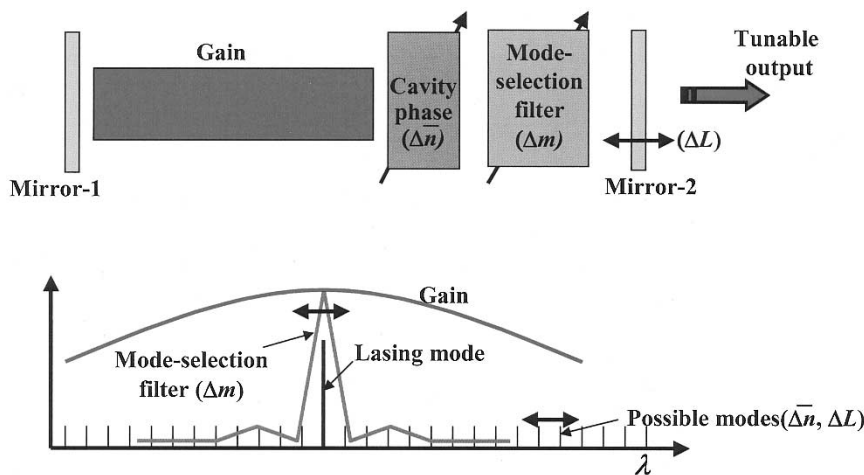


Fig. 3. Schematic of generic tunable laser together with relationship of the spectra of each element.

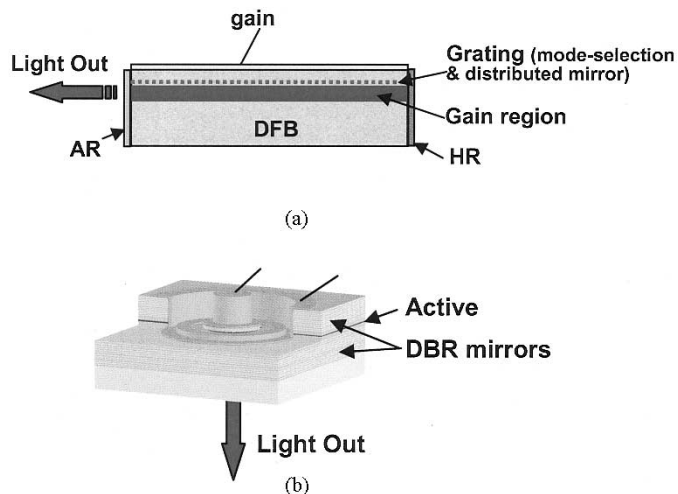


Fig. 4. Examples of single-frequency lasers (not tunable): (a) DFB laser and (b) VCSEL.

Equation (1) gives the relationship between the lasing wavelength, λ , and the cavity mode number, m , effective index of refraction seen by the cavity mode, \bar{n} , and the effective cavity length, L . Quite obviously, if one changes m , \bar{n} , or L , the wavelength must also change. The relative change in wavelength derived from (1) is given in (2). As indicated the relative wavelength change is directly proportional to the relative change in either the length, index or mode number

$$\begin{aligned}
 & \text{Mode number} \quad \text{Effective cavity length} \\
 & \quad \quad \quad \searrow \quad \quad \quad \swarrow \\
 & \quad \quad \quad \frac{m\lambda}{2} = \bar{n}L \\
 & \quad \quad \quad \swarrow \quad \quad \quad \searrow \\
 & \text{Wavelength} \quad \quad \quad \text{Effective index} \\
 & \quad \quad \quad \quad \quad \quad \downarrow \\
 & \quad \quad \quad \quad \quad \quad \text{Tuned by mode-selection filter} \\
 & \quad \quad \quad \quad \quad \quad \text{(via index or grating angle)} \\
 & \frac{\Delta\lambda}{\lambda} = \frac{\Delta\bar{n}}{\bar{n}} + \frac{\Delta L}{L} - \frac{\Delta m}{m} \\
 & \quad \quad \quad \swarrow \quad \quad \quad \downarrow \quad \quad \quad \searrow \\
 & \text{Tuned by net cavity} \quad \quad \quad \text{Tuned by physical} \\
 & \text{index change} \quad \quad \quad \text{length change}
 \end{aligned}
 \tag{1}$$

IV. EXAMPLES OF TUNABLE SEMICONDUCTOR LASERS

Fig. 5 shows several different types of tunable single-frequency lasers that have been commercialized. (Since tunable lasers need to be single frequency to be of much use, we will now drop this qualifier.) In the figure we have only included the widely-tunable varieties that are capable of full *C* or *L*-band coverage from a single device.

The first example shows a selectable array of DFB lasers that are combined in a multimode interference coupler. The DFBs are excited one at a time and each is manufactured with a slightly different grating pitch to offset their output wavelengths by about 3 or 4 nm. The chip is then temperature tuned by some 30–40 C to access the wavelengths between the discrete values of the array elements. With *N*-DFB elements, then, a wavelength range of up to about 4*N* nm can be accessed, or with 8–10 elements the entire *C*-band can be accessed. The schematic included in Fig. 5(a) is from NEC[11]; however, similar work is also being carried out at Fujitsu [12] and other mostly Japanese labs. Santur Corporation uses a similar concept, but with an external micro-electromechanical (MEMS) mirror to select which element is coupled to the output fiber [13], thus eliminating the 1/*N* combiner loss, but at the expense of one more element to package and control. In all cases, this approach must deal with the requirement of having a number of closely spaced DFBs all working to tight specifications. The losses in combining, inherent in most varieties, are also significant, and the need to temperature tune over a fairly large tuning range leads to relatively high power dissipation for this approach.

Fig. 5(b) is an example of an external-cavity laser. In this case a “gain block” is coupled to external mode-selection filtering and tuning elements via bulk optical elements. The cavity phase adjustment, necessary to properly align the mode with the filter peak and the desired ITU grid wavelength, can be included in one of several places—e.g., on the gain block or by fine tuning the mirror position. In most external-cavity approaches the mode selection filter is a diffraction grating that can also double as a mirror. The so-called Littman-Metcalf cavity arrangement is illustrated. In this case, a retro-reflecting mirror is translated as it is rotated. This combined motion changes the ef-

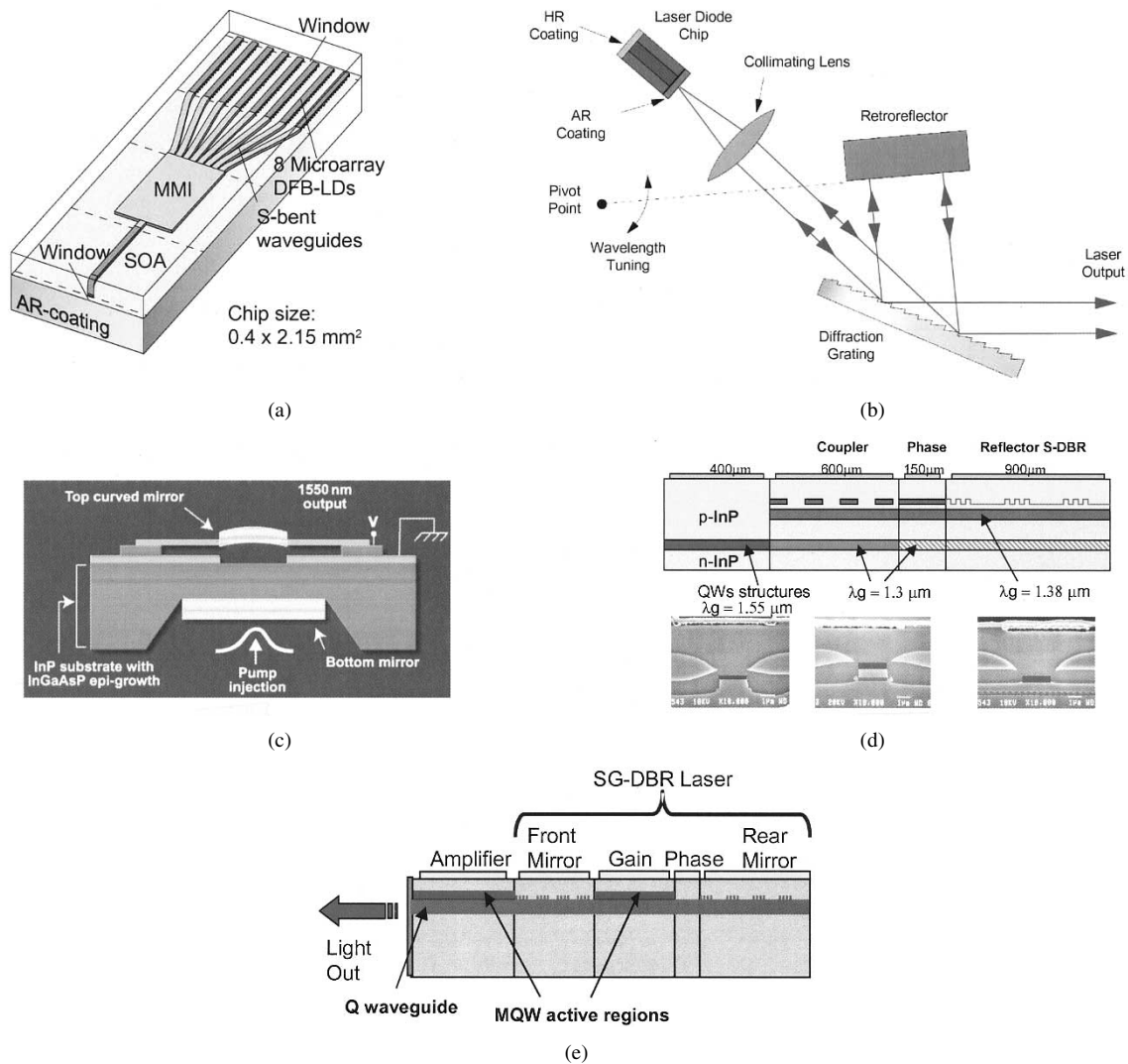


Fig. 5. Examples of widely-tunable laser types: (a) selectable DFB array, (b) external-cavity, (c) MEMs/VCSEL, (d) grating-coupled sampled-reflector (GCSR), and (e) sampled-grating DBR (SGDBR) with integrated SOA.

fective cavity length in proportion to the change in center wavelength of the mode-selection filter to track the movement of a single cavity mode. The Littman-Metcalf geometry provides continuous tuning over some range, but due to cavity dispersion, one in general still needs to correct the cavity phase at each ITU channel. This approach has been used by Iolon [14] and New Focus [15] in their products. Other companies tend to just rotate the mirror and let the mode selection filter scan across the modes. This is most common in scientific instruments, where the cavities are quite long and the mode spacing very small. Intel also has reported some research [16] in which the external cavity contains two temperature-tuned etalons with slightly different resonance frequencies, which act in combination to create a widely-tunable filter. A standard external mirror completes the cavity. All of the external cavity approaches appear to provide useable specs for telecommunications, although at this writing we are not aware of any that has completed the full Telcordia qualification exercise. An obvious concern with these structures is their manufacturability and reliability, given the need for assembling numerous micro-optical parts and holding them in precise alignment.

Fig. 5(c) shows a tunable VCSEL that is created by mounting one mirror on a flexible arm and using an electrostatic force to translate it up and down. This MEMs approach has been employed by Coretek [17]—later acquired by Nortel—[as shown in Fig. 5(c)] and Bandwidth 9 [18]. In Coretek's case external optical pumping was used, and in Bandwidth 9's case electrical pumping was employed. Both efforts appear to have been discontinued. The Coretek approach used dielectric mirrors for wide reflection bandwidth. Thus, it was able to show full C-band operation; the Bandwidth 9 device had a somewhat smaller tuning range. The use of optical pumping also provides for more power output, although advertised products from Nortel did include an external amplifier to boost the fiber-coupled power to the 20 mW range. A primary appeal for the VCSEL approaches is the wafer-scale manufacturing platform that it appears to provide. The hope here was to make tunable devices for nearly the same cost as the 850 nm VCSELs used in Gigabit Ethernet. However, at 1550 nm VCSEL construction is more difficult, and limited output power together with wide optical linewidth appear to be serious limitations with the VCSEL approaches at 1550 nm.

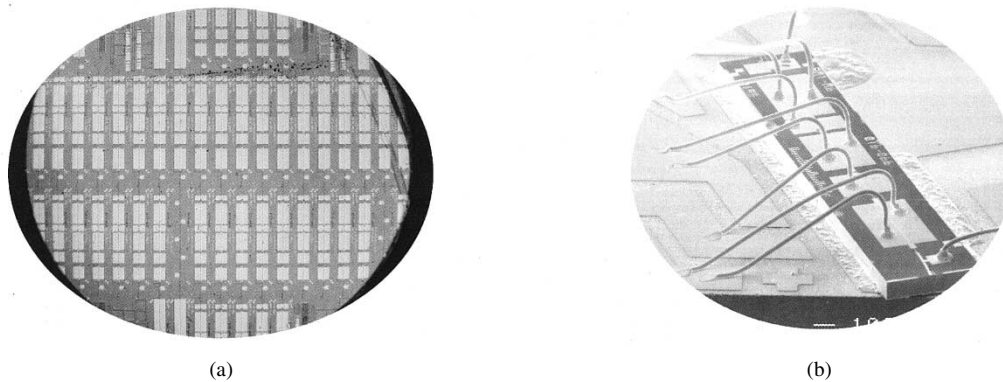


Fig. 6. Photo of wafer and SEM of mounted single-chip transmitter.

Fig. 5(d) and (e) show monolithic widely-tunable semiconductor laser approaches that employ electronic tuning of the index in a single cavity to provide for full *C*- or *L*-band wavelength coverage. Both are variations on older DBR laser approaches [19]–[21], but both employ concepts to tune the relative wavelength by up to an order of magnitude more than the index of any section can be tuned. In the case of Fig. 5(d), the so-called grating-coupled sampled-reflector (GCSR) laser [22], [23], this is accomplished by using a property of a grating-assisted co-directional coupler which has a tuning proportional to the index tuning relative to the *difference* in index between two coupled waveguides, $\Delta n/(n_1 - n_2)$, rather than $\Delta n/n_1$ as in most other filters. However, because the filter is also broad, a back multiple-order sampled-grating reflector is required for good mode selectivity in this case. In the SGDBR of Fig. 5(e) [24], [25], the wider tuning range filter is provided by the product of the two differently spaced and independently tuned reflection combs of the SGDBRs at each end of the cavity. This product, $R_1 R_2$, is what appears in the laser cavity loss factors, and the variation in the beating effect between the two different mirror reflection combs is sometimes referred to as the vernier effect. In this case the net mode selection filter wavelength tuning is that of a single grating, $\Delta n/n$, multiplied by $\delta\lambda/\Delta\lambda$, the difference in spacing between the mirror reflection peaks of the two mirrors, $\delta\lambda$, divided by the mean mirror peak spacing, $\Delta\lambda$. Similar physics is involved in the superstructure-grating DBR developed at NTT [26]. In both cases, good side-mode suppression has been demonstrated, and tuning of over 40 nm is easily accomplished, but due to grating losses resulting from current injection for tuning, the differential efficiency and chip output powers can be somewhat limited. In the case of the SGDBR, this is easily addressed by the incorporation of another gain section on the output side of the output mirror, and fiber-coupled powers of up to 40 mW have been reported. In fact, this is the embodiment illustrated in Fig. 5(e). Incorporating such a semiconductor-optical-amplifier (SOA) is not as easy for the GCSR, so fiber-coupled powers of typically less than 10 mW result. The integrated SOA also has other benefits for the SGDBR as will be discussed in the following.

V. CHARACTERISTICS OF SGDBR LASERS AND SINGLE-CHIP TRANSMITTERS

Work at UCSB and Agility Communications has aimed to develop widely tunable lasers and transmitters with monolithically

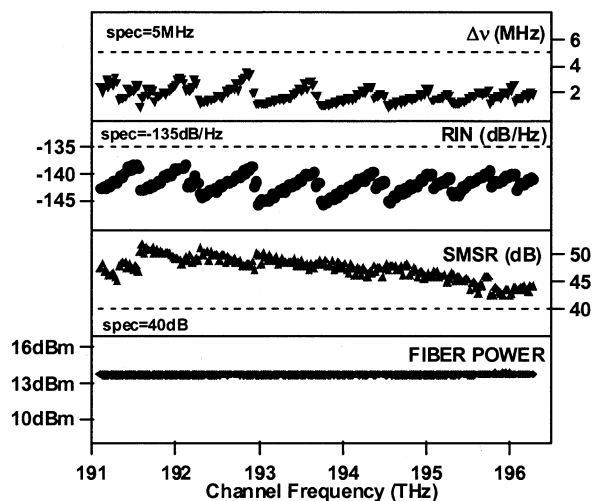


Fig. 7. CW characteristics of SGDBR-SOA device for 100 channels—calibrated for 20 mW of fiber power. The linewidth, $\Delta\nu$, relative intensity noise, RIN, and side-mode suppression ratio, SMSR shown for all *C*-band channels.

integrated modulators. A low-cost “platform technology” that is capable of providing a wide variety of photonic ICs (PICs) without changing the basic manufacturing process has been developed. Fig. 6 shows a photograph of a 2” InP wafer with arrays of seven-section photonic IC transmitters, each consisting of a full-band-tunable four-section SGDBR laser integrated with a monitoring detector, optical amplifier, and modulator. The SEM inset shows one of these mounted on a carrier ready to be inserted into a package. It is important to note that the wafer layer structure and processing procedure used is identical to that developed for the SGDBR laser alone. This same structure and processing procedure is also used in the more complex laser PICs to be discussed below. Note also a key advantage of photonic integration—only one optical coupling to fiber is required, as would be necessary for a simple DFB laser alone.

The basic SGDBR-SOA shown in Fig. 5(e) above as well as the integrated SGDBR-SOA-EAM transmitter illustrated in Fig. 6 have been productized and Telcordia qualified for telecom applications [27]. In Fig. 7 we give a summary of the characteristics of a 20 mW cw product similar to Fig. 5(e) at each of 100 channels spaced by 50 GHz across the *C*-band. A common quaternary waveguide extends throughout the entire device and offset quantum-well gain layers are included at the laser gain and SOA sections.

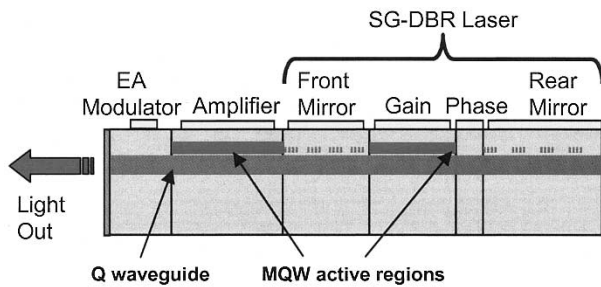


Fig. 8. Single-chip widely-tunable transmitter schematic showing a SGDBR laser integrated with an SOA and EAM.

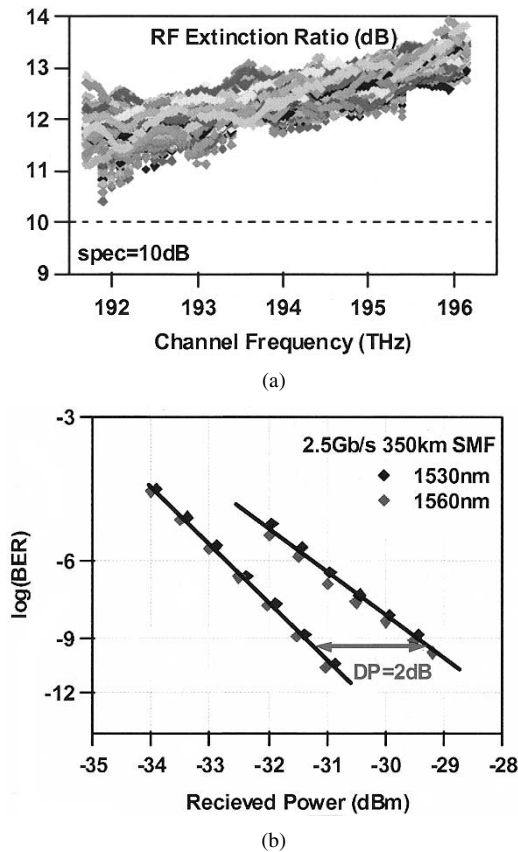


Fig. 9. (a) RF extinction ratio for 100 superimposed SGDBR/EAM transmitters across the C-band. (b) Bit-error-rate results after transmission through 350 km of standard fiber at 2.5 Gb/s.

Fig. 8 shows a schematic cross section of an InP-based transmitter chip [28] as included in the photos of Fig. 6. The modulator bias is varied across the 40 nm tuning range to enable efficient modulation and good extinction across this entire range.

Fig. 9(a) shows superimposed rf-extinction ratio versus wavelength characteristics for 100 transmitter chips across the C-band, and Fig. 9(b) shows the bit-error rate after transmission through 350 km of standard single-mode fiber for two different wavelengths. The data is applied directly to the EAM of the chip. The average modulated output power is about 3 dBm in this case. Error-free operation was observed.

The transmitter illustrated in Figs. 6 and 8 and characterized in Fig. 9 provides good results at 2.5 Gb/s for distances up to 350 km. However, for longer distances and/or higher bit

rates, some sort of chirp control is necessary. Thus, work at both Agility [6], [29] and UCSB [30] has explored replacing the EAM with a Mach-Zehnder modulator (MZM) as shown in Fig. 10. Such modulators have been used widely for long-haul applications, and they allow negative chirp with only one drive signal, although dual drive of both arms of the MZM are necessary for truly programmable chirp. In the past, researchers have had difficulties in integrating such MZM's directly with lasers because of reflections. However, the UCSB-Agility effort appears to have solved these difficulties. By monolithically integrating the MZM a much smaller footprint and low power dissipation is possible as compared to hybrid packaged or fiber-coupled devices. In addition, the chirp can be tailored for each channel across the wavelength band by adjusting the biases to the two legs of the MZM. Chirp values from +1 to -1 are readily available. Error free transmission over 80 km of standard fiber was demonstrated for all channels at 10 Gb/s using a negative chirp configuration.

VI. RELIABILITY OF THE SGDBR LASER

Fig. 11 summarizes some of the reliability data taken on the 10 mW cw product by Agility [31]. Both the integrated EAM transmitter and the 10 mW cw version have undergone complete Telcordia qualification. Because of the InP single-chip architecture, these PICs can be qualified in much the same way as simple laser chips. Such is not the case with other types of widely-tunable transmitters in which separated optical parts are involved in some sort of hybrid package.

A quantitative model of failure rates was developed for each section of the device by fully characterizing failure modes and determining failure mode accelerants. The activation energy, $E_a = 0.5$ eV was derived assuming an aging rate proportional to $\exp[E_a/kT]$. The current acceleration exponent, $n = 1.5$ was derived assuming the aging rate was also proportional to J^n , where J is the applied current density to the section in question. Mirror drift failure was set to be when the operating point moved half way from the center of a single-mode region toward a mode-hop boundary. For the SGDBRs in question this was equivalent to ± 100 pm of allowable open-loop wavelength drift of the mode boundaries. (Of course, with a wavelength locker in operation, the lasing mode wavelength only drifts as much as it does—typically < 1 pm over life.) The aging criteria for the gain and amplifier sections are as for other semiconductor lasers. The same approximate activation energies and current acceleration factors were observed for all sections.

The data indicate that no updating of mirror currents is necessary for a FIT rate of < 20 at 15 years. This includes reasonable margins for all device parameters. However, a mirror look-up table updating algorithm has also been developed that both monitors the mirror drift for setting possible alarms as well as updating the table. This mirror-control algorithm improves the FIT rate to < 3 at 15 years. The lifetime distribution taken from 200 parts using accelerated aging procedures shows a classical log-normal relationship with a mean lifetime of 186 years for room temperature, but with maximum channel currents assumed. In a normal WDM system populated with such devices, the channel currents would be distributed over lower values for the various channels, so Fig. 11 should be taken as a worst case

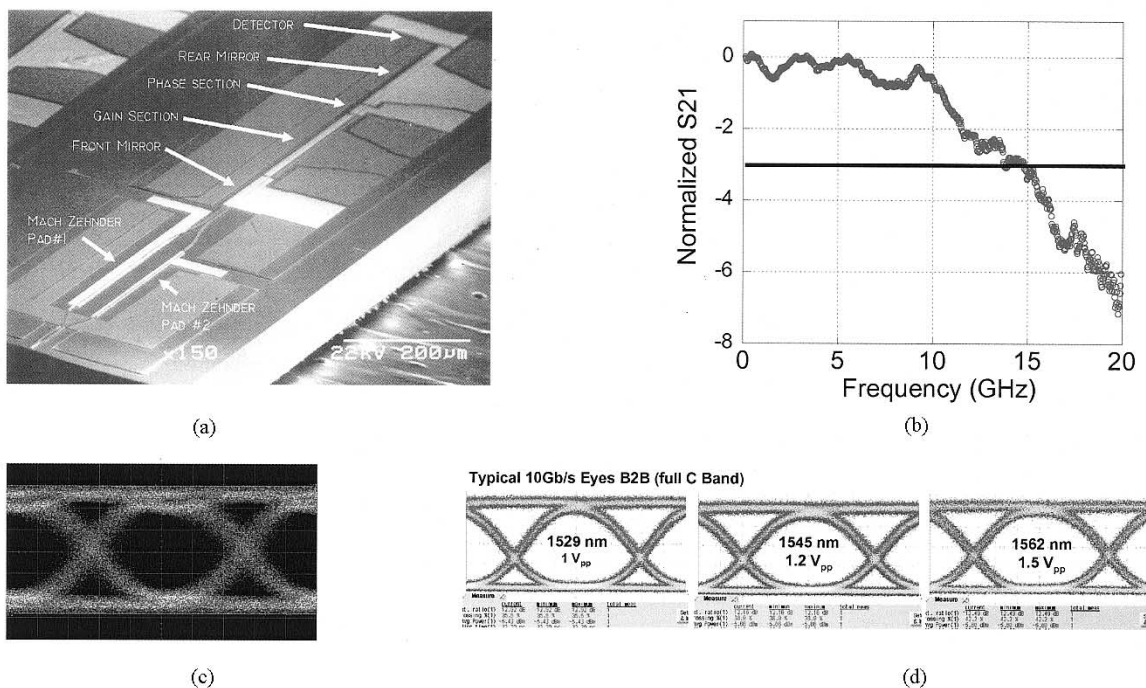


Fig. 10. (a) SEM photo of UCSB’s SGDBR integrated with a Mach-Zehnder modulator, (b) small-signal bandwidth, (c) unfiltered eye, and (d) filtered eye-diagrams at 10 Gb/s for three wavelengths across the band for Agility device.

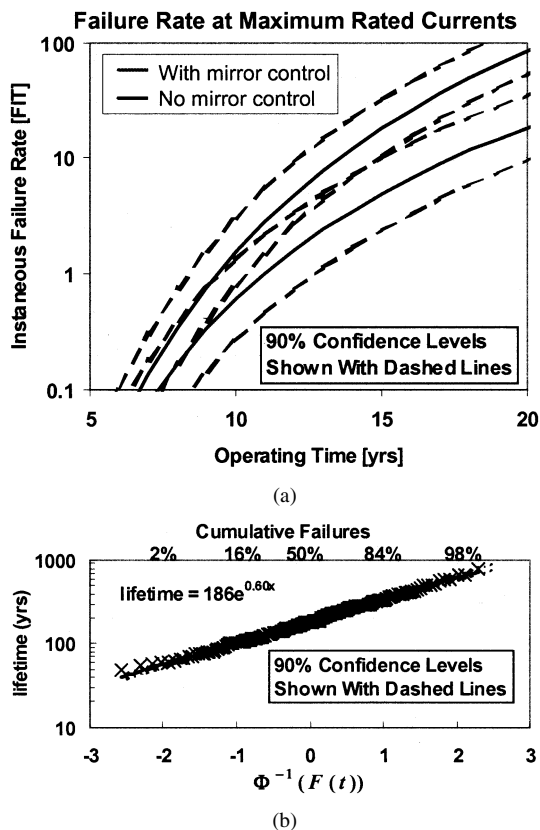


Fig. 11. (a) FIT rate versus time, assuming both original mirror biases as well as with bias updating-mirror control. (b) Lifetime distribution of 200 parts tested. Maximum channel currents assumed. Mean lifetime of 186 years shown.

result that would not occur over any distribution of components in a typical system. Taking a distribution of WDM channels into

account, the “no mirror control” FIT rate is estimated to be about 2 @ 15 years.

This relatively low wavelength drift for the SGDBR has been ascribed to the relatively small percentage of grating that fills the sampled-grating mirrors. About 90% of the mirror area is free from gratings in a typical design. Studies have shown that this results in much higher material quality within the mirrors [31]. Lack of gratings in most areas permits very high quality regrowth of the InP cladding following grating formation. Not only is the surface more planar and free from defects, it can be composed of InP rather than InGaAsP quaternary waveguide material in the large regions between the grating bursts. Thus, while standard DBR lasers, which contain gratings throughout the mirror tuning sections, continue to have wavelength drift problems, the SGDBR has emerged as being surprisingly stable.

VII. CONTROL OF WIDELY-TUNABLE LASERS

The control of multi-element tunable lasers, such as those illustrated in Fig. 5, has been a roadblock to their general acceptance for some time. Most system engineers are accustomed to incorporating a two-terminal device, such as a DFB laser, in their optical transmitters. Of course, even for the DFB the device temperature is used to fine tune and lock the wavelength in WDM systems. For the widely-tunable devices of Fig. 5, it seems apparent that we must simultaneously control some additional parameters, although in some cases we may only need to dynamically control the same number as in the DFB to lock the amplitude and wavelength at a given channel. However, there is always a need for a “look-up table” to give the specific set of currents or voltages for each channel to the several sections, and this indeed, does add a complication for the user. To gain

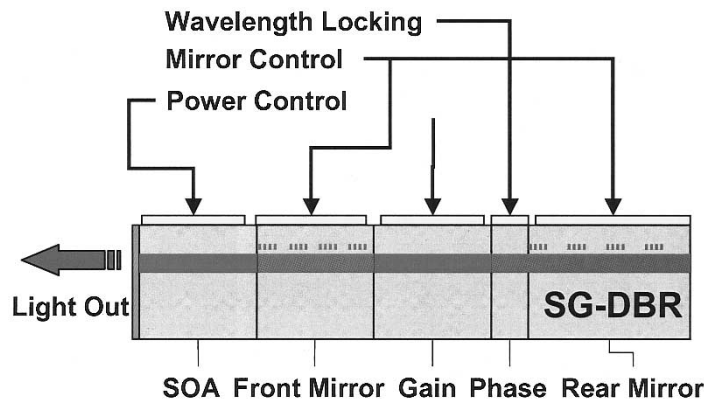


Fig. 12. SGDBR/SOA with connections for control circuit.

more wide-spread acceptance, suppliers of the multiple-section lasers in recent years have provided automatic control systems within the laser module so that the user doesn't have to deal with the control problem. The wavelength and amplitude are set via a digital command through a common interface. Nevertheless, users are justifiably concerned with the reliability and stability of such systems. So they remain of great interest.

The control system must be capable of two basic functions: 1) staying accurately on the desired wavelength channel and 2) reliably finding a new desired channel when a channel change is requested at some later time, and this time could be near the end of life. To accurately stay on a desired wavelength channel most lasers require a separate wavelength locker. If the wavelength channel plan is relatively coarse, perhaps >100 GHz, this locker may not be necessary. For example, given the low wavelength drift of the SGDBR outlined above, this locker may not be necessary for even 100 GHz channel spacing if a modest FIT rate is tolerable. But, more generally a locker is required. It usually contains an etalon with a free-spectral range roughly equal to the channel spacing, so that it can provide a feedback signal to capture and lock the wavelength within about one-third of a channel spacing on either side of some ITU frequency.

Switching to a new channel after some time is generally a more difficult problem. The immediate question is, will the original look-up table from factory calibration be good enough, or will aging have changed the values? To be able to use the original look-up table, the settings must get us to the correct channel within the capture range of the locker. For embodiments where tuning requires mechanical motion or significant swings in temperature, hysteresis and charging of MEMs elements tend to shift the look-up table. In some DBR structures, changes in carrier lifetime also may result in a shift in wavelength that exceeds the locker capture range. Possible solutions to these problems involve either some sort of global wavelength monitor, a channel counting algorithm, or some means of updating the look-up tables over life. All of these approaches have been demonstrated, but all require a more complex control system.

Fig. 12 illustrates the control signals necessary to operate the SGDBR/SOA. An electronic circuit supplies control currents in response to amplitude and wavelength errors derived from the locker. The temperature and the current to the gain section are held constant at factory-set values, so they are not part of the control system. All other currents are contained in a look-up

table for each channel. The locker signals are converted to error currents for that are added to the SOA and phase sections. The SOA is used to lock the amplitude and the phase section is used to lock the wavelength. In normal operation no corrections are supplied to the mirrors—this is called the “no mirror control” case referred to in Fig. 11. In this mode of operation then, the actual feedback control system is about the same as for the DFB, with the amplitude correction being added to the SOA instead of the DFB gain section and the wavelength correction being added to the phase section instead of the thermoelectric cooler of the DFB. Of course, there is a look-up table to set different initial values for each channel in the SGDBR case, but this involves no dynamic control, just set points.

It may also be seen that the use of an external SOA for amplitude control is desirable in a tunable laser relative to adjusting the gain current in the cavity. This is because the wavelength would also change in response to changing the gain current. In fact, this is one of the primary limitations on wavelength stability in widely-tunable laser embodiments that do not have the external SOA to level the amplitude as the device ages.

For “mirror control” the mirror currents are slowly dithered about their set points and the voltage on the gain section is monitored. Because the wavelength and amplitude locking circuits are operating, there is no change in external optical power or wavelength observed. Second order changes in cavity loss, caused by changing the mirror currents, are also removed in this process. The dithering of the reflectivity peaks of the mirrors cause the gain voltage to change slightly because it monitors the quasi-Fermi level separation in the gain region, and this is proportional to the cavity loss change. Thus, a local minimum in the gain voltage is observed when the mirror peaks are properly aligned with the mode wavelength, where the cavity loss is at a local minimum. The mode, of course, is set by the locker/phase-section feedback circuit to be at the proper ITU grid wavelength. So, it can be seen that this “mirror control” algorithm requires no additional optical elements or electrical connections. Again, this mirror control mode is probably not necessary for reliable device operation according to Fig. 11; however, monitoring of the mirror peaks relative to the cavity mode gives one assurance that the device is operating properly.

If the mirror currents must be corrected, then it may be assumed that the currents required to hit other channels must also change. This is the second aspect of control mentioned

TABLE I
CONTROL PARAMETERS FOR TUNABLE LASERS

Laser	Coarse Wavelength	Fine Wavelength	Amplitude	VOA
DFB Array/SOA	$V_{\text{array}}(j)$	T	$I_{\text{gain}}(j)$	ΔI_{SOA}
DFB/MEMs	$V_{m1}, V_{m2}(j)$	T	$I_{\text{gain}}(j)$	$V_{m1}, V_{m2}(j)$
SGDBR/SOA	I_{m1}, I_{m2}	I_{ϕ}	I_{SOA}	ΔI_{SOA}
Ext Cavity/ grating	V_{m0}	V_{mL} or I_{ϕ}	I_{gain}	V_{mshutter}
Ext. Cavity/ etalons	$T_{\text{et1}}, T_{\text{et2}}$	V_{mL} or I_{ϕ}	I_{gain}	-----
VCSEL/MEMs	V_{m1}	V_{m1}	I_{gain}	-----

above—finding a new channel. In the SGDBR case with mirror control the table can be updated dynamically without ever leaving the original channel. This is because the same reduction in carrier lifetime that requires a current increase to maintain a given carrier density and thus index of refraction, is also experienced by all the other channels. Most importantly, it has been verified that this carrier lifetime decrease is due to an increase in nonradiative recombination, and it is well known that this has a linear relationship to carrier density. Since carrier density is predominately determined by the radiative recombination rate, which depends upon the square of the carrier density, we can assume that the shift in the entire look-up table will be linear in the square root of current. Fortunately, extensive measurements have shown that this is indeed the case experimentally [31], [32], so updating the table is a valid approach in this case.

Table I summarizes the parameters that must be adjusted to enable the amplitude and wavelength of the various types of tunable lasers illustrated in Fig. 5 to be set. It also indicates the parameters for variable-optical-attenuator (VOA) operation. This function is desirable both to allow the user to adjust the amplitude as well as to blank the output during tuning between channels. As can be seen most of the widely-tunable lasers being considered require several parameters to be set, and in most cases, most of these must be controlled. In the VCSEL/MEMs case there are fewer parameters, but this is an example where changing channels requires some sort of global wavelength monitor or channel counting scheme, because one clearly can not depend upon the look-up table for channel selection, especially after some aging with the MEMs mirror. The case is similar in the other mechanically tuned embodiments.

VIII. CONCLUSION

As presented in the tutorial on tunable semiconductor lasers at OFC'03 we have outlined why tunable lasers might be beneficial, discussed basic tuning mechanisms involved in most tunable lasers, given some examples of tunable lasers that have been commercialized, discussed reliability issues, and outlined control techniques. A summary of performance data for the SGDBR type of laser and the monolithically integrated SGDBR

with both electroabsorption and Mach-Zehnder modulators was given. It was argued that tunable lasers can reduce operational costs, that full-band tunability is desirable for many applications, that monolithic integration offers the most potential for reducing size, weight, power and cost, and that sufficient reliability for system insertion has been demonstrated, at least in the SGDBR case.

REFERENCES

- [1] L. Coldren, "Monolithic tunable diode lasers," *IEEE J. Select. Topics Quantum Electron.*, vol. 6, p. 988, Nov./Dec. 2000.
- [2] R.-C. Yu *et al.*, presented at the Proc. APOC'03, Wuhan, China, Sept. 3, 2003.
- [3] G. Fish and K. Affolter, "Tunable lasers and their impact on optical networks," presented at the Communications Design Conf., San Jose, CA, Aug. 2002.
- [4] D. J. Blumenthal, B. E. Olsson, G. Rossi, T. Dimmick, L. Rau, M. L. Ma'anovic', O. A. Lavrova, R. Doshi, O. Jerphagnon, J. E. Bowers, V. Kaman, L. A. Coldren, and J. Barton, "All-Optical label swapping networks and technologies," *IEEE J. Lightwave Technol., Special Issue Optical Networks*, vol. 18, pp. 2058–2075, Dec. 2000.
- [5] M. L. Mašanović, V. Lal, J. S. Barton, E. J. Skogen, L. A. Coldren, and D. J. Blumenthal, "Monolithically integrated Mach-Zehnder interferometer wavelength converter and widely-tunable laser in InP," *IEEE Photon. Technol. Lett.*, vol. 15, pp. 1115–1117, Aug. 2003.
- [6] L. A. Coldren, "Widely-tunable chip-scale transmitters and wavelength converters," in *Integrated Photonics Research Tech. Dig.*, Washington, DC, June 2003, Paper IMB-1, pp. 6–8.
- [7] A. Carena, M. D. Vaughn, R. Gaudino, M. Shell, and D. J. Blumenthal, "OPERA: An optical packet experimental routing architecture with label swapping capability," *IEEE J. Lightwave Technol., Special Issue Photonic Packet Switching Technologies, Techniques, and Systems*, vol. 16, pp. 2135–2145, Dec. 1998.
- [8] M. Duell, J. Gripp, J. Simsarian, A. Bhardwaj, P. Bernasconi, M. Zirngibl, and O. Laznicka, "Fast packet routing in a 2.5 Tb/s optical switch fabric with 40 Gb/d duobinary signal at 0.8 b/s/Hz spectral efficiency," presented at the OFC 2003, 2003, postdeadline paper PD8-1.
- [9] L. A. Coldren and S. W. Corzine, *Diode Lasers and Photonic Integrated Circuits*. New York: Wiley, 1995.
- [10] M. C. Amann and J. Buus, *Tunable Laser Diodes*. London: Artech, 1998.
- [11] N. Natakeyama, K. Naniwae, K. Kudo, N. Suzuki, S. Sudo, S. Ae, Y. Muroya, K. Yashiki, S. Satoh, T. Morimoto, K. Mori, and T. Sasaki, "Wavelength-Selectable microarray light sources for S-, C-, and L-band WDM systems," *IEEE Photon. Technol. Lett.*, vol. 15, pp. 903–905, 2003.
- [12] M. Bouda, M. Matsuda, K. Morito, S. Hara, T. Watanabe, T. Fujii, and Y. Kotaki, "Compact high-power wavelength selectable lasers for WDM applications," in *Proc. OFC 2000*, vol. 1, Mar. 2000, pp. 178–180.

- [13] J. Heanue, E. Vail, M. Sherback, and B. Pezeshki, "Widely tunable laser module using DFB array and MEM's selection with internal wavelength locker," in *Proc. OFC 2003*, vol. 1, 2003, pp. 82–83.
- [14] D. Anthon, J. D. Brerger, J. Drake, S. Dutta, A. Fennema, J. D. Grade, S. Hrinya, F. Ilkov, H. Jerman, and D. King, "External cavity diode lasers tuned with silicon MEMS," in *Proc. OFC 2003*, 2002, pp. 97–98.
- [15] T. Day, "External-cavity tunable diode lasers for network deployment". presented at Proc. OFC 2001. [Online]. Available: http://www.new-focus.com/Online_Catalog/Literature/Tunable2.pdf
- [16] *Intel Work* [Online]. Available: <http://www.commsdesign.com/story/OEG20030110S0053>
- [17] K. J. Knopp, D. Vakhshoori, P. D. Wang, M. Azimi, M. Jiang, P. Chen, Y. Matsui, K. McCallion, A. Baliga, F. Sakhtab, M. Letsch, B. Johnson, R. Huang, A. Jean, B. DeLargy, C. Pinzone, F. Fan, J. Liu, C. Lu, J. Zhou, H. Zhu, and R. Gurjar, "High power MEMS-tunable vertical-cavity surface-emitting lasers," in *Proc. Advanced Semiconductor Lasers, Dig. LEOS Summer Topical Meet.*, Copper Mountain, CO, July–Aug. 30–1, 2001, pp. 31–32.
- [18] C. J. Chang-Hasnain, "Tunable VCSEL's," *IEEE J. Select. Topics Quantum Electron.*, vol. 6, pp. 978–987, Nov.–Dec. 2000.
- [19] T. L. Koch, U. Koren, and B. I. Miller, "High-performance tunable 1.55 mm InGaAs/InGaAsP multiple-quantum-well distributed-bragg-reflector lasers," *Appl. Phys. Lett.*, vol. 53, pp. 1036–1038, 1988.
- [20] J. E. Johnson, L. J. Ketelsen, D. A. Ackerman, L. Zhang, M. S. Hybertsen, K. G. Glogovsky, C. W. Lentz, W. A. Asous, C. L. Reynolds, J. M. Geary, K. K. Kamath, C. W. Ebert, M. Park, G. J. Przybyl, R. E. Leibenguth, S. L. Broutin, and J. W. Stayt Jr, "Fully stabilized electroabsorption-modulated tunable DBR laser transmitter for long-haul optical communications," *IEEE J. Select. Topics Quantum Electron.*, vol. 7, pp. 168–177, Mar.–Apr. 2001.
- [21] H. Debergeas-Sillard, A. Vuong, F. Delorme, J. David, V. Allard, A. Bodere, O. LeGouezigou, F. Gaborit, J. Rotte, M. Goix, V. Voinit, and J. Jacquet, "DBR module with 20 mW constant coupled output power, over 16 nm (40 × 50 GHz spaced channels)," *Photon. Technol. Lett.*, vol. 13, no. 1, pp. 4–6, Jan. 2001.
- [22] M. Oberg, S. Nilsson, K. Streubel, J. Wallin, L. Backborn, and T. Klinga, "74 nm wavelength tuning range of an InGaAsP/InP vertical grating assisted codirectional coupler laser with rear sampled grating reflector," *IEEE Photon. Tech. Lett.*, vol. 5, pp. 735–738, 1993.
- [23] B. Broberg, P. J. Rigole, S. Nilsson, L. Andersson, and M. Renlund, "Widely tunable semiconductor lasers," in *Proc. OFC/IOOC '99*, vol. 2, Feb. 1999, pp. 137–139.
- [24] V. Jayaraman, A. Mathur, L. A. Coldren, and P. D. Dapkus, "Theory, design, and performance of extended tuning range in sampled grating DBR lasers," *IEEE J. Quantum Electron.*, vol. 29, pp. 1824–1834, June 1993.
- [25] B. Mason, J. Barton, G. A. Fish, L. A. Coldren, and S. P. Denbaars, "Design of sampled grating DBR lasers with integrated semiconductor optical amplifiers," *IEEE Photon. Technol. Lett.*, vol. 12, pp. 762–764, 2000.
- [26] Y. Tohmori, Y. Yoshikuni, H. Ishii, F. Kano, T. Tamamura, Y. Kondo, and M. Yamamoto, "Broadrange wavelength-tunable superstructure grating 9SSG) DBR lasers," *IEEE J. Quantum Electron.*, vol. 29, pp. 1817–1823, 1993.
- [27] C. Coldren *et al.*, "Workshop on tunable lasers," presented at the OFC'03 Proc., Atlanta, GA, Mar. 2003.
- [28] Y. A. Akulova, G. A. Fish, P.-C. Koh, C. L. Schow, P. Kozodoy, A. P. Dahl, S. Nakagawa, M. C. Larson, M. P. Mack, T. A. Strand, C. W. Coldren, E. Hegblom, S. K. Penniman, T. Wipiejewski, and L. A. Coldren, "Widely tunable electroabsorption-modulated sampled-grating DBR laser transmitter," *IEEE J. Select. Topics Quantum Electron.*, vol. 8, no. 6, pp. 1349–1357, 2002.
- [29] T. Wipiejewski, Y. Akulova, G. Fish, P. Koh, C. Show, P. Kozodoy, A. Dahl, M. Larson, M. Mack, T. Strand, C. Coldren, E. Hegblom, S. Penniman, T. Liljeborg, and L. Coldren, "Performance and reliability of widely-tunable laser diodes," in *Proc. Electronic Components and Technology Conf.*, New Orleans, LA, May 2003, pp. 789–795.
- [30] J. S. Barton, E. J. Skogen, M. L. Masanovic, S. P. DenBaars, and L. A. Coldren, "Widely-tunable high-speed transmitters using integrated SGDBR's and Mach-Zehnder modulators," *IEEE J. Select. Topics Quantum Electron.*, vol. 9, 2003.
- [31] C. Coldren, T. Strand, E. Hegblom, Y. Akulova, G. Fish, M. Larson, and L. Coldren, "Reliability of widely-tunable SGDBR lasers suitable for deployment in agile networks," in *OFC Tech. Dig.*, Atlanta, GA, Mar. 2003, Paper MF60.
- [32] D. A. Ackerman, J. E. Johnson, G. Chu, S. Nee, Z. Liming, E. J. Dean, and L. J.-P. Ketelsen, "Assessment and modeling of aging in electro-absorption distributed bragg reflector lasers," *IEEE J. Quantum Electron.*, vol. 37, pp. 1382–1387, Nov. 2001.

Larry A. Coldren (S'67–M'72–SM'77–F'82) received the Ph.D. degree in electrical engineering from Stanford University, Stanford, CA, in 1972.

He is the Fred Kavli Chair of Optoelectronics and Sensors at the University of California, Santa Barbara (UCSB). He is also Chairman and Chief Technology Officer of Agility Communications Inc., Santa Barbara, a company he cofounded in 1998 to develop widely tunable transmitters for wavelength-division multiplexed networks. After 13 years in the research area at Bell Laboratories, he joined UCSB in 1984, where he now holds appointments in Materials and Electrical & Computer Engineering and is Director of the Optoelectronics Technology Center. At UCSB, his efforts have included work on guided-wave and vertical-cavity modulators and lasers as well as the underlying materials growth and fabrication technology. His current work includes the integration of these devices to create novel optical transmitters, receivers, and wavelength converters for optical networking and interconnection. He has authored or coauthored over 500 papers, 5 book chapters, 1 textbook, and has been issued 36 patents.

Prof. Coldren is a Fellow of the Optical Society of America and the Institute of Electrical Engineers (U.K.).

G. A. Fish, photograph and biography not available at the time of publication.

Y. Akulova, photograph and biography not available at the time of publication.

J. S. Barton, photograph and biography not available at the time of publication.

L. Johansson, photograph and biography not available at the time of publication.

C. W. Coldren (S'97–M'00), photograph and biography not available at the time of publication.

Scalable and Reliable Photonic Integrated Circuits for Scalable and Reliable WDM Networks

(Plenary paper)

Larry A. Coldren

University of California and Agility Communications, Inc.

Santa Barbara, CA 93106

Tel: (805) 893-4486; Fax: (805) 893-4500; email: coldren@ece.ucsb.edu

Abstract

Photonic ICs that function as reliable single-chip widely-tunable transmitters have been developed on a simple InP-based platform technology. This same platform has been shown to be scalable to more than a dozen optical elements for more complex functionalities such as full-band wavelength converters. Much higher levels of integration are anticipated.

Summary

The allure of monolithically integrating many photonic components to form high-performance photonic integrated circuits (PICs) has been with us for many years. Such devices, as their electronic-IC counterparts, should provide improved performance and reliability, while having lower power, size, weight, and cost than their discrete-component embodiments. Moreover, the integration technology should be scalable so that more and more photonic components can be integrated as the technology matures to provide further improvements in these key parameters. This is a nice vision, but until recently most efforts to create such PICs have largely fallen short of the goal. In this paper we shall summarize recent progress in developing a robust InP-based platform technology that is capable of providing scalable and reliable PICs, which in some forms are now ready for wide-scale deployment in WDM networks.

Figure 1 gives a schematic and an SEM photo of an integrated PIC transmitter, which includes a widely-tunable laser, a back-side monitoring detector, a semiconductor optical amplifier (SOA), and an electroabsorption modulator (EAM)[1]. The integration platform includes only one regrowth step to form the gratings and define the active and passive regions. The entire transmitter is fabricated with the same layer structure and the same fabrication process as the laser alone.

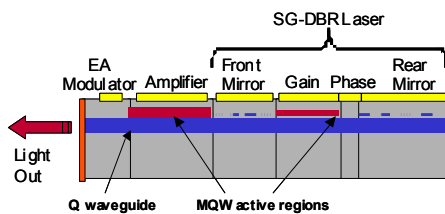


Figure 1. Schematic and SEM of single-chip transmitter.

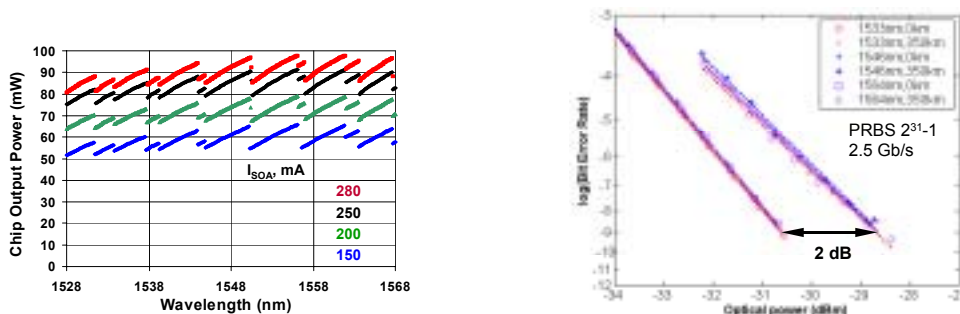


Figure 2. Unleveled cw chip power vs. wavelength (left) and BER of the packaged transmitter for several wavelengths (right) across the C-band after transmission over 350 km on standard fiber.

Figure 2 shows that relatively high powers are available from these chips and that the packaged chips can give very competitive transmitter performance.

These devices have undergone extensive reliability testing and have shown very stable operation over life[2]. In fact, the open-loop wavelength is surprisingly stable on these SGDBR lasers as compared to previous reports on DBR lasers[3], and the results compare favorably to the stability of DFB lasers. The explanation for this seems to lie in the fact that the SGDBR mirrors only contain a small fraction of grating, and the space between the grating bursts, which provides an InP-on-InP regrowth surface, actually determines the mirror peak position. Thus, mode hops never occur within the lifetime of the gain section, which extends to several hundred years for a 20% roll off in power as determined by rigorous Telcordia standards. Moreover, the dual grating SGDBR laser design has a much larger design window than simple DBRs. Mirrors can be misaligned by more than 50% without degrading the side-mode-suppression ratio (SMSR) to less than 40dB.

More recently, state-of-the-art Mach-Zehnder modulators have been successfully integrated on the same chip as the SGDBR, detector, and SOA[4,5]. Figure 3 illustrates a schematic and SEM of the chip as well as transmission results at 10Gb/s. This represents a still higher level of integration, because the chip now includes MMI power splitters and combiners and additional phase shifters for the ultimate in chirp control. The effective chirp parameter has been shown to be programmable from +1 to -1. In Fig. 3, a chirp parameter of approximately -0.7 was set to provide error-free transmission over 100km of standard fiber across the entire C-band.

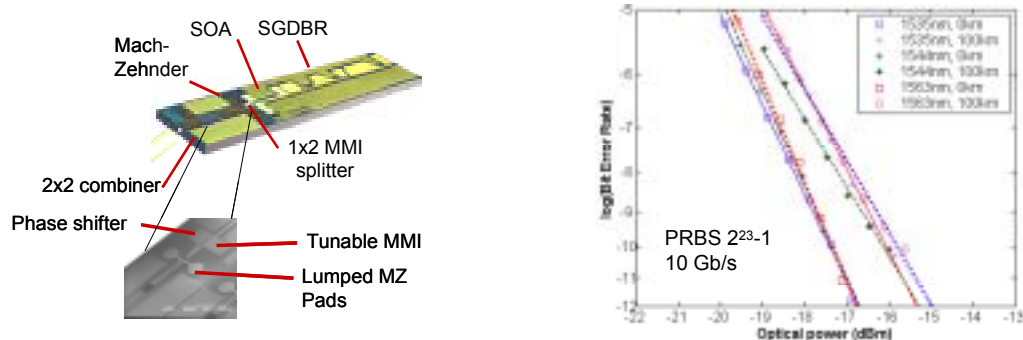


Figure 3. Schematic, SEM blowup, and transmission results with integrated transmitter using an integrated Mach-Zehnder modulator.

Most recently, the integration platform has been extended to include additional functionalities as well as to make arrays of devices. All-optical wavelength converters, incorporating SOAs modulated by optical data on preamplified inputs[6], as well as photocurrent-driven wavelength converters that used SOA-PIN input stages directly coupled to either the SGDBR gain section or the integrated external modulator[7] have been demonstrated with error free operation over a wide bandwidth of input and output wavelengths. Yields for these complex devices appear to be similar to the SGDBR itself, and these have been reported to exceed DFB yields.

Conclusions

A PIC integration platform on InP has been demonstrated to provide high-performance, high-reliability devices with significant numbers of elements on a single chip. The design rules require that all other devices must be integrable with the same layer structure and processing steps as required for the widely-tunable SGDBR laser alone. Future plans call for significant increases in the level of integration from this platform.

References:

- [1] Y. A. Akulova, G. A. Fish, et al., "Widely tunable electroabsorption-modulated sampled-grating DBR laser transmitter", *IEEE Journal of Selected Topics in Quantum Electron.*, v.8, no. 6, pp.1349-1357, 2002.
- [2] C. Coldren, T. Strand, E. Hegblom, Y. Akulova, G. Fish, M. Larson, and L. Coldren, *OFC Tech Dig.*, pap. MF60, Atlanta, Mar. 2003.
- [3] D. A. Ackerman, J.E. Johnson, George Chu, Sung Nee, Zhang Liming, E.J. Dean, L.J.-P. Ketelsen, "Assessment and modelling of aging in electro-absorption distributed Bragg reflector lasers," *IEEE J Quantum Electron.*, **37**, pp1382-1387, 2001.
- [4] J. S. Barton, E.J. Skogen, M.L. Masanovic, S. P. DenBaars, and L. A. Coldren, "Widely-tunable high-speed transmitters using integrated SGDBRs and Mach-Zehnder modulators," *JSTQE*, **9**, Semi. Lasers issue, 2003.
- [5] L.A.Coldren, "Integrated tunable transmitters for WDM networks," *Proc. ECOC-IOOC'03*, Rimini, pp. 878-881, Sept, 2003.
- [6] M. L. Mašanović, V.Lal, J.S. Barton, E.J. Skogen, L.A. Coldren, D.J. Blumenthal,, "Monolithically Integrated Mach-Zehnder Interferometer Wavelength Converter and Widely-Tunable Laser in InP", *IEEE Photonics Technology Letters*, August 2003.
- [7] J.M. Hutchinson, J.A. Henness, L.A. Johansson, et al, "2.5 Gb/s wavelength conversion using monolithically-integrated photodetector and directly modulated widely-tunable SGDBR laser," *Proc. LEOS'03*, Tucson, Oct. 2003.

Sampled-grating DBR laser integrated with SOA and tandem electroabsorption modulator for chirp-control

L.A. Johansson, Y.A. Akulova, G.A. Fish and L.A. Coldren

Chirp-controlled optical modulation is demonstrated using a voltage division scheme applied to a long-section phase modulator to compensate for the positive chirp of an electroabsorption modulator arranged in a tandem configuration. Both modulators are integrated with a semiconductor optical amplifier (SOA) and a sampled-grating distributed Bragg reflector (DBR) laser. The effective chirp factor can be controlled from +1 to -0.86 with less than 2 dB penalty in extinction ratio and insertion loss.

Introduction: Widely tunable lasers integrated with electroabsorption modulators generally use a Franz-Keldysh modulator for wide spectral bandwidth [1]. The positive chirp of these modulators is a limiting factor for data transmission over long spans of fibre. Negative chirp and wide spectral bandwidth can be offered by integration of a widely tunable laser with a Mach-Zehnder modulator [2] at the cost of more complex modulator design and increased passive loss of the modulator. An alternative approach to generate negative chirp is using two EA modulators in a tandem configuration, one biased for amplitude modulation, the other biased for phase modulation using an inverted driver signal, compensating for the residual phase modulation of the amplitude modulator [3]. This approach is limited by the voltage swing available at the phase modulator, determined on the high voltage side by the diode threshold voltage, where carrier injection is causing distortion, and limited on the low voltage side by the onset of absorption that ultimately makes the insertion loss prohibitive and deteriorates the extinction ratio. One possibility to enhance the available performance of this approach is to use different bandgap EA modulators, possible to achieve using quantum-well intermixing techniques [4]. A second possibility that applies to Franz-Keldysh modulators is to use a simple voltage division scheme, which is described in this Letter.

Device design: Fig. 1 shows a schematic diagram of the device used in this work together with the voltage division scheme used. The electroabsorption modulator is split in two parts arranged in a tandem configuration. The device is mounted onto an aluminium nitride RF carrier, with integrated thin-film resistors. The amplitude modulator is terminated in parallel to $50\ \Omega$ in series with a capacitor. In contrast, the phase modulator is terminated in parallel by a lower value resistor and in series by a second resistor, such that $R_1 + R_2 = 50\ \Omega$. The resulting voltage division factor, n , is given by $n = 50\ \Omega / R_1$. To compensate for the lower modulation voltage, the phase modulator is made n times longer than the amplitude modulator. To a first-order estimate, the RC-limited bandwidth of the modulators remains the same. The main advantage of the described voltage division scheme is that while the modulation voltage is now scaled down by a factor of n , the threshold voltage stays constant, increasing the available phase swing while keeping amplitude modulation in the phase modulator low.

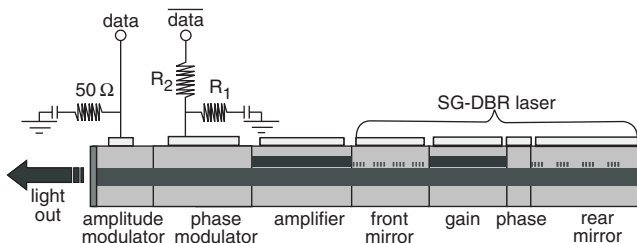


Fig. 1 Schematic diagram of tandem EAM modulator, integrated with SOA and sampled-grating DBR laser; simple schematic of voltage division scheme also shown

Two devices are investigated, the first having a $200\ \mu\text{m}$ amplitude modulator and an $800\ \mu\text{m}$ phase modulator, with a voltage division factor of $n = 4$. The second device has equal length sections of $120\ \mu\text{m}$, and is used for verification of the benefits of the principle. The sampled-grating

DBR lasers are similar to the one described in [2], with more than 10 mW output power, lower than 2 MHz linewidth, and more than 40 dB side-mode suppression ratio, achieved over more than 40 nm wavelength tuning range.

Experimental results: The amplitude modulator is modulated at 2.5 Gbit/s datastream while the phase modulator is complementary modulated by the inverted signal. By varying the attenuation/amplification of the signal applied to the phase modulator, the resulting chirp of the device can be controlled. The time-resolved chirp characteristics of the modulated optical signal is measured using an Advantest Q7606B optical chirp form test set and an Agilent 86100A oscilloscope. The effective chirp factor, α_{eff} , is then derived from the time-resolved chirp data. Previously, using the amplitude modulator only, the effective chirp parameter has been shown to correlate well to the fibre dispersion penalty for this type of device [5].

Fig. 2 shows the measured chirp forms for the device when voltage division of $n = 4$ was used. The phase modulator was biased at 0 V and the amplitude modulator at $-2.6\ \text{V}$. The upper plot shows the chirp characteristics of the amplitude modulator alone, corresponding to an α_{eff} of 0.97. Applying a modulation signal to the phase modulator of equal amplitude as to the amplitude modulator, results in the characteristics shown by the centre plot, corresponding to α_{eff} of 0.03. The remaining frequency chirping, particularly apparent at the falling edge, is a result of different impulse response between the phase and amplitude modulator. The different impulse response can be attributed in part to the inductance of the bondwire used to connect the modulators to the RF lines of the carrier. A more careful RF design should further decrease the envelope of the frequency chirp. The lower plot in Fig. 2 shows α_{eff} of -0.86 for a phase modulation signal amplified by 3 dB relative to that of the amplitude modulator.

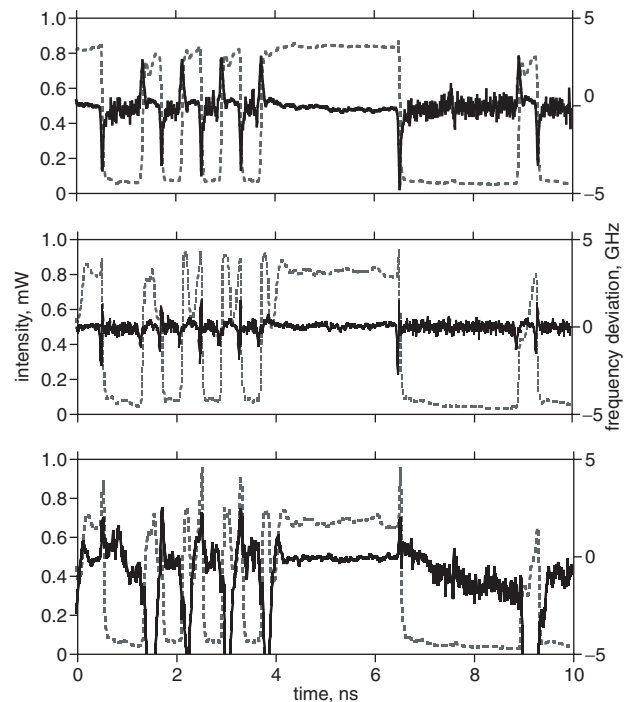


Fig. 2 Measured output amplitude (dotted line) and time-resolved frequency chirping (solid line) of tandem EAM configuration. Resulting effective chirp factors 0.97, 0.03, -0.86 , respectively, top to bottom

Fig. 3 shows the extinction and excess insertion loss compared to amplitude modulation only against achieved effective chirp factor for a device using voltage division and a control device with equal length modulators. Significant penalties are shown for the control device at lower chirp values, as a result of counteracting amplitude modulation in the phase modulator. Using voltage division, α_{eff} down to -0.86 is observed with $<2\ \text{dB}$ excess insertion loss and $<2\ \text{dB}$ degradation of extinction ratio. For even lower values of achieved effective chirp, further degradation is observed, partly due to too high applied voltage in the phase modulator. This can be traded-off with a slightly degraded

insertion loss and extinction by lowering the bias point of the phase modulator.

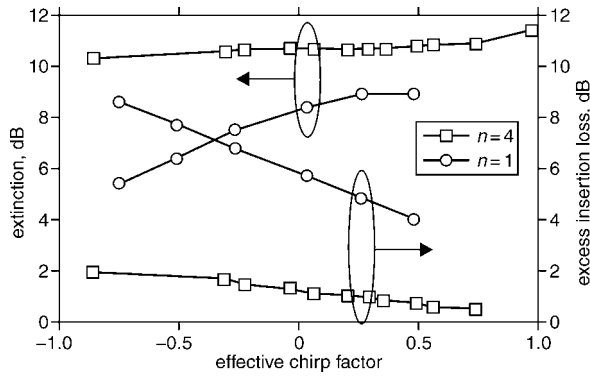


Fig. 3 Extinction ratio and resulting penalty in terms of insertion loss, compared to amplitude modulation only, against measured large-signal chirp factor for $n=4$ and $n=1$

The control device achieves negative chirp with lower phase modulation voltage. The cause for this is believed to be localised heating at the front edge of the phase modulator that for the control device experiences significant optical absorption, with the higher applied modulation voltage and therefore necessarily lower bias point: -2 V.

Conclusion: We have demonstrated how two Franz-Keldysh modulators arranged in a tandem configuration can be used to produce chirp-controlled optical modulation with an effective chirp factor down to -0.86 . It is shown how using a long phase modulating section in combination with a simple voltage division scheme to one

of the modulator sections can improve the performance of the tandem modulator to <2 dB excess insertion loss and <2 dB degradation of extinction ratio compared to a single section modulator for effective chirp factors down to -0.86 .

© IEE 2004

24 October 2003

Electronics Letters online no: 20040016

doi: 10.1049/el:20040016

L.A. Johansson and L.A. Coldren (*Department of Electrical and Computer Engineering, University of California, Santa Barbara, CA 93106, USA*)

E-mail: leif@ece.ucsb.edu

Y.A. Akulova and G.A. Fish (*Agility Communications, Inc., 600 Pine Ave, Santa Barbara, CA 93117, USA*)

References

- 1 Akulova, Y.A., *et al.*: 'Widely-tunable electroabsorption-modulated sampled grating DBR laser transmitter', *IEEE J. Sel. Top. Quantum Electron.*, 2002, **8**, pp. 1349–1357
- 2 Barton, J.S., *et al.*: 'Widely-tunable high-speed transmitters using integrated SGDBRs and Mach-Zehnder modulators', *IEEE J. Sel. Top. Quantum Electron.* (accepted for publication)
- 3 Claassen, M., Harth, W., and Stegmüller, B.: 'Two-section electroabsorption modulator with negative chirp at low insertion loss', *Electron Lett.*, 1996, **32**, pp. 2121–2122
- 4 Skogen, E.J., *et al.*: 'A quantum-well-intermixing process for wavelength-agile photonic integrated circuits', *IEEE J. Sel. Top. Quantum Electron.*, 2002, **8**, pp. 863–869
- 5 Koh, P.C., *et al.*: 'Correlation between dispersion penalty and time-resolved chirp for widely tunable electroabsorption-modulated SGDBR laser across the EDFA gain bandwidth', *IEEE Photonics Technol. Lett.*, 2003, **15**, pp. 1011–1013

High-Speed Optical Frequency Modulation in a Monolithically Integrated Widely-Tunable Laser - Phase Modulator

L.A. Johansson, J.S. Barton and L.A. Coldren

Department of Electrical and Computer Engineering, University of California, Santa Barbara, CA 93106.
Email: leif@ece.ucsb.edu

G.A. Fish

Agility Communications, Inc., 600 Pine Ave, Santa Barbara, CA 93117.

Abstract: A factor of ten improvement of modulation bandwidth, from 2GHz to 20GHz, is demonstrated using phase modulator monolithically integrated to a semiconductor amplifier and a widely-tunable SG-DBR laser. This is achieved by generating optical frequency modulation converted to intensity modulation in an optical ASE filter.

OCIS codes: (250.5300) Photonic integrated devices; (060.2630) Frequency modulation

1. Introduction

Optical frequency modulation (FM) has been considered mainly for analog or coherent links. A frequency modulated, coherently detected link has been shown to exhibit advantages relative to intensity modulated, directly detected links both in terms of SFDR when the received optical power is limited [1] and available SNR [2]. Frequency modulation combined with an optical frequency discriminator has also been considered for analog links [3] in order to reduce the required drive power and therefore to reduce link loss and improve potential link noise figure. In a discriminator-aided FM-link, the SFDR is determined limited by the nonlinear characteristics of the discriminator and can be improved by using special linearized FM discriminators [4]. Recently, increasing interest has also been focused at alternative modulation formats for data transmission when receiver sensitivity, spectral efficiency, constant envelope, or long haul performance is of importance [5].

Common for most FM links is that a directly modulated semiconductor laser diode is used as source because of the relative ease a frequency modulated output can be produced. The drawback of using directly modulated devices is the modulation bandwidth, typically limited to ~ 10 GHz. Optical phase modulators can produce FM at higher modulation frequencies utilizing the transient chirp preceded by signal integration to produce linear frequency modulation. In this paper, we will show how an optical phase modulator can be used to produce optical frequency modulation by operating beyond the conventional RC -limited bandwidth of the modulator and how this operating point eliminates the requirement for any preceding signal integration. Combined with an optical frequency discriminator, this modulation scheme also provides a method of greatly extending the available bandwidth of optical modulators. In this work, the modulation bandwidth is increased by a factor of ten.

2. Frequency modulation scheme

An optical phase modulator produces an output optical phase dependent on the applied voltage over the modulator. Within the conventional RC -limited bandwidth of the modulator, the phase shift is proportional to the applied signal, ($=V_0$ at DC) and determined by the resistive part of the impedance. The frequency dependence of the phase modulation is given by:

$$\partial\varphi(\omega_m) = \frac{\partial\varphi}{\partial V} \cdot V(\omega_m) = \frac{\partial\varphi}{\partial V} \cdot \frac{1}{j\omega_m RC + 1} \cdot V_0(\omega_m) \underset{\omega_m RC \gg 1}{\approx} \frac{\partial\varphi}{\partial V} \cdot \frac{1}{j\omega_m RC} \cdot V_0(\omega_m) \quad (1)$$

The phase modulation sensitivity is at lower modulation frequency, ω_m , constant, while at higher frequencies inversely proportional to the modulation frequency. The 3-dB bandwidth is given by the RC -constant. Phase modulation can then be converted into amplitude modulation using for example a Mach-Zehnder configuration.

An alternative way of looking at the phase modulator is to consider the frequency modulation at the output of the modulator. The modulator will produce an optical frequency shift, $\delta\omega$, given by:

$$\partial\omega(\omega_m) = -\frac{\partial\phi}{\partial V} \cdot \frac{\partial V}{\partial t} = -\frac{\partial\phi}{\partial V} \cdot \frac{1}{j\omega_m RC + 1} \cdot \frac{\partial\{V_0(\omega_m)\}}{\partial t} \approx \frac{\partial\phi}{\partial V} \cdot \frac{1}{RC} \cdot V_0(\omega_m) \quad (2)$$

At low modulation frequency, the frequency modulation is proportional to the slope of the modulating signal, which increases as the modulation frequency. At high modulation frequency, the increased slope of the modulating signal is compensated by the capacitive roll-off, and the frequency response will be that of a high-pass filter with a 3-dB cut-off frequency again given by the RC -constant. Above the 3-dB point, the frequency dependence of the FM is flat. For a very long modulator, the increased capacitance will be compensated for by increased phase modulation sensitivity, leaving the FM sensitivity constant, according to eq. 2, the low-frequency cut-off will however be improved. The frequency modulated signal can be demodulated in a number of ways, including coherent detection schemes [2] or FM to IM conversion using an optical frequency discriminator [4,6].

When using demodulation by FM to IM conversion, there is a tradeoff in required modulation efficiency and bandwidth. The spectral bandwidth of an FM signal is given by Carson's rule, $B_{FM} \approx 2(\delta\omega + \omega_m)$. The modulation bandwidth is limited by the response of the discriminator, that can only sustain a high slope sensitivity over a limited frequency range. Meanwhile, the instantaneous frequency shift required to achieve a high modulation depth is similarly determined by the discriminator response. A relative comparison of phase modulation and the corresponding frequency modulation of a modulator can be obtained by considering the modulation voltage required to switch the output between maximum and minimum transmission, the equivalent V_π . For frequency modulation, the equivalent V_π is given by the voltage needed to generate a frequency shift of $\delta\omega_\pi$, corresponding to maximum and minimum transmission through the discriminator. From the bandwidth-efficiency limit outlined above, $\delta\omega_\pi$ also roughly corresponds to the bandwidth limit. Assuming a Mach-Zehnder-type discriminator chosen to achieve a FM bandwidth n times that of the modulator RC -limit. Inserting this into equation 2, we obtain the equivalent V_π :

$$V_\pi = \frac{n\pi}{\partial\phi/\partial V_{\max}} \quad (3)$$

The factor of π in the numerator results from the sinusoidal response of the Mach-Zehnder discriminator. The expression for V_π corresponds to the bandwidth-modulation efficiency limit of the corresponding MZ modulator that is obtained by changing the length of the modulator arms, assuming the first order approximation of linear dependency of capacitance to modulator length.

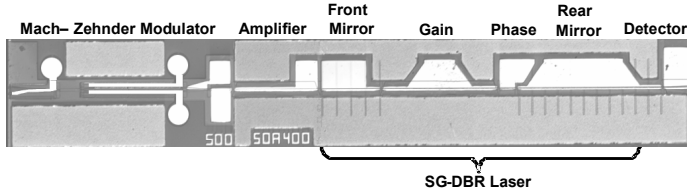


Fig. 1. Outline of SG-DBR laser integrated with an SOA and a Mach-Zehnder modulator.

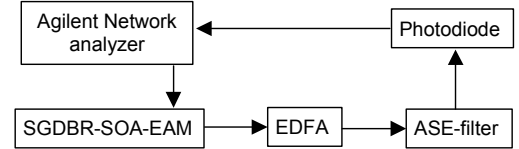


Fig. 2. Outline schematic of experimental Arrangement.

3. Experiment

The monolithically integrated device is similar to that described in [7], where a sampled-grating DBR laser is integrated with a semiconductor optical amplifier and a Mach-Zehnder modulator, all on a single InP-substrate. An outline of the device is shown in Fig. 1. The modulator electrodes are 500 μm long with a 97 μm long 1x2 MMI coupler at the laser input and a 170 μm long 2x2 MMI to the waveguide outputs. The total device length is then 3400 μm long consisting of the 1.75mm SGDBR 0.4mm SOA and 1000 μm MZ device with integrated curved waveguide passive regions at the facets.

Figure 2 shows a schematic of the experimental setup. An Agilent 50GHz network analyzer was used to modulate the phase modulator. For characterization of phase modulation performance, the MZ modulator is biased for maximum slope sensitivity, while for characterization of frequency modulation, one arm of the MZ modulator is reverse biased for absorption such that the output consists only of the output of the second arm. The output of the device is then amplified to compensate for the filter insertion loss. After the EDFA, a 0.4nm optical filter is used, partly to remove the ASE noise and partly to provide an optical frequency dependent element for discriminator FM to IM conversion. The IM signal is then detected by a U^2T photodiode and the output signal is fed back to the Agilent network analyzer.

Figure 3 shows the measured bandwidth using phase modulation and frequency modulation of one arm of the MZ modulator. The phase modulator is unmatched with a bandwidth of 2GHz. The bandwidth of a 50Ω-matched, equally long modulator is on the order of 5GHz. Switching off the output of the second arm, the output consists of the phase/frequency modulated output of the first arm of the MZ-modulator. Tuning the optical filter to maximum slope sensitivity at center frequency, the bandwidth of the modulator is increased by a factor of ten to 20GHz. The measured bandwidth corresponds well to what is expected from the filter FWHM bandwidth; 0.4nm \approx 50GHz at 1566.4nm, the emission wavelength of the SG-DBR laser. A wider bandwidth optical filter will sustain a wider frequency swing and therefore produce a wider modulation bandwidth, though the efficiency of the FM to IM conversion will be compromised.

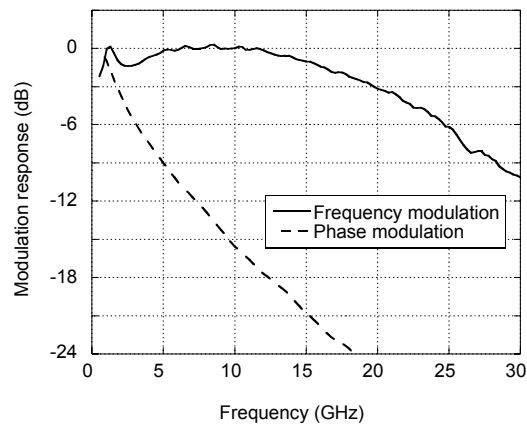


Fig. 3. Measured bandwidth for phase modulation converted to intensity modulation in the Mach-Zehnder modulator and for frequency modulation converted to intensity modulation using an optical frequency discriminator.

4. Summary

In this paper we have showed how an optical phase modulator monolithically integrated to a semiconductor amplifier and a widely-tunable SG-DBR laser can be used to produce optical frequency modulation at modulation frequencies beyond the RC -limited bandwidth of the phase modulator. Combined with FM to IM conversion using an optical frequency discriminator, the available modulation bandwidth is limited to frequencies between the conventional RC -limit on the low frequency side and the maximum frequency swing accommodated by the frequency discriminator. Further, it is shown how the available bandwidth-modulation efficiency product is comparable to that of using phase modulation to intensity modulation conversion in a Mach-Zehnder configuration. The bandwidth-modulation efficiency product can be improved by using a coherent detection scheme, instead of FM to IM conversion. Finally, the described modulation scheme is demonstrated modulating one electrode of a Mach-Zehnder modulator integrated with an SG-DBR laser and an SOA. The available FM bandwidth is shown to increase by a factor of ten, from 2GHz to 20GHz, compared to that of the Mach-Zehnder modulator. The FM bandwidth can be further increased by selecting a frequency discriminator with lower slope sensitivity at the price of lower conversion efficiency.

5. References

- [1] R.F. Kalman, J.C. Fan and L.G. Kazovsky, "Dynamic range of coherent analog fiber-optic links," *IEEE J. Lightwave Technol.*, 12, pp.1263-1277, (1994).
- [2] B. Cai and A.J. Seeds, "Optical frequency modulation links: Theory and experiments," *IEEE Trans. Microwave Theory Tech.* 45, pp 505-511 (1997).
- [3] Qiangsheng Xiang, Yang Zhao and Fow-Sen Choa, "A high-performance RF-lightwave transmitter for analog fiber links," *IEEE LEOS Annual Meeting 2000*, Vol. 1, pp. 13-16 (2000).
- [4] Xiaobo Xie, J. Khurgin, Jin Kang and Fow-Sen Choa, "Ring-assisted frequency discriminator with improved linearity," *IEEE Photon. Technol. Lett.*, 14, pp 1136-1138 (2002).
- [5] A. H. Gnauck, G. Raybon, S. Chandrasekhar, J. Leuthold, C. Doerr, L. Stulz, A. Agrawal, S. Banerjee, D. Grosz, S. Hunsche, A. Kung, A. Marhelyuk, D. Maymar, M. Movassaghi, X. Liu, C. Xu, X. Wei, and D. M. Gill, "2.5 tb/s (64 \times 42.7 Gb/s) transmission over 40 \times 100 km NZDSF using RZ-DPSK format and all-raman-amplified spans," *Proc. OFC, 2002*, Postdeadline Paper FC2.
- [6] G. Fikshan, R. Gross, J. Fan and L. Kazovsky, "Performance optimization of directly modulated FM-SCM systems with optical discriminator," *IEEE Photon. Technol. Lett.*, 5, pp 845-848 (1993).
- [7] J.S. Barton, E.J. Skogen, M.L. Mašanović, S.P. Denbaars, and L.A. Coldren, "Widely-tunable high-speed transmitters using integrated SGDBRs and Mach-Zehnder modulators," to be published in *IEEE J. Sel. Top. Quantum Electron.*

10 Gb/s Mach-Zehnder modulator integrated with widely-tunable sampled grating DBR Laser

Y. A. Akulova, G. A. Fish, P. Koh, P. Kozodoy, M. Larson, C. Schow,
E. Hall, H. Marchand, P. Abraham, L. A. Coldren

Agility Communications, Inc., 475 Pine Ave, Santa Barbara, CA 93117
yakulova@agility.com

Abstract: We report on a sampled grating DBR laser monolithically integrated with a Mach-Zehnder modulator and a semiconductor optical amplifier. Transmission over 100 km of standard fiber at 10 Gb/s is demonstrated across 30 nm tuning range.

© 2003 Optical Society of America

OCIS codes: (250.5300) Photonic integrated circuits; (060.2330) Fiber optics communications

1. Introduction

A compact, high-performance widely-tunable integrated laser/modulator chip is a key component of a tunable transmitter that can dramatically lower the barriers to deployment and operation of high capacity DWDM networks. Several tunable laser technologies with integrated electroabsorption (EA) modulator operating at a bit rate of 2.5 Gb/s and beyond have been demonstrated [1-3]. Integrated transmitters based on EA-modulators although successfully deployed in metropolitan networks have received only limited acceptance in long-haul transmission systems at 10 Gb/s. The main limitations of the EA-modulator are inherent wavelength dependence of extinction ratio (ER) and chirp and trade-off between these characteristics and insertion loss. In contrast to EA-modulators, Mach-Zehnder (MZ) modulators offer the capability of precise control over chirp and extinction ratio over wide wavelength range without introducing excess loss [4]. Co-packaging of a tunable laser with a lithium niobate or III-V MZ modulator is being widely pursued by component manufactures to minimize cost and size of tunable transmitters [5]. The advantage of the co-package approach is the possibility to select laser and modulator chip characteristics independently and to ensure good optical and electrical isolation between the laser and modulator. However, further reduction of package complexity, cost, and size is achievable only through monolithic integration of a laser and a MZ modulator. Reports on a monolithically integrated III-V MZ modulator with a very narrowly-tunable gain-coupled DFB laser have demonstrated feasibility of integration and acceptable system performance at 2.5 and 10 Gb/s [6].

In this paper we discuss the design and performance of a widely tunable transmitter chip based on a Sampled Grating Distributed Bragg Reflector (SG-DBR) laser monolithically integrated with a semiconductor optical amplifier (SOA), and a Mach-Zehnder modulator (MZM). Negative and zero chirp of the transmitted signal were demonstrated by adjusting the drive voltages for two arms of MZM. Error-free transmission at 10 Gb/s for 100 km of standard single mode fiber over 30 nm wavelength range has been demonstrated for the first time for a widely-tunable laser monolithically integrated with a modulator.

2. Device design and fabrication

As illustrated in Fig. 1, the device consists of a four-section SG-DBR laser, an SOA, and a MZM, all integrated on the same InP chip. The integrated SOA compensates on-state modulator loss and cavity losses caused by free carrier absorption in the tuning sections and allows wavelength independent power leveling, beam blanking during wavelength switching, and variable optical attenuator functionality. The MZ modulator consists of two multi-mode interference (MMI) sections with curved waveguides and 400 um long lumped electrodes. The integration of the laser and SOA active regions with the tuning and modulator sections of the device has been accomplished by using an offset quantum-well structure [7]. In this simple integration technology the active region of the modulator uses the same bulk quaternary waveguide as the tuning sections of the laser. The composition of the bulk waveguide can be optimized to achieve high tuning efficiency for the laser and a target V_{π} over the required wide spectral bandwidth for the modulator. The device is fabricated using shallow-ridge technology to ensure low optical reflections as compared to the deep-ridge structures due to reduced index step between optical waveguides and MMI

sections [8]. An angled waveguide and wide-band anti-reflection coating at the output of the device were used to suppress the facet feedback.

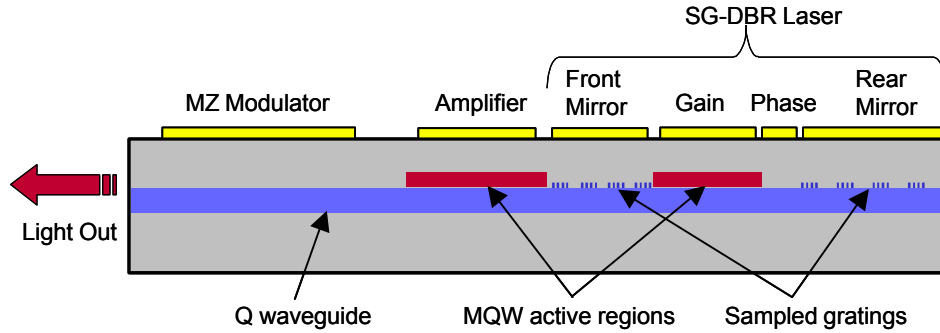


Fig. 1. Schematic of SG-DBR laser integrated with SOA and MZ modulator.

3. Results and discussion

The fabricated devices were mounted on ceramic carriers with co-planar waveguides and integrated matching resistors. For transmission measurements the chip-on-carrier was packaged into a cooled butterfly module with a co-planar RF input.

The output power vs. wavelength for a SG-DBR-SOA-MZM chip is shown in Fig. 2a). For this measurement the nominally π -phase shifted MZM is biased to produce differential phase shift of 0 radians between the two arms. The integrated chips are capable of producing more than 15 mW of power across 40 nm tuning range in the C-band. Figure 2b) shows normalized transmission characteristics for a packaged SG-DBR-SOA-MZM chip at three wavelength across C-band. DC ER in excess of 20 dB is achieved with less than 3.3 V. In single-ended drive configuration RF ER of 12 dB was measured across 40 nm tuning range with less than 3 V peak-to-peak modulation voltage (Fig. 2c).

The key for achieving uniform transmission performance of the integrated SG-DBR-SOA-MZM transmitter over wide wavelength range is in eliminating optical and electrical crosstalk and precise control of the transient chirp of the modulator. Measurements of the time-resolved chirp characteristics of the integrated chips confirmed that extrinsic chirp components due to optical feedback or electrical crosstalk are completely eliminated. The remaining chirp component is transient chirp determined by a MZM design and drive conditions. The transient chirp of p-i-n InP MZ modulator is a function of electrooptic properties of active material, splitting ratio of the two MMI sections, the differential phase shift between two arms, and the format of the modulation voltages applied to each arm of the modulator [9]. These features provide flexibility of optimizing device performance for zero or negative chirp over wide wavelength range. Figure 2c) shows wavelength dependence of the effective α -parameter extracted from the time-resolved chirp characteristics in a 3 dB region of the most transparent state of the modulator in single-ended drive configuration. Uniform chirp of -0.74 ± 0.1 is maintained across the tuning range.

Figure 3a) shows output and transmitted eye diagrams for dual- and single-ended drive conditions at 10 Gb/s for a π -shifted MZM. Maximum peak-to-peak modulation voltage for 12 dB RF ER across the C-band is 1.5 and 3 V for dual- and single-ended drive, respectively. The dual-drive condition results in “zero” chirp configuration, while single-ended operation results in “negative” chirp. Wide open eye diagrams after 50 km (“zero” chirp) and 100 km (“negative” chirp) of standard non-dispersion shifted fiber indicate that the integrated chips are capable of meeting stringent requirements for 10 Gb/s transmission. The back-to-back and 100 km BER curves were measured for negative chirp configuration for three wavelength across C-band. The lowest wavelength for this measurement was limited to 1535 nm by the tunable bandpass filter. The BER data presented in Fig. 3 b) shows error free transmission for 1600-1800 ps/nm dispersion for 1535-1563 nm wavelength range. Evaluation of dispersion penalty for longer transmission distances is currently in progress.

4. Summary

In summary, we have demonstrated a widely-tunable, 10 Gb/s transmitter chip based on a SG-DBR laser monolithically integrated with a SOA and MZ modulator. RF extinction ratio > 12 dB with less than 3 V modulation

voltage and negative chirp across a 40 nm tuning range have been achieved. Error-free transmission at 10 Gb/s has been demonstrated for 100 km of standard single mode fiber.

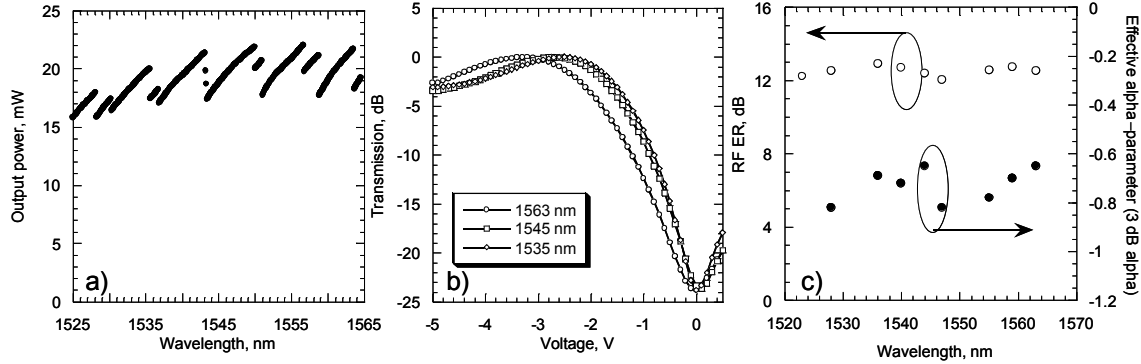


Fig. 2. a) Unlevelled SG-DBR-SOA-MZM output power across the tuning range. b) Normalized transmission characteristic for three wavelengths. c) RF ER and 3 dB alpha parameter in single-ended drive configuration across the tuning range.

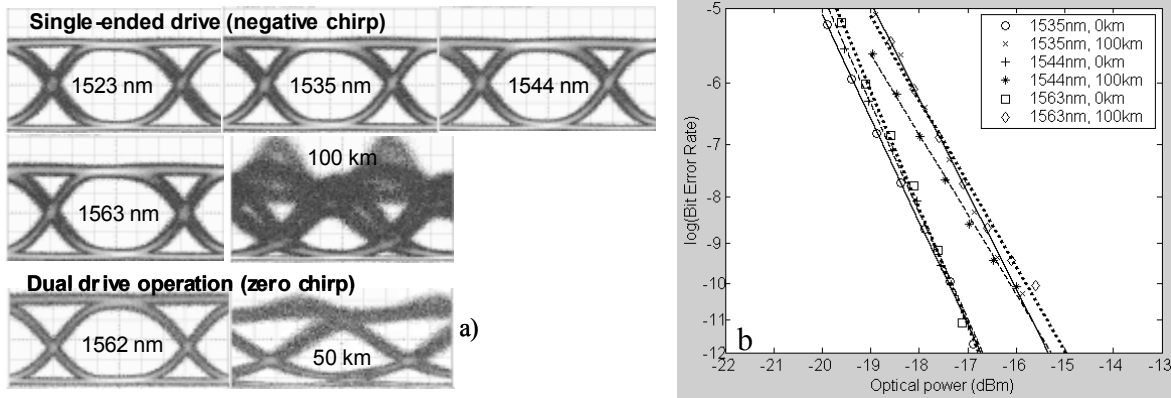


Fig. 3. a) Output eye diagrams and eye after fiber in single and dual drive configurations. b) Bit error rate curves for 0 and 100 km of standard single-mode fiber spans for three different wavelengths (10 Gb/s NRZ, $2^{21}-1$ PRBS).

5. References

- [1] J.E. Johnson, L.J.-P. Ketelsen, D.A. Ackerman, Zhang Liming, M.S. Hybertsen, K.G. Glogovsky, C.W. Lentz, W.A. Asous, C.L. Reynolds, J.M. Geary, K.K.; Kamath, C.W. Ebert, M. Park, G.J. Przybylek, R.E. Leibenguth, S.L. Broutin, and J.W. Stayt, Jr, "Fully stabilized electroabsorption-modulated tunable DBR laser transmitter for long-haul optical communications", *IEEE J. Select. Topics Quantum Electron.*, **7**, 168-177 (2001).
- [2] T. Marimoto, K. Yashiki, K. Kudo, and T. Sasaki, "Wavelength-selectable microarray light sources for DWDM photonics networks", *IEICE Trans. Electron.*, **E85-C**, 982-989 (2002).
- [3] Y.A. Akulova, G.A. Fish, Ping-Chiek Koh, C.L. Schow, P. Kozodoy, A.P. Dahl, S. Nakagawa, M.C. Larson, M.P. Mack, T.A. Strand, C.W. Coldren, E. Hegblom, S.K. Penniman, T. Wipiejewski, L.A. Coldren, "Widely tunable electroabsorption-modulated sampled-grating DBR laser transmitter", *IEEE J. Select. Topics Quantum Electron.*, **8**, 1349-1357 (2002).
- [4] J.S. Barton, E.J. Skogen, M.L. Masanovic, S.P. DenBaars, L.A. Coldren, "Tailorable chirp using integrated Mach-Zehnder modulators with tunable sampled grating distributed Bragg reflector lasers", *Proc. IEEE 18th International Semiconductor Laser Conference*, 49-50 (2002).
- [5] R. A. Griffin, R. I. Johnstone, R. G. Walker, J. Hall, S. D. Wadsworth, K. Berry, A. C. Carter, M. J. Wale, J. Hughes, P. A. Jerram, and N. J. Parsons, "10Gb/s optical differential quadrature phase shift key (DQPSK) transmission using GaAs/AlGaAs Integration", *OFC'02, FD6-1* (2002).
- [6] C. Rolland, "InGaAsP-based Mach-Zehnder modulators for high-speed transmission systems", *OFC Technical Digest*, 283-284 (1998).
- [7] B. Mason, G. A. Fish, S. P. DenBaars, and L. A. Coldren, "Widely tunable sampled grating DBR laser with integrated electroabsorption modulator", *IEEE Photon. Technol. Lett.*, **11**, 638-40 (1999).
- [8] S. Lovisa, N. Bouche, H. Helmers, Y. Heymes, F. Brillouet, Y. Gottesman, K. Rao, "Integrated laser Mach-Zehnder modulator on indium phosphide free of modulated-feedback", *IEEE Photon. Technol. Lett.*, **13**, 1295-1297 (2001).
- [9] C. Lawetz, J.C. Cartledge, C. Rolland, J. Yu, "Modulation characteristics of semiconductor Mach-Zehnder optical modulators", *J. of Lightwave Technol.*, **15**, 697-703 (1997).

Wavelength Agile, Integrated Analog Optical Transmitters

G. A. Fish, Y. A. Akulova, and L. A. Coldren

Agility Communications, Inc., 475 Pine Ave, Santa Barbara, CA 93117

1-(805) 690-1722 / gfish@agility.com

L. A. Johansson, L. A. Coldren

Department of Electrical and Computer Engineering University of California, Santa Barbara, CA 93106

1-(805) 893-4543 / leif@ece.ucsb.edu

Abstract

We report on analog modulation characteristics of a widely-tunable sampled grating DBR laser monolithically integrated with an electroabsorption or Mach-Zehnder modulators and a semiconductor optical amplifier. A sub-octave SFDR of 125-127 dB/Hz^{4/5} and a broadband SFDR of 103-107 dB/Hz^{2/3} limited by third order intermodulation products is demonstrated over a 1528 to 1573 nm wavelength range.

1. INTRODUCTION

Analog optical links have found applications areas such as wireless over fiber or antenna remoting for radar applications. In both cases, the optical link provides a low loss, wide band with medium, transparent to modulation format. The antenna units can be simplified, while system complexity can be located at a centralized location. The merging of WDM and wireless over fiber technologies will further enhance system reconfigurability and capacity, particularly for wireless over fiber applications [1]. Signal routing will enable dynamic allocation of radio resources and increased overall system capacity.

In this work, we have investigated the performance of an integrated photonic transmitter module based on a monolithically integrated InP chip comprising of a sampled-grating distributed Bragg grating (SG-DBR) laser, a semiconductor optical amplifier (SOA), and an electroabsorption modulator (EAM) or a Mach-Zehnder modulator (MZM), for high-performance analog optical link application. The paper is structured as follows. In section 2, a brief overview of the SG-DBR laser platform that these analog transmitters are based upon is presented. In section 3.2, the performance of transmitter including an EAM is reviewed. The performance of transmitters including a MZM is summarized in section 3.2, and the summary, section 4 gives a brief comparison of the performance of the two types of transmitters.

2. DEVICE DESIGN AND FABRICATION

As illustrated in Figure 1, the device consists of a four-section SG-DBR laser, an SOA, and an EAM or MZM, all integrated on the same InP chip. Formed by sampling (periodically blanking) front and back grating mirror sections longitudinally integrated in-plane with active and phase tuning sections, the SG-DBR lasers rely on refractive index tuning through current injection combined with the vernier effect for wide (>40 nm) wavelength coverage [2]. The integration of the laser and SOA active regions with the tuning and modulator sections of the device has been accomplished by using an offset quantum-well structure. In this simple integration technology the active region of the modulator uses the same bulk quaternary InGaAsP waveguide as the tuning sections of the laser. The composition of the bulk waveguide can be optimized to achieve high tuning efficiency for the laser and a target V_p over the required wide spectral bandwidth for the modulator. The developed integration technology is compatible with reliable, low cost, wafer-scale InP manufacturing process. The monolithic integration of laser and modulator also results in reduced cost and complexity of the package assembly [3].

3. DEVICE CHARACTERISTICS

3.1 EAM Transmitter

The spurious-free dynamic range (SFDR) of the packaged SG-DBR-SOA-EAM device was measured at 0.5 GHz using two-tone modulation at 1 MHz offset of between -5 dBm to 8 dBm modulation power each. Figure 2a shows the broadband and sub-octave spurious-free dynamic range, both for 1Hz and 1MHz noise bandwidth. The broadband SFDR is taken at 1552 nm, 180mA bias current to gain section and SOA and at the bias point of minimum second order distortion. The noise level is -157 dBm/Hz, limited by shot noise and laser RIN. The SFDR limited by second order distortion is 97.19 dB in 1 Hz bandwidth and the SFDR limited by third order distortion is 106.09 dB in 1 Hz

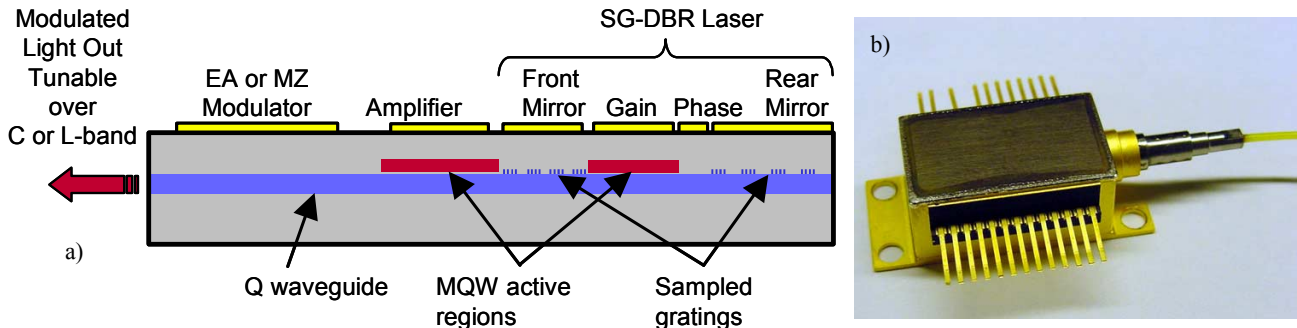


Figure 0 a) Schematic cross-section of an SGDBR-SOA-Modulator chip (chip dimensions 3x0.5 mm²). b) Packaged widely-tunable optical transmitter (package size 1x0.5x0.5 in³).

bandwidth, corresponding to 66.09 dB in 1 MHz bandwidth. The broadband SFDR was also measured at several wavelengths over the tuning range of the laser. At each wavelength the dc bias on the modulator was adjusted to the minimum second order distortion. The SFDR remains within a 103-107 dB/Hz^{2/3} range limited by third order intermodulation products, dominant for noise bandwidths above 1MHz, or 95-98 dB/Hz^{1/2} range limited by second order intermodulation products. The sub-octave SFDR is taken at 1552 nm, 180mA bias current to gain section, 120 mA SOA bias and at the bias point of minimum third order distortion (Figure 2b). The noise floor is mainly limited by shot noise. The SFDR is 126.28 dB in 1 Hz bandwidth and remains within a 125-127 dB/Hz^{4/5} range, all limited by fifth order intermodulation products over the tuning range of the laser. RF gain of +10.5 dB and noise figure of 5.07 dB were simultaneously measured for pre-amplified optical link.

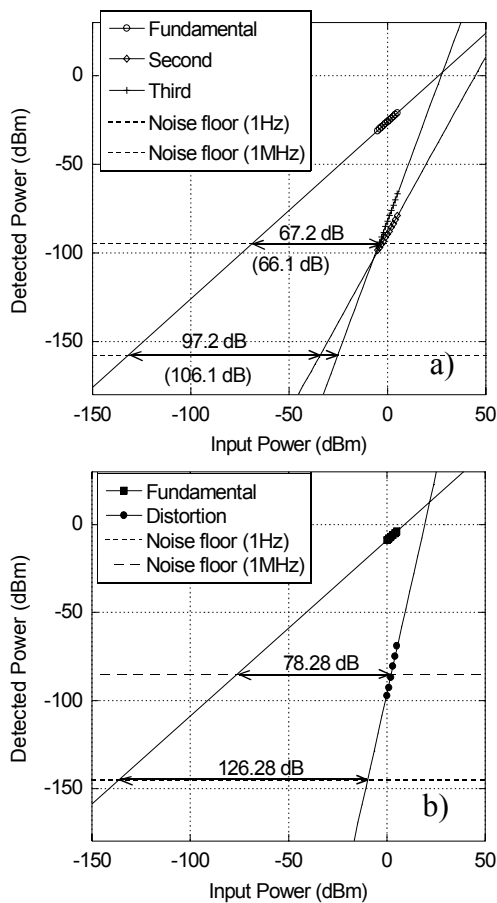


Figure 1 a) Power of noise floor, fundamental, second and third order intermodulation products at -1.1V EAM bias. Broadband SFDR is shown in 1Hz and 1MHz bandwidth. b) Power of noise floor, fundamental and third order intermodulation products at -2.5 V EAM bias. Sub-octave spurious-free dynamic range is also shown in 1Hz and 1MHz bandwidth.

The spurious-free dynamic range (SFDR) of the device is measured using two-tone modulation at 1 MHz offset of between -5 dBm to 8 dBm modulation power each.

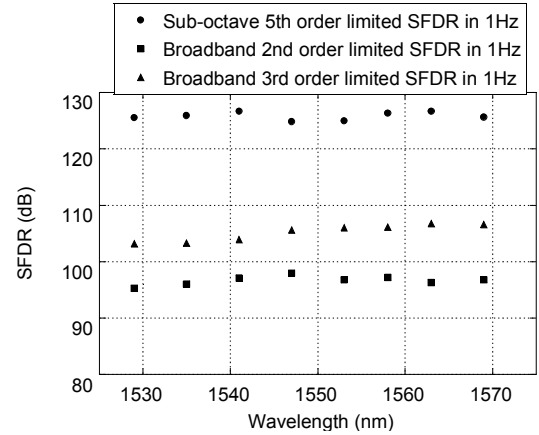


Figure 2 Measured sub-octave and broadband spurious-free dynamic range, left scale, normalized to 1 Hz bandwidth for different wavelengths. Sub-octave SFDR limited by fifth shown is relative effect on SFDR from the RIN level of the order intermodulation products and broadband SFDR limited source.

Figure 1 a) and b) show the broadband and sub-octave spurious-free dynamic range, both for 1Hz and 1MHz noise bandwidth. The broadband SFDR is taken at 1552 nm, 180mA bias current to gain section and SOA and at the bias point of minimum second order distortion. The noise level is -157 dBm/Hz, limited by shot noise and laser RIN. The SFDR limited by second order distortion is 97.19 dB in 1 Hz bandwidth and the SFDR limited by third order distortion is 106.09 dB in 1 Hz bandwidth, corresponding to 66.09 dB in 1 MHz bandwidth. Figure 2 shows the broadband SFDR over the tuning range of the laser. The SFDR remains within a 103-107 dB/Hz^{2/3} range limited by third order intermodulation products, dominant for noise bandwidths above 1MHz, or 95-98 dB/Hz^{1/2} range limited by second order intermodulation products. The sub-octave SFDR is taken at 1552 nm, 180mA bias current to gain section, 120 mA SOA bias and at the bias point of minimum third order distortion. The noise floor is mainly limited by shot noise. The SFDR is 126.28 dB in 1 Hz bandwidth and remains within a 125-127 dB/Hz^{4/5} range, all limited by fifth order intermodulation products over the tuning range of the laser, Figure 2.

3.2 Mach-Zehnder Transmitter

The Mach-Zehnder modulator has a number of advantages compared to EA modulators. First of all, the RF link gain of a EA modulated optical link becomes limited by the absorbed photocurrent [4]. MZ modulators do not have this limitation, being based on interferometric modulation. Second, by choosing inverting, non-inverting or a combined push-pull modulation, the modulator chirp can be controlled from positive to negative values. In terms of linearity, Mach Zehnder modulators have one disadvantage. With its sinusoidal response, the third order inflection points appear at the same bias point as zero slope sensitivity, limiting the available sub-octave SFDR [5]. Figure 1 shows a simple schematic of an SG-DBR laser integrated to an SOA and a Mach-Zehnder modulator. Since the MZ modulator is defined in the same material and with the same fabrication steps as the SG-DBR laser and SOA, the fabrication process is not

much more complex than for the SG-DBR laser alone. The composition of the bulk waveguide can be optimized to achieve high tuning efficiency for the laser and a target V_p over the required wide spectral bandwidth for the modulator. The length of the electrodes of the Mach-Zehnder is in the 300 μm to 700 μm range.

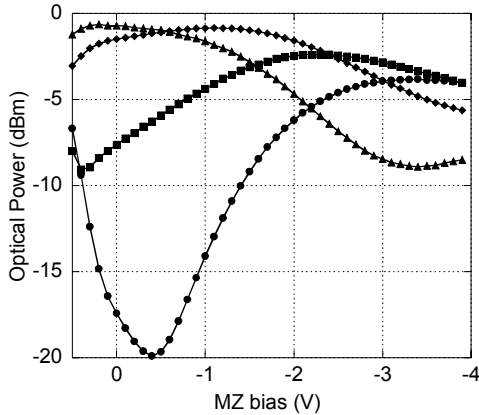


Figure 3 Typical extinction curves for various differential MZ phase settings.

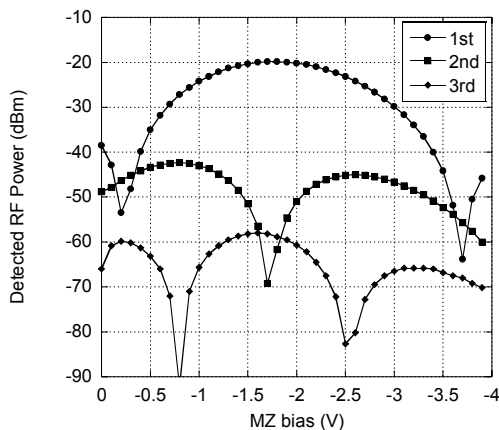


Figure 4 Detected RF power of fundamental and intermodulation products for 0 dBm modulation power.

Figure 3 shows a typical set of extinction curves for different values of phase difference between the arms of the Mach-Zehnder. In order to achieve high extinction, both the phase and the amplitude of the field passing through the arms of the Mach-Zehnder need to be matched. When both arms are biased around 0V, good extinction is achieved by design. When the phase offset is tuned to a different value, the available extinction ratio is obtained away from 0V and is degraded. The reason is the onset of Franz-Keldysh absorption in the bulk material. This can be a problem for digital applications and is the reason that it has been designed for good extinction around 0V. For analog applications, the altered response of the Mach-Zehnder can be taken advantage of in order to enhance the SFDR of the modulator. This is illustrated in Figure 4 for 300 μm electrode length, where the detected power of fundamental, second and third order intermodulation products are plotted as a function of MZ bias. As expected, the points of minimum second order distortion

coincides with the point of maximum slope efficiency. However, unlike the typical Mach-Zehnder modulator, the points of maximum second order distortion, and therefore minimum third order distortion, do not coincide with minimum power of the fundamental. Therefore, by tuning the MZ bias point for minimum third order distortion, there is only about 3.3 dB penalty in the RF power of the fundamental, and optimized linearity for sub-octave applications is obtained. At this bias point, the sub-octave SFDR is 107.5 dB/Hz^{2/3}, limited by third order intermodulation products as shown in Figure 6. The broadband SFDR is obtained by choosing the bias point where second order distortion has a minimum and is 92.8 dB/Hz^{2/3}, when limited by second order distortion or 103.6 dB/Hz^{2/3}, when limited by third order distortion products, as show in Figure 7. In both cases, the noise floor was limited mainly by shot noise. It is worth noting that even though the fiber coupled output power of the MZ-devices, a peak 2mW, was much smaller than for the EA-devices, a peak 10mW, the broadband SFDR was comparable for both devices. MZ-devices with similar output power as the EA-devices should deliver improved broadband SFDR.

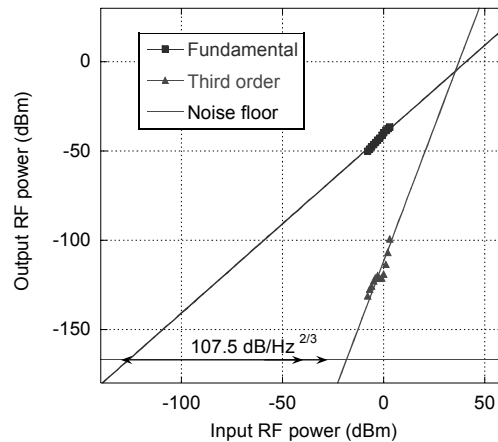


Figure 5 Measured power of noise floor, fundamental and 3rd order intermodulation products at 1547 nm.

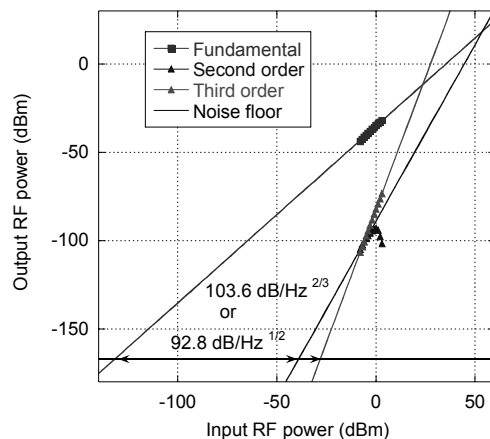


Figure 6 Measured power of noise floor, fundamental, 2nd and 3rd order intermodulation products at 1547 nm.

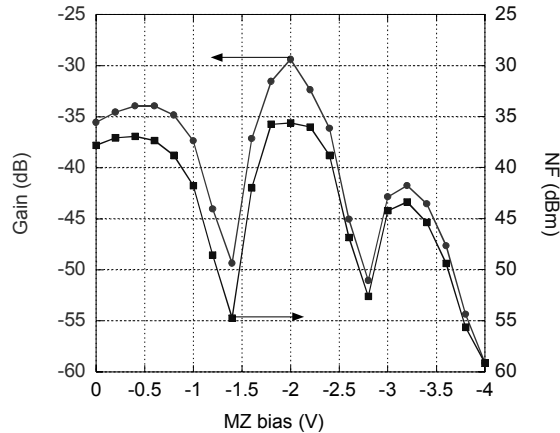


Figure 7 MZ-modulated link gain and noise figure as a function of electrode bias point.

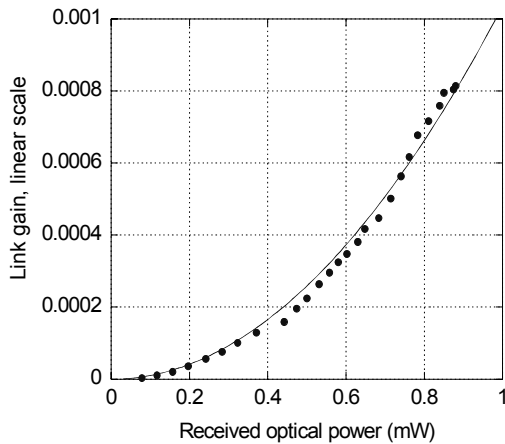


Figure 8 MZ-modulated optical link gain as a function of received optical power.

A 700 μm electrode MZ-device was used for a link experiment, measuring link gain and noise figure. The longer electrode length was chosen to improve gain and noise figure in the absence of any preamplification. The link gain peaks at slightly above -30 dB, with an attributed noise figure of just below 35 dB, as shown in Figure 7. Again, despite that the peak output power is about five times lower for the MZ-devices than for the EA-devices, the link noise figure is comparable, mainly as a result of the steeper slope sensitivity of the long electrode MZ. A second contributing reason is the fact that this is an interferometric modulator, not as severely affected by that the absorbed photocurrent that had such a drastic impact on the response of the EA-devices. In fact, plotting the link gain on a linear scale as a function of received optical power (Figure 8), an almost perfect square relationship between link gain and power is obtained, indicating no compression of the modulator response with optical power. This relationship may be extrapolated at higher output power, such that a MZ-device with 10mW peak output power would have superior link performance of the corresponding EA-device.

4. SUMMARY

In this paper, SG-DBR laser based devices integrated to an SOA and either an electroabsorption modulator or a Mach-Zehnder modulator have been investigated for application as an analog transmitter. The performance has been evaluated in terms of spurious-free dynamic range, conversion efficiency and link noise figure. Using the EA device, a sub-octave SFDR of 126.3 dB/Hz^{4/5} and a broadband SFDR of 106.1 dB/Hz^{2/3} limited by third order intermodulation products or 97.2 dB/Hz^{1/2}, limited by second order intermodulation products is measured. A link gain up to -20.7 dB and noise figure up to 32.1 dB is also measured. For the MZ-device, the sub-octave SFDR was slightly worse, 107.5 dB/Hz^{2/3}, mainly determined by the lower output power of the MZ-device and the third order power dependence of the distortion. The broadband SFDR was comparable to the EA-modulator at 103.6 dB/Hz^{2/3} limited by third order intermodulation products or 92.8 dB/Hz^{1/2}, limited by second order intermodulation products. A link gain of -30 dB and noise figure of 35 dB is measured. These numbers would greatly benefit from higher output power as the MZ-modulator is not limited by photocurrent effects.

5. ACKNOWLEDGEMENTS

This work was in part funded by DARPA/MTO under the RFLICS program and in part under the CS-WDM program.

6. References

- [1] C. Lim, A. Nirmalathas, M. Attygalle, D. Novak, R. Waterhouse, "The merging of a WDM fiber-radio backbone with a 25 GHz WDM ring network," *2003 IEEE MTT-S Microwave Symposium Digest*, vol.1, pp. 273 -276, June 8-1,3 2003.
- [2] V. Jayaraman, Z.-M. Chuang, L. A. Coldren, "Theory, Design, and Performance of Extended Tuning Range Semiconductor Laser with Sampled Grating", *IEEE J. of Quantum Electron.*, 29, pp. 1824–1834, 1993.
- [3] Y. A. Akulova, G. A. Fish, P. C. Koh, C. Schow, P. Kozodoy, A. Dahl, S. Nakagawa, M. Larson, M. Mack, T. Strand, C. Coldren, E. Hegblom, S. Penniman, T. Wipiejewski, and L. A. Coldren, "Widely-Tunable Electroabsorption-Modulated Sampled Grating DBR Laser Transmitter", *IEEE Journal on Selected Topics in Quantum Electronics*, 8, pp. 1349-1357, 2002.
- [4] G.L. Li, P.K.L. Yu, W.S.C. Chang, K.K. Loi, C.K. Sun and S.A. Pappert, "Concise RF equivalent circuit model for electroabsorption modulators," *Electron. Lett.* 36, pp. 818-820, 2000.
- [5] M. Farwell, W. Chang, and D. Huber, "Increased linear dynamic range by low biasing the Mach-Zehnder modulator," *IEEE Photon. Technol. Lett.*, 5, pp. 779-782, Jul. 1993.

7. BIBLIOGRAPHY (IES)

None available at the time of submission.

High-efficiency ‘receiverless’ optical interconnects

Larry A. Coldren, University of California, Santa Barbara, CA 93106

Joe C. Campbell, University of Texas, Austin, TX

The objective of this work is to develop new chip-to-chip optical interconnect architectures using novel transmitter and receiver modules for terabit data throughput in multi-chip modules. High-efficiency, high-speed, high-power photodetectors and integrated surface-emitting laser-modulators are being explored to enable minimal or no additional electronics at the receiver.

On the transmitter side we are developing high-efficiency, high-power, ~980 nm, integrated in-plane laser-modulator arrays for this architecture. Quantum-well intermixing (QWI) is being used to define the grating and modulator regions as well as for lateral carrier confinement. New levels of power efficiency are expected in a relatively small footprint. The QWI can provide simultaneous optimization of the gain and modulator characteristics for high power (~20mW), modulation bandwidth (~40GHz), and low modulation voltage. CAIBE etched 45-degree facets at the end of the modulator will be explored in the future for reduced back reflections and vertical emission through the substrate. In this case monolithically integrated microlenses on the backside of the substrate will also be investigated. Comparisons of this architecture to alternative VCSEL approaches will be given.

“Digital” receiver circuits in which the photodiodes are directly connected to the logic circuitry are being developed. In order to generate the required drive voltage, it is necessary for the photodiode to operate at higher input optical power levels than telecommunication optical receivers. Conventional photodiode structures exhibit saturation at high frequencies. Recently, we have designed and characterized a new photodiode structure that has achieved a record current-bandwidth product of >1000mA GHz to above 40 GHz. These photodiodes are uniquely positioned to directly drive digital logic circuits with no degradation in the frequency response.

As illustrated in Fig. 1, an in-plane surface-emitting laser-modulator (IPSEL-Mod) array having elements with short cavities and highly-reflecting rear mirrors for high efficiency, high power, and high speed at relatively high temperatures is being developed. Wavelengths of both 980nm (GaAs-based) and 1300 nm (InP-based) are being will investigated. Also illustrated in Fig. 1 are backside microlenses. These have been previously developed on the backside of VCSELs and will be explored in the future. Elliptical shapes will be explored for collimation into circular beams.

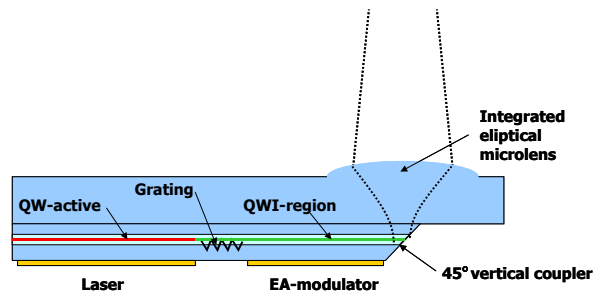


Figure 1. In-plane surface-emitting laser with integrated EA-modulator (IPSEL-Mod).

In the photodetector high saturation current at high bandwidth is required. In order to reduce the space charge effect and thus increase the operating current, we have developed an $\text{In}_{0.53}\text{Ga}_{0.47}\text{As}$ photodiode with a partially depleted absorber (PDA). The primary motivation for the PDA structure is charge balance in the depletion region, which reduces the space-charge effect. A schematic cross section and initial frequency response data is shown in Figure 2. Unlike conventional, long-wavelength PINs, for the PDA structure, the $\text{In}_{0.53}\text{Ga}_{0.47}\text{As}$ depletion region is sandwiched between p-type and n-type undepleted $\text{In}_{0.53}\text{Ga}_{0.47}\text{As}$ absorbers. The doping in the undepleted absorbers is graded to build in a small electric-field ($\sim 10^3\text{V/cm}$) to facilitate transport into the depletion region. In a conventional p-i-n photodetector the electron-hole pairs are generated in the i-region and travel in opposite directions. Since the overshoot velocity of electrons is much higher than the saturation velocity of holes, the i-region of a conventional p-i-n photodetector is strongly influenced by the hole density. For the PDA photodiode, there is a p-doped absorber and an n-doped absorber on each side of the i-region. The p-doped absorber injects electrons into the i-region while the n-doped absorber injects holes. However, electron injection is much stronger than that of holes due to the different thickness of the absorber on each side. By proper design, the electron and hole currents can be tailored to greatly reduce the space charge effect, i.e., electron injection from the p-side into the i-region can balance the hole-dominated i-region.

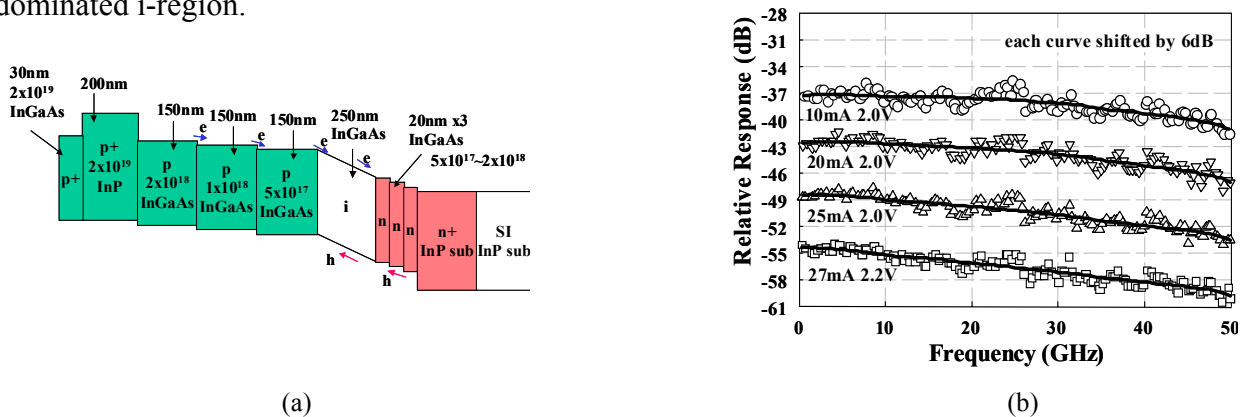


Figure 2. (a) Partially-depleted-absorber photodiode structure. (b) Frequency response of 8 μm -diameter partially-depleted-absorber photodiode.

This new photodiode achieved a compression current of 27mA at 40 GHz, which yields a saturation current-bandwidth product $>1000\text{mA}\cdot\text{GHz}$. An 18 μm -diameter device achieved an output power level of 10 dBm at 20 GHz (41 mA, 2.2 V). The PDA structure has achieved the highest current-bandwidth products reported to date for any photodetector.

In summary, new advances in overall link power efficiency are anticipated at higher data rates ($>20\text{Gb/s}$) with a combination of novel integrated laser-modulators capable of delivering relatively high output powers ($>10\text{mW}$) at the transmitter side and high-saturation power photodetectors directly coupled to the electronic logic circuits at the receiver side. Electronic driver and receiver circuits identical to those being developed on longer distance on-chip electrical interconnects should be useable to avoid any further on-chip O/E interface electronics.

Efficient, Integrated Optical Transmitters for High-Speed Optical Interconnect Applications

Chad S. Wang[†], Erik J. Skogen[†], Gordon B. Morrison[†], James W. Raring^{*}, and Larry A. Coldren^{†*}

[†]ECE Dept. University of California, Santa Barbara, CA 93106
^{*}Materials Dept. University of California, Santa Barbara, CA 93106

Phone: 805.893.7065, Fax: 805.893.4500, Email: cswang@engineering.ucsb.edu

1. SUMMARY

For a variety of fiber optic data link, optical access, and computer interconnect applications, it is desired to have a coolerless, small-footprint, high-speed, high-efficiency transmitter in the 1300 – 1550 nm range. Chip to chip optical interconnects (C2OI) have the potential to demonstrate numerous advantages over traditional electrical I/O integrated circuits. Applications requiring high bandwidth-path length products will be best served through an optical free-space type interconnect [1]. This technology will also lead to advantages in power dissipation, crosstalk, and susceptibility to electro-magnetic interference (EMI) than electrical connections. Highly integrated transmitters would also be desired for low cost as well as the prospect of generating arrays of such elements.

In order to meet and exceed existing electrical I/O specifications, it is necessary to design and develop short cavity lasers with a small footprint (<250 μm pitch), high efficiency, low power dissipation, and high output power. Here we demonstrate a short cavity, high output power, single mode, high efficiency, distributed Bragg reflector (DBR) laser, monolithically integrated with an electro-absorption modulator (EAM). The devices were fabricated in the InGaAsP/InP material system and exhibited both good static and dynamic characteristics.

The short-cavity DBR lasers were designed to have a high-reflectivity (HR) rear mirror, short gain section (150 μm), and front DBR mirror (40 μm). The DBR lasers were monolithically integrated with an optional semiconductor optical amplifier (SOA) (75 & 110 μm) and EAMs (75 – 175 μm) using a quantum well intermixing processing platform that allows for the formation of a unique quantum well band edge for each integrated component. With this process it is possible to achieve any number of band-edges across the wafer, limited only by the practical number of lithographic process steps as shown in Fig. 1a and 1b. Therefore, each component of the device can be tailored for optimum performance. For this work, three band-edges were needed: the as grown band-edge for the gain regions ($\lambda_{\text{pl}} = 1540$ nm), a band-edge ideal for the EAM ($\lambda_{\text{pl}} = 1500$ nm), and a band-edge used in the low loss passive waveguide regions ($\lambda_{\text{pl}} = 1430$ nm). The photoluminescence curves for the band-edges used in this work are shown in Fig. 1c. The epitaxial base structure and fabrication details are given in Ref. 2. Fig. 2 illustrates this integrated laser-modulator.

The devices demonstrated both good static and dynamic characteristics. A low threshold current of 7 mA was measured, and output powers greater than 10mW were achieved with a gain section current of 30 mA, as shown in Fig. 3a. The wall plug efficiency exceeded 18%. The DBR lasers also demonstrated single-mode emission at 1543 nm with a SMSR greater than 40 dB, as shown in Fig 3b. The DC modal extinction characteristics of a 125 μm long EAM are presented in Fig. 3c. Greater than 20 dB optical extinction was measured at a reverse bias of 4 V. Modulation bandwidths were measured to be 25 GHz, and open eye diagrams were achieved at 10 Gbit/s NRZ bit patterns, as shown in Fig. 4a and 4b.

A first-generation of small footprint, high power laser-modulator devices have been designed, fabricated, and tested. The devices employed a QWI-based processing platform for the monolithic integration of multiple section photonic integrated circuits. Lasers exhibited excellent characteristics in terms of output power (>10 mW) and wall plug efficiency (>18%). The modulator demonstrated >20 dB DC extinction at a length of 125 μm , with 3 dB bandwidths up to 25 GHz. Taken together, the next generation of long-wavelength efficient transmitters will be implemented into arrays with vertically coupled output emission. Efficient transmitters in the 980 nm and 1300 nm wavelength range are also beginning to be explored.

2. REFERENCES

- [1] M. R. Feldman, S. C. Esener, C. C. Guest, and S. H. Lee, "Comparison between optical and electrical interconnects based on power and speed considerations," *Applied Optics*, vol. 27, pp. 1742-1751, 1988.
- [2] E. J. Skogen, C. S. Wang, J. W. Raring, G. B. Morrison, and L. A. Coldren, "Small Footprint, High-Efficiency, Integrated Transmitter for High-Speed Optical Interconnect Applications," to be published at *Integrated Photonics Research Conference 2004*.

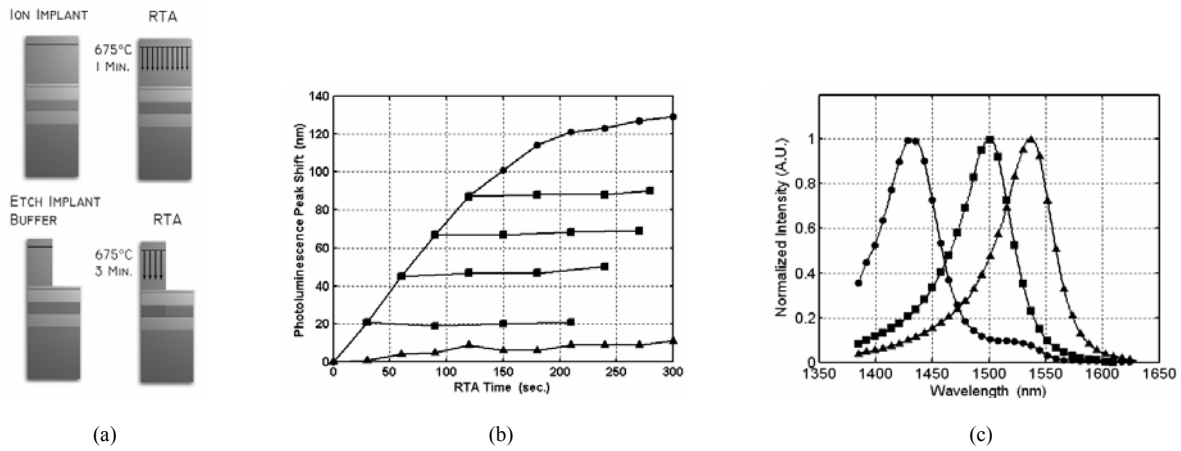


FIGURE 1. (a) Illustration of the intermixing processing platform used in this work. (b) Peak photoluminescence peak shift as a function of anneal time, showing the initial linear increase in the peak shift and the complete halting of the peak shift for samples for which the implant buffer layer has been etched. Symbols indicate non-implanted (triangles), implanted (circles), and samples with partial anneal followed by the removal of the implant buffer layer (squares). (c) Photoluminescence spectra for device shown in this work. Symbols indicate active region photoluminescence (triangles), EAM photoluminescence (squares), and passive section photoluminescence (circles).

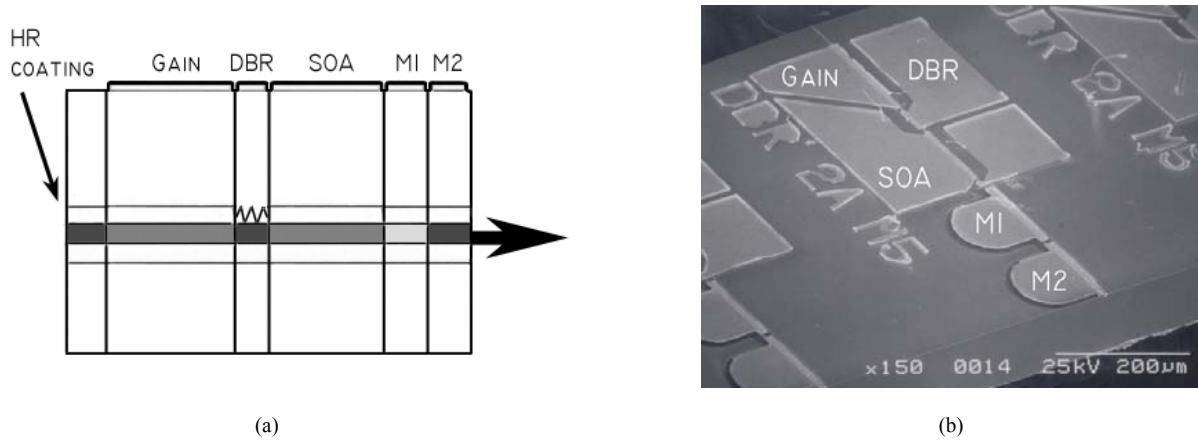


FIGURE 2. (a) Side view schematic and (b) electron micrograph of the completed short-cavity DBR laser, illustrating the Gain, DBR, optional SOA, and 2-section EAM. This QWI platform takes advantage of the capability to integrate multiple band-edges across different sections of the device.

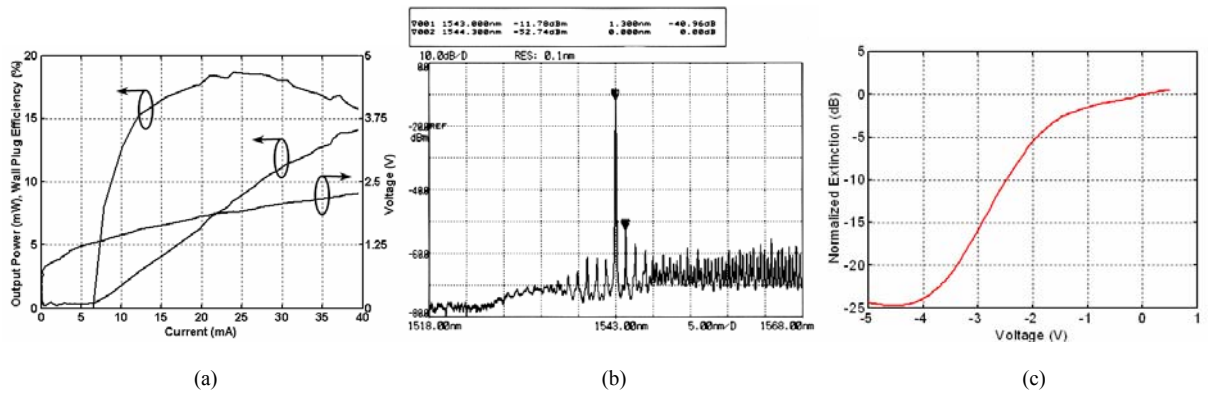


FIGURE 3. (a) LIV and wall plug efficiency under pulse testing. (b) CW lasing spectra showing emission at 1543 nm with greater than 40 dB SMSR. (c) DC optical extinction of a 125 μm modulator M1.

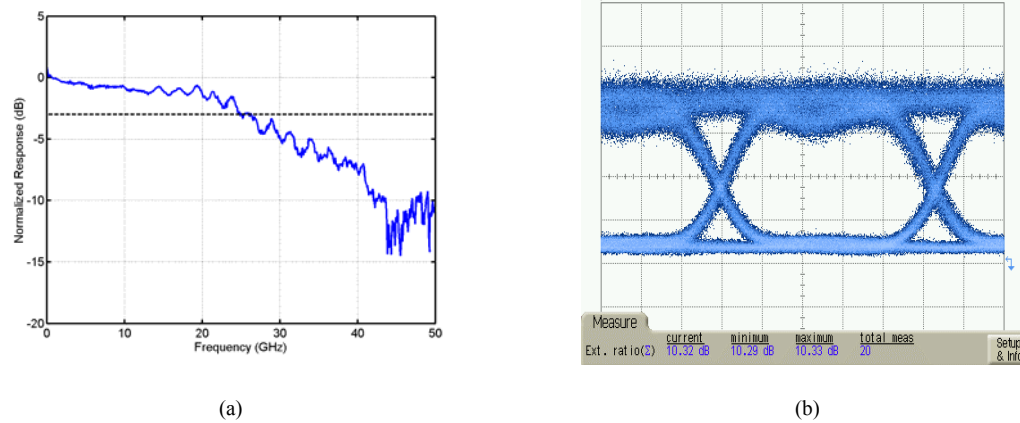


FIGURE 4. (a) Modulation bandwidth of integrated DBR laser with 125 μm long modulator, showing 3dB bandwidth of 25 GHz. (b) Open eye diagram for 10 Gb/s transmission.

Monolithically integrated 40GHz pulse source with >40nm wavelength tuning range

L.A. Johansson, Zhaoyang Hu, D.J. Blumenthal and L.A. Coldren

Department of Electrical and Computer Engineering, University of California, Santa Barbara, CA 93106.

Email: leif@ece.ucsb.edu, Tel: (805) 893 2875, Fax: (805) 893 4500

Y.A. Akulova and G.A. Fish

Agility Communications, Inc., 475 Pine Ave, Santa Barbara, CA 93117.

Abstract: A monolithically integrated device combines 40 GHz dual mode-locked operation with the wide tuning range (>40nm) of sampled-grating DBR lasers, while further being integrated to an SOA and a potentially high-speed modulator.

OCIS codes: (250.5300) Photonic integrated devices; (140.3600) Lasers, tunable; (140.4050) Mode-locked lasers

1. Introduction

High-speed optical communications systems with transmission rates of 40 Gbps have been developed for future wavelength multiplexed high-capacity systems. One key enabling component, not previously demonstrated, is an integrated, wavelength-agile return-to-zero (RZ) optical pulse source. Although several integrated configurations have been reported in the literature to generate 40 GHz RZ pulse sources [1-3], none have been widely wavelength tunable. The topic of this paper is to demonstrate, for the first time, a single monolithically integrated device combining generation of spectrally compact RZ pulses with the wide tunability offered by an SG-DBR laser integrated with a semiconductor amplifier and an electroabsorption modulator. The modulator is at this stage not sufficiently fast for 40Gbps data encoding. However, MZ modulators integrated with widely tunable SG-DBR lasers, sufficiently fast for 40Gbps data encoding have recently been built and can be integrated with the dual-mode-locked laser.

In an extended perspective, this device would be well suited for integration to form a 40Gbps RZ transmitter. A conventional 40Gbps RZ transmitter typically consists of several optical and electrical components, including an optical source, two external modulators and drivers; one for pulse carving and one for encoding, and additional optical amplification, illustrated by Fig. 1a. The type of monolithically integrated device presented here has the potential to replace the majority of the components in an RZ-transmitter, as indicated by Fig. 1b. This proposed transmitter would consist of a dual-mode-locked widely-tunable SG-DBR laser integrated with a semiconductor amplifier and a high-speed data encoder. Because the clock-reference is used only to synchronize the two modes, not to drive a modulator, the clock drive amplifier can in principle be eliminated.

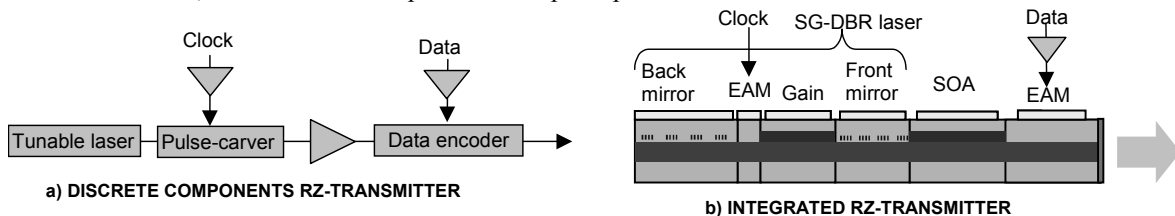


Fig. 1. a: Schematic of conventional wavelength tunable RZ optical transmitter. b: Schematic of proposed monolithically integrated RZ optical transmitter.

2. Experiment

The device used for this demonstration is the same as described in greater detail in reference [6]. It is based on a widely tunable sampled grating (SG) DBR laser with the structure shown in Fig 1b. The SG-DBR laser includes gain and phase sections positioned between two “sampled grating” distributed reflectors, sampled at different periods such that only one of their multiple reflection peaks can coincide at a time. An offset quantum-well structure provides a platform for integration of the laser with other active regions, such as detectors or semiconductor optical amplifiers (SOA), and passive regions, such as phase or amplitude modulators. Typical performance of an SG-DBR laser integrated to an SOA is more than 20mW fiber-coupled output power, lower than 2MHz linewidth, lower than

-140dB/Hz RIN and more than 40dB sidemode suppression ratio over more than 40nm wavelength tuning range. Also integrated in the device used in these experiments is an EA modulator designed for 2.5Gbps operation.

The sampled grating mirrors are designed so that only one single stable axial mode can be supported at a time. Mode-jumps between axial modes can be achieved by tuning the phase section, and at the mode boundary unstable operation is observed due to mode competition. By reverse biasing the phase section, it will take the function of an intracavity Franz-Keldysh modulator. Phase control must then be achieved by a combination of mirror and gain section tuning. A stable and synchronized dual-mode operation can be generated by modulating the phase section at the axial mode spacing frequency. Although the phase section has not been designed for efficient modulation at 40 GHz, the response is at the axial resonance sufficiently strong to correlate and stabilize the two lasing modes. In principle, if a high-speed modulator section is integrated in the laser, a much weaker drive signal can be used than for driving the equivalent external modulator, as only a small modulation is required to achieve mode synchronization.

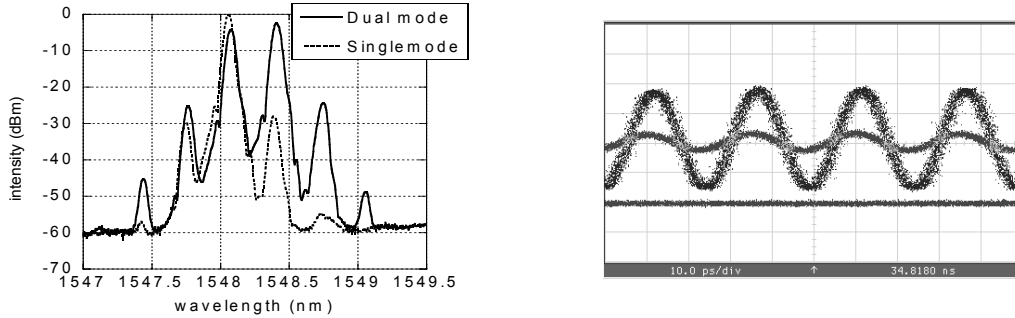


Fig. 2. a: Optical spectra for single and dual mode operation. b: Captured oscilloscope waveforms contrasting 40GHz dual-mode-locked and modulated single-mode SG-DBR laser operation.

3. Results

The optical spectra in Fig. 2a contrasts single and dual-mode operation under phase section modulation by a 19.3dBm signal. At single mode operation, weak modulation sidebands can be generated when the drive frequency matches the axial mode spacing; $\sim 0.32\text{nm}$. Adjusting the cavity round-trip phase, stable and synchronized dual-mode operation is observed. Figure 2b shows the comparison between the detected 40GHz waveforms generated under modulated single-mode and locked dual mode operation. The zero-level is also shown in the figure. At single-mode operation, a weak sinusoidal waveform was observed and it demonstrates that 40GHz optical pulses cannot be generated directly through strong modulation; while at locked dual-mode operation, a strong beat signal is obtained as a result of the heterodyne beat between the two locked modal frequencies. Based on the observed oscilloscope waveform, zero level, and the frequency roll-off of the 50GHz detector and 50GHz sampling oscilloscope used for detection, it is estimated that the actual extinction ratio is better than 10dB under dual-mode lasing.

The mode-beating can be synchronized over a 0.9GHz locking range, centered around 40.2GHz, corresponding to the cavity mode spacing of these devices, and illustrated by Fig. 3. At the boundaries of the locking range, a penalty in signal power was observed due to unbalanced mode amplitude. The 1-dB frequency range was on the order of 300MHz.

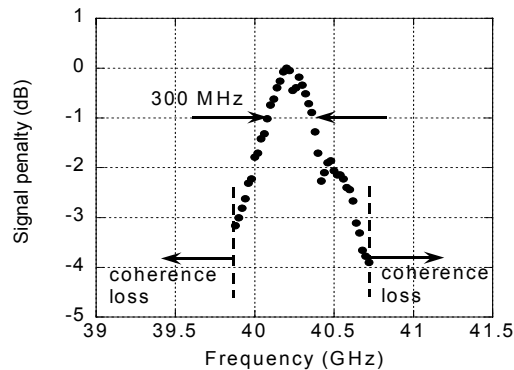


Fig. 3: Measured mode-locking range, where synchronized dual mode operation can be obtained. Also indicated is the 1-dB frequency range.

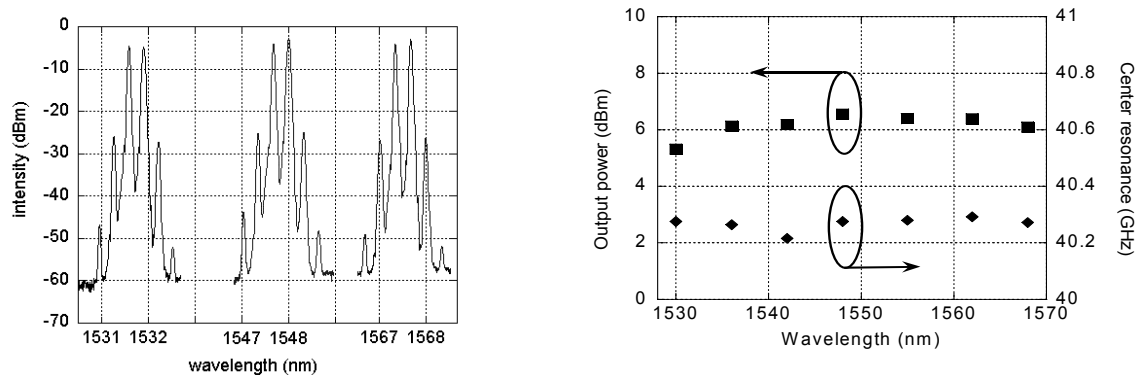


Fig. 4. a: Optical spectra taken through the tuning-range of the laser; low, center and high wavelength, illustrating a sidemode suppression ratio better than 20dB. (Res. bandwidth $\sim 0.08\text{nm}$). b: Fiber-coupled output power and center cavity resonance frequency over the wavelength tuning range of the laser.

Stable dual-mode lasing is obtained over the entire tuning-range of the laser; $>40\text{nm}$, illustrated by Fig. 3b, where dual-mode optical spectra at low, center and high wavelength are shown. The sidemode suppression ratio is at all wavelengths better than 20dB at a spectrum analyzer resolution bandwidth of $\sim 0.08\text{nm}$. The mode spacing remains well within the 1-dB lock-frequency range of Fig.3 over the wavelength tuning range of the laser, as shown in Fig. 4b, and is equally insensitive to chip operating temperature. The relative stability of generated modal beat frequency would allow the design of a widely-tunable dual-mode mode-locked laser for 40.0GHz or 42.7GHz applications. The fiber-coupled output power over the wavelength tuning range is consistent to that of single-mode operation and is also shown in Fig. 4b, where the gain section and SOA are kept at constant bias current.

4. Summary

In this paper we have demonstrated, for the first time, a single monolithically integrated device that combines generation of spectrally compact 40GHz pulses with wide wavelength tunability. This has been achieved by locking two axial modes of a widely-tunable SG-DBR laser to an external 40GHz reference used to modulate the reverse-biased phase section of the laser. The device is integrated with an SOA and an EAM that could potentially be designed sufficiently fast for data encoding, which would then be the realization of an integrated 40Gbps RZ transmitter. 40.2GHz pulse-generation is demonstrated with 0.9GHz locking range and uniform performance over the entire 40nm tuning range of the laser.

5. References

- [1] C. Bobbert, J. Kreissl, L. Molle, F. Raub, M. Rohde, B. Sartorius "Novel Compact 40GHz RZ-Pulse-Source based on Self-Pulsating PhaseCOMB Lasers," in *Optical Fiber Communication Conference on CD-ROM (Optical Society of America, Washington, DC, 2004)*, WL5.
- [2] C. Bornholdt, B. Sartorius, S. Schelhase, M. Mohrle, and S. Bauer, "Self-pulsating DFB-laser for all-optical clock recovery at 40 Gb/s," *Electron. Lett.*, vol. 36, pp. 327-328, 2000.
- [3] K. Sato, A. Hirano, N. Shimizu, T. Ohno, and H. Ishii, "Dual mode op-eration of semiconductor mode-locked lasers for anti-phase pulse gen-eration," in *Proc. OFC 2000*, 2000, Paper ThW3.
- [4] Y. A. Akulova, G. A. Fish, P. C. Koh, C. Schow, P. Kozodoy, A. Dahl, S. Nakagawa, M. Larson, M. Mack, T. Strand, C. Coldren, E. Hegblom, S. Penniman, T. Wipiejewski, and L. A. Coldren, "Widely-Tunable Electroabsorption-Modulated Sampled Grating DBR Laser Transmitter", *IEEE J. Selec. Top. in Quantum Electron.*, vol. 8, pp. 1349-1357, Nov/Dec 2002.

Small-Footprint, High-Efficiency, Integrated Transmitters for High-Speed Optical Interconnect Applications

Erik J. Skogen[†], Chad S. Wang[†], James W. Raring^{*}, Gordon B. Morrison[†], and Larry A. Coldren^{†*}

[†]ECE Dept. University of California, Santa Barbara, CA 93106

^{*}Materials Dept. University of California, Santa Barbara, CA 93106

Phone: 805.893.8465, Fax: 805.893.4500, Email: skogen@engineering.ucsb.edu

Abstract: Short-cavity InGaAsP/InP DBR lasers with integrated SOA and EAM were fabricated using a quantum well intermixing processing platform. >10mW output power and 17.5% wall-plug efficiency was achieved at 30mA. EAM extinction was >15dB at -4V.

©2004 Optical Society of America

OCIS codes: (140.5960) Semiconductor lasers; (250.5300) Photonic Integrated Circuits

1. INTRODUCTION

Chip to chip optical interconnects (C2OI) have the potential to demonstrate numerous advantages over traditional electrical I/O integrated circuits. Applications requiring high bandwidth-path length products will be best served through an optical free-space type interconnect [1]. This technology will also lead to advantages in power dissipation, crosstalk, and susceptibility to electro-magnetic interference (EMI) than electrical connections.

In order to meet and exceed existing electrical I/O specifications, it is necessary to design and develop short cavity lasers with a small footprint (< 250 μm pitch), high efficiency, low power dissipation, and high output power. Here we demonstrate a short cavity, high output power, single mode, high efficiency, distributed Bragg reflector (DBR) laser, with monolithically integrated semiconductor optical amplifier (SOA) and electro-absorption modulator (EAM).

2. EXPERIMENT

The short-cavity DBR lasers were designed to have a high-reflectivity (HR) rear mirror, short gain section (150 μm), and front DBR mirror (40 μm). The DBR lasers were monolithically integrated with an SOA (110 μm) and EAMs (125 μm) using a quantum well intermixing processing platform that allows for the formation of a unique quantum well band edge for each integrated component. In this device architecture, two modulators with differing band-edge placement were included, one at the passive waveguide band-edge (M1), and one at the EAM band-edge (M2). A side-view schematic of the device and an electron micrograph are shown in Fig. 1a and 1b, respectively.

With this process it is possible to achieve any number of band-edges across the wafer, limited only by the practical number of lithographic process steps as shown in Fig. 2a and 2b. For this work, only three band-edges were needed: the as grown band-edge for the gain regions, a band-edge ideal for the EAM, and a band-edge used in the low loss passive waveguide regions. The photoluminescence curves for sample used in this work are shown in Fig. 2c.

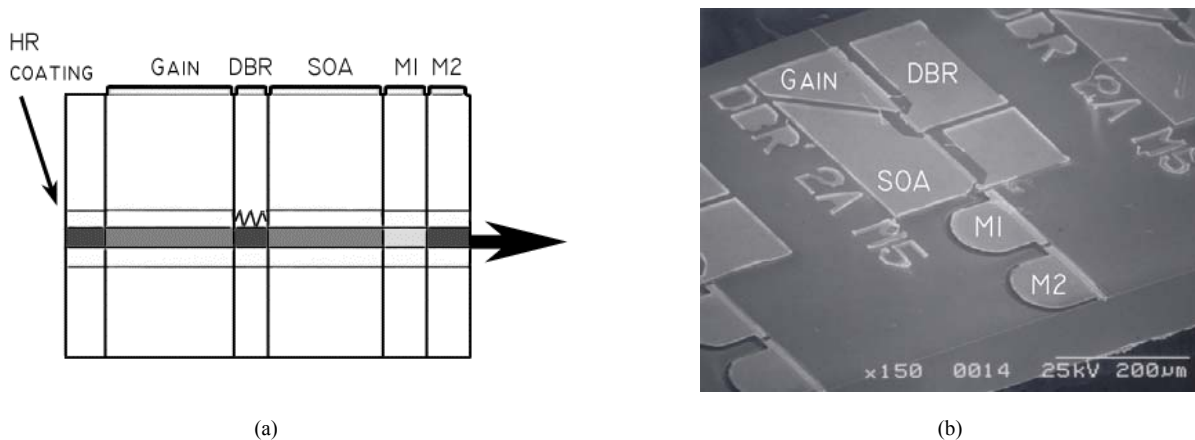


FIGURE 1. (a) Side view schematic and (b) electron micrograph of the completed short-cavity DBR laser, illustrating the Gain, DBR, SOA, and 2 section EAM.

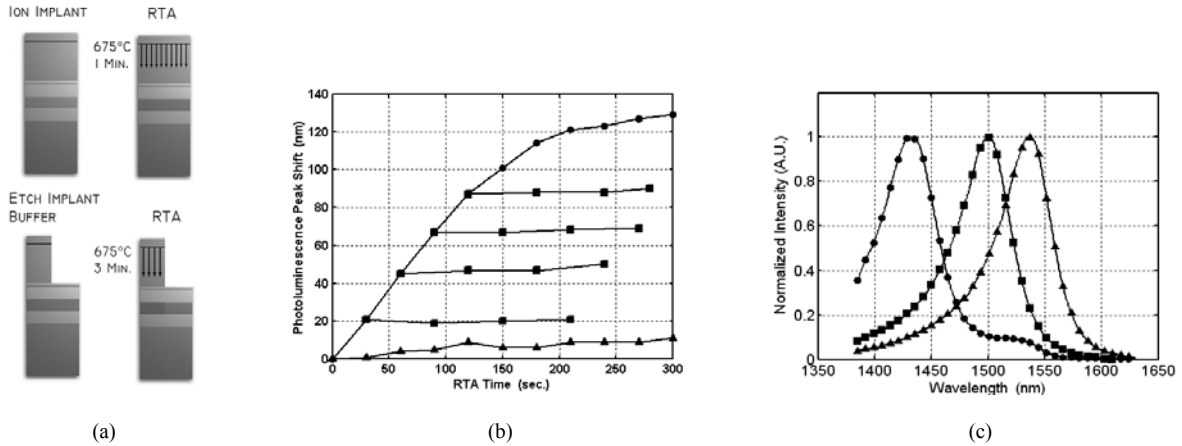


FIGURE 2. (a) Illustration of the intermixing processing platform used in this work. (b) Peak photoluminescence peak shift as a function of anneal time, showing the initial linear increase in the peak shift and the complete halting of the peak shift for samples for which the implant buffer layer has been etched. Symbols indicate non-implanted (triangles), implanted (circles), and samples with partial anneal followed by the removal of the implant buffer layer (squares). (c) Photoluminescence spectra for device shown in this work. Symbols indicate active region photoluminescence (triangles), EAM photoluminescence (squares), and passive section photoluminescence (circles).

3. PROCESS

The epitaxial base structure, grown on a S-doped InP substrate using a Thomas Swan horizontal-flow rotating-disc MOCVD reactor, contained an n-InP buffer region below a multi-quantum well (MQW) active region centered within a 1.3Q waveguide. The MQW consists of 7 InGaAsP 6.5 nm compressively strained (0.6%) quantum wells, separated by 8.0 nm tensile strained (0.3%) InGaAsP barriers. Following the active region, a 15 nm InP stop etch, a 20 nm 1.3Q stop etch, and a 450 nm InP implant buffer layer was grown.

A 500 nm Si_xN_y mask layer was deposited using plasma enhanced chemical vapor deposition and lithographically patterned such that it remained only where the as-grown band-edge was desired. Ion implantation was performed using P^+ at an energy of 100 keV, yielding a range of 90 nm, with a dose of $5\text{E}14 \text{ cm}^{-2}$, at a substrate temperature of 200 °C [2]. The sample was subjected to rapid thermal processing at a temperature of 675 °C, promoting the diffusion of vacancies through the MQW region. Once the desired band-edge for the EAM was achieved ($\lambda_{\text{pl}} = 1500 \text{ nm}$) the diffusion process was halted. This is accomplished by selectively removing the implant buffer layer, removing the vacancies, thereby halting the intermixing in that region; the regions in which the implant buffer layer remains will continue to intermix along the curve, as shown in Fig. 2b. Using this method, we can achieve multiple band edges across the wafer from a single implant process. The sample was then subjected to an additional rapid thermal anneal, further blue-shifting the regions where the implant buffer layer remained. This second anneal was used to obtain the desired band edge ($\lambda_{\text{pl}} = 1430 \text{ nm}$) for the mirror and passive waveguide sections. A schematic illustrating the intermixing process and the photoluminescence of the active, EAM, and passive regions are shown in Fig. 2a and 2c, respectively.

Once the implant buffer layer was removed, the deeply etched gratings, with a coupling coefficient of 250 cm^{-1} , were formed in the DBR region using holography. This was followed by an optimized MOCVD regrowth process of the upper p-cladding and p-type InGaAs contact layer. Ridge waveguides, 3 μm wide, were patterned; Si_xN_y and benzocyclobutene (BCB) were patterned beneath the laser and EAM contacts, respectively. Isolation was accomplished by proton implantation, and p-type metal deposited. The wafers were thinned, backside metalized, and devices were cleaved into bars. Subsequently, the rear facet of cleaved bars was HR-coated.

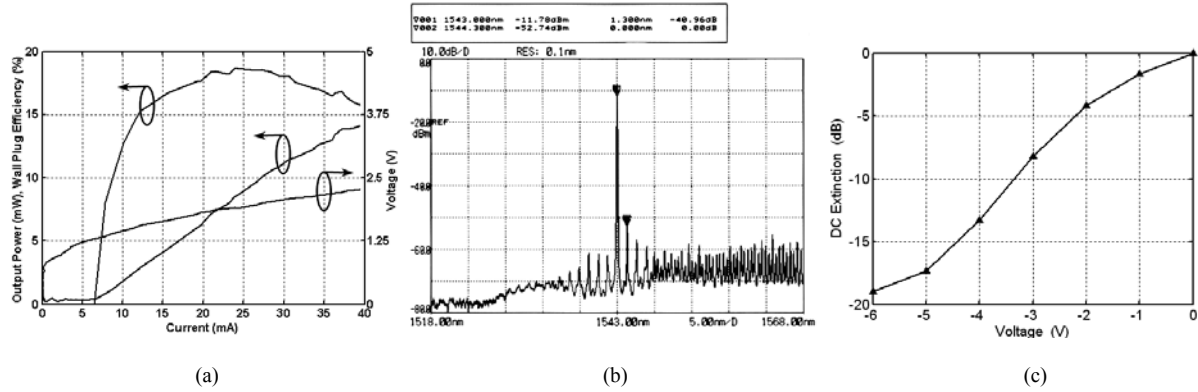


FIGURE 3. (a) LIV and wall plug efficiency under pulse testing. (b) CW lasing spectra showing emission at 1543 nm with greater than 40 dB SMSR. (c) DC optical extinction of a 125 μm modulator M1.

4. RESULTS

Material parameters were extracted from all-active and active/passive Fabry-Perot lasers, resulting in a modal gain of 67 cm^{-1} , an active internal loss of 9.7 cm^{-1} , and a passive internal loss of 3.5 cm^{-1} extracted as described in [3]. The power reflectivity of the HR-coating was extracted using all-active Fabry-Perot lasers and found to be $> 95\%$. A DBR mirror power reflectivity of 30% was extracted by analysis of DBR laser threshold current and differential efficiency before and after HR-coating.

The devices demonstrated good characteristics in terms of output power, efficiency, side mode suppression ratio (SMSR), and DC optical extinction. A low threshold current of 7 mA was measured, and output powers greater than 10 mW were achieved with a gain section current of 30 mA, as shown in Fig. 3a. The wall plug efficiency exceeded 18% and at 30 mA was 17.5%. The DBR lasers also demonstrated single-mode emission with a SMSR greater than 40 dB, as shown in Fig 3b. The DC modal extinction characteristics of EAM (M1) are presented in Fig. 2c. Greater than 15 dB optical extinction was measured at a reverse bias of 4 V. The laser, at an operating point of 30 mA, had a power dissipation of 50 mW, while the EAM dissipated 30 mW at a reverse voltage of 3.0 V.

5. CONCLUSION

Small footprint, high power laser/modulator devices have been designed, fabricated, and tested. The devices employed a QWI-based processing platform for the monolithic integration of multiple section photonic integrated circuits. Lasers exhibited excellent characteristics in terms of output power ($>10\text{ mW}$) and efficiency ($> 18\%$). The modulator demonstrated $> 15\text{ dB}$ DC extinction at a length of 125 μm , with expected bandwidth simulated to exceed 15 GHz.

6. REFERENCES

- [1] M. R. Feldman, S. C. Esener, C. C. Guest, and S. H. Lee, "Comparison between optical and electrical interconnects based on power and speed considerations," *Applied Optics*, vol. 27, pp. 1742-1751, 1988.
- [2] E. Skogen, J. Raring, J. Barton, S. DenBaars, and L. Coldren, "Post-Growth Control of the Quantum-Well Band Edge for the Monolithic Integration of Widely-Tunable Lasers and Electroabsorption Modulators," Accepted for publication in *IEEE J. Sel. Topics in Quantum Electron.*, vol. 9, September/October, 2003.
- [3] E. Skogen, J. Barton, S. DenBaars, and L. Coldren, "A Quantum-Well-Intermixing Process for Wavelength-Agile Photonic Integrated Circuits," *IEEE J. Sel. Topics Quantum Electron.* vol. 8, pp. 863-8, 2002.

Short-Cavity 1.55 μm DBR Lasers Integrated with High-Speed EAM Modulators

Chad S. Wang[†], Erik J. Skogen[†], James W. Raring^{*}, Gordon B. Morrison[†], and Larry A. Coldren^{†*}

[†]ECE Dept. University of California, Santa Barbara, CA 93106

^{*}Materials Dept. University of California, Santa Barbara, CA 93106

Phone: 805.893.7065, Fax: 805.893.4500, Email: cswang@engineering.ucsb.edu

Abstract: Short-cavity InGaAsP/InP DBR lasers with integrated EAMs were designed and fabricated using a quantum well intermixing processing platform. RF bandwidths up to 25GHz were achieved and open eyes at 10Gbit/s observed with >10dB dynamic extinction.

1. INTRODUCTION

Short-cavity lasers can have improved efficiency if properly designed. Integrated laser-modulators can also provide high-speed operation with good chirp management. Such characteristics are desirable in future datacom and telecom applications, as well as proposed chip-to-chip optical interconnects. Results with directly modulated distributed feedback laser (DFB) have been reported with operation at 10 Gbit/s [1, 2], but operation to higher data rates appears problematic. Also, the wall-plug efficiency in such devices is not particularly high. Integrated DFB-EAM structures are being used with some success at higher speeds, but overall power efficiency remains low, and the footprint is too large for optical interconnect applications [3]. In this work, we present the design and results from a short-cavity distributed Bragg reflector (DBR) laser at 1.55 μm monolithically integrated with an electro-absorption modulator (EAM) that can simultaneously have high-efficiency, high-speed, and a small footprint. This is facilitated by the use of a quantum well intermixing process to individually optimize the laser and modulator sections.

2. DEVICE

In designing a short-cavity laser, considerations and trade-offs have to be made regarding the mirror reflectivity, operating current, and temperature rise in the device. First, the cavity requires the length to be sufficiently short such that the mode spacing is wide enough on the DBR stopband to maintain single mode emission. With a high reflectivity (HR) coated back mirror, the front mirror needs to be optimized for low current operation in the laser at high powers (>10 mW). Here, we chose to design a short-cavity DBR laser with a high-reflectivity (HR) rear mirror, short gain section (150 μm), and front DBR mirror (40 μm). The short front mirror is enabled by deep gratings resulting in a high coupling coefficient ($\kappa = 250 \text{ cm}^{-1}$). This does not adversely affect the laser performance since it lies outside the gain region. Fig. 1a shows design curves of operating current and temperature rise as a function of front mirror grating length for various power levels for the design detailed above. A side-view schematic of the designed device is shown in Fig. 1b. A quantum well intermixing process was used to monolithically integrate high-speed EAM modulators with the DBR laser [4, 5]. By selectively implanting and annealing individual regions of the wafer, it is possible to achieve any number of band-edges across the wafer, limited only by the practical number of lithographic process steps as shown in Fig. 2a and 2b. A complete description of this quantum well intermixing process can be found in [5]. For this work, three band-edges were needed: the as grown band-edge for the gain region, a band-edge ideal for the EAM, and a band-edge used in the low loss passive waveguide regions. The photoluminescence curves for sample used in this work are shown in Fig. 2c. By detuning the modulator's quantum well band edge from the Bragg wavelength, the EAM can be optimized

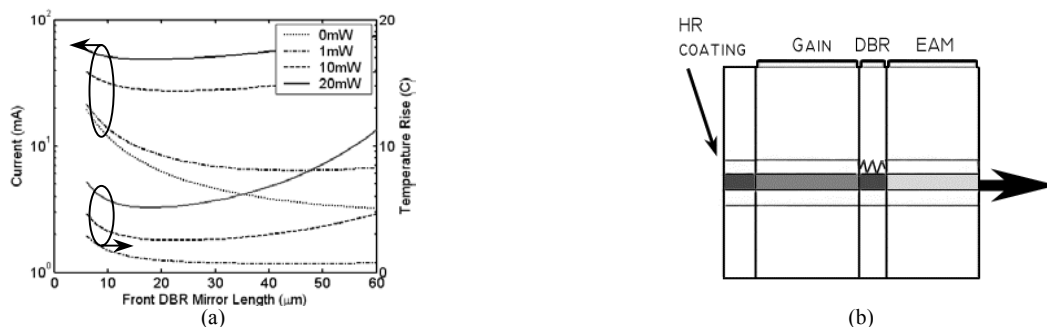


FIGURE 1. (a) Design curves for short-cavity DBR laser with 150 μm long active region at 0, 1, 10 and 20 mW output powers and (b) side view schematic of an integrated short-cavity DBR laser-modulator, illustrating the Gain, DBR, and EAM.

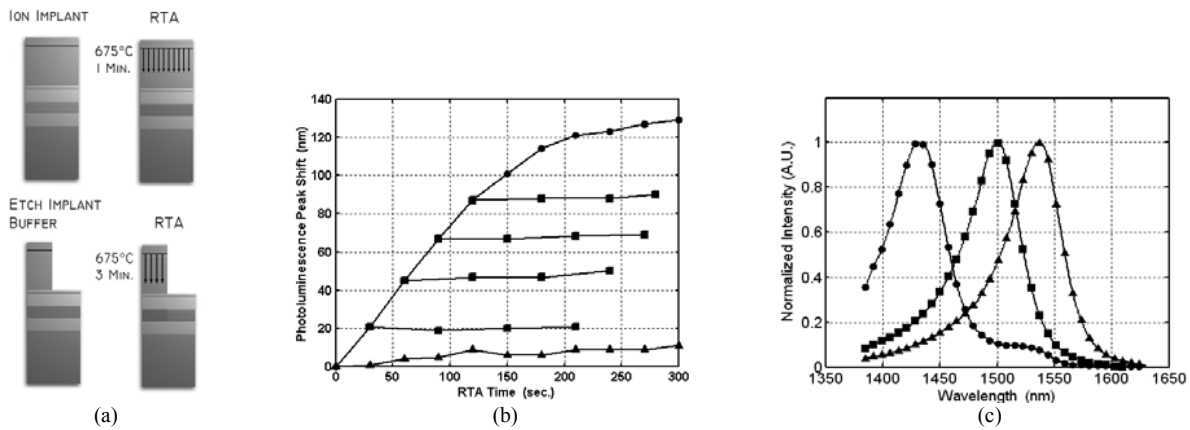


FIGURE 2. (a) Illustration of the intermixing processing platform used in this work. (b) Peak photoluminescence peak shift as a function of anneal time, showing the initial linear increase in the peak shift and the complete halting of the peak shift for samples for which the implant buffer layer has been etched. Symbols indicate non-implanted (triangles), implanted (circles), and samples with partial anneal followed by the removal of the implant buffer layer (squares). (c) Photoluminescence spectra for device shown in this work. Symbols indicate active region photoluminescence (triangles), EAM photoluminescence (squares), and passive section photoluminescence (circles).

for high extinction at low-voltage. Fabrication details of these ridge lasers with integrated EAM modulators are described in [4].

3. RESULTS

The devices demonstrated good characteristics in terms of output power, efficiency, and side mode suppression ratio (SMSR) [4]. A threshold current of 7 mA was measured, and output powers greater than 10 mW were achieved with a gain section current of 30 mA, as shown in Fig. 3a. Greater than 20 dB optical extinction with >10 dB/V extinction efficiency was measured for a 125 μm modulator, and 3dB modulation bandwidth was measured to be 25 GHz, as shown in Fig. 3b. Open eye diagrams were achieved at 10 Gbit/s with greater than 10 dB dynamic extinction at a DC bias of -3 V and a 0.6 V swing, as shown in Fig. 3c.

4. CONCLUSION

The design space for short-cavity lasers has been investigated, and short-cavity DBR lasers integrated with EAM modulators have been fabricated and tested. The devices employed a QWI-based processing platform for the monolithic integration of multiple section photonic integrated circuits. By individually optimizing the band edge of each section of the device, high-performance, short-cavity, DBR lasers can be monolithically integrated with high-performance EAMs.

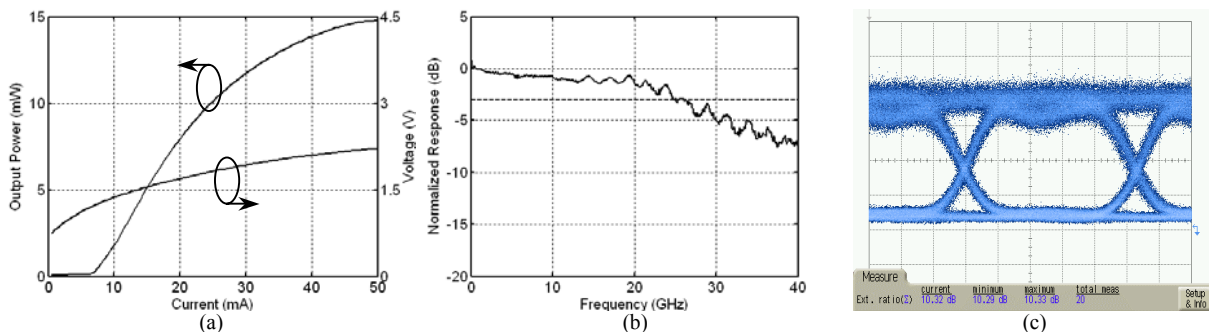


FIGURE 3. (a) CW LIV of DBR laser with rear HR coating of 94% reflectivity. (b) 3 dB modulation bandwidth of 25 GHz and (c) open eye diagram at 10 Gbit/s with a 125 μm long EAM.

5. REFERENCES

- [1] R. Paoletti, M. Agresti, G. Burns, G. Berry, D. Bertone, P. Charles, P. Crump, A. Davies, R.Y. Fang, R. Ghin, P. Gotta, M. Holm, C. Kompocholis, G. Magnetti, J. Massa, G. Meneghini, G. Rossi, P. Ryder, A. Taylor, P. Valenti, and M. Meliga, *Postdeadline Proceedings, European Conference on Optical Communications*, vol. 6, pp. 84-5, 2001.
- [2] K. Nakahara, T. Tsuchiya, T. Kitatani, K. Shinoda, T. Taniguchi, S. Fujisaki, T. Kikawa, E. Nomoto, F. Hamano, M. Sawada, and T. Yuasa, *Technical Digest, Optical Fiber Communication Conference*, paper no. ThD1, 2004.
- [3] A. Ramdane, F. Devaux, N. Souli, D. Delprat, and A. Ougazzaden, *IEEE J. of Sel. Topics in Quantum Electron.*, vol. 2, pp. 326-34, 1996.
- [4] E.J. Skogen, C.S. Wang, J.W. Raring, G.B. Morrison, and L.A. Coldren, *Integrated Photonics Research Conference*, paper no. ITHD2, 2004.
- [5] E.J. Skogen, J.W. Raring, J.S. Barton, S.P. DenBaars, and L.A. Coldren, *IEEE J. of Sel. Topics in Quantum Electron.*, vol. 9, pp. 1183-90, 2003.

InGaAsP/InP gain-levered tunable lasers

John M. Hutchinson[‡], Leif A. Johannson[†], Jonathan T. Getty[†], Jeffrey A. Hennes^{*},
Larry A. Coldren^{*†}

^{*}Materials Engineering, University of California, Santa Barbara, CA 93106

[†]Electrical and Computer Engineering, University of California, Santa Barbara, CA 93106

[‡]Intel Corporation, Strategic Technology

Phone: 805-893-3831, Fax: 805-893-4500, Email: john.hutchinson@intel.com

Abstract

A tunable gain-levered laser is fabricated on an InGaAsP ridge waveguide, and demonstrates increased CW differential efficiency and sharp DC turn-on, with hysteretic characteristics. The devices can be directly modulated up to > 2.5 Gb/s.

I. Introduction

Bistable laser diodes have been proposed for use in optical networks due to their enhanced differential quantum efficiency (DQE), signal regeneration properties, and even implementation of all-optical flip-flops[1]. Gain-levered lasers have demonstrated improved noise figure (NF) in passive microwave fiber-optic links[2]. Fabry-Perot ridge lasers with saturable absorber sections are one additional implementation and have demonstrated sharp DC turn-on characteristics[3].

In this work, we report on the implementation and performance of a gain-levered widely-tunable laser. The design utilizes a tunable sample-grating distributed Bragg reflector (SGDBR) laser [4] and splits the laser gain cavity into two electrically segmented sections. The gain-levered cavity yields high quantum efficiency and sharp turn-on. The SGDBR mirrors ultimately allow full C-band tunability from the vernier effect. The gain levered SGDBR may be particularly useful getting the most efficient modulation out of a limited photocurrent for optical wavelength converters[5].

II. Gain levered SGDBR Laser Design

The device is illustrated schematically in Fig. 1(left) and consists of six sections with (from right-to-left) a SGDBR rear mirror, phase section, the QW cavity split into a $460 \mu\text{m}$ long section (gain) and a $90 \mu\text{m}$ long section (lever), a SGDBR front mirror and a $550 \mu\text{m}$ long output SOA. The device is fabricated with a common $1.4 Q$ InGaAsP waveguide, offset $1.55 \mu\text{m}$ QW for the amplifier, gain and lever sections, and a single blanket InP ridge regrowth. Details of the fabrication process are given in [5]. The output SOA is provided to boost the laser output power. Typical operation conditions are $I_{\text{gain}} = 50 \text{ mA}$, $I_{\text{lever}} = 5 \text{ mA}$, $I_{\text{SOA}} = 50 \text{ mA}$ for $T_{\text{subs}} = 16^\circ\text{C}$.

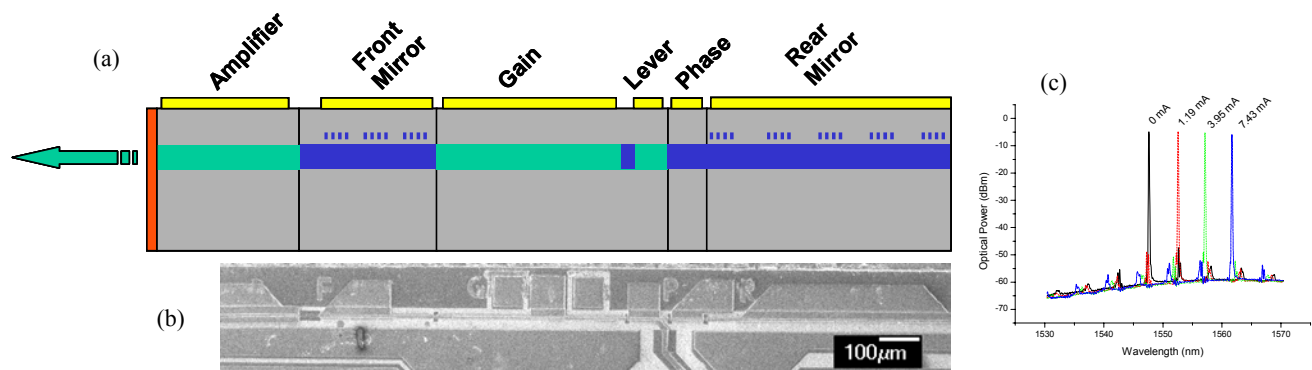


Figure 1. (a) Cross-section schematic of gain lever SGDBR (b) Top-down micrograph of fabricated device (c) optical spectra for as a function of rear mirror current.

III. Device Results

The optical spectra for various rear mirror currents are superimposed in Figure 1(c) showing $\sim 15\text{nm}$ of tuning with $>35\text{dB}$ side mode suppression ratio. Continuous wave room temperature light-lever current measurements were taken as a function of gain section current (Figure 2a). With separately biased gain and lever contacts, I_{th} is reduced and slope efficiency at threshold is increased for increasing I_{Gain} . With shorted gain and lever contacts, threshold current (I_{th}) was 30 mA. The L-I curve also shows hysteretic effects (Figure 2b). Small signal modulation response was measured on un-terminated devices (Figure 3a). Although we see hysteretic behavior in the L-I curve, the modulation bandwidth is at least as good as a conventional laser produced by shorting the contacts, 5.0 GHz for $I_{\text{gain}} = 60\text{mA}$ and $I_{\text{lever}} = 8\text{mA}$. The devices were digitally modulated at 2.5 and 5 Gb/s and demonstrated open eyes as shown in Figure 3b and c.

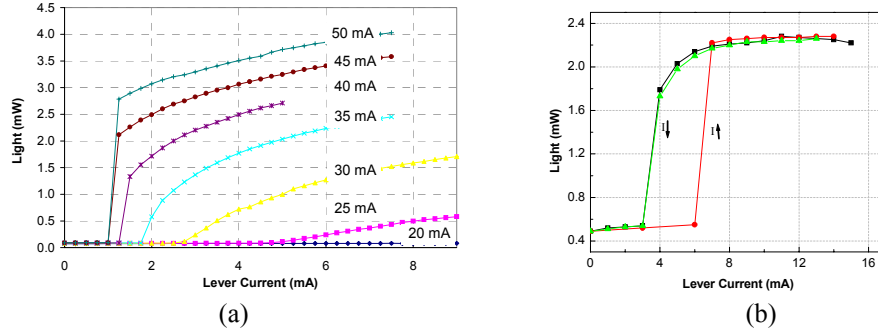


Figure 2. (a) CW L-I data for gain-levered SGDBR with I_{gain} as a parameter (1548nm emission, 30 mA I_{SOA}) (b) hysteresis L-I curve showing dependence of L-I on increasing vs. decreasing lever current (1548nm emission, 70 mA I_{SOA}).

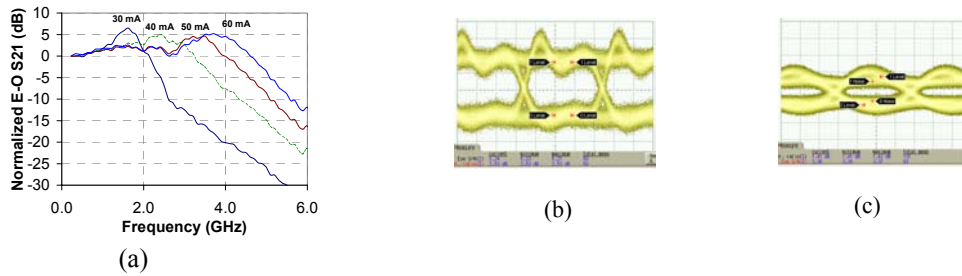


Figure 3. (a) Small signal gain lever laser bandwidth with I_{GAIN} as a parameter ($I_{\text{SOA}} = 30\text{mA}$, $I_{\text{LEVER}} = 8\text{mA}$) (b) 2.5 Gb/s NRZ eyes ($2^{31}-1$ PRBS, $I_{\text{SOA}} = 30\text{mA}$, $I_{\text{GAIN}} = 60\text{mA}$, $I_{\text{LEVER}} = 11\text{mA}$, $V_{\text{RF}} = 1\text{V}$) (c) 5 Gb/s NRZ eyes ($2^{31}-1$ PRBS) (same conditions as b)

IV. Conclusions

We have presented our design and the performance of a tunable gain-levered ridge laser. The gain-levered SGDBR tunable laser is fabricated on a robust InGaAsP waveguide, InP ridge process suitable for standard ridge lasers, and demonstrates increased differential efficiency and sharp DC turn-on characteristics. Small-signal RF bandwidth of 5 GHz and clearly open eyes at 2.5 Gb/s were demonstrated.

This work was supported by DARPA/MTO CS-WDM under grant No. N66001-02-C-8026 and by Intel Corporation under grant No. TXA001630000.

References

- [1] H. Kawaguchi, "Bistable Laser Diodes and Their Applications: State of the Art," *IEEE J. Sel. Topics in Quantum Electronics*, vol. 3, no. 5, pp. 1254-1270, October 1997.
- [2] K. Y. Lau, "Passive Microwave Fiber-Optic Links with Gain and a Very Low Noise Figure," *IEEE Photonics Tech. Letters*, vol. 3, no. 6, pp.557-559, June 1991.
- [3] J. Lee, P. Zory, "Sharp Turn-on Diode Lasers", *2003 IEEE LEOS Annual Meeting Conference Proceedings*, vol 2, pp987-988, 2003.
- [4] B. Mason, G.A. Fish, S.P. Denbaars, and L.A. Coldren, "Widely Tunable Sampled Grating DBR Laser with Integrated Electroabsorption Modulator," *IEEE Photon. Tech. Letters*, vol. 11, pp638-640, 1999.
- [5] J.M. Hutchinson, J. S. Barton, M. L. Masanovic, M. N. Sysak, J. A. Hennes, L. A. Johansson, D. J. Blumenthal, L. A. Coldren "Monolithically integrated InP-based tunable wavelength conversion", *SPIE Proceedings of Optoelectronics 2004: Integrated Optoelectronic Devices*, paper 5349-25, San Jose, CA, January 24-29, 2004.

Widely-Tunable Single-Mode Bipolar Cascade SGDBR Lasers

Jonathan Klamkin^{*}, Jonathan T. Getty[†], John M. Hutchinson[‡], Leif A. Johansson[†],
Erik J. Skogen[†], Larry A. Coldren^{*†}

^{*}Materials Engineering, University of California, Santa Barbara, CA 93106

[†]Electrical and Computer Engineering, University of California, Santa Barbara, CA 93106

[‡]Intel Corporation

Phone: 805-893-8465, Fax: 805-893-4500, Email: klamkin@engineering.ucsb.edu

Abstract

A novel widely-tunable sampled-grating DBR laser with an electrically segmented gain section is presented. The lasers tune over 38nm and exhibit differential efficiencies that nearly scale with the number of gain section segments.

I. Introduction

The Sampled-grating distributed Bragg reflector (SGDBR) laser is a widely tunable laser source that can be monolithically integrated with other components, such as modulators, receivers, and amplifiers [1]. Previous direct modulation measurements showed that single-mode operation was possible, that good extinction could be obtained, and that reasonable spur-free dynamic range was available for analog applications [2]. An SGDBR laser transmitter has also been integrated with an input semiconductor optical amplifier (SOA) and photodetector (PD) receiver in order to perform on-chip wavelength conversion [3]. However the performance of such devices was limited by the amount of photocurrent that could be generated on chip to directly modulate the laser. In order to improve on the extinction ratio and overall performance of such a photocurrent driven wavelength converter, the differential efficiency of the SGDBR laser can be scaled by series connecting electrically isolated segments of the gain section as already demonstrated in Fabry-Perot lasers [4]. Using ion implantation to electrically isolate stages of the gain section, a chain of diodes sharing the same optical cavity can be formed, and the differential efficiency will scale nearly with the number of segments. The cost is increased voltage and input impedance, but the latter can be tailored to meet impedance matching requirements. We here report for the first time the implementation of this so called “bipolar cascade” concept into the gain section of a widely tunable SGDBR laser by a robust process that allows for monolithic integration with other optical components.

II. Device Design

The bipolar cascade SGDBR lasers fabricated consist of a segmented gain section, front and rear SGDBR mirrors, phase section, and backside absorber as shown in Figure 1. The segmenting of the gain section is accomplished by implanting Helium ions in $3\mu\text{m}$ stripes and interconnecting adjacent stages forcing the current through the diodes in series. As a result the threshold current nearly scales by $1/N$ (where N is the number of stages), and the differential efficiency nearly scales by N , as described in [4]. The sub-linear dependence of differential efficiency on the number of stages is due to a relatively small segmentation loss resulting from implanting through the waveguide. Lasers were fabricated with 1, 3, 4, and 8 stage gain sections. In all cases, the gain section is approximately $550\mu\text{m}$ long. The quantum wells in the implanted regions are disordered using a novel quantum well intermixing technique as described in [5] in order to prevent unwanted saturable absorber regions in the gain section.

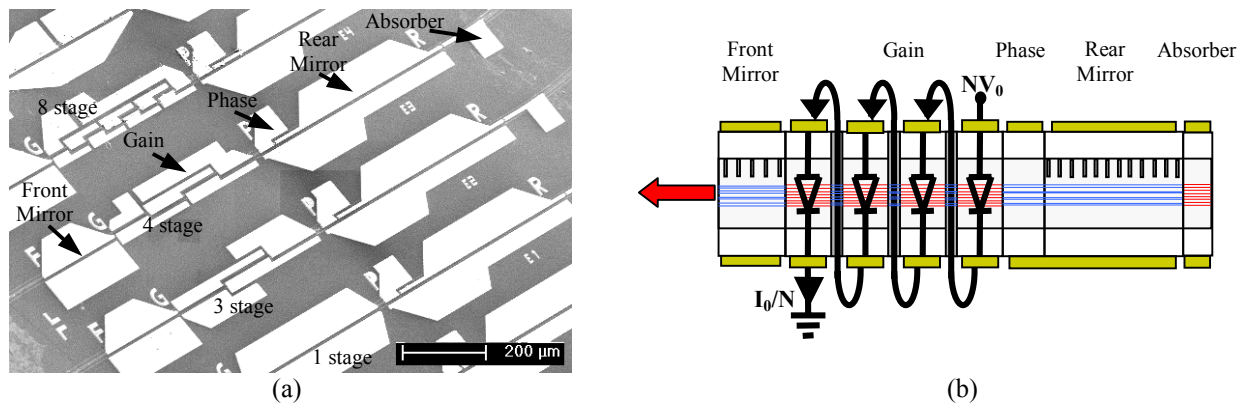


Figure 1. (a) Scanning electron micrograph of 1, 3, 4, and 8 stage bipolar cascade SGDBR lasers indicating sections. (b) Schematic of bipolar cascade SGDBR laser illustrating connection of a gain section with 4 stages. Shaded regions in gain section are implanted with Helium ions to provide isolation between stages.

III. Device Results

Continuous wave room temperature light-current measurements were taken, and relative values of threshold current and differential efficiency, as well as absolute input impedance are shown in Table 1. The threshold current, and single-ended differential efficiency for the 1, 3, 4, and 8 stage devices are 42.5mA and 9%, 15.4mA and 25%, 11.1mA and 31%, and 7.1mA and 40%. The threshold current and differential efficiency scales as expected, however due to a processing error resulting in poor current injection, the values are not optimal. A segmentation loss of 0.12dB per pass was extracted by plotting the differential efficiency versus the number of stages and fitting to a theoretical curve. The effect of this loss on differential efficiency is more severe when a higher number of stages are used. The tuning range was measured by injecting current into the front mirror and leaving the rear mirror and phase section unbiased. The optical spectra for various front mirror currents are superimposed in Figure 2(a) showing 38nm of tuning with nearly 40dB side mode suppression ratio without fine tuning of the wavelength. Measurements of the modulation response were performed on the devices and the results for a 3 stage SGDBR laser, whose input impedance is around 50Ω, are shown in Figure 2(b). The 1, 3, and 4 stage devices were digitally modulated at 2.5 Gb/s and demonstrate open eyes as shown in Figure 2(c). Because the input impedance of the 3 stage device is more closely matched to the RF power source, the modulation voltage required is lower.

Stages	Threshold Current	Differential Efficiency	DC Input Impedance
1	1	1	8.5Ω
3	0.36	2.8	50Ω
4	0.26	3.4	77Ω
8	0.17	4.4	222Ω

Table 1. Normalized threshold current and differential efficiency, and absolute input impedance.

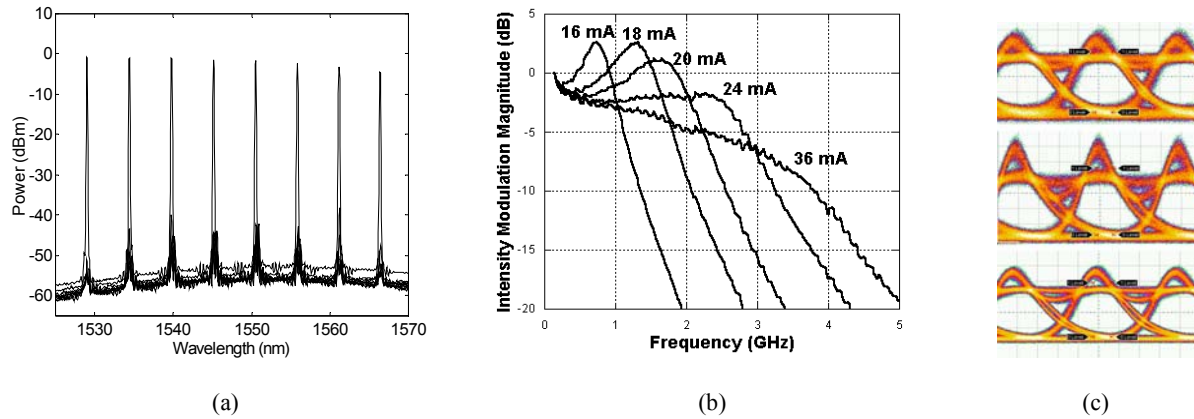


Figure 2. (a) Optical Spectra for 3 stage device showing 38nm of tuning with good SMSR. (b) Small signal modulation response at varying gain section bias currents for 3 stage SGDBR laser operating at 1567nm. (c) 2.5 Gb/s NRZ eye diagrams. From top, 1 stage SGDBR with $I_{bias}=70\text{mA}$, $V_{p-p}=1.27\text{V}$, $ER=6.8\text{dB}$, 3 stage SGDBR with $I_{bias}=18\text{mA}$, $V_{p-p}=0.25\text{V}$, $ER=7.5\text{dB}$, 4 stage SGDBR with $I_{bias}=17.5\text{mA}$, $V_{p-p}=0.6\text{V}$, $ER= 8.0\text{dB}$.

IV. Conclusions

Bipolar cascade SGDBR lasers have been successfully fabricated and demonstrate proper scaling of the differential efficiency, threshold current, and input impedance. These widely-tunable single-frequency devices have advantages in rf-photonics because of their higher differential efficiencies, which can lead to improved signal-to-noise ratio, as well as a possible 50Ω input impedance. The fabrication process readily allows for monolithic integration with other components in order to perform such functions as on chip wavelength conversion. Less current swing is needed to directly modulate the segmented lasers, therefore less input power and less SOA gain should be required resulting in enhanced conversion efficiency.

References

- [1] B. Mason, G.A. Fish, S.P. Denbaars, and L.A. Coldren, "Widely Tunable Sampled Grating DBR Laser with Integrated Electroabsorption Modulator," *IEEE Photon. Tech. Letters*, **11**, 638-640, (1999).
- [2] M.L. Majewski, J. Barton, L.A. Coldren, Y. Akulova, M.C. Larson, "Direct Intensity Modulation in Sampled-Grating DBR Lasers," *IEEE Photon. Tech. Letters*, **14**, 747-749, (2002).
- [3] J.M. Hutchinson, J.A. Henness, L.A. Johansson, J.S. Barton, M.L. Mašanović, L.A. Coldren, "2.5 Gb/sec Wavelength Conversion Using Monolithically-integrated photodetector and directly modulated widely-tunable SGDBR laser," *IEEE/LEOS annual meeting, 2003*.
- [4] J.T. Getty, E.J. Skogen, L.A. Coldren, "Multistage Segmented Lasers with Record Differential Efficiency, Low Thresholds, and 50Ω Matching," *IEEE/LEOS annual meeting, 2002*.
- [5] E.J. Skogen, J.S. Barton, S.P. Denbaars, L.A. Coldren, "A Quantum-Well-Intermixing Process for Wavelength-Agile Photonic Integrated Circuits," *IEEE Journal of Selected Topics in Quantum Electronics*, **8**, 863-869, (2002).

Analog Performance of an InP Mach-Zehnder Modulator Integrated with a Widely Tunable Laser

L.A. Johansson, J.S. Barton and L.A. Coldren
University of California at Santa Barbara, ECE Department, Santa Barbara, CA 93106
Tel: (805) 893-2875, Fax: (805) 893-4500, email: leif@ece.ucsb.edu

Abstract – The performance of an InP Mach-Zehnder modulator integrated with a widely tunable sampled grating DBR laser and a semiconductor amplifier has been characterized for analog applications. Extinction, RIN, bandwidth and SFDR have been measured.

I. INTRODUCTION

Photonic integrated devices are attractive candidates for analog optical transmitters for several reasons. By integrating the electro-optical modulator with the optical source, efficient optical coupling is achieved by eliminating fiber to device interfaces. The amount of optical power that can be coupled is no longer limited by potential damage at the input facet of the modulator. Lower cost is expected by integrating several optical functions on a single chip and reducing the number of active alignment steps that is required in either hybrid integrated devices or using discrete components. Finally, the transmitter will be compact, having a small footprint.

We have previously reported on the analog performance of a Franz-Keldysh electroabsorption modulator (EAM) integrated with a widely tunable sampled-grating (SG) DBR laser and a semiconductor optical amplifier (SOA) [1]. It was found that as a result of the high coupled power; more than 70 mA absorbed photocurrent was absorbed in the EAM, and the low relative intensity noise; less than -153 dB/Hz, a high spurious-free dynamic range (SFDR) of between 125 - 127 dB·Hz^{4/5} was measured over the tuning range of the laser. One limitation to the potential performance of EA-modulated transmitters is the effect of absorbed photocurrent, limiting the maximum achievable gain and noise figure (NF) of the optical link [2]. The gain of a Mach-Zehnder (MZ) modulated link need not be limited by photocurrent effects as the MZ relies on interferometric modulation. Indeed, MZ modulated links with RF gain have been demonstrated, using a LiNbO₃ MZ-modulator [3].

Integrated SG-DBR/MZ modulators have been reported previously [4]. Unlike Franz-Keldysh modulators, integrated MZ modulators can generate negative chirp signals, allowing data transmission over extended fiber spans [5]. In this paper, we present the first investigation of the analog performance of an InP Mach-Zehnder modulator integrated with a widely tunable sampled grating DBR laser and an SOA.

II. DEVICE

The device used for this work consists of Mach-Zehnder modulator, a widely-tunable sampled-grating (SG) DBR laser and an SOA, all integrated on a single InP chip. The SG-DBR laser includes gain and phase sections positioned between two “sampled grating” distributed reflectors, sampled at different periods such that only one of their multiple reflection peaks can coincide at a time. Introducing a small index change in one mirror relative to the other causes adjacent reflectivity maxima to come into alignment, shifting the lasing wavelength a large amount for small index change. Continuous tuning between the reflectivity maxima is obtained by tuning both mirrors. The integrated SOA compensates for on-state modulator loss, and for cavity losses caused by free carrier absorption in the tuning sections, and allows wavelength independent power leveling. The chip is mounted on an Aluminum Nitride ceramic carrier with coplanar RF lines connecting the MZ electrodes.

The device uses a bulk waveguide common to all sections. An offset quantum-well structure then provides gain in the active regions in the laser and the SOA. Passive regions, such as used for the laser mirror sections or in the MZ modulator, are defined by selective removal of the quantum-well material. A schematic of the device structure is shown in Fig. 1. Also inset in Fig. 1 is a detail of the MZ modulator, incorporating $300\ \mu\text{m}$ long RF electrodes on each arm, allowing single or dual drive. Separate phase tuning sections provide amplitude-independent phase adjustment. More details of the processing and characteristics of this type of device can be found in reference [4].

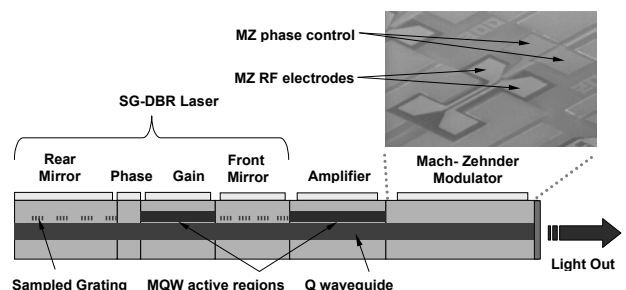


Fig. 1. Simple schematic of the integrated device including a detail picture of the MZ modulator.

III. PERFORMANCE

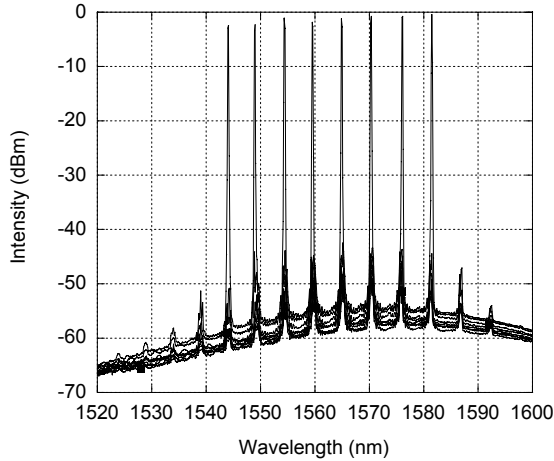


Fig 2. Overlapped optical spectra taken over the tuning range of the SG-DBR laser.

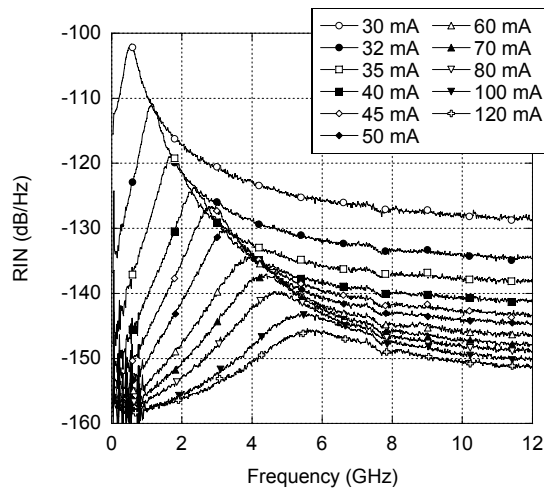


Fig 3. Measured RIN at 1555 nm for different gain section bias and 100 mA SOA bias current.

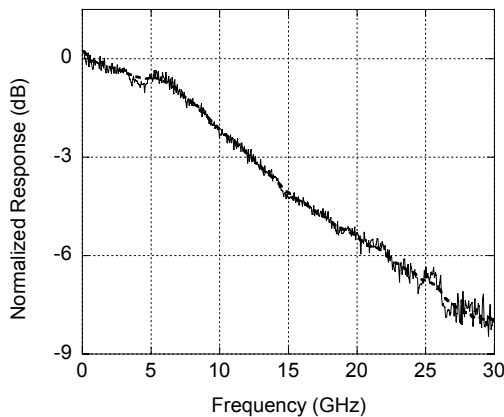


Fig 4. Mach-Zehnder frequency response taken at 1555 nm and at $-3V$ bias.

The SG-DBR laser has over 38 nm wavelength tuning range, from 1544 nm to 1482 nm with more than 40 dB sidemode suppression ratio and a fiber-coupled output power better than 2mW over the tuning range. Figure 2 shows the overlapped optical spectra taken over the tuning range of the SG-DBR laser, varying the front mirror current only. The relative intensity noise has been measured and is shown in Fig. 3 for a wavelength of 1555 nm. The SOA current was kept fixed at 100 mA, while the gain section current was varied. At 120 mA gain section current, the RIN was lower than -146 dB/Hz. The 3-dB bandwidth of the MZ modulator is 12.4 GHz. Figure 4 shows the measured frequency response for the 300 μm long lumped RF electrodes. When applying the modulation voltage, both amplitude and phase are modulated, resulting in a modulator response slightly different than the conventional sinusoidal response of a MZ modulator. This is illustrated in Fig. 5, where the measured transmitted optical power of the device is mapped out as a function MZ electrode biases. It can be seen that for equal voltage to the arms of the MZ, the amplitude of the arms is balanced and high extinction is achieved, while for unequal applied voltage, a high extinction cannot be obtained even though the output of the two arms is in antiphase. This is because the absorption in the arms at lower applied bias creates an amplitude imbalance.

The slightly modified MZ response creates an opportunity for linear operation. Different from the purely sinusoidal response of the conventional MZ modulator, the minimum of the power the third harmonic intermodulation products does not appear at the same bias as for the minimum of the fundamental as shown by Fig. 6, where the detected RF power of fundamental and intermodulation products are plotted together with the transmitted optical power.

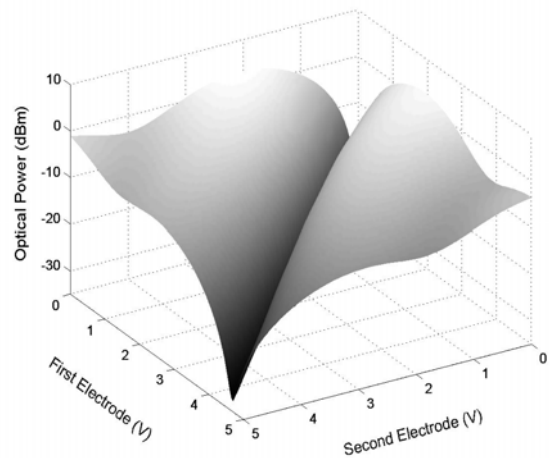


Fig 5. Measured transmitted optical power of the device as a function MZ electrode biases.

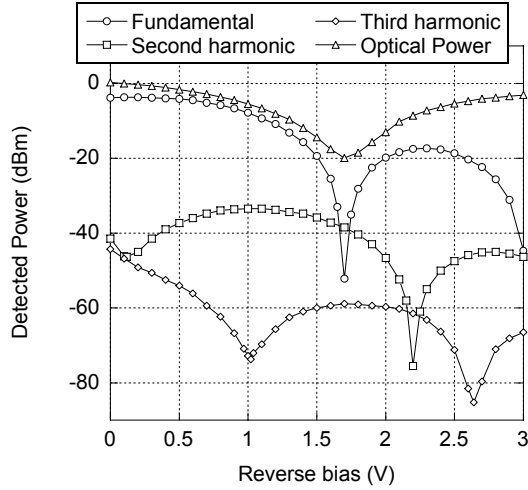


Fig. 6. Detected average optical power and RF power of fundamental and intermodulation products for 0 dBm modulation power.

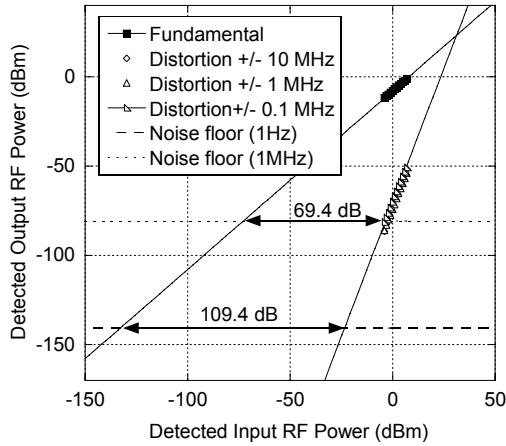


Fig. 7. Measured power of noise floor, fundamental, second and third order intermodulation products at 1555 nm at $-1V$ MZ bias. Intermodulation products are measured at different carrier separation. Sub-octave spurious-free dynamic range is shown in 1Hz and 1MHz bandwidth.

The bias point for sub-octave linear operation is $-1V$. This is a compromise between maximizing the output power of both MZ arms in order to achieve high slope sensitivity, and the requirement for some intensity modulation in the MZ electrode to achieve the modified MZ response described above. The MZ phase is then adjusted to the point of minimum third order distortion, as shown in Fig. 6. For broadband operation, both second and third order intermodulation products need to be considered. The optimum bias point is then at minimum second order distortion and maximum slope; $-0.1V$.

Figure 7 shows the sub-octave SFDR at 1555 nm. The SFDR is determined around 0.5 GHz modulation frequency using two-tone modulation for a range of frequency separations between the tones. The SFDR is

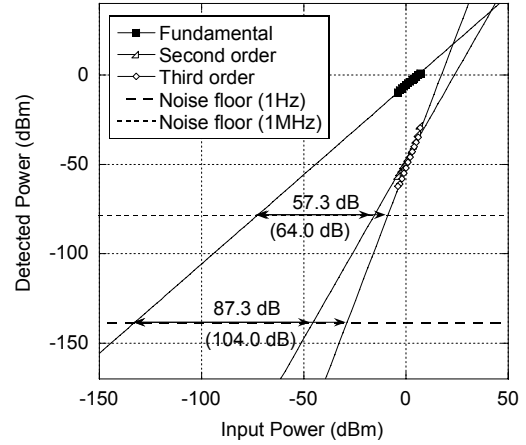


Fig. 8. Measured power of noise floor, fundamental, second and third order intermodulation products at 1555 nm and $-0.1V$ MZ bias. Broadband spurious-free dynamic range is shown in 1Hz and 1MHz bandwidth.

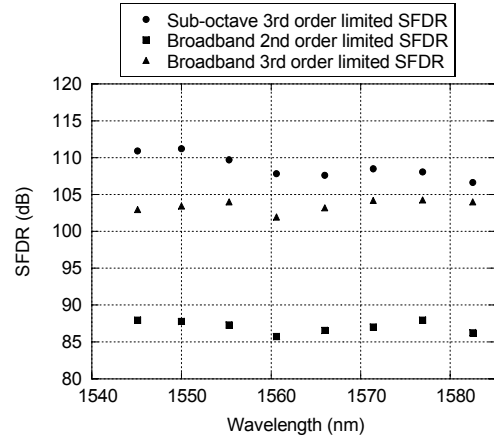


Fig. 9: Measured sub-octave and broadband spurious-free dynamic range, left scale, normalized to 1 Hz bandwidth for different wavelengths. Sub-octave SFDR limited by third order intermodulation products and broadband SFDR limited by second and third order intermodulation products are shown.

$109.4 \text{ dB}\cdot\text{Hz}^{2/3}$, determined from the tone separation displaying the worst nonlinear behavior. Compared to the bias point of maximum slope; $-0.1V$, shifting the bias to minimum third order distortion, $-1V$, results in 27dB suppression of third order intermodulation products with only 4 dB modulator gain penalty.

Figure 8 shows the broadband SFDR; $87.3 \text{ dB}\cdot\text{Hz}^{1/2}$ limited by second order intermodulation products, or $104.0 \text{ dB}\cdot\text{Hz}^{2/3}$ limited by third order intermodulation products. Similar performance is obtained throughout the tuning range of the laser. As shown in Fig. 9, the sub-octave SFDR varies between $106.6 \text{ dB}\cdot\text{Hz}^{2/3}$ to $111.2 \text{ dB}\cdot\text{Hz}^{2/3}$ and the broadband over $85.7 \text{ dB}\cdot\text{Hz}^{1/2}$ to $87.9 \text{ dB}\cdot\text{Hz}^{1/2}$, limited by second order intermodulation products, or $102.0 \text{ dB}\cdot\text{Hz}^{2/3}$ to $104.3 \text{ dB}\cdot\text{Hz}^{2/3}$, limited by third order intermodulation products.

IV. CONCLUSION

In this paper, the performance of a sampled-grating DBR laser based integrated with an SOA and a MZ modulator has been characterized for analog applications. The laser has a tuning range greater than 38nm, with more than 40 dB sidemode suppression ratio. The peak RIN is lower than -146 dB/Hz for higher bias currents to the SOA and gain sections.

The combination of phase and amplitude modulation in the MZ electrodes results in a response different from conventional MZ modulators. A shift in the bias point of minimum third order distortion away from minimum slope sensitivity is observed, and this effect is taken advantage of for linear operation. The sub-octave spurious-free dynamic range of the MZ modulator varies between 106.6 dB·Hz^{2/3} and 111.2 dB·Hz^{2/3} over the tuning range. The broadband spurious-free dynamic range is taken at minimum second order distortion and maximum slope, and varies over the tuning range between 85.7 dB·Hz^{1/2} and 87.9 dB·Hz^{1/2}, limited by second order intermodulation products, or 102.0 dB·Hz^{2/3} to 104.3 dB·Hz^{2/3}, limited by third order intermodulation products.

These results do not represent an overall improvement compared to previous results using electroabsorption modulation. However, the difference can be attributed to the slightly lower optical power operation of the laser/SOA and for a similar power performance, the dynamic range would not be worse using an MZ modulator than using an EAM. Ultimately a MZ modulator has the potential for much higher optical power tolerance and therefore higher E/O conversion gain, as the optical power does not need to be absorbed within the modulator. Also, no or low photocurrent is absorbed and the degradation in conversion efficiency due to photocurrent effects observed in EAM's is not nearly as severe.

REFERENCES

- [1] L.A. Johansson, J.T. Getty, Y.A. Akulova, G.A. Fish and L.A. Coldren, "Sampled-Grating DBR Laser-Based Analog Optical Transmitters," *IEEE J. Lightwave Technol.*, **21**, pp. 2968-2976, Dec. 2003.
- [2] L.A. Johansson, Y.A. Akulova, G.A. Fish, and L.A. Coldren, "Photocurrent effects in an electro-absorption modulator integrated with SG-DBR laser," *Proc. Microwave Photonics*, pp. 161-164, Budapest, Hungary, Sep. 2003.
- [3] W. K. Burns, M. M. Howerton and R. P. Moeller, "Broad-Band Unamplified Optical Link with RF Gain Using a LiNbO₃ Modulator," *IEEE Photon. Technol. Lett.*, **11**, pp. 1656-1658, Dec. 1999.
- [4] J.S. Barton, E.J. Skogen, M.L. Mašanović, S.P. Denbaars, and L.A. Coldren, "Widely-tunable high-speed transmitters using integrated SGDBRs and Mach-Zehnder modulators," *IEEE J. Sel. Top. Quantum Electron.* **9**, pp. 1113-1117, Sept./Oct. 2003.
- [5] Y.A. Akulova, G.A. Fish, P. Koh, P. Kozodoy, M. Larson, C. Schow, E. Hall, M. Marchand, P. Abraham and L.A. Coldren, "10 Gb/s Mach-Zehnder modulator integrated with widely-tunable sampled-grating DBR laser," in *Optical Fiber Communication Conference on CD-ROM (Optical Society of America, Washington, DC, 2004)*, TuE4.

LINEARIZED MODULATOR FOR MONOLITHICALLY INTEGRATED PHOTONIC DEVICES

L.A. Johansson¹, Y.A. Akulova, G.A. Fish and L.A. Coldren¹
Agility communications, Inc., 475 Pine Ave, 93117 Santa Barbara, CA 93117
Tel: (805) 879-9282, Fax: (805) 690-1850, email: ljohansson@agility.com
¹Also with University of California, Santa Barbara, ECE department.

Abstract – An electroabsorption-modulator in an unbalanced Mach-Zehnder configuration is shown to generate a broadband linearized response, with simultaneous suppression of second and third order intermodulation products. The modulator is monolithically integrated with a widely-tunable SG-DBR laser.

I. INTRODUCTION

Monolithic integration of a modulator with the optical source has several advantages to using discrete components, including lower cost, smaller size and improved power budget due to reduced coupling losses, the last point being particularly important for analog links. However, to realize a truly high-performance analog link, a linearized modulator is required. Furthermore, the modulator should be compatible to integration with the optical source, have the potential to operate over a wide RF frequency range and, if integrated with a tunable laser, must be compatible to a WDM environment.

Several linearized modulator architectures exist, including those using engineered waveguide material [1], dual modulator configurations [2,3], using two optical sources [4], polarization diversity [5] or a directional coupler modulator [6]. Engineering the waveguide material requires very precise control of material parameters, and leaves little flexibility to fine-tune the response to changing operating conditions, such as optical power, temperature and wavelength. Dual modulator configuration requires careful adjustment of path length and gain of the split RF paths, which are difficult to achieve over a large frequency range. Using two optical sources bypasses the need for a split RF path. However, a more complicated optical arrangement is required, not suitable for WDM applications. Utilizing the different responses for TE and TM polarization to linearize the response of a MZ elegantly eliminates the need for either dual RF paths or wavelengths, but is not compatible to photonic integration. Finally, the directional coupler modulator can be used with a

single RF path and operated at single wavelength, but this modulator has been less investigated than electroabsorption or Mach-Zehnder modulators.

In this paper, we propose and demonstrate a broadband linearized modulator architecture that is well suited for integration with a laser in an InP material system. It requires only a single RF path, operates at a single, but adjustable wavelength and is based on a combination of two standard modulation mechanisms; an electroabsorption modulator inserted into an unbalanced Mach-Zehnder.

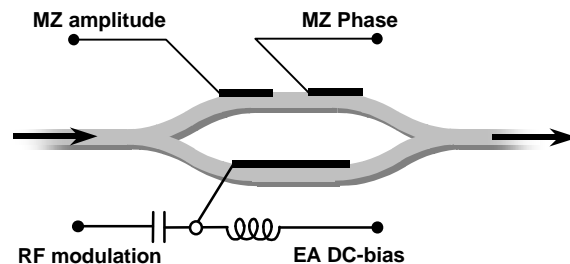


Fig. 1. Simple schematic of proposed modulator.

II. LINEARIZATION SCHEME

The proposed linearized modulator is based on a standard electroabsorption modulator (EAM). The EAM is inserted in a Mach-Zehnder (MZ) configuration, where the other arm of the MZ is not being modulated. Figure 1 shows a simple schematic of the proposed modulator. The electroabsorption is modeled after the response of a Franz-Keldysh modulator, where both phase and amplitude is modulated. The total response of the modulator is then a combination of EA and MZ modulation. The EA modulator is biased at maximum slope sensitivity with minimum second order intermodulation products. The phase control of the MZ is regulated to the corresponding operating point, but with opposite slope. A linearized response is then generated by regulating the amplitude balance between the two arms of the MZ, such that third order intermodulation products of the EA and MZ are cancelled out.

This work was funded by DARPA/MTO CS-WDM program

Figure 2 shows a sample of simulated linearized responses for different ratio between the equivalent V_{π} of the EAM and MZ V_{π} . For a high ratio, the power of third order intermodulation products generated by the MZ is large relative to those produced by the EAM. In this case, a highly unbalanced MZ is required for third order intermodulation cancellation. As the V_{π} ratio decreases, the voltage range where a constant slope is obtained increases as the cancellation of higher order intermodulation terms also improves. Reducing the V_{π} ratio even more, a penalty in overall slope sensitivity appears, as the absolute slope of the MZ becomes comparable to that of the EAM. A V_{π} ratio of 2 represents a good operating point with low penalty in slope sensitivity, and still a wide voltage range with constant slope.

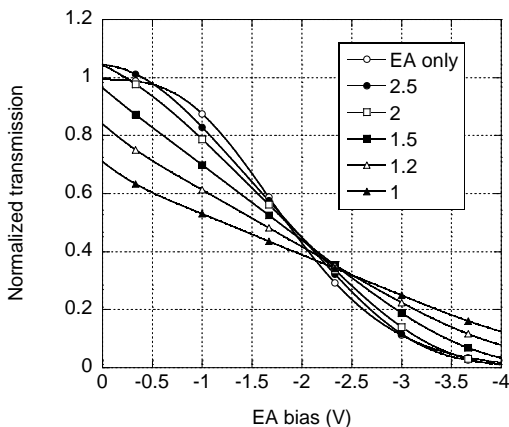


Fig 2. Simulated linearized DC extinction curves for different ratios of equivalent EAM V_p to Mach-Zehnder V_p

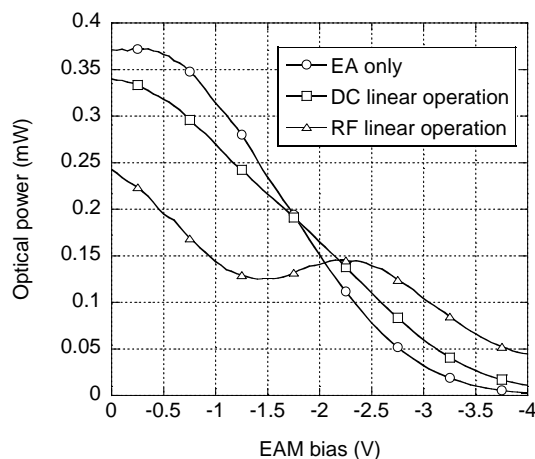


Fig. 3. Measured modulator extinction using the EAM only, and for the bias points of DC and RF linearized operation.

Further, in addition to simultaneous cancellation of second and third order intermodulation, the model shows that careful adjustment of the three DC controls would allow additional cancellation of fourth order intermodulation products. In practice, this operating point was never reached.

III. EXPERIMENTAL VERIFICATION

The device used to experimentally verify the proposed linearized modulator configuration is similar to that described in [7]. It consists of a widely-tunable sampled grating DBR laser, a semiconductor optical amplifier (SOA) and a Mach-Zehnder modulator, all integrated on the same InP chip. The modulator consists of multimode interference (MMI) sections and 600 μm long lumped electrodes. The laser-modulator uses a common waveguide structure, where passive sections, such as used in the MZ modulator, are defined by selective removal of an offset active quantum-well material. The bulk material of the electrodes of the MZ exhibits both electro-refraction and electro-absorption at reverse bias. This makes this MZ a suitable candidate for demonstration of the linearization scheme described above, which requires both effects. The amplitude balance of the MZ arms is controlled when reverse bias is applied to the second MZ electrode, absorbing part of the light. Amplitude independent phase control is obtained in a separate phase control section. The SOA bias current is reduced to limit MZ input optical power so that the I - V product of each MZ electrode remained less than 100mW at -6V , I being the absorbed photocurrent. The reduced optical power limits the total available link gain and SFDR in these experiments.

Figure 3 shows the DC extinction at 1542 nm wavelength. The extinction of EA only is obtained when the second electrode of the MZ is deeply reverse biased ($<-6\text{V}$). With the correct balance between EA and MZ effects, an overall linearized response at DC is obtained, shown in Fig. 3. This operating point is not the same as for linear operation at RF modulation. The response at DC is affected by slow heating effects that do not affect the response at RF modulation around a constant DC bias point. The DC response obtained at the linear bias point for RF, shown in Fig. 3, indicates that the electro-refractive effect is affected by slow heating, with a slightly higher MZ V_{π} at RF than is indicated by DC data.

The spurious-free dynamic range (SFDR) was evaluated using two-tone modulation at $f_1, f_2 = 500 \pm 10 \text{ MHz}$. Odd-order intermodulation products were measured at either $2f_1-f_2$ or $2f_2-f_1$, whichever term

was overall the greater. Even-order intermodulation products were measured at $f1+f2$.

Figure 4 and 5 gives a comparison between using EA only and the linearized modulator. The powers of fundamental and intermodulation products are shown as a function of applied electrode bias. Using EA modulation only, a characteristic behavior for most optical modulators is observed, where at maximum slope, second order intermodulation products are minimized, while third order intermodulation products are prevalent. For the linearized modulator, local minima for both odd and even order products are obtained at the same bias voltage, -1.67 V. Due to DC heating effects, the power of the fundamental does not stay constant over a wide voltage range. Instead, a local minimum is found around the linear bias point.

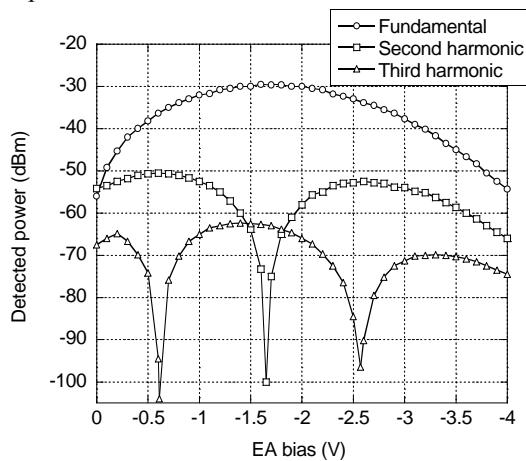


Fig. 4. Detected power of fundamental and intermodulation products using EA modulation only for 4 dBm modulation power per tone and at 1542nm.

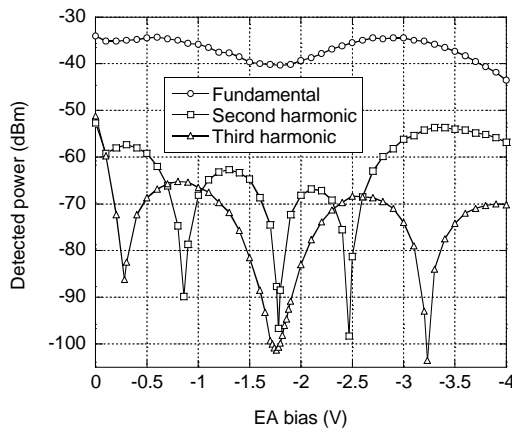


Fig. 5. Detected power of fundamental and intermodulation products using the linearized modulator for 4 dBm modulation power per tone and at 1542nm.

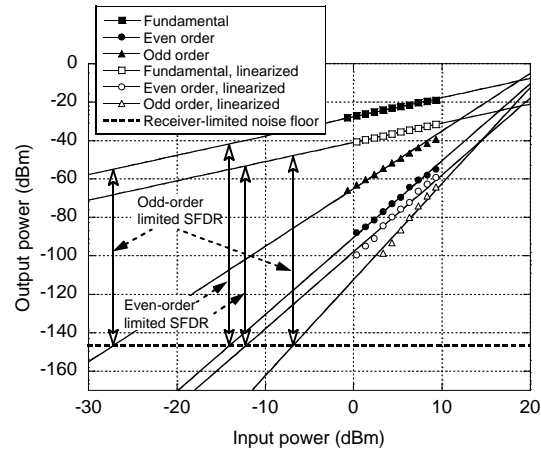


Fig.6. Measured SFDR, limited by even or odd order intermodulation products for the EAM and for the linearized modulator at 1542 nm and for receiver limited noise floor.

The measured SFDR is shown in Fig. 6 for both EAM and the linearized modulator. It is seen that odd-order intermodulation products are suppressed by 25dB to 40dB compared to that of using the EAM alone. Using the EAM alone, second order intermodulation was cancelled at maximum slope. The SFDR, as limited by odd or even order products was $91.9 \text{ dB}\cdot\text{Hz}^{2/3}$ or $104.9 \text{ dB}\cdot\text{Hz}^{3/4}$, respectively. For the linearized modulator, both second and third order intermodulation products could be cancelled, and odd order limited SFDR increased to $98.9 \text{ dB}\cdot\text{Hz}^{4/5}$. Even order limited SFDR was reduced to $93.4 \text{ dB}\cdot\text{Hz}^{3/4}$. The main reason for this reduction is lower slope sensitivity of the linearized modulator. The noise floor was in all cases mainly limited by receiver noise.

Linearized modulation was obtainable over the entire tuning range of the integrated SGDBR laser. To investigate the dependence on emission wavelength, the laser was tuned to the extremes of the tuning range and the SFDR was measured. At 1520.9 nm, odd order limited SFDR increased by 7.9 dB to $97.8 \text{ dB}\cdot\text{Hz}^{4/5}$ and even order limited SFDR was reduced by 10.8 dB to $92.7 \text{ dB}\cdot\text{Hz}^{3/4}$ using the linearized modulator, compared to the EAM. At 1574.4 nm, odd order limited SFDR increased by 7.6 dB to $99.3 \text{ dB}\cdot\text{Hz}^{4/5}$ and even order limited SFDR was reduced by 12.3 dB to $92.2 \text{ dB}\cdot\text{Hz}^{3/4}$. Compared to EA-modulation, the modulation sensitivity of the linearized modulator was reduced by more than 10 dB over the tuning range.

Currently, the overall performance of the linearized modulator is not improved compared to that using the EAM only. In order to achieve a real improvement, the relative strength of MZ modulation must be increased to generate a linearized response

with a low penalty in modulation sensitivity, as shown by Fig. 2. Further improvements would be achieved using adjustable splitting ratio in the MMI couplers of the MZ. Then, the amplitude balance would not be adjusted by electroabsorption for better utilization of available optical power. It has been shown that a similar integrated EAM can produce high sub-octave SFDR of $126.3 \text{ dB}\cdot\text{Hz}^{4/5}$ [8]. It is expected that this type of linearized modulator should be able to produce a comparable or greater broadband SFDR performance if the transmitted optical power would be as high. Future work will focus on improving the optical output power, incorporating tunable MZ couplers and balancing EA and MZ modulation for higher linearized slope sensitivity.

IV. CONCLUSION

We have proposed and demonstrated an architecture for a linearized modulator that is well-suited for monolithic integration to an optical source in an InP based material system. The modulator is based on a combination of electroabsorption and Mach-Zehnder modulation, and requires only one optical source and one single RF path. The principle is demonstrated, using a Mach-Zehnder modulator integrated with a widely tunable SG-DBR laser and a semiconductor amplifier. Simultaneous cancellation of both second and third order intermodulation products is observed over the tuning range of the laser, with 25dB to 40dB suppression of odd-order intermodulation products and 7dB to 8dB of improvement in odd-order limited SFDR, compared to using electroabsorption modulation alone. It is expected that a MZ modulator with tunable couplers and a tailored balance between MZ and EA modulation would further enhance odd-order limited SFDR and reduce the large penalty in even-order limited SFDR that is currently seen as a result of reduced modulation slope sensitivity in the linearized modulator.

REFERENCES

- [1] R.B. Welstand, J.T. Zhu, W.X. Chen, A.R. Clawson, P.K.L Yu and S.A Pappert, "Combined Franz-Keldysh and quantum-confined Stark effect waveguide modulator for analog signal transmission," *J. Lightwave Technol.*, **17**, pp. 497-502, 1999.
- [2] D.J.M. Sabido, I.X. Tabara, M. Fong, T.K. Chung-Li and L.G. Kazovsky, "Improving the dynamic range of a coherent AM analog optical link using a cascaded linearized modulator," *IEEE Photon. Technol. Lett.*, **7**, pp. 813-815, 1995.
- [3] W.B. Bridges and J.H. Schaffner, "Distortion in linearized electrooptic modulators," *IEEE Trans. Microwave Theory Tech.*, **43**, pp. 2184-2197, 1995.
- [4] E.I. Ackerman, "Broad-band linearization of a Mach-Zehnder electrooptic modulator," *IEEE Trans. Microwave Theory Tech.*, **47** pp. 2271-2279, 1999.
- [5] L.M. Johnson and H.V. Roussell, "Reduction of intermodulation distortion in interferometric optical modulators," *Opt. Lett.*, **13**, pp 928-930, 1988.
- [6] M. Farwell, Z. Lin, E. Wooten, and W. Chang, "An electrooptic intensity modulator with improved linearity," *IEEE Photon. Technol. Lett.*, **3**, pp. 792-795, 1991.
- [7] Y.A. Akulova, G.A. Fish, P. Koh, P. Kozodoy, M. Larson, C. Schow, E. Hall, M. Marchand, P. Abraham and L.A. Coldren, "10 Gb/s Mach-Zehnder modulator integrated with widely-tunable sampled-grating DBR laser," in *Optical Fiber Communication Conference on CD-ROM (Optical Society of America, Washington, DC, 2004)*, TuE4.
- [8] L.A. Johansson, J.T. Getty, Y.A. Akulova, G.A. Fish and L.A. Coldren, "Sampled-Grating DBR Laser-Based Analog Optical Transmitters," *IEEE J. Lightwave Technol.*, **21**, pp. 2968-2976, Dec. 2003.

InP-based Active Photonic Integrated Circuits

[Invited]

Jonathon S. Barton, Matt Dummer, Anna Tauke-Pedretti, Erik J. Skogen, James Raring,
Matt Sysak, Milan Mašanović, Leif A. Johansson, Larry A. Coldren

University of California Santa Barbara, Engineering II Santa Barbara, CA 93106
Tel: (805)893-8465, FAX: (805) 893-4500, email: jsbarton@engineering.ucsb.edu

Abstract-This talk will outline a number of state-of-the-art photonic integrated circuits including photocurrent-driven wavelength converters, optical receivers and optical tunable transmitters using SGDBR lasers with Mach-Zehnder and Electro-absorption modulators.

I. INTRODUCTION

There are many advantages to the integration of discrete photonic devices into more complex Photonic Integrated Circuits (PICs)[1]. PICs reduce the optical and electrical losses in between components, allow for much higher functionality, and lower costs in packaging. Tunable lasers[2], modulators, semiconductor optical amplifiers (SOAs), detectors, and passive waveguiding components such as multi-mode interference devices (MMIs), have all been successfully integrated – on both Offset Quantum Well (OQW) and Quantum Well Intermixed[3] (QWI) integration platforms. The time-tested OQW platform permits the formation of active and passive regions across the device structure suitable for the fabrication of high-gain SOAs, high-speed modulators, and detectors. Alternatively, the QWI platform gives more flexibility and allows the creation of multiple band-gaps across the device – leading to the optimization of each component with regard to absorption properties, refractive index shifts, and chirp characteristics.

One such Photonic Integrated Circuit that is widely regarded as critical to the scalability, flexibility, and cost of future optical networks is the monolithic wavelength converter. These devices have opportunities for deployment in optical switches, routers and add/drop multiplexers. Essentially, they enable Wavelength Division Multiplexed (WDM) signals to be transferred from one wavelength channel to another wavelength channel without requiring off-chip electronic circuitry. Many different implementations have been proposed using cross phase modulation (XPM)[4], differential phase modulation (DPM)[5], and/or cross absorption modulation (XAM) of SOAs. High performance has been obtained with both discrete[4] and monolithically-integrated tunable all-optical wavelength converters (TAO-WC)[6].

Another approach to wavelength conversion – and pursued henceforth in this paper is that of the photocurrent-driven (PD-WC) variety [7]. These devices rely on compact tunable transmitters that consist of a SGDBR laser, SOA and either an Electro-absorption (EA)[3], or Mach-

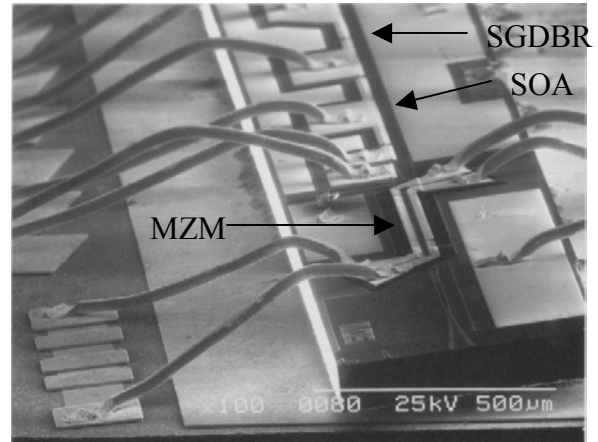


Fig. 1. Scanning electron micrograph of an integrated transmitter with series push-pull modulator (500µm long), SOA and SGDBR laser

Zehnder(MZ)[8] modulator – with one implementation shown in fig. 1. Figure 2 gives an equivalent circuit diagram of a PD-WC that incorporates an SOA-PIN receiver driving a Mach-Zehnder laser, all integrated with a widely-tunable SGDBR laser on a single InP chip.

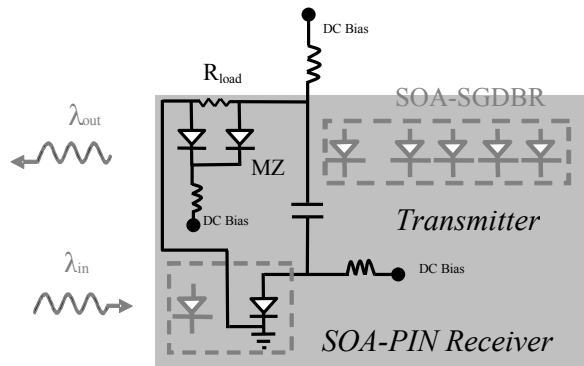


Fig.2. Series Push-pull MZ photocurrent-driven wavelength converter configuration

PD-WCs do not require an optical filter to reject the input signal at the output which is desirable particularly with wavelength tunable applications where the response time of a filter could limit system performance. Integrating SOAs

with detectors allows the fabrication of high-gain, high saturation power receivers as shown in Fig. 3.

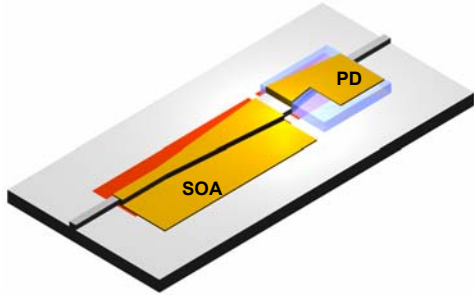


Fig. 3. Device Schematic of integrated SOA-Photodiode Receiver

As illustrated in Figs. 1 & 3, these sub-components are monolithically integrated in a parallel configuration as a photocurrent-driven wavelength converter. 2.5Gbit/s operation has been demonstrated for devices with this structure [7]. In order to improve the bandwidth, tunable transmitters using a series push-pull Mach-Zehnder modulator structure were fabricated similar to the structure shown in [9]. This structure can improve the bandwidth of the modulator by roughly a factor of two. The device configuration is shown in Fig. 2. Despite some additional bias circuitry, this configuration has the added benefit that the device may be biased to achieve zero chirp for inverting and non-inverting operation, and no DC power is dissipated across the resistive load.

II. DEVICE RESULTS

The small-signal optical-to-optical bandwidth (S_{21}) was measured for the wavelength converter with an input signal at 1545nm and converted signal at 1555nm using a 500 μ m long MZ modulator connected as shown in fig. 2 for various biases on each branch of the Mach-Zehnder modulator.

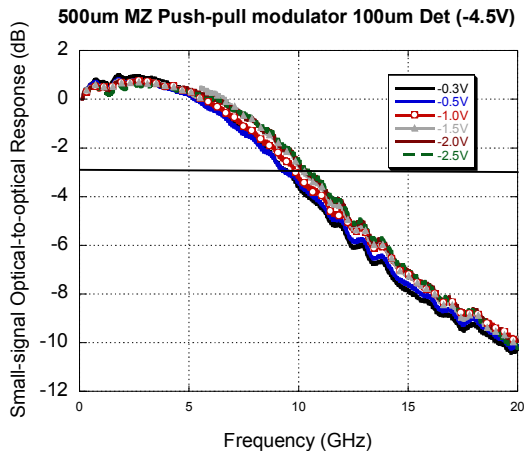


Fig 4. Small-signal optical-to-optical response for a MZ based wavelength converter 1545nm – 1555nm

The receiver for this device consisted of a 300 μ m long SOA with a 100 μ m long (3 μ m wide) Franz-Keldysh PIN detector that was reverse-biased to -4.5V. As can be seen in fig. 4, an optical bandwidth suitable for 10Gbit/s operation is obtained with a 50ohm termination on the detector and modulator.

III. CONCLUSION

We demonstrate a variety of different photonic integrated circuits suitable as building block elements on a couple of different integration platforms. The use of high-gain, high saturation power receivers coupled with high bandwidth efficient modulators will allow the realization of viable monolithic wavelength converters.

REFERENCES

- [1] TL, Koren U. "Semiconductor photonic integrated circuits." IEEE Journal of Quantum Electronics, vol.27, no.3, March 1991, pp.641-53.
- [2] Coldren, L. A. , "Monolithic Tunable Diode Lasers", IEEE. Journal Special Topics Quantum Electronics., 6, No. 6, Nov. 2000.
- [3] Raring J.W., E. J. Skogen, L. A. Johansson, M. N. Sysak, J. S. Barton, M. L. Mašanović, L. A. Coldren Demonstration of Widely-Tunable Single-Chip 10 Gb/s Laser-Modulators Using Multiple-Bandgap InGaAsP Quantum-Well Intermixing, Photonics Technology Letts. July 2003.
- [4] Nielsen ML, Nord M, Petersen MN, Dagens B, Labrousse A, Brenot R, Martin B, Squedín S, Renaud M. 40 Gbit/s standard-mode wavelength conversion in all-active MZI with very fast response. Electronics Letters, vol.39, no.4, 20 Feb. 2003, pp.385-6.
- [5] Suzuki Y, Ito T, Shibata Y. "Monolithically integrated wavelength converter: Sagnac interferometer integrated with parallel-amplifier structure (SIPAS) and its application." 2002 LEOS Summer Topical Meetings IEEE.2002, ppWB2-12.
- [6] Masanovic M.L., V. Lal, J. S. Barton, E. J. Skogen, L. A. Coldren, and D. J. Blumenthal, "Monolithically integrated Mach-Zehnder interferometer wavelength converter and widely tunable laser in InP," IEEE Photonics Technology Letters, vol. 15, pp. 1117-19, 2003.
- [7] Hutchinson J.M., J. F. Zheng, J. S. Barton, M. L. Masanovic, M. N. Sysak, J. A. Hennes, L. A. Johansson, D. J. Blumenthal, L. A. Coldren, H. V. Demir, V. A. Sabnis, O. Fidaner, J. S. Harris, and D. A. B. Miller, " Indium Phosphide based Wavelength Conversion for High Speed Optical Networks," Intel Technology Journal, 2004.
- [8] Barton J.S., Skogen E.J., Mašanović M.L., DenBaars S.P., and Coldren L.A., "Widely-tunable high-speed transmitters using integrated SGDBRs and Mach-Zehnder modulators." IEEE Journal of Selected Topics in Quantum Electronics, Vol. 9, No. 5, pp.1113-17. September/October 2003.
- [9] Walker RG. "High-speed III-V semiconductor intensity modulators." IEEE Journal of Quantum Electronics, vol.27, no.3, March 1991, pp.6

Demonstration of negative chirp characteristics over wide wavelength range using monolithically integrated SG-DBR laser/electroabsorption modulator

J.W. Raring, E.J. Skogen, S.P. DenBaars and L.A. Coldren

For the first time negative large signal chirp characteristics from a widely-tunable laser/electroabsorption modulator transmitter are reported. This device employed an intermixed quantum well absorption region in the modulator. Large signal time resolved chirp measurements were made at wavelengths from 1542 to 1569 nm and were shown to exhibit negative characteristics at all wavelengths.

Introduction: It is desirable that future 10 Gbit/s transmitters employed in dense wavelength division multiplexing metro-area networks possess both wavelength tunability and negative chirp characteristics. Wavelength-agile transmitters will enable next generation network technologies such as dynamic provisioning. Negative chirp characteristics are essential for 10 Gbit/s transmission over fibre spans implemented in metro-area networks to limit the dispersion penalty.

It has been shown that quantum well electroabsorption modulators (EAMs), whose absorption characteristics are governed by the quantum confined Stark effect, can provide a negative chirp parameter at a single laser operating wavelength [1]. More complicated monolithically integrated Mach-Zehnder laser/modulator designs have been traditionally employed to provide desirable chirp characteristics across wide tuning ranges.

Recently, we have demonstrated 10 Gbit/s transmission through 75 km of fibre with under 0.5 dB dispersion penalty at a wavelength of 1564 nm [2]. In this Letter we report time resolved large signal chirp measurements at 10 Gbit/s to demonstrate, for the first time, a widely-tunable laser/EAM transmitter exhibiting negative large signal chirp over the tuning range of the device. Furthermore, we demonstrate the onset of the negative chirp characteristics in an EAM operating regime which provides over 10 dB of signal extinction and only 3–4 dB of total insertion loss. A novel quantum well intermixing (QWI) processing platform provided the enabling technology for achieving a quantum well band edge blue-shifted from that of the laser gain peak. The relatively simple QWI process employed in this work enables the precise placement of the band edge for each component within the device. This allows for partially intermixed QWs to remain in the modulator while leaving the axial waveguide undisturbed.

Experiment: The transmitter, Fig. 1, consists of a five-section widely tunable sampled-grating (SG) distributed Bragg reflector (DBR) laser followed by an electroabsorption modulator. The five sections of the SG-DBR laser are, from left to right in Fig. 1, are backside absorber, rear mirror, phase, gain, and front mirror. The phase and mirror sections function to tune the wavelength of the laser. The lithographically-defined mirrors make the SG-DBR laser ideal for monolithic integration since no facets are required for operation.

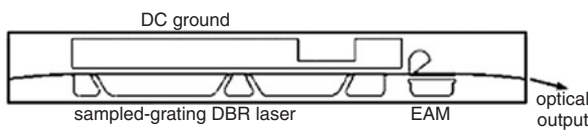


Fig. 1 Top view schematic of SG-DBR/EAM transmitter architecture

This work employs a modified ion implantation enhanced QWI process, described in [3], as the fabrication platform. In this process, vacancies are created by ion implantation into an InP buffer layer over the multiquantum well (MQW) active region. During a high temperature anneal, the vacancies are diffused through the MQW region, promoting the interdiffusion of group V atoms between the wells and barriers. The interdiffusion reshapes the QW profile by reshaping the QW/barrier interface. The result is a shift in the quantised energy levels in the well, and hence a shift in the band edge energy.

Results: The MOCVD-grown epitaxial base structure contained an n-contact InGaAs layer 1 μm below an MQW active region centred within a 1.1Q waveguide. The MQW consists of 15 InGaAsP 8.0 nm compressively strained (0.6%) quantum wells, separated by 8.0 nm

tensile strained (0.3%) InGaAsP barriers grown on an Fe-doped InP substrate. The fabrication process was identical to that described in [3] with modifications for top-side n-contacts for capacitance reduction. The devices were thinned, cleaved into bars, and mounted on AlN carriers for characterisation

The SG-DBR lasers demonstrated over 25 nm of wavelength tuning, threshold currents of 13 mA, and output powers up to 10 dBm were captured in an integrating sphere at a gain section current of 100 mA. At the same gain section bias, the average fibre coupled power from the transmitters with no bias on the EAM ranged from 0 to 5 dBm. A more thorough description of the DC and RF characteristics of these transmitter devices can be found in [4].

To demonstrate the viability for these devices to operate as widely-tunable 10 Gbit/s transmitters, the modal extinction characteristics and large signal alpha parameter were extracted at several wavelengths. The DC modal extinction characteristics of the device in question are shown in Fig. 2. The 175 μm-long EAM achieved over 35 dB of modal extinction for wavelengths between 1542 and 1569 nm, with efficiencies greater than 15 dB/V. The unbiased insertion loss was measured at 1–2 dB for a wavelength of 1575 nm. The same modulators possessed a small signal 3 dB bandwidth of over 10 GHz.

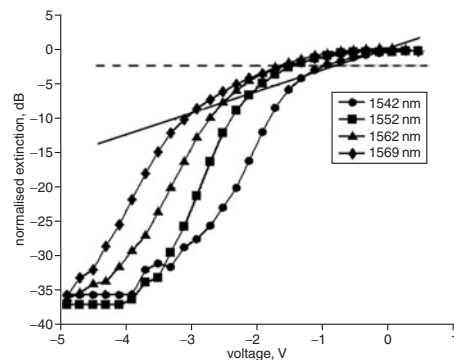


Fig. 2 DC extinction of 175 μm modulator for wavelengths from 1542 to 1569 nm

Dashed and dotted lines indicate approximate EAM on state DC bias to achieve chirp parameter of 0 and -0.7, respectively, with 2 V peak-to-peak swing

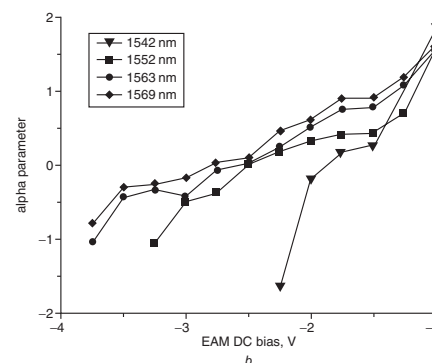
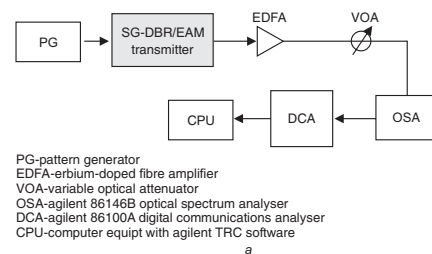


Fig. 3 Test setup, and alpha parameter against EAM bias

a Test setup used to extract time resolved large signal alpha parameter
b Alpha parameter against EAM bias at 1542, 1552, 1563, 1569 nm extracted at 10 Gb/s with 2 V peak-to-peak swing

The dynamic chirp measurements were made using Agilent's Time Resolved Chirp (TRC) software coupled with an Agilent 86146B optical spectrum analyser and 86100A digital communications analyser. The complete test setup is illustrated in Fig. 3a. The alpha parameter was measured at 10 Gbit/s against the DC bias applied to the EAM for

wavelengths of 1542, 1552, 1563 and 1569 nm. The peak-to-peak voltage swing applied to the EAM was 2 V.

Considering the proximity of the modulator band edge to the laser operating wavelength, it is clear that a larger reverse bias is required to achieve efficient absorption at longer wavelengths. As the reverse voltage is increased, the onset of absorption occurs at longer wavelengths and the absorption efficiency is decreased slightly, however the general shape of the absorption curves remain similar. In view of the fact that the alpha parameter is related to the operating point on the modulator absorption curve, and the fact that similar absorption characteristics are observed for all wavelengths, it is reasonable to conclude that a negative alpha parameter can be obtained over a wide tuning range. As shown in Fig. 3b, the measured alpha parameter follows this trend with larger reverse biases required for negative chirp at longer wavelengths. The measured alpha parameters were found to transition from positive to negative for all wavelengths, occurring at 1.9 V at 1542 nm and 2.8 V at 1569 nm.

By comparing the extinction characteristics in Fig. 2 with the chirp characteristics of Fig. 3b, the modulator extinction and insertion loss can be estimated for a given alpha parameter at all tested wavelengths. The intersections of the dashed and dotted lines in Fig. 2 represent the on-state operating voltage of the EAM to achieve alpha parameters of 0 and -0.7 , respectively. The on-state operating voltage was calculated by adding half of the peak-to-peak voltage swing (1V) to the DC bias necessary to achieve the alpha parameter values in question. It is clear that for both alpha parameter values, a 2 V swing on the EAM provides over 10 dB extinction at all tested wavelengths. Fig. 2 indicates that to achieve an alpha parameter of 0, the modulator must be biased such that there is ~ 2 dB of signal extinction for all tested wavelengths. By adding the necessary signal extinction to the unbiased EAM loss of 1–2 dB, we arrive at a total insertion loss of 3–4 dB necessary to attain an alpha parameter of 0. To achieve an alpha parameter of -0.7 , the on-state signal extinction ranged from 3.5 to 9 dB, depending on the operating wavelength. By performing the same operation as above, we arrive at a total insertion loss of 4.5 to 11 dB necessary to attain an alpha parameter of -0.7 . The extinction properties coupled with the dynamic chirp data of the EAM demonstrates the ability to achieve ample signal extinction along with reasonable insertion loss in an EAM operating regime exhibiting negative chirp characteristics.

Conclusion: We have demonstrated the first widely-tunable laser/electroabsorption modulator transmitter exhibiting negative large signal chirp over a wide tuning range. The negative chirp characteristics were achieved in a device operating regime in which 10 dB of extinction and reasonable insertion loss were achieved. The SG-DBR lasers possess a tuning range of over 27 nm and high output power. The integrated EAM provided 15 dB/V of absorption efficiency and a 3 dB modulation bandwidth of over 10 GHz. As expected, the time resolved large signal chirp parameter was shown to transition to a negative value at larger reverse biases for increasing operating wavelength.

© IEE 2004

7 October 2004

Electronics Letters online no: 20047306

doi: 10.1049/el:20047306

E.J. Skogen and L.A. Coldren (*Electrical and Computer Engineering Department, University of California, Santa Barbara, CA 93106, USA*)

J.W. Raring and S.P. DenBaars (*Materials Department, University of California, Santa Barbara, CA 93106, USA*)

References

- 1 Morito, K., *et al.*: 'Penalty free 10 Gb/s NRZ transmission over 100 km of standard fiber at 1.55 μm with a blue-chirp modulator integrated DFB laser', *IEEE Photonics Technol. Lett.*, 1996, **8**, pp. 431–433
- 2 Raring, J., *et al.*: 'Minimal dispersion penalty at 10 Gb/s, over 75 km, using a quantum-well-intermixed electroabsorption-modulator/widely-tunable laser transmitter'. Optical Fiber Communications Conf. (OFC). Postconference Tech. Dig., Optical Society America, PDP 13, 2004
- 3 Skogen, E., *et al.*: 'Post growth control of the quantum-well band edge for the monolithic integration of widely-tunable lasers and electroabsorption modulators', *J. Sel. Top. Quantum Electron.*, 2003, **9**, (5), pp. 1183–1190
- 4 Raring, J., *et al.*: 'Demonstration of widely-tunable single-chip 10 Gb/s laser-modulators using multiple-bandgap InGaAsP quantum-well intermixing', *IEEE Photonics Technol. Lett.*, 2003, **16**, (7), pp. 1613–1615

I. Photonic Integrated Circuits and Related Technology

B. Widely-Tunable Wavelength Converters

3D Simulation of an Integrated Wavelength Converter

Joachim Piprek,ⁱ Nicolas Trenado, John Hutchinson,^a Jeffrey Hennes, and Larry A. Coldren
Electrical and Computer Engineering Department,
University of California, Santa Barbara, CA 93106
^a also with Intel Corporation, Portland, OR

ABSTRACT

In this paper, we present three-dimensional (3D) simulation results for an integrated wavelength converter which monolithically combines a pre-amplifying receiver with a post-amplified sampled-grating distributed Bragg reflector tunable laser diode. The self-consistent physical model used in the simulation takes into account gain and absorption in the quantum wells, carrier drift and diffusion, and optical wave-guiding. In order to validate and calibrate the model, we compare the results to available experimental data. Microscopic physical processes inside the converter components are revealed and analyzed, such as receiver saturation effects.

Keywords: Optoelectronic integrated circuits, OEIC, wavelength converter, numerical simulation

1. INTRODUCTION

Our wavelength converter electrically couples an optical receiver for any input wavelength of the C band, e.g., $\lambda_{in} = 1530$ nm, with an optical transmitter for any other output wavelength of the C band, e.g., $\lambda_{out} = 1550$ nm (Fig. 1). The receiver integrates signal pre-amplification by a 500 μm long semiconductor optical amplifier (SOA) and signal detection by a 50 μm long waveguide photodiode (WPD). The optical signal is converted into an electrical signal that directly modulates a sampled-grating distributed-Bragg-reflector (SGDBR) laser diode which is integrated with a semiconductor optical amplifier (SOA) for signal enhancement.¹ The SGDBR laser can be tuned to emit at any wavelength of the C band.

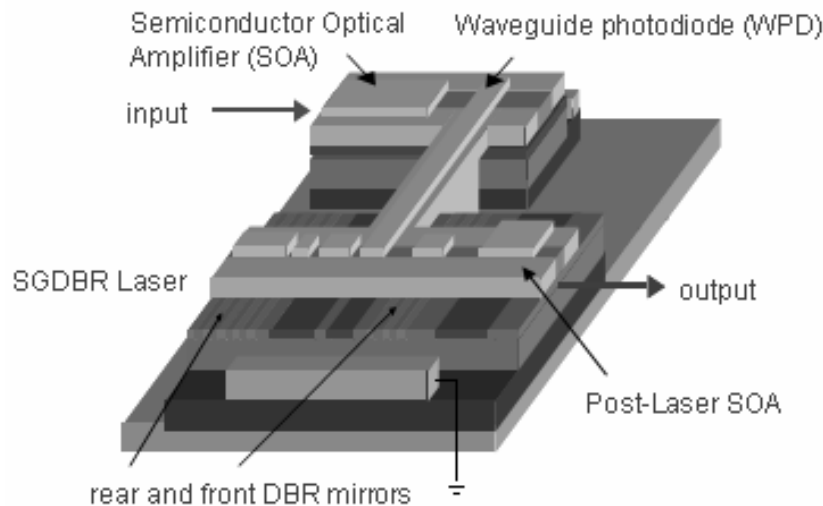


Fig. 1: Schematic view of the InP-based integrated wavelength converter.

ⁱ Corresponding author, e-mail: piprek@ieee.org

The structure of the different components is very similar as all are based on the same epitaxial growth (Tab. 1). An offset multi-quantum-well (MQW) active region is grown on top of the waveguide region. A ridge waveguide structure is etched through the MQW region. Passive device sections are formed by etching off the MQWs completely.

Layer	Material	Thickness nm	Doping 10^{18} cm^{-3}	Refractive index
p-contact	InGaAs	100	30 (p)	3.72
upper cladding	InP	1600	1 (p)	3.167
upper cladding	InP	200	0.3 (p)	3.167
doping setback	InP	50	-	3.167
quantum barrier (8x)	$\text{In}_{0.735}\text{Ga}_{0.265}\text{As}_{0.513}\text{P}_{0.487}$	8	-	3.396
quantum well (7x)	$\text{In}_{0.735}\text{Ga}_{0.265}\text{As}_{0.845}\text{P}_{0.155}$	6.5	-	3.616
etch stop	InP	10	-	3.167
waveguide	$\text{In}_{0.612}\text{Ga}_{0.338}\text{As}_{0.728}\text{P}_{0.272}$	350	0.1 (n)	3.455
lower cladding	InP	1400	1 (n)	3.167
etch stop / n-contact	InGaAs	100	1 (n)	3.72
Buffer	InP	1000	-	3.167

Tab. 1 Epitaxial layer sequence of the devices simulated.

The self-consistent numerical simulation² includes band-structure and gain calculations for the strained quantum wells, carrier transport, optical waveguiding, and Bragg reflection. Field effects on MQW gain and absorption (quantum confined Stark effect) are considered as well as free-carrier and intervalence band absorption. InGaAsP material parameters are adjusted based on recent publications.³

The next section discusses 2D simulation results and general device physics. The following section addresses the specifics of each device based on 3D simulation. Section 4 compares simulation results to available receiver measurements and discusses parameter calibration issues.

2. TWO-DIMENSIONAL SIMULATION

2.1 Optical Waveguiding

The software solves the scalar Helmholtz equation in two dimensions to obtain the intensity of the fundamental mode $W_0(x,y)$. The vertical profile $W_0(0,y)$ is plotted in Fig. 2 together with the refractive index profile. The unsymmetrical index profile results in an optical confinement factor for the quantum wells of $\Gamma=0.06$. The 2D mode profile is given in Fig. 3. It is well confined by the p-InP ridge. In agreement with experimental results, fundamental mode operation is assumed here. Near $1.55\mu\text{m}$ wavelength, optical losses are mainly caused by intervalence band absorption (IVBA). The IVBA coefficient is considered proportional to the local hole density, i.e., it is only relevant within the quantum wells and within p-doped regions. The total local absorption coefficient is calculated as

$$\alpha(x,y) = \alpha_b + k_n n + k_p p \quad (1)$$

with the background loss α_b , the electron density n and the hole density p . The hole coefficient $k_p = 25 \times 10^{-18} \text{ cm}^2$, the electron coefficient $k_n = 1 \times 10^{-18} \text{ cm}^2$, and the background value $\alpha_b = 10 \text{ cm}^{-1}$ are employed in our calculations.

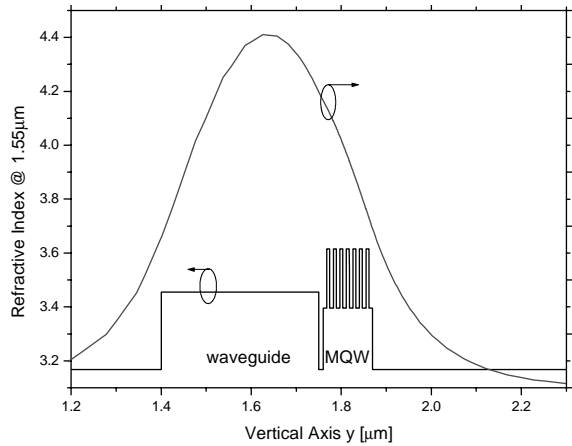


Fig. 2: Vertical profile of refractive index and optical intensity of the fundamental mode.

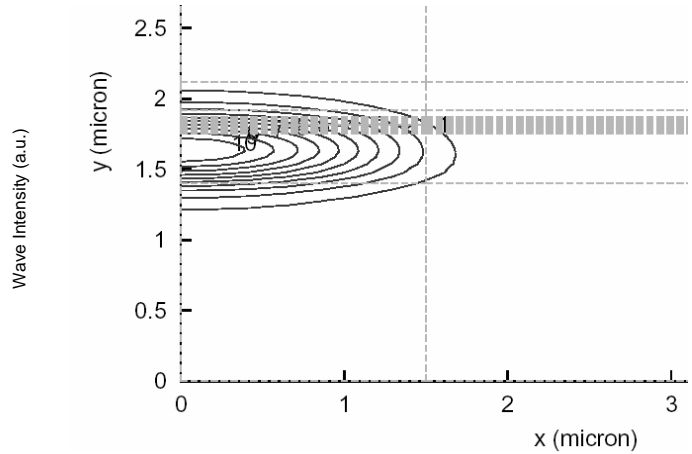


Fig. 3: 2D intensity profile of the fundamental waveguide mode for half the device (y – symmetry plane, ridge width = 3 micrometers).

2.2 Multi-Quantum Well Active Region

The energy band diagram of the multi-quantum well active region is plotted in Fig. 4. The etch stop layer is needed for longitudinal integration of different devices, however, it constitutes a barrier for electron injection into the MQW which requires thermionic emission of electrons from the waveguide layer. The common conduction band edge offset ratio $\Delta E_c / \Delta E_g = 0.4$ is employed at all interfaces (E_c – conduction band edge, E_g – band gap). On the other hand, the etch stop layer also generates a barrier in the valence band, which helps to prevent holes from escaping the MQW.

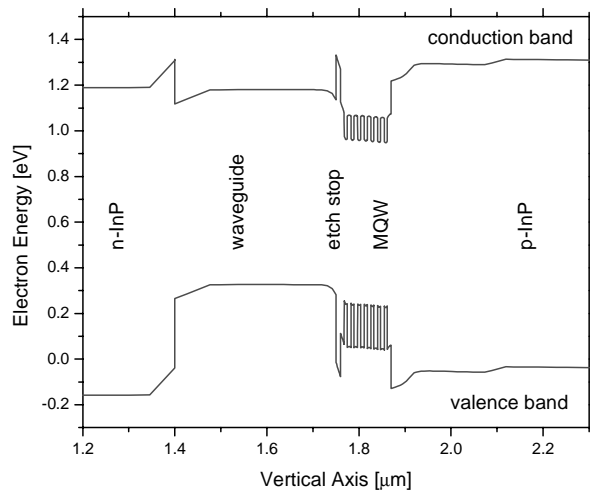


Fig. 4 Energy band diagram of the active region.

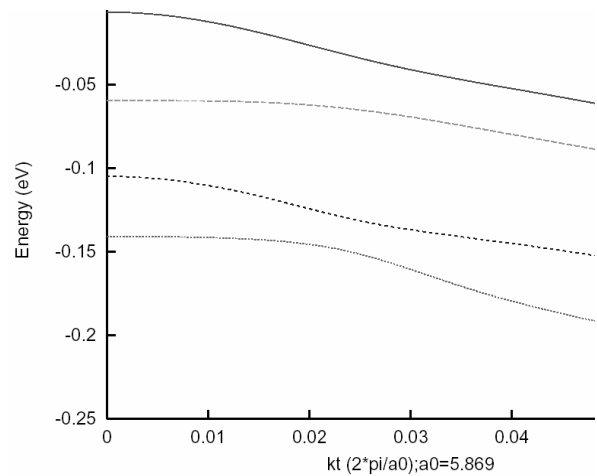


Fig. 5: Energy vs. transversal wavenumber for the quantum well valence subbands (from top: HH1, HH2, LH1, HH3).

For the quantum wells, compressive strain of 0.88% is calculated. The tensile strain in the barrier is -0.2%. The conduction bands are assumed parabolic with an in-plane effective mass of 0.0447. The non-parabolic valence bands are calculated using the popular 4x4 **kp** method including valence band mixing (Fig. 5). Three heavy hole (HH) levels and one light hole (LH) level are found. The relevant top level has an effective HH mass of 0.3 at the Γ point.

2.3 Carrier Transport

The drift and diffusion of electrons and holes is calculated by solving the semiconductor transport equations.³ For forward bias operation (95 mA) of amplifier or laser, Fig. 6 gives the vertical carrier density profile in the center of the device. The average quantum well carrier density is about $2 \times 10^{18} \text{ cm}^{-3}$. The lateral carrier density profile reveals relatively strong lateral carrier diffusion away from the waveguide ridge. The corresponding lateral profiles of the recombination rates are plotted in Fig. 7. Stimulated recombination is restricted to the fundamental optical mode profile (cf. Fig. 3). The strongest carrier loss is caused by the Auger recombination rate

$$R_{\text{Aug}} = n p (C_n n + C_p p) \quad (2)$$

with the preliminary Auger parameters $C_n=0$ and $C_p= 8 \times 10^{-29} \text{ cm}^6/\text{s}$. Those parameters can later be adjusted to fit experimental characteristics. Spontaneous emission is calculated by integrating the spontaneous emission rate, it is proportional to the square of the carrier density. Shockley-Read-Hall (SRH) recombination at crystal defects and interfaces is inversely proportional to the SRH lifetime of the carriers. We here assume a uniform SRH lifetime of 20 ns for electrons and holes throughout the device. This value is longer than the total (measured) lifetime which includes all recombination mechanisms.

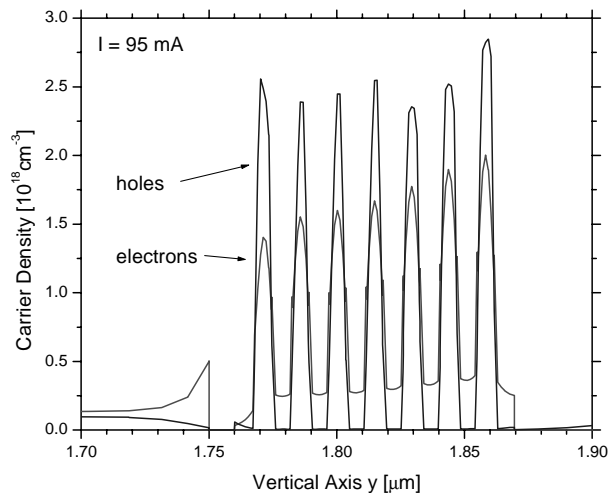


Fig. 6: Vertical carrier density profile in the center of the device.

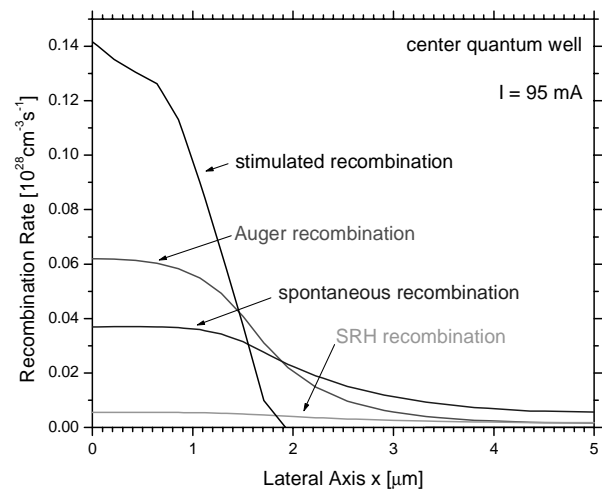


Fig. 7: Lateral profile of the quantum well recombination rates.

2.4 Quantum Well Gain and Absorption

Calculated gain spectra are shown in Fig. 8 under flat-band condition (zero field) using a free carrier model including Lorentz broadening with 0.1 ps intraband relaxation time. The gain peak wavelength blue-shifts slightly due to band filling, however, it is close to the target wavelength of 1550 nm. Figure 9 plots calculated quantum well absorption spectra for different reverse bias conditions of the photodetector. Higher reverse bias gives a stronger internal field which moves the absorption edge towards longer wavelength (quantum confined Stark effect). At the same time, the maximum possible absorption is reduced. At 2V reverse bias, our quantum well shows an absorption edge near 1610 nm. It absorbs light almost uniformly from 1500nm to 1600nm wavelength.

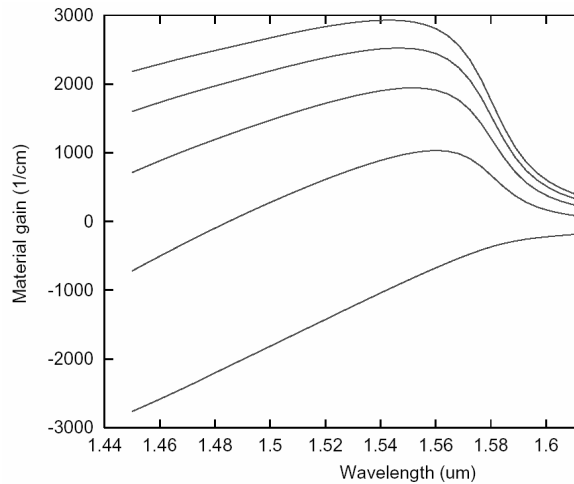


Fig. 8: Flat-band quantum well gain spectra for different carrier densities (from bottom: 1, 2, 3, 4, and $5 \times 10^{18} \text{cm}^{-3}$).

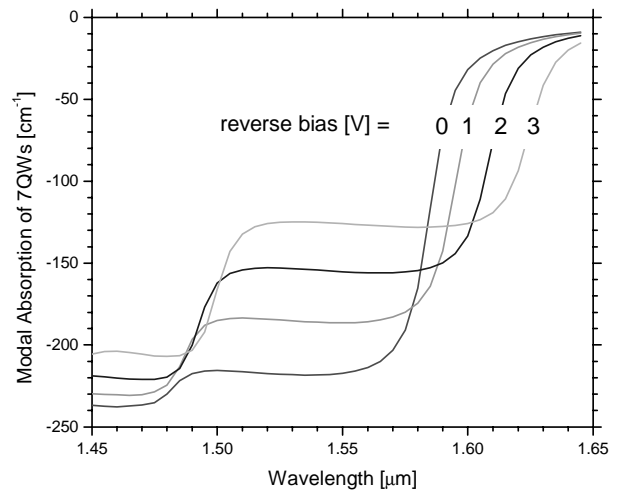


Fig. 9: Quantum well absorption spectrum at different bias.

3. THREE-DIMENSIONAL SIMULATION

3.1 Waveguide Photodetector

Figure 10 shows a 3D plot of the optical intensity calculated for the fundamental mode with 0.01 mW input power. The optical power decays exponentially in travel direction (z) and it is almost completely absorbed at the other end.

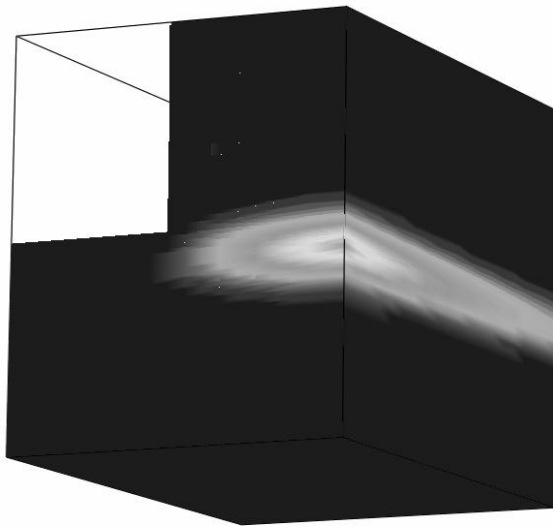


Fig. 10: Fundamental optical mode intensity for half the photodetector.

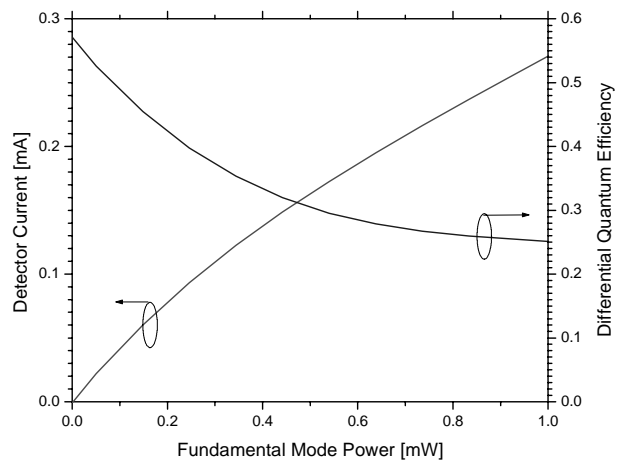


Fig. 11: Photocurrent and quantum efficiency vs. input power.

Photocurrent and quantum efficiency are given in Fig. 11. The calculation considers a front facet reflectance of $R=0.29$, which reduces the maximum possible quantum efficiency to 71%. At low input power, the calculated quantum efficiency is 58%, due to the incomplete absorption of the lightwave. With higher input power, the efficiency decays and it is only 25% at 1 mW. The decay in efficiency is reflected by the non-linear current-power characteristic in Fig.

11. The non-linear response of the photodetector is mainly attributed to the reduction of the quantum well absorption with increasing carrier density. The photon density is highest at the input facet. With increasing power, it generates an increasing number of electron-hole pairs in the quantum wells (QWs). The average QW carrier density is shown in Fig. 12 for different input power. Due to band filling, higher carrier density leads to lower absorption (Fig. 13) which affects the decay of the optical power along the waveguide (Fig. 14). With higher input power, the detection is less efficient, i.e., a larger part of the input power remains undetected. While the intensity decays by a factor of about 14 for low input power, it only decays by a factor of 5 for 1 mW input power in Fig. 14. This mechanism is the main reason for the non-linear photocurrent response shown in Fig. 11. The photocurrent is non-uniform in longitudinal direction (Fig. 15).

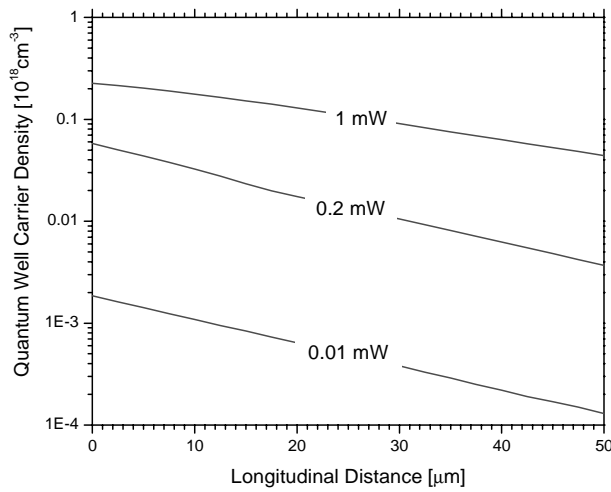


Fig. 12: Longitudinal profile of the quantum well carrier density at different input power.

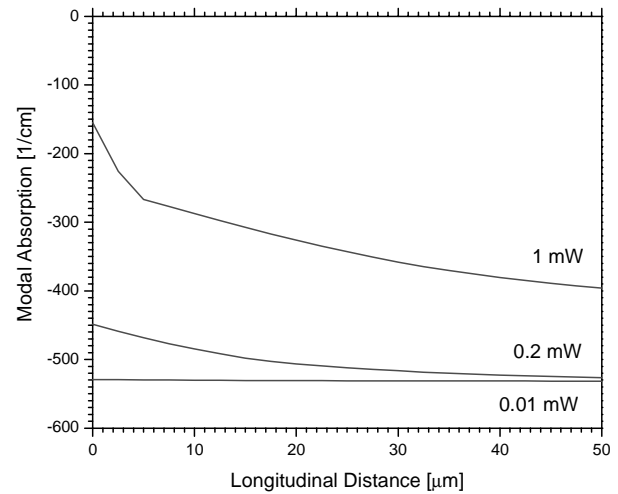


Fig. 13: Longitudinal profile of the modal absorption at different input power (1550 nm).

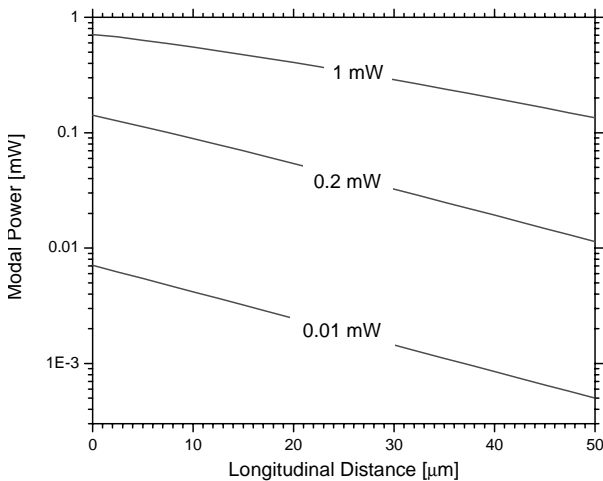


Fig. 14: Longitudinal decay of the modal power at different input power.

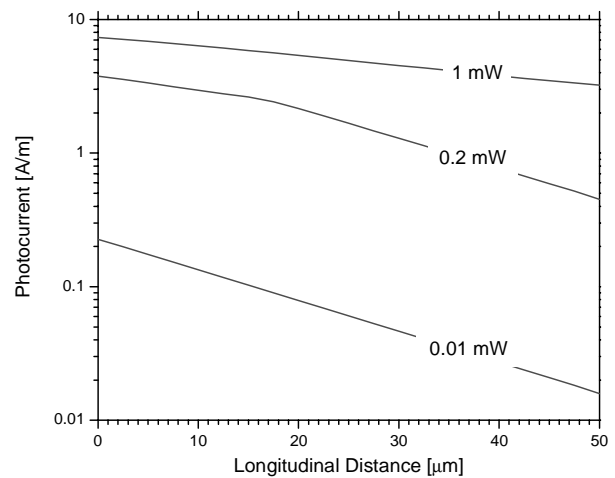


Fig. 15: Non-uniform distribution of the photocurrent at different input power.

However, it needs to be mentioned that PICS3D simulations are not truly 3D since carriers cannot move in longitudinal z direction. The device is rather sliced up into many 2D sections (x,y) within which the device equations are solved self-consistently. The only difference between all the 2D sections is the photon density $S(z)$ which varies in longitudinal direction (Fig. 10). Thus, the quantum well carrier density $N(x,y)$ varies among the 2D sections. Iteratively, a balance between $S(z)$ and $N(x,y)$ is achieved by the software which can be called quasi-3D solution.

3.2 Integrated Receiver

The optical gain of the MQW active region depends on the applied bias: if it is positive, the gain is positive and the region is an amplifying region, if the bias is negative, the gain is negative and the region is an absorbing region. The energy bands of the SOA region are plotted in Figure 16. The bands are flat due to presence of the doping region and the fact that a forward bias is applied to the SOA. In this case, the overlap between electron and hole wave function is optimum and the modal gain is positive (cf. Fig. 8). The energy bands of the WPD region are shown in Figure 17. A reverse bias is applied so that the bands are not flat and the absorption is dominant (cf. Fig. 9). The modal gain is positive for the SOA region and negative for the WPD region (Fig. 18). Accordingly, the wave intensity in Fig. 19 is increasing within the SOA region and decreasing within the WPD region.

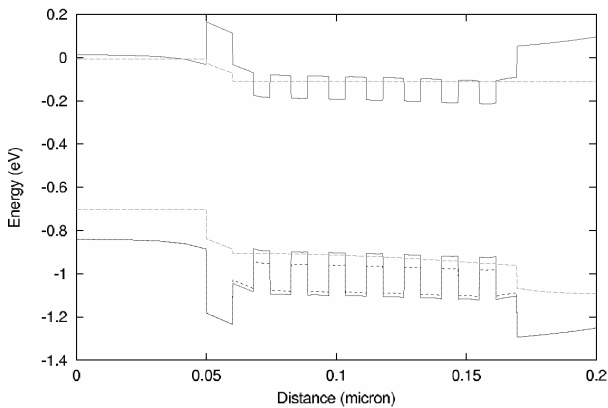


Fig. 16: Conduction (upper) and valence (lower) bands in the SOA region along the vertical y direction (dashed: quasi-Fermi levels)

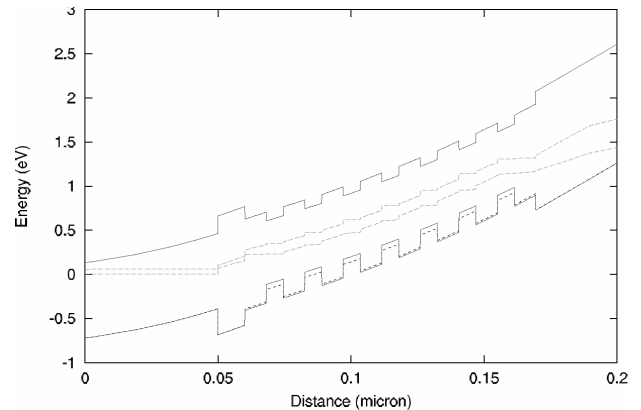


Fig. 17: Conduction (upper) and valence (lower) bands in the WPD region along the vertical y direction (dashed: quasi-Fermi levels)

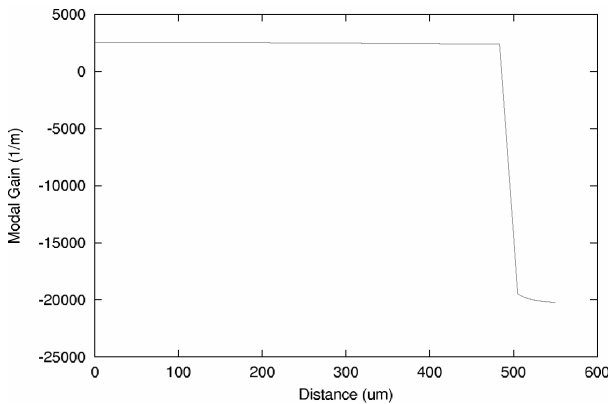


Fig. 18: Receiver modal gain along the longitudinal propagation direction z.

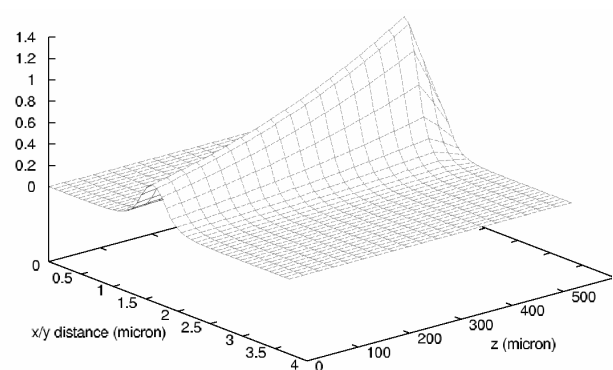


Fig. 19: Wave intensity surface plot (a.u.) within the vertical symmetry plane of the receiver ($x=0$).

3.3 Integrated Transmitter

Simulation of the sampled-grating DBR laser diode⁴ is the most challenging part of this project. The laser includes five longitudinal sections (Tab. 2). Optical gain is provided in the active section of the laser as well as in the amplifier. For this example simulation, both mirrors are tuned to exhibit reflectivity peaks at 1550 nm (Fig. 20). Laser emission is therefore at the same wavelength (Fig. 21). A 3D plot of the calculated wave intensity is shown in Fig. 22. In this case, the laser is biased well above threshold (25 mA). The amplifier current of 20 mA gives additional photon multiplication, resulting in a strong enhancement of the optical intensity towards the right facet of the emitter. The same situation is shown in Fig. 23 as longitudinal intensity profile, comparing two different amplifier currents. Within the SGDBR sections, each grating burst reflects part of the wave and gives a stepwise change in wave intensity. At low amplifier current (5 mA), the SOA region exhibits net optical loss and the optical intensity decays as the light approaches the right facet. SOA transparency is obtained at 16.5 mA. At higher SOA current net amplification is achieved.

The corresponding light-current (LI) characteristic is given in Fig. 24. Lasing threshold is calculated at about 14 mA. At first, the amplifier current is kept constant at 5 mA and the laser current is ramped up to 25 mA. The slope of the LI curve is 0.043 W/A which corresponds to a differential quantum efficiency of only 5% for the right facet, due to the photon losses in the amplifier. Second, the SOA current is ramped up to 20 mA keeping the laser current constant at 25 mA. The SOA slope efficiency is 0.23 W/A. At the SOA current of 20 mA, the laser slope efficiency would be 0.273 W/A, which translates into 34% differential quantum efficiency of the laser. At higher SOA currents, more than 100% differential quantum efficiency can be achieved this way, i.e., each electron injected into the laser above threshold leads to more than one emitted photon, due to the photon multiplication in the SOA region. The side mode suppression ratio is only about 20 dB (Fig. 21) and it decreases with higher amplifier current (Fig. 25).

Section name	Length [μm]	κ [1/cm]	DBR Sampled Grating
Left mirror	552	250	12 x 6 μm grating bursts with 46 μm period
Phase tuning	75	-	-
Active	500	-	-
Gain lever	100	-	-
Right mirror	307.5	250	5 x 4 μm grating bursts with 61.5 μm period
Amplifier	500	-	-

Tab. 2 Longitudinal sections of the integrated transmitter (κ – optical coupling coefficient).

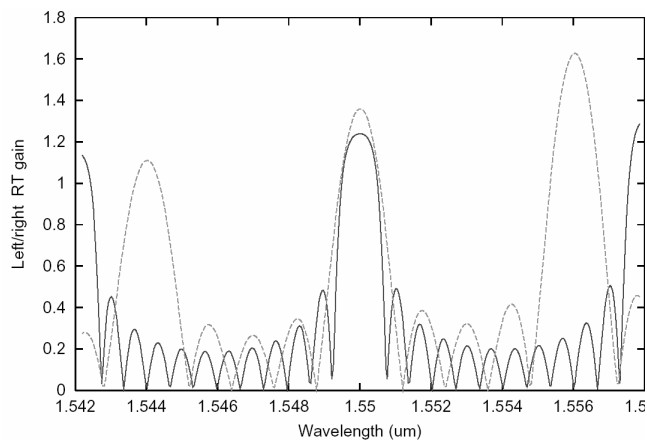


Fig. 20: Round trip gain spectra for left mirror (dashed) and right mirror (solid).

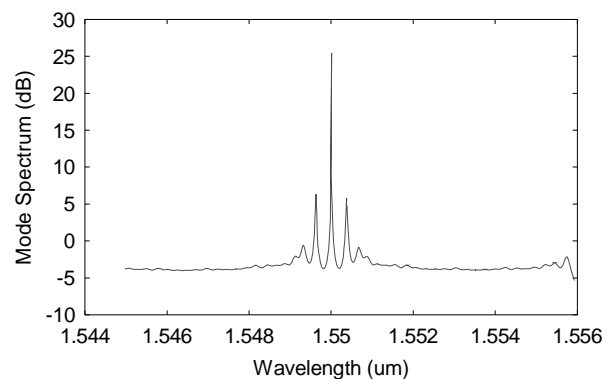


Fig. 21: Calculated mode spectrum (laser current = 25 mA, SOA current = 20 mA).

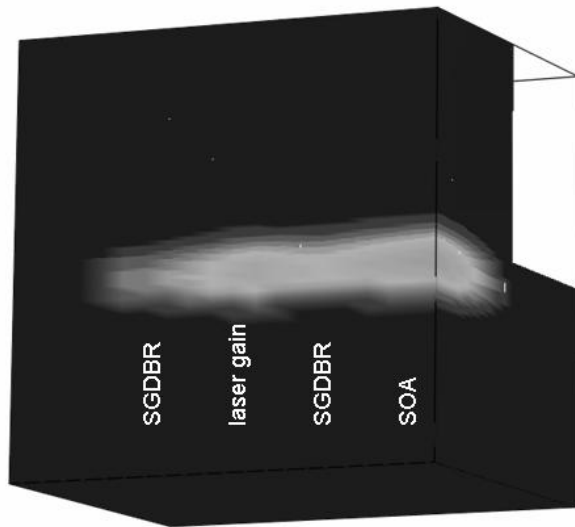


Fig. 22: 3D visualization of the internal light intensity for half the device (laser current = 25 mA, amplifier current = 20 mA).

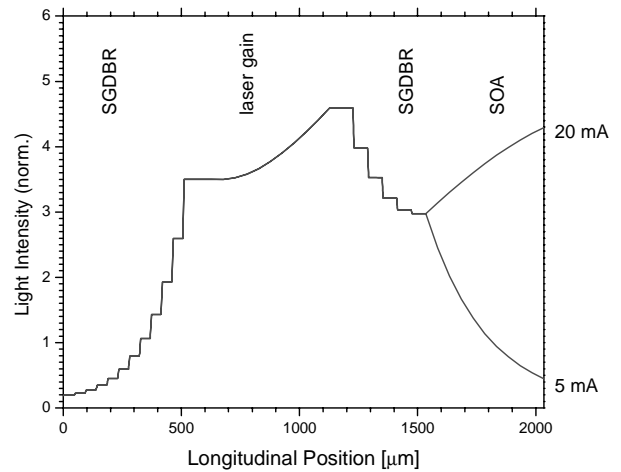


Fig. 23: Longitudinal light intensity profile with 25 mA laser current and with the amplifier current given as parameter.

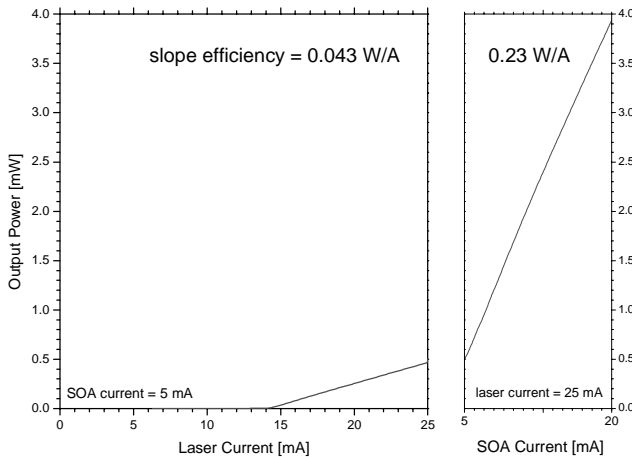


Fig. 24: Calculated light-current characteristics.

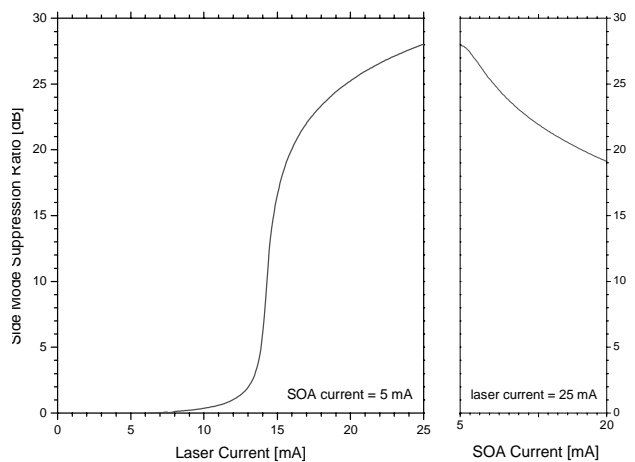


Fig. 25: Calculated side mode suppression ratio vs. current.

4. COMPARISON TO MEASUREMENTS AND PARAMETER CALIBRATION

In this section, we compare our results to the first available receiver measurements in order to validate the model and to calibrate critical material parameters. First, X-ray and photoluminescence (PL) measurements are utilized to adjust MQW parameters. Slight variations from the intended numbers (Tab. 1) are unavoidable during the growth process. For both the quantum wells and the barriers, we extract a slightly lower Ga mole fraction of 0.2367. In addition, the width of both layers is smaller than intended (well: 56.8 Å, barriers: 70.4 Å). Quantum well band-gap renormalization (BGR) is taken into account in order to find agreement with the measured PL peak wavelength (Fig. 26). BGR leads to

decreasing band gap energy with higher carrier density (spectral shift to longer wavelength). The formula used to express BGR is

$$\Delta E_g = A_x \left(\frac{n+p}{2} \right)^{1/3} \quad (3)$$

with $A_x = 0.8 \times 10^{-10}$ eV/m. The difference to the PL measurement at high energies (low wavelengths) is attributed to the fact that the common free carrier model is currently considered in our gain calculation. Many-body models are expected to correctly reproduce the entire gain spectrum.

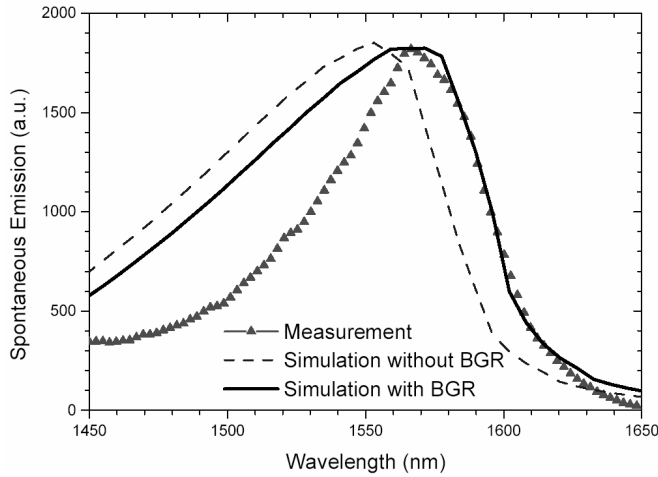


Fig. 26: Comparison between MQW photoluminescence measurement (triangles) and calculated spontaneous emission spectra with and without band-gap renormalization (BGR).

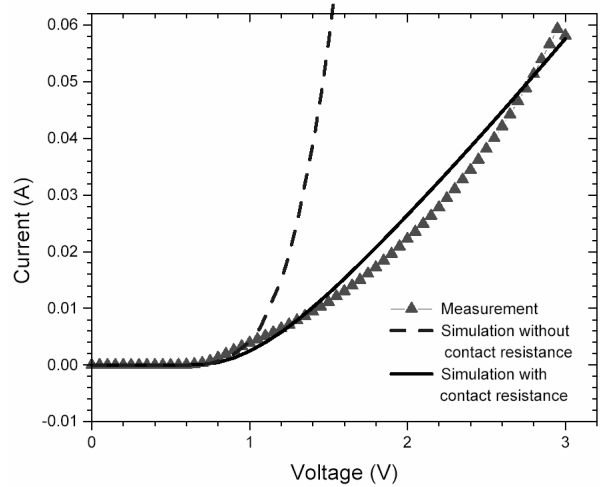


Fig. 27: Dark current versus voltage curve for a 300 μm long SOA.

The measurement of the dark current of a 300 μm long SOA is shown and compared to our simulation in Figure 27. This curve depends on the mobility of the carriers. The mobility depends on the composition of the layer and the doping. Since exact numbers for doping and mobility are unknown, we use 2200 cm^2/Vs for the electron mobility and 70 cm^2/Vs for the hole mobility in all layers. The resulting current-voltage (IV) curve is much steeper than measured (dashed line in Fig. 27). The inclusion of an additional contact resistance of 52 Ω in the simulation gives a much better agreement with the measurement (solid line in Fig. 27). Future measurements of the contact resistance will allow us to adjust the mobility values.

The contact resistance is known to vary from device to device. IV curves for a 500 μm long SOA are shown in Fig. 28 for different input light power. Here, a contact resistance of 8.5 Ω is extracted from the fit. Another crucial input parameter is the optical coupling factor between fiber and SOA. Best agreement with the measurements in Fig. 28 is obtained when a coupling factor of 0.163 is assumed for this measurement. With ideal fiber adjustment, a maximum coupling factor of 0.25 is estimated. Thus, less than one quarter of the light power is coupled into our receiver waveguide.

Figure 29 compares the calculated receiver photocurrent to the measurement. In this measurement, the ideal fiber coupling factor of 0.25 was achieved. In order to fit the measurement, gain and absorption need to be scaled down by a factor of 0.5 (dip_factor). This indicates significant inaccuracies of the free carrier model used for gain and absorption calculation.

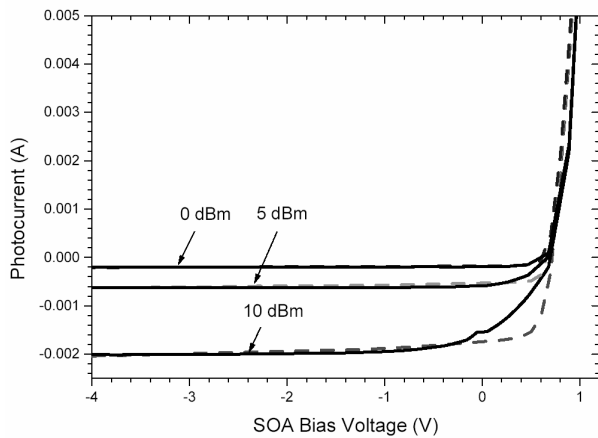


Fig. 28: Photocurrent versus applied reverse voltage for a 500 μm long SOA at different light power in the fiber (dashed: measurement, solid – simulation).

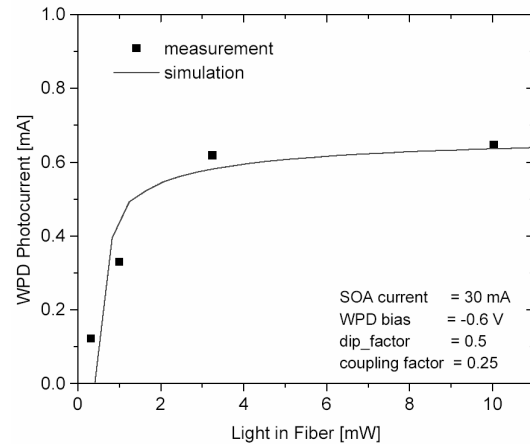


Fig.29: Receiver photocurrent vs. fiber input power.

Finally, light vs. current (LI) measurements on broad-area Fabry-Perot laser structures are compared to simulations in Fig. 30. The main fit parameters are the Auger recombination coefficient $C = 10^{-28} \text{cm}^6/\text{s}$ and the modal loss parameter $\alpha_i = 24 \text{cm}^{-1}$, which is larger than expected and attributed to an overestimation of the quantum well gain within the free carrier model. The corresponding recombination rates are plotted in Fig. 31. Auger recombination is by far the dominating mechanism, spontaneous photon emission and defect related SRH recombination are less important.

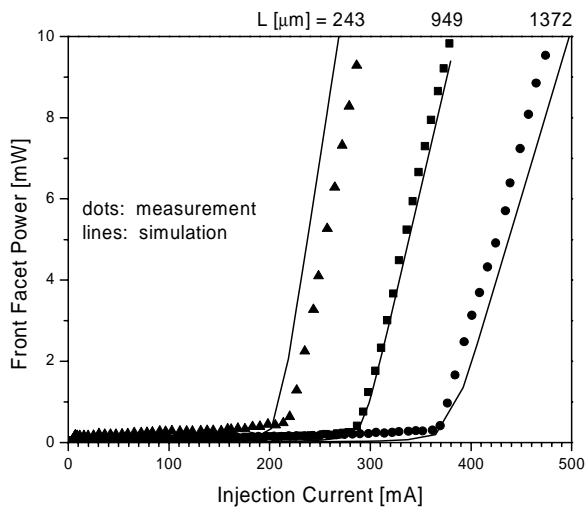


Fig.30: Light-current characteristics for 50 μm wide Fabry-Perot lasers of different length L.

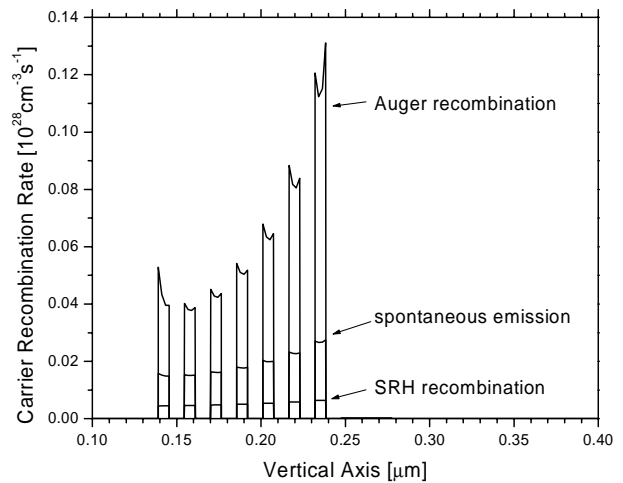


Fig.31: Quantum well recombination rate at 380 mA ($L=949\mu\text{m}$).

5. SUMMARY

We have presented first results on the self-consistent numerical simulation of an InP-based integrated wavelength converter that monolithically combines optical amplifier, waveguide photodetector, and sampled-grating DBR laser diode. Comparison to available measurements reveals crucial parameters such as the contact resistance, the fiber coupling efficiency, and the Auger coefficient. The free carrier model used for quantum well gain and absorption calculations is found to be not accurate enough to achieve good agreement with measurements and to predict the device performance. More advanced models will be employed in future simulations.

ACKNOWLEDGEMENT

This research project is sponsored by the Semiconductor Research Corporation (Award 2001-NJ-968) and by Intel.

REFERENCES

1. B. Mason, J. Barton, G. A. Fish, L. A. Coldren, S. P. Denbaars, "Design of sampled grating DBR lasers with integrated semiconductor optical amplifiers," *IEEE Phot. Techn. Lett.*, vol. 12, pp. 762-764 (2000).
2. PICS3D by Crosslight Software, 2003.
3. J. Piprek, *Semiconductor Optoelectronic Devices – Introduction to Physics and Simulation*, Academic Press, San Diego, 2003.
4. V. Jayaraman, A. Mathur, L. A. Coldren, and P. D. Dapkus, "Theory, design, and performance of extended tuning range in sampled grating DBR lasers," *IEEE J. Quantum Electron.*, vol. 29, pp. 1824–1834, 1993.

Monolithically integrated InP-based tunable wavelength conversion

John M. Hutchinson*¹, Jonathon S. Barton, Milan L. Mašanović, Matthew N. Sysak, Jeffrey A. Henness, Leif A. Johansson, Daniel J. Blumenthal, Larry A. Coldren

¹Intel Corporation, MS FM6-30, 1900 Prairie City Rd. Folsom, CA 95630-9598;
University of California, ECE Dept, Santa Barbara, CA 93106

ABSTRACT

In this work, we describe tunable wavelength converters based on a photodiode receiver integrated with a tunable laser transmitter. Devices are fabricated on a robust InP ridge/InGaAsP waveguide platform. The photodiode receiver consists of an integrated SOA pre-amplifier and a PIN diode to improve sensitivity. The laser transmitter consists of a 1550 nm widely tunable SGDBR laser modulated either directly or via an integrated modulator outside the laser cavity. An SOA post-amplifier provides high output power. The integrated device allows signal monitoring, transmits at 2.5 GB/s, and removes the requirements for filtering the input wavelength at the output. Integrating the SGDBR yields a compact wavelength agile source that requires only two fiber connections, and no off-chip high speed electrical connections. Analog and digital performance of directly and externally modulated wavelength converters is also described.

Keywords: Optoelectronics, Indium Phosphide, Wavelength Conversion, Tunable lasers

1. INTRODUCTION

Tunable wavelength converters represent a novel class of highly sophisticated photonic integrated circuits that are crucial in the functions or functioning or for functions of future optical networks[1]. They allow for the manipulation of wavelengths in WDM optical switches, routers and add/drop multiplexers. Many different implementations of non-tunable wavelength converters have been proposed: using cross phase modulation (XPM) in semiconductor optical amplifiers (SOAs), and fiber [2,3], and cross absorption modulation (XAM) in EAMs[4]. In our previous work, we have demonstrated tunable photocurrent driven wavelength converters utilizing a photodiode driving a laser or a modulator[5, 6]. High-speed integrated photodiodes and electroabsorption modulators suitable for wavelength conversion have also been proposed by other groups [7, 8]. Many of these architectures have been demonstrated to perform the significant feature of digital signal regeneration – including improvements in extinction ratio, signal to noise ratio, pulse width control, etc. Monolithically integrated, widely-tunable all-optical wavelength converters (TAO-WC)[9] have been demonstrated and have shown promise to allow for the conversion of one wavelength to another without requiring the signal to pass through electronics. In this paper, we will describe our work on *tunable* photocurrent driven WC's, and compare them against one another as well as against the TAO-WC approach pursued at UCSB.

2. PHOTOCURRENT DRIVEN TUNABLE WAVELENGTH CONVERSION

The simplest photocurrent-driven wavelength converter (PD-WC) consists of a photodiode receiver directly modulating a laser diode (Figure 1 left). Optical input is incident upon a reverse biased photodiode, which generates a photocurrent directly modulating the gain section of an integrated laser. The laser, and therefore the wavelength converter, can be made tunable by embedding the gain section within tunable mirrors such as implemented in the sampled-gating distributed Bragg reflector (SGDBR) laser [10]. A separate DC electrode connected to the gain section can bias the laser to a level suitable for high output extinction. Above laser threshold, the design affords linear operation, which is of importance for application in analog links. In the direct mod. approach, the extinction ratio of the converted output is proportional to the photocurrent and the laser differential efficiency. In order to improve the extinction ratio, we implement integrated optical pre-amplifiers with on-chip SOAs to generate increased photocurrent.

Modulation bandwidth of the directly modulated PD-WC is ultimately limited by the relaxation resonance frequency of the laser, typically ~ 6GHz in SGDBRs. External modulation of the laser, via an electro-absorption modulator (EAM)

or a Mach-Zehnder modulator (MZM), represents a second important class of tunable photocurrent-driven wavelength converter approaches (Figure 1 right). In these configurations, the photocurrent generates a voltage via a load resistor, which in turn, modulates the transmission of the light through an EAM or MZM. Utilizing either EAMs or MZMs may lower the photocurrent requirements, and offers reduced (and perhaps tunable) chirp suitable for higher data rates.

The semiconductor optical amplifier Mach-Zehnder interferometer (SOA-MZI) wavelength converter is another important class of tunable integrated wavelength converters that also implements the significant feature of digital signal regeneration. Instead of being photocurrent driven, the SOA-MZI WC is based upon the cross-phase modulation, where all of the light interaction between the original data and the new signal takes place in the one arm of an MZI. The monolithically integrated SOA-MZI WC consists of an InP SGDBR laser integrated with a MZI (Figure 2). The laser and the interferometer are connected via a multimode interference (MMI) splitter. The input signal is coupled onto the chip through a tapered input waveguide, and then amplified by an 800 μm long input semiconductor optical amplifier. The same MMI splitter/combiner design is used to connect the data input waveguide with one of the interferometer's SOAs, as well as to combine the light from the two branches at the interferometer output. Waveguides in Mach-Zehnder branches are of the same width and length, hence, with no external stimuli the signal traversing the two interferometer arms will experience no phase change, compared to each other, and thereby add constructively at the output.

All of the designs described in this section have the significant capability for electronic signal monitoring which is a key function required for high speed data networks.

3. DEVICE DESIGN

3.1. Device structure design

Tunable PD-WC's consist of a receiver stage, which collects, amplifies, absorbs and converts the light into a photocurrent, and a transmitter stage which has a tunable laser and perhaps a modulator. Our designs are fabricated on a robust exposed InP ridge platform with a quarternary InGaAsP waveguide. SOAs are used for optical pre-amplification of the input signal, and to boost the converted output signal. Photodiodes are all waveguide type utilizing either Franz-Keldysh (no QWs) or quantum confined stark effect (QW) absorption. SOAs are typically 3 μm wide by 500 to 800 μm long. Photodiode ridges are 3 μm wide by 50 to 100 μm long.

The transmitter stage consists of a SGDBR laser, tunable over the entire C-band. The exposed ridge waveguide laser consists of 5 sections: front and rear SGDBR mirror sections, phase section, gain section and a backside absorber. The Laser output wavelength tuning is achieved by current injection into the SGDBR front and rear mirrors that utilize the vernier effect to select dominant lasing mode. The front mirror consists of 5 4 μm wide burst on a 68.5 μm pitch. The rear mirror consists of 12 6 μm wide bursts on a 68.5 μm pitch. The gain section is 550 μm long and the phase section is 75 μm long.

3.2. Device fabrication and testing

The devices are fabricated on an exposed ridge strip design with a single blanket P-type InP regrowth. The layer structure consists of a 350 nm thick 1.4Q quarternary waveguide with seven compressively strained (1%) 1.55 μm quantum-well active regions grown on top, separated by a thin InP etch stop layer (Figure 3). Epi growth is performed in a Thomas Swan near-atmospheric MOCVD reactor using tertiary-butyl phosphine and tertiary-butyl arsine for the group V precursors, and diethylsilane and diethylzinc for the dopants. Passive sections, such as SGDBR mirrors, phase and franz-keldysh modulators/detectors are formed by selectively etching off the quantum wells in a wet etch process. The sampled grating DBR laser mirrors are defined using a two-step lithography/holography process and etched directly into the top of the waveguide using a $\text{CH}_4/\text{H}_2/\text{Ar}$ RIE process. Blanket regrowth of a thick p-InP cladding and an InGaAs cap. 3 μm wide exposed ridges are formed after regrowth lithographically using a combined dry-wet etch process to provide smooth sidewalls and minimize scattering loss. E-beam evaporated Ni/AuGe/Ni/Au metal is used to contact the N-type semiconductor and Ti/Pt/Au is used to contact the P-type semiconductor. Selectively removing the regrown P-type InGaAs and implanting protons provides carrier confinement between adjacent device sections. The

temperature of the N-type contact anneal is $\sim 430\text{C}$, which significantly repairs the proton induced damage used for section isolation, requiring that N-metal formation and anneal occur prior to proton implant. The implant is designed to penetrate through the p-InP cladding and stop just above the waveguide to avoid creating defects in the intrinsic region that would lead to increased optical loss. In order to reduce the capacitance, a multiple layer dielectric stack of PECVD silicon nitride and biscyclobutene (Dow Chemical Cyclotene 4024) is used to separate the semiconductor from the pad metallization. Following Ti/Pt/Au P-type metallization and anneal, devices are lapped back to 100 μm thickness, cleaved into bars and AR coated. Working devices are mounted on probable AlN carriers with Pb/Sn/Ag solder.

Figure 4 shows a schematic of the experimental arrangement. An Agilent 70841A 2.5 Gbps pseudo-random bit sequencer (PRBS) was used to drive an Agilent 83433A optical transmitter. The modulated optical signal was amplified and coupled into the wavelength converter. Flextronics conical tip lensed fibers mounted on Melles Griot piezo-electric three axis stages were used to couple the light onto and off of the wavelength converters. Wavelength converters were mounted on AlN carriers on top of a thermoelectric cooler to provide temperature stabilization. The output power of the wavelength converter is controlled by an optical attenuator before it is received by an Agilent 83434A optical receiver, connected to an Agilent 70842B 2.5 Gbps bit error rate tester (BERT). The received eye could also be directly observed in an Agilent 86100A high-speed oscilloscope. The amplified monitor signal from the OEIC-WC device could also be observed in the oscilloscope. For back-to-back testing, i.e. without wavelength conversion, the optical transmitter was directly connected to the optical receiver via an optical attenuator.

4. WAVELENGTH CONVERTER COMPONENT RESULTS

Crucial to the operation of photocurrent driven wavelength converters is a high efficiency receiver. Two types of photodiodes have been investigated: Franz-Keldysh and QW absorbers. Figure 5 (left) shows the detected photocurrent of an optically pre-amplified QW photodiode of 50 and 100 μm length. Current saturation is observed and is due to both power saturation in the SOA, and QW band filling. An improved photodetector can be fabricated using Franz-Keldysh absorption. Figure 5 (right) shows the detected photocurrent vs. reverse bias for different fiber optical power levels for such a device without any optical pre-amplification on chip. No saturation is observed up to photocurrents of at least 30 mA. Others using the same structure have observed even higher saturation currents, up to 70 mA [11]. Coupling efficiency from the lensed fiber to the waveguide mode was $\sim 25\%$.

Figure 6 shows the modulation bandwidth of the directly modulated SGDBR tunable laser. The relaxation resonance frequency of the laser limits the modulation bandwidth to a few GHz. To obtain a flat bandwidth response to above 2.5 GHz, the laser must be DC biased at least to 100 mA. For directly modulated wavelength converters, the resulting extinction ratio is limited by the available photocurrent from the receiver

Externally modulated wavelength converters utilize a DC biased SGDBR laser with an additional EAM or MZM modulator. The potential used to drive the modulator is developed across a 50 Ω load resistor connected in parallel. As discrete components, the crucial figure of merit for modulators is modulation efficiency in dB/Volt. Figure 7 (left) shows the extinction of a bulk Franz-Keldysh EAM and Figure 7 (right) shows the extinction vs. bias for a MZM. The maximum obtained EAM efficiency, for a 10 dB transmission loss is ~ 10 dB/V at 1530 nm, and the efficiency drops as the wavelength moves away from the waveguide absorption edge. Higher modulation efficiencies can be obtained by operating at larger DC biases, at the expense of overall transmission. The MZM exhibits an increased ~ 20 dB/V modulation efficiency, at the expense of device area and complexity compared to the EAM.

5. WAVELENGTH CONVERTER MODULATION RESULTS

All of the wavelength converter implementations were successfully fabricated and were tested using the setup described in Figure 4 previously. Figure 8 shows input and output eye diagrams at 2.5 GB/s for the directly modulated WC, the MZM WC and the SOA-MZI WC. All three demonstrated clearly open eyes at 2.5 GB/s data rates across at least a 20 nm SGDBR laser tuning range. Extinction ratio for the directly modulated WC was ~ 3 dB as the photocurrent was limited in fully integrated devices due to a fabrication error resulting in higher than expected contact resistance. Extinction ratio for both MZM-WC and SOA-MZI WC was greater than ~ 8 dB.

All of the wavelength converter approaches fabricated demonstrated error-free operation at 10^{-9} BER with a 2.5 GB/s 2^{31} -1 PRBS signal (Figure 9). Power penalties were 8 dB, 1-2 dB and <1 dB for the direct mod WC, MZM and SOA-MZI WC respectively. The larger power penalty for the direct mod WC was due to the lower than expected extinction.

6. CONCLUSIONS

We described tunable wavelength converters based on a photodiode receiver integrated with a tunable laser transmitter. Devices are fabricated on a robust InP ridge/InGaAsP waveguide platform. The photodiode receiver consists of an integrated SOA pre-amplifier and a PIN diode to improve sensitivity. The laser transmitter consists of a 1550 nm widely tunable SGDBR laser modulated either directly or via an integrated modulator outside the laser cavity. An SOA post-amplifier provides high output power. The integrated device allows signal monitoring, transmits at 2.5 GB/s, and removes the requirements for filtering the input wavelength at the output. Integrating the SGDBR yields a compact wavelength agile source that requires only two fiber connections, and no off-chip high speed electrical connections. Analog and digital performance of directly and externally modulated wavelength converters is also described.

7. ACKNOWLEDGEMENTS

The financial support of Intel Corporation, DARPA CS-WDM and NSF IGERT is gratefully acknowledged. Tom Mates (Materials Department, UCSB) provided SIMS.

REFERENCES

1. S. J. B. Yoo, "Wavelength Conversion Technologies for WDM Network Applications", IEEE J. Lightwave Technology, 14, 944-966 (1996).
2. L.H. Spiekman, U. Koren, M.D. Chien, B.I. Miller, J.M. Wiesenfeld, J.S. Perino, "All-Optical Mach-Zehnder Wavelength Converter with Monolithically Integrated DFB Probe Source", IEEE Photonics Technology Letters, 9, IEEE, 1349-51. (1997)
3. B.-E. Olsson, P. Ohlen, L. Rau, D. J. Blumenthal, "A simple and robust 40-Gb/s wavelength converter using fiber cross-phase modulation and optical filtering", IEEE Photonics Technology Letters, 12, IEEE, 846-848 (2000)
4. N. Edagawa, M. Suzuki, S. Yamamoto, "Novel wavelength converter using an electroabsorption modulator," IEICE Trans. Electron., E81-C, 1251-1257 (1998).
5. J. M. Hutchinson, J. A. Hennes, L. A. Johansson, J. S. Barton, M. L. Masanovic, "2.5 Gb/sec wavelength conversion using monolithically-integrated photodetector and directly modulated widely-tunable SGDBR laser," IEEE LEOS 2003 Annual meeting proceedings, WU4, 6 50-651 (2003).
6. J. S. Barton, M. L. Mašanović, M. N. Sysak, J. M. Hutchinson, E. J. Skogen, D. J. Blumenthal, L. A. Coldren, "A novel monolithically-integrated widely-tunable wavelength converter based on a SGDBR-SOA-MZ transmitter and integrated photodetector" Photonics in Switching proceedings, Versailles France (2003).
7. H. Demir, V. Sabnis, O Fidaner, S. Latif, J. Harris, D. A. B. Miller, J Zheng, "Novel optically controlled optical switch based on intimate integration of surface-normal photodiode and waveguide electroabsorption modulator for wavelength conversion," IEEE LEOS 2003 Annual Meeting proceedings, WU1, 644-645, (2003).
8. H. Takeuci, T. Saoitoh, H. Ito, "High-speed electroabsorption modulators with traveling-wave electrodes," OFC 2002 Technical Digest, 336-338 (2002).
9. M. L. Masanovic, V. Lal, J. S. Barton, E. J. Skogen, D. J. Blumenthal, L.A. Coldren, "Monolithically Integrated Mach-Zehnder Interferometer wavelength converter and widely-tunable laser in InP", IEEE Photonics Technology Letters, 15, 1117-1119 (2003)
10. B. Mason, G. A. Fish, J. Barton, L. A. Coldren, S. P. DenBaars, "Design of sampled grating DBR lasers with integrated semiconductor optical amplifiers", IEEE Photonics Technology Letters, 12, 762-764 (2000).
11. L.A. Johansson, Y.A. Akulova, G.A. Fish, L.A. Coldren, "High optical power electroabsorption waveguide modulator," Electron. Lett., 39, 364-365 (2003).

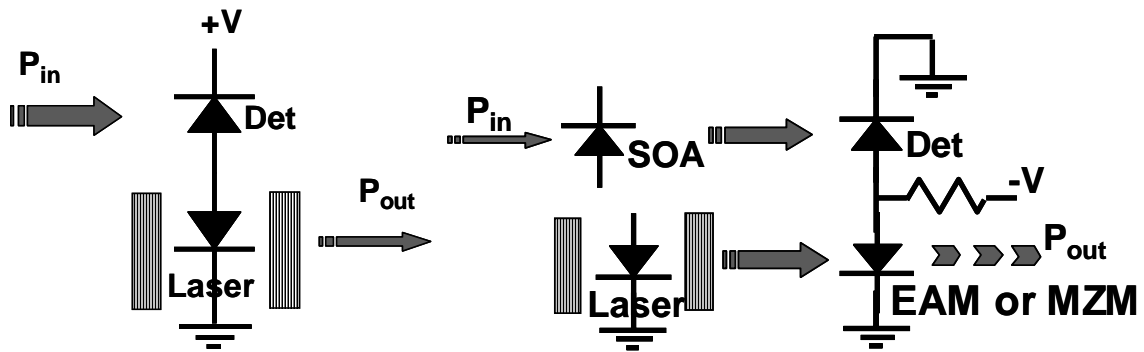


Figure 1. Left: Equivalent circuit of directly modulated wavelength converter
 Right: Equivalent circuit of externally modulated wavelength converter

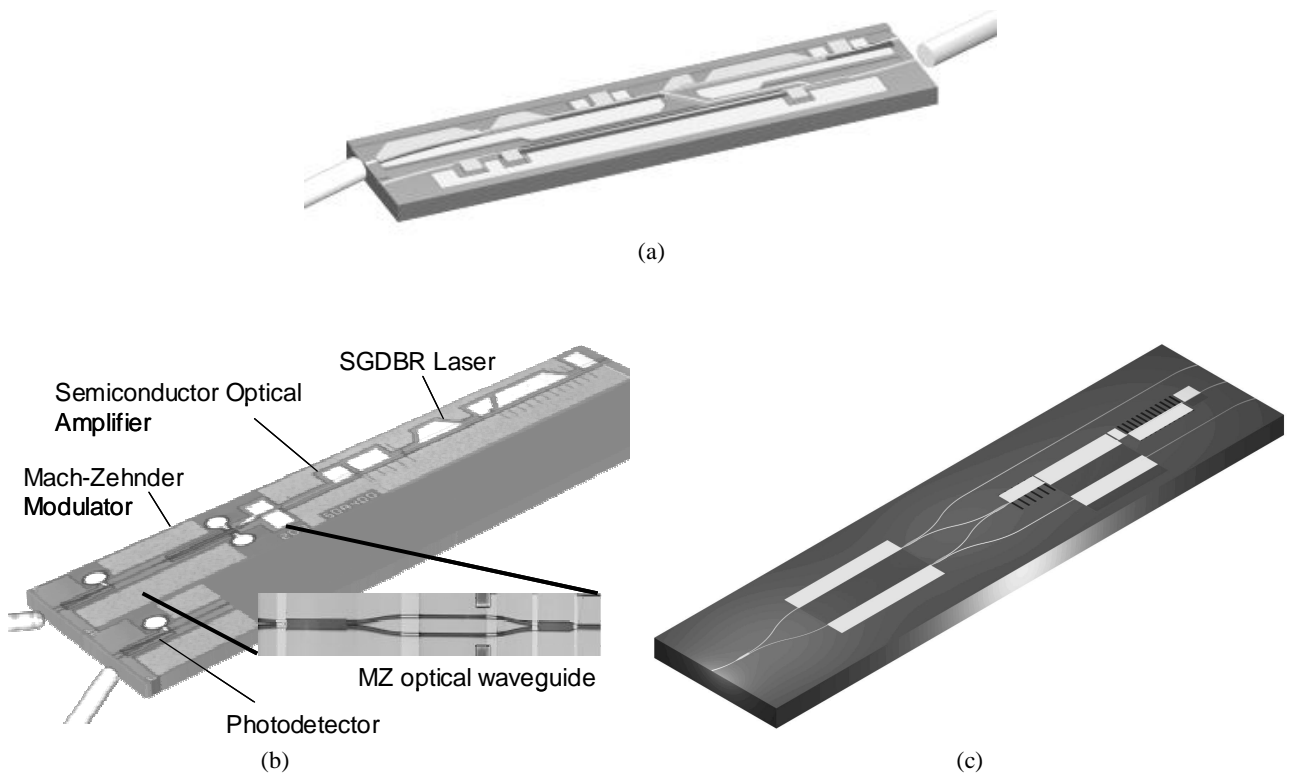


Figure 2. Schematic of three different wavelength converters based on a common InP SGDBR laser process, (a) directly modulated, (b) MZM modulated and (c) SOA-MZI all-optical

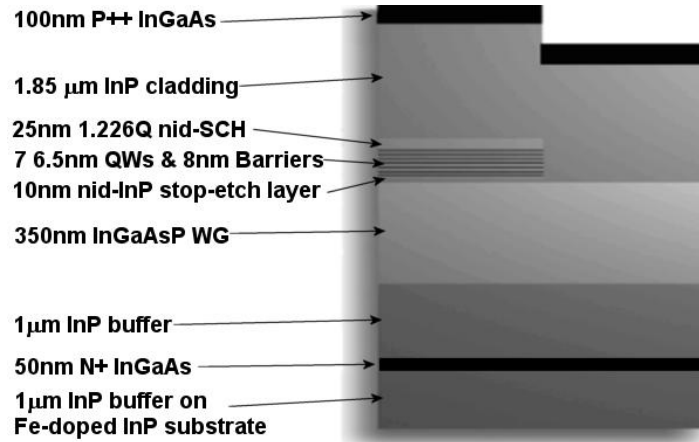


Figure 3. InP MOCVD epitaxial structure of directly modulated WC.

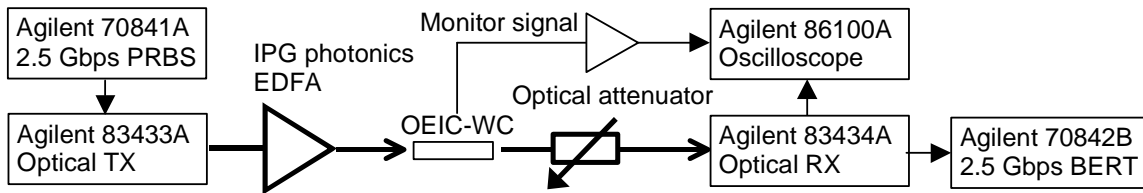


Figure 4. Experimental arrangement for 2.5 Gbps wavelength conversion demonstration. Thick line indicates optical path while thin line indicated electrical path.

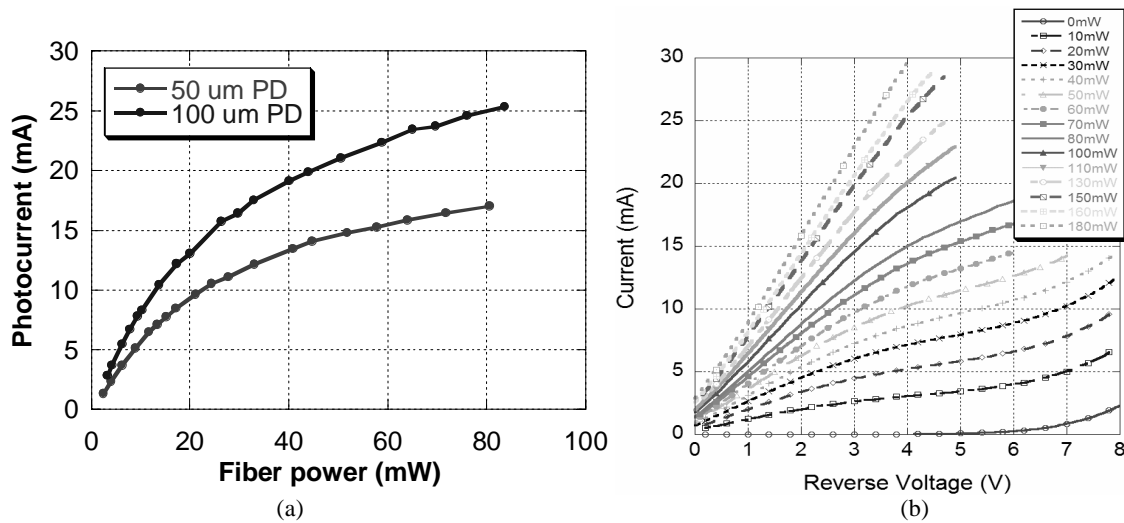


Figure 5. (a) QW absorber photodiode I-L response and (b) Franz-Keldysh absorber photodiode I-V.

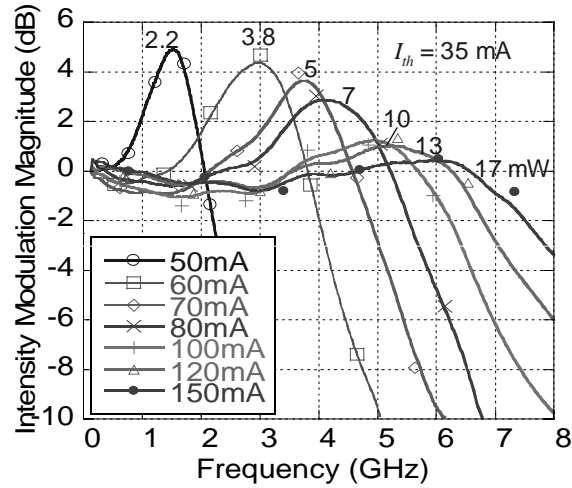


Figure 6. Modulation bandwidth of an SGDBR laser as a function of gain section bias current. Optical power output is labeled on individual curves.

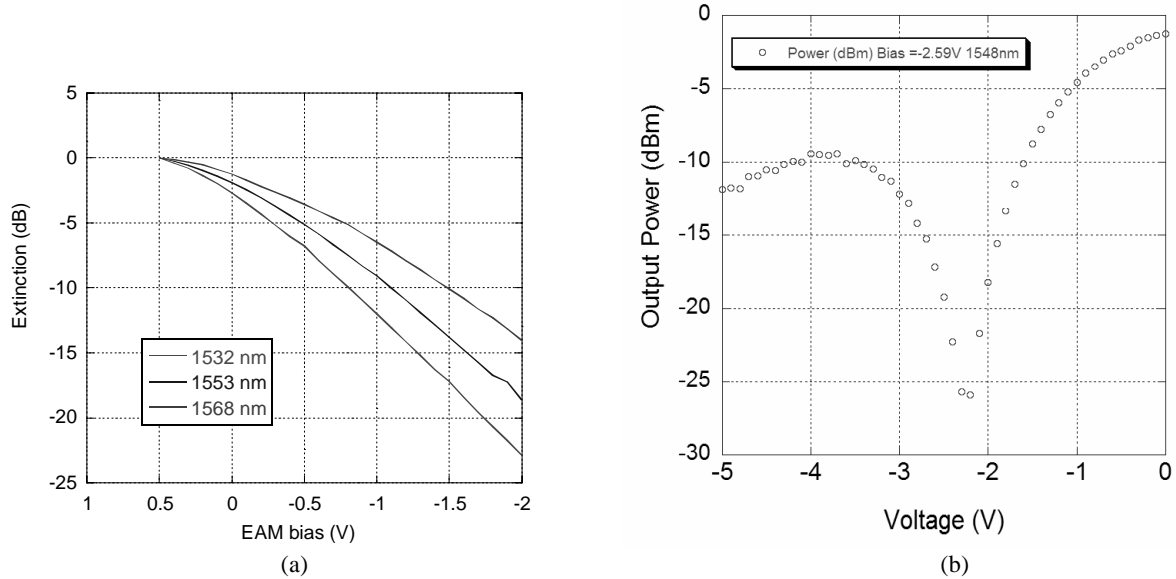


Figure 7. Optical Extinction vs. Voltage for (a) 600 um long EAM and (b) Mach-Zender modulator

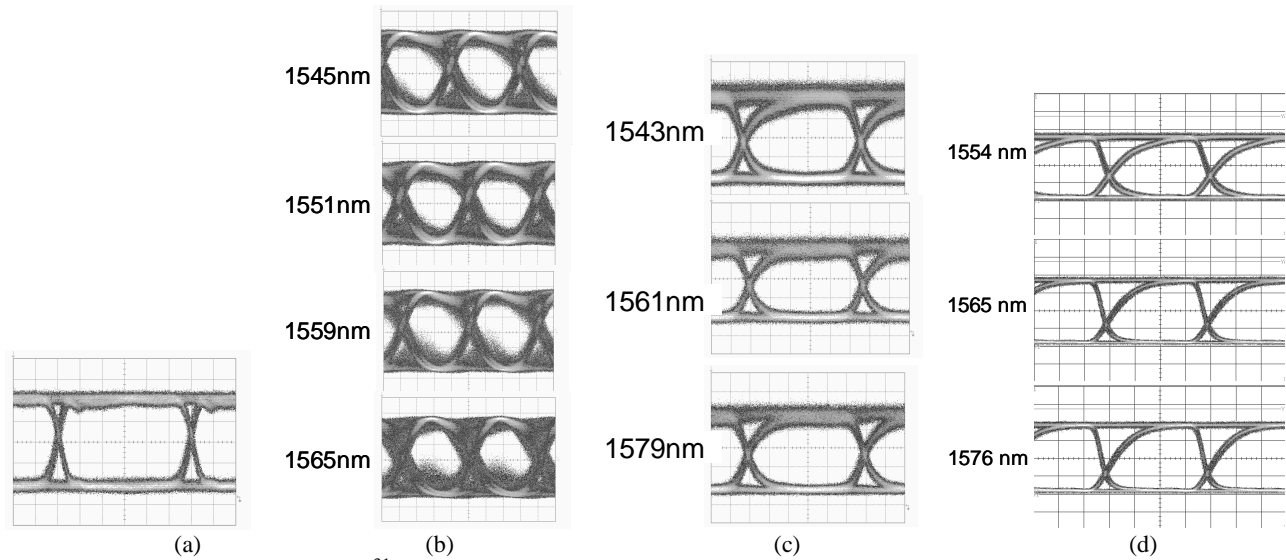
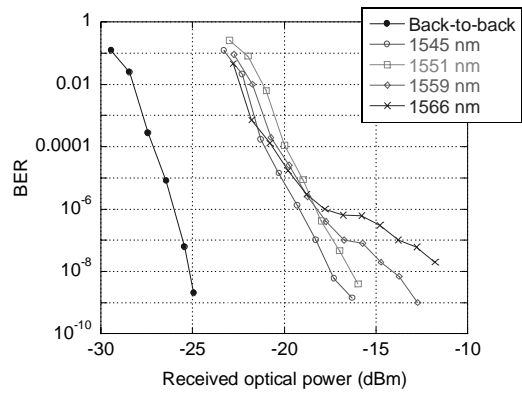
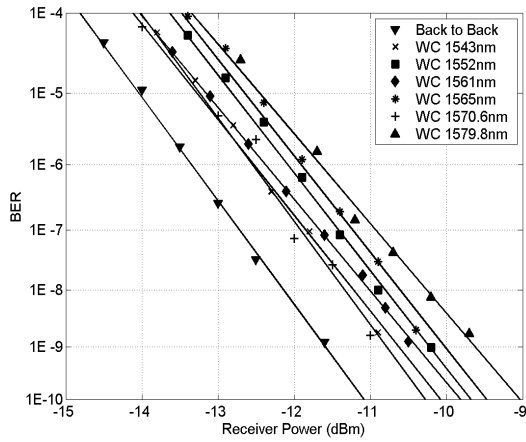


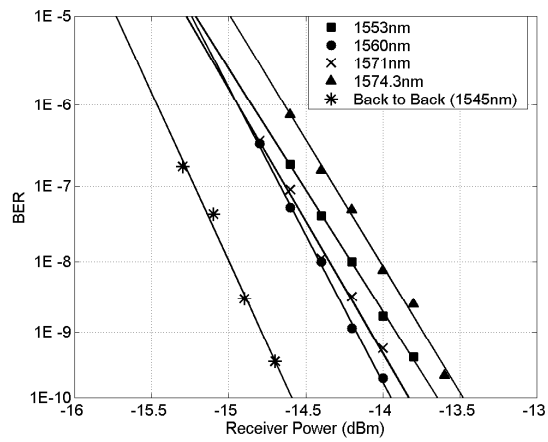
Figure 8. 2.5 Gb/s optical eyes, $2^{31}-1$ NRZ pattern, (a) input signal, (b) directly modulated WC output eye, (c) MZM WC output eye and (d) SOA-MZI all-optical output eyes.



(a)



(b)



(c)

Figure 9. 2.5 GB/s bit-error rates as a function of received optical power for (a) directly modulated WC, (b) MZM WC and (c) all-optical SOA-MZI WC.

10 Gbps and 2.5 Gbps error-free operation of a monolithically integrated widely-tunable all-optical wavelength converter with independent phase control and output 35nm tuning range

Milan L. Mašanović, Vikrant Lal, Joseph A. Summers, Jonathon S. Barton, Erik J. Skogen, Larry A. Coldren, Daniel J. Blumenthal

*Electrical and Computer Engineering Department, University of California Santa Barbara, CA 93106-9560, USA
mashan@ece.ucsb.edu*

Abstract: This paper reports on the first demonstration of 2.5 Gbps and 10 Gbps operation of a new InP MZI-SOA all-optical wavelength converter with independent interferometer phase control monolithically integrated with a widely-tunable SGDBR laser. We show a 35nm output tuning range with less than 0.8dB power penalty at -10 dBm input at 2.5Gbps NRZ and error-free operation with -5 dBm input power at 10Gbps NRZ.

©2003 Optical Society of America

OCIS codes: (250.5300) Photonic integrated circuits; (230.4320) Nonlinear optical devices

1. Introduction

The development of photonic integrated circuits (PICs) with increased functionality and monolithic integration on a single chip is a critical step for the deployment of optical networks. The tunable all-optical wavelength converter is a critical component for reconfigurable WDM systems that employ optical switching, wavelength routing and add/drop multiplexing. Integration of the tunable laser and all-optical wavelength converter on a single chip is necessary to meet performance, yield, cost and footprint requirements of these networks. This level of chip-scale integration has a number of benefits including reduced coupling loss between laser and converter, faster operating speed, improved converter noise figure and improved conversion efficiency. Tunable all-optical wavelength converters allow data to be transferred from an input wavelength to a tunable output wavelength without passing the signal through electronics. For wavelength conversion, the semiconductor optical amplifier based Mach-Zehnder Interferometer (SOA-MZI) wavelength converter is an important class of integrated wavelength converters that work for both RZ and NRZ data formats while also acting as a 2R signal regenerator due to their nonlinear transfer function. [1-3]. Previously, we have reported on the first widely tunable all-optical wavelength converter with 22nm tuning range working at 2.5 Gbps [4].

In this paper, we report for the first time a new tunable wavelength converter with independent interferometer phase control, which has a tuning range of 35nm with average converted output power of 0dBm. This device operates error free out to 10 Gbps with -5 dBm input power and shows very low power penalties (<0.8 dB) across the tuning range at 2.5 Gps with very low input signal power (-10 dBm).

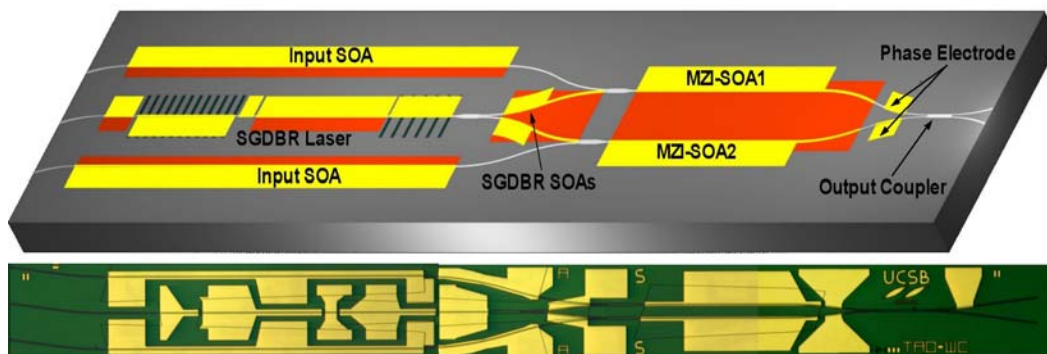


Fig. 1. Schematic and actual die shot of the widely tunable 10 Gbps all-optical wavelength converter with independent phase control using the phase electrodes in the interferometer arms.

2. Device Design and Fabrication

The new tunable wavelength converter design reported consists of a widely tunable sampled grating distributed Bragg reflector (SGDBR) laser monolithically integrated with a semiconductor optical amplifier based Mach-Zehnder Interferometer wavelength converter (MZI-WC) and is shown in Figure 1. The laser is 1.5mm long and has five sections: front mirror, gain section, phase section, back mirror and back facet detector and its operation is described in detail in [5]. The interferometer branches are defined by two S-bends and 1.5 mm long SOAs. The output light of the SGDBR laser is equally split using a 1x2 multimode interference (MMI) based light splitter, and then amplified by 2 in-line SOAs that also serve as part of the interferometer S bends. This amplified light is then coupled with light from the input waveguides using 2x1 MMI combiners into the SOAs in the branches of the MZI. 1.5 mm long MZI SOAs are used to achieve 10 Gbps operation. Each branch of the MZI has a 100 μ m long passive section contacted by a metal pad which is used to adjust the relative phase of the MZI independently of the SOA bias current. This separation of phase control provides for easier optimization of the operating bias point of the wavelength converter as well as better extinction for both inverting and non-inverting modes of operation.

The branches of the MZI are coupled by a MMI based 2x2 coupler at the output. Depending on the relative phase of the MZI branches, the output light will be split between the two output waveguides with two extreme cases: for the phase difference of -90 deg, all of the light will be coming out of one waveguide whereas for the phase difference of +90 deg, all of the light will be coming out of the other waveguide. The two outputs are used to constantly remove the light from the chip (this is different from our previous design [4]), which helps prevent light resonance buildup. Both of the output waveguides are curved and tapered before they reach the facet in order to minimize the back reflections.

The input signal is coupled onto the chip through a tapered, angled input waveguide, and then amplified by 2 SOAs running alongside the laser. In order to reduce the thermal crosstalk, the input SOAs are about 200 μ m away laterally from the SGDBR active regions. The total chip size is 0.5x5.3mm.

This device is fabricated using an MOCVD grown offset quantum well integration platform [4]. The layer structure consists of a 350nm thick 1.4Q quarternary waveguide followed by a 7 quantum well active region and a thin InP cap. The fabrication process requires only a single MOCVD regrowth and is similar to [4].

3. Results

The input signal at 1570nm was externally modulated with NRZ 2^{31} -1 PRBS data at both 2.5 and 10 Gbps. Light was coupled into and out of the device using conically-tapered lensed fiber. The converted output wavelength was filtered using a thin-film tunable filter and detected with an Agilent 83434A 10Gb/s lightwave receiver. For non-inverting mode of operation, both of the SOAs are biased by equal electrical currents, and the relative phase of the two branches is adjusted using the phase electrodes to cancel out the two signals. As can be seen in Fig. 2, it takes about 5 mA to turn the interferometer off completely; therefore, the new method of phase control is very efficient. For inverting mode of operation, the MZI-SOA bias needs to be adjusted in such a way that the powers of the CW signals in the MZI branches are equal for maximum input power of the data stream. Representative tuning of the device to 4 different output wavelengths over a 35nm tuning range is shown in Fig. 3 and these are the same wavelengths used in the BER measurements.

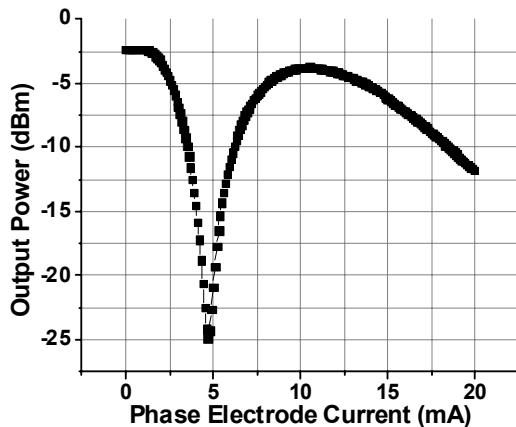


Fig. 2. Static extinction curve of the MZI

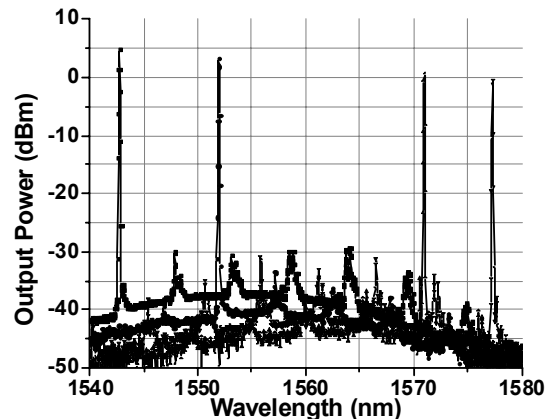


Fig. 3. Overlapped optical spectra of the on-chip tunable laser

The measured BER curves are shown in Fig. 4. The data input power was only -10dBm at 2.5Gbps and -5dBm at 10Gbps. The average output power of the wavelength converter was around 0dBm. At 2.5 Gbps the maximum power penalty measured was 0.8dB which can be attributed mainly to the ASE noise generated by on-chip SOAs. At 10Gbps, the power penalty was measured as low as 1.4dB for output wavelengths between 1542-1555nm. The penalty increased to around 3dB, and the BER slope decreased for longer wavelengths (above 1570nm), which can be attributed to SNR and extinction ratio degradation for wavelengths near the band edge. We expect that these numbers could improve with future device designs.

4. Conclusions

We have demonstrated for the first time error-free operation at 2.5 and 10 Gbps of a novel all-optical widely-tunable wavelength converter monolithically integrated in InP. The output tuning range of the device is 35nm (1542-1578nm), and less than 0.8dB power penalty is measured for 2.5Gbps NRZ operation at -10dBm input power. Error-free operation at 10Gbps NRZ with less than 3 dB is measured over the entire tuning range with input power of -5dBm. The average output power of the device is 0dBm. This work is supported by the DARPA/MTO CS-WDM Program under Grant No. N66001-02-C-8026

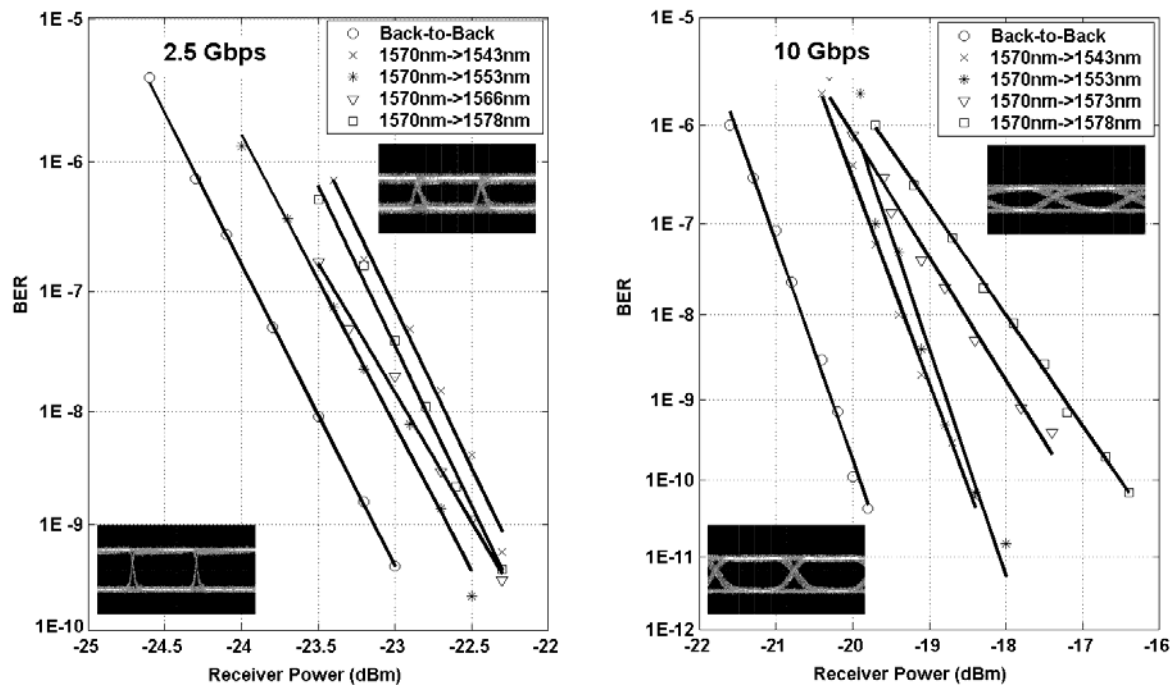


Fig. 4. BER plots for 2.5Gbps operation with -10dBm input power, and for 10Gbps operation with -5dBm input power. The insets also show the back-to-back received eye (bottom) and the converted eye from the device (Top) at the respective data rates

- [1] X. Pan, J.M. Wiesenfeld, J.S. Perino, T.L. Koch, G. Raybon, U. Koren, M. Chien, M. Young, B.I. Miller, C.A. Burrus, "Dynamic Operation of a Three-Port, Integrated Mach-Zehnder Wavelength Converter", *IEEE Photonics Technology Letters*, 7, IEEE, 995-97. (1995)
- [2] W. Idler, K. Daub, G. Laube, M. Schilling, P. Wiedemann, K. Dutting, M. Klenk, E. Lach, K. Wunstel, "10 Gb/s Wavelength Conversion with Integrated Multiquantum-Well 3-Port Mach-Zehnder Interferometer" *IEEE Photonics Technology Letters*, 8, IEEE, 1163-65. (1996)
- [3] C. Janz, F. Poingt, F. Pommereau, W. Grieshaber, F. Gaborit, D. Leclerc, I. Guillemot, M. Renaud, "New All Active Dual Order Mode (DOMO) Mach-Zehnder Wavelength Converter For 10 Gbit/s Operation", *ECOC 99, Nice, France*
- [4] "Monolithically Integrated Mach-Zehnder Interferometer Wavelength Converter and Widely-Tunable Laser in InP" M. L. Masanovic, V. Lal, J. S. Barton, E. J. Skogen, L. A. Coldren and D. J. Blumenthal, *IEEE Photonics Technology Letters*, 15 (8), August (2003).
- [5] V. Jayaraman, Z. Chuang, and L. Coldren, "Theory, Design, and Performance of Extended Tuning Range Semiconductor Lasers with Sampled Gratings," *IEEE J. Quantum Electron.*, vol. 29, pp. 1824-1834, 1993.

Indium Phosphide-Based Optoelectronic Wavelength Conversion for High-Speed Optical Networks

John M. Hutchinson, Technology and Manufacturing Group, Intel Corporation
Jun-Fei Zheng, Technology and Manufacturing Group, Intel Corporation
Jonathon S. Barton, Dept. of Materials and Electrical & Computer Engineering, U.C. Santa Barbara
Jeffrey A. Henness, Dept. of Materials and Electrical & Computer Engineering, U.C. Santa Barbara
Milan L. Mašanović, Dept. of Electrical & Computer Engineering, U.C. Santa Barbara
Matthew N. Sysak, Dept. of Electrical & Computer Engineering, U.C. Santa Barbara
Leif A. Johansson, Dept. of Electrical & Computer Engineering, U.C. Santa Barbara
Daniel J. Blumenthal, Dept. of Electrical & Computer Engineering, U.C. Santa Barbara
Larry A. Coldren, Dept. of Materials and Electrical & Computer Engineering, U.C. Santa Barbara
Hilmi Volkan Demir, Edward. L. Ginzton Laboratory, Stanford University, CA
Vijit A. Sabnis, Edward. L. Ginzton Laboratory, Stanford University, CA
Onur Fidaner, Edward. L. Ginzton Laboratory, Stanford University, CA
James S. Harris, Edward. L. Ginzton Laboratory, Stanford University, CA
David A. B. Miller, Edward. L. Ginzton Laboratory, Stanford University, CA

Index words: optical, wavelength conversion, monolithic, indium phosphide, tunable

ABSTRACT

Monolithic approaches to wavelength converters have been demonstrated and show promise to allow for the high-speed conversion of one wavelength to another without requiring the signal to pass through off-chip electronics. In this paper, we describe our research, undertaken jointly with the University of California at Santa Barbara and with Stanford University, into novel approaches for monolithically integrating Wavelength Converters (WCs) in Indium Phosphide.

In the first approach, undertaken jointly with the University of California at Santa Barbara, we describe Photonic-IC (PIC) tunable wavelength converters that are based on a photodiode receiver integrated with a tunable laser transmitter. Devices are fabricated on a robust InP ridge/InGaAsP waveguide platform. The photodiode receiver consists of an integrated optical pre-amplifier and a pin photodiode to improve sensitivity. The laser transmitter consists of a 1550 nm widely tunable Sampled Grating Distributed Bragg Reflector (SGDBR) laser modulated either directly or via an integrated modulator outside the laser cavity. An optical post-amplifier provides high output power. The Photonic-IC (PIC) tunable WC (PIC-WC) device allows signal monitoring,

transmits at 2.5 Gb/s, and removes the requirements for filtering the input wavelength at the output. Integrating the widely tunable laser on-chip yields a compact wavelength agile source that requires only two fiber connections, and no off-chip high-speed electrical connections.

In the second approach, undertaken jointly with Stanford University, we present a compact, low-power, dual-diode photonic switch architecture that allows for scalable multi-channel wavelength conversion. These photonic switches are scaled into a two-dimensional array to construct the first wavelength-converting crossbar switch on a single chip. Each of the wavelength-converting switches in the crossbar consists of an InGaAsP/InP quantum-well waveguide modulator monolithically integrated with a surface-normal InGaAs photodiode in its close vicinity as a part of a novel integrated optoelectronic circuit. The confinement of optically induced high-speed electrical signals within the lumped circuit elements of each switch node leads to efficient wavelength conversion, requiring low optical input power (mW range) for high extinction ratio (>10 dB), and eliminating the need for on-chip transmission lines and off-chip high-speed electrical connections. In addition to optical switching, the ability to enable and disable the

switch nodes electrically further allows for the electrical reconfiguration of the wavelength-converting crossbar switch as necessary. Experimental demonstrations include unlimited wavelength conversion at 2.5 Gb/s using single switch elements and multi-channel wavelength conversion at 1.25 Gb/s using 2x2 crossbar switches, all exhibiting >10 dB extinction ratio and spanning the entire C-band. Theoretical analysis predicts the feasibility of operation at 10 Gb/s with a 10 dB extinction ratio.

INTRODUCTION

The high-speed fiber optic network of today forms the backbone of the Internet. As the Internet data bandwidth continues to climb, the optical devices used to manipulate these data must demonstrate increased line data rates, functionality, and efficiency while maintaining small size and low cost. Wavelength Converters (WC) represent a novel class of highly sophisticated photonic integrated circuits that are crucial in the function of future optical networks [1]. They allow for the manipulation of wavelengths in Wavelength Division Multiplexing (WDM) optical switches, routers, and add/drop multiplexers.

A key application of WCs is in all-optical “wavelength continuous” networks. In such networks, the interconnection between two nodes (typically optical fiber) is fixed to a given wavelength that cannot be changed along the route. Any new connection to the network must use a different wavelength; if a new connection uses a wavelength already allocated to another connection, it is blocked. Two connections cannot use the same wavelength on a given portion of the same fiber. Wavelength conversion at the nodes of the networks enables the network to avoid this “wavelength-continuity constraint” improving efficiency and flexibility.

The lowest risk and also the most expensive and bulky implementation of wavelength conversion is the use of an Optical/Electrical/Optical (O/E/O) line card that incorporates a tunable laser for its output. The additional problem with this approach is that because of the digital regeneration circuits, the line card typically only functions at a particular data rate. Such O/E/O line cards may be undesirable, because they are one of the major high-cost items that have thwarted the scaling down of system costs as needed to bring optical networking, especially WDM networking, into the metropolitan and local area distribution networks.

Many different implementations of non-tunable WCs have been proposed: using Cross-Phase Modulation (XPM) in Semiconductor Optical Amplifiers (SOAs), fiber [2,3], and Cross Absorption Modulation (XAM) in Electro-Absorption Modulators (EAMs) [4,5]. In our previous work, we have demonstrated photocurrent-

driven WCs utilizing a photodiode driving a laser or a modulator [5,6,7]. High-speed integrated photodiodes and EAMs suitable for wavelength conversion have also been previously proposed [8]. Many of these architectures have been demonstrated to perform digital signal regeneration—including improvements in extinction ratio, signal to noise ratio, pulse width control, etc. The SOA Mach-Zehnder interferometer (SOA-MZI) WC is another important class of tunable integrated WC that also implements the significant feature of digital signal regeneration [9,10]. Instead of being photocurrent driven, the SOA-MZI WC is based upon the XPM, where all of the light interaction between the original data and the new signal takes place in the one arm of an MZI. These previous demonstrations of WCs exhibited promising results for a single-channel operation [2-8]; however, a multi-channel wavelength conversion system has not been previously proposed.

In this paper, we first describe our work at the University of California at Santa Barbara on *tunable* photocurrent driven WCs made by monolithically integrating a widely tunable laser source with detectors and modulators. Next, we discuss our work at Stanford University based on a scalable, compact, dual-diode optical switch suitable for reconfigurable multi-channel wavelength conversion.

WIDELY TUNABLE APPROACH (UCSB)

Design

The simplest photocurrent-driven wavelength converter (PD-WC) consists of a photodiode receiver directly modulating a laser diode (Figure 1 top). Optical input is incident upon a reverse-biased photodiode, which generates a photocurrent directly modulating the gain section of an integrated tunable laser. The Sampled Grating Distributed Bragg Reflector (SGDBR) tunable laser is a four-section device consisting of SGDBR front and rear mirrors and phase and gain sections [11]. A separate DC electrode connected to the gain section can bias the laser to a level suitable for high output extinction. Above threshold, the directly modulated design affords linear operation, which is important for applications in analog links. In this approach, the extinction ratio of the converted output is proportional to the photocurrent, and the laser differential efficiency. In order to improve the extinction ratio, we implement integrated optical pre-amplifiers with on-chip Semiconductor Optical Amplifiers (SOAs) to generate increased photocurrent.

Modulation bandwidth of the directly modulated PD-WC is limited by the relaxation resonance frequency of the laser, typically ~6 GHz. External modulation of the laser, via an Electro-Absorption Modulator (EAM) or a Mach-Zehnder Modulator (MZM), represents a second important class of tunable photocurrent-driven WC

approaches (Figure 1 bottom). In these configurations, the photocurrent generates a voltage via a load resistor, which in turn modulates the transmission of the light through an EAM or MZM. Utilizing either EAMs or MZMs may lower the photocurrent requirements and offer reduced (and perhaps tunable) chirp, suitable for higher data rates.

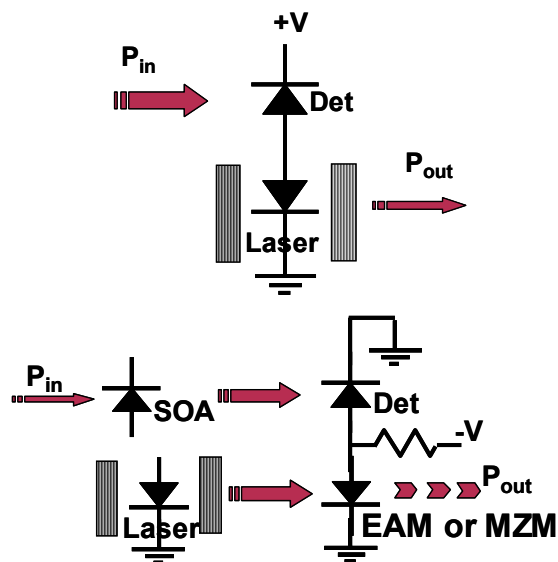


Figure 1: Schematic of UCSB Tunable WCs in direct modulation (top) and external modulation (bottom) implementations

Fabrication

The UCSB design uses a quaternary InGaAsP waveguide structure for the laser, modulator, amplifier, and photodetector sections grown on a semi-insulating Fe-doped InP substrate. Removing conducting semiconductor down to the semi-insulating substrate between the two ridges electrically isolates the ridge waveguides for the photodetector and laser sections. An N⁺ InGaAs layer underneath the quaternary waveguide material provides contacts to the n side of the diodes. The optically passive sections are formed by etching off the offset quantum wells down to the 10nm InP stop-etch layer prior to blanket InP regrowth. Completed devices vary in size depending on the specific design and are typically 0.5 mm wide and 2.5 to 3.5 mm long. An example micrograph of a fabricated wavelength converter with an SGDBR laser, MZM, and receiver is shown in Figure 2. More details on fabrication can be found in Reference 12.

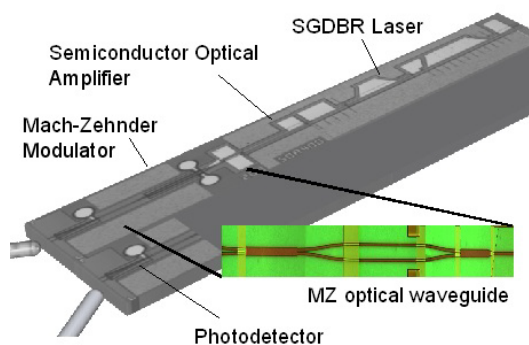


Figure 2: Fabricated MZM WC (~0.5 mm x 3 mm)

RESULTS

Laser, Receivers, and Modulators

Crucial to the operation of photocurrent-driven WCs is a high-efficiency receiver. Two types of photodiodes have been investigated: bulk absorbers, utilizing the Franz-Keldysh (FK) effect, and Quantum Well (QW) absorbers, utilizing the quantum confined Stark effect. Figure 3 (top) shows the detected photocurrent of an optically pre-amplified QW photodiode of 50 and 100 μm length. Current saturation is observed and is due to both power saturation in the SOA and QW band filling. An improved saturation photodetector can be fabricated using FK effect absorption. Figure 3 (bottom) shows the detected photocurrent vs. reverse bias for different fiber optical power levels for such a device, without any optical pre-amplification on chip. No saturation is observed up to photocurrents of at least 30 mA. Others using the same structure have observed even higher saturation currents, up to 70 mA [13]. Coupling efficiency from the lensed fiber to the waveguide mode was $\sim 25\%$. Note that the QW photodiodes incorporate an on-chip SOA preamp, and the bulk photodiodes do not.

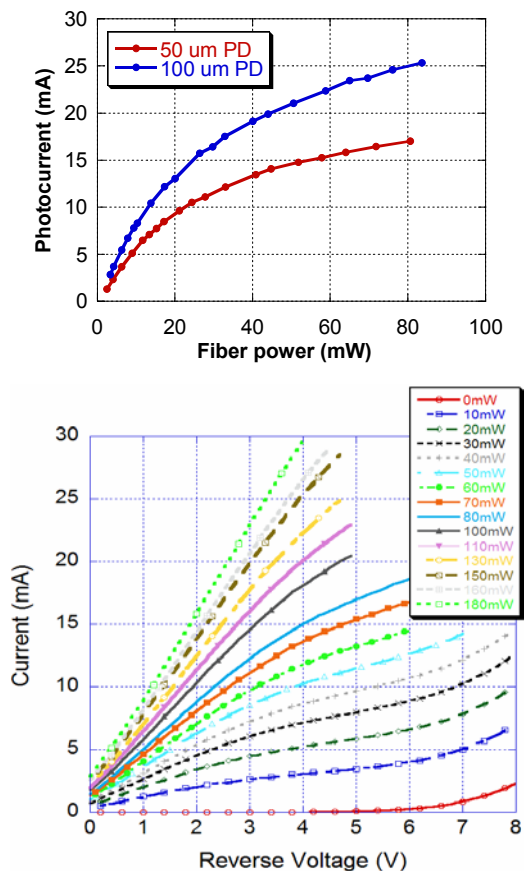


Figure 3: Photodiode optical response for quantum-well photodiodes of 2 lengths with 350 μm SOA preamp (top) and bulk photodiodes (200 μm long, No SOA preamp)

Figure 4 shows the modulation bandwidth of the directly modulated SGDBR tunable laser. The relaxation resonance frequency of the laser limits the modulation bandwidth to a few GHz. To obtain a flat bandwidth response to above 2.5 GHz, the laser must be DC biased at least to 100 mA. For directly modulated wavelength converters, the resulting extinction ratio is limited by the available photocurrent from the receiver.

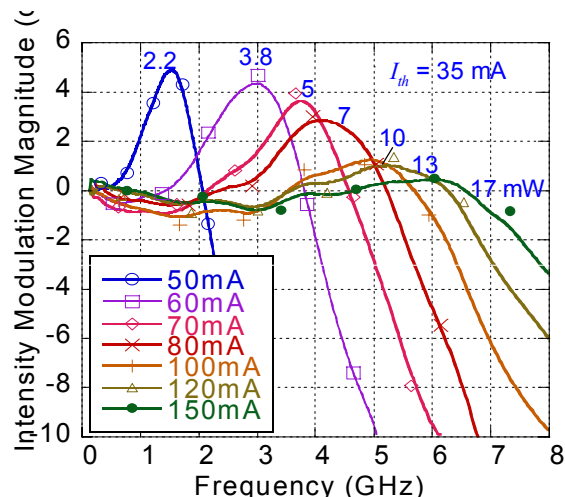


Figure 4: SGDBR laser direct modulation bandwidth

For improved chirp and larger extinction, WCs incorporating external modulators become attractive. In our implementation, we achieve external modulation in the WC with a DC-biased SGDBR laser followed by an EAM or MZM. The transmission of the modulator is varied through an applied voltage that is developed across a 50 Ω load resistor connected in parallel with the EAM/MZM and the photodetector. As discrete components, one crucial figure of merit for modulators is modulation efficiency in dB/Volt. Figure 5 (top) shows the extinction of a bulk FK EAM and Figure 5 (bottom) shows the extinction vs. bias for an MZM. The maximum obtained EAM efficiency for a 10 dB transmission loss is ~5 dB/V at 1535 nm for a 200 μm long EAM; the efficiency drops as the wavelength moves away from the waveguide absorption edge. Higher modulation efficiencies can be achieved, but at the expense of a larger insertion loss. The MZM exhibits an increased ~15 dB/V modulation efficiency, at the expense of device area and complexity, compared to the EAM.

2.5 Gb/s Wavelength Conversion

All of the WC implementations were successfully fabricated and were tested using a 2.5 Gb/s Non-Return to Zero (NRZ) optical input signal. Figure 6 shows input and output eye diagrams at 2.5 Gb/s for the directly modulated WC, the EAM WC, and the MZM WC. All three demonstrated clearly open eyes at 2.5 Gb/s NRZ data rates across at least a 20 nm SGDBR laser tuning range. Extinction ratio for the directly modulated WC was ~3 dB as the photocurrent was limited in fully integrated devices, due to a fabrication error resulting in higher than expected contact resistance. The extinction ratio for the EAM WC and MZM-WC devices was > 10 dB for all wavelengths.

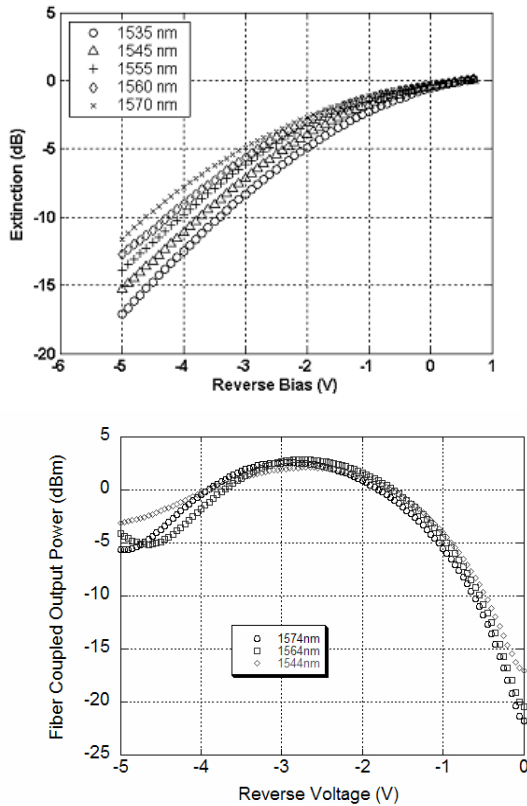


Figure 5: Extinction vs. bias for a 200 μm long EAM (top) and a MZM with 200 μm long electrodes (bottom)

All of the WC approaches fabricated demonstrated error-free operation at 10^{-9} Bit-Error Rate (BER) with a 2.5 Gb/s $2^{31}-1$ Pseudo Random Bit Stream (PRBS) signal. Power penalties compared to back-to-back operation without a WC were 6 dB, 1-2 dB, and < 1 dB for the directly modulated WC, EAM, and MZM WC, respectively. The larger power penalty for the directly modulated WC was due to the lower than expected photocurrent and consequently extinction, due to undesirable heating resulting from a fabrication error.

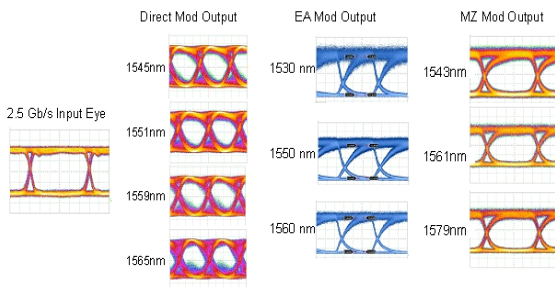


Figure 6: WC output eye diagrams with 2.5 Gb/s NRZ input signal

SCALABLE APPROACH (STANFORD)

Design and Fabrication

The approach taken by the Stanford team is based on the *intimate* integration of an electroabsorption modulator with a photodiode into a compact wavelength-converting switch [8]. Figure 7a illustrates such a dual-diode switch structure that incorporates a waveguide modulator diode and a surface-illuminated photodiode integrated as a part of the novel on-chip lumped optoelectronic circuit shown in Figure 7b. This dual-diode switch is designed to confine the optically generated high-speed electrical signals within its integrated circuit. The localization of the optical switching yields efficient wavelength conversion with a low optical input power requirement (mW range) to achieve high extinction ratios (> 10 dB). Furthermore, this photonic switch architecture naturally leads to a two-dimensional integrated array of these photonic switches to implement a reconfigurable wavelength-converting crossbar switch [14]. Such a photonic switch architecture also provides a convenient photonic integration platform; for example, a (tunable) laser diode and an optical semiconductor amplifier could be conveniently incorporated into the switch because of the fabrication compatibility, if desired [15].

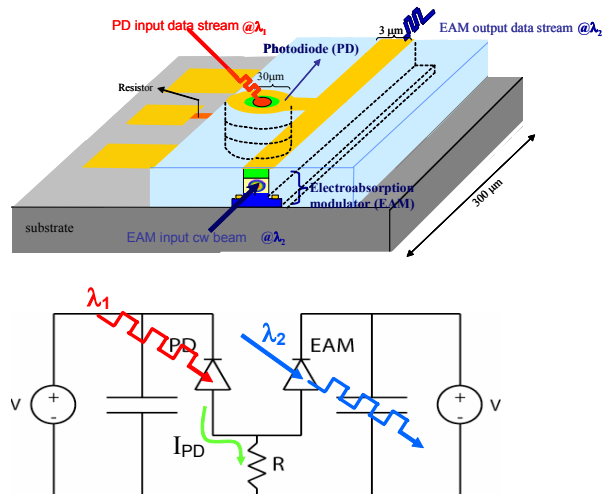


Figure 7 (a): A schematic of dual-diode photonic switch, and (b) its simplified circuit diagram

These wavelength-converting switches are completely insensitive to input signal polarization due to the surface-normal input configuration. They operate over a wide range of wavelengths (e.g., over the C-band) because of the broad-band absorption of the InGaAs photodiode and because of the electroabsorption of the InGaAsP/InP quantum-well modulator that is shifted and broadened with the application of DC bias. These switches provide unconstrained, bi-directional wavelength conversion and multi-wavelength broadcasting in the C-band.

Figure 7b shows a simplified circuit diagram of the integrated photodiode-modulator structure including a local resistor and a pair of bypass capacitors. Because of the lumped circuit operation of the integrated parts, transmission lines are not necessary. In operation, the high-speed optical input signal at λ_1 incident on the photodiode, PD, generates a photocurrent, I_{PD} , that creates a voltage drop across the resistor, R , and swings the voltage across the electroabsorption modulator. Such an optically-induced voltage change across EAM changes the transmission of the EAM quantum wells at λ_2 . Thus, the input data at λ_1 is bit-by-bit transferred to the output at λ_2 , which thus converts the carrier wavelength from λ_1 to λ_2 . The DC biases applied to the EAM and PD can further be used to electrically enable or disable the wavelength conversion.

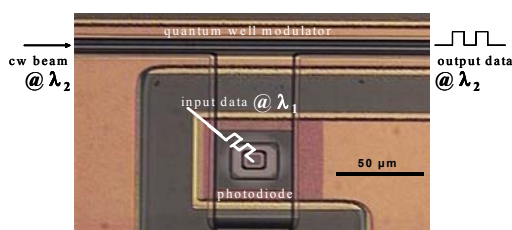


Figure 8: A picture of fabricated dual-diode device

Figure 8 is a part of the optical micrograph of a fabricated wavelength-converting switch that consists of an InGaAsP/InP waveguide quantum-well modulator and an InGaAs surface-normal pin photodiode monolithically integrated through two-step epitaxial growths. The switch is $300 \mu\text{m} \times 300 \mu\text{m}$ in size. It comprises a waveguide modulator with a width of $2 \mu\text{m}$, a length of $300 \mu\text{m}$ and a $0.37 \mu\text{m}$ thick i-region; a photodiode with a $30 \mu\text{m} \times 30 \mu\text{m}$ mesa and a $1.25 \mu\text{m}$ thick i-region; and a local resistor with values from 340 to 650 Ohms depending the designed speed of operation. The device is built on a semi-insulator InP substrate to lower parasitic capacitance and to isolate the individual switches. For monolithic integration, a new selective area regrowth technique is used [16]. For the further reduction of the parasitic capacitance and leakage current, a self-aligning polymer planarization and passivation method is developed [17].

The switch simulation that includes the on-chip, integrated optoelectronic circuit and off-chip, biasing circuit predicts optical switching requiring $< 10 \text{ mW}$ absorbed optical power for $> 10 \text{ dB}$ extinction ratio at 10 Gb/s. The RC time constant of the integrated optoelectronic circuit determines the operation speed. Figure 9 shows the simulated eye diagram at 10 Gb/s with $> 10 \text{ dB}$ extinction ratio [17].

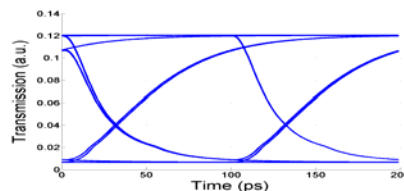


Figure 9: Simulation of 10 Gb/s operation

RESULTS

Figure 10 shows two open eye diagrams from the modulator output in (a) Return-to-Zero (RZ) and (b) NRZ schemes from the WC with a designed operation speed of 2.5 Gb/s. These diagrams exhibit RF-extinction ratios of $> 10 \text{ dB}$ with absorbed average optical power of $< 8 \text{ mW}$ at 2.5 Gb/s [18]. In both cases, the input wavelength is 1550 nm, and the output wavelength is 1530.0 nm. With the input beam photogenerating $\sim 5 \text{ mA}$ of current, an electric field swing of $\sim 6.5 \text{ V}/\mu\text{m}$ is optically induced across the modulator, comparable to the field swing typically required by an electrically driven, conventional EAM. These wavelength-converting switches cover an operation range of 45 nm, from 1525 nm to 1570 nm, centered on the C-band [17].

The switches also allow for multi-channel broadcasting across the entire C-band [17]. For dual-wavelength broadcasting, two CW beams at different wavelengths are coupled into the EAM to be simultaneously modulated by the same optical input signal incident on the PD. Figure 11 (b1-b3 and c) shows the two output optical signals from the EAM with channel spacings of 10 nm and 20 nm, respectively in C-band at 1.25Gb/s [17].

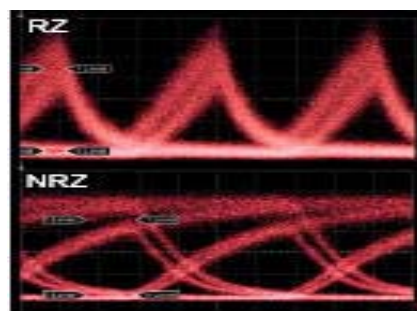


Figure 10: Optical switching in (a1) NRZ and (a2) RZ formats with $>10 \text{ dB}$ RF-extinction ratios at 2.5 Gb/s

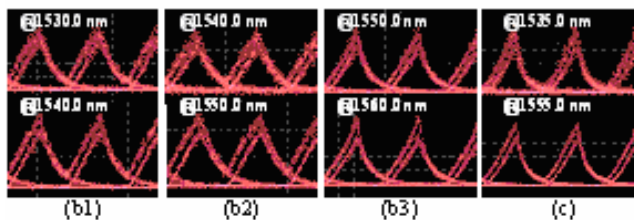


Figure 11: C-band dual-wavelength broadcasting with channel spacings of 10 nm in (b1)–(b3) and 20 nm in (c)

Figure 12 shows a fabricated 2x2 wavelength-converting crossbar switch [13]. Figure 13 depicts the eye diagrams taken from each of the four switch elements at 1.25 Gb/s, all measured with > 10dB extinction ratio. While one of the switch elements is tested, the unused switch along the same waveguide is disabled by slightly forward-biasing its photodiode and modulator. This removes the potential crosstalk between the two input channels and eliminates the background absorption of the quantum-well modulator in the unused WC.

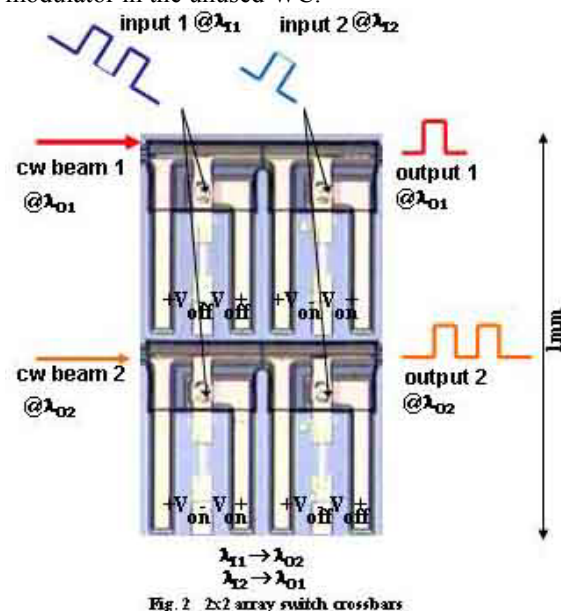


Figure 12: 2x2 wavelength-converting crossbar switch. The size is 1 mm x 600 μm

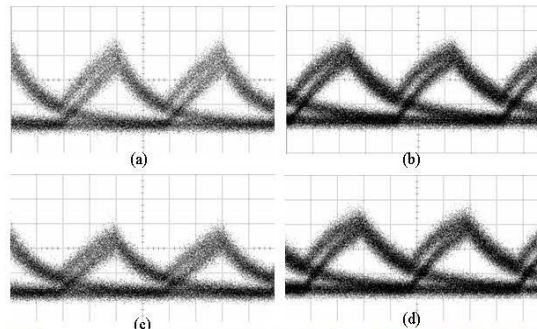


Figure 13: Eye diagrams from each of the four switch elements in a 2x2 array

DISCUSSION

We presented our design and experimental results on a wide variety of wavelength-converter implementations, and showed how these approaches can achieve the desired wavelength-conversion functionality at high bit rates and extinction ratio.

The Directly Modulated (DM) laser approach to wavelength conversion remains the most compact device incorporating an on-chip tunable optical source, but is ultimately limited by the modulation bandwidth of SGDBR lasers, and would achieve bit rates of 10 Gb/s or higher only with significant redesign. In addition, “chirping” in directly modulated lasers would result in an undesirable dispersion penalty.

For bit rates of 10 Gb/s and above, the externally modulated approach, utilizing an EAM or MZM to modulate the laser output, becomes more attractive. Both modulator types have been implemented by the UCSB project, and demonstrate higher extinction at 2.5 Gb/s compared to the direct modulated approach. Our EAM approach utilizes FK absorption. The EAM WC and MZM WC designs incorporate FK photodiodes, in order to take advantage of their improved linearity.

Modulator-type WCs will benefit from increased modulator extinction efficiency (dB/V). Longer EAMs provide increased extinction efficiency at the expense of increasing capacitance (hence lower bandwidth) and on-state transmission. The MZM, by utilizing phase change-induced interference, exhibits higher extinction efficiency than the EAM of similar electrode length allowing it to maintain high bandwidth.

The photonic switch architecture based on the intimate integration of a quantum-well waveguide modulator with a surface-normal photodiode allows for the two-dimensional scalability of the wavelength-converting switches to realize the first reconfigurable wavelength-converting crossbar switches. This technology relies on the tight confinement of optically induced high-speed

electrical signals in a single, compact, integrated optoelectronic chip for efficient wavelength conversion with low switching power for high extinction ratios in high-speed operations. Experimental results include unconstrained wavelength conversion up to 2.5 Gb/s and across 45 nm around the C-band, multi-wavelength broadcasting over 20 nm across the C-band, and multi-channel wavelength conversion with a 2x2 wavelength-converter array. Theoretical simulations predict 10 Gb/s operation.

CONCLUSION

In this paper, we described our research into novel approaches for monolithically integrating WCs in InP. The first approach, undertaken with UCSB, consists of an integrated widely tunable laser-transmitter and waveguide photodiode receiver. Several implementations have been designed, fabricated, and tested to exhibit modulation up to 2.5 Gb/s with high extinction ratio and error-free operation. The second approach, undertaken with Stanford University, consists of a scalable, compact, low-power, dual-diode photonic switch architecture that confines high-speed electrical signals in its novel photodiode-modulator integrated optoelectronic circuit. This technology enables reconfigurable multi-channel wavelength conversion. Both approaches are scalable to 10 Gb/s and higher bit rates, crucial for the implementation of advanced optical networking and the continuing explosion of Internet data bandwidth.

ACKNOWLEDGMENTS

We gratefully acknowledge the financial support of Intel Corporation, DARPA via the CS-WDM project, UC MICRO, and NSF IGERT for financial support, and the backing of George Bourianoff, Frank H. Robertson, and Valluri (Bob) Rao, all of Intel. Stanford researchers also acknowledge Jesper Hanberg of Intel/GIGA for sharing his InP expertise and for wafer and epi processing support, OEPIC Corporation for supplying epitaxial wafers, Japan ULVAC for advanced InP etch process support, Melles Griot for providing waveguide alignment setup, and PTAP (funded by NSF and DARPA) for the additional support.

REFERENCES

- [1] S. J. B. Yoo, "Wavelength Conversion Technologies for WDM Network Applications," *IEEE J. Lightwave Technology*, 14, 944-966, 1996.
- [2] L.H. Spiekman, U. Koren, M.D. Chien, B.I. Miller, J.M. Wiesenfeld, J.S. Perino, "All-Optical Mach-Zehnder Wavelength Converter with Monolithically Integrated DFB Probe Source," *IEEE Photonics Technology Letters*, 9, IEEE, 1349-51, 1997.
- [3] B.-E. Olsson, P. Ohlen, L. Rau, D. J. Blumenthal, "A simple and robust 40-Gb/s wavelength converter using fiber cross-phase modulation and optical filtering," *IEEE Photonics Technology Letters*, 12, IEEE, 846-848, 2000.
- [4] N. Edagawa, M. Suzuki, S. Yamamoto, "Novel wavelength converter using an electroabsorption modulator," *IEICE Trans. Electron.*, E81-C, 1251-1257, 1998.
- [5] L. Xu, L.K. Oxenlowe, N. Chi, J. Mork, P. Jeppesen, K. Hoppe, J. Hanberg, "Basic characterization of wavelength conversion at 40 Gb/s based on electroabsorption modulators," *IEEE Lasers and Electro-optics Society 2002 Annual meeting proceedings*, 111-112, 2002.
- [6] J. M. Hutchinson, J. A. Henness, L. A. Johansson, J. S. Barton, M. L. Masanovic, "2.5 Gb/sec wavelength conversion using monolithically-integrated photodetector and directly modulated widely-tunable SGDBR laser," *IEEE Lasers and Electro-optics Society 2003 Annual meeting proceedings*, 650-651, 2003.
- [7] J. S. Barton, M. L. Mašanović, M. N. Sysak, J. M. Hutchinson, E. J. Skogen, D. J. Blumenthal, L. A. Coldren, "A novel monolithically-integrated widely-tunable wavelength converter based on a SGDBR-SOA-MZ transmitter and integrated photodetector," *Photonics in Switching proceedings*, Versailles France, 2003.
- [8] H. Demir, V. Sabnis, O Fidaner, S. Latif, J. Harris, D. A. B. Miller, J Zheng, "Novel optically controlled optical switch based on intimate integration of surface-normal photodiode and waveguide electroabsorption modulator for wavelength conversion," *IEEE LEOS 2003 Annual Meeting proceedings*, WU1, 644-645, 2003.
- [9] H. Takeuci, T. Saoitoh, H. Ito, "High-speed electroabsorption modulators with traveling-wave electrodes," *OFC 2002 Technical Digest*, 336-338, 2002.
- [10] M. L. Masanovic, V. Lal, J. S. Barton, E. J. Skogen, D. J. Blumenthal, L.A. Coldren, "Monolithically Integrated Mach-Zehnder Interferometer wavelength converter and widely-tunable laser in InP," *IEEE Photonics Technology Letters*, 15, 1117-1119, 2003.
- [11] B. Mason, G. A. Fish, J. Barton, L. A. Coldren, S. P. DenBaars, "Design of sampled grating DBR lasers with integrated semiconductor optical amplifiers," *IEEE Photonics Technology Letters*, 12, 762-764, 2000.

- [12] J.M. Hutchinson, J. S. Barton, M. L. Mašanović, M. N. Sysak, J. A. Hennes, L. A. Johansson, D. J. Blumenthal, L. A. Coldren "Monolithically integrated InP-based tunable wavelength conversion," in *Proceedings of SPIE Photonics West Conference*, paper 5349-25, San Jose, CA, January 24-29, 2004.
- [13] L.A. Johansson, Y.A. Akulova, G.A. Fish, L.A. Coldren, "High optical power electroabsorption waveguide modulator," *Electron. Letters*, 39, 364-365, 2003.
- [14] H. V. Demir, V. A. Sabnis, O. Fidaner, J. S. Harris, Jr., D. A. B. Miller, J.-F. Zheng, N. Li, T.-C. Wu, and Y.-M. Houg, "Novel scalable wavelength-converting crossbar," *Proceedings of IEEE-OSA Optical Fiber Communications Conference (OFC)*, Los Angeles, CA, February 22-27, 2004, Paper FD5.
- [15] L. A. Coldren, "Widely-tunable chip-scale transmitters and wavelength converters," *Integrated Photonics Research (IPR) OSA Technical Digest*, Optical Society of America, Washington, DC, 2003, pp. 6-8.
- [16] V. A. Sabnis, H. V. Demir, O. Fidaner, J. S. Harris, Jr., D. A. B. Miller, J.-F. Zheng, N. Li, T.-C. Wu, Y.-M. Houg, "Optically-switched dual-diode electroabsorption modulators," *Integrated Photonics Research (IPR) OSA Technical Digest*, Optical Society of America, Washington, DC, pp.12-14 2003.
- [17] J.-F. Zheng, J. P. Hanburg, H. V. Demir, V. A. Sabnis, O. Fidaner, J. S. Harris, Jr., D. A. B. Miller, "Novel passivation and planarization in the integration of III-V semiconductor devices," in *Proceedings of SPIE Photonics West Conference*, paper 5356-9, San Jose, CA, January 24-29, 2004.
- [18] H.V. Demir, V. Sabnis, O. Fidaner, J. Harris Jr. and D. A.B. Miller, J.F. Zheng, "Dual-diode Quantum-Well Modulator for C-band Wavelength Converting and Broadcasting," *OSA Optics Express*, 12(2), pp. 310-316, 2004.
- [19] V. A. Sabnis, H. V. Demir, O. Fidaner, J. S. Harris, Jr., D. A. B. Miller, J.-F. Zheng, N. Li, T.-C. Wu, H.-T. Chen, and Y.-M. Houg, "Optically-controlled electroabsorption modulators for unconstrained wavelength conversion," *Applied Physics Letters*, 84 (4), pp. 469-471, 2004.

AUTHORS' BIOGRAPHIES

John M. Hutchinson received a Ph.D. degree in Electrical Engineering from the University of California, Berkeley in 1994. He worked in Intel Corporation's Components Research Department from 1994 to 2001

where his focus was on advanced silicon process technology. He is currently with Intel's Strategic Technology Group as a researcher-in-residence at the University of California, Santa Barbara. His research focuses on in-plane InP-based optoelectronics design and fabrication technology through design, fabrication, and testing of optical wavelength converters. His email is john.hutchinson at intel.com.

Jun-Fei Zheng received a Ph.D. degree in Materials Science from the University of California at Berkeley in 1994. Since then he has been with Intel Corporation working on silicon process technology development, advanced MOS transistors, memory devices, optoelectronic devices and their applications in optical interconnections. Currently, he is with the Intel Strategic Technology Group and an Intel researcher-in-residence at Stanford University and a Visiting Fellow at Yale University. His e-mail is jun.f.zheng at intel.com.

Jonathon S. Barton received a B.S. degree in Materials Engineering in 1998 from the University of California, at Davis. He is currently pursuing a Ph.D. at the University of California, Santa Barbara, and is working on the growth, processing, and testing of long wavelength photonic integrated circuits. His research involves Sampled Grating Distributed Bragg Reflector lasers with integrated modulators and amplifiers as well as monolithically integrated wavelength converters.

Jeffrey A. Hennes received a B.S. degree in Materials Engineering from Cal Poly, San Luis Obispo in 2000 and is pursuing a Ph.D. at the University of California, Santa Barbara. He is involved with the MOCVD growth of photonic integrated circuits. His current research interests include use of quantum-well intermixing for lateral carrier confinement within in-plane tunable lasers.

Milan L. Mašanović received an M.S. degree in Electrical Engineering, from the University of California, Santa Barbara, in 2000 and is currently pursuing a Ph.D. there. He is working on monolithically integrated, widely tunable all-optical wavelength converters in InP. The device design is based on the Sampled Grating DBR Laser and different versions of a Mach-Zehnder interferometer semiconductor optical amplifier-based wavelength converter.

Matthew N. Sysak received an M.S. degree in Electrical Engineering from the University of California, Santa Barbara in 2002 and is currently pursuing a Ph.D. there. His research interests include the monolithic integration of EAMs and widely tunable Sampled Grating DBR lasers, Semiconductor Optical Amplifiers and photodetectors for high-speed wavelength conversion in broadband WDM systems.

Leif A. Johansson received a Ph.D. degree in Engineering from University College, London, in 2002 and took up a post-doctoral position at the University of California at Santa Barbara in 2002. His current research interests include design and characterization of integrated photonic devices for analog and digital applications.

Daniel J. Blumenthal received a B.S.E.E. degree from the University of Rochester, New York, in 1981, an M.S.E.E. degree from Columbia University in 1988, and a Ph.D. degree from the University of Colorado at Boulder in 1993. From 1993 to 1997 he was Assistant Professor in the School of Electrical and Computer Engineering at the Georgia Institute of Technology. He is currently a Professor in the Department of Electrical and Computer Engineering at the University of California, Santa Barbara. Dr. Blumenthal is co-founder of Calient Networks, a manufacturer of photonic switching systems based in San Jose, CA. His current research areas are in optical communications, photonic packet switched and all-optical networks, all-optical wavelength conversion, photonic integration, and nanophotonics. He has authored and co-authored over 100 papers in these and related areas. Dr. Blumenthal is the recipient of a 1999 Presidential Early Career Award for Scientists and Engineers (PECASE), a 1994 NSF Young Investigator (NYI) award, and a 1997 Office of Naval Research Young Investigator Program (YIP) award. He is a Fellow of IEEE, and a member of the Optical Society of America and the Lasers and Electro-optic Society.

Larry A. Coldren holds a Ph.D. degree from Stanford University and is a Professor of Materials and Electrical and Computer Engineering at the University of California, Santa Barbara. He worked on guided surface-acoustic-wave devices, microfabrication techniques, and tunable diode lasers at AT&T Bell Laboratories until 1984. At UCSB since then, he has worked on a variety of opto-electronic materials and devices currently focusing on components and fabrication techniques for III-V opto-electronic integrated circuits. His group has made seminal contributions to vertical-cavity lasers and widely tunable lasers, and they are now involved in optical switching and noiseless amplification research. The fundamentals of such components are detailed in his recent book entitled *Diode Lasers and Photonic Integrated Circuits*, published by Wiley-Interscience. Professor Coldren is also heavily involved in new materials growth and fabrication technology essential to the fabrication of such integrated opto-electronic components. Most recently, his group has become actively involved in the fabrication of GaN-based edge- and vertical-cavity lasers that will emit in the blue and green wavelengths. Professor Coldren has been a Fellow of IEEE since 1982 and a Fellow of OSA since 1990.

Hilmi Volkan Demir received a B.S. degree in Electrical and Electronics Engineering from Bilkent University in 1998 and an M.S. degree in Electrical Engineering from Stanford University in 2000. He is an Intel Research Assistant at E. L. Ginzton Laboratory, and is working towards the completion of his Ph.D. degree in Electrical Engineering under the supervision of Professor David A. B. Miller at Stanford University. He defended his thesis on "Multifunctional Photonic Switches" in January 2004; his doctoral work has led to the world's first chip-scale wavelength-converting crossbar switches. His e-mail is volkan at stanford.edu.

Onur Fidaner received a B.Sc. degree in Electrical and Electronics Engineering from Middle East Technical University (METU), Ankara, Turkey, in 2001, and an M.S. degree in Electrical Engineering from Stanford University Stanford, CA in 2003. He is a Lucent Technologies Stanford Graduate Fellowship Student at Stanford University and he is currently working toward a Ph.D. degree in Electrical Engineering under Professor David A. B. Miller. His research involves development of novel ultrafast photonic devices incorporating quantum-well structures for future optical networks.

Vijit A. Sabnis received a B.Sc. degree (highest honors, honors program) from the University of California, Berkeley, in Electrical Engineering and Computer Sciences in 1995. He received an M.S. and Ph.D. degree in Electrical Engineering from Stanford University in 1997 and 2003, respectively. His doctoral research was conducted in the areas of epitaxial growth, fabrication, simulation, and characterization of optically controlled electroabsorption modulators.

James S. Harris, Jr. received B.S., M.S., and Ph.D. degrees in Electrical Engineering from Stanford University in 1964, 1965, and 1969, respectively. He joined Rockwell International in 1969 where he was a leader in establishing their preeminent position in GaAs heterojunction technology. In 1982, he joined Stanford University as Professor of Electrical Engineering and served as Laboratory Director from 1984-98. He has supervised over 65 Ph.D. students, has over 650 publications, 14 US patents, and is a Fellow of both APS and IEEE. He received the 2000 IEEE Morris N. Liebmann Award, the 2000 ISCS Welker Medal, and IEEE Third Millennium Medal.

David A. B. Miller received his B.Sc. degree from St. Andrews University and Ph.D. degree from Heriot-Watt University in 1979. He worked at Bell Laboratories from 1981 to 1996, being a Department Head from 1987, latterly of the Advanced Photonics Research Department. He is currently the W.M. Keck Foundation Professor of Electrical Engineering at Stanford University and Director of the Ginzton and Solid State and Photonics

Laboratories. His research interests include quantum-well opto-electronic physics and devices, and fundamentals and applications of optics in information, sensing, switching, and processing. He has published more than 200 scientific papers and holds over 50 patents. He has served as a board member for both OSA and IEEE Lasers and Electro-Optics Society (LEOS), and in various other society and conference committees. He was President of the IEEE Lasers and Electro-Optics Society in 1995. He was awarded the Adolph Lomb Medal and R. W. Wood Prize from the OSA, the International Prize in Optics from the International Commission for Optics, and an IEEE Third Millennium Medal. He is a Fellow of the Royal Societies of London and Edinburgh, IEEE, OSA, and APS, and holds honorary degrees from Vrije Universiteit, Brussel and Heriot-Watt University. His e-mail is dabm at ee.stanford.edu.

Copyright © Intel Corporation 2004. This publication was downloaded from <http://developer.intel.com/>.

Legal notices at <http://www.intel.com/sites/corporate/tradmarx.htm>.

Widely tunable, photocurrent-driven wavelength converter for narrowband analog applications

L.A. Johansson¹, Y.A. Akulova², G.A. Fish² and L.A. Coldren^{1,2}

¹ Department of Electrical and Computer Engineering, University of California, Santa Barbara, CA 93106.
Tel: (805) 893 2875, Fax: (805) 893 4500, Email: leif@ece.ucsb.edu. ²Agility Communications, Inc.

Abstract: A widely-tunable photocurrent-driven, directly modulated wavelength converter is demonstrated for narrowband applications. Wavelength conversion RF gain up to 30 dB and spurious-free dynamic range up to 105 dB·Hz^{2/3} are measured at 2.5 GHz.

©2004 Optical Society of America

OCIS codes: (190.2620) Frequency conversion; (140.3600) Lasers, tunable; (250.5300) Photonic Integrated Circuits

Summary

A widely-tunable, photocurrent driven optical wavelength converter for digital, broadband applications have been demonstrated using direct modulation of a sampled-grating DBR (SGDBR) laser, monolithically integrated with an optical receiver [1]. The overall performance of such device is ultimately limited by the requirement to produce sufficient photocurrent for various applications. One approach to increase the performance of photocurrent-driven wavelength converters is to trade-off bandwidth to modulation sensitivity in a resonated configuration.

In this work, a hybrid approach to achieve a wavelength converter for narrowband applications has been adopted using separate receiver and transmitter chips, as illustrated by the schematic of Fig. 1. The SG-DBR laser is integrated with an SOA and has >20mW output power and >40dB sidemode suppression ratio over >40nm tuning range [2]. The receiver consists of a bulk waveguide detector that can produce more than 70mA of linear photocurrent [3], also integrated with an SOA. The detector, with on the order of ~1pF total capacitance, was directly wirebonded by a ~5mm long bondwire (~1nH/mm) to the gain section of the SGDBR laser. Decoupled DC-biasing was achieved by separated, but AC-shorted ground planes.

The resulting optical-to-optical wavelength conversion frequency response is shown by Fig. 2. A resonantly enhanced peak is seen around 2.6 GHz with a 3dB passband of 370 MHz. The greatest signal gain occurs at around 40mA bias current when the resonance frequency of the directly modulated laser matches in frequency. It is estimated that the resonant configuration enhances the response by 20-30 dB, compared to using no resonance. Figure 3 shows the gain and spurious-free dynamic range (SFDR) of the wavelength converter as a function of gain section bias. The SFDR was measured by wavelength converting the output of two 1555nm DFB lasers, separated in wavelength by 60GHz and modulated at 2.505 GHz and 2.495 GHz, respectively, and detecting the 1547nm converted signal in a linear detector. The peak SFDR is 105 dB·Hz^{2/3} and occurs away from peak conversion gain, due to worsened distortion at laser resonance. At higher gain section bias, the SFDR degrades due to non-linearities of the preamplified receiver, as higher photocurrent is needed to compensate for the reduced conversion gain.

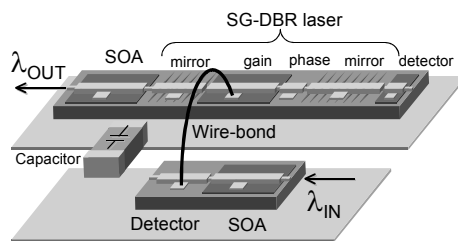


Fig. 1. Schematic overview of photocurrent-driven wavelength converter.

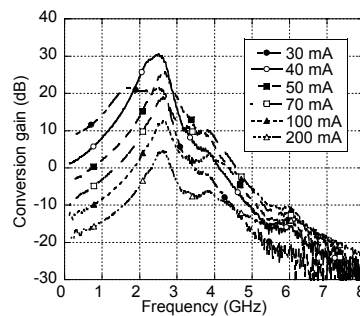


Fig. 2. Wavelength conversion RF frequency response for different gain section bias currents.

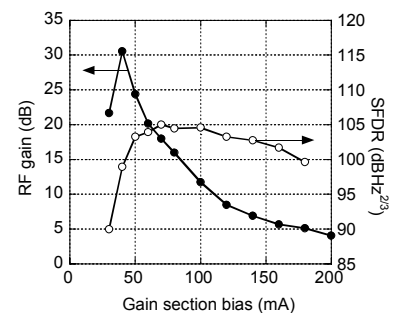


Fig. 3. Conversion gain and SFDR as a function of gain section bias current at 2.5 GHz.

References

1. J.M. Hutchinson, J.A. Hennes, L.A. Johansson, J.S. Barton, M.L. Mašanović and L.A. Coldren, "2.5 Gb/sec wavelength conversion using monolithically-integrated photodetector and directly modulated widely-tunable SGDBR laser," *LEOS Annual Mtg. 2003, WU4*.
2. Y. A. Akulova, G. A. Fish, P. C. Koh, C. Schow, P. Kozodoy, A. Dahl, S. Nakagawa, M. Larson, M. Mack, T. Strand, C. Coldren, E. Hegblom, S. Penniman, T. Wipiejewski, and L. A. Coldren, "Widely-Tunable Electroabsorption-Modulated Sampled Grating DBR Laser Transmitter", *IEEE J. Sel. Top. in Quantum Electron.*, 8, 1349-1357, Nov/Dec 2002.
3. L.A. Johansson, Y.A. Akulova, G.A. Fish, L.A. Coldren, "High optical power electroabsorption waveguide modulator," *Electron. Lett.*, 39, pp. 364-365, 2003.

2.5Gbit/s error free wavelength conversion using a monolithically-integrated widely-tunable SGDBR-SOA-MZ transmitter and integrated photodetector

Jonathon S. Barton, Milan L. Mašanović, Matthew N. Sysak, John M. Hutchinson, Erik J. Skogen, Daniel J. Blumenthal, Larry. A. Coldren, *Member, IEEE*

Abstract— Error free operation at 2.5 Gbit/s with a 2^{31} -1 PRBS is demonstrated for the first monolithically-integrated widely-tunable photocurrent-driven Mach-Zehnder based wavelength converter (TPDMZ-WC). A power penalty of 1-2dB is measured across the 37nm wavelength range of the SGDBR.

Index Terms—Tunable laser, RF modulation, Photonic Integrated circuits, high speed lasers. Wavelength conversion

I. INTRODUCTION

Future optical networks will benefit greatly from the development of widely-tunable wavelength converters. This novel class of sophisticated photonic integrated circuits allow for the dynamic manipulation of wavelengths in WDM optical switches, routers and add/drop multiplexers. A number of different implementations of wavelength converters have been proposed using optical gates comprised of a photodiode and electro-absorption modulator[1], cross-phase modulation in SOAs and fiber[2,3], and cross-absorption modulation(XAM) of EAMs[4]. Many of these architectures have been demonstrated to perform digital signal regeneration – including improvements in extinction ratio, signal to noise ratio, pulse width etc. More recently, fixed wavelength integrated laser sources have been explored [5] and monolithically-integrated widely-tunable all-optical wavelength converters(TAO-WC)[6] have been demonstrated. This approach has shown promise to allow for wavelength conversion

without requiring the signal to pass through electronics. In this paper we describe results from one configuration of a new class of wavelength converters that consist of a monolithically integrated tunable transmitter[7] with waveguide photodetector to generate photocurrent that is used to drive the modulation of the transmitter. The broad class of tunable photocurrent driven wavelength converters (TPD-WC) can use either an external modulator – or directly modulate the gain section of an SGDBR tunable laser[8].

This particular implementation uses a monolithically-integrated widely-tunable wavelength converter based on a SGDBR-SOA-MZ transmitter and integrated frantz-keldysh photo-detector (TPD-MZ-WC) (fig.1). The Mach-Zehnder design has high extinction with a low drive voltage making it suitable as a driving modulator for the device (fig. 2). The modulation efficiency is high due to the large change in index and absorption in the branches of the waveguide (band-gap energy corresponds to $\lambda=1.4\mu\text{m}$). The integrated device also allows wavelength monitoring, transmits at high speed, and removes the requirements for filtering the input wavelength at the output[5,6]. Integrating the SGDBR gives a compact wavelength agile source that requires only two fiber connections – with low loss coupling between the SGDBR and the modulator. This design ultimately yields a small footprint and low cost.

II. WAVELENGTH CONVERTER DESIGN

The device uses a ridge-based SGDBR with laser and modulator design similar to the one described in [7]. An absorber section is on the back-end of the device for measurement of power, and to decrease the requirements of the backside Anti-Reflective coating. The Mach-Zehnder modulator utilizes one 1x2 Multimode interference (MMI) coupler (97 μm long) at the input of the interferometer with curved waveguides extending to a separation of 20 μm in between the two branches and a 172 μm 2x2 MMI at the output of the MZ modulator

Manuscript received Oct 30, 2003. This work was supported by Intel Corporation and DARPA MTO – CS-WDM grant number N66001-02-C-8026. The authors are at the University of California at Santa Barbara, Materials and Electrical and Computer Engineering Dept. 93106 USA (telephone: 805-893-8465, e-mail: jsbarton@engineering.ucsb.edu).

section (inset of fig.1). The outputs are angled to reduce the AR coating requirements. The total device chip size is 1mm x 3.5mm. For the TPD-MZ-WC, the pads on both the bulk (Franz-Kelydsh) detector and the MZ are both 200 μ m long. This bulk detector drives one of the branches of a SGDBR-SOA-MZ transmitter at the output wavelength λ_2 .

This design uses a common waveguide structure in which the passive sections are formed by etching off the QWs down to the 10nm InP stop-etch layer. The process is similar to other SGDBR based Photonic Integrated Circuits (PIC's) [6,7,8]. The epi-layer structure consists of an offset quantum well structure (QW) as shown in table 1.

TABLE I
EPI-LAYER STRUCTURE

Layer	Thickness (nm)	Composition – Doping
InGaAs	100	Lattice Matched $1e19 \text{ cm}^{-3}$ Zn
<i>p</i> -InP	1800	$1e18 \text{ cm}^{-3}$ Zn
1.226LM	25	
7QWs		Nid 8nm barriers 6.5nm wells
<i>nid</i> InP	10	
Waveguide	350	Emission wavelength 1.4 μ m
<i>n</i> -InP Buffer	1800	$1e18$ Si InP
S Doped	10000000	$5e18$ Sulfur doped
Substrate		

III. PHOTO-DETECTOR CHARACTERISTICS

The bulk Franz-Kelydsh detector in this wavelength converter offers high photocurrent generation without saturation at high optical input powers. Fig. 3 demonstrates the photocurrent characteristics as a function of reverse bias and optical input power. In other designs[8], SOA preamps were employed to reduce the input power requirements to <1mW. In this case no on-chip SOA was used. Determination of the bias point of the detector is based on concerns of excessive device heating with high bias(-6V) and optical facet damage with high optical power (>200mW). For these reasons, the detector was biased at -4V to generate 30mA photocurrent using 180mW of optical power. Due to the flaring and angling of the waveguide and the use of lensed fiber – we experience approximately 5dB of coupling losses at the facet.

IV. BIAS CONFIGURATION

Conceivably the two devices could be directly connected together with a metal trace with proper design. In this device configuration, one would like to reverse bias the detector highly (-4V) to achieve sufficient photocurrent and resulting voltage swing, but leave the

MZ at a lower bias(-1V) where there isn't excessive absorption. For the purposes of this paper, both devices were probed with CPS probes using Picosecond labs model 5542 bias Ts. For improvement of the lumped bandwidth, a 50 ohm parallel resistor was connected between the MZ p-metal and ground contactss.

V. EXPERIMENT

BER curves as a function of receiver power were generated using an experimental setup as shown in fig. 4. NRZ 2^3-1 PRBS 2.5Gbit/s data was generated at an input wavelength of 1548.1nm using a 3 Gbit/s BERT and Agilent 83433A transmitter. An EFDA was used to boost the power to 180mW and generate 30mA of photocurrent in the detector at a bias of -4V on the detector which provides adequate drive voltage on the modulator – and ultimately high extinction ratio output. The converted signal from the integrated transmitter at λ_2 was fed into an EDFA/Filter then attenuated and the power measured just before the PIN receiver as shown in fig. 4 (Agilent 11982A). Separate filters were tuned for each wavelength in the C and L bands.

VI. RESULTS

Typical BER measurements are shown in fig. 5. The PBRS 2.5 Gbit/s output waveforms corresponded to 7.5-8.3 dB extinction across the wavelength range. Error free wavelength conversion was achieved over a wide range (37nm output) corresponding to a 1-2dB power penalty over this range. The device was biased with the following currents. Gain section = 120mA, SOA = 70mA, MZ branch1(modulated) = -1V, MZ branch2 = -3.6V. The tuning was performed by current injection into the rear mirror.

VII. CONCLUSION

We have demonstrated error free wavelength conversion over 37nm with <2dB power penalty using a novel TPD-MZ-WC wavelength converter. We see great promise in this monolithically integrated approach to wavelength conversion. These devices should become practical for implementation with improvement of on-chip coupling losses and with the eventual integration of a preamplifier before the photo-detector, which will provide significant optical gain and provide sufficient photocurrent to drive the Mach-Zehnder modulator with much lower optical power requirements. Improvements in biasing can be made using either an integrated capacitor on chip or devices isolated on semi-insulating substrates so that bias-T's are not required or an active detector employed that can absorb more of the light with lower bias.

ACKNOWLEDGEMENT

The authors acknowledge Agility Communications for the regrowth of the material.

REFERENCES

- [1] Kodama S, Yoshimatsu T, Ito H. 320 Gbit/s error-free demultiplexing using ultrafast optical gate monolithically integrating a photodiode and electroabsorption modulator. *Electronics Letters*, vol.39, no.17, 21 Aug. 2003, pp.1269-70. Publisher: IEE, UK.
- [2] Wolfson D, Fjelde T, Kloch A, Janz C, Poingt F, Pommereau F, Guillemot I, Gaborit F, Renaud M. Detailed experimental investigation of all-active dual-order mode Mach-Zehnder wavelength converter. *Electronics Letters*, vol.36, no.15, 20 July 2000, pp.1296-7. Publisher: IEE, UK.
- [3] Olsson B-E, Ohlen P, Rau L, Blumenthal DJ. A simple and robust 40-Gb/s wavelength converter using fiber cross-phase modulation and optical filtering. *IEEE Photonics Technology Letters*, vol.12, no.7, July 2000, pp.846-8. Publisher: IEEE, USA.
- [4] N. Edagawa, M. Suzuki, S. Yamamoto, "Novel wavelength converter using an electroabsorption modulator," *IEICE Trans. Electron.*, E81-C, 1251-1257 (1998).
- [5] **Spiekman LH, Koren U**, Chien MD, Miller BI, Wiesenfeld JM, Perino JS. **All-optical Mach-Zehnder wavelength converter with monolithically integrated DFB probe source.** [Journal Paper] *IEEE Photonics Technology Letters*, vol.9, no.10, Oct. 1997, pp.1349-51. Publisher: IEEE, USA.
- [6] Milan L. Mašanović, Vikrant Lal, Jonathon S. Barton, Erik J. Skogen, Larry A. Coldren, Daniel J. Blumenthal "Monolithically Integrated Mach-Zehnder Interferometer Wavelength Converter and Widely-Tunable Laser in InP." *IEEE Photonics Technology Letters*, Aug. 2003, Publisher: IEEE, USA.
- [7] J.S. Barton, E.J. Skogen, M.L. Masanovic, SP DenBaars, L.A. Coldren. "Tailorable chirp using integrated Mach-Zehnder modulators with tunable sampled grating distributed Bragg reflector lasers." *2002 IEEE 18th International Semiconductor Laser Conference. IEEE. 2002, pp.49-50. Piscataway, NJ, USA.*
- [8] Coldren, L.A., "Widely-Tunable Chip-Scale Transmitters and Wavelength Converters," *2003 Integrated Photonics Research. OSA. 2003, pp. xx. Washington DC, USA*

Figure Captions

Figure 1 : TPD-MZ-WC wavelength converter

Figure 2: DC extinction data for a 200 μ m long electrode Mach-Zehnder modulator – with 0 phase shift

Figure 3 Photodetector IV characteristics as a function of incident optical power at 1548.1nm

Figure 4. Schematic of BER test setup

Figure 5: BER data for different wavelengths with original wavelength at 1548.1nm [1-2dB power penalty]

Fig. 1.

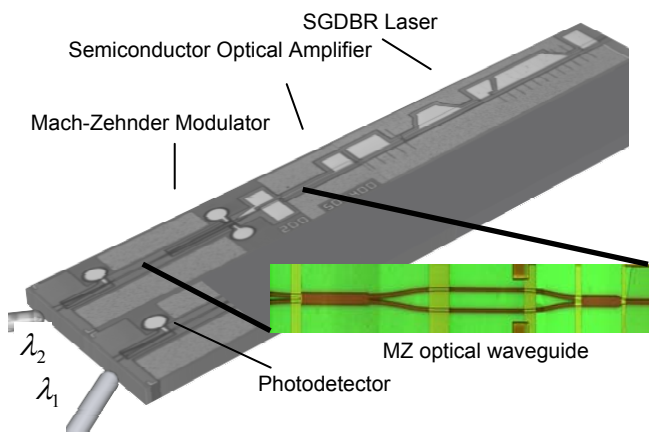


Fig. 2.

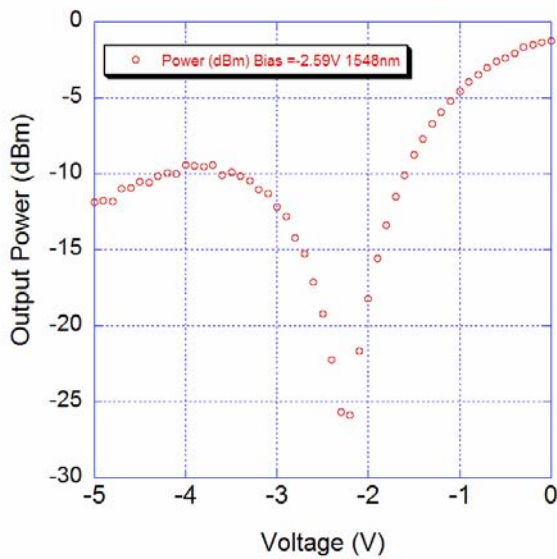


Fig.3.

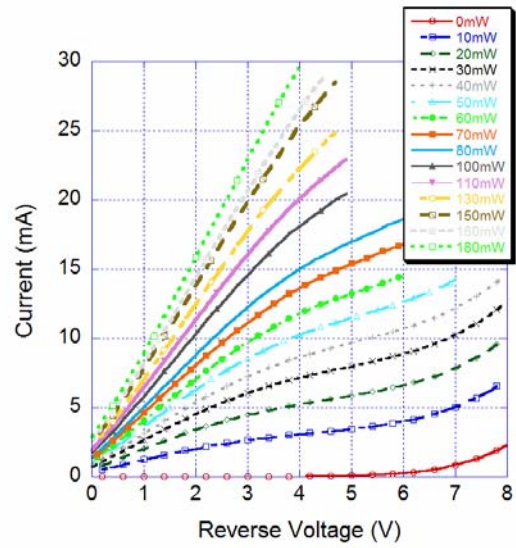


Fig. 4.

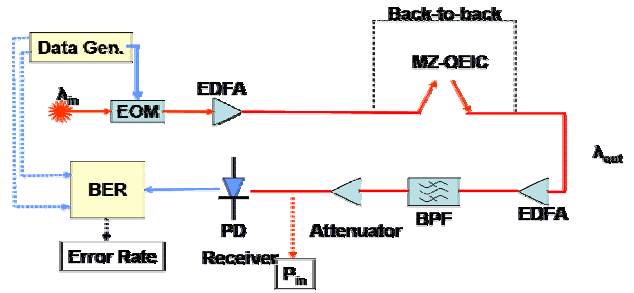
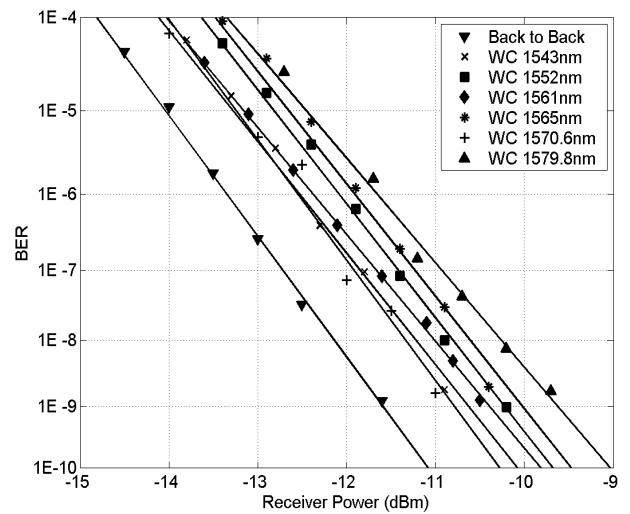


Fig. 5.



Many-Body Effects on InP-based Optoelectronic Wavelength Converters for WDM Applications

Joachim Piprek, John Hutchinson,* Jeff Hennes, Larry Coldren, and Jörg Hader #

ECE Department, University of California, Santa Barbara, CA 93106

* Intel Corporation, Portland, OR

Non-Linear Control Strategies, Tucson, AZ

Wavelength converters are a novel class of photonic integrated circuits that is crucial for future wavelength-division multiplexing (WDM) fiber-optic communication systems. Their main purpose is to transfer signals from one WDM wavelength to another. We present the simulation and analysis of an optoelectronic InP-based tunable wavelength converter (Fig. 1) which monolithically combines a pre-amplified receiver with a post-amplified sampled-grating distributed Bragg reflector (SG-DBR) laser diode [1]. The SG-DBR laser can be tuned to any wavelength of the C-band.

The commercial software PICS3D [2] is employed which was modified for the purpose of this investigation. The three-dimensional (3D) physics-based model takes into account interband gain and absorption in the multi-quantum well (MQW) InGaAsP active region, carrier transport including Fermi statistics and thermionic emission, and optical wave-guiding. For the first time, we integrate advanced many-body gain theory [3] into the 3D simulation of an optoelectronic device [4]. Measured photoluminescence (PL) spectra are used to adjust the inhomogeneous energy broadening in the many-body model, which represents unpredictable growth imperfections of the quantum wells (Fig. 2). The bulk transition matrix element for our quantum well is obtained from non-linear interpolation of binary compound data [5]. Good agreement with device measurements is achieved by adjusting the quantum well Auger coefficient. Figure 3 shows light vs. current characteristics for the laser-amplifier transmitter. Performance limitations of the wavelength converter are investigated in detail. Wavelength dependence and non-linear response to increasing current are strongly affected by the many-body gain model. Significant saturation effects with increasing input power are calculated for the receiver and are connected to the nonuniform carrier density in the quantum wells. Further results will be presented at the conference.

- [1] J. Hutchinson, J. Barton, M. Masanovic, M. Sysak, J. Hennes, L. Johansson, D. Blumenthal, and L. A. Coldren, "Monolithically integrated InP-based tunable wavelength conversion." In: *Physics and Simulation of Optoelectronic Devices XII*, SPIE Proc. Vol. 5349, pp. 176-184, 2004.
- [2] PICS3D by Crosslight Software, 2004.
- [3] J. Hader, J.V. Moloney, S.W. Koch, and W.W. Chow: IEEE J. Sel. Topics in Quantum Electron. 9, 688 (2003)
- [4] J. Piprek, S. Li, P. Mensz, and J. Hader, "Monolithic Wavelength Converter: Many-Body Effects and Saturation Analysis." In: *Optoelectronic Devices – Advanced Simulation and Analysis*, Springer, New York, 2004 (to be published).
- [5] I. Vurgaftman, J. R. Meyer, and L. R. Ram-Mohan: J. Appl. Phys. 89, 5815 (2001)

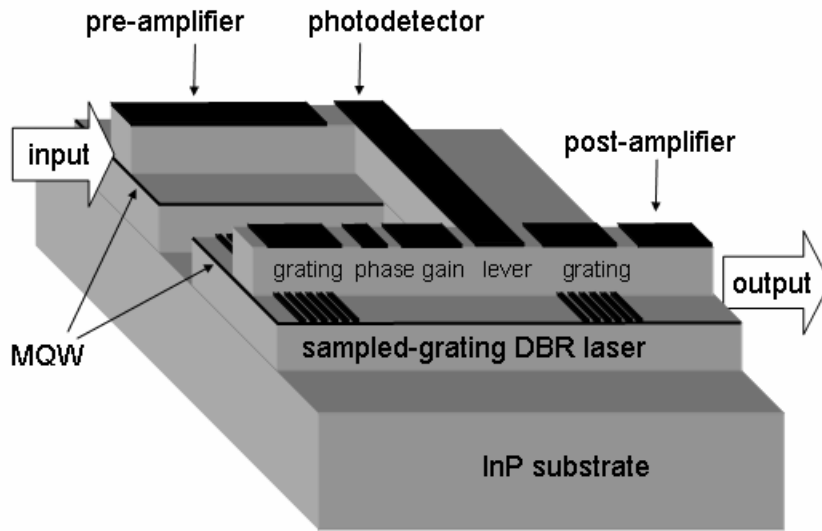


Fig. 1: Schematic view of the monolithic wavelength converter.

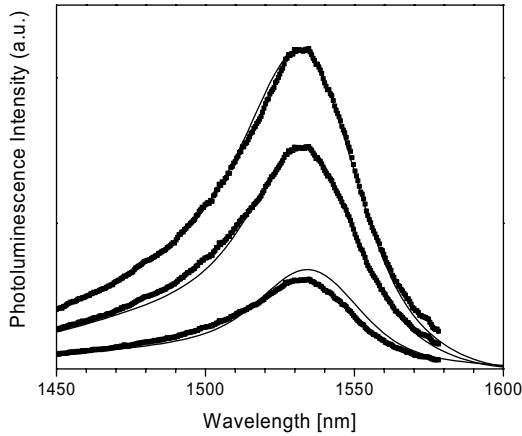


Fig. 2: PL spectra of our MQW active region (dots – measured at 1 \times , 2 \times , and 3 \times pump intensity; solid lines - many-body calculations at carrier densities of 3.8, 6.2, and $7.7 \times 10^{17} \text{ cm}^{-3}$).

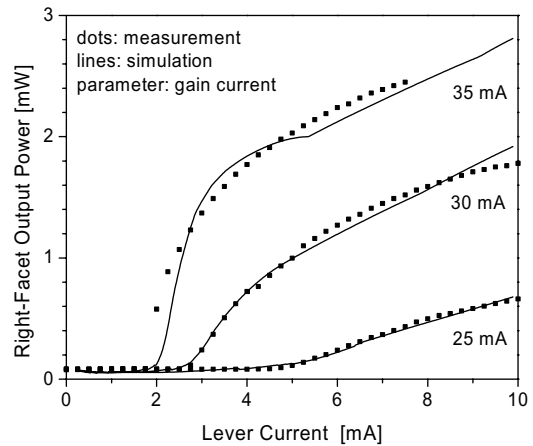


Fig. 3: Sampled-grating DBR laser characteristics with post-amplifier current of 30 mA. The gain section is divided into a constant pump region (parameter) and a lever region that is connected to the photodetector (cf. Fig. 1).

Single-Chip Wavelength Conversion Using a Photocurrent-Driven EAM Integrated With a Widely Tunable Sampled-Grating DBR Laser

Matthew N. Sysak, Jonathon S. Barton, *Student Member, IEEE*, Leif A. Johansson, James W. Raring, *Student Member, IEEE*, Erik J. Skogen, *Member, IEEE*, Milan L. Mašanović, *Student Member, IEEE*, Daniel J. Blumenthal, *Fellow, IEEE*, and Larry A. Coldren, *Fellow, IEEE*

Abstract—Tunable photocurrent-driven wavelength converters using widely tunable sampled grating distributed Bragg reflector lasers, electroabsorption modulators, semiconductor optical amplifiers, and an optically preamplified receiver have been fabricated and tested. Dynamic wavelength conversion has been achieved over 40 nm with optical bandwidths up to 10 GHz.

Index Terms—Electroabsorption modulators (EAMs), offset quantum well, sampled grating distributed Bragg reflector (SGDBR) laser, semiconductor lasers, semiconductor optical amplifier (SOA)-PIN receiver, semiconductor optical amplifiers (SOAs), wavelength converters (WCs).

I. INTRODUCTION

NEXT-GENERATION networks using wavelength-division multiplexing will benefit greatly from increased functionality of advanced photonic integrated circuits (PICs). Of particular importance are network functions like wavelength provisioning, add-drop multiplexing, and packet switching that require the use of fast, dynamic wavelength conversion. The InP-InGaAsP offset quantum-well shallow-ridge technology platform has been shown to be convenient for monolithic integration of advanced wavelength agile PICs that promise to perform these functions [1], [2], [4], [6]. Of particular importance are devices that can perform dynamic wavelength conversion. Recently, all-optical wavelength conversion in a Mach-Zehnder interferometer (MZI) monolithically integrated with a widely tunable transmitter [sampled grating distributed Bragg reflector (SGDBR)] has been demonstrated. In this device, no complicated electronics are necessary and it is possible to perform 2R regeneration [tunable all-optical wavelength converter (WC)] [2]. In addition, broad-band, high-speed, field-based, photocurrent-driven (PD) WC designs have been proposed and demonstrated with both MZI and electroabsorption modulators (EAMs) [1], [3]. In this class of WCs, photocurrent from a photodetector is used to modulate the electric field in a reverse biased modulator. Device performance is not limited to carrier modulation effects and inherently

Manuscript received April 16, 2004; revised May 17, 2004. This work was supported by DARPA/MTO CS-WDM under Grant N66001-02-C-8026 and by Intel Corporation under Grant TXA001630000.

The authors are with the Department of Electrical Engineering and the Department of Materials, University of California Santa Barbara, Santa Barbara, CA 93116 USA (e-mail: mnsysak@engineering.ucsb.edu).

Digital Object Identifier 10.1109/LPT.2004.833069

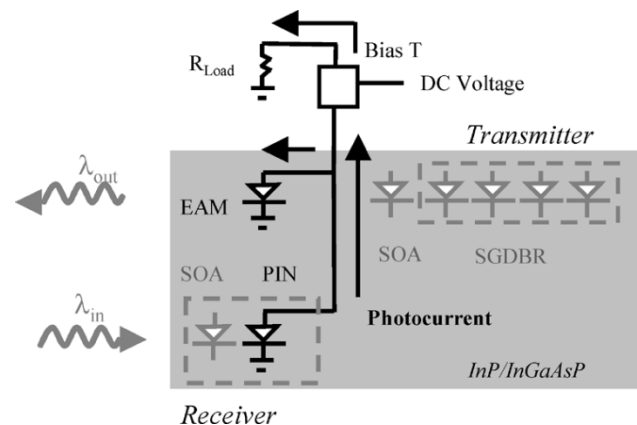


Fig. 1. Diagram of integrated PD-EAM WC with equivalent circuit schematic.

higher modulation bandwidth products are possible. PD-EAM devices traveling-wave EAM/unitraveling-carrier photodiode have been shown to support data rates up to 320 Gb/s [5].

In this work, a widely tunable SGDBR laser has been monolithically integrated with a Franz-Keldysh (FK) EAM, semiconductor optical (SOA) amplifiers, and an FK waveguide photodetector in a PD-EAM arrangement. This design allows for broadband wavelength conversion using high-speed field-based modulation with no required off-chip control wavelength source, no electrical amplification, and no complex optical filtering of output data signals.

II. WAVELENGTH CONVERTER DESIGN

The WC architecture consists of two neighboring ridges interconnected with a gold trace or wirebond. A basic device schematic is shown in Fig. 1. The transmitter ridge consists of an SGDBR laser integrated with a 300- μm -long SOA and an EAM [6]. The receiver ridge contains an input optical preamplifier and an FK-EAM used as a photodetector. The device fabrication process is similar to other SGDBR-based PICs [1], [2], [4], [6] and the final epilayer structure is shown in [1]. For the modulator and detector, a low K dielectric, photo-bis-benzocyclobutene is employed to reduce parasitic pad capacitance. The output and input waveguides are angled to reduce the antireflection coating requirements. Devices have been thinned, and individual bars mounted on aluminum nitride carriers and wirebonded for characterization.

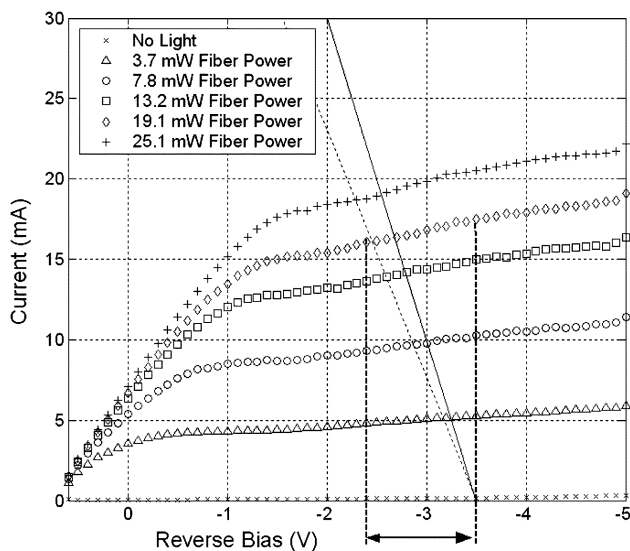


Fig. 2. 200- μm photodetector characteristics as a function of input fiber power. 65- (dotted lines) and 50- (solid lines) Ω load lines shown at -3.5-V bias. Note $>1\text{-V}$ swing with 19-mW fiber power using a 65- Ω load.

III. OPTICAL RECEIVER

It is well known that including an optical preamplifier into integrated optical receiver architectures greatly improves performance by providing optical gain. In the receiver section a broad-band high-saturation power [7] 200- μm -long FK PIN photodiode has been integrated with a 300- μm -long SOA preamplifier similar to that described in [4]. The amplifier provides between 4 and 5 dB of gain and shows 1 dB of gain compression at 10.4-mW input fiber power with 100-mA bias. The compression point is rather high and may be a result of reduced differential gain due to heating. It is important to note that 10.4 mW does not necessarily represent a maximum level of input power to the receiver. It is only for input powers significantly above the 1-dB compression point (above ~ 20 mW) that diminished increases in photocurrent swing can be seen as a result of comparative rolloffs in the optical gain between the input signal “1” and “0” level.

IV. DEVICE BIAS AND OPERATION

Due to the complexity of integrating the individual components, care must be taken to select optimum operating conditions. Electrically, the WC consists of two reverse biased diodes (photodetector and EAM) connected to a common DC reverse bias and terminated with a load resistor through a bias-T (Fig. 1). As an example of device operation, load lines (50 and 65 Ω) have been added to show the peak-to-peak voltage swing at a given fiber power level (Fig. 2). This voltage is then translated into a change in extinction in the EAM (~ 6 dB for about 1 V, Fig. 3). Generally, it is advantageous to bias the modulator at higher voltages since both the bandwidth (Fig. 4) and slope efficiency is greater. However, operation in this regime increases insertion loss. From Figs. 2 and 3, it is clear that most of the input light is absorbed in the PIN at voltages greater than -2 V and that >10 dB of attenuation of light input into the EAM is also expected. As a result, when the signal photocurrent from the

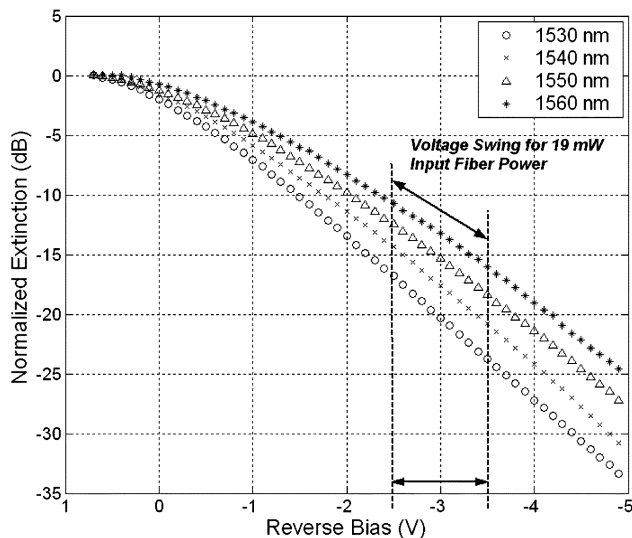


Fig. 3. DC extinction results for 400- μm FK EAM. Note $\sim 6\text{-dB}$ extinction change with 1-V swing (see Fig. 2) at -3.5-V bias.

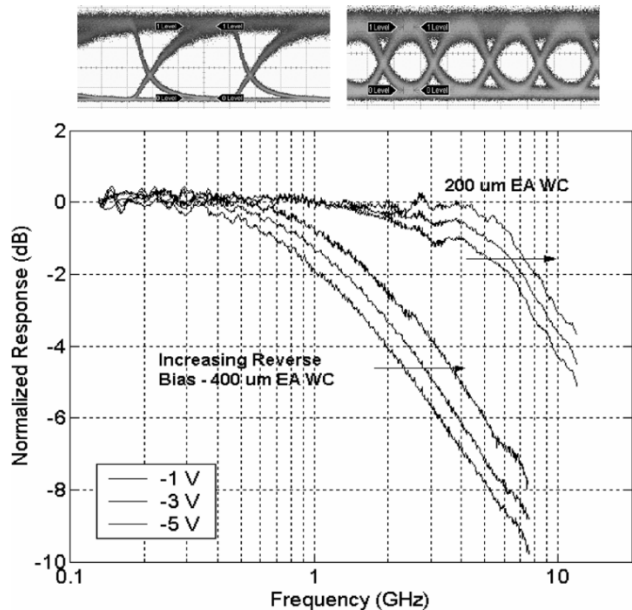


Fig. 4. Optical bandwidth for 75- Ω terminated WC with 400- μm EAM (left) and 50- Ω terminated WC with 200- μm EAM (right) at various reverse bias with 5 mW of input fiber power. Optical eyes at 2.5 (left) and 10 Gb/s (right) are shown above for input power levels of 19.2 mW. Extinction ratios are 14 and 5 dB, respectively, with the limited ER at 10 Gb/s and the slow rise time of the 2.5-Gb/s signal mainly due to the frequency response rolloff.

PIN swings the voltage over the EAM, very little parasitic photocurrent swing is generated that would compete with the PIN signal. This allows the bias point of the entire device beyond -2 V to be selected based on desired EAM efficiency, bandwidth, and output power.

V. EXPERIMENT

Optical bandwidth measurements and bit-error-rate (BER) curves with eye diagrams have been generated. Optical bandwidth measurements were performed using a lightwave optical component analyzer as a function of reverse bias on the device. Light at λ_1 is input from a lensed fiber into the receiver section

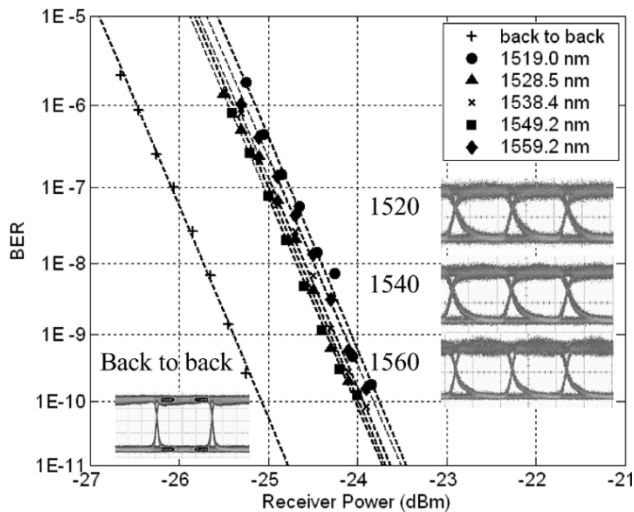


Fig. 5. BER Curves for wavelength conversion. Input wavelength is 1548.1 nm. Eye diagrams are shown for back-to-back operation and conversion to 1520, 1540, and 1560 nm.

of the WC and the output from the transmitter ridge at λ_2 is fed back into a high-speed detector. For the BER measurements, a nonreturn-to-zero $2^{31} - 1$ pseudorandom bit stream at 2.5 Gb/s from a 10-Gb/s BER tester transmitter (Agilent 83433A) at a wavelength of 1548.1 nm was input into a high-power Erbium-doped fiber amplifier followed by a polarization controller and transmitted to the device under test using a conically tipped lensed fiber. In this experiment, 19.2 mW of optical fiber power was used and the extinction ratio of the input signal was 14 dB. The output optical signal of the WC was then input into a variable optical attenuator before entering the PIN receiver. Note that no output filtering or amplification was required. The BER testing schematic is similar to that in [1]. The laser gain section, preamplifier SOA, and transmitter SOA are biased at 160, 120, and 100 mA, respectively, and the device was maintained at 16 °C with a thermoelectric cooler.

VI. RESULTS

Three separate devices under slightly different conditions have been examined. Optical bandwidth of a 75- Ω terminated 400- μm -long EAM integrated with a 200- μm detector/tunable laser/optical amplifier shows a small signal 3-dB rolloff frequency response of between 2–3 GHz. For a 200- μm -long EAM integrated with a 200- μm passive detector/tunable laser/optical amplifier configuration terminated at 50 Ω , the bandwidth can be extended to 10 GHz (Fig. 4). Small signal circuit models show agreement with experimental results taking into account wirebond inductance from the connection between the chip and carrier.

BER results at 2.5 Gb/s for wavelength conversion are shown in Fig. 5 for the 400- μm -based electroabsorption WC that has been terminated with a 65- Ω load resistor. The device operating point was chosen to maximize output power levels while targeting acceptable system performance and input power requirements. Output waveforms correspond to an extinction ratio of

between 8–8.5 dB over output wavelengths spanning 40 nm with peak output power levels increasing from -7 dBm at 1519 nm to -2.6 dBm at 1559.2 nm. Error-free operation has been achieved with a power penalty of less than 1.5 dB and is in good agreement with expected dispersion penalties given this extinction ratio.

It is possible to improve many of the device characteristics such as extinction ratio, output power, and bandwidth. Higher saturation power preamplifiers will significantly increase the photocurrent generated in the receiver and the voltage drop across the EAM. In addition, narrowing exposed ridge width will provide lower junction capacitance and decrease the resistance–capacitance time constant that limits device bandwidth. Additional approaches for device improvements include increasing the reverse bias, increasing the load resistance, and increasing the EAM length for increased efficiency and extinction ratio.

Optical transmission over 25 and 50 km of fiber at 2.5 Gb/s has also been performed. No noticeable power penalty was observed which is to be expected with a low-chirp FK-based device at these transmission distances [6].

VII. CONCLUSION

We have demonstrated wavelength conversion over a wide wavelength range with optical bandwidths up to 10 GHz. At 2.5 Gb/s, less than 1.5-dB power penalty has been observed with a 65- Ω terminated device that includes a 400- μm -long EAM. In addition, the integrated optical on-chip preamplifier has been shown to provide gain, reducing the fiber power drive requirements considerably from previously reported devices on a similar material platform [1].

REFERENCES

- [1] J. S. Barton, E. J. Skogen, M. L. Masanovic, M. N. Sysak, D. J. Blumenthal, and L. A. Coldren, "2.5-Gb/s error-free wavelength conversion using a monolithically-integrated widely-tunable SGDBR-SOA-MZ transmitter and integrated photodetector," *IEEE Photon. Technol. Lett.*, vol. 16, pp. 1531–1533, June 2004.
- [2] M. L. Mašanović, V. Lal, J. S. Barton, E. J. Skogen, L. A. Coldren, and D. J. Blumenthal, "Monolithically integrated Mach–Zehnder interferometer wavelength converter and widely-tunable laser in InP," *IEEE Photon. Technol. Lett.*, vol. 15, pp. 1117–1119, Aug. 2003.
- [3] H. V. Demir, V. A. Sanabis, O. Fidaner, J. S. Harris Jr., D. A. B. Miller, and J. F. Zheng, "Dual-diode quantum-well modulator for C-band wavelength conversion and broadcasting," *OSA Opt. Express*, vol. 12, no. 2, pp. 310–316, 2004.
- [4] B. Mason, J. Barton, G. Fish, and L. Coldren, "Design of sampled grating DBR lasers with integrated semiconductor optical amplifiers," *IEEE Photon. Technol. Lett.*, vol. 12, pp. 762–764, July 2000.
- [5] S. Kodama, T. Yoshimatsu, and H. Ito, "320 Gbit/s optical gate monolithically integrating photodiode and electroabsorption modulator," *Electron. Lett.*, vol. 39, no. 4, pp. 383–385, Feb. 2003.
- [6] Y. A. Akulova, G. A. Fish, P. C. Koh, C. Schow, P. Kozodoy, A. Dahl, S. Nakagawa, M. Larsen, M. Mack, T. Strand, C. Coldren, E. Hegblom, S. Penniman, T. Wipiejewski, and L. A. Coldren, "Widely tunable electroabsorption-modulated sampled grating DBR laser transmitter," *IEEE J. Select. Topics Quantum Electron.*, vol. 8, pp. 1349–1357, Nov/Dec. 2002.
- [7] L. A. Johansson, Y. A. Akulova, G. A. Fish, and L. A. Coldren, "High optical power electroabsorption waveguide modulator," *Electron. Lett.*, vol. 39, no. 4, pp. 364–365, Feb. 2003.

Design and Performance of a Monolithically Integrated Widely Tunable All-Optical Wavelength Converter With Independent Phase Control

Milan L. Mašanović, *Student Member, IEEE*, Vikrant Lal, *Student Member, IEEE*, Joseph A. Summers, *Student Member, IEEE*, Jonathon S. Barton, *Student Member, IEEE*, Erik J. Skogen, *Member, IEEE*, Larry A. Coldren, *Fellow, IEEE*, and Daniel J. Blumenthal, *Fellow, IEEE*

Abstract—We report on a new widely tunable all-optical wavelength converter consisting of a sampled-grating distributed Bragg reflector (SGDBR) laser monolithically integrated with a Mach–Zehnder interferometer semiconductor optical amplifier (MZI-SOA)-based wavelength converter. The new design incorporates independent phase control of the interferometer and SOAs for amplification of the SGDBR output. For the first time, error-free operation for data rates of up to 10 Gb/s is reported for 35-nm output tuning range. The high-speed operation is enabled by high photon density in the SOA due to large power transfer from the on-board tunable laser and amplifiers. We also report on device sensitivity of -10 dBm at 2.5 Gb/s and -5 dBm at 10 Gb/s, with an average output power of 0 dBm.

Index Terms—Mach–Zehnder interferometer (MZI), photonic integrated circuits (PICs), tunable laser, wavelength conversion, wavelength converter.

I. INTRODUCTION

FUTURE optical networks and their deployment represent the main driving force for the development of photonic integrated circuits (PICs). PICs utilize a single substrate for the monolithic integration of optically interconnected guided-wave optoelectronic devices. The primary objectives of photonic integration are similar to those of electronic integration: enhancing the performance, efficiency, reliability, and increasing the functionality while lowering the manufacturing and utilization cost. One of the key new PICs being developed for deployment in reconfigurable and packet-switched wavelength-division-multiplexing networks is the tunable all-optical wavelength converter (TAO-WC). Integration of the tunable laser and an all-optical Mach–Zehnder interferometer (MZI)-based wavelength converter on a single chip allows data to be transferred from an input wavelength to a tunable output wavelength without passing the signal through electronics. This class of wavelength converters was shown to work for both return-to-zero and non-return-to-zero (NRZ) data formats while acting as a 2R signal regenerator due to their highly nonlinear transfer function [1].

Manuscript received March 9, 2004; revised April 28, 2004. This work was supported by the DARPA/MTO CS-WDM Program under Grant N66001-02-C-8026.

The authors are with the Electrical and Computer Engineering Department, University of California Santa Barbara, Santa Barbara, CA 93106 USA (e-mail: mashaan@ece.ucsb.edu).

Digital Object Identifier 10.1109/LPT.2004.834448

Previously, we have reported on the demonstration of the first widely TAO-WC [2]. With TAO-WC, we demonstrated regenerative, error-free operation at 2.5 Gb/s, with 22-nm output tuning range, -6 -dBm input sensitivity, and -2 dBm in fiber converted signal power [3]. However, in this prior work, there were issues with optimization of the extinction ratio in the noninverting mode of operation, as well as the gain recovery time of the MZI semiconductor optical amplifiers (MZI-SOAs).

In this letter, we address these issues with a new device design. The major differences in the new design are the inclusion of an independent MZI-SOA interferometer phase control mechanism, and the addition of the two booster SOAs after the SGDBR laser. With this improved PIC design, we achieved error-free power efficient operation for bit rates up to 10 Gb/s, with increased output tuning range of 35 nm, and an increased input sensitivity and converted signal power.

II. WAVELENGTH CONVERTER DESIGN

The new tunable wavelength converter design incorporates an SGDBR laser and a Mach–Zehnder SOA-based wavelength converter, but it differs from our previous design [2] in several key aspects: optimized sampled-grating DBR mirror design, two independent (for redundancy) longer input SOA, two booster-amplifier SOAs located in the branches of the MZI after the SGDBR laser, passive waveguide phase sections in the MZI, and finally, a dual-output multimode interference (MMI) 2×2 coupler at the wavelength converter output.

The electron micrograph of the chip on a carrier, as well as the wavelength converter schematic are shown in Fig. 1. The tunable SGDBR laser is 1.7 mm long and its operating principles are described in detail in [4]. The interferometer branches are defined by four S-bends and two 1.5-mm-long SOAs. The output light of the SGDBR laser is equally split using a 1×2 MMI-based light splitter, and then amplified by the two booster-amplifier SOAs that are located after the splitter, in the interferometer S-bends. This amplified laser light is then coupled with the light from the input waveguides using 2×1 MMI combiners into the SOAs in the branches of the MZI. The input signal is coupled onto the chip through a tapered, angled input waveguide, and then amplified by the input SOA running alongside the laser. In order to reduce the thermal crosstalk, the input SOAs, on the sides of the SGDBR laser, are about 200 μm away

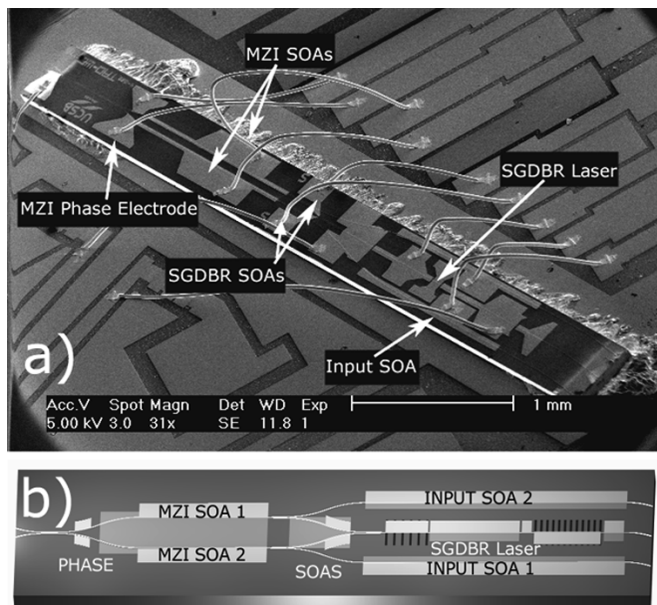


Fig. 1. (a) Electron micrograph of the wavelength converter. (b) Device schematic.

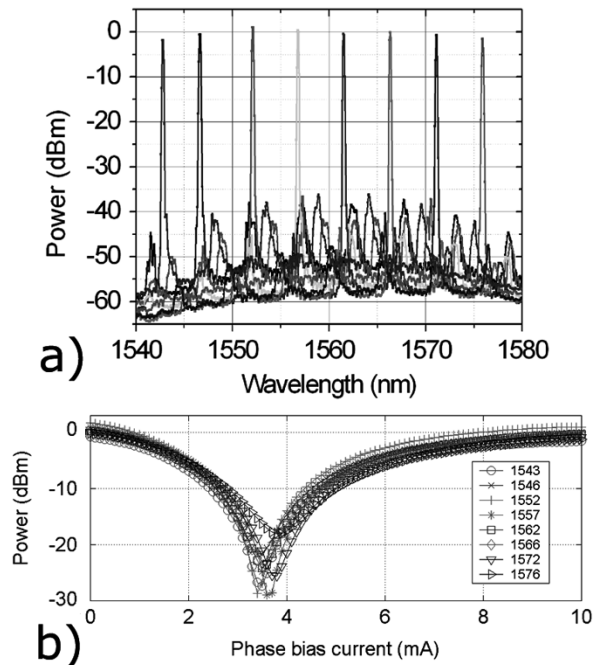


Fig. 2. (a) Spectra of the integrated laser. (b) Control of the interferometer using phase electrodes (Port 2: $I_{mzisoas} = 200$ mA).

laterally from the SGDBR active region. The total chip size is 0.5×5.3 mm.

The laser mirror design was optimized for wide tunability, resulting in 35-nm output tuning range [see Fig. 2(a)].

Longer input SOA helps improve the device sensitivity by providing a large amount of gain, as seen in Fig. 3(b). The total gain shown represents the gain measured at the input to the left MZI-SOA, and therefore, includes the propagation loss of the signal through the passive waveguides and light splitters. The power measurements on chip for both Fig. 3(a) and (b) were

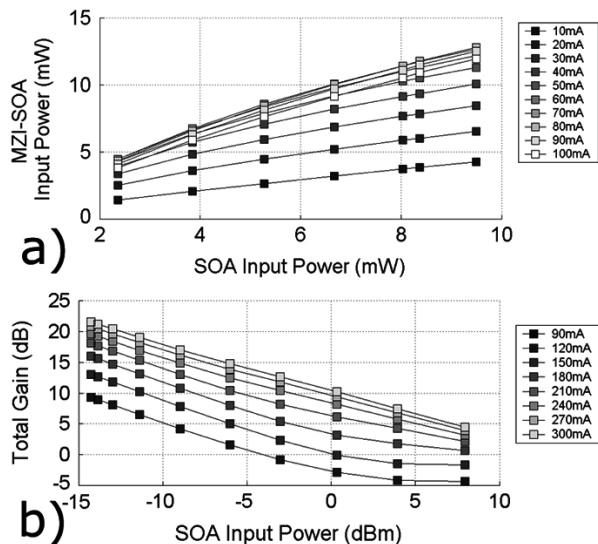


Fig. 3. (a) Power of the SGDBR-generated light that reaches the MZI-SOA as a function of the booster amplifier bias current. (b) Gain of the preamplifier SOA measured at the MZI-SOA.

performed by reverse biasing the SOAs and measuring the photocurrent.

Two $250\text{-}\mu\text{m}$ -long SOAs are used to amplify the continuous-wave (CW) light from the SGDBR laser. These amplifiers provide about 5 dB of gain resulting in more than 12 mW of optical power entering each MZI-SOAs. This high-power optical pumping sets the MZI-SOAs in the high-photon density operation regime, thereby reducing the gain recovery time to less than 60 ps and enabling 10-Gb/s operation. The gain recovery time was measured from the optical eye diagram. Measured SGDBR light power in the MZI-SOAs in function of the SGDBR output power is shown in Fig. 3(a).

For independent adjustment of the SOA gain in the MZI and the relative phase between the two branches, two phase control sections consisting of $100\text{-}\mu\text{m}$ -long passive waveguides were incorporated into this design. The effect used to achieve the index change is carrier plasma effect, which is observed when a diode is in forward bias and the carriers are flowing through the waveguide. This method of phase control is fairly wavelength insensitive, as shown in Fig. 2(b). We observe better than 25 dB of extinction over 30-nm range. The measurements show absolute power coupled and were taken without an output filter, therefore, we notice a degradation in the extinction observed for wavelengths more than 20 nm away from the gain peak due to reduced amplified spontaneous emission (ASE) suppression at those wavelengths. This separation of phase control provides for easier optimization of the operating bias point of the wavelength converter as well as better extinction for both inverting and noninverting modes of operation, in part because the gain of the MZI-SOA can be adjusted to compensate for high ASE light power of the input amplifier in the OFF state of the wavelength converter.

The branches of the MZI are joined by an MMI-based 2×2 coupler at the output. Depending on the relative phase of the CW light in the MZI branches, the total light power will be distributed between the two output waveguides with two extreme cases: For the phase difference of -90° , all of the light will be

coming out of one waveguide, whereas, for the phase difference of $+90^\circ$, all of the light will be coming out of the other waveguide. This output scheme is useful because it allows for the CW light to be continuously removed from the chip (this is different from our previous design [2]), which helps with light evacuation from the chip. Both of the output waveguides are curved and tapered before they reach the facet in order to minimize the back reflections [3].

The device was fabricated using an offset quantum-well integration platform and process, and the details about the process have been reported in [3]. For this work, we used a lower loss $1.4Q$ quaternary waveguide.

III. DEVICE PERFORMANCE

Device characterization was performed using two lensed fibers to couple light into and out of the device. Tuning results of the on-chip laser are shown in Fig. 2(a)—device tuning range is 35 nm with better than 35-dB side-mode suppression ratio.

The relative phase of the two branches is adjusted using the phase electrodes to cancel out the CW signals. As can be seen from Fig. 2(b), less than 4 mA is required to turn the interferometer off completely; therefore, the new method of phase control is very efficient.

For wavelength conversion, a transverse-electric polarized input signal at 1570 nm was generated using an electrooptic modulator with NRZ $2^{31} - 1$ pseudorandom bit sequence data at both 2.5 and 10 Gb/s. The converted output wavelength was filtered using a thin-film tunable filter and detected with a PIN-photodiode-based receiver. The MZI SOA biases were set to cancel out the preamplifier ASE influence. Measured bit-error-rate (BER) curves are shown in Fig. 4. The signal input power to the device was -10 dBm for 2.5-Gb/s operation and -5 dBm for 10-Gb/s operation. The bias currents were kept constant for all wavelength. The average output power of the wavelength converter was 0 dBm. At 2.5 Gb/s, the maximum power penalty measured was 0.8 dB which can be attributed mainly to the ASE noise generated by the on-chip SOAs. At 10 Gb/s, the power penalty was measured as low as 1.4 dB for output wavelengths between 1542–1555 nm. The penalty increased to around 3 dB, and the BER slope decreased for longer wavelengths (above 1570 nm), which can be attributed to different SNR redistribution due to optical transfer function change for wavelengths near the band edge. The dynamic extinction ratios were better than 10 dB for both bit rates.

IV. CONCLUSION

Design and performance of a new monolithically integrated widely tunable all-optical wavelength converter in InP were reported in this letter. This new design allowed for both simple optimization of the device operating point and superior performance relative to our previous work [2]. Error-free operation for data rates up to 10 Gb/s over 35-nm output tuning range of the device was demonstrated for the first time for a monolithically integrated tunable wavelength converter. The device input sensitivity for error-free operation was -10 dBm at 2.5 Gb/s and

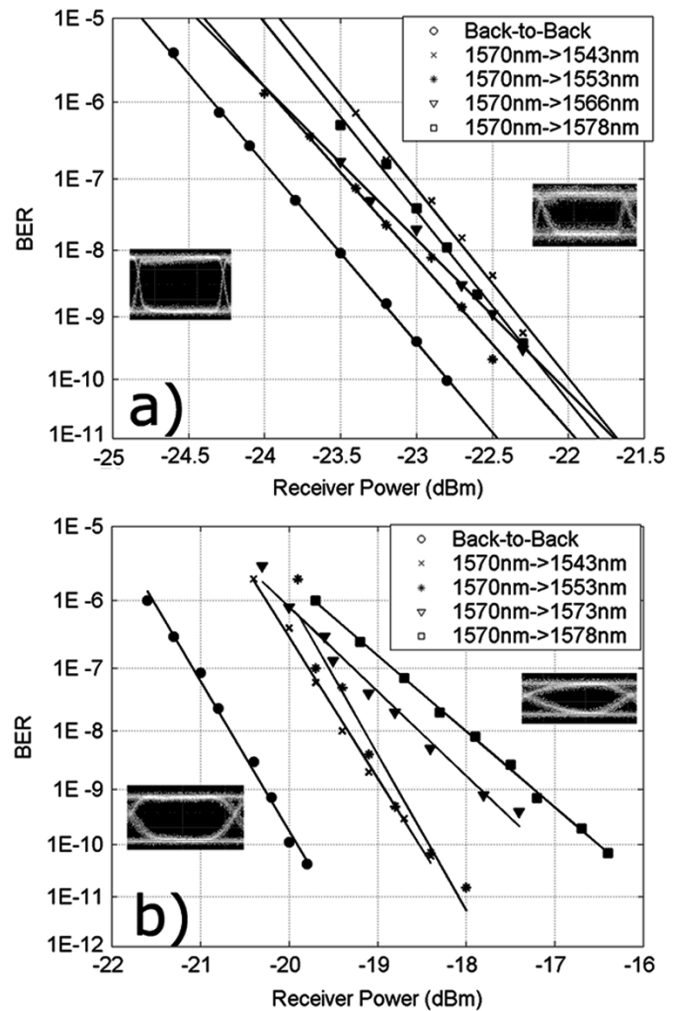


Fig. 4. (a) BER testing results for operation at 2.5 Gb/s. (b) BER testing results for operation at 10 Gb/s. The device bias currents were $I_{\text{gain}} = 93$ mA, $I_{\text{mzisoa-left}} = 300$ mA, $I_{\text{mzisoa-right}} = 265$ mA, $I_{\text{input}} = 200$ mA, $I_{\text{booster}} = 45$ mA.

-5 dBm at 10 Gb/s. The average converted signal output power of the device was 0 dBm.

ACKNOWLEDGMENT

The authors would like to thank Agility Communications for MOCVD growth and AR coating services, and Marcelo Davanço from UCSB for help with the FE-SEM.

REFERENCES

- [1] D. Wolfson, T. Fjelde, A. Kloch, C. Janz, F. Poingt, F. Pommereau, I. Guillemot, F. Gaborit, and M. Renaud, "Detailed experimental investigation of all-active dual-order mode Mach-Zehnder wavelength converter," *Electron. Lett.*, vol. 36, pp. 1296–1297, 2000.
- [2] M. L. Mašanović, V. Lal, J. A. Summers, E. J. Skogen, L. A. Coldren, and D. J. Blumenthal, "Monolithically integrated Mach-Zehnder interferometer wavelength converter and widely-tunable laser in InP," *IEEE Photon. Technol. Lett.*, vol. 15, no. 8, pp. 1117–1119, Aug. 2003.
- [3] M. L. Mašanović, V. Lal, J. A. Summers, E. J. Skogen, L. G. Rau, L. A. Coldren, and D. J. Blumenthal, "Widely-tunable monolithically-integrated all-optical wavelength converters in InP," *J. Lightwave Technol.*, submitted for publication.
- [4] V. Jayaraman, Z. Chuang, and L. Coldren, "Theory, design, and performance of extended tuning range semiconductor lasers with sampled gratings," *IEEE J. Quantum Electron.*, vol. 29, pp. 1824–1834, June 1993.

Saturation Analysis of a Monolithic Wavelength Converter

Joachim Piprek,ⁱ John Hutchinson,^a Jeffrey Hennes, Milan Masanovic, and Larry A. Coldren

Electrical and Computer Engineering Department,
University of California, Santa Barbara, CA 93106
^a Intel Corporation, Portland, OR

ABSTRACT

We investigate the nonlinear response of an InP-based optoelectronic wavelength converter by three-dimensional device simulation including an advanced many-body model for gain and absorption in the InGaAsP quantum wells. The wavelength converter combines a pre-amplified receiver with a post-amplified sampled-grating distributed Bragg reflector tunable laser diode. Good agreement between simulation and measurements is obtained. The nonlinear signal transmission is mainly attributed to quantum well saturation effects in amplifier and photo-detector. Saturation related microscopic physical processes are analyzed in detail.

Keywords: Optoelectronic integrated circuit, wavelength converter, semiconductor optical amplifier, waveguide photo-detector, nonlinear signal transmission, saturation effect, many-body model, three-dimensional numerical simulation

1. INTRODUCTION

Wavelength converters are a novel class of photonic integrated circuits that is crucial for future wavelength-division multiplexing (WDM) fiber-optic communication systems. Their main purpose is to transfer signals from one WDM wavelength to another. Here we report on the simulation and analysis of an optoelectronic InP-based tunable wavelength converter as shown in Fig. 1.

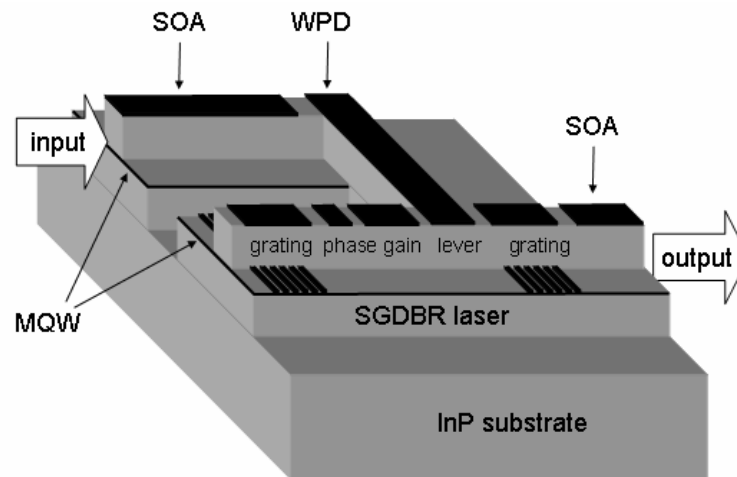


Fig. 1: Schematic view of the InP-based integrated wavelength converter.

ⁱ Corresponding author, e-mail: piprek@ieee.org

The receiver integrates signal pre-amplification by a semiconductor optical amplifier (SOA) and signal detection by a waveguide photodiode (WPD). The optical signal is converted into an electrical signal that directly modulates a sampled-grating distributed-Bragg-reflector (SGDBR) laser diode which is integrated with a semiconductor optical amplifier (SOA) for signal enhancement.¹ The SGDBR laser can be tuned to emit at any wavelength of the C band.²

Layer	Material	Thickness nm	Doping 10^{18} cm^{-3}
p-contact	InGaAs	100	30 (p)
upper cladding	InP	1600	1 (p)
upper cladding	InP	200	0.3 (p)
doping setback	InP	50	-
quantum barrier (8x)	$\text{In}_{0.685}\text{Ga}_{0.315}\text{As}_{0.595}\text{P}_{0.405}$	8	-
quantum well (7x)	$\text{In}_{0.685}\text{Ga}_{0.315}\text{As}_{0.864}\text{P}_{0.136}$	6.5	-
etch stop	InP	10	-
waveguide	$\text{In}_{0.612}\text{Ga}_{0.338}\text{As}_{0.728}\text{P}_{0.272}$	350	0.1 (n)
lower cladding	InP	1400	1 (n)
etch stop / n-contact	InGaAs	100	1 (n)
Buffer	InP	1000	-

Tab. 1 Epitaxial layer sequence of the devices simulated.

The structure of the different components is very similar as all are based on the same epitaxial growth (Tab. 1). An offset multi-quantum-well (MQW) active region is grown on top of the waveguide region. A ridge waveguide structure is etched through the MQW region. Passive device sections are formed by etching off the MQW completely.

2. THEORETICAL MODEL

The three-dimensional (3D) physics-based model takes into account interband gain and absorption in the InGaAsP active region, carrier transport including Fermi statistics and thermionic emission, and optical wave-guiding.³ However, previous investigations revealed that the free-carrier gain model does not give consistent agreement with experimental results.⁴ We therefore combine our 3D simulation with an advanced many-body gain theory⁵ which is calibrated to measured photoluminescence spectra of our MQW active region (Fig. 2). Details of the 3D model and of the many-body gain integration are published elsewhere.⁶ In the following, we apply this model to the investigation of saturation effects in amplifier and detector.

3. COMPARISON TO MEASUREMENTS

In order to calculate realistic many-body spectra, photoluminescence (PL) measurements on our quantum well structure are used to calibrate the inhomogeneous energy broadening in the model, which represents imperfections of the practical growth process. Fig. 2 shows measured and calculated PL spectra. The emission peak at 1532 nm indicates a slight growth deviation from the intended MQW composition. The PL peak wavelength can be matched in the simulation by adjustment of the MQW composition, maintaining the measured biaxial MQW strain: 0.6% compressive strain in the quantum wells and 0.3% tensile strain in the barriers. This way, we obtain $\text{In}_{0.685}\text{Ga}_{0.315}\text{As}_{0.864}\text{P}_{0.136}$ for the quantum well composition and $\text{In}_{0.685}\text{Ga}_{0.315}\text{As}_{0.595}\text{P}_{0.405}$ for the barrier composition. The adjustment may also reflect inaccuracies in the calculation of the strained quaternary energy band gap. A full-width half maximum (FWHM) value of 14 meV for the inhomogeneous energy broadening gives good agreement with the experimental PL spectra in Fig. 2, much better than with the free-carrier model.⁴

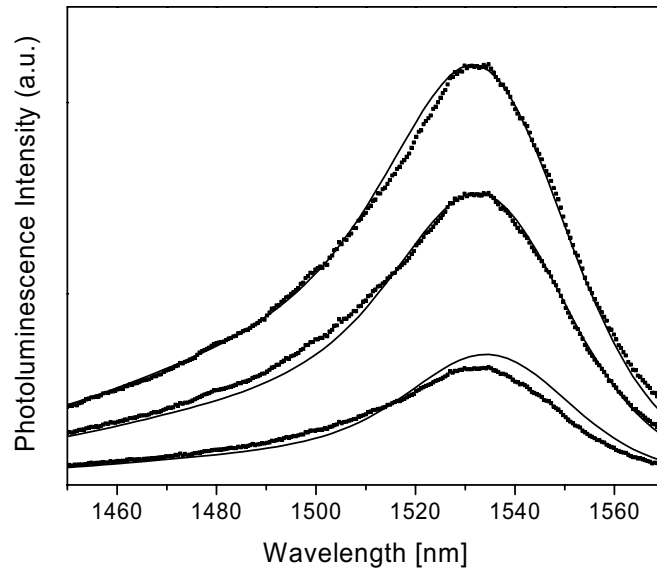


Fig. 2: Photoluminescence spectra of our MQW active region (dots – measured at 1×, 2×, and 3× pump intensity; solid lines - many-body calculations at carrier densities of 3.8 , 6.2 , and $7.7 \times 10^{17} \text{ cm}^{-3}$).

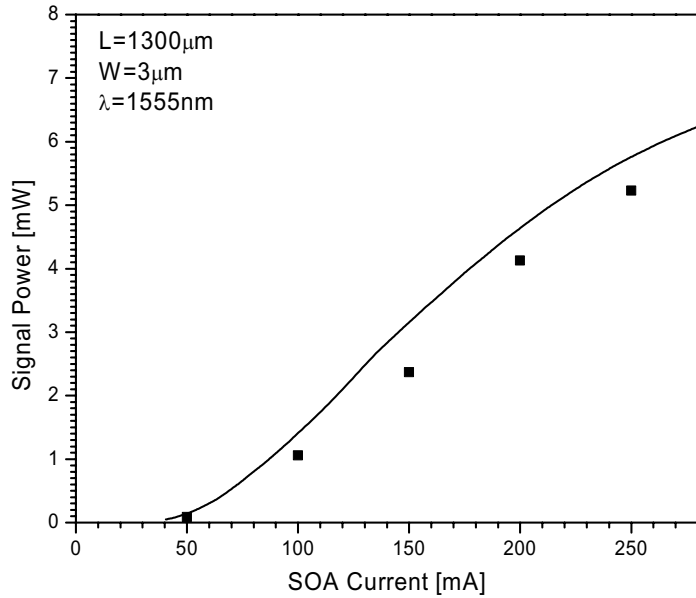


Fig. 3: Comparison of measured (dots) and simulated (lines) amplifier characteristics without ASE (L - amplifier length, W - ridge width, λ - signal wavelength).

Figure 3 shows a comparison between the measured and the simulated signal output power as function of SOA current. We use the same model and parameters as in Ref.⁶ without any parameter adjustment. The measurements are performed on individual SOAs with a length of $1300 \mu\text{m}$ which are not integrated into the wavelength converter. Amplified spontaneous emission (ASE) contributions are subtracted from the experimental output power using a

measurement without input signal. The ASE is expected to be lower when an input signal is present, so the dots in Fig. 3 somewhat underestimate the actual signal power.

4. AMPLIFIER SATURATION

Amplification enhances the optical signal and it compensates for any losses during wavelength conversion. Our semiconductor optical amplifier (SOA) should provide maximum signal gain while maintaining linearity between input and output signal. However, with increasing input power, amplifier saturation results in a sub-linear response which significantly limits the performance of our wavelength converter. In the following, we simulate and analyze the physical mechanisms that cause amplifier saturation. Figure 4 shows the calculated SOA transmission characteristics for three different amplifier currents. Optical coupling losses are neglected. Hardly any performance improvement is achieved by increasing the SOA current from 150 mA to 300 mA, due to the saturation of the material gain with rising quantum well carrier density.⁶ Thus, we consider the case with 150 mA current in the following. Transmission nonlinearity becomes obvious at a signal input power of about 1 mW.

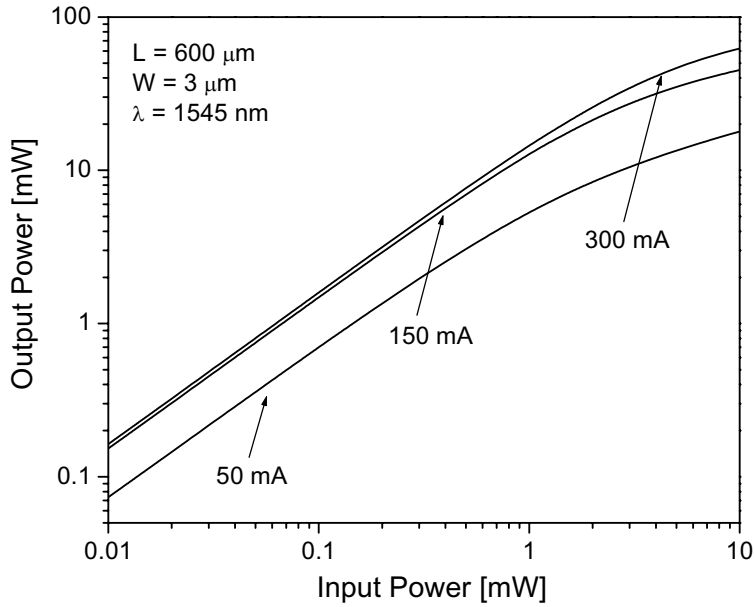


Fig. 4: SOA output power vs. input power with the SOA current as parameter.

Figure 5 plots longitudinal profiles of different physical quantities within the center of the SOA active region. With increasing travel distance of the signal, its optical intensity rises due to stimulated carrier recombination within the quantum wells. The recombination rate is proportional to the local optical intensity, reducing the quantum well carrier density towards the output facet. This leads to the reduction of the local material gain, which limits the amplification of the signal power and causes the sub-linear response in Fig. 4. The transmission characteristic is linear only as long as the internal material properties remain independent of the signal power. The reduction of the quantum well carrier density by enhanced stimulated recombination is the main reason for the nonlinearity of our SOA transmission characteristics.

Figure 6 shows lateral profiles of the same parameters at the output facet. The optical field is laterally confined by the 3 μm wide waveguide ridge. The high power of 12 mW at the output facet causes lateral hole burning by enhanced stimulated emission, i.e., the electron density as well as the gain profile exhibit a local minimum in the center of the device where the optical intensity is maximum.

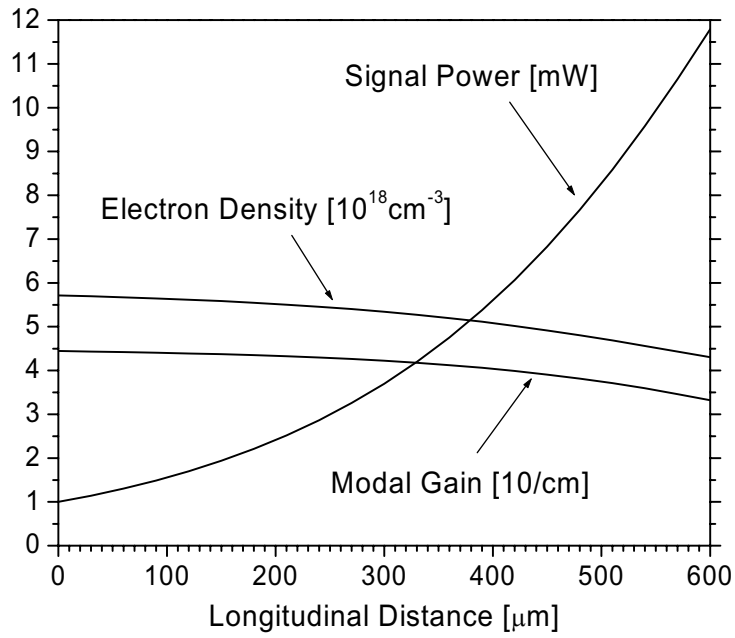


Fig. 5: Longitudinal profiles of internal amplifier parameters in the center quantum well.

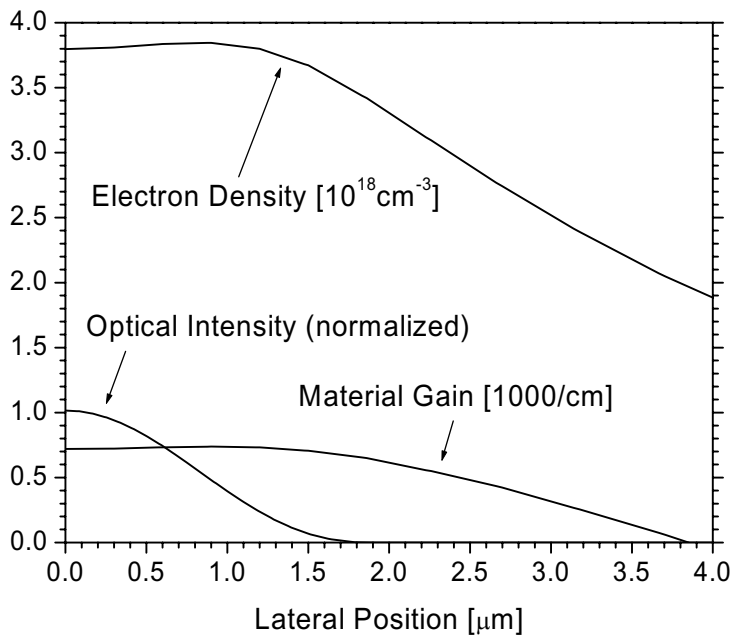


Fig. 6: Lateral profiles of internal amplifier parameters at the output facet.

5. DETECTOR SATURATION

The waveguide photodetector (WPD) is coupled monolithically to the pre-amplifier and we neglect any optical coupling loss. The WPD length is $L = 100 \mu\text{m}$ in our simulation and the ridge width is $W = 3 \mu\text{m}$. Figure 7 shows the calculated detector response function for two cases with different reverse bias. At lower reverse bias of 1V, the photocurrent is a sublinear function of the input power even for weak signals. At larger reverse bias, the detector response is more linear. We investigate the strongly nonlinear low-voltage case in the following.

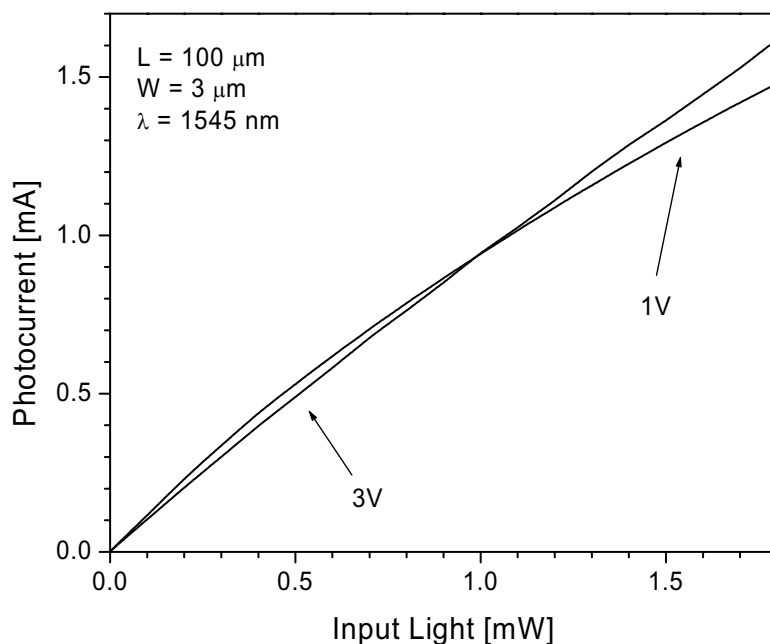


Fig. 7: WPD photocurrent vs. optical input power with the reverse bias as parameter.

Detector saturation effects are mainly related to the accumulation of photo-generated carriers within the quantum wells. Such accumulation depends on the local light power and therefore on the longitudinal position within the detector. Figure 8 shows longitudinal variations within the detector for 1 mW input power. The modal power decays exponentially with light penetration depth due to local photon absorption. The optical power is highest near the front facet causing photo-generated carriers to pile up there. The increased band filling leads to a blue-shift of the absorption edge and a reduction of the signal absorption at 1545 nm wavelength. Therefore, the light penetrates deeper into the WPD and about 5% of the light power remains undetected (light reflection at the rear facet is neglected). The amount of undetected light grows with higher input power, leading to a non-linear detector response in Fig. 7.

The vertical profiles of electron density and conduction band edge are plotted in Fig. 9. The carrier pile-up in the quantum wells causes a partial screening of the electrostatic field flattening the conduction band edge profile. As a consequence, the carriers are less quickly removed from the quantum wells and the saturation effect is worsened. A higher reverse bias enhances the carrier removal from the quantum wells leading to a more linear response in Fig. 7. However, the strong saturation calculated for our quantum well detector at relatively low input power may require the use of Franz-Keldysh-type detectors in our wavelength converter. Such photon absorption by the reverse biased waveguide layer shows less saturation effects due to the missing carrier confinement.¹

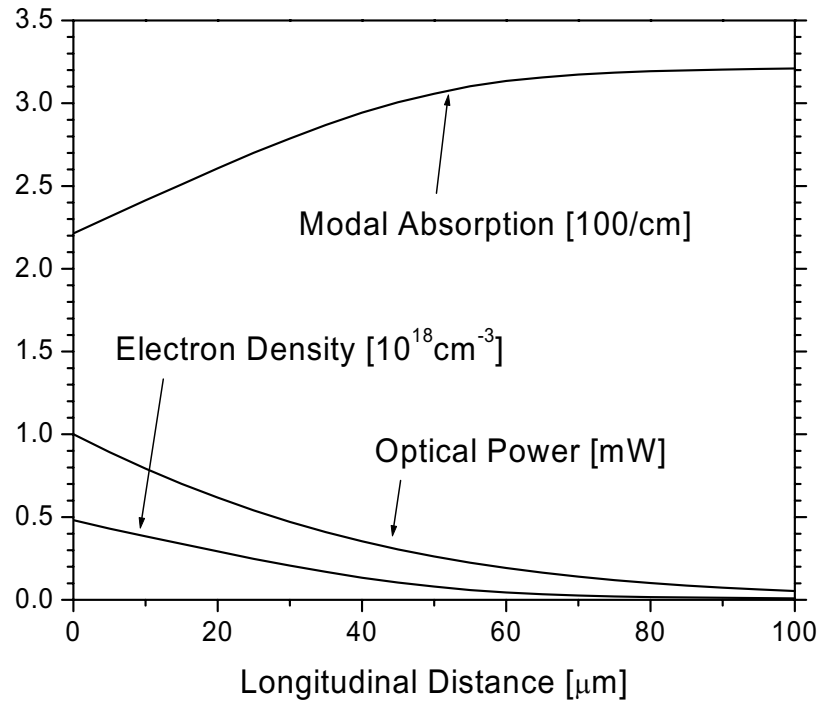


Fig. 8: Longitudinal variations of internal photodetector parameters.

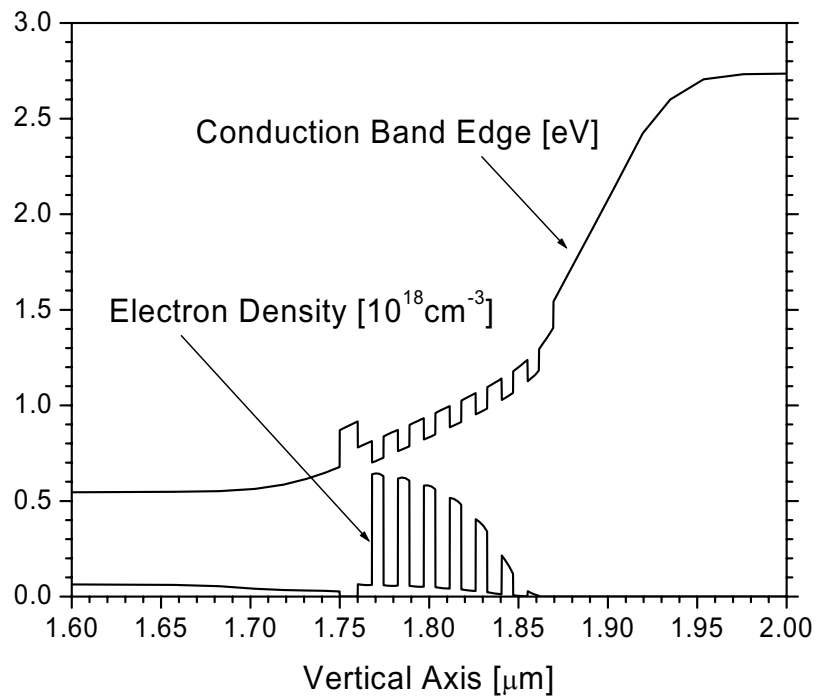


Fig. 9: Vertical variations of internal photodetector parameters.

6. SUMMARY

Advanced three-dimensional simulation of wavelength converter components including a realistic many-body model for gain and absorption is used to analyze quantum well saturation mechanisms that cause nonlinear signal transmission. Both amplifier and detector show a nonlinear response for input signal powers near 1 mW and above, which is mainly caused by quantum well carrier depletion and accumulation, respectively. The detector saturation is found to be most severe, due to the blue-shift of the absorption edge with increasing photo-generation of carriers.

ACKNOWLEDGMENT

This research project is sponsored by the Semiconductor Research Corporation (Award 2001-NJ-968) and by the Intel Corporation.

REFERENCES

-
- ¹ J. Hutchinson, J. Barton, M. Masanovic, M. Sysak, J. Henness, L. Johansson, D. Blumenthal, and L. A. Coldren, "Monolithically integrated InP-based tunable wavelength conversion." In: *Physics and Simulation of Optoelectronic Devices XII*, SPIE Proc. Vol. 5349, pp. 176-184, 2004.
 - ² V. Jayaraman, A. Mathur, L. A. Coldren, and P. D. Dapkus, "Theory, design, and performance of extended tuning range in sampled grating DBR lasers," *IEEE J. Quantum Electron.*, vol. 29, pp. 1824–1834, 1993.
 - ³ PICS3D by Crosslight Software, 2004.
 - ⁴ J. Piprek, N. Trenado, J. Hutchinson, J. Henness, and L. A. Coldren, "3D Simulation of an integrated wavelength converter." In: *Physics and Simulation of Optoelectronic Devices XII*, SPIE Proc. Vol. 5349, pp. 185-196, 2004.
 - ⁵ S.W. Koch, J. Hader, A. Tränhardt, and J.V. Moloney, "Gain and Absorption: Many-Body Effects," Chapter 1 in: *Optoelectronic Devices – Advanced Simulation and Analysis*, J. Piprek (ed.), Springer Verlag, New York, 2004.
 - ⁶ J. Piprek, S. Li, P. Mensz, and J. Hader, "Monolithic Wavelength Converter," Chapter 14 in: *Optoelectronic Devices – Advanced Simulation and Analysis*, J. Piprek (ed.), Springer Verlag, New York, 2004.

Photocurrent Driven Widely-Tunable Wavelength Converter based on a Directly Modulated Bipolar Cascade SGDBR Laser

Jonathan Klamkin*, Leif A. Johansson†, Jonathan T. Getty†, John M. Hutchinson‡, Erik J. Skogen†, Larry A. Coldren*†

*Materials Engineering, University of California, Santa Barbara, CA 93106

†Electrical and Computer Engineering, University of California, Santa Barbara, CA 93106

‡Intel Corporation

Phone: 805-893-8465, Fax: 805-893-4500, Email: klamkin@engineering.ucsb.edu

Abstract

A monolithically integrated tunable wavelength converter based on a bipolar cascade SGDBR laser is presented. Enhanced conversion efficiency is achieved and error free operation at 2.5Gb/s with a NRZ 2^{31} -1 PRBS is demonstrated.

I. Introduction

Tunable wavelength converters represent a novel class of integrated components for WDM systems [1]. A widely-tunable SGDBR laser transmitter has been monolithically integrated with an input semiconductor optical amplifier (SOA) and photodetector (PD) receiver in [2], however the performance of such devices is limited by the amount of photocurrent that could be generated on chip to directly modulate the laser. In order to improve on the overall performance of such a photocurrent driven wavelength converter, the differential efficiency of the SGDBR laser can be scaled by series connecting electrically isolated segments of the gain section as described in [3]. We report here the integration of such a bipolar cascade SGDBR laser with an input SOA-PD receiver for wavelength conversion.

II. Device Design

The design and operation of the tunable bipolar cascade SGDBR laser transmitters used in this work are described in [3,4]. The laser consists of a front SGDBR mirror (FM), bipolar cascade gain section, phase section (PH), rear SGDBR mirror (RM), and rear absorber (ABS) as shown in Figure 1. The integrated input optical receiver consists of a 750 μ m long SOA followed by a 200 μ m long PD. In all cases the ridge width is 3 μ m. A metal interconnect provides a means for transferring photocurrent from the PD to the gain section of the laser. Independent bias is provided to the laser through an off-chip bias-T to a metal pad shared by the laser and PD.

III. Testing Results

Experiments were performed on devices with 1, 3, and 8-stage bipolar cascade SGDBR laser transmitters. The optical-to-optical bandwidth was measured for a 3-stage device and the results are shown in Figure 2(a) demonstrating a 3dB bandwidth in excess of 5GHz. For wavelength conversion, a modulated input signal with NRZ 2^{31} -1 PRBS data at 2.5Gb/s was provided with a wavelength of 1548.1nm. Wavelength converted output eyes are shown in Figure 2. The 1-stage device has poor eye opening and poor extinction due to the combination of limited photocurrent and differential efficiency. With its enhanced differential efficiency, the 3-stage device exhibits good extinction and a clearly opened eye with a similar amount of photocurrent. The 8-stage device can operate at low input powers and maintain good extinction, however its performance is limited by the roll-off of the light-current characteristic due to heating. Increasing the number of segments beyond 3 should increase device performance, however in this particular process run the 3-stage device is superior due to a processing error resulting

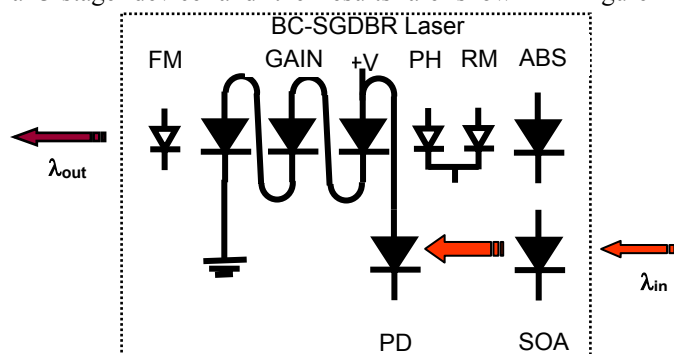


Figure 1. Schematic of tunable wavelength converter showing input optical receiver and bipolar cascade SGDBR laser transmitter.

Large diodes have as-grown quantum wells, small diodes have disordered quantum wells.

in poor current injection. BER measurements were performed over a wide tuning range, and the corresponding curves are shown in Figure 3(a). The measured power penalty was 2.7-3.2dB over the wavelength range. Extinction ratio and output fiber power were also measured for various input powers. Thus conversion efficiency, defined as the ratio of output signal power to input signal power, is calculated and shown in Figure 3(b).

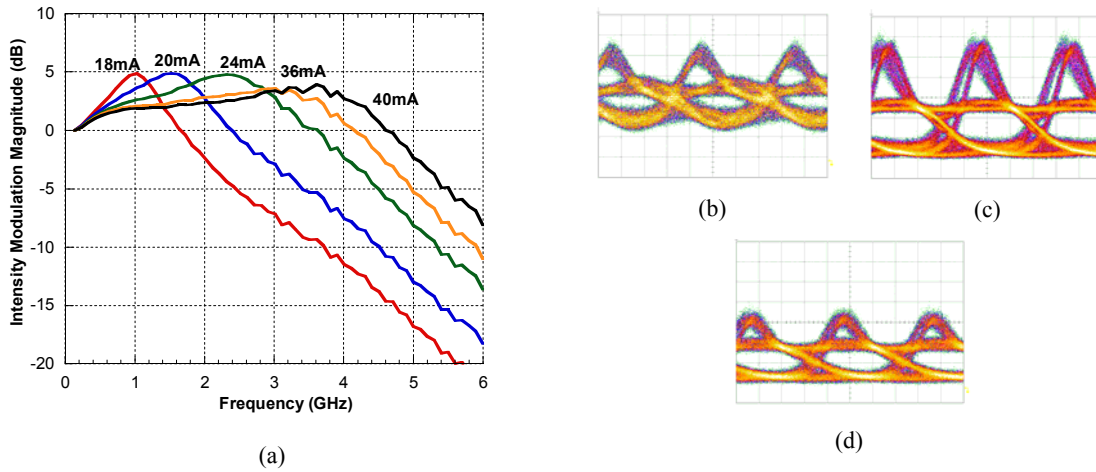


Figure 2. (a) Small signal modulation response for 3-stage SGDBR wavelength-converter at varying gain section bias currents operating at 1565.5nm. 2.5Gb/s output eye diagram for (b) 1-stage device with $I_{ph}^{avg}=8.2mA$, $ER=2.3dB$, $\lambda_{out}=1565nm$ (c) 3-stage device with $I_{ph}^{avg}=8.65mA$, $ER=7.9dB$, $\lambda_{out}=1566nm$ (d) 8-stage device with $I_{ph}^{avg}=5.5mA$, $ER=6.5dB$, $\lambda_{out}=1565nm$.

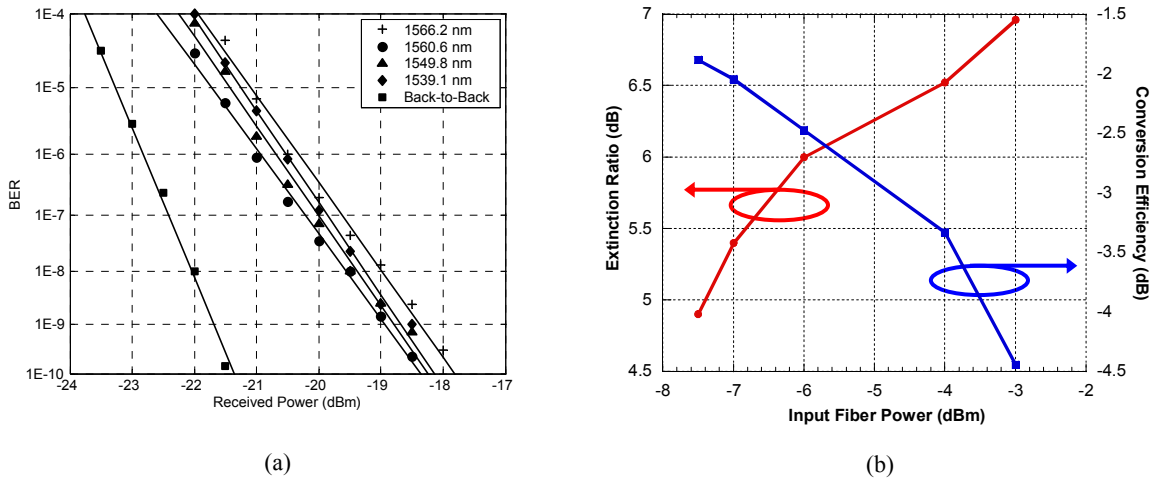


Figure 3. (a) BER at 2.5Gb/s for various output wavelengths for 3-stage device with $\lambda_{in}=1548.1nm$. (b) Extinction ratio and conversion efficiency as a function of input fiber power for 3-stage device.

IV. Conclusions

Bipolar cascade SGDBR based wavelength converters have been successfully fabricated and tested and demonstrate error free operation at 2.5Gb/s with between 2.7-3.2dB power penalty over a wide wavelength range. Vast improvements in conversion efficiency are achieved as a result of the enhanced differential efficiency of the lasers, which in turn allows for lower input powers and thus more linear amplification.

References

- [1] S.J.B. Yoo, "Wavelength Conversion Technologies for WDM Network Applications," *IEEE J. Lightwave Technology*, **14**, 955-966, (1996).
- [2] J.M. Hutchinson, J.A. Hennes, L.A. Johansson, J.S. Barton, M.L. Mašanović, L.A. Coldren, "2.5 Gb/sec Wavelength Conversion Using Monolithically-integrated photodetector and directly modulated widely-tunable SGDBR laser," *IEEE/LEOS annual meeting, 2003*.
- [3] J. Klamkin, J.T. Getty, J.M. Hutchinson, L.A. Johansson, E.J. Skogen, L.A. Coldren, "Widely-Tunable Single-Mode Bipolar Cascade SGDBR Lasers," *to be presented at ISLC 2004*.
- [4] J.T. Getty, E.J. Skogen, L.A. Johansson, L.A. Coldren, "CW Operation of 1.55 μm Bipolar Cascade Laser with Record Differential Efficiency, Low Threshold, and 50 Ω Matching," *IEEE Photon. Tech. Lett.*, **15**, 1513-1515, (2003)

I. Photonic Integrated Circuits and Related Technology

C. Quantum-Well Intermixing Technology

Low Dispersion Penalty at 10 Gb/s, Over 75 km, Using a Quantum-Well-Intermixed Electroabsorption-Modulator/Widely-Tunable Laser Transmitter

James W. Raring[†], Erik J. Skogen^{*}, Leif A. Johansson, Matthew N. Sysak, and Larry A. Coldren^{*†}

[†]Materials Dept. University of California, Santa Barbara, CA 93106

^{*}ECE Dept. University of California, Santa Barbara, CA 93106

Phone: 805.893.8465, Fax: 805.893.4500, Email: jraring@engineering.ucsb.edu

Abstract: 10Gb/s low power penalty (<0.5 dB) error-free transmission was achieved through 75km using a high-performance widely-tunable EAM/laser transmitter operating under negative chirp conditions. An integration-oriented quantum-well-intermixing process was employed for the realization of these devices.

©2004 Optical Society of America

OCIS codes: (140.5960) Semiconductor lasers; (140.3600) Lasers, tunable; (250.5300) Photonic Integrated Circuits

1. INTRODUCTION

For the first time, a widely-tunable transmitter demonstrating negative chirp performance at 10 Gb/s has been fabricated using a simple, robust quantum-well-intermixing (QWI) processing platform. The transmitter consists of a quantum-well electroabsorption modulator (QW-EAM) monolithically integrated with a widely-tunable sampled grating (SG) DBR laser. Less than 0.5 dB power penalty was measured for transmission at 10 Gb/s through 75 km of standard fiber. The QWI process allows for the circumvention of the traditional processing complexity necessary for the integration of negative chirp EAMs with diode lasers.

Electroabsorption-modulated lasers are candidate sources for optical metropolitan area network applications, as they are compact and potentially low-cost. The monolithic integration of EAMs with widely-tunable lasers allows for inventory reduction and wavelength agile functionality. A common method used to realize this integration employs an offset QW epitaxial architecture, in which the QW active region is grown on top of a bulk waveguide. For EAM definition, the QWs are selectively etched away and an upper cladding regrowth is performed [1]. This process produces Franz-Keldysh type modulators with a positive chirp factor, not suitable for 10 Gb/s transmission through standard fiber over distances required for metro networks. If QWs are used in the EAM, the quantum confined stark effect can be exploited, and negative chirp factors can be achieved. Power-penalty-free transmission through over 100 km of standard fiber using QW EAMs has been reported [2]. The traditional method for the realization of monolithically integrated QW-EAM/laser involves the selective removal of the as-grown waveguide/multiple QW (MQW) region followed by the regrowth of waveguide/MQW material with the desired band edge. This tedious method is commonly referred to as butt-joint regrowth [3]. Although the butt-joint regrowth process does allow each integrated component to possess a unique band edge, the difficulty associated with matching thickness and achieving the desired composition to avoid reflection and loss at the interface is great. Another technique used to realize multiple band edges across a wafer is selective area growth. However, as discussed in [4] the abruptness of the transition region is limited by the surface diffusion of the growth constituents, which may be on the order of tens of microns. Additionally, the optical mode overlap with the MQW may not be ideal in all sections due to the thickness variation. The relatively simple QWI process employed in this work enables for the precise placement of the band-edge of each component within the device, allowing for blue-shifted QWs to remain in the modulator while leaving the axial waveguide undisturbed.

2. EXPERIMENT

The device architecture (Fig. 1a dark outline) consists of two adjacent parallel buried ridges, which can function independent of one another with the lower ridge operating as an optical transmitter. The transmitter consists of a five section widely tunable sampled-grating (SG) distributed Bragg reflector (DBR) laser followed by an EAM. The 5 sections of the SG-DBR laser are, from left to right in Fig. 1a; backside absorber, rear mirror, phase, gain, and front mirror. The phase and mirror sections function to tune the wavelength of the laser [5]. The lithographically defined mirrors make the SG-DBR laser ideal for monolithic integration since no facets are required for operation.

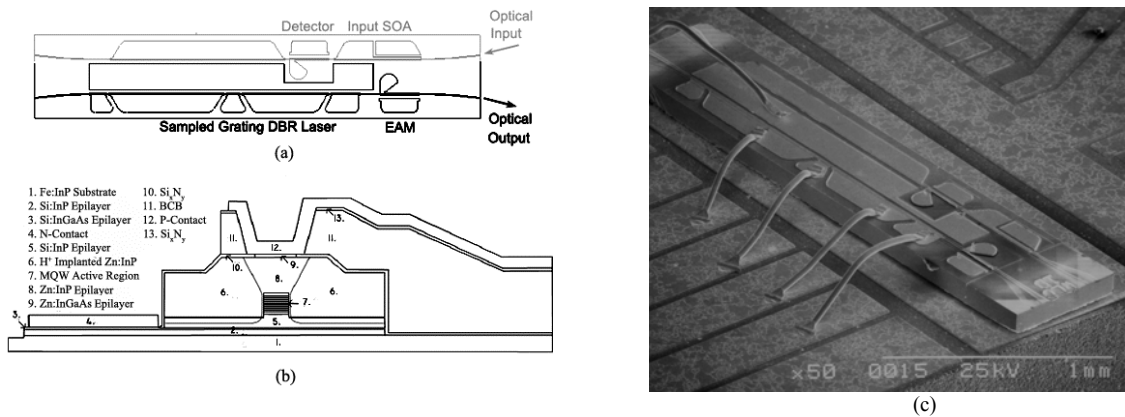


FIGURE 1. (a) Top view schematic of the device architecture, where the transmitter device used in this work is shown with a dark outline. (b) Cross- sectional schematic of modulator sections (c) Electron micrograph of completed transmitter device mounted on a carrier.

This work employs a modified ion-implantation enhanced QWI process described in [4], as the fabrication platform. In this process, vacancies are created by ion implantation into an InP buffer layer over the MQW active region. During a high temperature anneal, the vacancies are diffused through the MQW region, promoting the interdiffusion of group V-atoms between the wells and barriers. The interdiffusion reshapes the QW profile by distorting the QW/barrier interface. The result is a shift in the quantized energy levels in the well, and hence a shift in the band edge energy.

3. PROCESS

The epitaxial base structure and cross-sectional device architecture is illustrated in Fig. 1b and an electron micrograph of the completed device is shown in Fig. 1c. The MQW active region, consisting of 15 InGaAsP 8.0 nm compressively strained (0.6%) QWs and 8.0 nm tensile strained (0.3%) InGaAsP barriers, is centered within a 1.1Q waveguide. Using the intermixing process described in [4] and illustrated in Figure 2a, the EAM and passive section band-edges were blue-shifted such that the peak photoluminescence wavelengths were 1510 nm and 1450 nm, respectively. The photoluminescence results are shown in Fig. 2b.

4. RESULTS

The SG-DBR lasers demonstrated low threshold currents of 13mA, with output powers of 10mW at a gain section current of 100mA. At this operating point, a side mode suppression ratio (SMSR) greater than 35 dB was achieved. The EAM (175 um) demonstrated over 40 dB of DC extinction for wavelengths of 1558, 1570, and 1580

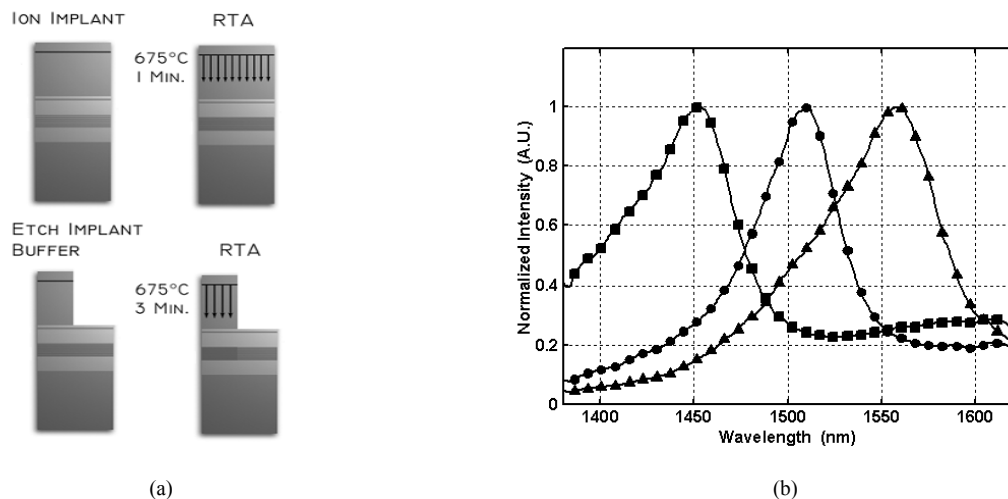


FIGURE 2. (a) Schematic of intermixing process. From left to right on top; ion implantation followed by rapid thermal annealing. From left to right on bottom; selective removal of vacancy point defects required for blue-shifting, followed by an additional anneal (b) Photoluminescence spectra of active section (triangles), modulator section (circles), and passive sections (squares).

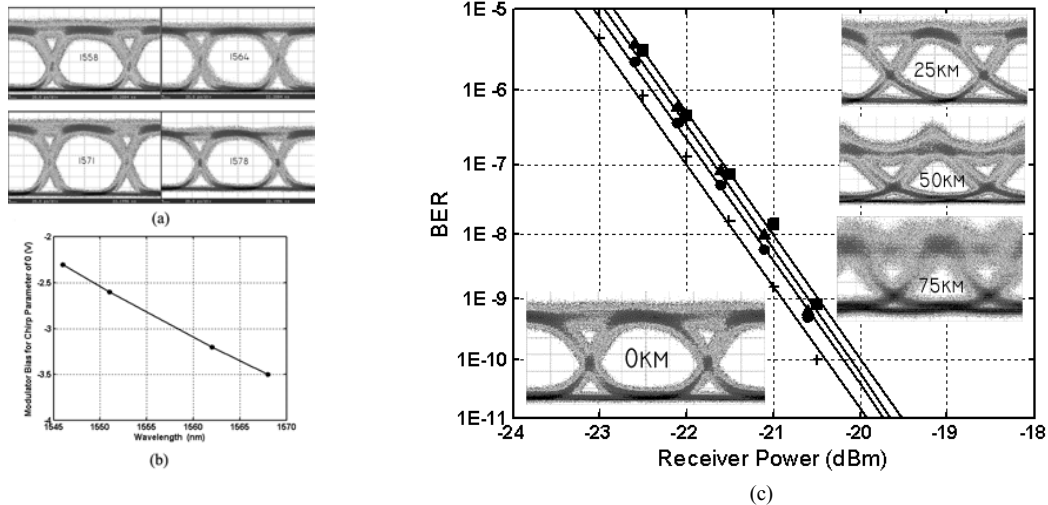


FIGURE 3. (a) Back-to-back eye diagrams from transmitter at wavelengths of 1558 nm, 1564 nm, 1571 nm, and 1578 nm. (b) Reverse bias zero chirp crossing point as a function of laser wavelength (c) BER curves and respective eye diagrams for back-to-back (cross), and transmission through 25 km (circles), 50 km (triangles), and 75 km (squares) of fiber at a wavelength of 1564 nm.

nm, with efficiencies greater than 20 dB/Volt. The 3dB bandwidth of the same modulator was greater than 19 GHz. 10 Gb/s eye diagrams were taken over the tuning range of the SG-DBR laser demonstrating RF extinction ratios greater than 10 dB using driving voltages between 2.4 V and 3.4 V. The small-signal chirp parameter was characterized using the fiber-response method described in [6]. Fig. 3b shows the wavelength dependency of the small signal zero-chirp parameter bias point, varying from -2.3V at 1546 nm to -3.5V at 1568 nm.

Transmission experiments at 10 Gb/s were performed using a non-return to zero (NRZ) pseudo-random-bit-sequence (PRBS) of $2^{31}-1$. A booster erbium doped fiber amplifier (EDFA) was used to launch optical powers on the order of 30 mW through Corning SMF-28 fiber. A variable optical attenuator was used to regulate the optical power into a non-preamplified receiver. Bit error rate (BER) curves through 25, 50, and 75 km of fiber at a wavelength of 1564 nm are shown in Fig. 3c. Error-free operation was achieved through 75km of fiber with a power penalty of less than 0.5 dB, while transmission through 100km of fiber resulted in a significantly larger power penalty. The low power penalty at 75 km confirms the negative effective chirp operation for large signal modulation, as indicated by small-signal chirp measurements. The shaping of the eye diagrams due to dispersion is clearly seen inset in Fig. 3c where the optical eye diagrams are shown after transmission through fiber. The noise performance for transmission through 75km is limited by the signal attenuation of the fiber and the noise of the oscilloscope optical receiver.

5. CONCLUSION

For the first time, a high performance widely-tunable EAM/laser transmitter operating under negative chirp conditions demonstrated error-free low-power-penalty operation through 75 km of standard fiber at 10 Gb/s. The transmitters demonstrated a 3dB bandwidth over 19 GHz and an RF extinction greater than 10 dB. This work was made possible by the use of a simple, robust QWI processing platform for the monolithic integration of blue-shifted QW-EAMs with SG-DBR lasers.

6. REFERENCES

- [1] Y Akulova, G. Fish, P Koh, C. Schow, P Kozodoy, A. Dahl, S. Nakagawa, M. Larson, M. Mack, T. Strand, C. Coldren, E. Hegblom, S. Penniman, T. Wipiejewski, L. Coldren, "Widely Tunable Electroabsorption-Modulated Sampled Grating DBR Laser Transmitter" *IEEE J. Sel. Topics in Quantum Electron.*, vol. 8, November/December, 2002
- [2] K. Morito, R. Sahara, K. Sato, and Y. Kotaki, "Penalty Free 10 Gb/s NRZ Transmission over 100 km of Standard Fiber at 1.55 μm with a Blue-Chirp Modulator Integrated DFB Laser", *IEEE Photon. Technol. Lett.*, vol. 8, pp.431-433, 1996.
- [3] J. Binsma, P. Thijs, T. VanDongen, E. Jansen, A. Staring, G. VanDenHoven, and L. Tiemeijer, "Characterization of Butt-Joint InGaAsP Waveguides and Their Application to 1310 nm DBR-Type MQW Ganin-Clamped Semiconductor Optical Amplifiers," *IEICE Trans. Electron.*, vol. E80-C, pp. 675-681, 1997.
- [4] E. Skogen, J. Raring, J. Barton, S. DenBaars, and L. Coldren, "Post-Growth Control of the Quantum-Well Band Edge for the Monolithic Integration of Widely-Tunable Lasers and Electroabsorption Modulators," *IEEE J. Sel. Topics Quantum Electron.* To be published 2004.
- [5] V. Jayaraman, Z. Chuang, and L. Coldren, "Theory, Design, and Performance of Extended Tuning Range Semiconductor Lasers with Sampled Gratings," *IEEE J. Quantum Electron.*, vol. 29, pp. 1824-1834, 1993.
- [6] B. Dvaux, Y. Sorel, and J.F. Kerdiles, "Simple Measurement of Fiber Dispersion and of Chirp Parameter of Intensity Modulated Light Emitter," *IEEE J Lightwave Technology*, vol. 11, no. 12, pp. 1937-1940, (1993).

Enhanced Frequency Response in Buried Ridge Quantum Well Intermixed SGDBR Laser Modulators

James W. Raring, Erik J. Skogen, Leif A. Johansson, and Larry A. Coldren

Materials Dept. University of California, Santa Barbara, CA 93106

Phone: 805.893.8465, Fax: 805.893.4500, Email: jraring@engineering.ucsb.edu

Abstract: We have studied the effects of various proton implant profiles on the performance of buried-ridge-stripe electro-absorption modulators monolithically integrated with SG-DBR lasers. Two implant profiles were performed adjacent to the buried ridge, enhancing the bandwidth.

© 2003 Optical Society of America

OCIS codes: (140.5960) Semiconductor lasers; (140.3600) Lasers, tunable; (250.5300) Photonic Integrated Circuits

1. Introduction

We present an investigation into the effects of proton implantation on the performance of monolithically integrated buried ridge stripe (BRS) sampled grating (SG) DBR lasers with electro-absorption modulators (EAM). Two different proton implant profiles were performed, demonstrating a reduction in parasitic capacitance associated with the BRS structure. The modulation bandwidth, DC extinction, and optical loss of the modulators were characterized. It is shown that by using a proton implant profile that is in close proximity to the buried ridge and penetrates the homojunction, a 2X improvement in modulation bandwidth and a decreased optical loss can be achieved.

2. Experiment

A complete description of the device fabrication process and epilayer structure can be found in [1]. A schematic of the device is shown in Figure 1. In order to create a non-absorbing waveguide and an efficient EAM, QWI has been applied to two different extents, yielding a total of three unique band-edges on chip [2].

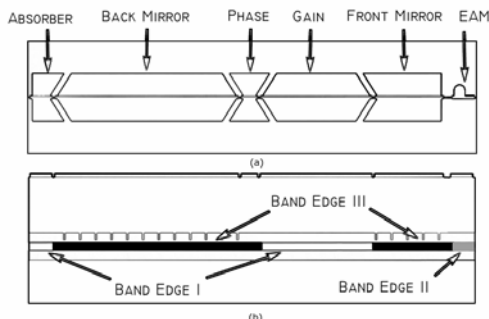


Figure 1: (a) Top view and (b) side view SG-DBR laser schematic illustrating the various sections and band-edges.

The fabrication process calls for two proton implants, the first is used for electrical isolation between laser sections and has a width of 10 μm over the buried ridge. The second, the BRS implant studied here, is a higher energy implant used to decrease leakage current in the laser and to lower parasitic capacitance in the EAM. In order to study the effects of proton implantation, two different BRS implant profiles were used. As a control, one sample was not BRS implanted. The second sample used a straight implant profile with a 4 μm wide implant mask over the EAM section, and a 10 μm wide implant mask was used over all other sections of the device. The third sample used a 28° angle implant with a 6 μm wide implant mask over the EAM section, and again used a 10 μm implant mask over all other sections. Figure 2 illustrates the implant profile for both samples with a BRS implant.

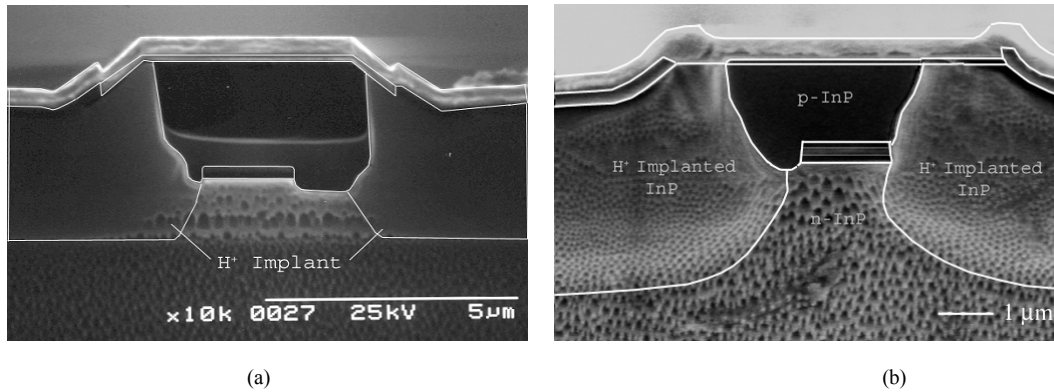


Figure 2: Electron micrograph of (a) 4 μm wide straight implant profile, (b) 6 μm wide angled implant profile.

3. Results and Conclusions

The injection efficiency of the SG-DBR laser was shown to increase as the proton implant approached the buried ridge. The injection efficiencies were extracted to be 76%, 82%, and 85% for the non BRS implanted, 4 μm wide straight implant, and 6 μm wide angled implant, respectively. This can be explained by the reduction in the InP total homojunction area reducing the leakage current. The optical loss in the regions containing the passive band-edge and 10 μm wide BRS implant was found to be between 2.3 and 3.5 cm^{-1} . A significant reduction in optical loss, from 6.0 cm^{-1} to 1.8 cm^{-1} , was observed in the sample with the 6 μm wide angled implant compared to the sample without the BRS implant in the regions with the EAM band-edge. This can be attributed to less free carrier absorption associated with p-type doping [3].

The modulator characteristics for all implant profiles are shown in Figure 3. The decreased extinction for the implanted samples is likely due to proton straggle causing lattice damage within the quantum wells. The 6 μm wide angle implanted EAM demonstrates 11.5 GHz 3dB bandwidth, a greater than 2X improvement over the non BRS implanted sample, while the 4 μm wide straight implant demonstrated a 3dB bandwidth of 8.5 GHz. Although the DC extinction was observed to suffer as the implant approached the ridge, with further optimization of the active region design and implant profile, proton implantation holds promise as a technique that could make the BRS more viable for use in high-speed devices.

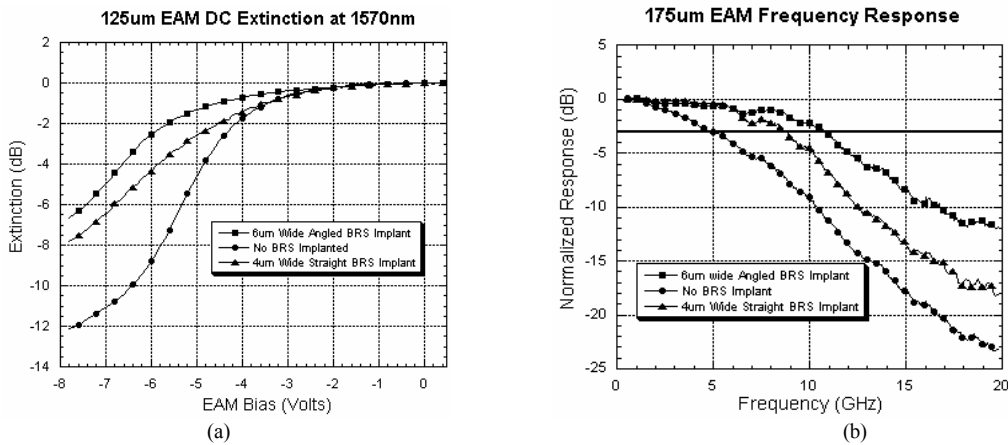


Figure 3: (a) DC Extinction for 125 μm EAMs of all implant profiles, (b) Frequency response for 175 μm EAMs of all implant profiles.

3. References

- [1] E. Skogen, J. Barton, S. DenBaars, and L. Coldren, "A Quantum-Well-Intermixing Process for Wavelength-Agile Photonic Integrated Circuits," *IEEE J. Sel. Topics in Quantum Electron.*, vol.8, pp. 863-869, 2002.
- [2] E. Skogen, J. Raring, J. Barton, S. DenBaars, and L. Coldren, "Post-Growth Control of the Quantum-Well Band Edge for the Monolithic Integration of Widely-Tunable Lasers and Electroabsorption Modulators," *IEEE J. Sel. Topics Quantum Electron.* To be published 2004.
- [3] E.V. Rao, Y. Gottsman, M. Allovon, E. Vergnol, D. Sigogne, A. Talneau, H. Sik, S. Slempekes, B. Theys, and J. Chevallier, "CA Significant Reduction in Propagation Losses in InGaAsP-InP Buried-Stripe Waveguides by Hydrogenation," *IEEE Photon. Technol. Lett.*, vol. 10, no. 3, pp. 370-372, (1998).

Quantum Well Intermixing for Monolithic Integration: A Demonstration of Novel Widely-Tunable 10Gb/s Transmitters and Wavelength Converters

James W. Raring[†], Erik J. Skogen^{*}, Leif A. Johansson, Matt Sysak^{*}, Jonathon S. Barton[†],
Milan L. Masanovic^{*}, and Larry A. Coldren^{**†}

^{*}Materials Dept. University of California, Santa Barbara, CA 93106

[†]ECE Dept. University of California, Santa Barbara, CA 93106

Phone: 805.893.8465, Fax: 805.893.4500, Email: jraring@engineering.ucsb.edu

Abstract: Wavelength-agile InGaAsP/InP photonic integrated circuits were fabricated using a quantum well intermixing processing platform. 10Gb/s operation was achieved with widely-tunable laser/modulator transmitters and optoelectronic wavelength converters in the 1550 nm range.

©2004 Optical Society of America

OCIS codes: (140.5960) Semiconductor lasers; (140.3600) Lasers, tunable; (250.5300) Photonic Integrated Circuits

1. INTRODUCTION

Optical networks employing wavelength division multiplexing (WDM) will benefit tremendously by exploiting photonic integrated circuits (PICs) with wavelength-agile capabilities. Widely-tunable transmitters are the key to achieving cost savings through inventory reduction and are an enabling technology for future applications such as dynamic provisioning [1,2]. The integration of an optical receiver with a widely-tunable transmitter can provide wavelength conversion functionality, making applications such as wavelength routing and reconfigurable optical add/drop multiplexes (ROADMs) possible [3].

The capacity to fabricate such wavelength-agile PICs requires a processing platform ideal for the monolithic integration of components with differing functionality. These components inherently require a specific band edge for optimum performance. Quantum well intermixing (QWI) has been shown to provide device specific band edge definition orthogonal to the growth direction [4], with high controllability and resolution. The work presented herein utilizes QWI to realize a high performance wavelength-agile transmitter and wavelength conversion at 10Gb/s.

2. EXPERIMENT

The lithographic mask contains two variations of the photonic integrated circuit architecture, which are shown in Fig. 1. Both architectures consist of two adjacent parallel buried ridges, which can function independent of one another, with one ridge operating as an optical receiver and the adjacent ridge operating as an optical transmitter. The receiving ridge consists of a semiconductor optical amplifier (SOA) and a photo-detector for the amplification and detection of the input optical signal, respectively. The adjacent transmitting ridge consists of a four section widely tunable sampled-grating (SG) distributed Bragg reflector (DBR) laser followed by an electro-absorption

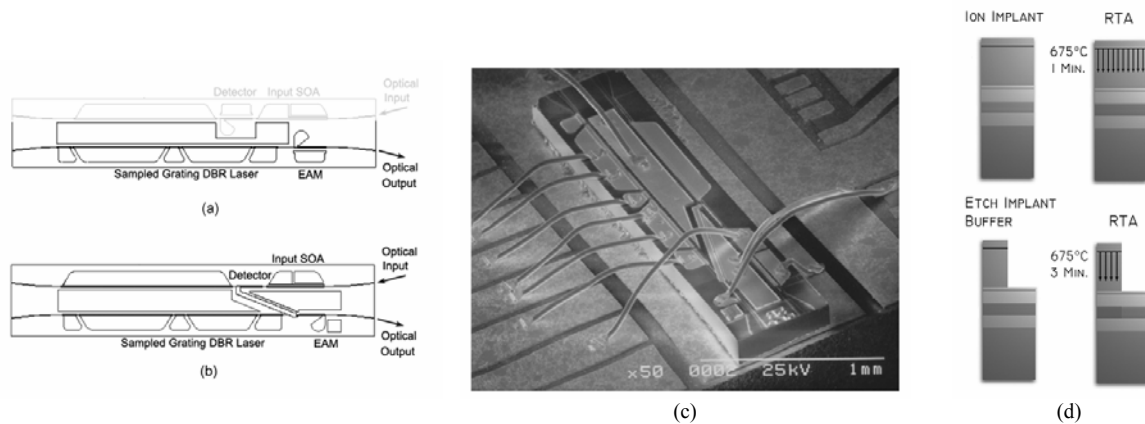


FIGURE 1. (a) Top view schematic of the device with discrete detector/modulator architecture, where the transmitter device used in this work is shown with dark outline. (b) Top view schematic of the interconnected device used in the wavelength converter work. (c) Electron micrograph of the completed wavelength converter device mounted on carrier (d) Illustration of the intermixing processing platform used in this work.

modulator (EAM). The 4 sections of the SG-DBR laser are: gain, back mirror, phase, and front mirror of which, the latter three function to tune the wavelength of the laser. The lone difference between the two architectures is the electrode scheme placed on the detector and EAM. In the first scheme, Fig 1a, the detector and EAM have discrete electrodes such that they can each be biased independently, allowing for the testing of the SG-DBR/EAM ridge solely as a transmitter. In the second architecture, termed the optoelectronic integrated circuit (OEIC) wavelength converter, the detector and EAM electrodes are joined by a CPS interconnect. In this configuration, the photocurrent generated in the detector by the input optical signal will pass through a termination load, resulting in the small signal voltage swing across the EAM identical to that of the input data sequence. The EAM functions to write the data on the continuous wave output of the SG-DBR laser operating at any wavelength within the tuning band hence wavelength conversion is achieved. A scanning electron micrograph of the second architecture is shown in Fig. 1c.

In this work, we employ a modified ion-implantation enhanced QWI process described in [1], as the fabrication platform for the realization of the described OEIC architectures. This method relies on the diffusion of point defects, specifically vacancies, created during an ion implantation. As the vacancies diffuse through the MQW active region during a high temperature anneal, group V atoms interdiffuse between the wells and barriers. This results in a more parabolic shaped well, increasing the quantized energy level separation between the conduction and valence bands, and hence blue shifting the band edge.

To achieve 10Gb/s operation, several measures were taken for the reduction of parasitic capacitance. The epilayer base structure was grown on a semi-insulating substrate, benzocyclobutene (BCB) was defined below the EAM electrodes to serve as a low-K dielectric, and an angled proton implant was performed adjacent to the buried ridge to eliminate the parasitic capacitance associated with the homojunction.

3. PROCESS

The epitaxial base structure contained an n-contact InGaAs layer 1 μm below a multi-quantum well (MQW) active region centered within a 1.1Q waveguide. The MQW consists of 15 InGaAsP 8.0 nm compressively strained (0.6%) quantum wells, separated by 8.0 nm tensile strained (0.3%) InGaAsP barriers grown on a Fe-doped InP substrate using a Thomas Swan horizontal-flow rotating-disc MOCVD reactor. Following the active region, a 15 nm InP stop etch, a 20 nm 1.3Q stop etch, and a 450 nm InP implant buffer layer was grown.

A 500 nm Si_xN_y mask layer was deposited using plasma enhanced chemical vapor deposition and lithographically patterned such that it remained only where the as-grown band-edge was desired. Ion implantation was performed using P^+ at an energy of 100 keV, yielding a range of 90 nm, with a dose of $5 \times 10^{14} \text{ cm}^{-2}$, at a substrate temperature of 200 $^\circ\text{C}$ [4]. The sample was subjected to rapid thermal processing at a temperature of 675 $^\circ\text{C}$, promoting the diffusion of vacancies through the MQW region. Once the desired band-edge for the EAM was achieved ($\lambda_{\text{pl}} = 1510 \text{ nm}$) the diffusion process was halted. The implant buffer layer above the EAM sections was removed using a wet etching process, stopping on the 1.3Q stop etch layer. The sample was then subjected to an additional rapid thermal anneal, further blue-shifting the regions where the implant buffer layer remained. This second anneal was used to obtain desired band edge ($\lambda_{\text{pl}} = 1450 \text{ nm}$) for the mirror, phase, and passive waveguide sections. A schematic illustrating the intermixing process and the photoluminescence of the active, EAM, and passive regions are shown in Fig. 1d and 2a, respectively.

The remainder of the process was carried out as described in [1] with the modifications for top-side n-contacts and the addition of BCB beneath the EAM contacts. The wafers were thinned, the devices were cleaved into bars

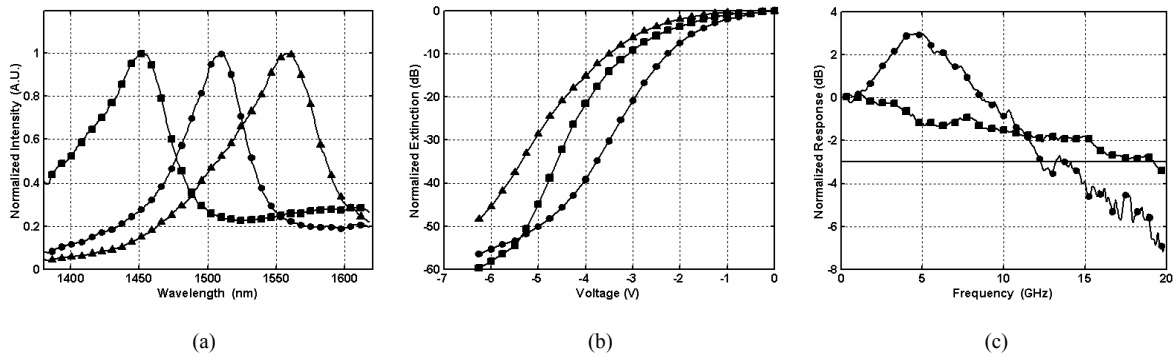


FIGURE 2. (a) Photoluminescence spectra of active section (triangles), modulator section (circles), and passive sections (squares). (b) DC extinction of a 175 μm modulator for wavelengths of 1558 nm (circles), 1570 nm (squares), and 1580 nm (triangles). (c) Electrical to optical frequency response of the transmitter device (squares) and optical to optical frequency response for wavelength converter device.

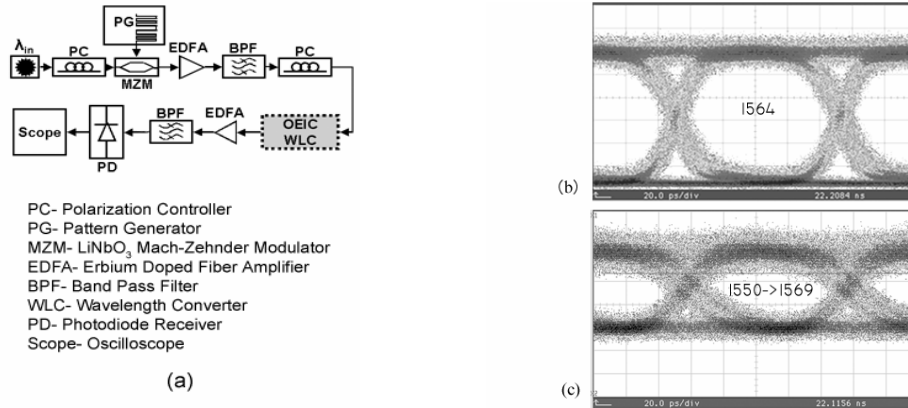


FIGURE 3. (a) Test set used to measure the eye diagrams for the wavelength converter device. (b) 10 Gb/s transmitter device representative eye diagram at 1564 nm (c) 10 Gb/s representative eye diagrams for wavelength conversion from 1550 nm to 1569 nm.

and anti-reflection coated. The die were separated, soldered to aluminum nitride carriers, and wire bonded (Fig. 1c) for characterization.

4. RESULTS

The SG-DBR lasers demonstrated low threshold currents of around 13mA, with output powers of 10mW at a gain section current of 100mA, with a side mode suppression ratio (SMSR) greater than 35 dB. The DC modal extinction characteristics of a 175 μm long EAM are presented in Fig. 2b. Over 40 dB of extinction was demonstrated for wavelengths of 1558, 1570, and 1580 nm, with efficiencies greater than 20dB/Volt. The 3dB bandwidth of the same modulator was greater than 19 GHz as shown in Fig. 2c. The optical to optical frequency response of a wavelength converter with a 225 μm photo-detector interconnected to a 175 μm modulator demonstrated a 3dB bandwidth of over 12 GHz, also shown in Fig. 2c. The resonance in the response at lower frequencies of this device is believed to be caused by inductance in the wire bond from the modulator to the RF pad on the carrier.

To demonstrate operation of both wavelength conversion and transmission at 10Gb/s, eye diagrams were taken for each type of device and bit error rate (BER) testing was performed through various fiber lengths for the SG-DBR/EAM transmitters. The test scheme used to obtain eye diagrams from the wavelength converter is shown Fig. 3a. The scheme used to obtain eye diagrams from the transmitter differs from the scheme in Fig. 3a such that electrically amplified data from the pattern generator was supplied to the device. Eye diagrams from the transmitter device and wavelength converter device, demonstrating conversion from 1550 nm to 1569 nm, are shown in Fig. 3b and 3c, respectively. Greater than 10 dB extinction was realized at wavelengths of 1558, 1564, and 1571 nm from the transmitter device, and error-free operation was achieved through 75km of fiber, with a power penalty of less than 0.5 dB. Error-free operation was achieved for conversion from 1550 to 1561, with a power penalty of 8dB. The high power penalty is a result of insufficient extinction (2 dB) due to the poor efficiency of the receiver.

5. CONCLUSION

A QWI processing platform has been employed for the fabrication of wavelength-agile photonic integrated circuits. Both discrete SG-DBR/EAM transmitters and OEIC wavelength converters have been confirmed at 10 Gb/s. The transmitters demonstrated a 3dB bandwidth over 19 GHz, an RF extinction greater than 10 dB, and error-free transmission through 75 km of non-dispersion shifted fiber with a minimal power penalty. The concept of OEIC wavelength conversion at 10 Gb/s has been realized. Significant improvements in the receiver design will yield increased RF extinction, reducing the power penalty of conversion.

6. REFERENCES

- [1] E. Skogen, J. Raring, J. Barton, S. DenBaars, and L. Coldren, "Post-Growth Control of the Quantum-Well Band Edge for the Monolithic Integration of Widely-Tunable Lasers and Electroabsorption Modulators," *IEEE J. Sel. Topics Quantum Electron.* To be published 2004.
- [2] J. Barton, M. Mašanovic, E. Skogen, and L. Coldren, "Widely-Tunable High-Speed Transmitters Using Integrated SGDBRs and Mach-Zehnder Modulators," Accepted for publication in *J. Sel. Topics in Quantum Electron.*, vol. 9, September/October, 2003.
- [3] M. Mašanovic, V. Lal, J. Barton, E. Skogen, L. Coldren, and D. Blumenthal, "Monolithically Integrated Mach-Zehnder Interferometer Wavelength Converter and Widely-tunable Laser in InP," *IEEE Photon. Technol. Lett.*, vol. 15, pp.1117-1119, 2003.
- [4] E. Skogen, J. Barton, S. DenBaars, and L. Coldren, "Tunable Sampled-Grating DBR Lasers Using Quantum-Well-Intermixing," *IEEE Photon. Technol. Lett.*, vol. 14, pp.1243-5, 2002.

Demonstration of Widely Tunable Single-Chip 10-Gb/s Laser–Modulators Using Multiple-Bandgap InGaAsP Quantum-Well Intermixing

James W. Raring, *Student Member, IEEE*, Erik J. Skogen, *Member, IEEE*, Leif A. Johansson, Matt N. Sysak, Jonathon S. Barton, *Student Member, IEEE*, Milan L. Mašanoviæ, *Student Member, IEEE*, and Larry A. Coldren, *Fellow, IEEE*

Abstract—High-speed wavelength-agile laser–modulators were fabricated for the first time using a quantum-well intermixing processing platform for monolithic integration. Over 19-GHz 3-dB modulator bandwidth was achieved and 10-Gb/s error-free transmission was demonstrated through 75 km of standard fiber.

Index Terms—Electroabsorption modulators (EAMs), ion implantation, laser tuning, quantum-well intermixing (QWI), semiconductor lasers, wavelength-division multiplexing.

I. INTRODUCTION

PHOTONIC integrated circuits (PICs) with wavelength-agile capabilities are key to next-generation optical networks employing wavelength-division multiplexing. Widely tunable transmitters will provide cost savings through inventory reduction and will facilitate the enabling technologies for future applications such as dynamic provisioning and wavelength routing.

The work presented here utilizes quantum-well intermixing (QWI) to provide device-specific band-edge definition orthogonal to the growth direction [1] for the realization of high performance wavelength-agile transmitters at 10 Gb/s. We demonstrate, for the first time, 10-Gb/s operation across the tuning band of a widely tunable laser using partially quantum-well-intermixed material in an integrated electroabsorption modulator (EAM). The viability of the devices for high-speed transmission applications was confirmed with the first demonstration of 10-Gb/s transmission using a widely tunable sampled-grating (SG) distributed Bragg reflector (DBR) laser/EAM transmitter. The device exhibited error-free/low-dispersion-penalty transmission through 75 km of standard fiber and a small signal chirp parameter capable of being tuned to negative values.

II. EXPERIMENT

The transmitter device consists of a five-section widely tunable SG-DBR laser followed by an EAM. The five sections of

Manuscript received February 4, 2004; revised March 30, 2004. This work was supported by Defense Advanced Research Projects Agency (DARPA)/MTO CS-WDM under Grant N66001-02-C-8026 and by Intel Corporation under Grant TXA001 630 000.

The authors are with the Materials Engineering Department, University of California, Santa Barbara, CA 93106 USA (e-mail: jraring@engineering.ucsb.edu).

Digital Object Identifier 10.1109/LPT.2004.828853

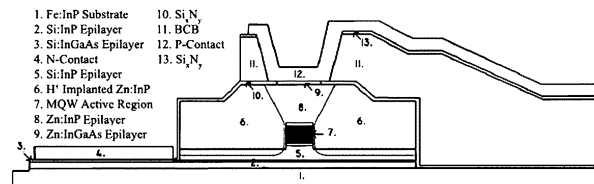


Fig. 1. Cross-sectional schematic of modulator sections, illustrating the placement of BCB and the angled implant profile used for capacitance reduction.

the SG-DBR laser are, from rear facet to front facet, backside absorber, rear mirror, phase, gain, and front mirror. The phase and mirror sections function to tune the wavelength of the laser [2]. The lithographically defined mirrors make the SG-DBR laser ideal for monolithic integration due to the fact that no facets are required for operation.

This work employs a modified ion-implantation enhanced QWI process described in [1], as the fabrication platform. In this process, an InP buffer layer, situated above the multiquantum-well (MQW) active region, functions to capture the vacancies created during an ion implantation. During a high-temperature anneal, the vacancies are diffused through the MQW region, promoting the interdiffusion of group V-atoms between the wells and barriers. The interdiffusion reshapes the quantum-well profile by distorting the quantum-well–barrier interface. The result is a shift in the quantized energy levels in the well, and hence, a shift in the band edge energy [3].

Several design and processing measures were taken to reduce parasitic capacitance in the EAM regions to achieve 10-Gb/s operation. The epilayer base structure was grown on a semi-insulating substrate. A 3- μm -thick layer of benzocyclobutene (BCB) was defined below the EAM bond pads to serve as a low-K dielectric. An angled proton implantation was performed adjacent to the buried ridge to eliminate the parasitic capacitance associated with the homojunction. The implant was designed such that proton concentration was maintained at a level greater than $2 \times 10^{19} \text{ cm}^{-2}$ to a depth beyond the InP homojunction on either side of the buried ridge. Fig. 1 is a schematic cross-sectional view of the EAM, illustrating these described features.

III. FABRICATION

The metal–organic chemical vapor deposition (MOCVD)-grown epitaxial base structure contained an n-contact InGaAs layer 1 μm below an MQW active region centered within a



Fig. 2. Electron micrograph of transmitter device.

1.1Q waveguide. The MQW consists of 15 InGaAsP 8.0-nm compressively strained (0.6%) quantum wells, separated by 8.0-nm tensile-strained (0.3%) InGaAsP barriers grown on a Fe-doped InP substrate. Following the active region, a 15-nm InP stop etch, a 20-nm 1.3Q stop etch, and a 450-nm InP implant buffer layer was grown.

The process was as follows: The gain sections and the absorber sections were masked with 500 nm of Si_xN_y and the sample was subjected to a P^+ implant at 100 keV and a dose of $5 \times 10^{14} \text{ cm}^{-2}$, yielding a range of 900 Å into the implant buffer layer. The sample was subjected to rapid thermal processing at a temperature of 675 °C, promoting the diffusion of vacancies through the MQW region. Once the desired band-edge for the EAM was achieved ($\lambda_{pl} = 1510 \text{ nm}$) the diffusion process was halted. The implant buffer layer above the EAM sections was removed using a wet etch process, stopping on the 1.3Q stop etch layer. The sample was then subjected to an additional rapid thermal anneal, further blue-shifting the regions where the implant buffer layer remained. This second anneal was used to obtain desired band edge ($\lambda_{pl} = 1450 \text{ nm}$) for the mirror, phase, and passive waveguide sections.

The remainder of the process was carried out as described in [1] with the modifications for top-side n-contacts and the addition of BCB beneath the EAM contacts. The wafers were thinned and the devices were cleaved into bars and antireflection coated. The die were separated, soldered to aluminum nitride carriers, and wire bonded (Fig. 2) for characterization.

IV. RESULTS

The SG-DBR lasers demonstrated low threshold currents of 13 mA, with an output power of 10 mW at a gain section current of 100 mA. At this operating point, a sidemode suppression ratio (SMSR) greater than 35 dB was achieved. The devices demonstrated over 25 nm of wavelength tunability. For the testing discussed in this letter, the rear mirror was held at a bias of 0 mA while the front mirror was biased at levels between 0 and 15 mA to tune across super modes within the tuning range. The low threshold current can be attributed to the high modal gain offered by the centered quantum-well design. This design results in optimum modal overlap with the quantum wells, increasing the confinement factor by 50% over the offset quantum-well architecture found in traditional SG-DBR laser designs [4]. The dc modal extinction characteristics of a 175- μm -long EAM are presented in Fig. 3. Over 40 dB of extinction was demonstrated for wavelengths of 1558, 1570, and 1580 nm, with efficiencies greater than 20 dB/V. The efficient extinction properties are due

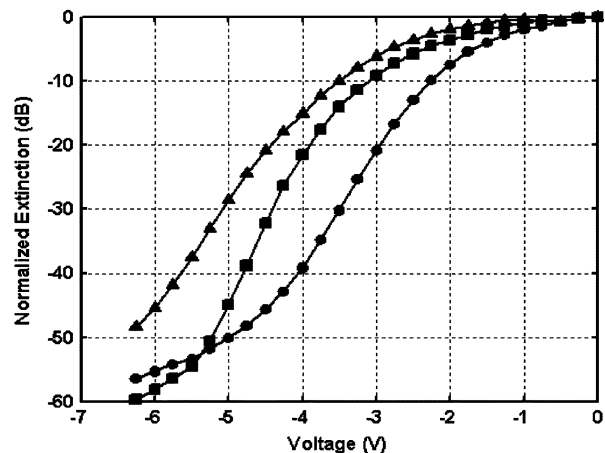


Fig. 3. DC extinction of a 175- μm modulator for wavelengths of 1558 (circles), 1570 (squares), and 1580 nm (triangles).

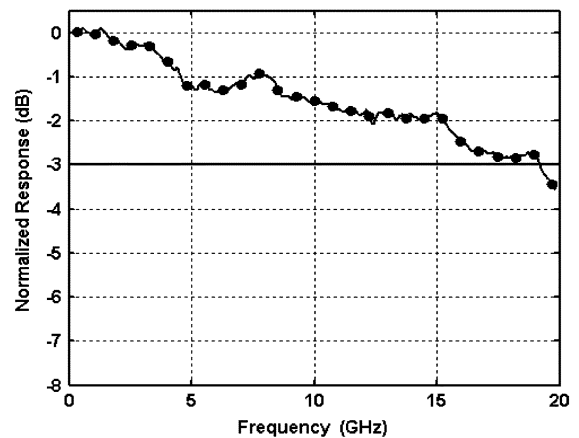


Fig. 4. Electrical to optical frequency response of a 175- μm modulator. The circular markers represent every 30th data point.

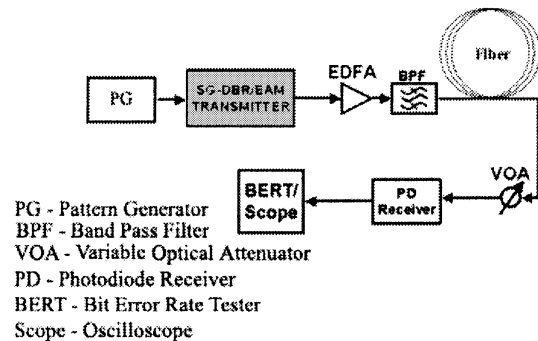


Fig. 5. Test set used to obtain BER and eye-diagrams from transmitter.

to the combination of the centered quantum-well design and the intermixing process that allows for precise placement of the modulator band edge. The 3-dB bandwidth of the same modulator was greater than 19 GHz, as shown in Fig. 4.

To demonstrate operation and transmission at 10 Gb/s, eye diagrams were taken and bit-error-rate (BER) testing was performed through various fiber lengths for the SG-DBR/EAM transmitters. BER testing was performed using a pseudorandom bit sequence of $2^{31} - 1$. A schematic of the test setup is shown in Fig. 5. Eye diagrams, shown in Fig. 6, were taken at wavelengths of 1558, 1564, 1571, and 1578 nm with dc biases ranging from

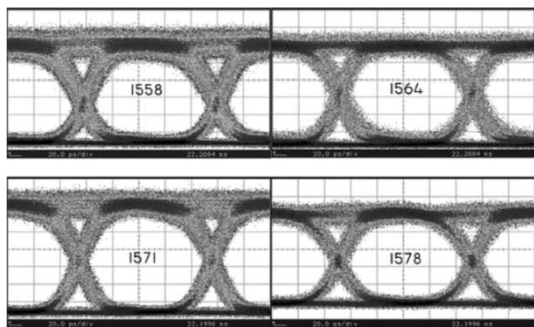


Fig. 6. Back-to-back eye diagrams from transmitter at wavelengths of 1558, 1564, 1571, and 1578 nm.

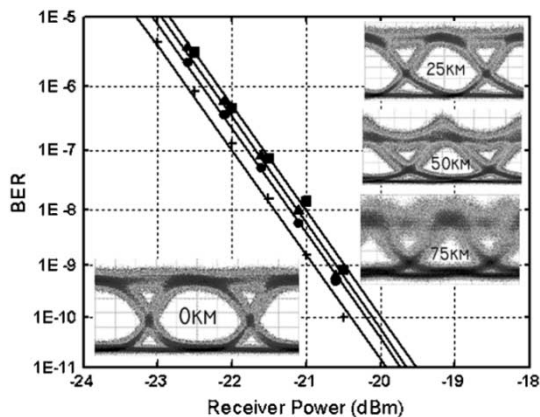


Fig. 7. BER curves and respective eye diagrams for back-to-back (cross), and transmission through 25 (circles), 50 (triangles), and 75 km (squares) of fiber at a wavelength of 1564 nm.

−2.1 to −3.8 V and peak-to-peak voltage swings ranging from 2.2 to 3.4 V. Greater than 10-dB extinction was achieved at all wavelengths. We believe that the less efficient dynamic extinction behavior compared to the dc behavior is due to the use of an erbium-doped fiber amplifier (EDFA) and the application of a lower gain section bias (50 mA) during dynamic testing. The amplified spontaneous emission from the EDFA significantly raises the noise floor, decreasing the amount of total extinction read by the digital communications analyzer. The higher gain section bias (100 mA) used during dc testing will result in a greater amount of optical power entering the EAM, creating more heat, inducing more bandgap shrinkage, and hence increasing the absorption efficiency. Fig. 7 presents BER results and eye-diagrams for back-to-back and through 25, 50, and 75 km of Corning SMF-28 fiber at a wavelength of 1564 nm and a dc bias of −3.4 V. Error-free operation was achieved through 75 km of fiber, with a dispersion power penalty of less than 0.5 dB. The variation in the signal-to-noise ratio in the eyes of Fig. 7 is due to receiver noise, which becomes more pronounced as the received optical power decreases with longer fiber spans.

The low dispersion penalties of Fig. 7 are indicative of a slightly negative large signal chirp parameter. Using the fiber response frequency domain method described in [5], the small signal chirp parameter of the device was extracted for various EAM bias points at 1564 nm, as shown in the inset of Fig. 8. The transition from a positive to a negative chirp parameter occurred at −3.5 V. To demonstrate the capability for efficient 10-Gb/s

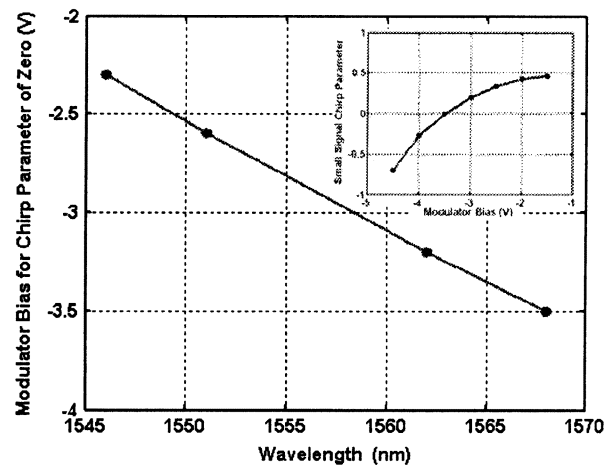


Fig. 8. Required EAM bias to achieve small signal chirp parameter of zero versus operating wavelength. The inset depicts the small signal chirp parameter characteristics versus reverse bias at 1563 nm for a separate device.

transmission across the wide tuning range of the devices, small signal chirp parameters were extracted at wavelengths of 1546, 1552, 1563, and 1568 nm on a separate device. At all wavelengths tested, the chirp parameter was shown to go negative, requiring a larger reverse bias with increasing wavelength. The required EAM bias points to achieve a chirp parameter of zero at these wavelengths are shown in Fig. 8. This behavior is expected since a larger reverse bias is required at longer wavelengths to position the EAM band edge at the correct proximity to the operating wavelength.

V. CONCLUSION

A QWI processing platform coupled with several measures for capacitance reduction were utilized for the realization of high-performance widely tunable transmitters. The 175- μm EAMs possessed a dc absorption efficiency of over 20 dB/V, radio-frequency extinctions greater than 10 dB, and over 19-GHz 3-dB bandwidth. Error-free transmission through 75 km of fiber was demonstrated with a monolithically integrated laser-modulator operating at 10 Gb/s. The power penalty of transmission was less than 0.5 dB, indicative of a negative large signal chirp parameter. The small signal chirp parameter was extracted and was shown to go negative across the tuning range of the device.

REFERENCES

- [1] E. Skogen, J. Raring, J. Barton, S. DenBaars, and L. Coldren, "Post-growth control of the quantum-well band edge for the monolithic integration of widely-tunable lasers and electroabsorption modulators," *J. Select. Topics Quantum Electron.*, vol. 9, pp. 1183–1190, Sept./Oct. 2003.
- [2] V. Jayaraman, Z. Chuang, and L. Coldren, "Theory, design, and performance of extended tuning range semiconductor lasers with sampled gratings," *IEEE J. Quantum Electron.*, vol. 29, pp. 1824–1834, June 1993.
- [3] E. Skogen, J. Barton, S. DenBaars, and L. Coldren, "Tunable sampled-grating DBR lasers using quantum-well-intermixing," *IEEE Photon. Technol. Lett.*, vol. 14, pp. 1243–1245, Sept. 2002.
- [4] B. Mason, J. Barton, G. Fish, and L. Coldren, "Design of sampled grating DBR lasers with integrated semiconductor optical amplifiers," *IEEE Photon. Technol. Lett.*, vol. 12, pp. 762–764, July 2000.
- [5] B. Dvaux, Y. Sorel, and J. F. Kerdiles, "Simple measurement of fiber dispersion and of chirp parameter of intensity modulated light emitter," *J. Lightwave Technol.*, vol. 11, pp. 1937–1940, Dec. 1993.

Improved Ridge Lasers Utilizing Laterally-Intermixed Active Regions

Jonathan T. Getty, Erik J. Skogen, Larry A. Coldren

Electrical & Computer Engineering, Univ. of California, Santa Barbara, CA 93106

Phone: 805-893-7163, Fax 805-893-4500, Email: beans@mrows.org

Abstract: The submicron abruptness of an intermixing transition is used to create current and carrier confinement in a ridge laser. Compared to a control laser, a 27% threshold reduction and 10% efficiency enhancement are demonstrated.

Introduction:

Buried heterostructures (BH) are employed in high-performance in-plane lasers because they concentrate both light and carriers in the same narrow waveguide. Ridge lasers confine light and carriers unevenly, and generally must use wider waveguides (to avoid sidewall scattering). Despite these problems, ridge lasers are still widely employed because they are much easier to grow and fabricate. Lateral current and carrier confinement (LCC) seek to squeeze the current under a ridge or pillar, reducing the active volume (and threshold current), and better align the gain with the mode (improving both threshold current and differential efficiency).[1] In InP-based ridge lasers, such LCC schemes must refrain from overcomplicating the process, such that a BH would be easier.

Concept:

This work demonstrates the first use of quantum well intermixing (QWI) to create surprisingly abrupt energy barriers under an InP ridge (Fig. 1), resulting in strong lateral carrier and current confinement. Implant-induced QWI [2] uses the defects caused by a shallow implant (100keV) to diffuse down through the QW's and enhance intermixing, as in Fig. 2. By implanting a thinner InP layer and annealing at a cooler temperature[3], lateral defect diffusion should be greatly reduced (from 4-6 μ m when a 2 μ m cap is implanted in [2]), and the intermixed-unintermixed junction should be sharper.

Experiment:

After the anneal, the implanted layer is removed, and a full cap is regrown on the planar surface above the waveguide, though gratings could be etched at this point. A 4 μ m ridge waveguide is centered over unimplanted stripes of widths ranging from 4-40 μ m, contacts are deposited through SiN vias, and Fabry-Perot bars are cleaved. At this point, the width of the un-intermixed material under the ridge is unknown, but certainly a fixed amount less than the unimplanted width. By measuring the parameters of lasers of different unimplanted width, we can observe the extent of LCC, and by fitting a simple abrupt-junction model, measure defect diffusion more accurately than has been done before.

Results:

After a four-minute anneal at 675 $^{\circ}$ C, the implanted material blueshifted 76nm more than unimplanted regions, as shown in Fig. 2. This results in a 40.6meV bandgap difference between the two region, and an approximately 1kT lateral energy barrier to holes in the valence band. The lower photon voltage in the active region should cause 2.4 times more current to flow under the center of the ridge than at its edges. Carrier confinement is more difficult to confirm, but must be sufficient to preserve the benefits of current confinement. Modeling both effects allows us to predict the threshold current and differential efficiency scaling as the intermixing moves laterally under the ridge.

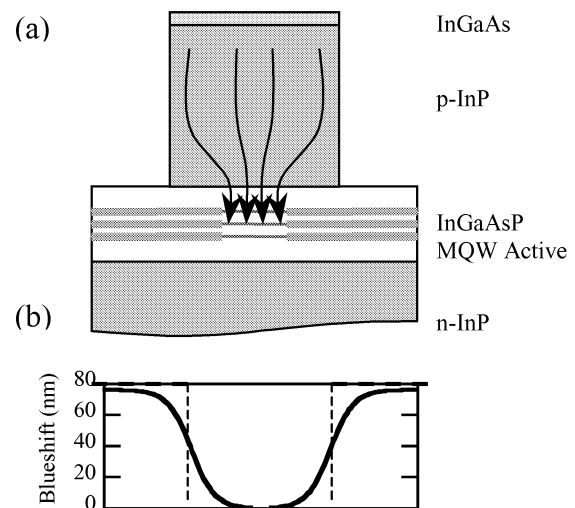


Fig. 1(a) By intermixing on either side of the center of the ridge, current is funneled under the center of the ridge, and the lateral energy barrier provides carrier confinement. (b) shows the simulated bandgap across the ridge, and the abrupt-junction model used in this work.

Differential efficiency and threshold current were measured for lasers on each bar and plotted against unimplanted (mask) width, as shown in Fig. 3. All bars scaled similarly, regardless of laser length. Successful lateral current confinement is clearly shown by the reduction in threshold and increase in efficiency over wide-mask control lasers (for all mask widths >12 μm , intermixing shows no effect on threshold or efficiency). Differential efficiency is improved by as much as 10% before falling off at unintermixed widths less than 2 μm . Threshold reductions of up to 27% are observed while maintaining the efficiency observed in control lasers; further reductions are possible at the expense of efficiency (due to current leakage through intermixed regions), and results from these ongoing experiments will be presented at the conference. The excellent fit to the model indicates that the intermixing transition occurs $0.7\pm 0.2\mu\text{m}$ from the implant, and is fairly abrupt. This represents both an excellent measurement of lateral intermixing effects, and twice as abrupt a junction as reported for similar work in GaAs [4] with cap-induced intermixing.

Conclusions:

We have demonstrated, for the first time, improved laser characteristics by using QWI to create current and carrier confinement under a laser ridge. Close agreement with an abrupt-junction model indicates that the intermixing is confined to less than a micron from the implant, the best measurement to date for a large blueshift in the InP/InGaAsP system. Although threshold current was not reduced to the levels seen in buried heterostructures, modeling indicates that the enhancement seen here should be reproduced for narrower ridges, and increased for larger blueshifts. Finally, because a large blueshift maximizes the LCC benefit, lateral intermixing is fully compatible with photonic integration platforms [3,5] that use QWI to create passive regions without removing the active region.

References:

- [1] S.Y. Hu, *et al.*, *IEEE Photon. Technol. Lett.*, **7**, 712-714
- [2] S. Charbonneau, *et al.*, *J. Appl. Phys.*, **78**, 3697-3705 (1995).
- [3] E.J. Skogen, J.S. Barton, S.P. DenBaars, L.A. Coldren, *IEEE J. Sel. Top. Quant. Electron.*, **8**, 863-869 (2002).
- [4] C.L. Walker, A.C. Bryce, J.H. Marsh, *IEEE Photon. Technol. Lett.*, **14**, 1391-1393 (2002).
- [5] S. Charbonneau, *et al.*, *IEEE J. Sel. Top. Quant. Electron.*, **4**, 772-793 (1998).

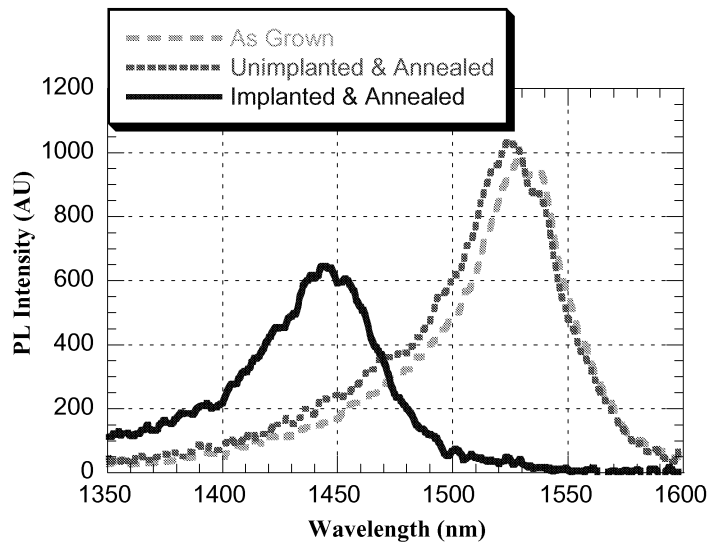


Fig. 2. Room-temperature microphotoluminescence measurements of implanted and unimplanted material after the intermixing anneal. A 76nm relative blueshift is observed.

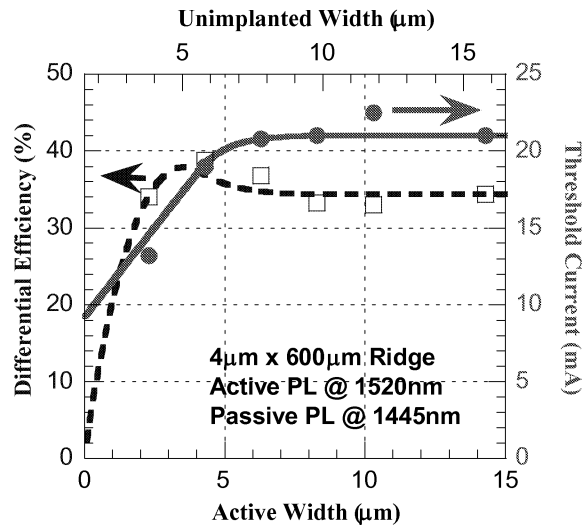


Fig. 3. Threshold current and differential efficiency for 600 μm -long ridge lasers, plotted against the unimplanted width and fit to the unintermixed width. Improvements in threshold and efficiency are observed over a wide range.

I. Photonic Integrated Circuits and Related Technology

D. Sensors

A monolithic evanescent field spore detector

D. A. Cohen, C. S. Wang, J. A. Nolde, D. D. Lofgreen, L. A. Coldren

Department of Electrical and Computer Engineering, University of California, Santa Barbara, CA 93106-9560
cohen@ece.ucsb.edu

Abstract: We demonstrate a monolithically integrated particle sensor based on evanescent field scattering, well suited for use with affinity assays for pathogen recognition. Single micron sized particles may be detected, representative of spores and small bacteria.

©2004 Optical Society of America

OCIS codes: (250.5300) Photonic integrated circuits; (140.5960) Semiconductor lasers

1. Introduction

Particle detection and identification is an important task in many industrial, pharmaceutical, medical, and security applications, and there is a growing need for particle sensors that are small, lightweight, fast, robust, and low enough in cost for widespread distribution. These requirements suggest that photonic integrated circuits may fill a significant market need. There have been many reports of integrated optic biochemical sensors achieving high sensitivity for both small and large molecules [1-3], but all required external light sources or optics which added significant size and manufacturing cost. We previously reported an optoelectronic sensor that included a monolithic laser to avoid this alignment task [4]. Those experiments all focused on the detection of molecular antigens captured on a waveguide surface by high affinity binding to antibodies or nucleotides, and careful control was needed to achieve sensitivity and stability. In contrast to molecular targets, there is an important class of pathogens that includes bacteria and bacterial spores, which range in size from one to ten microns in diameter. Cellular species have also been detected with miniature diode laser based instruments [5], but not previously with fully integrated devices. We report here the use of a simple monolithic particle sensor based on scattering of the evanescent field from a novel sensing waveguide. In conjunction with an appropriate affinity assay, the sensor may detect specific pathogens at the single cell level.

The sensor has been described previously, within the context of molecular sensing [6]. It consists of a gain section, a passive sensing region, and a waveguide photodetector all coupled by a single ridge waveguide, as shown in Fig. 1. A coupled cavity laser is formed between the cleaved facet at one end of the gain section, and the pair of etched facets bounding the passive section. The evanescent field of the optical mode penetrates slightly above the waveguide, and interacts with the sample fluid surrounding the waveguide. Optical scattering by particles bound to the waveguide surface increase both the cavity loss and reduce the light coupled to the waveguide photodetector, resulting in a reduction in photocurrent for a given laser bias current.

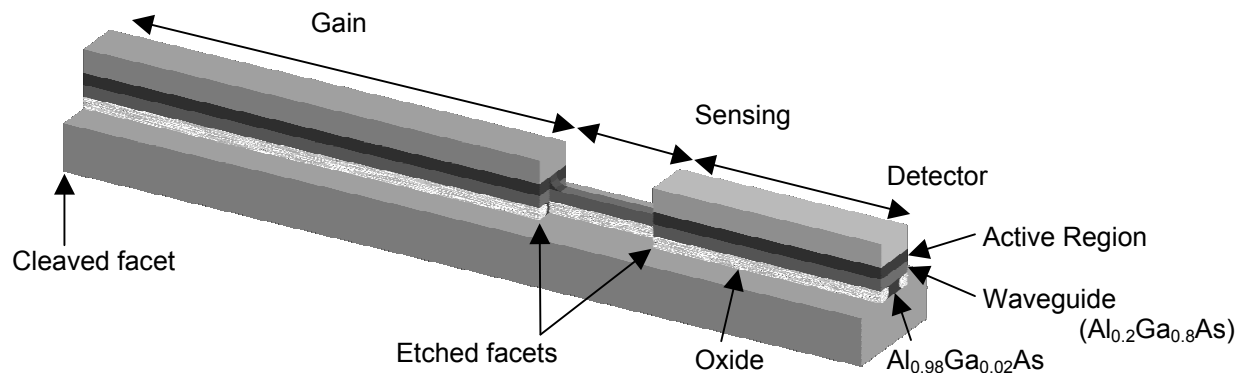


Fig. 1. Schematic of the coupled cavity laser sensor. Note the narrower ridge width in the sensing region, allowing complete oxidation beneath the waveguide layer to form a quasi-symmetrically clad waveguide.

It has been shown that for optimal sensitivity to thin chemical layers surface-bound to the sensing waveguide, as used, for example, in affinity assays, the sensing waveguide must be symmetrically clad, with a large index contrast between core and cladding [7]. Symmetrically clad dielectric waveguides have been demonstrated with very high sensitivity for bulk sensing, but due to the small index contrast, they offer only modest optical overlap with thin surface-bound layers. The need for careful alignment between the integrated laser's semiconductor waveguide and the dielectric waveguide also makes fabrication difficult. An all-semiconductor waveguide has also been demonstrated, but the highly asymmetric cladding limited the mode overlap with an analyte to 0.02% [4]. We developed a process for fabricating a self-aligned, semiconductor core, quasi-symmetric sensing waveguide monolithically-integrated with a conventional ridge laser. The resulting mode optical mode was tightly bound near the waveguide surface, with a 4.8% overlap with the analyte.

2. Fabrication

The major obstacle in constructing a symmetric waveguide was incorporating a low index material below the semiconductor core. This was accomplished without using a difficult regrowth or etching process, but rather by oxidizing a 300 nm $\text{Al}_{0.98}\text{Ga}_{0.02}\text{As}$ layer below the core. The laser itself employed an offset quantum well structure. The active region consisted of three 8 nm InGaAs wells with 8 nm GaAs barriers, grown above a 200 nm thick waveguide core composed of $\text{Al}_{0.2}\text{Ga}_{0.8}\text{As}$. Fabrication began by etching down to the waveguide in the middle region, thereby eliminating the absorbing quantum wells and forming a trench for the sensing region. Next, the ridge was patterned such that the middle region was narrower than the gain and absorber sections. Upon exposing the $\text{Al}_{0.98}\text{Ga}_{0.02}\text{As}$ after etching, a wet oxidation was performed to completely oxidize the sensing region in the middle but not completely oxidize under the gain and absorber sections. Thus, the effective widths of all three sections were nearly the same, 3 microns, providing a single lateral mode. The gain, sense, and absorber sections were 400, 40 and 200 microns long, respectively. The process was finalized with Ti/Pt/Au p-contacts, and AuGe/Ni/Au n-contacts on the back of the thinned substrate.

3. Results

To measure the mode overlap with an analyte, the shift in the optical spectrum due to changes in the analyte's index of refraction was measured, as described in [6]. The shift occurred because the passive cavity formed a Fabry Perot mode filter whose center wavelength depended on the refractive index of the medium surrounding the passive waveguide. The filter wavelength shifted nearly linearly with the index of refraction of the bathing fluid. To rule out errors due to temperature effects, the entire device was submerged in a temperature-controlled bath of fluid held at $18^\circ\text{C} \pm 0.1^\circ\text{C}$, and the gain section was biased with 500 ns pulses at a repetition rate of 10 kHz. From the data, the mode overlap with the fluid was calculated to be 4.8%, a hundred-fold improvement over previous work with an asymmetrically-clad waveguide, and in good agreement with 2D mode simulations.

We demonstrated a monolithic particle detector by reverse biasing the absorber section, and using it as an integrated photodetector. The gain section was biased at a fixed current, and the resulting photocurrent was monitored. A nanoliter drop of water containing about one thousand 1 micron diameter latex spheres was placed on the sensing region. The reflectivity at the etched facet between the gain and sensing regions was lowered by the presence of water, and so the laser's threshold current increased and the output power at fixed current decreased, as shown in Fig. 2. After 15 seconds, the water evaporated, and the signal increased again, but not quite to the original level. A photomicrograph of the sensing region revealed that a cluster of particles landed on the waveguide when the water evaporated, also shown in Fig. 2. Such a cluster is similar in size to a cluster of Anthrax spores. The sensitivity was high enough to detect single 1 μm latex particles.

4. Discussion

As with other sensors based on refractometry, for example surface plasmon resonance sensors or waveguide interferometers, this particle detector relies on selective binding chemistry to differentiate between target analytes and all other species. Thus, a useful device would also require a layer of ligand molecules deposited on the surface of the sensing waveguide, and a microfluidic means to deliver the sample and perhaps wash away contaminating particles. We note that the nearly instantaneous response of this sensor allows easy discrimination between discreet

particle binding events and slow changes due to an accumulation of serum proteins, a problem that has plagued other affinity sensors. Also, if the binding layer is restricted to the central two microns of waveguide width, where the field intensity is relatively uniform, then the magnitude of the response can also be used as a measure of the particle size, providing some additional discrimination against fouling by unsought particles.

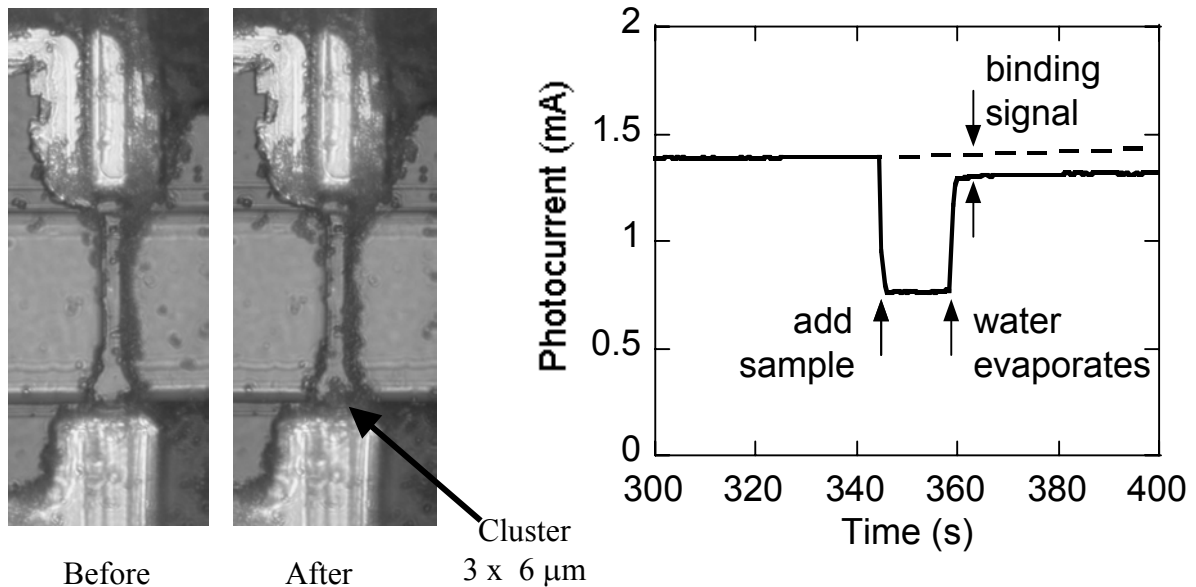


Fig. 2. Particle sensing with the coupled cavity laser sensor. A nanoliter droplet of water containing 1 micron diameter latex spheres is placed on the sensing waveguide and allowed to evaporate, leaving behind spheres or small clusters of spheres. The difference in photocurrent measured at the absorber indicates the presence of particles, seen in this case to be a single cluster similar in size to a cluster of anthrax spores.

5. References

- [1] R. G. Heidemann et al., "Remote opto-chemical sensing with extreme sensitivity: design, fabrication and performance of a pigtailed integrated optical phase-modulated Mach-Zehnder interferometer system," *Sensors and Actuators B*, **B61**, 100-127, (1999).
- [2] W. Lukosz, "Integrated optical chemical and direct biochemical sensors," *Sensors and Actuators B*, **B29**, 37-50, (1995).
- [3] C. F. R. Mateus et al., "Ultra sensitive optoelectronic label-free biosensor for static and dynamic monitoring of protein interactions," in *2003 LEOS Annual Meeting Conference Proceedings*, (Institute of Electrical and Electronics Engineers, New York, 2003), paper PD 2.4.
- [4] D. A. Cohen et al., "Monolithic chemical sensor using heterodyned sampled grating DBR lasers," *Electronics Letters*, **37**, 1358-1360, (2001).
- [5] P. L. Gourley et al., "Nanolaser/microfluidic biochip for realtime tumor pathology," *Biomedical Microdevices*, **2**, 111-122, (1999).
- [6] C. S. Wang et al., "A diode laser chemical sensor utilizing an oxidized lower cladding layer for high sensitivity," in *2003 LEOS Annual Meeting Conference Proceedings*, (Institute of Electrical and Electronics Engineers, New York, 2003), pp. 989-990.
- [7] O. Parriaux et al., "Normalized analysis for the sensitivity optimization of integrated optical evanescent-wave sensors," *IEEE J. Lightwave Technology*, **16**, 573-582, (1998).

A monolithic diode laser chemical sensor with a quasi-symmetrical sensing waveguide for improved sensitivity

C. S. Wang,^{a)} J. A. Nolde, D. D. Lofgreen, L. A. Coldren, and D. A. Cohen
*Department of Electrical and Computer Engineering, University of California, Santa Barbara,
 Santa Barbara, California 93106*

(Received 5 February 2004; accepted 18 May 2004)

We demonstrate a diode laser chemical sensor incorporating a self-aligned, symmetrically clad high index contrast evanescent field sensing waveguide. This is accomplished by selectively oxidizing the lower cladding layer of the sensing waveguide. An analyte overlap of 4.8% is obtained with a tightly confined mode, ideal for sensitive affinity assays. © 2004 American Institute of Physics. [DOI: 10.1063/1.1769080]

There is a growing need for biochemical sensors that are sensitive, fast, small, low powered, and inexpensive for use in medical, industrial, and military applications. To date, some of the highest sensitivities have been demonstrated using interferometric or refractometric techniques, but with nonmonolithic approaches.¹⁻³ A few monolithically integrated evanescent field sensors have been demonstrated based on waveguide interferometers or on-chip heterodyne detection.^{4,5} For optimal sensing of thin chemical layers surface bound to the sensing waveguide, as used in affinity assays, for example, it has been shown that the sensing waveguide must be symmetrically clad, with a large index contrast Δn between core and cladding.⁶ Symmetrically clad dielectric waveguides have been demonstrated with a very high sensitivity for bulk sensing, but due to the small index contrast, they offer only modest optical overlap with thin, surface-bound layers.⁴ The need for careful alignment between the integrated laser's semiconductor waveguide and the dielectric waveguide also makes fabrication difficult. An all-semiconductor waveguide has also been demonstrated, but the highly asymmetric cladding limited the mode overlap with an analyte to $\sim 0.02\%$.⁷ In this letter, we report results from, and a process for, fabricating a self-aligned, semiconductor core, quasi-symmetric sensing waveguide that is monolithically integrated with a conventional ridge laser. A 4.8% overlap with an analyte in a tightly confined optical mode is demonstrated.

The major obstacle in constructing a symmetric waveguide is incorporating a low index material below the semiconductor core. In this work, this is accomplished without using a difficult regrowth or etching process, but rather by oxidizing an $\text{Al}_{0.98}\text{Ga}_{0.02}\text{As}$ layer below the sensing waveguide core. This process is fully self-aligned, resulting in no excess loss from lateral misalignment. The vertical misalignment, to be explained later, resulting from abrupt changes in the refractive index, leads to an increased reflection. However, we use this reflection to build a simple three-mirror resonator,⁸ as shown in Fig. 1. The cleave at the front (gain) end, the etched facet at the interface between the gain and sensing regions, and the etched facet at the interface between the sensing and absorber regions comprise the three mirrors. In operation, the absorber region is grounded so that no light

returns from the rear cleaved facet. The net reflectivity is modulated by the resonance in the passive cavity, producing a mode filter whose center wavelength depends on the modal index of refraction in the passive section. This, in turn, is influenced by the evanescent interaction with the medium surrounding the passive waveguide.

The laser itself employs an offset quantum well structure, as shown in the refractive index profile of the layer structure in Fig. 2. The epilayers, grown by molecular beam epitaxy on an $n\text{-GaAs}(100)$ substrate, consist of $1.4\ \mu\text{m}$ $\text{Al}_{0.8}\text{Ga}_{0.2}\text{As}$ n -cladding doped $1 \times 18\ \text{cm}^{-3}$, $300\ \text{nm}$ $\text{Al}_{0.98}\text{Ga}_{0.02}\text{As}$ oxidation layer doped $5 \times 17\ \text{cm}^{-3}$ n -type, $200\ \text{nm}$ $\text{Al}_{0.2}\text{Ga}_{0.8}\text{As}$ waveguide core, graded from $5 \times 17\ \text{cm}^{-3}$ to unintentionally doped, an active region consisting of three $8\ \text{nm}$ InGaAs wells with $8\ \text{nm}$ barriers, $70\ \text{nm}$ $\text{Al}_{0.3}\text{Ga}_{0.7}\text{As}$ p -SCH ($5 \times 17\ \text{cm}^{-3}$) graded to $1.4\ \mu\text{m}$ $\text{Al}_{0.8}\text{Ga}_{0.2}\text{As}$ p -cladding ($2 \times 18\ \text{cm}^{-3}$), and a $120\ \text{nm}$ heavily doped $p\text{-GaAs}$ contact layer.

This structure, as grown, has an asymmetrical 1D mode profile, as shown in Fig. 2. With the p -cladding and active region removed and the $\text{Al}_{0.98}\text{Ga}_{0.02}\text{As}$ oxidized, a more symmetrical mode results. The Al_xO_y ($n \approx 1.6$) and sensing fluid ($n \approx 1.3$) are thus the low-index cladding layers sandwiching the semiconductor waveguide core. The mode overlap between the active and passive sections is 70%, and the modal power reflectivity is calculated to be 5.8%.

The initial fabrication step was to dry etch down to the waveguide in the middle section, thereby eliminating the absorbing quantum wells and forming a trench for the sensing region. Next, the ridge was patterned perpendicular to the trench and a second dry etch was used to define the ridge structure, which abruptly changes width from $6\ \mu\text{m}$ in the gain and absorber sections to $2.5\ \mu\text{m}$ in the sensing region.

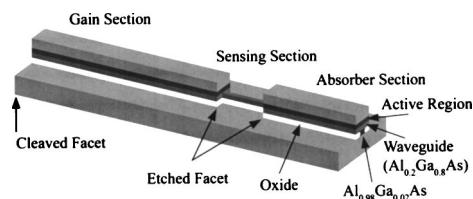


FIG. 1. The device schematic of the coupled-cavity laser sensor. Note the narrower ridge width in the sensing region, allowing complete oxidation beneath the waveguide layer to form a quasi-symmetrically clad waveguide.

^{a)} Author to whom correspondence should be addressed; electronic mail: cswang@engineering.ucsb.edu

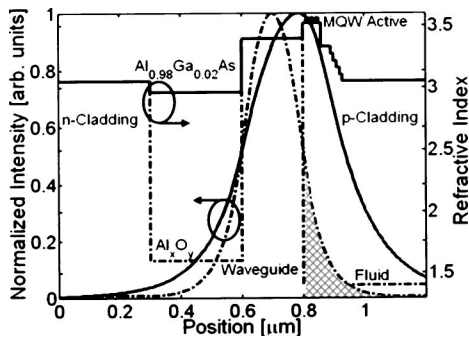


FIG. 2. The labeled epitaxial layer structure of the laser sensor, showing the index of refraction of each layer. The solid line represents the gain section of the laser. The dashed line represents the sensing region, in which the active region has been etched away and the $\text{Al}_{0.98}\text{Ga}_{0.02}\text{As}$ has been oxidized. Superimposed are the one-dimensional mode profiles of each section. The crosshatched area represents the modal overlap of the evanescent field with the fluid analyte.

The etch penetrated through the waveguide and the 300-nm-thick $\text{Al}_{0.98}\text{Ga}_{0.02}\text{As}$ layer beneath the waveguide core. A low temperature (420 °C) wet oxidation was then used to convert this $\text{Al}_{0.98}\text{Ga}_{0.02}\text{As}$ layer to Al_xO_y . The oxidation was timed to completely convert the material below the narrow sensing region, but leave an unoxidized width of approximately 3 μm below the active and absorber waveguides. Similar processes have also been used to fabricate structures utilizing oxide apertures for index and current confinement.⁹ Figure 3 shows an SEM image of the gain section with this partial oxidation. This self-aligned process left a high-index-contrast quasi-symmetrically clad waveguide coupled to a more conventional laser waveguide. The gain, sense, and absorber sections were 400, 40, and 200 μm long, respectively. The process was completed with Ti/Pt/Au p-contacts and AuGe/Ni/Au n-contacts on the back of the thinned substrate. The devices were cleaved and mounted onto copper studs for pulsed testing. Pulse testing was used to avoid self-heating in the device, which would skew the data.

To measure the mode overlap with an analyte, the entire device was submerged in a temperature-controlled bath of fluid held at 18±0.1 °C, monitored with a thermistor. The bath was covered to minimize evaporative cooling. The gain

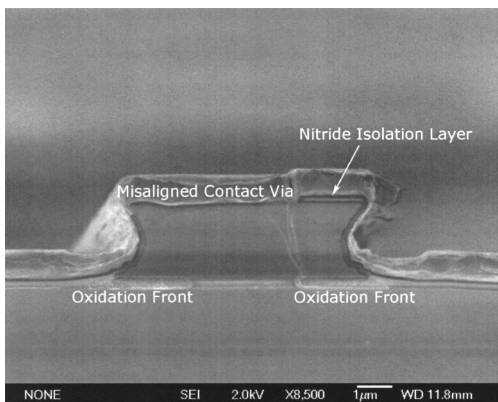


FIG. 3. The scanning electron micrograph of a cross section of the gain region. The oxidation front can be seen approaching from both sides of the etched sidewall, leaving a 3 μm wide current path through the $\text{Al}_{0.98}\text{Ga}_{0.02}\text{As}$. The defect running from the oxidation front to the misaligned nitride layer on top of the ridge is possibly due to strain between these two layers.

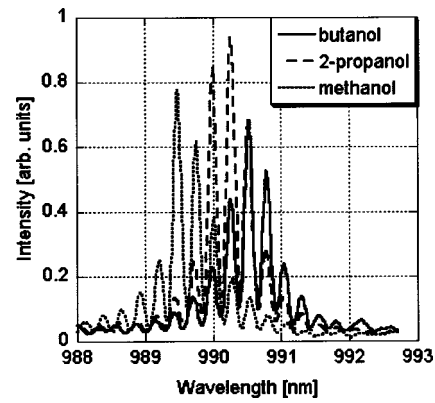


FIG. 4. The lasing spectra for three different fluids bathing the sensor. The mode filter center wavelength depends on the fluid index of refraction, and is found by interpolation between the dominant modes.

section was biased at 45 mA, 5 mA above the threshold, with 500 ns pulses at a repetition rate of 10 kHz. Five different alcohol mixtures were tested; for clarity, only three of the lasing spectra are shown in Fig. 4. An interpolation scheme was used to determine the filter center wavelength from the intensities of the three strongest lasing modes:

$$\lambda_c = \lambda_o + \left(\frac{P_{+1} - P_{-1}}{P_{+1} + P_{-1}} \right) \left(\frac{\lambda_{+1} - \lambda_o}{2} \right), \quad (1)$$

where λ_c is the center wavelength, λ_o is the dominant mode wavelength, $\lambda_{\pm 1}$ are the wavelengths of modes adjacent to λ_o , and $P_{\pm 1}$ are the powers of modes adjacent to λ_o . As shown in Fig. 5, this filter wavelength shifted nearly linearly with the index of refraction of the bathing fluid. The modal overlap with the fluid to be sensed, Γ , is related to the filter wavelength by,

$$\frac{\Delta\lambda_c}{\lambda_c} = \Gamma \frac{\Delta n_{\text{fluid}}}{n_{\text{eff}}}, \quad (2)$$

where $\Delta\lambda_c$ is the shift in λ_c due to a shift in fluid index Δn_{fluid} , and n_{eff} is the modal effective index in the passive section. From the data, Γ was calculated to be 4.8%, a hundredfold improvement over previous work with an asymmetrically clad waveguide and in good agreement with two-dimensional mode simulations of 4.45%.

In conclusion, we have developed a manufacturable technique to monolithically couple symmetrically clad high index contrast waveguides to conventional semiconductor la-

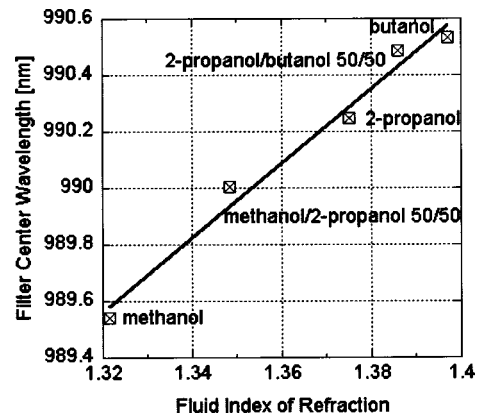


FIG. 5. The filter center wavelength as a function of the fluid index of refraction. All fluid indices were measured with an Abbe refractometer.

ser waveguides. The tight optical confinement is ideal for the sensing of thin analyte layers surface bound to the sensing waveguide. Integration of this structure into sensors based on either interferometric or heterodyne detection would yield femtogram sensitivities from picoliter volumes.

This work was supported by DARPA within the Bioflips and Simbiosys programs under Contract Nos. DAAD 19-00-1-0400 and F30602-01-2-0538.

¹R. G. Heidemann and P. V. Lambeck, *Sens. Actuators B* **B61**, 100 (1999).

²C. F. R. Mateus, M. C. Y. Huang, J. E. Foley, R. Beatty, C. J. Chang-

Hasnain, P. Li, and B. Cunningham, LEOS 16th Annual Meeting, paper no. PD 2.4, Tucson, AZ (2003).

³W. Lukosz, *Sens. Actuators B* **B29**, 37 (1995).

⁴B. Maisenhölder, H. P. Zappe, R. E. Kunz, P. Riel, M. Moser, and J. Edlinger, *Sens. Actuators B* **38-39**, 324 (1997).

⁵D. A. Cohen, E. J. Skogen, H. Marchand, and L. A. Coldren, *Electron. Lett.* **37**, 1358 (2001).

⁶O. Parriaux and G. J. Veldhuis, *J. Lightwave Technol.* **16**, 573 (1998).

⁷D. A. Cohen, J. A. Nolde, A. Tauke Pedretti, C. S. Wang, E. J. Skogen, and L. A. Coldren, *IEEE J. Sel. Top. Quantum Electron.* **9**, 1124 (2003).

⁸L. A. Coldren and S. W. Corzine, *Diode Lasers and Photonic Integrated Circuits* (Wiley, New York, 1995), p. 79.

⁹S. A. Maranowski, A. R. Sugg, E. I. Chen, and N. Holonyak, Jr., *Appl. Phys. Lett.* **63**, 1660 (1993).

Biophotonic Integrated Circuits

Daniel A. Cohen^{*a}, J. A. Nolde^a, C. S. Wang^a, E. J. Skogen^a, A. Rivlin^b, L. A. Coldren^a

^aDept. of Electrical and Computer Engineering, University of California, Santa Barbara, CA 93106

^bThauMDx, Santa Barbara, Ca

ABSTRACT

Biosensors rely on optical techniques to obtain high sensitivity and speed, but almost all biochips still require external light sources, optics, and detectors, which limits the widespread use of these devices. The optoelectronics technology base now allows monolithic integration of versatile optical sources, novel sensing geometries, filters, spectrometers, and detectors, enabling highly integrated chip-scale sensors. We discuss biophotonic integrated circuits built on both GaAs and InP substrates, incorporating widely tunable lasers, novel evanescent field sensing waveguides, heterodyne spectrometers, and waveguide photodetectors, suitable for high sensitivity transduction of affinity assays.

Keywords: sensor, biochemical sensor, biomedical measurements, tunable diode laser, photonic integrated circuit, optoelectronic integrated circuit

1. INTRODUCTION

There is a growing need for biochemical sensors that are sensitive, fast, small, low-powered and inexpensive, for use in medical, industrial, and military applications. Potential markets include monitoring food and water supplies, insuring purity in the food and pharmaceutical industries, environmental monitoring, industrial process and pollution control, clinical diagnosis, battlefield monitoring and casualty assessment. Biochemical targets include hazardous industrial chemicals, pesticides, toxins, biowarfare agents, viruses and bacterial pathogens. As shown in Table 1, these species range in size from a few nanometers to a few microns, and hazardous or infective doses range from 1 to 8,000 particles or as little as 30 nanograms. Optical techniques based on absorption spectroscopy, Raman scattering, fluorescence, and surface plasmon resonance are the most sensitive for biochemical detection, and some of these approaches have been commercialized^{1,2}. However, attempts to adapt these laboratory techniques to the microscale have suffered by not integrating the light source with the sensor. A number of interferometric sensors have been demonstrated utilizing integrated optics in conjunction with an off-chip laser^{3,4}. Refractive index changes as low as $5 \cdot 10^{-8}$ have been detected in bulk fluids, using an interaction length of 4 millimeters⁵. Sensors have also been demonstrated utilizing diode lasers monolithically integrated with Mach Zehnder interferometers⁶. The results are encouraging, and suggest a promising new market for photonic integrated circuits.

Pathogen	Size	Infective Dose
Anthrax spores	1-5 micron cluster	8,000
Plague bacteria	.5 x 1 micron rod	100
Smallpox virus	200-400 nm	10

Table 1. Pathogen size and infective dose.

We have previously reported chemical sensing with a monolithically integrated device comprising a pair of sampled-grating distributed Bragg reflector (SGDBR) lasers, a field combiner, and a photodiode⁷. The sensor consists of a pair of tunable single frequency ridge waveguide diode lasers, integrated with a waveguide field combiner and a photodetector, as shown in Fig. 1. The lasers' optical fields produce a heterodyne signal at the photodetector, with the heterodyne frequency dependent on the relative lasing frequencies. A portion of one laser's waveguide is left free of metal or dielectric, so that the optical evanescent field penetrates into the region adjacent to the ridge. The round trip phase in the laser cavity is then sensitive to the index of refraction of the surrounding medium, so that the lasing frequency shifts as the index changes, for example due to a change in the chemical concentration or the binding of an antigen to an antibody coating the ridge sidewall. The shift in heterodyne frequency, Δf , is then given by

$$\frac{\Delta f}{f} = \Gamma \frac{\Delta n}{n_{eff}}, \quad (1)$$

where f is the optical frequency, Δn is the change in refractive index in the region of the evanescent field, n_{eff} is the effective modal index averaged over the entire cavity, and Γ is the fraction of the sensing laser's optical energy that resides in the exposed evanescent field. The high sensitivity of this technique originates from the relative precision with which the frequency may be measured: the heterodyne linewidth is below 20 MHz, and with simple processing a frequency shift of only 2 MHz can be detected, while the optical frequency is 200 THz. Thus, with a Γ of 1%, and an effective index of 3.3, the detector would sense an index shift of only $3 \cdot 10^{-6}$.

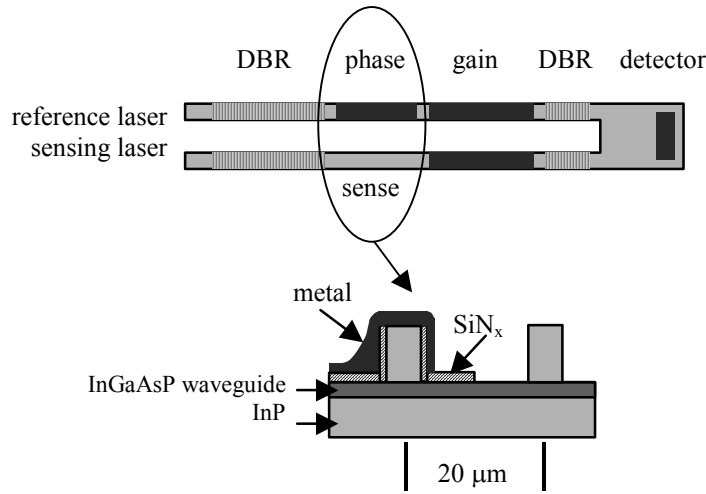


Figure 1. Heterodyned laser biochemical sensor.

Such a shift in refractive index may signal contamination of bulk fluids, but will not directly indicate the source or nature of contamination. To obtain this information, a variety of thin surface coatings are available that capture and bind specific chemical species or organisms with very high selectivity. Examples include antibodies, DNA, and chemically selective polymers, and the detection processes are collectively known as affinity assays. These coatings may be applied directly to optical components or waveguides, resulting in very sensitive affinity assay transducers.

Once the light source is included on the sensor chip, wafer-scale manufacturing techniques such as flip-chip bonding may be used to integrate the optical sensor with silicon control electronics and microfluidics, as shown in Fig. 2. This eliminates the need for optical alignment, and enables mass production and mass deployment of the sensors.

The standard ridge waveguide structure as used in the experimentally demonstrated sensor cannot achieve the 1% optical overlap with the analyte, and so the index sensitivity was limited to $\sim 1 \cdot 10^{-4}$. We have explored two approaches to improve this. By narrowing the ridge width to below a micron, we can increase the mode overlap by one order of magnitude. To do this inside the laser cavity, however, the ridge width must be gently tapered to avoid scattering losses and reflections. The optical overlap can be increased by another order of magnitude, if the waveguide's lower cladding is removed, or converted to a low-index material. We verified this in a novel sensor built in the AlGaAs material system, using wet oxidation to convert an AlAs layer to AlO_x . Experimentally, we obtained a mode overlap of 4.8%, in good agreement with numerical modeling. We also found that this device is sensitive to scattering loss, and may be useful as a spore detector for security applications. Experimental work on these approaches will be presented below.

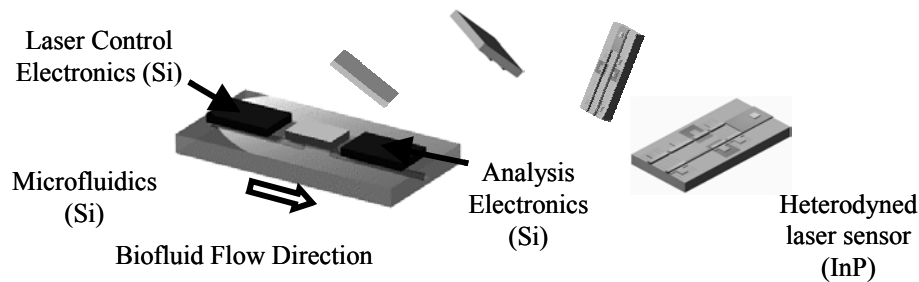


Figure 2. Schematic of the heterodyned laser sensor flip-chip attached to a silicon microfluidic circuit, with silicon control and analysis electronics also attached.

2. HETERODYNE REFRACTOMETER

2.1 Experimental performance

We used sampled grating distributed Bragg reflector (SGDBR) lasers in this sensor because the very large tuning range provides a tremendous dynamic range. SGDBR laser performance and fabrication details have been detailed elsewhere⁸. We mention here that they consist of a 350 nm thick GaInAsP waveguide layer, clad by InP. Seven compressively strained quantum wells are grown above the waveguide, and are etched away prior to MOCVD regrowth, to form passive waveguide regions. The quantum wells are left intact to form the detector. A ridge waveguide structure is used, with a nominal ridge width of 2.5 μm , etched chemically down to the top quantum well barrier in the active region, or to the top of the waveguide in the passive regions. The two laser ridges are 20 μm apart, and terminate in a common slab waveguide 23 μm wide. Imbedded in the slab, approximately 200 μm from the input end is the photodetector. The sampled DBR mirrors and the phase adjustment region in the reference laser are tuned by current injection. The corresponding phase adjustment region of the sensing laser is left without contact or dielectric layers, so that the evanescent field from the waveguide can interact with the surrounding medium.

Fig. 3 shows the heterodyne signal of the sensor chip in air, for two different currents in the reference laser's phase control section. The signal linewidth is less than 20 MHz in this example, and dropped to 15 MHz at higher gain section currents, as expected. Bulk chemical sensing was tested in an open reservoir containing one of five different fluids, including air. Alcohol mixtures were used instead of aqueous or aromatic solvents, to avoid excessive bubbling due to electrolysis at the contacts, and to insure clean exchange of fluids. The reservoir, in turn, rested upon a temperature-controlled stage. The optical signal from the back facets of the two lasers was coupled through single mode fiber to a high-resolution optical spectrum analyzer, used as an independent measure of wavelength shift. The device was biased with DC electrical probes, and the microwave signal from the photodetector was coupled by way of a coplanar waveguide probe to an electrical spectrum analyzer, without amplification. Fluids were exchanged by pipette.

The heterodyne frequency shifted approximately linearly with the index of refraction of the fluid, as shown in Fig. 4. Indeed, the linearity was quite good, except when exchanging the fluid to air. This is probably the result of a significant change in the field profile when the surrounding index changed from approximately 1.3 to 1.0. Also shown is the tuning current supplied to the reference laser's phase section, to maintain a fixed heterodyne frequency. This feedback technique provides a very wide dynamic range without the need for an integrated high-speed detector, because the SGDBR laser is tunable over 5 THz. It also allows the use of narrow band electrical filters for an improved signal-to-noise ratio.

At 1550 nm, the index difference between 1-propanol and 2-propanol is 0.009. The heterodyne signal shifted 93 MHz when these two fluids were exchanged. The modal index of this ridge structure is 3.3, so from (1) we calculate the experimental mode overlap with all of the surrounding fluid to be $1.8 \cdot 10^{-4}$. The sensing region occupied 40% of the total cavity length, that is $\Gamma_z = \Gamma / \Gamma_{xy} = 0.4$, so that $\Gamma_{xy} = 4.4 \cdot 10^{-4}$.

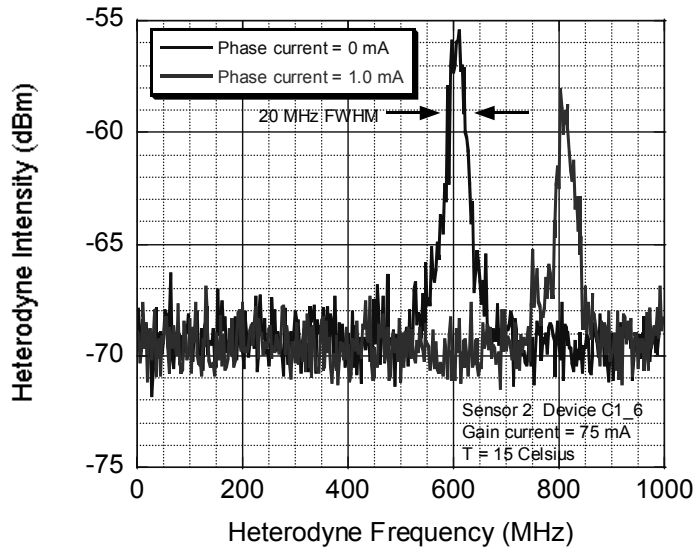


Figure 3. Heterodyne signal in air, for different reference laser phase section currents.

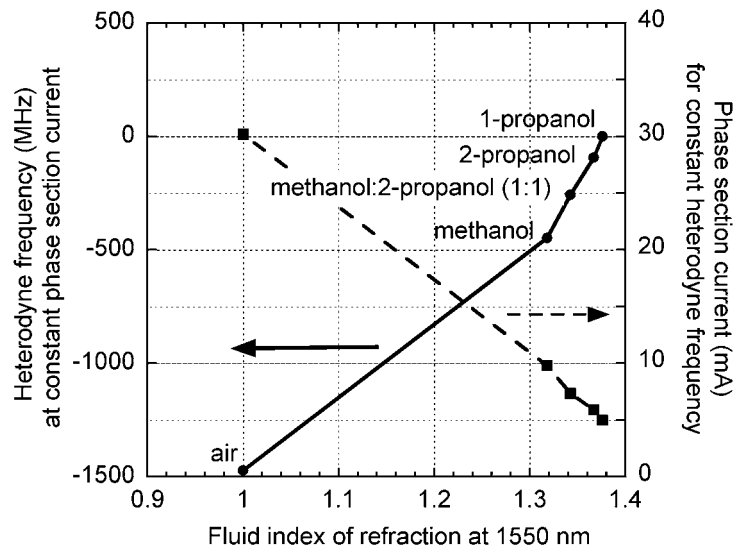


Figure 4. Response of the sensor to different refractive index fluids.

The optical frequency of an SGDBR laser drifts with temperature at 13-15 GHz/K, as does any single frequency diode laser at this wavelength. However, since the heterodyne frequency is the difference between two nominally identical lasers, it should be orders of magnitude more stable than the individual lasers. We tested this by varying the heatsink temperature below the sensor. As shown in Fig. 5, the signal drift was 106 MHz/K, less than 1% of the drift of the individual lasers. The residual drift arises because the two lasers may have slightly different scattering or absorption losses, and thus operate at slightly different carrier densities. The absorption losses, in particular, depend on the tuning currents applied to the phase and mirror sections, so the temperature sensitivity will be influenced by the current needed to align the two lasers' frequencies. In principle, additional loss could be added to one laser to better match the operating point of the other laser. Alternatively, a reference pair of lasers, neither of which has an exposed

sensing region, may be used as an on-chip temperature monitor. In this case, increasing the difference in loss between the two lasers in the reference pair will increase the temperature sensitivity, as desired for a temperature monitor.

With the present temperature sensitivity, a substrate temperature drift of 10 mK would produce a 1 MHz error in the heterodyne frequency, comparable to the anticipated frequency resolution. For clinical applications, thermoelectric temperature controllers are commercially available with 5 mK stability. For many portable or cost-sensitive applications, however, the sensor must operate unstabilized. In this case, we can use the known temperature response in conjunction with an on-chip temperature measurement (perhaps from a reference pair as above), to interpret the heterodyne signal. We note that the 35 nm tuning range of the SGDBR lasers will allow nulling the heterodyne signal over the lasers' entire 80 degree operating range.

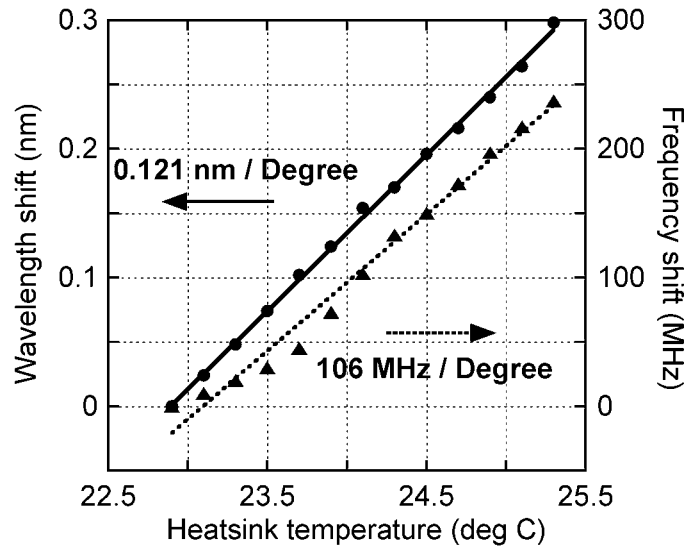


Figure 5. Response of the sensor to varying temperature.

2.2 Sensitivity Improvement

Equation 1 shows that the key to achieving high sensitivity is to obtain a high overlap, I , between the optical mode and the region to be sensed. In Fig. 6(a) we show a standard ridge waveguide structure consisting of a lower InP ridge, an InGaAsP waveguide core layer, and an InP upper ridge. The upper ridge is surrounded by the fluid sample. Contour lines representing the optical field intensity propagating out of the page are also shown. The high index of the upper ridge prevents the optical mode from penetrating significantly into the fluid, and so must be narrowed or completely removed, as in Fig. 6(b) and Fig. 6(c). Reducing the thickness of the waveguide layer may further increase the mode overlap, but due to the asymmetric structure, propagation is eventually cut off. Fig. 7 shows the improvement in mode overlap, relative to the standard ridge structure of Fig. 6(a), for the case of a 350 nm thick waveguide and varying upper

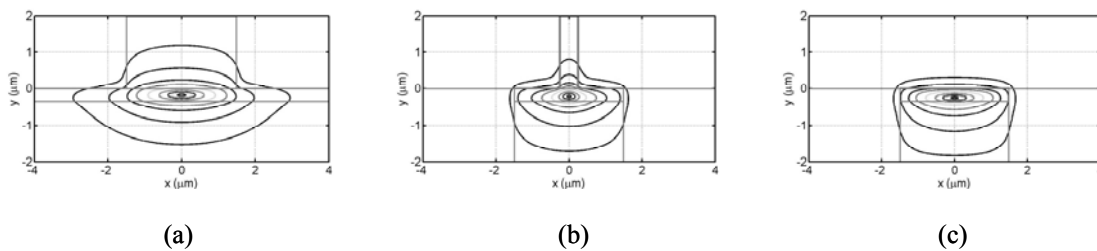


Figure 6. Mode profiles for various waveguide geometries.

ridge width. Also shown is the case of a quasi-symmetrically clad waveguide in which the lower ridge (or substrate) has been completely replaced by a low index material, forming a channel waveguide. We see that a thirty-fold improvement may be obtained by tapering the upper ridge to zero width, without the need to replace or remove the lower substrate.

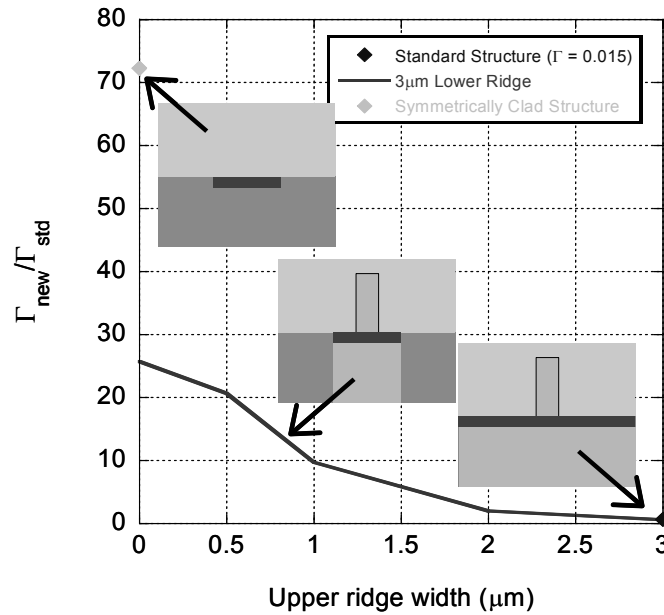


Figure 7. Relative improvement of the mode overlap with an analyte, for various waveguide geometries.

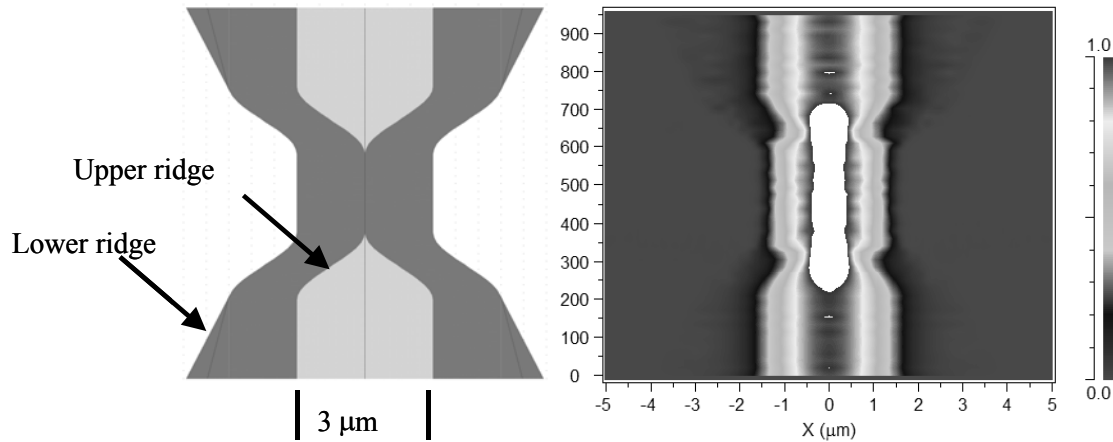


Figure 8. Taper design and beam propagation simulation.

To avoid spurious reflections and scattering losses, the standard ridge structure used in the gain section of the laser must be tapered gently to the asymmetric waveguide used in the sensing region. This taper is shown in Fig. 8 (note that the longitudinal and transverse scales are very different.) The taper length is approximately 175 microns. The

accompanying beam propagation simulation shows the optical intensity along a taper down and a taper back up to the ridge structure. The net loss in power due to this double taper is only 0.16 dB.

Fabry Perot cleaved-facet ridge lasers coupled to taper and sensing waveguides were fabricated from MOCVD-grown epitaxial wafers, using standard microfabrication techniques. A comparison of the differential efficiency versus passive waveguide length, shown in Fig. 9 for different sensing ridge widths, indicates that there is some excess propagation loss distributed over the narrow sensing ridge. The spectrum shown in Fig. 10 shows that there are also some spurious reflections inside the cavity. The mode spacing between the main lasing modes corresponds to a distance equal to the separation between the ends of the tapers, rather than the full cleave-to-cleave distance. Even small internal reflections can give rise to such a mode filtering. The fine ripple in the tails of the spectrum agrees with the mode spacing expected for the full cavity length, and shows that light does propagate from end to end. Improved etching, and a redesign of the taper ends, should reduce this reflection and scattering loss.

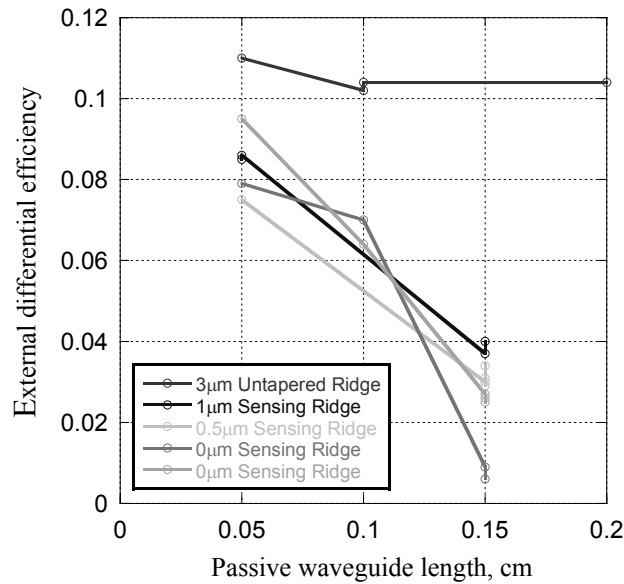


Figure 9. Differential efficiency versus passive waveguide length, showing excess loss in the sensing waveguide.

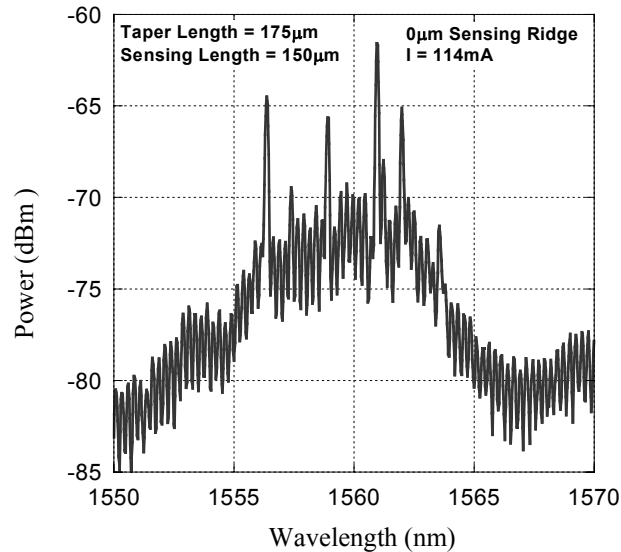


Figure 10. Spectrum of the active-passive laser, showing effect of spurious intracavity reflections.

symmetrically-clad waveguide as described above¹⁰. The result is shown in Fig. 14. Also shown is the sensitivity limit of the heterodyne sensor, assuming a frequency precision of 1 MHz. We see that for protein antigens 5 nm in radius, $2 \cdot 10^5$ copies must be bound. This corresponds to about 150 femtograms of material. For macromolecules or pathogens larger than 50 nm in radius, single copies should be detectable.

A number of authors have used polystyrene beads bound to the target antigens to enhance the sensitivity of refractometric measurements¹¹. This is particularly useful when the target is a small molecule such as a drug. A thousand-fold improvement in sensitivity has been reported, easily understood by reference to Fig. 14.

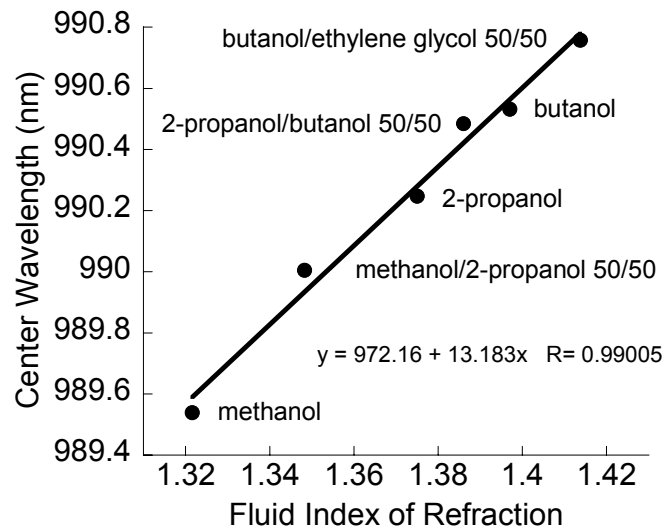


Figure 12. Bulk chemical sensing with the coupled cavity sensor.

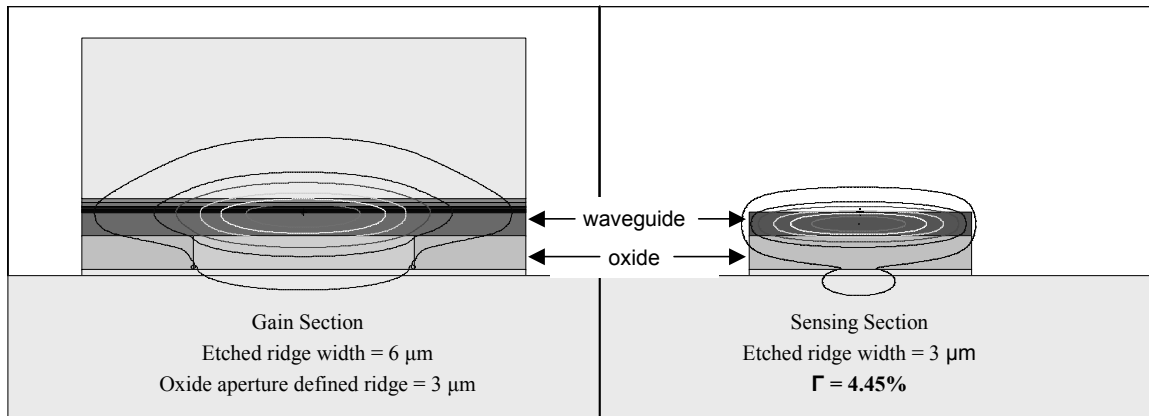


Figure 13. Mode contours in the active and sensing regions of the coupled cavity sensor.

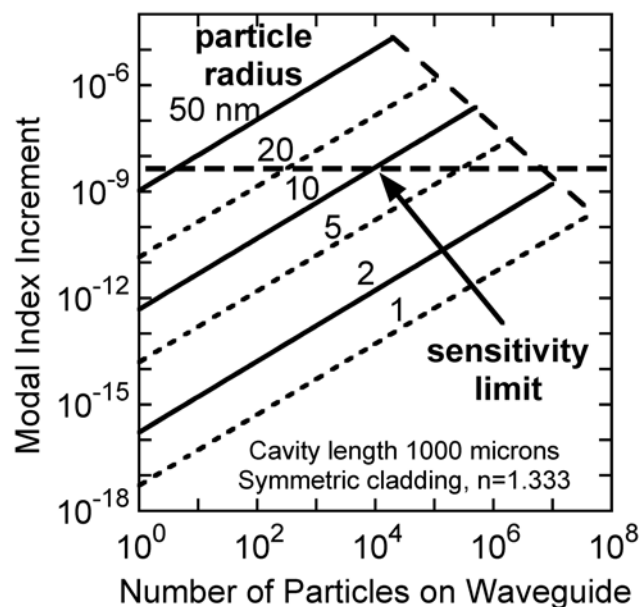


Figure 14. Sensitivity limit of the heterodyned laser sensor with a symmetrically-clad sensing waveguide.

3. SPORE DETECTION

In contrast to molecular targets, there is an important class of pathogens that includes bacteria and bacterial spores, which range in size from one to ten microns in diameter. Cellular species have been detected with miniature diode laser based instruments¹², but not previously with fully integrated devices. The AlGaInAs coupled-cavity sensor described in the preceding section was not itself useful as a refractometric sensor for bulk fluids or small molecules, because it required an external spectrometer to observe the shift in filter wavelength. However, it did serve as a chip-scale particle detector, because the high optical overlap with the region adjacent to the sensing waveguide led to significant scattering loss when wavelength-sized particles bound to the surface¹³.

We demonstrated particle detection by reverse biasing the absorber section, and using it as an integrated photodetector. The gain section was biased at a fixed current, and the resulting photocurrent was monitored. A nanoliter drop of water containing about one thousand 1 micron diameter latex spheres was placed on the sensing region. The reflectivity at the etched facet between the gain and sensing regions was lowered by the presence of water, and so the laser's threshold current increased and the output power at fixed current decreased, as shown in Fig. 15. After about 15 seconds, the water evaporated, and the signal increased again, but not quite to the original level. The photomicrograph of the sensing region reveals that a cluster of particles landed on the waveguide when the water evaporated,. Such a cluster is similar in size to a cluster of Anthrax spores. The sensitivity was high enough to detect single 1 μm latex particles.

We note that the nearly instantaneous response of this sensor allows easy discrimination between discrete particle binding events and slow changes due to an accumulation of serum proteins, a problem that has plagued other affinity sensors. Also, if the binding layer is restricted to the central two microns of waveguide width, where the field intensity is relatively uniform, then the magnitude of the response can also be used as a measure of the particle size, providing some additional discrimination against fouling by unsought particles.

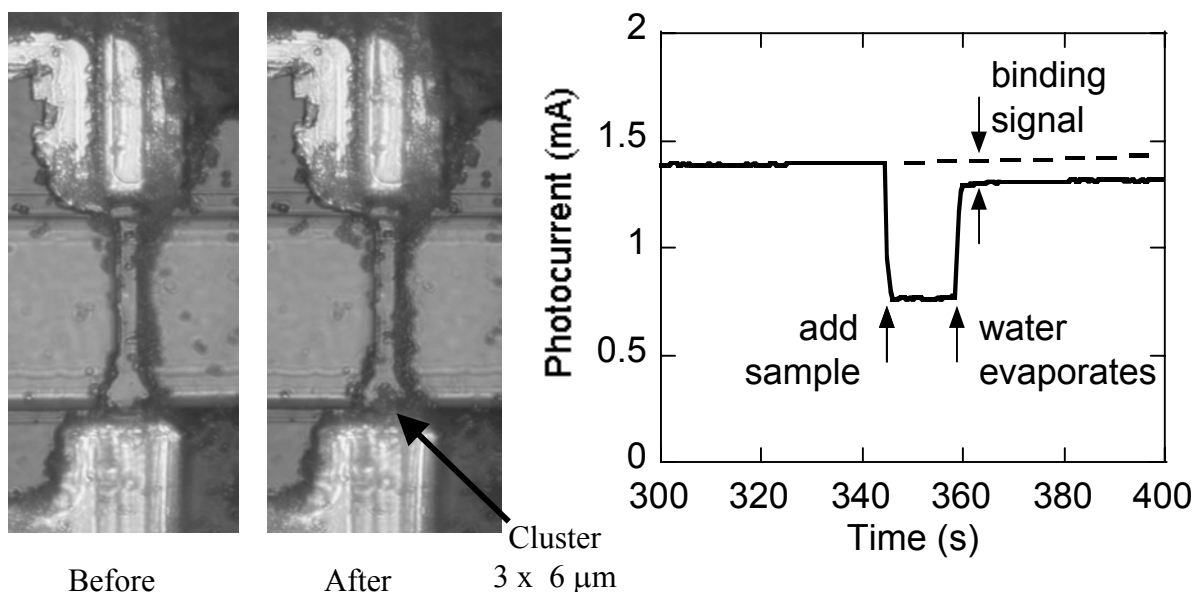


Figure 15. Particle sensing with the coupled cavity laser.

4. ANTIBODY IMMOBILIZATION

As with other sensors based on refractometry, such as surface plasmon resonance sensors or integrated optic interferometers, the sensors described here rely on selective binding chemistry to differentiate between target analytes and all other species. Thus, a useful device would also require a layer of ligand molecules deposited on the surface of the sensing waveguide, and a microfluidic means to deliver the sample and perhaps wash away contaminating particles. Many different reagents and protocols have been developed for coating surfaces with capture ligands, either antibodies or nucleotides, depending on the target species. In all cases, some linking molecule between the surface and the capture ligand is used: thiol-based linkers are commonly used on gold-coated surfaces, while silane-based molecules are used on silica surfaces. The quality of this linking film is very important, for it determines both the effectiveness of the ligand and the inhibition of binding of unwanted species. While such films have been successfully applied to silica, polymer, and gold-coated optical components and waveguides, there are no reports of use with III-V semiconductor surfaces.

Antibodies may be attached to silicon by first forming a thin, well-controlled oxide layer prior to deposition of a silane linker, and protocols are available from the reagent manufacturers. We have adapted this approach to coat InP and GaInAsP surfaces, by depositing a relatively thin SiO₂ layer by electron beam evaporation. The primary advantage of a semiconductor waveguide, that the evanescent field decays very rapidly for high sensitivity to surface-bound species, also requires that the SiO₂ and chemical binding layers must be kept very thin, preferably below 10 nm, so that the target species is bound within the evanescent field. Layers 3, 10, 20, and 30 nm thick were tested, all deposited on planar InP wafers or InP wafers with a planar GaInAsP epitaxial layer. No difference between InP or GaInAsP was observed. We tried a number of commercially available linkers, including APTES (3-aminopropyltriethoxysilane), MPTS (3-mercaptopropyl trimethoxysilane), GOPS (glycidoxypropyl trimethoxysilane), BioConext (trimethoxysilane aldehyde), CDI (1,1'-carbonyldiimidazole) and GMBS. Goat anti-glucose oxidase antibody, and glucose oxidase from *A. niger*, anti- β -galactosidase antibody and β -galactosidase, anti-mouse antibodies, and mouse gamma globulin were used as model antibody/antigen pairs. Proteins were labeled with NBD-X (succinimidyl 6-(N-(7-nitrobenz-2-oxa-1,3-diazol-4-yl)amino)hexanoate) or FITC (fluorescein isothiocyanate) fluorescent dyes when necessary for detection and quantitative measurements. Labeling was performed according to the manufacturer's recommendations. Labeled antigens were captured from solution in PBS-milk.

Immobilization of antibodies to the surface was quantified by using fluorescently labeled antibodies. The ability of the immobilized antibody to capture the corresponding antigen was quantified by using unlabeled antibodies and fluorescently labeled antigens. The results are summarized in Fig. 16, showing the fluorescent signal for both the

antibody immobilization and antigen capture, for several linker molecules, and on 10 nm and 30 nm oxide layers upon InP. We found that the highest antibody immobilization did not provide the best antigen capture efficiency, an effect well documented in the literature. We also found that both the immobilization and capture efficiency were poor on films less than 20 nm thick. Experiments using different ionic strength buffers during the silane deposition suggest that there is a surface charge at the InP-SiO₂ interface that interferes with saline binding. We expect that this can be rectified, so that a SiO₂ layer only a few nm thick will be effective.

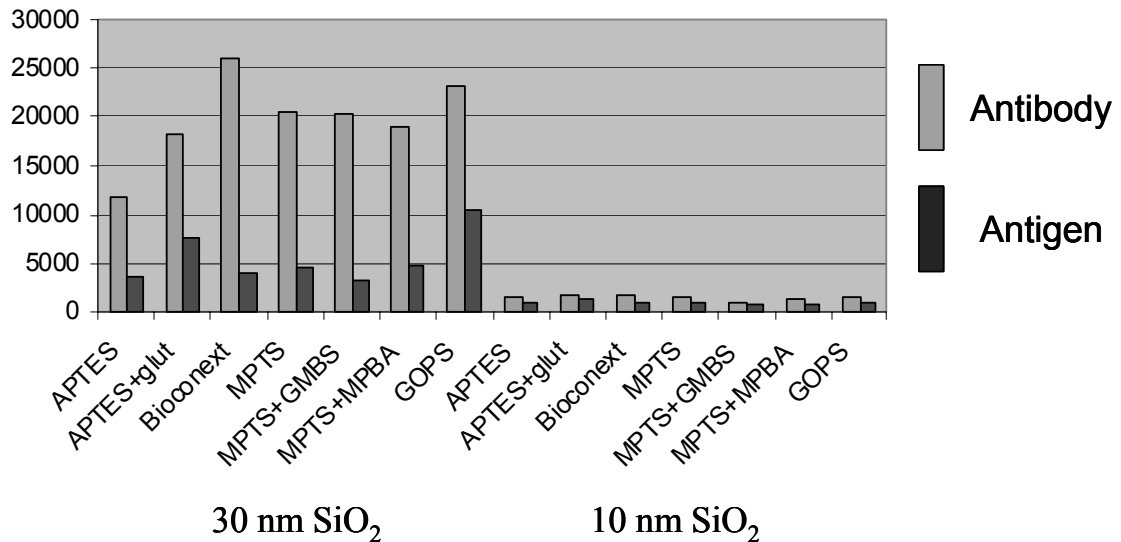


Figure 16. Antibody binding and activation on SiO₂-coated InP, with various linker molecules.

5. SUMMARY

We have discussed a novel monolithic sensor suitable for monitoring the purity of bulk fluids and capable of sensitive biochemical detection when coated with suitable capture ligands. Heterodyne detection was used to detect refractive index changes as small as $1 \cdot 10^{-4}$ within the evanescent field of the semiconductor optical waveguide, and the sensitivity may be improved to $1 \cdot 10^{-6}$ by replacing the asymmetrically clad ridge waveguide with a quasi-symmetrically clad structure. We verified this prediction with a simple coupled cavity sensor fabricated with a self-aligned technique based on oxidation of an AlAs cladding layer to AlO_x. We also demonstrated that this coupled-cavity device is useful for detection of cell-sized pathogens such as bacterial spores. Further development of these mass-deployable sensors may significantly improve our ability to monitor patient health, product quality, environmental conditions, and public safety.

ACKNOWLEDGEMENTS

This work was supported by the Defense Advanced Research Projects Agency (DARPA) through the BioFlips program, and the Army Research Office through the Institute for Collaborative Biotechnology.

REFERENCES

1. S. Y. Rabbany, B. L. Donner, and F. S. Ligler, "Optical immunosensors," *Critical Reviews in Biomedical Engineering*, **22**, 307-46, 1994.
2. G. Ramsay, *Commercial Biosensors*, John Wiley and Sons, New York, 1998.
3. W. Lukosz, "Integrated optical chemical and direct biochemical sensors," *Sensors & Actuators B*, **29**, 37-70, 1995.
4. K. M. Grace, K. Shrouf, S. Honkanen, P. Ayras, P. Katila, M. Leppihalme, R. G. Johnston, X. Yang, B. Swanson, and N. Peyghambarian, "Waveguide Zeeman interferometry for thin-film chemical sensors," *Electronics Letters*, **33**, 1651-1653, 1997.
5. R. G. Heidemann and P. V. Lambeck, "Remote opto-chemical sensing with extreme sensitivity: design, fabrication and performance of a pigtailed integrated optical phase-modulated Mach-Zehnder interferometer system," *Sensors & Actuators B*, **B61**, 100-127, 1999.
6. B. Maisenholder, H. P. Zappe, R. E. Kunz, M. Moser, and P. Riel, "Optical refractometry using a monolithically integrated Mach-Zehnder interferometer," presented at 1997 International Conference on Solid-State Sensors and Actuators, Chicago, IL, 16-19 June, 1997.
7. D. A. Cohen, E. J. Skogen, H. Marchand, and L. A. Coldren, "Monolithic chemical sensor using heterodyned sampled grating DBR lasers," *Electronics Letters*, **37**, 1358-1360, 2001.
8. B. Mason, G. A. Fish, S. P. DenBaars, and L. A. Coldren, "Widely tunable sampled grating DBR laser with integrated electroabsorption modulator," *IEEE Photonics Technology Letters*, **11**, 638-640, 1999.
9. C. S. Wang, D. A. Cohen, J. A. Nolde, D. D. Lofgreen, L. A. Coldren, "A monolithic diode laser chemical sensor with a quasi-symmetrical sensing waveguide for improved sensitivity," *Applied Physics Letters*, **85**, 320-322, 2004.
10. D. A. Cohen, J. A. Nolde, A. Tauke Pedretti, C. S. Wang, E. J. Skogen, L. A. Coldren, "Sensitivity and scattering in a monolithic heterodyned laser biochemical sensor," *IEEE Journal of Selected Topics in Quantum Electronics*, **9**, 1124-1131, 2003.
11. S. Kubitschko, J. Spinke, T. Bruckner, S. Pohl, and N. Oranth, "Sensitivity enhancement of optical immunosensors with nanoparticles," *Analytical Biochemistry*, **253**, 112-122, 1997.
12. P. L. Gourley, A. E. McDonald, J. K. Hendricks, G. C. Copeland, J. Hunter, O. Akhil, J. L. Dunn, S. L. Skirboll, L. Nihlen, H. Capps, "Nanolaser/microfluidic biochip for realtime tumor pathology," *Biomedical Microdevices*, **2**, 111-122, 1999.
13. D. A. Cohen, C. S. Wang, J. A. Nolde, D. D. Lofgreen, L. A. Coldren, "A monolithic evanescent field spore detector," paper IthB3, OSA Integrated Photonics Research Conference, San Francisco, CA, June 30-July 2, 2004.

* cohen@ece.ucsb.edu; phone 805-893-8489; fax 805-893-4500

I. Photonic Integrated Circuits and Related Technology

E. Materials Technology

Wafer-fused n-AlGaAs/p-GaAs/n-GaN Heterojunction Bipolar Transistor with uid-GaAs Base-Collector Setback

Sarah Estradaⁱ, James Champlain, Chad Wang, Andreas Stonas, Larry Coldren, Steven DenBaars, Umesh Mishra, and Evelyn Hu
Departments of Materials and Electrical & Computer Engineering, University of California, Santa Barbara, California 93106-5050
ⁱestrada@enr.ucsb.edu, <http://sarah.optimism.us/engineering/>

ABSTRACT

Recently we reported the first AlGaAs-GaAs-GaN heterojunction bipolar transistor (HBT), a device that potentially combines the high-breakdown voltage of an n-GaN collector with the high mobility of an AlGaAs-GaAs emitter-base.^{1,2} Because of the high degree of lattice mismatch between GaAs (lattice constant of 5.65Å) and GaN (3.19Å), we formed these devices through wafer fusion, also called direct wafer bonding. Measurements on the first generations of wafer fused HBTs revealed good current modulation, with modest output current (0.83 KA/cm²) and a current gain of 1.2.³ Limitations to the current gain may be related to traps and defects introduced by the fusion process, or may be a consequence of the natural conduction band offset between GaAs and GaN, which is not well known. This paper describes our new HBT structure that included a thin (20nm) uid-GaAs base-collector “setback” layer. The setback layer shifted the fused GaAs-GaN interface slightly into the collector. This new HBT structure also incorporated a reduced base thickness of 100 nm. HBTs with setback layers demonstrate increased output current (1.7 KA/cm²) and increased current gain (1.9).

INTRODUCTION

The large breakdown field and anticipated saturation velocity of GaN make this novel material particularly promising for high-frequency, high-power devices. With this goal in mind, quite a few researchers are working to develop GaN-based heterojunction bipolar transistors (HBTs).⁴⁻⁹ Although results thus far have been promising, there are still a number of outstanding materials issues. For example, AlGaN-GaN HBTs appear to be limited by large acceptor ionization energies and low hole mobilities.⁴ We describe the use of wafer fusion to form HBTs with an AlGaAs-GaAs emitter-base and a GaN collector. In this way, we hope to make use of both the high breakdown voltage of the GaN and the high mobility of the technologically more mature GaAs-based materials. Because the high degree of lattice mismatch between GaAs (lattice constant of 5.65Å) and GaN (3.19Å) precludes an all-epitaxial formation of this device, we fabricate the GaAs-GaN heterostructure via the novel technique of wafer fusion.

Our previous work on the wafer-fused (Al)GaAs-GaN HBTs identified the range of fusing conditions and temperatures to produce devices with modest output current and gain (1.2). In further improvements of the device performance, it is important to understand whether the

principal limitations to increased gain arise from defects, traps, and interface discontinuities associated with the wafer fusing process, or whether other means of bandgap engineering and device design can be used. The conduction band offset (ΔE_C) of the wafer-fused GaAs-GaN heterojunction is unknown. However, preliminary measurements and calculations indicated that a positive ΔE_C is likely.^{1,2} This positive ΔE_C would seriously impede current flow across the base-collector junction even in the absence of any defects or traps. To counteract a positive ΔE_C , our new device structure included a uid-GaAs base-collector “setback” layer. By decreasing the barrier in the conduction band at the base-collector junction, this new device structure increased collector current and hence current gain.

EXPERIMENT

Starting materials are depicted in Figure 1. The AlGaAs-GaAs emitter-base structure was grown by molecular beam epitaxy (MBE) at 585°C in a Varian Gen-II system. Carbon, rather than beryllium, was used as the p-GaAs dopant in order to minimize dopant diffusion during the high-temperature fusion procedure. The GaN collector structure was grown by metal-organic chemical vapor deposition (MOCVD) on c-plane (0001) sapphire at 1160°C. AlGaAs-GaAs and GaN were cleaved into rectangles (5-10mm), cleaned, rinsed in methanol, joined together in

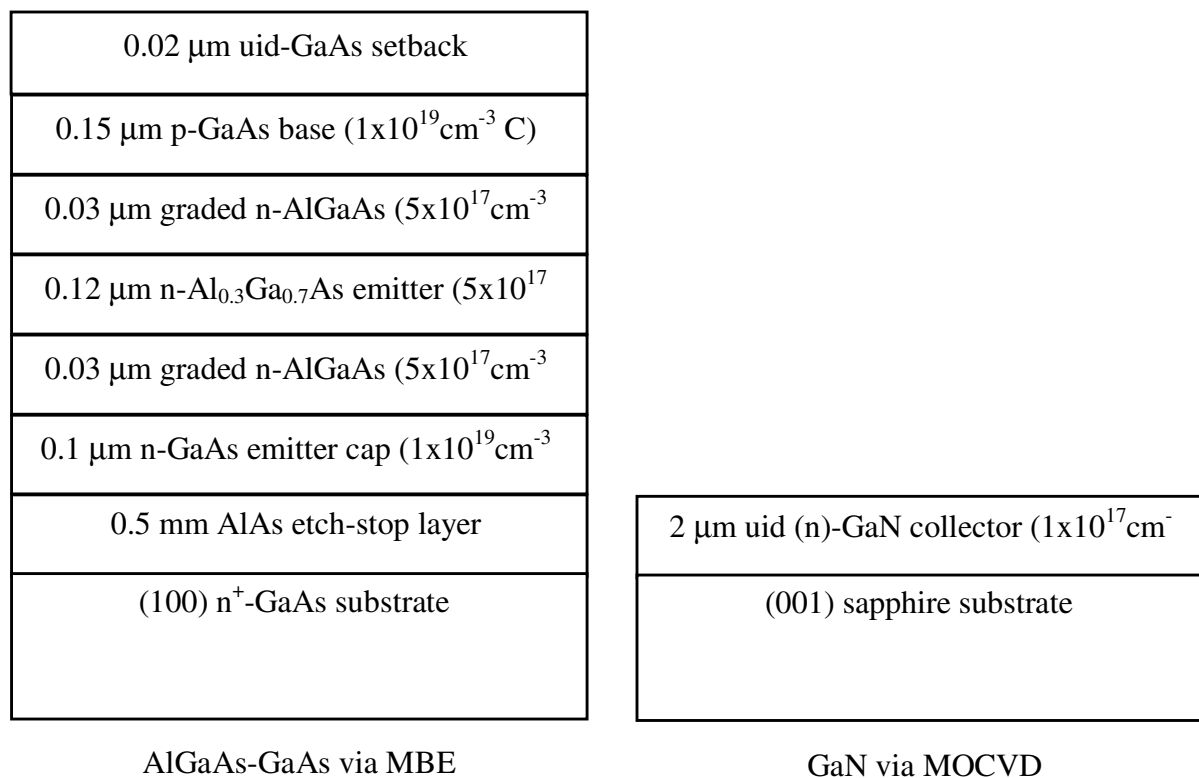


Figure 1. Starting materials for the wafer fusion of the third-generation n-AlGaAs/p-GaAs/n-GaN HBT. In the formation of the HBT, the GaAs and GaN top surfaces are fused together, and then the GaAs substrate and AlAs etch-stop layer are sequentially removed.

methanol, and annealed (“wafer-fused”) for one hour under a uniaxial pressure of 2 MPa in a nitrogen ambient. HBTs were fused over a wide range of systematically varied temperatures (550-750°C).

After fusion the GaAs substrate was removed via wet etching in $\text{H}_2\text{O}_2:\text{NH}_4\text{OH}$. This selective etch terminated at the AlAs layer, which was subsequently removed in HF. n-AlGaAs emitter mesas ($1 \times 10^{-5} \text{cm}^2$) and p-GaAs base mesas ($5 \times 10^{-5} \text{cm}^2$) were defined via wet etching in $\text{H}_3\text{PO}_4:\text{H}_2\text{O}_2:\text{H}_2\text{O}$. n-GaAs contacts were AuGeNi annealed at 415°C, p-GaAs contacts were ZnAu, and n-GaN contacts were unannealed AlAu.

RESULTS & CONCLUSIONS

This study demonstrated improved HBT electrical performance, due to the addition of a uid-GaAs base-collector setback layer. Figure 2 shows the materials structures and the common-

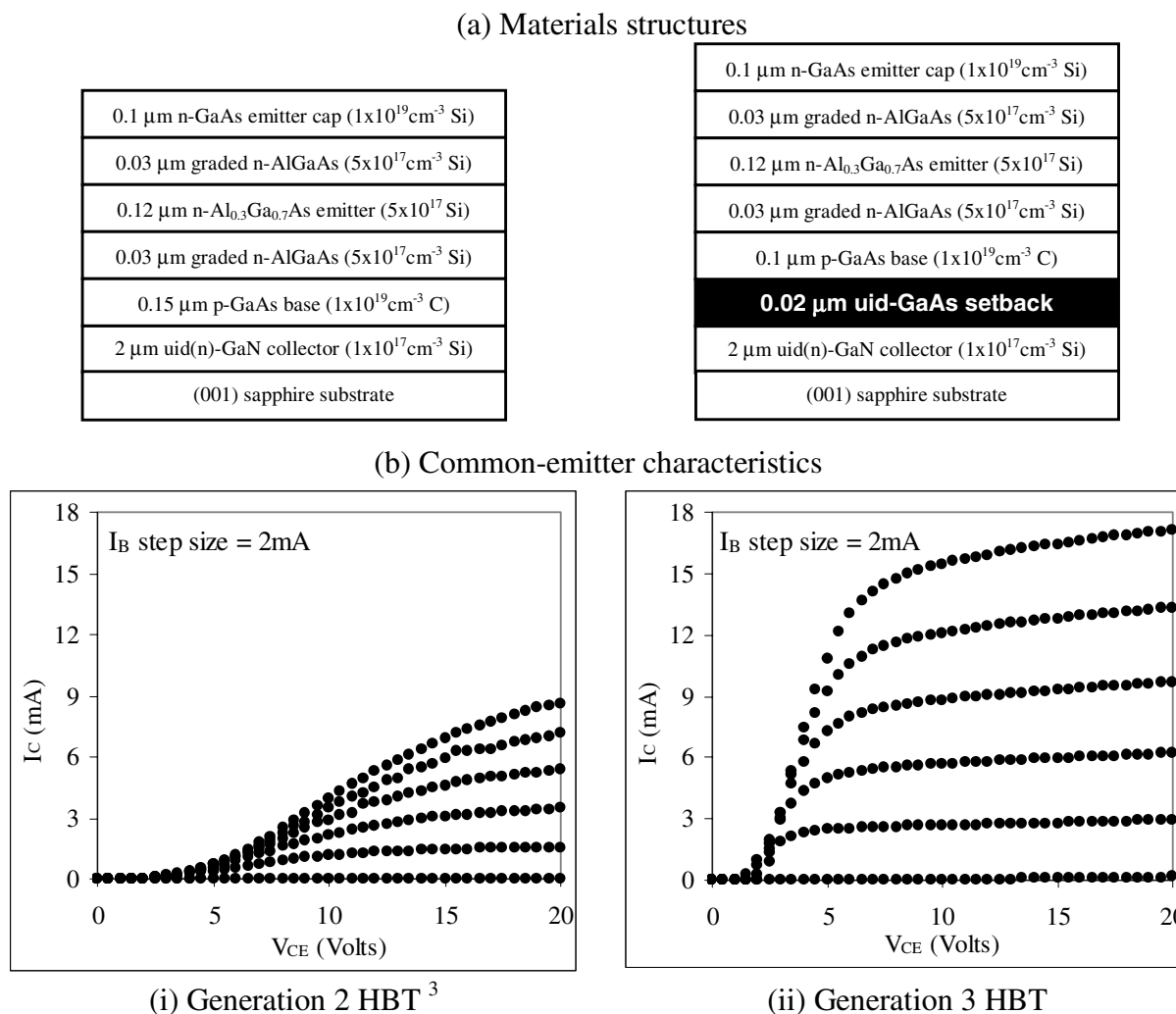


Figure 2. (a) Materials structures and (b) common-emitter characteristics of (i) Generation 2 and (ii) Generation 3 HBTs fused at 600°C. Generation 2 HBTs have no base-collector setback layer and have a thicker base.

emitter characteristics for Generation 2 and 3 HBTs fused at 600°C for one hour. Both generations of HBT devices were operable to a V_{CE} of 40V without breakdown. Devices were not tested at a V_{CE} greater than 40V, due to limitations of the testing equipment. A more detailed study of second-generation HBTs has been published elsewhere.³ Unlike Generation 2, Generation 3 HBTs include a base-collector setback layer. A setback layer shifts the fused GaAs-GaN interface slightly into the collector, decreasing the barrier prior to the conduction band spike at the fused junction. This accounts for the marked improvement in collector current and current gain demonstrated in Figure 2. Also, the Generation 3 HBT utilizes a thinner base (100nm rather than 150nm).

ACKNOWLEDGMENTS

This work was supported by the Department of Defense Multidisciplinary University Research Initiative (MURI) program administered by the Office of Naval Research under Grant N00014-98-1-0654, with Project Monitors Drs. Harry Dietrich and John Zolper. We acknowledge the contributions of Santa Barbara High School Apprentice Researchers Chelsea Teall and Craig Silverman.

REFERENCES

- ¹ S. Estrada, A. Stonas, A. Huntington, H. Xing, L. Coldren, S. DenBaars, U. Mishra, and E. Hu, in *The First Wafer-Fused AlGaAs-GaAs-GaN Heterojunction Bipolar Transistor*, Boston, Massachusetts, Fall 2002 (Materials Research Society), p. L12.10.
- ² S. Estrada, H. L. Xing, A. Stonas, A. Huntington, U. Mishra, S. DenBaars, L. Coldren, and E. Hu, *Applied Physics Letters* **82**, 820-822 (2003).
- ³ S. Estrada, A. Huntington, A. Stonas, H. Xing, U. Mishra, S. DenBaars, L. Coldren, and E. Hu, *Applied Physics Letters* **83**, 560-562 (2003).
- ⁴ Y. M. Zhang, C. Cai, and P. P. Ruden, *Journal of Applied Physics* **88**, 1067-1072 (2000).
- ⁵ S. Y. Chiu, A. F. M. Anwar, and S. L. Wu, *MRS Internet Journal of Nitride Semiconductor Research* **4**, G6.7 (1999).
- ⁶ J. T. Torvik, M. Leksono, J. I. Pankove, and B. Van Zeghbroeck, *MRS Internet Journal of Nitride Semiconductor Research* **4** (1999).
- ⁷ S. Yoshida and J. Suzuki, *Japanese Journal of Applied Physics Part 2-Letters* **38**, L851-L853 (1999).
- ⁸ J. Han, A. G. Baca, R. J. Shul, C. G. Willison, L. Zhang, F. Ren, A. P. Zhang, G. T. Dang, S. M. Donovan, X. A. Cao, H. Cho, K. B. Jung, C. R. Abernathy, S. J. Pearton, and R. G. Wilson, *Applied Physics Letters* **74**, 2702-2704 (1999).
- ⁹ H. Xing, S. Keller, Y. F. Wu, L. McCarthy, I. P. Smorchkova, D. Buttari, R. Coffie, D. S. Green, G. Parish, S. Heikman, L. Shen, N. Zhang, J. J. Xu, B. P. Keller, S. P. DenBaars, and U. K. Mishra, *Journal of Physics-Condensed Matter* **13**, 7139-7157 (2001).

A Study of Regrowth Interface and Material Quality for a Novel InP Based Architecture

James W. Raring, Erik J. Skogen, Larry A. Coldren, and Steven P. DenBaars

Monolithic integration of photonic integrated circuits is at the forefront of research in the InP based material system. Innovative device architectures utilizing unique growth/processing schemes must be employed to maintain rapid progression. This work examines a new technology, coupling the use of a quantum-well-intermixing (QWI) processing platform and an offset quantum-well regrowth. By intermixing the centered-quantum-well base structure to render it non-absorbing, and then regrowing offset wells, the saturation power in semiconductor-optical-amplifiers can be greatly increased. Achieving a high material quality regrowth on a surface subjected to heavy processing and defect diffusion during the intermixing process is vital to the performance of the offset quantum-wells. Using photoluminescence we will show the effects of pre-regrowth surface preparation and QW/interface offset distance on the material quality of the offset wells. We have demonstrated for the first time that good material quality can be achieved when regrowing on surfaces with intermixed material beneath.

High-Quality Grating Regrowth Interface in the InP/InGaAsP Material System Using TBA and TBP

Erik J. Skogen, Jonathon S. Barton, Larry A. Coldren, and Steven P. DenBaars

A key aspect to the realization of wavelength-agile photonic-integrated-circuits is the formation of high index contrast InP/InGaAsP gratings. A matrix of reactive-ion etch and MOCVD regrowth experiments were used to study the quality of the regrowth interface in InP/InGaAsP grating regions as compared to regions without gratings (InP), using photoluminescence measurements. The modified regrowth procedure consists of a warm-up under tertiarybutylphosphine (TBP) and tertiarybutylarsine (TBAs) overpressure, and elimination of a high temperature pre-growth bake. The goal was to reduce the group-V exchange on the surface during warm-up, which can lead to highly strained interface layers. The photoluminescence intensity of the regions with gratings was strongly affected by the modification in the etch process and MOCVD regrowth program. This process was used in the fabrication of widely tunable sampled-grating (SG) distributed Bragg reflector (DBR) lasers, which exhibited excellent characteristics in terms of injection efficiency, modal loss, and carrier induced tuning.



A study of regrowth interface and material quality for a novel InP-based architecture

James W. Raring^{a,*}, Erik J. Skogen^b, Steven P. Denbaars^a, Larry A. Coldren^b

^aMaterials Department, University of California, Santa Barbara, CA 93106, Santa Barbara, USA

^bElectrical and Computer Engineering Department, University of California, Santa Barbara, USA

Received 28 July 2004; accepted 30 July 2004

Communicated by G.B. Stringfellow

Available online 5 October 2004

Abstract

This work examines a new technology, coupling the use of a quantum-well-intermixing processing platform and an offset quantum-well regrowth. Achieving a high material quality regrowth on a surface subjected to heavy processing and defect diffusion during the intermixing process is vital to the performance of the offset quantum wells. Using photoluminescence, atomic force microscopy, and fabricating broad area lasers, we demonstrate for the first time that good material quality can be achieved when regrowing on surfaces with intermixed material beneath. Further, we achieve regions of high and low optical confinement on the same chip.

© 2004 Elsevier B.V. All rights reserved.

PACS: 42.55.X; 85.60; 81.05.P

Keywords: A1. Atomic force microscopy; A2. Metalorganic chemical vapor deposition A3. Quantum wells; B1. Phosphides; B2. Semiconducting indium phosphide; B3. Laser diodes

1. Introduction

Monolithically integrated photonic circuits offer tremendous advantages for applications in optical networks. These advantages include high functionality, improved efficiency, decreased size, and

lower costs. As the degree of complexity within a photonic integrated circuit (PIC) increases, the realization of an optimally performing device becomes more intricate. Monolithic integration often imposes design constraints due to the difficulty achieving multiple quantum well bandedges (MQW) and the limitation of a two-dimensional growth platform on a single chip. These constraints often demand performance trade-offs in the individual components within

*Corresponding author. Tel.: 805-893-7163; fax: 805-893-4500.

E-mail address: jraring@engineering.ucsb.edu (J.W. Raring).

the PIC, thus limiting the overall performance of the device.

The integration of a diode laser with a semiconductor optical amplifier (SOA) is one such example in which traditional monolithic integration schemes impose trade-offs. High modal gain is desired in the laser such that low threshold currents and high output powers can be achieved. The threshold modal gain (Γg_{th}) is governed by Eq. (1), where Γ is the optical confinement factor, g_{th} is the threshold material gain, α_i is the optical loss in the cavity, and α_m is the mirror loss. From Eq. (1) it is clearly advantageous to maximize the optical confinement factor within the laser to achieve high modal gain.

$$\Gamma g_{\text{th}} = \alpha_i + \alpha_m, \quad (1)$$

$$P_s = \frac{wdhv}{a\Gamma\tau}. \quad (2)$$

Saturation power, P_s , defined as the input power at which the gain drops by 3 dB, is a critical consideration in SOA design. The saturation power (P_s) can be approximated by Eq. (2) [1], where w is the width of the gain region, d is the thickness of the gain region, a is the differential gain of the material, τ is the carrier lifetime, and again Γ is the optical confinement factor. From Eq. (2), it is clear that for the realization of high saturation power SOAs, a low optical confinement factor is desirable. Thus, there is clear performance trade-off between the integrated laser and SOA imposed by the optical confinement properties of the device architecture.

Here we present and study an innovative fabrication/growth scheme to circumvent the traditional trade-off discussed above by realizing regions of both high and low optical confinement on the same chip. We employ a robust quantum well intermixing (QWI) processing platform [2] coupled with a novel growth architecture to achieve regions possessing either a high optical confinement centered multiple quantum well (c-MWQ) gain section or regions possessing an offset MQW (o-MQW) gain section with an optical confinement which can be adjusted based on the offset regrowth.

We have demonstrated the ability to achieve high-quality quantum well material grown short distances above a regrowth interface which had been subjected to vacancy diffusion during the QWI process. Furthermore, we achieved a $7\times$ reduction in modal gain from Fabry–Perot broad area lasers possessing an o-MQW active region over those with the c-MQW active region fabricated on the same chip.

2. Theory

The optical confinement factor is defined as the electron–photon overlap in the gain region of a device [1]. However, assuming a uniform carrier distribution, it can be approximated by the volume of the optical mode within the gain medium divided by the total volume of the optical mode and is governed by both the geometry and the refractive indices of the materials comprising the optical waveguide of the device. It has been shown that placing the MQW region in the center of a symmetric waveguide results in a maximized confinement factor. Thus, the c-MQW structure is ideal for employment in the gain section of a diode laser [3]. By placing the MQW region in a manner such that it is offset from the waveguide, the optical confinement is reduced by an amount governed by the degree of offset.

In this work, we begin with the growth of a c-MQW base structure. In regions where low optical confinement is desired, the c-MQW region is subjected to a QWI process to blueshift the band edge, effectively rendering it a passive waveguide to the operating wavelengths of the final device. A regrowth is then performed over the entire chip consisting of an InP offset layer and a MQW region. The o-MQW and offset InP layer are then selectively removed in regions above the as-grown c-MQW. The result is two regions on a single chip, one with high optical confinement and the other with a reduced optical confinement, c-MQW and o-MQW, respectively. A schematic of this structure is presented in Fig. 1.

A finite difference technique was used to solve the wave equation and compute the optical confinement within the active quantum wells for

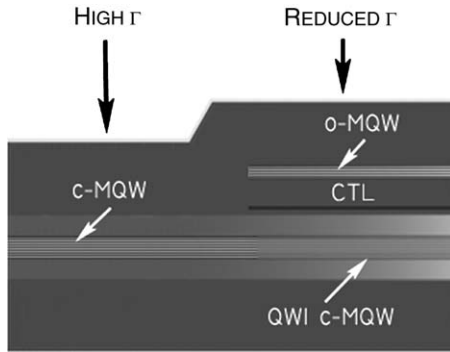


Fig. 1. Side view schematic of the device structure for the c-MQW high modal gain region (left) and the o-MQW with reduced modal gain (right).

both regions. The refractive index and simulated optical mode are plotted in Fig. 2. From the figure, it is clear that the optical mode overlap with the active wells is far higher in the c-MQW (Fig. 2a) than it is in the o-MQW (Fig. 2b).

As discussed above, the optical confinement in the o-MQW structure is governed by the degree of offset. Thus the optical confinement in the o-MQW architecture in this work can be tailored by the InP offset layer thickness. This layer will be referred to as the confinement tuning layer (CTL). To show how the optical confinement is influenced by the CTL and number of o-QWs, the finite difference technique was used to solve for the optical confinement as a function of the number of quantum wells for three different CTL thicknesses as shown in Fig. 3. The results of this simulation indicated no excitation of higher order transverse optical modes in the o-MQW regions.

3. Process

The process used to realize regions of both high and low optical confinement on a single chip suitable for device application is as follows. First, the epitaxial base structure is grown on an InP substrate using a Thomas Swan Scientific Equipment Ltd. horizontal-flow rotating-disc MOCVD reactor. The active region consists of ten 7.0 nm compressively strained (1.0%) quantum wells, separated by 8.5 nm tensile strained (0.3%) bar-

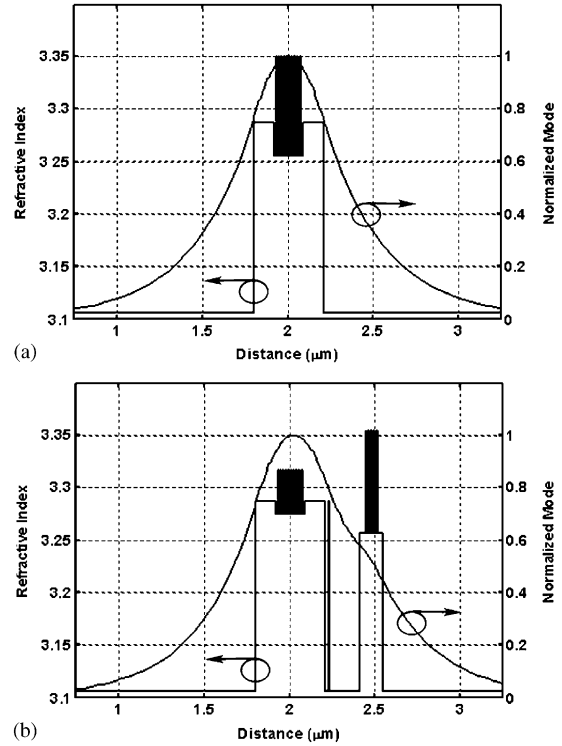


Fig. 2. Refractive index, and mode profile versus distance in the growth direction for (a) the c-MQW high modal gain region and (b) the o-MQW reduced modal gain region.

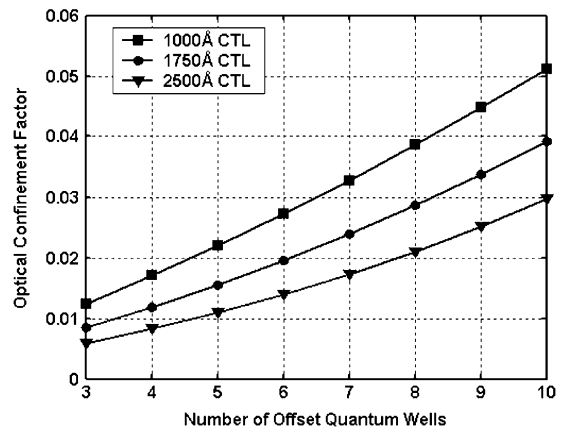


Fig. 3. Confinement factor versus the number of offset quantum wells for CTLs of 1000, 1750, 2500 Å.

riers, centered within two InGaAsP (1.3Q) layers designed to maximize the optical confinement in the quantum wells. Following the active region, a

15 nm InP regrowth layer, a 20 nm 1.3Q stop etch, and a 450 nm InP implant buffer layer are grown.

The regions in which high optical confinement is desired are masked with 500 nm of Si_xN_y , and a P^+ implant is carried out at an energy of 100 keV, yielding a range of 90 nm, with a dose of $5\text{E}14\text{cm}^{-2}$, at a substrate temperature of 200°C [2]. During a high-temperature anneal, the vacancies created during the implant above the unmasked regions are diffused through the c-MQW region, promoting the interdiffusion of group V-atoms between the wells and barriers. The interdiffusion reshapes the quantum well profile by distorting the quantum well/barrier interface, effectively blue-shifting the bandedge.

Following the QWI process, the implant buffer layer and 1.3Q stop etch layers are removed using selective wet chemical etching, leaving a thin InP regrowth layer on the surface. An MOCVD regrowth is performed for the growth of a thin InP:Si layer followed by a 1.3Q:Si stop etch layer, the InP:Si CTL (1750 Å), the o-MQW consisting of five quantum wells, and a thin InP:Zn cap. The wafer is then patterned with Si_xN_y and a selective wet chemical etch process is carried out such that the o-MQW remains only in regions where the c-MQW was blue-shifted. A second MOCVD regrowth process is performed to grow the p-type InP:Zn cladding and p-contact InGaAs:Zn layers. A step by step illustration of this process is shown in Fig. 4.

4. Experiment and results

4.1. Regrowth surface preparation

The ability to regrow high-quality MQW active regions in the o-MQW regions is essential for efficient device components operating in these sections. Since the offset wells will be placed in close proximity (2000 Å) and the optical mode will span and propagate parallel to the regrowth interface, it is of great importance to achieve a regrowth surface free from contaminants, which could act as non-radiative recombination sites. Thus the pre o-MQW regrowth surface preparation procedure should be optimal.

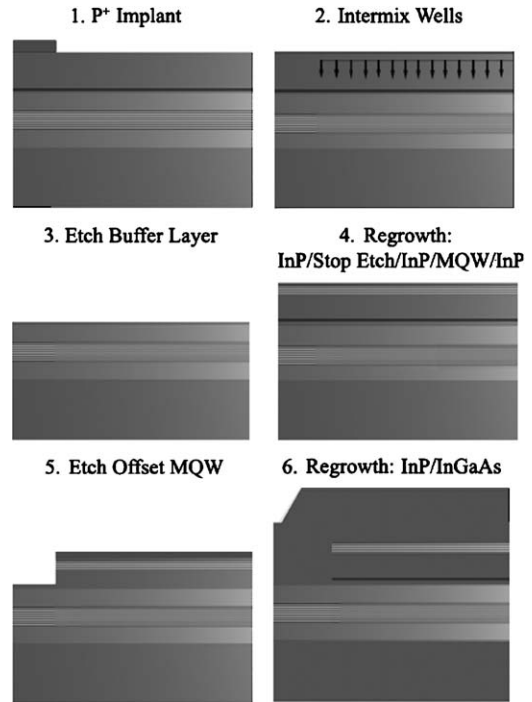


Fig. 4. Step-by-step illustration of the procedure required to achieve regions of both high and low optical gain in our architecture. The region on the left again contains the c-MQW with high optical confinement while that on the right possesses the o-MQW with a tunable optical confinement.

In order to study the effect of surface preparation on regrown MQW quality, the offset quantum well regrowth was performed on both epitaxial surfaces not subjected to the QWI process and on surfaces that had been subjected to QWI as described in the process section. The study characterized the influence of three different surface preparation procedures for two different CTL thicknesses, 500 and 2000 Å.

The first procedure, performed on the control samples, consisted of only blowing the sample surfaces with filtered N_2 . Following this step, the samples were immediately loaded into the MOCVD reactor. The second procedure required the placement of the samples in an oven where they were exposed to ultraviolet radiation and ozone (UV ozone) for 60 min in order to form an oxide on the sample surfaces. After they were removed from the oven, they were blown with N_2

and immediately loaded in the MOCVD reactor. The final regrowth preparation procedure was identical to that of the second with the addition of a 30' buffered hydrofluoric acid (BHF) dip and a 5' rinse with deionized (DI) water. After they were removed from the DI, the samples were blown dry with N_2 and immediately loaded into the MOCVD reactor.

Samples of all three cleaning procedures and of both QWI material and non-QWI epitaxial material were subjected to two growths, with the only difference being the CTL thickness. The growths began with the CTL layer of either 500 Å or 2000 Å of InP, followed by the o-MQW region containing four quantum wells ($\lambda = 1605$ nm) and a 1000 Å InP cap. Photoluminescence measurements were made on all samples and are presented in Fig. 5.

Fig. 5a shows the PL intensity of samples subjected to each of the three preparation procedures for a CTL thickness of 500 Å grown on non-QWI epitaxial material. From this plot, it is clear that the preregrowth sample preparation procedure has a large influence on the peak PL intensity at a CTL thickness of 500 Å. The sample that was only exposed to the UV ozone and no BHF demonstrated a $4 \times$ increase in intensity over the control sample and nearly a $3 \times$ increase in the sample dipped in BHF and rinsed with DI water. Fig. 5b shows the PL results from the same growth scheme grown on QWI material. The peaks centered at 1605 nm correspond to the o-MQW while those centered at 1480 nm correspond to the QWI c-MQW below. The same trend can be observed here as in Fig. 5a, with the sample only exposed to the UV ozone possessing the strongest intensity and the control sample the weakest.

Exposure to ultraviolet radiation and ozone at elevated temperatures promotes the formation of a thin oxide layer on the surface of the sample. The intention is to remove this oxide just prior to growth, such that a clean InP surface is exposed for deposition. The samples exposed to the UV ozone clearly demonstrated stronger PL intensities than the control sample, especially on the samples grown on QWI material.

The two procedures employing the UV ozone in this study relied on different mechanisms for oxide

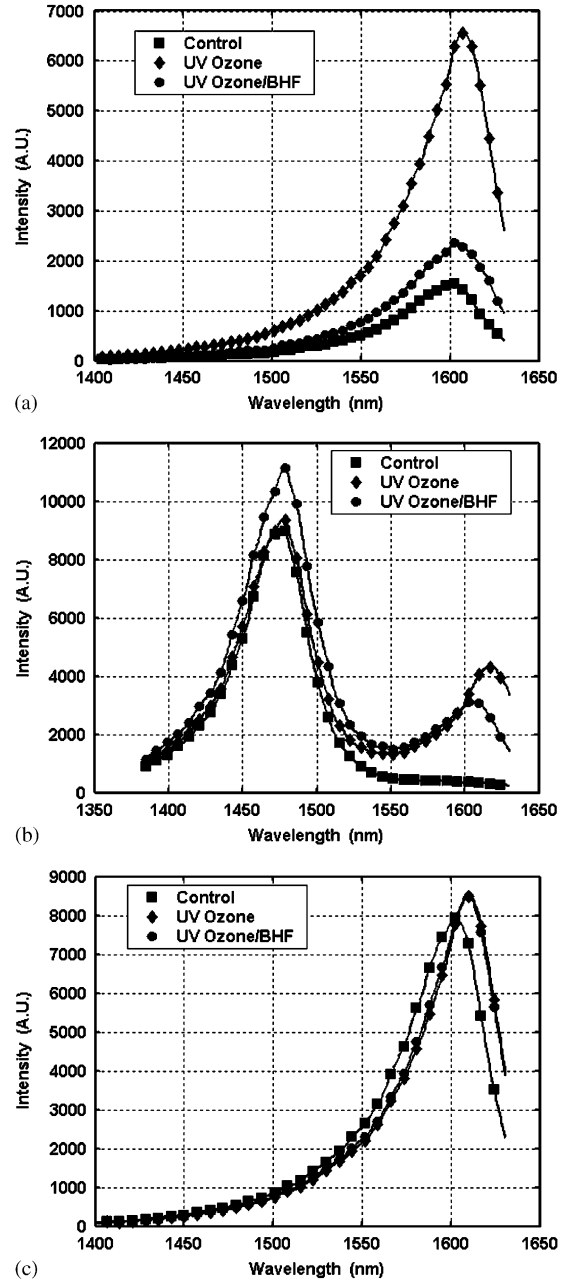


Fig. 5. Photoluminescence data for the three described surface preparation procedures with quantum wells grown on (a) an epitaxial InP layer 500 Å from the interface, (b) an InP regrowth layer with intermixed wells below 500 Å from the interface, and (c) an epitaxial InP layer 2000 Å from the interface.

removal prior to regrowth. The procedure resulting in the strongest intensity which did not contain the BHF dip relied on thermal desorption of the oxide during the temperature ramp in the reactor prior to the onset of growth. The sequence of steps and method of oxide removal in the process using the BHF dip intrinsically made the regrowth surface more susceptible to contamination, as it exposed the surface not only to acid and DI water, but also to the laboratory and MOCVD loading environments before the onset of growth. It is possible that the BHF dip procedure resulted in residual fluorine ions on the sample surface [4]. Thus the significantly lower PL intensity of the samples relying on the wet removal of the oxide can be attributed to contamination at the regrowth interface.

Fig. 5c presents the PL results from the growth on non-QWI material with a CTL thickness of 2000 Å. At this CTL thickness the peak PL intensities are nearly identical and it is clear that the sample regrowth interface does not strongly affect the PL properties. The slight difference in the peak PL intensities of all the samples with the 2000 Å CTL and that exposed to the UV ozone and no BHF with the 500 Å CTL illustrates the effectiveness of this surface preparation procedure.

4.2. *o*-MQW CTL layer smoothness

The QWI process requires the diffusion of defects, vacancies, through the InP implant buffer layer, 1.3Q stop etch, thin InP regrowth layer, and finally into the c-MQW region. Due to the compositional gradient present at the 1.3Q/InP regrowth layer interface, the diffusing vacancies will inevitably result in some degree of intermixing at this interface. As mentioned above, the 1.3Q stop etch is removed using a selective wet chemical etch, to expose the InP regrowth layer. The local intermixing that occurs at this interface in regions exposed to QWI will likely result in a roughening of the regrowth surface compared to regions not exposed to QWI.

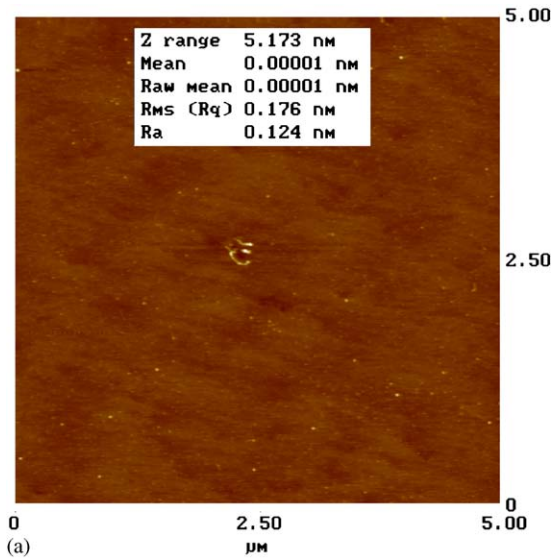
To study the effects of the QWI process on the regrowth surface, samples were grown and processed to simulate the regrowth surface without the intermixed c-MQW below. The samples con-

sisted of a 1 µm InP buffer layer followed by a 150 Å 1.3Q stop etch layer, and a 4500 Å implant buffer layer grown on top of an InP:S substrate. Half of these samples were implanted with P⁺ as described in the process section of this article, and all of the samples were subjected to the rapid thermal annealing process and the wet etch steps for removal of the implant buffer layer and stop etch. Without the intermixed c-MQW region below, these samples allowed for direct comparison of PL intensities of MQWs grown on regrowth surfaces both subjected to and not subjected to the QWI process.

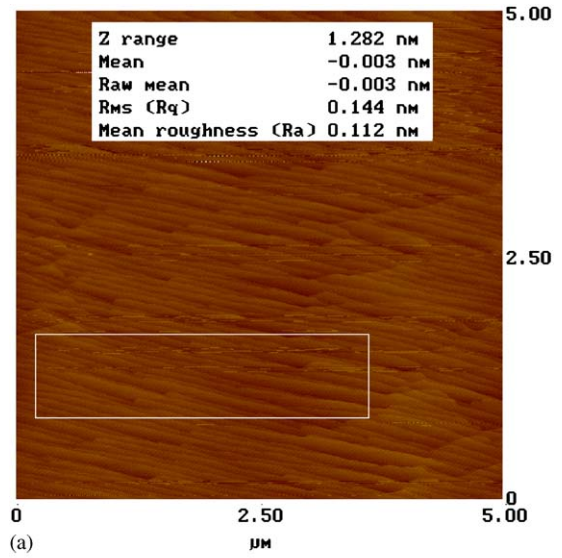
Fig. 6a shows a 5 µm by 5 µm atomic force microscopy (AFM) scan of a regrowth surface not subjected to the QWI process demonstrating an RMS smoothness of 0.176 nm. Fig. 6b shows an AFM scan of a regrowth surface which had been subjected to the QWI process demonstrating an RMS roughness of 1.728 nm. It is clear that the diffusion of vacancies through the 1.3 Q stop etch/InP regrowth layer interface degraded the regrowth surface characteristics.

To achieve high-quality quantum wells, it is essential that they are grown on a smooth surface such that thickness variations and scattering losses can be minimal. From the AFM scans shown in Fig. 6, it is obvious that for the realization of high-quality quantum wells in the regions subjected to QWI, the InP CTL must behave as a smoothing buffer layer for the growth of the *o*-MQW.

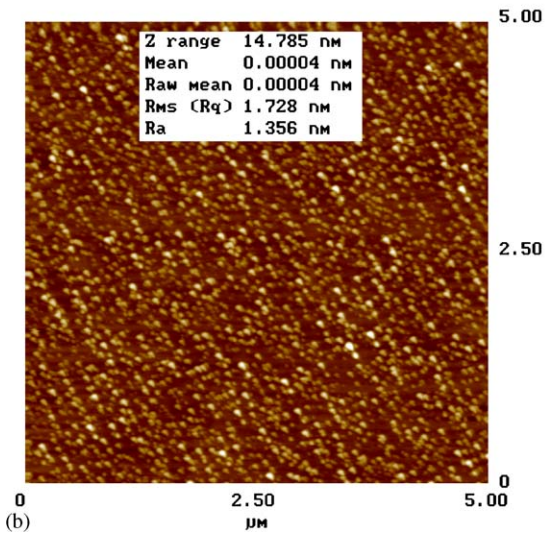
In order to characterize the smoothing characteristics of the CTL, an interrupted growth technique was performed. Samples with regrowth surfaces of both types shown in Fig. 6 were subjected to a regrowth procedure identical to that used for the *o*-MQW growth with the alteration of interrupting the growth immediately before the *o*-MQW. A 2000 Å smoothing CTL was grown under our standard conditions of a growth temperature at 590 °C, a reactor pressure at 350 Torr, a V/III ratio of 60, and a growth rate of 3.8 Å/s. AFM scans were performed on both surfaces following the growth and are presented in Fig. 7. Box analysis was employed on the AFM data in which the analysis results over the entire scan were not representative of the surface. As shown in Fig. 7, the CTL buffer layer RMS



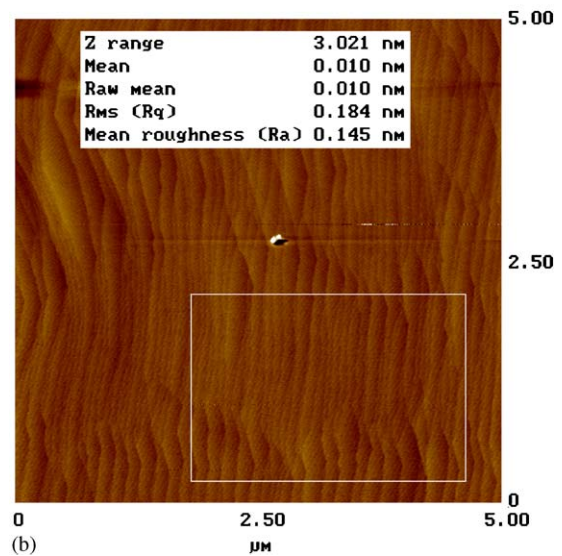
(a)



(a)



(b)



(b)

Fig. 6. AFM images of the regrowth surface on a sample (a) not subjected and (b) subjected to the intermixing process.

roughness over the non-intermixed region was only slightly higher than that subjected to the intermixing process, with RMS values of 0.144 and 0.184 nm, respectively. By decreasing the roughness by nearly $10\times$ with a 2000 \AA CTL layer, the ability to achieve a smoothing buffer layer for the growth of o-MQWs has been demonstrated.

Although the RMS roughness (0.184 nm) of the buffer layer over the intermixed regions appears suitable for the growth of high-quality quantum

Fig. 7. AFM images of the CTL layers grown on a sample not subjected (a) and subjected (b) to the intermixing process. The growth was interrupted just prior to onset of offset quantum well growth.

wells, a study was performed in an attempt to improve upon the smoothness and understand its significance at these low roughness values. Three separate interrupted regrowths on samples subjected to intermixing were performed, with only the following changes in the MOCVD growth parameters: the first growth was done at a reactor

pressure of 100 Torr, the second growth was performed at a V/III ratio of 30, and the third growth was done with both a 100 Torr reactor pressure and a V/III ratio of 30. These growth condition modifications were intended to increase the surface diffusion length of the group III adatoms, promoting a smoother growth surface. AFM scans from the buffer layers grown under the varying conditions are shown in Fig. 8. The RMS roughness data indicate that modified conditions provide a slightly smoother surface with the RMS values 0.151, 0.153, and 0.135 nm in the respective order that growth conditions were described.

In order to understand the degree of influence the slight improvements in smoothness would provide for the quantum well quality, the samples with the intermixed regrowth layer with the four different CTL smoothing layer growth condition schemes were subjected to another MOCVD regrowth. In this growth, five quantum wells were grown 500 Å above the interface. PL measurements were made on these samples and are presented in Fig. 9a. According to Fig. 9a, there is no correlation with the buffer layer smoothness and the quality of the MQW. With a slight exception of the sample with only the lowered V/III ratio, the full width at half of the maximum intensity (FWHM) and peak intensities are nearly identical. This is indicative that the slight improvements made in the RMS smoothness of the CTL layer by modifying the reactor conditions are not necessary for the realization of high-quality MQW active regions.

For final verification that our standard reactor conditions are sufficient for the growth of a smooth/high-quality MQW region above a regrowth interface subjected to vacancy diffusion, a non-interrupted growth experiment was performed. In this study, a 5 MQW region was grown 2000 Å on both surfaces which had and had not been subjected to QWI as shown in Figs. 6a and b, respectively. Photoluminescence measurements were made on the MQW regions and compared as shown in Fig. 9b. Since there is no significant difference in the FWHM of the spectra and the intensity is slightly higher for the MQW region grown above the intermixed regrowth surface, the sufficiency of the standard reactor conditions for this type of growth was confirmed.

4.3. Fabrication of Fabry–Perot broad area lasers

In the previous sections of this article, it was shown using AFM and photoluminescence analysis that good MQW material quality can be achieved on a regrowth surface exposed to QWI. In this section we describe our final experiment to determine the suitability of this material for employment in optoelectronic devices. Fabry–Perot lasers were fabricated out of material both exposed and not exposed to QWI on the same chip. Key figures of merit were then compared for both sets of devices such as threshold current density, injection efficiency, and optical loss.

Two device structures were fabricated on the same chip, one with a c-MQW gain region for high optical confinement and the second with a reduced optical confinement utilizing an o-MQW gain region. The fabrication sequence is as described in the process section of this article and illustrated in Fig. 4. Two chips were processed with slightly different doping schemes in the base structure waveguide in an attempt to optimize the injection efficiency of the o-MQW region.

The composition, layer thickness, and doping levels of the final epitaxial structure for both regions are given in Table 1. A and B indicated in the doping level column for the lower 1.3Q waveguide of the c-MQW represent the two different doping schemes used in this experiment. In sample A, neither the upper or lower waveguide were intentionally doped, and in sample B the lower waveguide was doped with Si at $1E17\text{ cm}^{-3}$. The $2.5E18\text{ cm}^{-3}$ Zn doping spike was employed to promote Zn diffusion to compensate the Si doping in the thin layers above the upper waveguide necessary for the o-MQW.

Fabry–Perot broad area lasers were fabricated from both structures on each chip with the two different doping schemes. In this work the peak photoluminescence wavelength of the c-MQW was shifted from 1548 to 1420 nm and the regrown o-MQW had a peak photoluminescence wavelength of 1560 nm in the regions where low optical confinement was desired. The photoluminescence data are presented in Fig. 10, showing the peak intensity for the as-grown c-MQW at 1548 nm, the

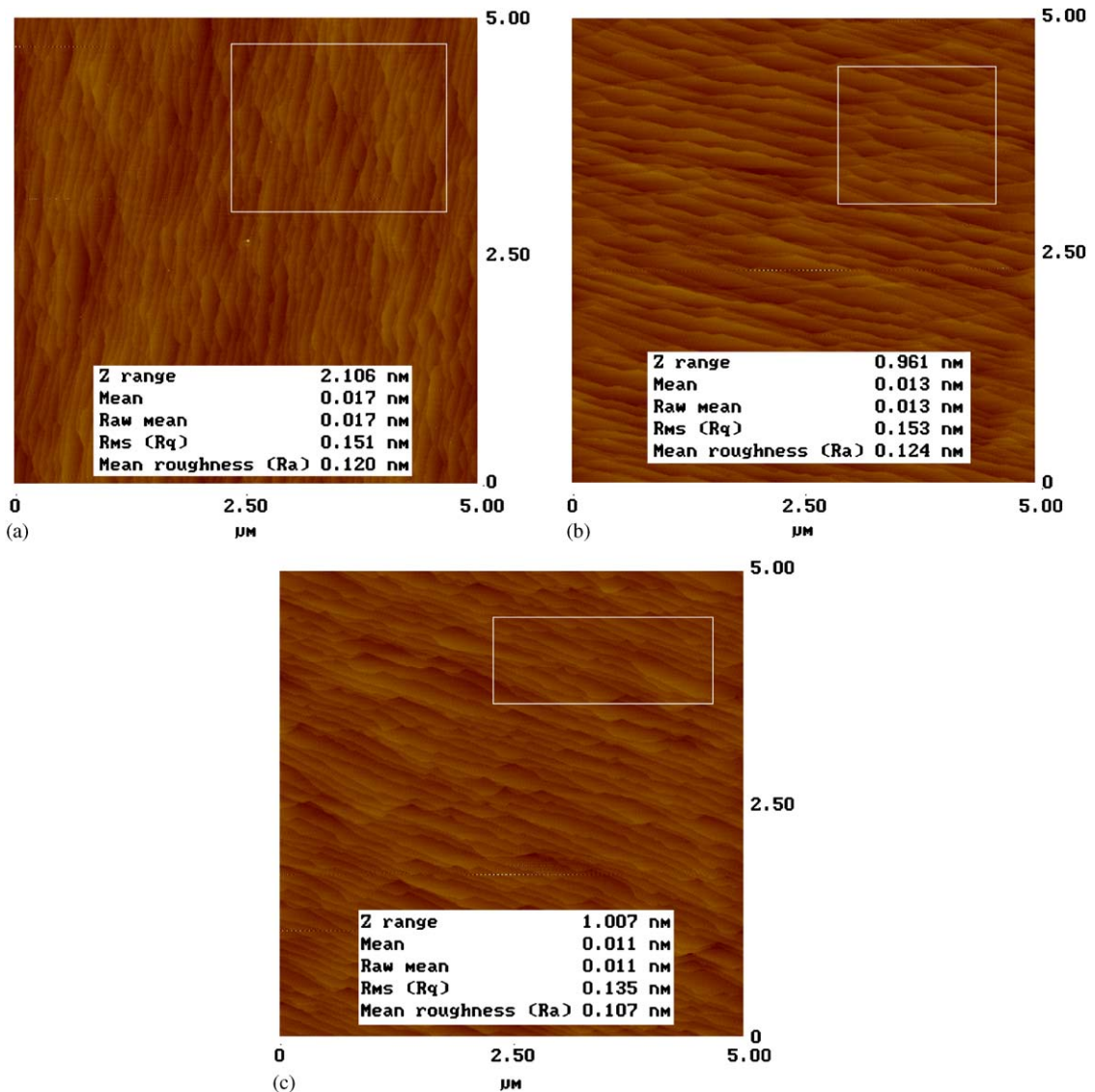


Fig. 8. AFM images of the 2000 Å CTL layers grown (a) at 100 Torr, (b) V/II = 30, and (c) at 100 Torr and V/III = 30.

intermixed c-MQW at 1420 nm, and the o-MQW at 1560 nm.

The 50 μm broad area lasers were cleaved into bars of various lengths and pulse tested. The inverse differential efficiency was plotted versus broad area laser length to extract the injection efficiency and modal loss associated with both device structures as shown in Fig. 11. The injection efficiency was extracted and found to be 86% for

the c-MQW for both doping schemes. This injection is in good agreement with past c-MQW broad area devices fabricated without the offset quantum well regrowth. The injection efficiency in the o-MQW gain region was found to be 61% for doping scheme A and 80% for doping scheme B. The improved injection efficiency with the lower waveguide doped at $1 \times 10^{17} \text{ cm}^{-3}$ in the o-MQW devices demonstrates the ability to effectively

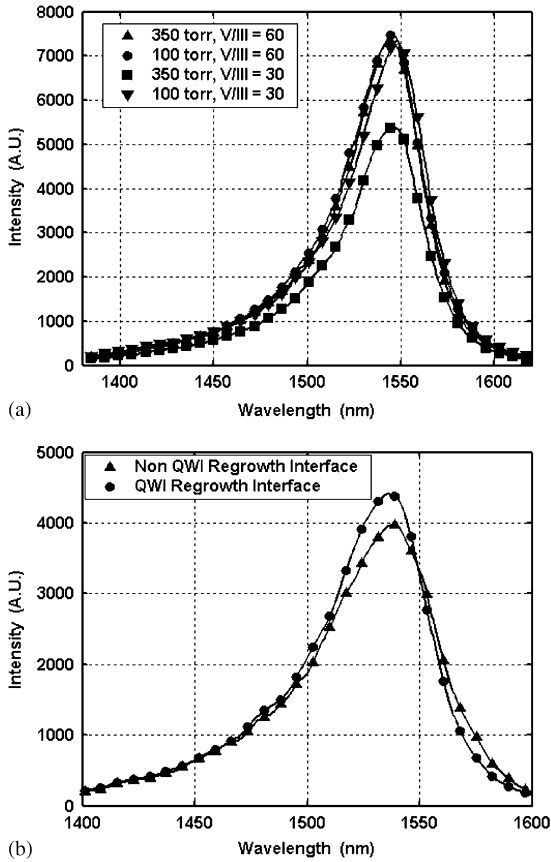


Fig. 9. Photoluminescence data for (a) a 5 MQW region grown 500 Å above CTL layers shown in Fig. 8 realized using the described MOCVD reactor conditions and (b) a 5 MQW region grown 2000 Å above intermixed and non-intermixed regrowth interface.

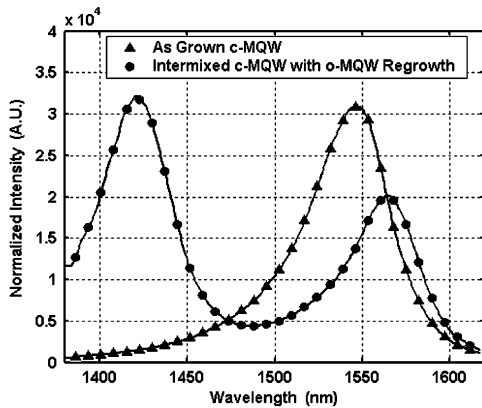


Fig. 10. Photoluminescence data for the as-grown c-MQW, intermixed c-MQW, and o-MQW realized on the same chip.

transport electrons across intermixed quantum wells, and is clearly suitable for insertion into a more complex PIC. The modal loss for the c-MQW regions was found to be 26 cm^{-1} , while the o-MQW devices exhibited a modal loss of 23 cm^{-1} . The nearly identical performance of c-MQW devices with the differing doping schemes indicates that the addition of Si doping in the lower waveguide does not impose adverse effects to the DC performance of the c-MQW region.

Using the finite difference method to solve the wave equation, the optical confinement was computed in the broad area devices to be 12.3% in the c-MQW region and 1.6% in the o-MQW region for a CTL thickness of 1750 Å. The experimental threshold modal gain was plotted as a function of threshold current density in order to extract the gain parameter and the transparency current density for both structures with doping scheme B, as shown in Fig. 12.

A two-parameter fit yielded transparency current densities of 43 and 41 A/cm^2 per well for the c-MQW and the o-MQW structures, respectively. The high correlation in transparency current density and optical loss for both structures strongly reinforces the AFM and photoluminescence studies demonstrating high-quality o-MQW material grown on a surface subjected to QWI. The extracted modal gain coefficient for the c-MQW was 140 cm^{-1} , while the o-MQW exhibited a modal gain coefficient of 20 cm^{-1} . Assuming a uniform carrier distribution in the MQW regions, the material gain coefficient can be estimated by dividing the modal gain coefficient by the optical confinement. Using the computed theoretical optical confinement values, the material gain coefficient was found to be in good agreement for both structures, at 1140 cm^{-1} for the c-MQW and 1250 cm^{-1} for the o-MQW. As shown in Eq. (2), the saturation power of an SOA is inversely proportional to the optical confinement. The reduction of the optical confinement increased the projected saturation power from 3.3 mW for the c-MQW structure to 22.9 mW for the o-MQW structure at a current density of 10 kA/cm^2 , as shown in Fig. 12.

Table 1
Epitaxial layer structures for the c-MQW and o-MQW regions

c-MQW			o-MQW		
Material	Thickness (Å)	Doping (cm ⁻³)	Material	Thickness (Å)	Doping (cm ⁻³)
InGaAs:Zn	1,000	2.00E+19	InGaAs:Zn	1000	2.00E+19
InP:Zn	8,000	1.00E+18	InP:Zn	8,000	1.00E+18
InP:Zn	12,000	7.00E+17	InP:Zn	12,000	7.00E+17
InP:Zn	1,250	2.50E+18	InP:Zn	1,250	2.50E+18
InP	300	NID	InP	300	NID
InP:Si	100	1.00E+17	InP:Zn	1500	5.00E+17
InP:Si	75	8.00E+16	InP	200	NID
InP:Si	75	5.00E+16	1.22Q	300	NID
1.3Q:Si	1,230	NID	o-MQW	5 × 70 Å wells 4 × 85 Å Bar	NID
c-MQW	10 × 70 Å wells 11 × 85 Å Bar	NID	1.22Q	300	NID
1.3Q:Si	1,230	A,B	InP:Si	1,500	5.00E+17
InP:Si	1,000	1.00E+17	InP:Si	300	3.00E+17
InP:Si	1,000	5.00E+17	InP:Si	100	2.00E+17
InP:Si	17,000	1.00E+18	1.3Q:Si	100	1.00E+17
InP:S	Substrate	5.00E+18	InP:Si	200	1.00E+17
			InP:Si	75	8.00E+16
			InP:Si	75	5.00E+16
			1.3Q:Si	1,230	NID
			Intermixed c-MQW	10 × 70 Å wells 11 × 85 Å Bar	NID
			1.3Q:Si	1,230	A,B
			InP:Si	1,000	1.00E+17
			InP:Si	1,000	5.00E+17
			InP:Si	17,000	1.00E+18
			InP:S	Substrate	5.00E+18

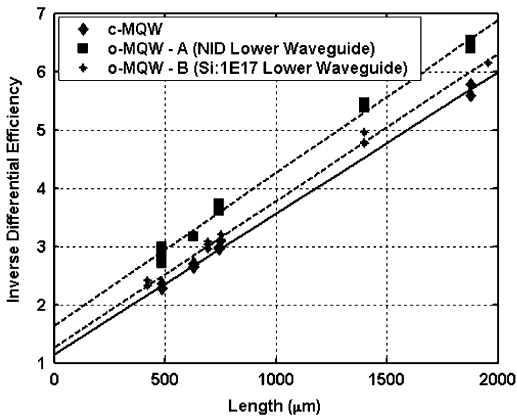


Fig. 11. Inverse differential efficiency versus broad area laser length for the c-MQW structure (solid lines) and the o-MQW structure (dotted lines) with two different doping schemes.

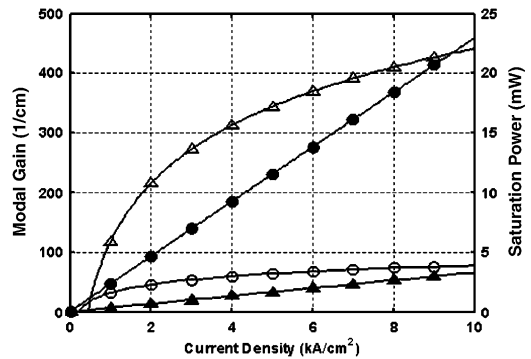


Fig. 12. Modal gain (hollow markers) and saturation power (solid markers) versus current density for the c-MQW (triangles) and o-MQW (circles) structures using a two-parameter fit and radiative recombination coefficient ($B = 0.3 \times 10^{-10} \text{ cm}^3/\text{s}$) and Auger recombination coefficient ($C = 6 \times 10^{-29} \text{ cm}^6/\text{s}$).

5. Conclusion

We have characterized the material growth aspects vital to a novel architecture allowing for the realization of regions with high and low modal gain on the same chip. This technology will enable the monolithic integration of high-modal gain diode lasers and high gain/saturation power SOAs.

A surface preparation procedure was devised allowing for the growth of high quality MQW active regions in close vicinity to the regrowth interface. The effects of vacancy diffusion through the stop etch/InP interface during the QWI process on the smoothness of the InP were shown, in which the intermixed interface had an RMS roughness $10\times$ greater than that not subjected to vacancy diffusion. However, it was shown that with a 2000 Å thick layer grown above this rough regrowth surface, the RMS roughness can be reduced by $10\times$, making it suitable for quantum well growth. Furthermore, it was demonstrated that at the RMS values we achieve using our standard MOCVD growth conditions, slight improvements in the smoothness realized by altering the growth parameters do not result in higher intensity or a narrower FWHM photoluminescence spectra.

Finally, Fabry–Perot broad area lasers were fabricated from both the c-MQW high confinement and o-MQW low confinement active regions realized on the same chip. By doping the lower waveguide of the c-MQW structure at $1E17\text{ cm}^{-3}$ with Si, the injection efficiency in the o-MQW was improved from 61% to 80% with no performance degradation of the c-MQW region. The high injection efficiency of the novel o-MQW structure implies effective electron transport through QWI

material. The o-MQW demonstrated nearly an order of magnitude reduction in the modal gain, which is in close correlation with our simulations. The photoluminescence and atomic force microscopy results coupled with the single-chip fabrication of efficient broad area lasers of both c-MQW and o-MQW active regions confirm our ability to achieve a device architecture that will enable the monolithic integration of high gain diode lasers with high gain/saturation power semiconductor optical amplifiers.

Acknowledgment

This work was supported by DARPA/MTO CS-WDM under Grant No. N66001-02-C-8026 and by Intel Corporation under Grant No. TXA001630000. This work made use of MRL Central Facilities supported by the National Science Foundation under Award No. DMR96-32716.

References

- [1] L. Coldren, S. Corzine, Diode Lasers and Photonic Integrated Circuits, Wiley, New York, 1995 (p. 456).
- [2] E. Skogen, J. Raring, J. Barton, S. DenBaars, L. Coldren, Post-growth control of the quantum-well band edge for the monolithic integration of widely tunable lasers and electro-absorption modulators. *J. Sel. Topics Quantum Electron.* 9 2003.
- [3] E. Skogen, J. Barton, S. DenBaars, L. Coldren, Tunable sampled-grating DBR lasers using quantum-well-intermixing, *IEEE Photon Technol. Lett.* 14 (2002) 1243–1245.
- [4] Mason, TGB. InP based photonic integrated circuits. Thesis from Department of Electrical and Computer Engineering #99–11, University of California Santa Barbara. June 1999.



High contrast InP/InGaAsP grating MOCVD regrowth using TBA and TBP

Erik J. Skogen^{a,*}, Jonathon S. Barton^b, James W. Raring^b, Larry A. Coldren^a, Steven P. Denbaars^b

^aElectrical and Computer Engineering Department, University of California, Santa Barbara, CA 93106, USA

^bMaterials Department, University of California, Santa Barbara, CA 93106, USA

Available online 8 October 2004

Abstract

High index contrast InGaAsP/InP gratings are useful in the design of next generation photonic integrated circuits. Here, we investigate the process conditions used in the formation of such gratings. We find that the reactive ion etch conditions have a strong influence on the radiative efficiency in the grating region. We also show that the use of a combination of TBP and TBA in the heat-up phase of growth results in a reduction of the group-V exchange in the grating region, thereby increasing the radiative efficiency, while not adversely affecting non-grating regions.

© 2004 Elsevier B.V. All rights reserved.

PACS: 81.10; 42.55.P; 81.05.D; 78.55.E

Keywords: A1. Photoluminescence; A3. Metalorganic chemical vapor deposition; B2. Semiconducting indium phosphide; B3. Laser diodes

1. Introduction

It is clear that as the InP-based opto-electronic devices industry matures, it is desirable to optically interconnect components with differing functionalities on the same chip. These photonic integrated circuits (PICs) will provide cost reduction, im-

proved performance, and increased functionality beyond what is capable presently with discrete components. Such PICs will be required to source and sink photons using devices such as lasers/amplifiers for the former, and modulators/detectors for the latter.

A key component within a PIC is the semiconductor laser. Monolithic integration of diode lasers with other components requires the lithographic definition of at least one reflector. Many of these lasers make use of the distributed Bragg reflector (DBR) or some variation, such as the

*Corresponding author. Tel.: +1-805-893-8465; fax: +1-805-893-4500.

E-mail address: skogen@engineering.ucsb.edu (E.J. Skogen).

sampled-grating (SG) DBR. In most cases, it is desirable to maximize the grating coupling coefficient κ , for the realization of strong reflectors and/or to minimize the length of the reflector [1].

We investigate the process and regrowth conditions for the formation of high- κ (250 cm^{-1}) gratings in the InP/InGaAsP material system using the low-toxicity group-V precursors tertiarybutylphosphine (TPB) and tertiarybutylarsine (TBA). Photoluminescence measurements were used as a qualitative comparison of the carrier radiative efficiency in the grating regions as opposed to non-grating regions for different etch and regrowth conditions.

2. Theory

It has been shown that for SG-DBR reflectors used in the widely tunable SG-DBR laser, it is advantageous to maximize κ in order to maintain a high reflectivity while minimizing the burst length [2]. A large value of κ is also beneficial in the design of short-cavity DBR laser structures, where the effective penetration depth of the DBR should be minimized to reduce loss in the mirror and maximize the cavity mode spacing [3]. The formation of strong κ gratings can be accomplished in several ways. Here, we use a two-step process, where gratings are first selectively etched into the waveguide core, as shown in Fig. 1 side B; this is followed by an epitaxial regrowth of InP to bury the gratings such that the refractive index contrast in the grating is an effective refractive index difference between the etched and non-etched portion of the waveguide core:

$$\kappa = \frac{4}{\pi} \left(\frac{2\Delta\bar{n}}{\lambda} \right). \quad (1)$$

The coupling coefficient of a grating structure is given by Eq. (1), where $\Delta\bar{n}$ is the difference in effective index in the grating region, λ is the wavelength, and $4/\pi$ a factor gained for a square grating profile. As described in Eq. (1), κ is directly proportional to the effective refractive index contrast between the grating teeth, and can be increased by increasing the difference in the refractive index of the material constituting the

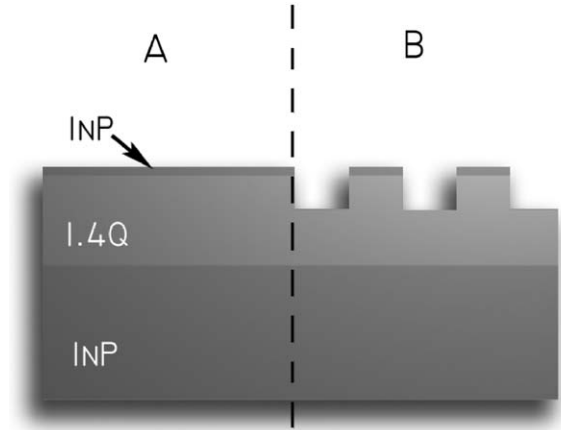


Fig. 1. Layer structure used for grating regrowth photoluminescence experiments indicating (A) non-grating region and (B) grating region. 1.4Q stands for InGaAsP whose bandgap wavelength is $1.4\ \mu\text{m}$.

waveguide structure, and/or an increase in the grating etch depth. The refractive index difference between the waveguide core and cladding is set by the design of the waveguide structure. Therefore, in this case, the grating etch depth is the only free parameter to control the strength of the grating.

3. Experiment

The epitaxial base structure used for these experiments was grown using a Thomas Swan Scientific Equipment Ltd. (TSSE) horizontal-flow rotating-disc metalorganic chemical vapor deposition (MOCVD) system. The base structure was grown on sulfur-doped InP misoriented 0.2° towards $\langle 111 \rangle_A$, and consisted of a $2\ \mu\text{m}$ InP:Si lower cladding layer, a $200\ \text{nm}$ 1.4Q (InGaAsP $\lambda_g = 1400\ \text{nm}$) waveguide core, followed by a $15\ \text{nm}$ InP:NID regrowth interface layer.

The quality of the regrowth in regions where gratings have not been patterned, as shown in Fig. 1 side A, has been previously investigated through visual inspection and measurement of the tuning efficiency in Ref. [4], and found that a thin InP layer is sufficient for achieving quality regrowth in those areas. In this work, we focus on the influence that the grating etch parameters, regrowth surface

preparation, and regrowth conditions have on producing a high-quality regrowth interface.

In order to study the grating etch, surface preparation, and regrowth conditions, two sets of experiments were conducted using samples with gratings patterned over 50% of the sample surface. The first investigated the grating etch and regrowth conditions, while the second investigated the grating surface preparation using the most favorable etch and regrowth conditions as determined from the previous experiment. A significant improvement in material quality was achieved as determined from photoluminescence experiments.

3.1. Reactive ion etch

The reactive ion etch (RIE) used for grating formation is an integral part of the grating process as it allows for a square grating profile. The conditions of the grating etch can have a great impact on the quality of the material (post) regrowth. It has been shown that a RIE using a high bias voltage (>300 V) produces damage in the remaining crystal [5].

In the past, a grating etch process based on a two-step RIE was used using a methane/hydrogen/argon (MHA) chemistry at flows of 4/20/10 sccm, respectively [4]. The two-step etch process consisted of a low-voltage, high-pressure (200 V, 14 W, 125 mTorr) etch, which forms a polymer on the surface of the resist, protecting it during a high-voltage, low-pressure etch (500 V, 85 W, 75 mTorr). Although this process yields a square grating profile, the etch rate for the high-voltage etch is extremely fast (~ 8 Å/s) making repeatability difficult, and leaving damage in the remaining crystal. In this study, the goal was to investigate a new set of etch conditions such that the square grating profile is maintained, while minimizing etch damage and improving repeatability.

The grating etch process was investigated using the epitaxial base structure described above. The wafer was cleaved into quarters, Q1–Q4, and 20 nm of SiO_xN_y was patterned to serve as a grating etch mask. Gratings with a pitch of 240 nm were defined holographically in 70 nm of photoresist. The samples were subjected to two etch processes A and B, summarized in Table 1. Etch A

Table 1

Summary of the experimental conditions for the grating etch and regrowth experiments

	Regrowth A	Regrowth B
	Ramp to 615 °C	Ramp to 615 °C
	P_{TBP}^* 1.0 Torr	P_{TBP}^* 1.0 Torr
	Hold 615 °C 5'	P_{TBA}^* 0.07 Torr
	Initial Rg 25%	Initial Rg 6.25%
Etch A		
MHA 4/20/10 sccm	Q1	Q2
200 V 125 mTorr		
500 V 75 mTorr		
Etch B		
MHA 4/20/10 sccm	Q3	Q4
200 V 75 mTorr		

uses the two-step etch method, discussed above. Etch B uses a reduced etch voltage of 200 V (14 W) at a pressure of 75 mTorr. The lower etch voltage yields a lower etch rate (~ 2 Å/s), allowing samples to be etched to a particular depth with more accuracy. The gas chemistry used for etch B did not change from etch A. All samples were etched to the same depth, 50 nm.

An identical surface preparation was performed on all samples post-grating etch; and consisted of a plasma etch with O_2 flow of 20 sccm, bias voltage of 300 V (40 W), and a pressure of 125 mTorr for 5 min, followed by immersion in a photoresist developer, an acetone and isopropyl alcohol soak. The process continued with a HF soak to strip the SiO_xN_y , a 60 min UV-ozone treatment, buffered-HF strip, and DI water rinse.

3.2. MOCVD regrowth

The MOCVD regrowth conditions are another important aspect of achieving high-quality grating overgrowth. There are a great deal of parameters that can influence the quality of the regrowth, such as the temperature, pressure, pre-growth bake time, and group-V overpressure ratio. As described in Ref. [6], an improved grating overgrowth profile and a reduction in the density of visible growth defects was accomplished by adding AsH_3 in the heat-up stage to stabilize the InGaAsP

surface, and by using a low initial growth rate to minimize growth defects and aid in grating preservation.

Here, we take a similar approach, using a low initial growth rate and the addition of an arsenic overpressure during the heat-up stage. A key difference in our process compared to that in Ref. [6], is the use of liquid group-V precursors TBP and TBA. Not only does the use of TBP and TBA offer greater flexibility in the growth temperature due to their lower pyrolysis temperatures, but also, unlike PH_3 and AsH_3 , they decompose without the aid of a surface. A homogeneous reaction results in greater controllability, repeatability, and uniformity [7].

In this study, the group-V overpressure ratio, pre-growth bake time, and the initial growth rate were varied from the standard conditions. The carrier flow and reactor pressure remained constant for both regrowth programs at 16slm and 350 Torr, respectively. The standard regrowth, regrowth A, consisted of a warm-up under a TBP overpressure of 1 Torr and a 5-min pre-growth bake at a growth temperature of 615°C . A stepped growth rate schedule was used with an initial growth rate of $\frac{1}{4}$ th that of the full growth rate. This growth procedure yielded good material quality in non-grating regions. Regrowth procedure B consists of a warm-up under TBP and TBA overpressure, 1 and 0.07 Torr, respectively, the elimination of the pre-growth bake, and an initial growth rate of $\frac{1}{16}$ th that of the full growth rate. The introduction of a slight arsenic overpressure stabilizes the quaternary material in the grating regions, while not allowing a significant arsenic/phosphorous exchange in the regions covered by InP in non-grating regions. The reduction in the initial growth rate is used to reduce the formation of defects and voids that may otherwise have formed using a higher initial growth rate. Table 1 summarizes the MOCVD regrowth conditions.

4. Results and discussion

The RIE and the MOCVD regrowth conditions play a crucial role in determining the quality of the material in the grating region. Photoluminescence

measurements, using a pump laser at 785 nm, were used to ascertain the quality of the material in the grating region as compared to the non-grating region. As discussed above, the first experiment involved a study of two grating etch processes and two MOCVD regrowth procedures. The photoluminescence results are summarized in Fig. 2.

As shown in Fig. 2, the photoluminescence intensity for the non-grating region is not affected by the change in the etch process or the modified regrowth program, as expected. However, the photoluminescence intensity of the regions with gratings are strongly affected by the change in the etch process and MOCVD regrowth program. Specifically, those samples subjected to regrowth program A yield virtually no photoluminescence intensity as compared to the regions without gratings. The samples subjected to regrowth program B show measurable photoluminescence intensity for both etch conditions, indicating greater radiative carrier efficiency. The samples subjected to etch process B and regrowth program B show the highest photoluminescence intensity. A summary of the photoluminescence intensity results is given in Table 2.

To further study how the etch process affects the photoluminescence intensity, another set of samples were prepared varying the surface preparation post-etch. For this experiment, a similar epitaxial

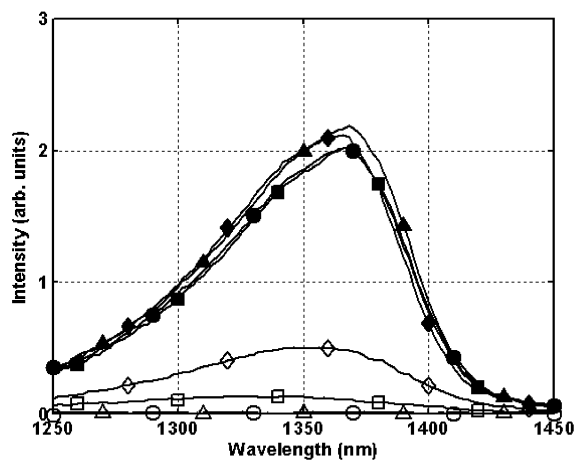


Fig. 2. Photoluminescence spectra in non-grating region (solid-symbols) and grating region (open-symbols) for experiments Q1 (circles), Q2 (squares), Q3 (triangles), and Q4 (diamonds).

Table 2

Photoluminescence intensity ratios for the grating region ($I_{\text{grating}}^{\text{PL}}$) versus the non-grating region ($I_{\text{non-grating}}^{\text{PL}}$) for the etch and regrowth conditions stated.

	Regrowth A	Regrowth B
	Ramp to 615 °C	Ramp to 615 °C
	P_{TBP}^* 1.0 Torr	P_{TBP}^* 1.0 Torr
	Hold 615 °C 5'	P_{TBA}^* 0.07 Torr
	Initial Rg 25%	Initial Rg 6.25%
Etch A		
MHA 4/20/10 sccm	0.90%	6.82%
200 V 125 mTorr		
500 V 75 mTorr		
Etch B		
MHA 4/20/10 sccm	0.92%	23.90%
200 V 75 mTorr		

base structure was grown and gratings patterned in an identical fashion. Gratings were etched using etch process B, the most favorable RIE conditions found in the previous experiment. From there, two surface preparations were conducted, the first, surface process A, was a control sample Q5, and was identical to that used in the previous set of experiments. The other, surface process B, sample Q6, made use of a lower voltage O_2 plasma etch (200 V, 23 W) at the same pressure and flow, and the addition of a 1 min H_2SO_4 soak prior to the SiO_xN_y strip, with all other steps the same. For both samples the process concluded with MOCVD regrowth B.

The results of the surface preparation study are shown in Fig. 3. As is evident from the figure, the surface preparation B, which included a reduced O_2 plasma etch and an additional H_2SO_4 soak, improved the photoluminescence intensity ratio over the control sample using etch process B, surface preparation A, and regrowth B. In this experiment, the ratio of the photoluminescence intensity for the control sample was 23.6%, almost identical to that found previously, 23.9%. The modified surface preparation, surface preparation B, demonstrated a marked improvement in the photoluminescence intensity ratio at 34.2%. From these experiments, it is clear that etch B, surface

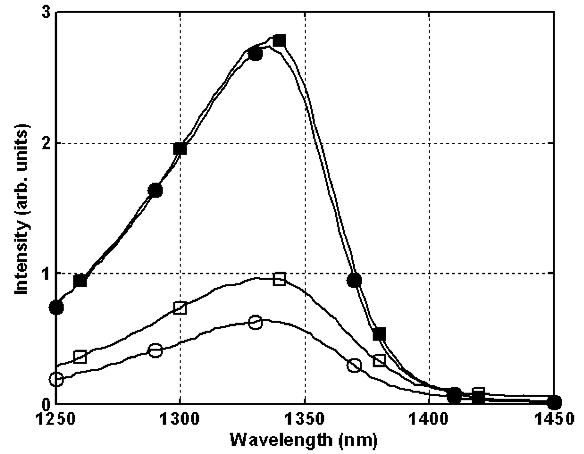


Fig. 3. Photoluminescence spectra in non-grating region (solid-symbols) and grating region (open-symbols) for experiments Q5 (circles), Q6 (squares).

preparation B, and regrowth B are the most favorable process conditions.

The photoluminescence intensity results indicate that the etch process, regrowth conditions, and surface preparation play a major role in determining the radiative carrier efficiency in the grating region. The addition of TBA as a source of arsenic during the heat-up phase of MOCVD regrowth, along with the other modifications, enhances the quality of the regrowth interface by the reduction of group-V exchange on the surface of the exposed InGaAsP. This surface stabilization results in an improved heterointerface, the absence of lattice mismatched interfacial layers, and the reduction of non-radiative recombination centers as suggested by photoluminescence intensity measurements.

The RIE, on the other hand, is directly responsible for the creation of non-radiative recombination centers in the InGaAsP material. The high bias voltage used in etch process A, creates noticeably more damage in the crystal versus the low-voltage etch process B, as indicated by the poor radiative recombination efficiency. Similarly, the surface preparation process B, incorporating a lower voltage O_2 plasma etch, is responsible for reducing the number of non-radiative recombination centers.

5. Conclusion

A large improvement in the radiative efficiency in regions where high-contrast InGaAsP/InP gratings are present was achieved through the manipulation of the process conditions. In regions where gratings were not patterned, the photoluminescence intensity remained constant, indicating that the modified process conditions do not adversely affect those regions. The radiative efficiency in the grating regions is improved using a lower RIE voltage and a lower voltage O₂ plasma etch. The combination of the addition of TBA as a source of arsenic in the heat-up phase of the MOCVD regrowth, the reduction of bake time prior to growth, and a reduced initial growth rate also contribute to an improved radiative efficiency.

The trends discussed may be extended such that a further refinement of the process conditions could be applied to gain an incremental improvement of the radiative efficiency in the grating regions.

References

- [1] E. Skogen, J. Barton, S. DenBaars, L. Coldren, A quantum-well-intermixing process for wavelength-agile photonic integrated circuits, *IEEE J. Selected Top. Quantum Electron.* 8 (2002) 863–869.
- [2] E. Skogen, Quantum well intermixing for wavelength-agile photonic integrated circuits, dissertation, University of California, Santa Barbara, CA, 2003.
- [3] E. Skogen, C. Wang, J. Raring, G. Morrison, L. Coldren, Small-footprint, high-efficiency, integrated transmitters for high-speed optical interconnect applications, To be presented at Integrated Photonics Research Conference (IPR) 2004, Paper ITHD2, San Francisco CA, 2004.
- [4] B. Mason, InP based photonic integrated circuits, dissertation, University of California, Santa Barbara, CA, 1997.
- [5] B. Qiu, B. Ooi, A. Bryce, S. Hicks, C. Wilkinson, R. DeLaRue, J. Marsh, Reduced damage reactive ion etching process for fabrication of InGaAsP/InGaAs multiple quantum well ridge waveguide lasers, *J. Vac. Sci. Technol. B* 16 (1998) 1818–1822.
- [6] D. Franke, H. Roehle, Highly reproducible and defect-free MOPVE overgrowth of InGaAsP-based DFB gratings, *J. Crystal Growth* 170 (1997) 113–116.
- [7] M. Heimbuch, Optimization of MOCVD growth using tertiarybutylarsine and tertiarybutylphosphine for the realization of 1.55 μm low threshold current lasers, dissertation, University of California, Santa Barbara, CA, 1997.

II. InP-Based Vertical Cavity Laser

Selectively Etched Tunnel Junction for Lateral Current and Optical Confinement in InP-Based Vertical Cavity Lasers

M.H.M. REDDY,^{1,3} T. ASANO,¹ D. FEEZELL,¹ D.A. BUELL,²
A.S. HUNTINGTON,² R. KODA,¹ and L.A. COLDREN^{1,2}

1.—Department of Electrical and Computer Engineering, University of California, Santa Barbara, Santa Barbara, CA 93106. 2.—Department of Materials Science, University of California, Santa Barbara, Santa Barbara, CA 93106. 3.—E-mail: mreddy@ece.ucsb.edu

We demonstrate a thin, selectively lateral-etched, AlIn(Ga)As tunnel-junction (TJ) layer as a current and optical confinement aperture in the InP-based long-wavelength vertical cavity surface-emitting lasers (VCSELs). A high etch selectivity was demonstrated by etching the aperture a distance of several microns without affecting the surrounding InP etch-resistant layer. Edge-emitting lasers enclosing the TJ aperture showed high injection efficiency and low current spreading underneath the aperture. Single-mode continuous-wave operation of a 1.55- μm VCSEL was demonstrated successfully with a room-temperature differential efficiency of 21% using a 6- μm -wide TJ aperture.

Key words: InP-based, tunnel junction, vertical cavity surface emitting lasers (VCSELs)

INTRODUCTION

Lateral current and optical confinement is essential to realize efficient single-mode vertical cavity surface-emitting lasers (VCSELs) by reducing the optical scattering losses and increasing the optical mode/charge-carrier profile overlap in the gain region. Short-wavelength VCSELs on GaAs showed exemplary improvement in terms of ultralow threshold current and high wall-plug efficiency because of an AlAs-oxide confinement layer.¹ In long-wavelength ($>1.3 \mu\text{m}$) devices, the need for a confinement layer is even more pronounced because of the enhanced Auger recombination, higher carrier leakage over the heterobarriers as a result of smaller carrier confinement, and the larger thermal impedance caused by the involvement of ternary and quaternary layers. Unfortunately, the highly successful AlAs-oxide confinement layer cannot be used in long-wavelength devices grown epitaxially on an InP substrate because of an extremely high lattice mismatch. Several approaches, such as metamorphically grown AlAs-oxide,² strained $\text{Al}_{0.6}\text{In}_{0.4}\text{As}$ -oxide,³ buried tunnel junction (TJ),⁴ and a selectively etched active region⁵ have been tried as

confinement layers in monolithically grown 1.55- μm VCSELs. Dislocation generation and their behavior with time and temperature may be a source of concern for the metamorphically grown AlAs-oxide and the strained $\text{Al}_{0.6}\text{In}_{0.4}\text{As}$ -oxide confined structures. Although the buried TJ has superior size control because of lithography definition, it requires complex processing steps and a regrowth, which increases the cost of fabrication. Our group reported a different approach, namely, the selective lateral etching of an AlGaInAs-based active region as the confinement layer with impressive results at no extra cost or processing steps.⁵ Though this aperture has been very successful in terms of exhibiting a low threshold current and a high continuous-wave output power, it has a few undesired features, namely, a large scattering loss caused by the thick and abrupt undercut aperture located at the optical, standing wave peak and a small overlap of the fundamental optical mode and the injected carrier-density profile. Also, there is the concern of the Al-containing active region getting exposed to ambient air, which may lead to reliability concerns.

In this work, we demonstrate a selectively lateral-etched thin (30–50 nm) AlInAs layer, which is a part of or the whole tunneling junction, enclosed in InP as the aperture. The same etch chemistry can also

(Received March 31, 2003; accepted September 23, 2003)

be used for the selective lateral etching of the lattice-matched quaternary, $\text{Al}_x\text{Ga}_y\text{In}_{1-x-y}\text{As}$. Edge-emitting stripe lasers were used for optimizing the selective lateral etching of the TJ and testing the dependence of the internal injection efficiency and current confinement characteristics on the aperture size. Finally, we have demonstrated the continuous-wave operation of a single-mode $1.55\text{-}\mu\text{m}$ VCSEL that encloses the TJ aperture.

APERTURE PLACEMENT

The VCSEL structure with the selectively etched TJ aperture is shown in Fig. 1. The TJ plays a crucial role in supplying the holes for the radiative recombination in the gain region. This helps eliminate the use of p-doping in the mirrors and the InP cavity of the device, which induces excess optical loss and a larger electrical resistance compared to n-doping. The TJ also works as an efficient lateral current spreader, thereby mitigating the problem of current crowding around the edges of the intracavity contacts. Because of this, it would not be beneficial to keep the aperture above the TJ. On the other hand, it would be desirable to place the TJ as close to the active region as possible for maintaining a high, hole injection efficiency. Therefore, it was decided to use the TJ itself as the aperture and place it as close to the active region as possible depending on the thickness of the InP necessary to carry out the selective etching.

Other factors of influence are the optical loss caused by free carrier absorption in the heavily doped TJ layers and the aperture thickness-dependent diffraction losses. We used a 30-nm-thick TJ aperture at the second null of the optical standing wave from the active region inside the cavity, as shown in Fig. 2. It has been demonstrated in short-wavelength VCSELs that thin apertures (30–50 nm) placed at a node show less diffraction losses and high single-mode output powers.^{6,7} As shown in Fig. 2, the TJ aperture needs to be incorporated inside the InP to facilitate selective wet etching. The energy band diagram (Fig. 3) shows a type-II band alignment between InP and InAlAs, offering a substantial barrier for the hole injection into the active region. To improve the hole injection efficiency, the InP underneath the aperture layer is lightly doped to $2 \times 10^{17} \text{ cm}^{-3}$ with a p-type (Be) impurity. The edge-emitting stripe lasers shown in Fig. 3 were fab-

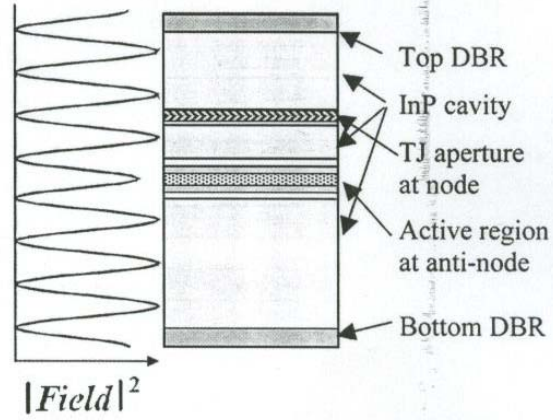


Fig. 2. Placement of different layers with respect to the optical standing wave field in the cavity. The TJ aperture is placed at the node to reduce optical free-carrier absorption and scattering losses.

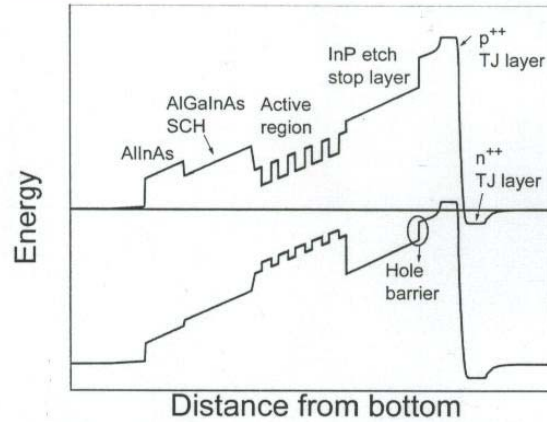


Fig. 3. Energy band diagram showing the effect of type-II band alignment between InP and InAlAs on the hole injection. We sought to overcome this problem by p-doping the InP layer.

ricated to extract the internal injection efficiency and the optical losses at different, selectively etched TJ widths. The same stripes were also used for measuring the etch rate with cross-sectional field-emission scanning electron microscopy (FESEM). To get an idea of current spreading, the distance between the aperture and the active region is maintained at the same value as that of the VCSEL.

EXPERIMENTAL

A Varian Gen II molecular-beam epitaxy machine was used for the growth of the VCSEL and the edge-emitting stripe lasers, as shown in Figs. 1 and 4, respectively. The active region in both the devices is digitally grown,⁸ and it consists of five compressively strained, $\text{Al}_{0.08}\text{Ga}_{0.23}\text{In}_{0.69}\text{As}$ quantum wells (QWs) and six partially strain-compensating tensile strained, $\text{Al}_{0.12}\text{Ga}_{0.44}\text{In}_{0.44}\text{As}$ barriers. The thickness and the amount of strain for each QW are 7 nm and -1.2%, respectively, and those of the barrier are

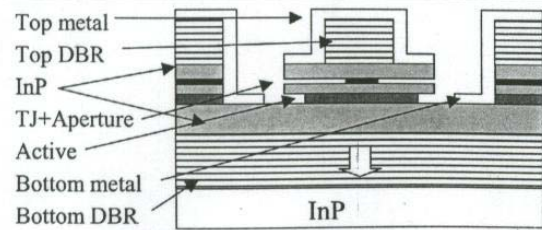


Fig. 1. Schematic of TJ-confined VCSEL grown lattice-matched to InP.

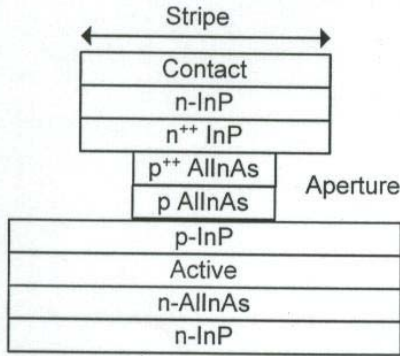


Fig. 4. Schematic of the edge-emitting laser structure, which enclosed the TJ aperture. The distance between the TJ aperture and the active region is the same as that of the VCSEL.

5 nm and 0.9%, respectively. The TJ consists of a 15-nm n^{++} -InP doped to $3 \times 10^{19} \text{ cm}^{-3}$ and a 15-nm p^{++} -AlInAs doped to $3 \times 10^{19} \text{ cm}^{-3}$. The aperture layer consists of a 15-nm p^{++} -AlInAs TJ layer and an additional 15-nm p-AlInAs layer doped to $5 \times 10^{17} \text{ cm}^{-3}$.

The edge-emitting stripe lasers were fabricated by dry etching mesas of 13–40- μm widths down to the AlInAs layer in the TJ. Then, the aperture was selectively lateral wet etched using a citric acid/hydrogen peroxide (10:1) solution to obtain the desired aperture size. Figure 5 shows an FESEM picture of selectively etched, 30-nm-thick p-AlInAs that does not affect the surrounding InP region. The measured etch rate of p-AlInAs was about 35-nm per minute. Subsequently, the remaining InP was dry etched vertically down to the active region using a mixture of $\text{CH}_4\text{-H}_2\text{-Ar}$. The active region was then etched down to the bottom-cladding layer using the

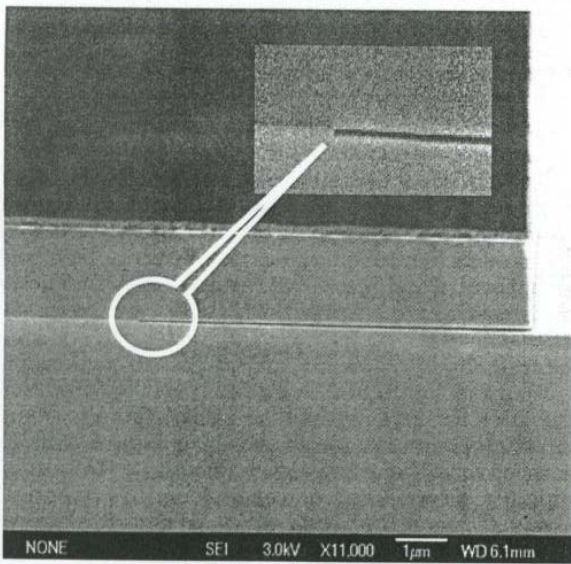


Fig. 5. FESEM cross-sectional picture of the selectively lateral-etched TJ layer. Inset shows the magnified image. Note that the surrounding InP is not affected.

same wet etchant, consisting of citric acid and H_2O_2 . Note that the aperture layer will also be etched during this process and, therefore, should be properly taken into account while designing the final aperture size. It should be mentioned that the active region, which is about 250-nm-thick, takes only 6–7 min to etch, and this time is insignificant when compared to the aperture etch time. After thinning the substrate down to 100 μm , the top and bottom contacts were deposited using Ni/AuGe/Ni/Au. Laser bars of different lengths were cleaved, and the facets were left uncoated during this study.

The VCSEL (Fig. 1) consists of a $\lambda/2$ -thick digital active region in a 3λ -thick InP cavity, which is enclosed by top and bottom distributed Bragg reflector (DBR) mirrors grown using 34.5 and 24.5 pairs of $\text{Al}_{0.15}\text{Ga}_{0.85}\text{As}_{0.52}\text{Sb}_{0.48}/\text{Al}_{0.95}\text{Ga}_{0.05}\text{As}_{0.56}\text{Sb}_{0.44}$ high-index contrast layers to achieve a reflectivity of 99.9% and 99.3%, respectively, on a semi-insulating (100)-oriented InP substrate. Device fabrication starts with the reactive ion etching (RIE) of the top of the DBR and InP down to the AlInAs layer in the TJ using Cl_2 and $\text{CH}_4\text{-H}_2\text{-Ar}$, respectively. Subsequently, a selective lateral wet etching of AlInAs in the TJ and beneath it, amounting to a total thickness of 30 nm, was carried out to form an aperture. Then, the remaining InP was etched using RIE, followed by a wet etching of the active region to expose the bottom InP contact layer. Selective lateral wet etching of the active region was performed for a limited time to reduce the lateral carrier diffusion in the QWs. Finally, Ni/AuGe/Ni/Au was evaporated on both InP layers to form the top and bottom intracavity contacts (Fig. 1).

RESULTS AND DISCUSSION

The pulsed light-current-voltage (L-I-V) characteristics of the stripe geometry edge-emitting lasers of different longitudinal cavity lengths at each underlying aperture size were measured. Figure 6 shows some of these curves for the aperture size less

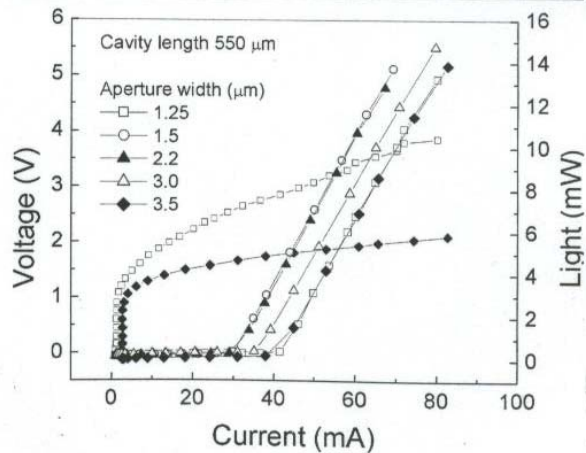


Fig. 6. Pulsed L-I-V characteristics of edge-emitting lasers with different TJ aperture widths.

than 3.5 μm . It can be seen that the threshold current (I_{th}) reduces with the aperture size down to 1.5 μm and then increases as the aperture size reduces further, though the slope efficiency remains the same. The device shows an impressive low I_{th} of 30 mA at the 2.2- μm aperture width for a cavity length of 550 μm . Figure 7 shows the inverse differential efficiency ($1/\eta_d$), which is derived from the slope efficiency of the L-I curves, as a function of cavity length at different aperture widths. From the linear fit of the preceding data, the internal injection efficiency (η_i) and the internal model loss ($\langle\alpha_i\rangle$) of the laser structure were derived. These devices showed a η_i of more than 90% even as the aperture reduces down to 4 μm . This high injection efficiency shows that the effect of the unfavorable band alignment at the InP/AlInAs interface can be effectively minimized by p-doping the InP layer between the active region and the aperture.

Figure 8 shows the variation of the differential efficiency and the threshold current density (J_{th}) with

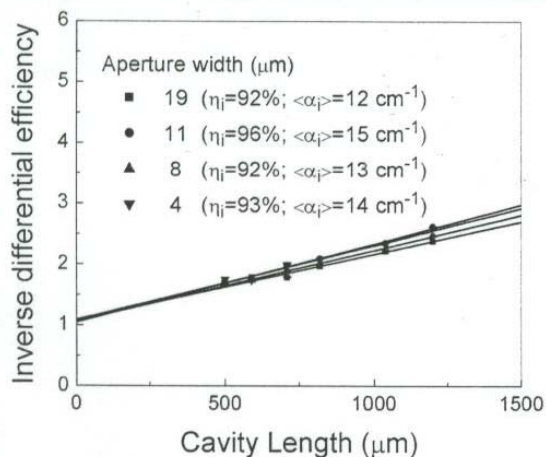


Fig. 7. Inverse differential efficiency versus cavity length for edge-emitting lasers with different TJ aperture widths.

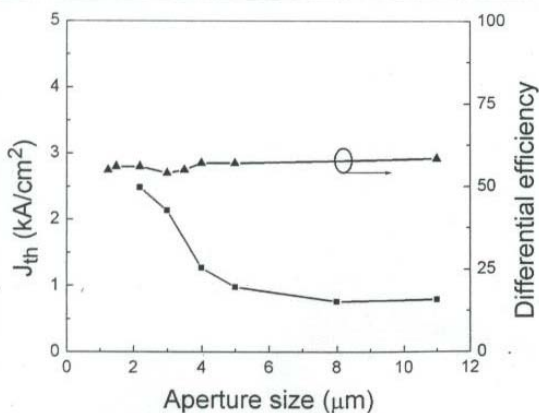


Fig. 8. Effect of aperture size on J_{th} and the differential efficiency of edge-emitting lasers.

respect to the aperture size. It can be seen that the J_{th} remains constant up to an 8- μm aperture width and increases mildly as the aperture size reduces to 4 μm . Further reduction in the aperture size results in a rapid increase of J_{th} . On the other hand, η_d remains constant even as the aperture size reduces to 0.75 μm , indicating that the injection efficiency and the internal optical loss remain unchanged. Therefore, the increase in J_{th} at smaller aperture size can be attributed to the current spreading in the p-InP layer below the aperture and in the QWs. Earlier reports^{5,9,10} have suggested that an aperture size of 5–8 μm would be ideal to realize efficient, single-mode 1.55- μm VCSELs. In this case, for edge-emitting lasers, we observed an increase in J_{th} from 0.8 kA/cm^2 to 0.98 kA/cm^2 (about 22%) when the aperture reduces to 5 μm , which is not very substantial. Also, our VCSEL design enables us to carry out a selective lateral wet etch of the active region, which should help minimize the carrier diffusion in QWs.

Figure 9 shows the continuous wave L-I-V characteristics of a VCSEL with 6- μm aperture. The device has a pillar size of 22 μm and an additional annular ring of 10- μm width to provide the top intracavity contact. To obtain an aperture size of 6 μm , selective etching up to a depth of 18 μm from each side was carried out. Using an etch rate of 35 nm per minute, it takes about 8.5 h. While testing, the device was not mounted on a heat sink and no antireflection coating was applied. The inset shows single-mode emission at 1,536 nm. This shows that the TJ aperture, though placed at optical null, provides a sufficient, effective lateral-index step to cause single-mode operation. The device showed an I_{th} of 1.2 mA, a η_d of 21%, and a maximum output power (P_{max}) of 0.26 mW at 20°C. These results are pretty impressive given the fact that the device shows a very large threshold voltage of 2.75 V, a differential resistance of 300 Ω , and an undesirable positive gain-mode offset of 12 nm. The higher V_{th} in our current device is partly because of the high turn-on

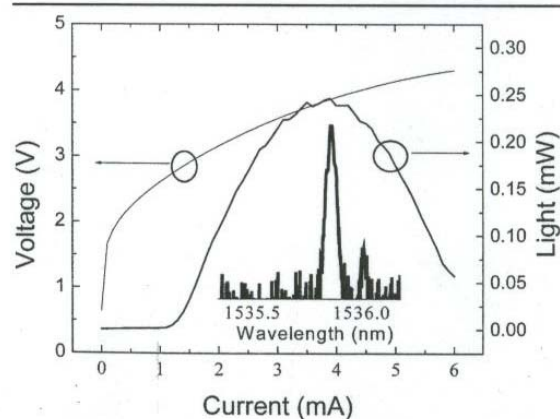


Fig. 9. Continuous-wave operation of a 1.55- μm VCSEL with an aperture size of 6 μm at 20°C.

voltage caused by the insufficient doping of the p++-layer in the TJ, which raised the voltage drop across the TJ. Because of a temporary problem with the CBr₄ source for C-doping, we used a Be δ -doped layer in the TJ. The carrier concentration of this layer was not as high as the desired value, which is greater than $1 \times 10^{20} \text{ cm}^{-3}$. This high electrical resistance and high V_{th} generates a large amount of heat, which, in turn, causes an increase in I_{th} , a reduction in η_d and gain,¹¹ and increases gain-cavity resonance mismatch as the gain peak shifts to longer wavelength at a much faster rate than the cavity resonance, which hastens power roll off. We anticipate that when the Be-doped layer in the TJ is again replaced with the C-doped layer, the device performance would be vastly improved.

CONCLUSIONS

The TJ, the most efficient lateral current spreader inside the cavity, is an ideal choice for an aperture to prevent carrier spreading below the aperture and, at the same time, allow efficient spreading within the aperture to avoid current crowding at the edges. We have demonstrated a high etch selectivity between the aperture layer and the InP to allow an aperture etch of several microns. It was demonstrated that the type-II staggered band alignment between InP and AlInAs would not affect the internal injection effi-

ciency when the InP between the aperture and the active region is doped with a p-type impurity. Finally, we have implemented the TJ aperture in a 1.55- μm VCSEL with no extra processing step, demonstrating successfully single-mode continuous-wave operation with a high room-temperature differential efficiency of 21%.

REFERENCES

1. E.R. Hegblom, N.M. Margalit, A. Fiore, and L.A. Coldren, *IEEE J. Sel. Top. Quant. Electron.* 5, 553 (1999).
2. W. Yuen et al., *Electron. Lett.* 36, 1121 (2000).
3. J.-H. Shin, B.-S. Yoo, W.-S. Han, O.-K. Kwon, Y.-G. Ju, and J.-H. Lee, *IEEE Photon. Technol. Lett.* 14, 1031 (2002).
4. M. Ortsiefer, R. Shau, G. Bohm, F. Kohler, and M.-C. Amann, *Appl. Phys. Lett.* 76, 2179 (2000).
5. S. Nakagawa, E. Hall, G. Almuneau, J.K. Kim, D.A. Buell, H. Kroemer, and L.A. Coldren, *Appl. Phys. Lett.* 78, 1337 (2001).
6. A.E. Bond, P.D. Dapkus, and J.D. O'Brien, *IEEE Photon. Technol. Lett.* 10, 1362 (1998).
7. B.J. Thibeault, E.R. Hegblom, P.D. Floyd, R. Naone, Y. Akulova, and L.A. Coldren, *IEEE Photon. Technol. Lett.* 8, 593 (1996).
8. M.H.M. Reddy, A. Huntington, D. Buell, R. Koda, E. Hall, and L.A. Coldren, *Appl. Phys. Lett.* 80, 3509 (2002).
9. Y. Ohiso, H. Okamoto, R. Iga, K. Kishi, and C. Amano, *IEEE Photon. Technol. Lett.* 14, 738 (2002).
10. A. Karim, P. Abraham, D. Lofgreen, Y.J. Chiu, J. Piprek, and J.E. Bowers, *Appl. Phys. Lett.* 78, 2632 (2001).
11. J. Piprek, Y.A. Akulova, D.I. Babic, L.A. Coldren, and J.E. Bowers, *Appl. Phys. Lett.* 72, 2632 (1998).

III. Photodetectors and Receivers

Recent Advances in Avalanche Photodiodes

Joe C. Campbell, *Fellow, IEEE*, Stephane Demiguel, Feng Ma, Ariane Beck, Xiangyi Guo, Shuling Wang, Xiaoguang Zheng, Xiaowei Li, Jeffrey D. Beck, *Senior Member, IEEE*, Michael A. Kinch, Andrew Huntington, Larry A. Coldren, *Fellow, IEEE*, Jean Decobert, and Nadine Tschertner

Invited Paper

Abstract—The development of high-performance optical receivers has been a primary driving force for research on III-V compound avalanche photodiodes (APDs). The evolution of fiber optic systems toward higher bit rates has pushed APD performance toward higher bandwidths, lower noise, and higher gain-bandwidth products. Utilizing thin multiplication regions has reduced the excess noise. Further noise reduction has been demonstrated by incorporating new materials and impact ionization engineering with beneficially designed heterostructures. High gain-bandwidth products have been achieved waveguide structures. Recently, imaging and sensing applications have spurred interest in low noise APDs in the infrared and the UV as well as large area APDs and arrays. This paper reviews some of the recent progress in APD technology.

Index Terms—Avalanche photodiodes (APDs), impact ionization, infrared, multiplication noise, photodetectors, ultraviolet (UV).

I. INTRODUCTION

INITIAL development of III-V compound avalanche photodiodes (APDs) was driven by fiber optic telecommunications, primarily for high-bit-rate, long-haul receivers. Compared to receivers with p-i-n photodiodes, those that utilize APDs achieve 5–10 dB better sensitivity. For these devices, research focused on reducing the excess noise and developing structures with high gain-bandwidth products to accommodate the ever-increasing bit rates of fiber-optic systems. Recently, imaging applications such as three-dimensional (3-D) imaging, sensing, and space-related spectroscopy have stimulated interest in APD arrays and large area devices that operate in the UV and short wavelength infrared (SWIR) range ($0.8 \mu\text{m} \leq \lambda \leq 2.2 \mu\text{m}$). For these tasks, speed is not critical, but it is essential to attain very low dark current densities and

low multiplication noise. In this paper, we will review some of the recent developments that have brought about improved APD performance.

II. LOW-NOISE APDS

The multiplication region of an APD plays a critical role in determining the gain, the multiplication noise, and the gain-bandwidth product. According to the local-field avalanche theory [1]–[3], both the multiplication noise and the gain-bandwidth product of APDs are determined by the electron, α , and hole, β , ionization coefficients of the material in the multiplication region; better performance is achieved when one of the ionization coefficients is much larger than the other, i.e., the β/α ratio (k) deviates markedly from unity. Since k is a material property, efforts to improve APD performance have focused on optimizing the electric field profile and characterizing new materials. For example, it has recently been reported that $k \sim 0.15$ to 0.19 for $\text{Al}_x\text{Ga}_{1-x}\text{As}$ ($x \geq 0.8$). [4]–[6]

Some compositions of $\text{Hg}_{1-x}\text{Cd}_x\text{Te}$ appear to exhibit even lower k values. Beck *et al.* [7] have observed exponential gain curve and extremely low multiplication noise ($F(M) \sim 1$ for multiplication, M , up to 100) in $\text{Hg}_{0.7}\text{Cd}_{0.3}\text{Te}$ APDs. These phenomena suggest that $k \sim 0$. Unlike most III-V semiconductors, $\text{Hg}_{0.7}\text{Cd}_{0.3}\text{Te}$ has a very small band gap (0.29 eV) for the Γ valley, and very high L and X valleys (1.5 and 2.5 eV, respectively [8]). The band structure suggests that in a $\text{Hg}_{0.7}\text{Cd}_{0.3}\text{Te}$ APD, electrons have a very small intervalley phonon scattering rate, which is the dominant scattering mechanism in most III-V semiconductors. In addition, the large effective mass ratio ($m_h/m_e \sim 30$) indicates that there is a large difference in the phonon and alloy scattering rates of holes and electrons for transport in $\text{Hg}_{0.7}\text{Cd}_{0.3}\text{Te}$. This picture is supported by the measured high electron mobility (two orders of magnitude higher than hole mobility) in HgCdTe materials. [9]

We have developed a Monte Carlo model to quantitatively study impact ionization in $\text{Hg}_{1-x}\text{Cd}_x\text{Te}$. For this study, the band structure of $\text{Hg}_{0.7}\text{Cd}_{0.3}\text{Te}$, including the Γ , L and X valleys of the conduction band, and heavy hole, light hole, and split-off valance bands, was incorporated into the model. Using a Keldysh formula [10] for impact ionizations, and threshold energies of 0.3 and 0.6 eV [11], respectively, for electrons and holes, the simulated gain and noise for an APD with a 3- μm -thick intrinsic region are shown as dashed lines in Fig. 1. This simulation assumes that electrons are injected from the

Manuscript received March 4, 2004; revised June 4, 2004. This work was supported by the Defense Advanced Research Projects Agency through the Center for Chips with Heterogeneously Integrated Photonics, the 3-D Imaging Program, and the Semiconductor Ultraviolet Optical Sources (SUVOS) Program.

J. C. Campbell, S. Demiguel, F. Ma, A. Beck, X. Guo, S. Wang, X. Zheng, and X. Li are with the Microelectronics Research Center, The University of Texas at Austin, Austin, TX 78712 USA (e-mail: jcc@mail.utexas.edu).

J. D. Beck and M. A. Kinch are with DRS Infrared Technologies, LP, Dallas, TX 75374 USA.

A. Huntington and L. A. Coldren are with the Materials Department, Optoelectronics Technology Center, University of California at Santa Barbara, Santa Barbara, CA 93106 USA.

J. Decobert and N. Tschertner are with Alcatel R&I, 91460 Marcoussis, France.

Digital Object Identifier 10.1109/JSTQE.2004.833971

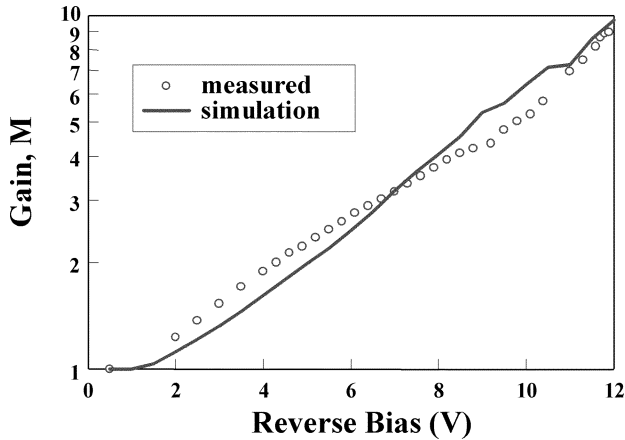


Fig. 1. Simulated (○) and measured (solid line) (a) gain and (b) excess noise factor of a 3- μm -thick cylindrical $\text{Hg}_{0.7}\text{Cd}_{0.3}\text{Te}$ APD.

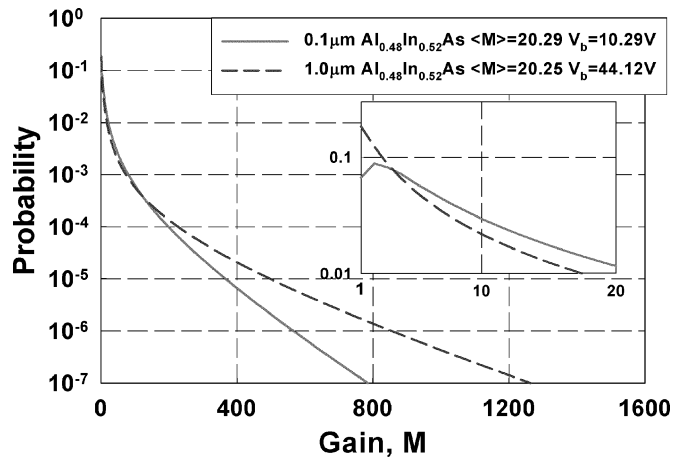


Fig. 2. Comparison of the gain distribution curves for $\text{Al}_{0.48}\text{In}_{0.52}\text{As}$ APDs having multiplication region widths of 1.0 (dashed line) and 0.1 μm (solid line). The average gain for both APDs is $M \sim 20$ but the excess noise factors for the 1.0 and 0.1 μm APDs is 6.9 and 4, respectively.

p side of the cylindrical APD structure in [8], and the electric field profile in the intrinsic region has been calculated for with a Poisson solver. The simulated exponential-shaped gain curve (solid line) is consistent with experimental data [circles in Fig. 1(a)]. The simulated noise [Fig. 1(b)] is very low, as would be expected if $\beta \sim 0$.

It has also been shown for a wide range of materials including InP [12]–[15], GaAs [14]–[20], $\text{Al}_x\text{In}_{1-x}\text{As}$ [14], [15], [21], Si [22], [23], $\text{Al}_x\text{Ga}_{1-x}\text{As}$ [14], [15], [24]–[26], SiC [27], and GaInP [28] that lower excess noise and higher gain-bandwidth products can be achieved, irrespective of the value of k , by sub-micron scaling of the thickness of the multiplication region. The origin of this effect is the nonlocal nature of impact ionization, which is frequently expressed in terms of the so-called “dead space,” the minimum distance over which carriers gain sufficient energy to impact ionize. The dead space effectively reduces the number of outlier high gain events [29], [30]. This, in turn, results in smaller deviations from the mean gain and, thus, lower excess noise factors. This is illustrated in Fig. 2, which shows the gain distributions of two $\text{Al}_{0.48}\text{In}_{0.52}\text{As}$ APDs with multiplication layer thickness of 1.0 (dashed line) and 0.1 μm (solid line).

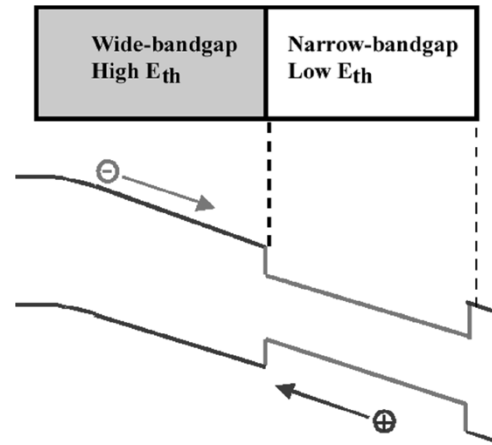


Fig. 3. Multiplication region of impact-ionization-engineered APD.

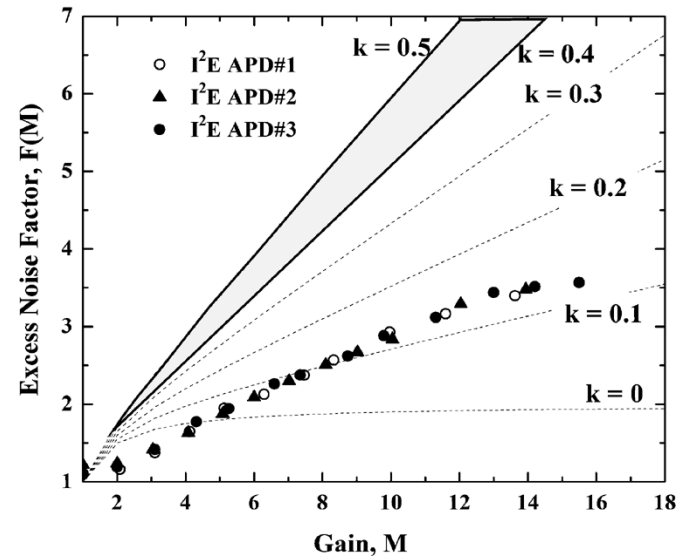


Fig. 4. Excess noise factor $F(M)$ versus gain for an $\text{In}_{0.52}\text{Ga}_{0.15}\text{Al}_{0.33}\text{As}/\text{In}_{0.52}\text{Al}_{0.48}\text{As}$ I^2E APD.

These APDs have the same average gain, $M \sim 20$, but the excess noise factor was 6.9 and 4.0 for the 1.0- and 0.1- μm APDs, respectively. The gain distribution of the 1.0- μm APD is broader than the 0.1- μm device, which is an indication of higher multiplication noise. This graph also shows that the thicker device has higher probabilities for both high gain ($M > 80$) and low gain ($M = 1$) than the 0.1- μm APD, while the probabilities for the thin device are higher for gains in the range $2 < M < 80$. This is reasonable since they have different standard deviations in M while keeping $\langle M \rangle$ the same. It is interesting that the 1.0- μm APD has a peak at $M = 1$, while the 0.1 μm APD has a peak at $M = 2$. It follows, somewhat counter intuitively, that for the same gain, it is less likely that the initial carrier will emerge from the i -region without ionization for the thinner device. This has also been observed in [19].

A third approach that has achieved low noise is impact ionization engineering (I^2E) with beneficially designed heterostructures. This approach utilizes heterojunctions to provide greater localization of impact ionization than can be achieved in spatially uniform structures. Initial work that demonstrated the efficacy of this approach utilized the $\text{GaAs}/\text{Al}_x\text{Ga}_{1-x}\text{As}$

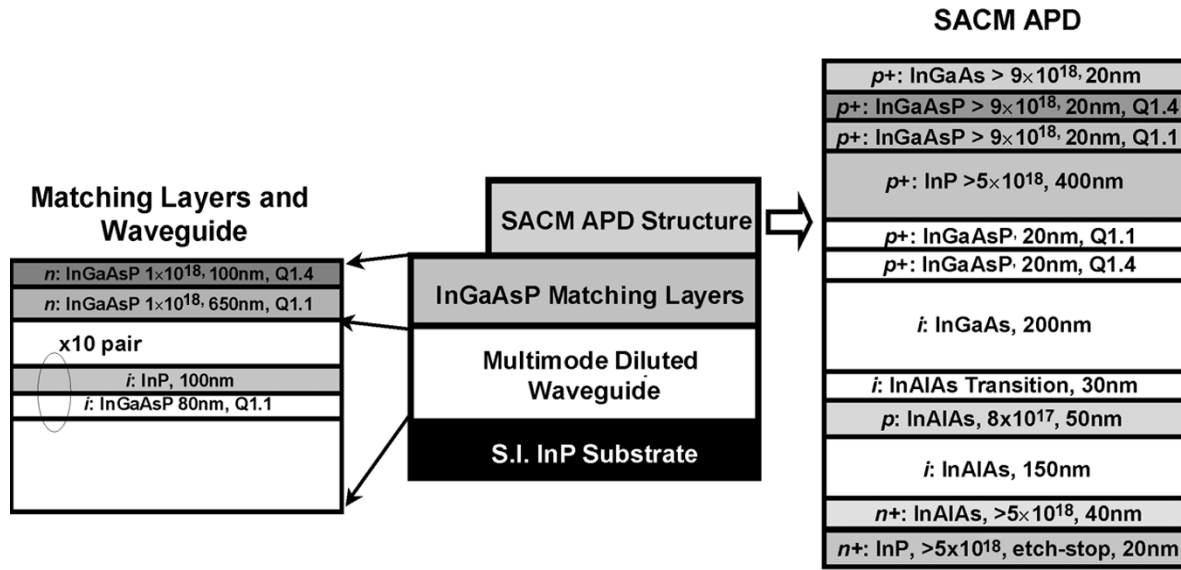


Fig. 5. Structure of evanescently-coupled waveguide APD.

material system. [31]–[35] More recently, InGaAlAs/InP implementations that operate at the telecommunications wavelengths have been reported. [36] The basic idea of I²E is to place thin narrow bandgap layers with relatively low threshold energies adjacent to wider bandgap regions with higher threshold energies. An implementation of the I²E structure is shown in Fig. 3. Structurally, the I²E is similar to a truncated multiple quantum well (frequently mislabeled as “superlattice”) APD [37], [38], however, operationally there is a fundamental difference in that the I²E does not invoke heterojunction band discontinuities.

Fig. 4 shows the excess noise factor $F(M)$ versus gain for three InGaAlAs I²E APDs grown lattice-matched to InP by molecular beam epitaxy. [36] The unintentionally doped multiplication region, which consisted of a 100-nm-thick In_{0.52}Al_{0.48}As layer and a 100-nm-thick In_{0.52}Ga_{0.15}Al_{0.33}As quaternary layer, was sandwiched between p-type ($3 \times 10^{18} \text{ cm}^{-3}$, 0.8 μm), and n-type ($5 \times 10^{18} \text{ cm}^{-3}$, 0.5 μm) In_{0.52}Al_{0.48}As layers, with a highly p-doped ($> 5 \times 10^{18} \text{ cm}^{-3}$, $\sim 30 \text{ nm}$) In_{0.53}Ga_{0.47}As contact layer on the top. The lower bandgap energy of In_{0.52}Ga_{0.15}Al_{0.33}As (estimated to be $E_g \sim 1.25 \text{ eV}$) as compared to In_{0.52}Al_{0.48}As ($E_g \sim 1.51 \text{ eV}$) results in lower carrier ionization threshold energy (E_{th}). There are relatively few ionization events in the In_{0.52}Al_{0.48}As layer, owing to the combined effects of “dead space” and the higher threshold energy in In_{0.52}Al_{0.48}As. The dotted lines in Fig. 4 are plots of $F(M)$ for $k = 0$ to 0.5 using the local field model [1], [2]. These plots are presented solely for reference because the k value has become a widely used figure of merit for excess noise. For $M \leq 4$, it appears that $k < 0$, which is unphysical and simply reflects the inapplicability of the local field model for this type of multiplication region. For higher gain, the excess noise is equivalent to a k value of ~ 0.12 . This is the lowest noise that has been reported for APDs that operate at the telecommunications wavelengths ($\lambda \sim 1300 \text{ nm}$ and 1550 nm). For reference, the excess noise factor for commercial InP/In_{0.53}Ga_{0.47}As APDs that have been widely deployed in fiber optic receivers

is shown as the shaded region in Fig. 4. Typically, these APDs exhibit $0.4 < k < 0.5$.

An intuitive explanation of the I²E APD is that carriers gain energy in the wide bandgap layer but since the threshold energy in that layer is relatively high, there are few ionization events. When the carriers enter the narrow bandgap layer, where the threshold energy is smaller, the energetic carriers ionize quickly. We conclude that the lower noise of the I²E structure is a result of the spatial modulation of the probability distribution for impact ionization. The heterojunction results in a more spatially localized process, which, in turn, reduces the noise.

III. HIGH-SPEED APDS

For high-speed applications, it is essential for the APDs to achieve high gain-bandwidth products without sacrificing responsivity. At present, the most attractive approach to meeting these goals is to incorporate separate absorption, charge, and multiplication (SACM) APDs with the waveguide structures that have proved successful for high-speed p-i-n photodiodes. To date, a few edge-coupled waveguide APDs have been demonstrated [39]–[41]. High external quantum efficiency of 72% was achieved by direct edge coupling into the absorbing layer of 0.5- μm , but the bandwidth was only 20 GHz at low gain [39]. A similar approach with a thinner multiplication layer achieved a higher bandwidth of 35 GHz at low gain; the external quantum efficiency was 58% and the gain-bandwidth product was 140 GHz [40]. A higher gain-bandwidth product of 320 GHz was demonstrated with a thinner absorbing layer (0.2- μm), however the quantum efficiency was only 16% [41]. Using an APD with a 0.12- μm absorbing thickness, an evanescently-coupled asymmetric twin-waveguide APD obtained a quantum efficiency of 48% [42], but at the expense of a more complex (and thus more difficult to fabricate) structure. The bandwidth at low gain was 31.5 GHz and the gain-bandwidth product was 150 GHz.

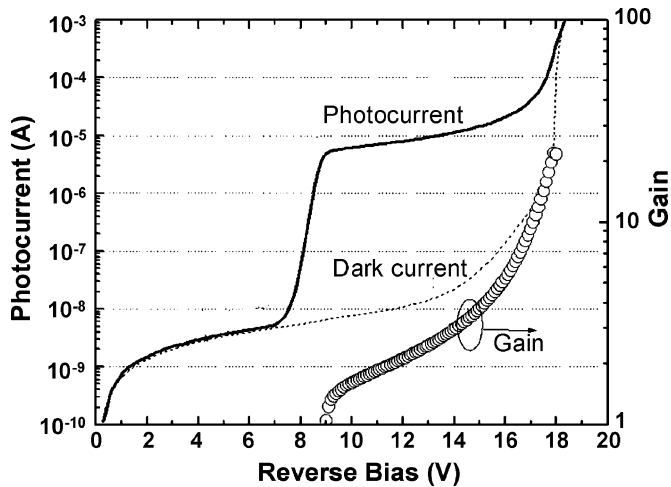


Fig. 6. Photocurrent, dark current, and gain of evanescently coupled waveguide APD.

Previously, it has been shown that high efficiency ($>80\%$) and broad bandwidth (>48 GHz) can be achieved with an evanescently coupled p-i-n having a planar short multimode input waveguide [43]. A strength of this approach is simplicity of fabrication. We have utilized this approach to fabricate an evanescently coupled waveguide SACM APD. A schematic cross section of the evanescently-coupled APD is shown in Fig. 5. The epitaxial structure was grown by low-pressure metal organic vapor phase epitaxy (LP-MOVPE) on semi-insulating InP substrate. The structure consists of a diluted waveguide and two optical matching layers [43] beneath the SACM APD. Proceeding sequentially from the bottom, the APD was comprised of an n-type AlInAs layer followed by an undoped AlInAs multiplication region of 150 nm. Then, a p-type AlInAs charge layer of 50 nm was grown with a nominal doping level of $8 \times 10^{17} \text{ cm}^{-3}$. An undoped graded layer of 30 nm was inserted between the AlInAs charge layer and the InGaAs absorbing layer in order to smooth the heterojunction. Two 20-nm InGaAsP layers (1.4- and 1.1- μm bandgap) were used for the same purpose at the InGaAs/InP heterojunction. The absorbing layer thickness was 190-nm, which resulted in a total active SACM thickness of 0.46- μm . The associated short transit time enabled high-speed operation at low gains. Processing was similar to that for the p-i-n photodiodes described in [43].

Fig. 6 shows a typical current-voltage characteristic for a $5 \times 20 \mu\text{m}^2$ evanescently-coupled APD. The light was coupled from a 3- μm spotsized lensed fiber to the multimode waveguide. The capacitance-voltage characteristic indicated that the punchthrough voltage was ~ 10 V. The breakdown occurred below 18.5 V and the dark current at 90% of the breakdown was in the range 100–500 nA. To determine the gain at punchthrough, the quantum efficiency was measured using top illumination on a large-area device and was compared to the maximum theoretical value [41]. Following this method, the minimum gain at punchthrough was estimated to be 1.6.

The -3 -dB bandwidths were measured with a heterodyne setup, based on the mixing of two single-mode DFB temperature-controlled lasers. Fig. 7 shows the -3 dB bandwidth versus dc gain achieved on $5 \times 20 \mu\text{m}^2$ photodiodes. The highest

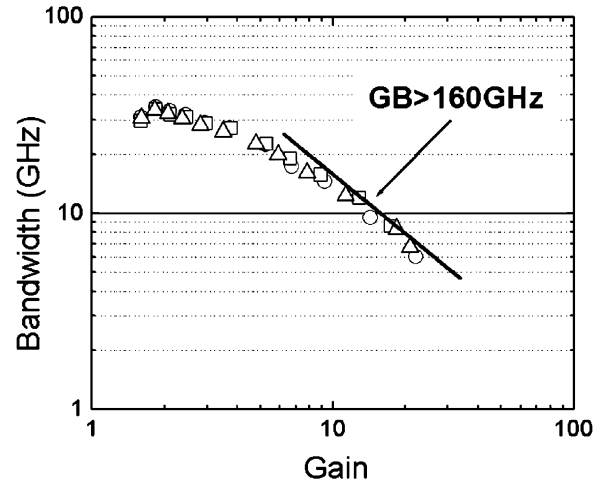


Fig. 7. Bandwidth versus gain for three evanescently-coupled waveguide APDs.

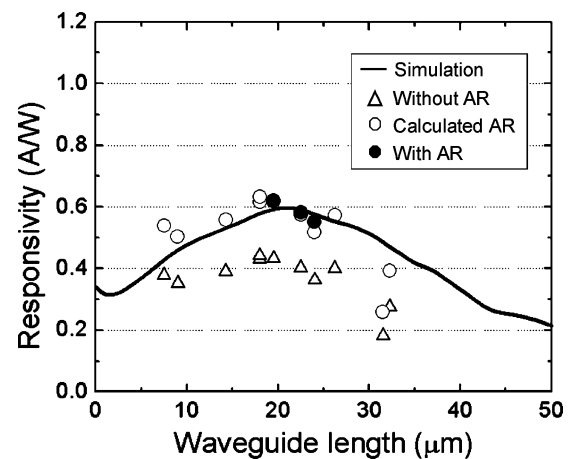


Fig. 8. Measured responsivity of evanescently-coupled waveguide APD with (\bullet) and without (Δ) antireflection (AR) coating versus length of multimode input waveguide. Also shown are the calculated responsivity with AR coating (\circ) and BPM simulated response (solid line).

bandwidth of 34.8 GHz was obtained at 11 V reverse bias corresponding to a gain of 1.84. At the same gain, 5×15 and $5 \times 30 \mu\text{m}^2$ diodes exhibited bandwidths of 35.5 and 31.8 GHz, respectively, which suggests that the low-gain bandwidth was transit-time limited. At high gain, the bandwidth was limited by the gain-bandwidth, which was ~ 160 GHz.

The thickness of the SACM layers were designed to obtain the best transfer of light from the input waveguide to the absorbing layer. The solid line in Fig. 8 presents the simulated responsivity of a $5 \times 20 \mu\text{m}^2$ diode versus the length of the multimode input waveguide. Owing to the low refractive index of the multiplication and charge layers, the projected responsivity was lower than for p-i-n photodiodes. In agreement with the modeling, the optimal waveguide length was $19 \pm 1 \mu\text{m}$. Using a 3- μm spotsized lensed fiber, a maximum responsivity of 0.62 A/W was achieved with AR coating at 1.543- μm wavelength with TE/TM polarization dependence less than 0.5 dB. The -1 -dB alignment horizontal and vertical tolerances for a 5- μm -wide diode were ± 1.8 and $\pm 0.9 \mu\text{m}$, respectively.

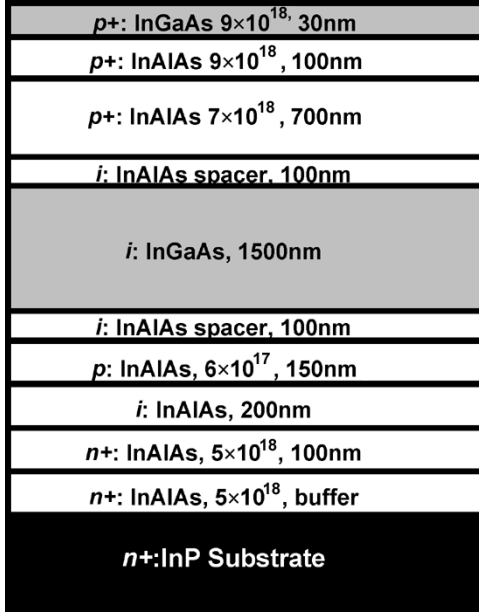


Fig. 9. Cross sectional schematic of $\text{Al}_{0.48}\text{In}_{0.52}\text{As}/\text{In}_{0.53}\text{Ga}_{0.47}\text{As}$ SACM structure utilized for the large-area APDs and arrays.

IV. ARRAYS AND LARGE-AREA APDS

Much of the research on III-V compound APDs has focused on achieving high-speed, low-noise operation for fiber optic receivers. For this application, small device size is preferred in order to reduce the RC time constant. On the other hand, emerging optical measurement systems that operate in the eye-safety wavelength range ($\sim 1.5 \mu\text{m}$) require long-wavelength, high-sensitivity photodiodes with large detection area. For many applications of this type an APD is preferable to a p-i-n photodiode since the APD can achieve higher sensitivity. Similar material uniformity is required by APD imaging arrays [44]. Both applications present daunting challenges to the quality and uniformity of the epitaxial layers from which the APDs are fabricated. In response to these emerging applications, we have developed $\text{Al}_{0.48}\text{In}_{0.52}\text{As}/\text{In}_{0.53}\text{Ga}_{0.47}\text{As}$ APDs with diameters up to $500 \mu\text{m}$ and 18×18 arrays.

The SACM structure that was utilized for the large-area APDs and arrays is shown in Fig. 9. The APD wafers were grown by molecular beam epitaxy on n -type InP (100) substrates. Mesas were etched in phosphoric etchant ($\text{H}_3\text{PO}_4 : \text{H}_2\text{O}_2 : \text{H}_2\text{O} = 1 : 1 : 8$) to the n^+ InP buffer layer where a Ni (20)/AuGe (30)/Au (80 nm) n -type ohmic contact was formed. The Cr (25)/Au (85 nm) p -type contacts were formed by standard evaporation and lift off. APDs with a wide range of diameters (from 20 to $500 \mu\text{m}$) were fabricated for characterization. Arrays of $50 \mu\text{m}$ -mesa-diameter APDs were also processed in order to evaluate the material quality, device uniformity, and device performance.

The typical photoresponse and dark current curves of a $500\text{-}\mu\text{m}$ -diameter APD are shown in Fig. 10. The punch-through voltage was $\sim 15.0 \text{ V}$, and the breakdown voltage was $\sim 39.2 \text{ V}$. The photocurrent was not flat above the punch-through voltage, an indication of gain prior to punch-through. The gain was estimated by comparing the measured external quantum efficiency with the theoretical

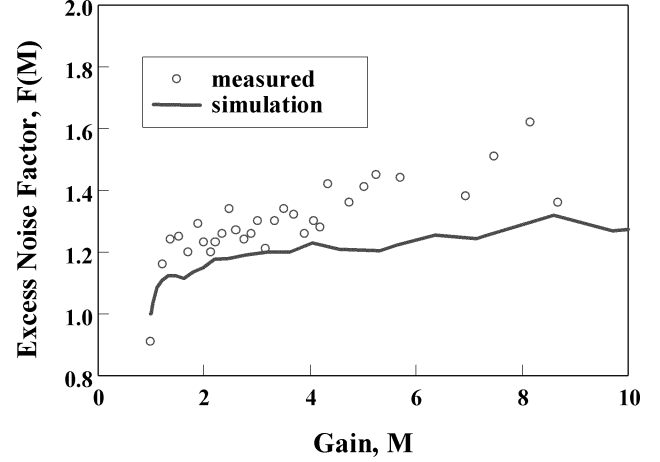


Fig. 10. Photocurrent, dark current, and gain curves for an $\text{Al}_{0.48}\text{In}_{0.52}\text{As}/\text{In}_{0.53}\text{Ga}_{0.47}\text{As}$ SACM APD.

maximum based on the reflected power at the surface and the thickness of the absorbing layer. This provided a lower limit to the gain. Using this approach the gain at 16.0 V was estimated to be ~ 1.8 . The assertion of gain at punch-through can be also corroborated by an estimate of the electric field intensity. At a reverse bias of 16.0 V , the electric field in the $\text{In}_{0.52}\text{Al}_{0.48}\text{As}$ multiplication region is $\sim 580 \text{ kV/cm}$, assuming a 200 nm $\text{In}_{0.52}\text{Al}_{0.48}\text{As}$ undoped multiplication region and a 150-nm p -type ($6 \times 10^{17} \text{ cm}^{-3}$) $\text{In}_{0.52}\text{Al}_{0.48}\text{As}$ charge region. This value of electric field is consistent with measurements on $\text{In}_{0.52}\text{Al}_{0.48}\text{As}$ homo-junction APDs [21], from which it was found that the electric field in a 200-nm -thick multiplication region at gain of 1.8 was $\sim 560 \text{ kV/cm}$.

The APD dark current consists of the bulk leakage current, which is proportional to the mesa area, and the sidewall leakage current, which scales with the mesa perimeter. The total dark current can be expressed as

$$I_{\text{total}} = J_{\text{sidewall}} \cdot \pi \cdot d + \frac{J_{\text{bulk}} \cdot \pi \cdot d^2}{4} \quad (1)$$

where J_{sidewall} is the sidewall leakage current density (in amps per micron) and J_{bulk} is the bulk leakage current density (in amps per micron squared). The measured dark current at bias voltage of $\sim 16 \text{ V}$ is plotted in Fig. 11 versus mesa diameter. The solid line is a quadratic fit, which shows that the bulk component of the dark current is dominant. From the fit, the surface dark current density J_{sidewall} was $0.19 \text{ nA}/\mu\text{m}$ and the bulk dark current density was $0.023 \text{ nA}/\mu\text{m}^2$. The total dark current can also be expressed in terms of the multiplied dark current and unmultiplied dark current using

$$I_{\text{total}} = I_{\text{unmultiplied}} + I_{\text{multiplied}} \cdot M. \quad (2)$$

By fitting the data to (2), it was found that the unmultiplied dark current (density) was $\sim 1.32 \text{ nA}$ and the multiplied dark current was $\sim 1.54 \text{ nA}$. The dependence of dark current on gain remains linear to gain values > 50 . The low value of the unmultiplied dark current (density) is an indication of good material quality and surface passivation; it can be neglected for APDs biased at high gains.

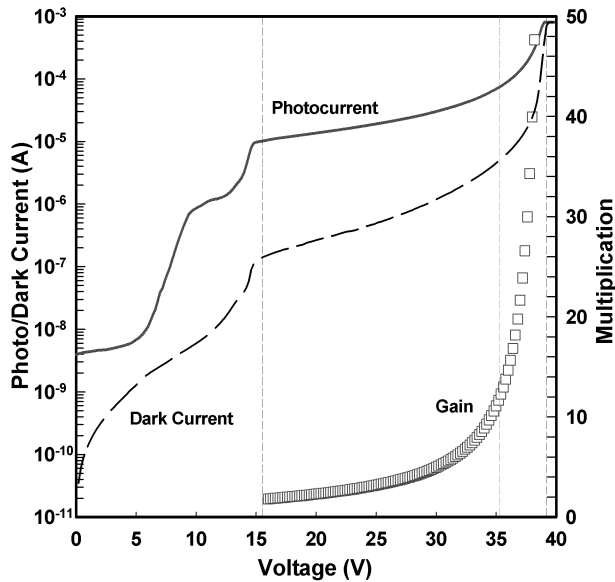


Fig. 11. Measured dark current and quadratic fit versus mesa diameter for $\text{Al}_{0.48}\text{In}_{0.52}\text{As}/\text{In}_{0.53}\text{Ga}_{0.47}\text{As}$ SACM APDs.

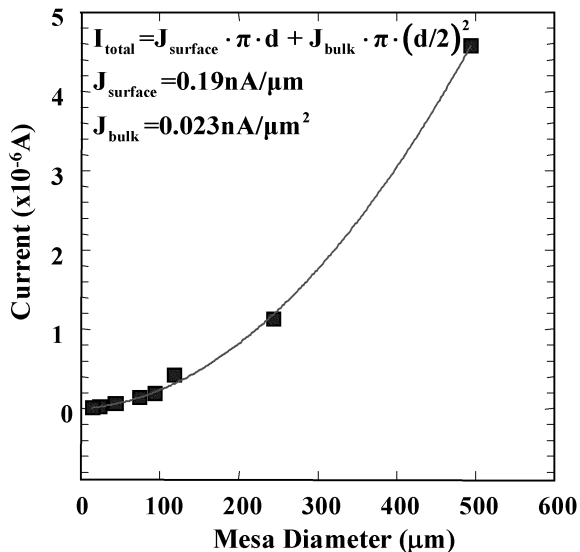


Fig. 12. Raster scan of photoresponse of a 500- μm -diameter $\text{Al}_{0.48}\text{In}_{0.52}\text{As}/\text{In}_{0.53}\text{Ga}_{0.47}\text{As}$ SACM APD for $M \sim 20$.

The spatial uniformity of a 500- μm -diameter APD was measured by raster-scanning. A 1.52- μm -wavelength He-Ne laser beam with a beam-waist $< 5 \mu\text{m}$ across a 500- μm -diameter APD at $M \sim 20$. A flat, uniform photoresponse profile was obtained across the whole mesa area, as shown in Fig. 12. No spikes in the interior or edge peaks were observed. The “hole” near the edge is due the probe and the top p-type contact.

The photocurrent, dark current, and gain of each device in an 18×18 array of 50- μm -diameter APDs were measured. Three devices on the array failed due to improper probing. Statistical analysis of the dark current for the other 321 devices exhibited a mean value of $\sim 4.4 \text{ nA}$ and a standard deviation of 1.5 nA at the punchthrough voltage of 16.0 V (gain ~ 1.8). The dark current distribution at 90% of the breakdown exhibited a mean value

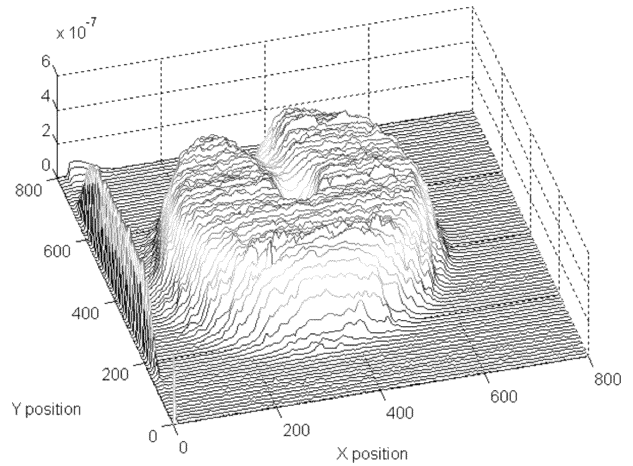


Fig. 13. Schematic cross section of 4H-SiC APD. The inset shows an SEM photograph of the etched mesa.

of $\sim 71 \text{ nA}$ and a standard deviation of 13 nA. Uniform photocurrent was consistently observed across the array. The mean value of gain was 10.9, 16.1, 22.1, and 43.4 at reverse bias voltages of 35.0, 36.4, 37.2, and 38.2 V, respectively. The standard deviations of the gain distribution at each of these reverse bias conditions were 0.9, 1.4, 2.1, and 5.6, respectively. The low-gain bandwidth of one of the 50- μm -diameter APDs in the array was $\sim 8 \text{ GHz}$. The bandwidth at low gain was limited by the transit time through the long carrier transport path ($\sim 3.9 \mu\text{m}$) associated with the depleted absorption, charge, and multiplication regions. At higher gains a gain-bandwidth product of 120 GHz was observed.

V. ULTRAVIOLET (UV) APDS

Detection of UV light has numerous medical, military, and environmental applications. Photomultiplier tubes (PMTs) are frequently used for these applications because they have high responsivity ($> 600 \text{ A/W}$), high speed, and low dark current. However, they are costly, large, and require high bias voltages (typically several hundred volts). For some applications another major drawback to using PMTs is that expensive filters are required, due to their high response in the visible and near IR. Thus, it is desirable to replace PMTs with solid-state, UV photodetectors that have high gain. To this end, UV-enhanced Si APDs have been utilized with limited success. The Si APDs have the benefits of a mature material system, easy integration with integrated circuit technology, low noise, and good quantum efficiency. However, they have relatively high dark currents at room temperature and, like PMTs, require complex, expensive filters.

Back-illuminated solar-blind $\text{Al}_x\text{Ga}_{1-x}\text{N}$ p-i-n's have recently demonstrated excellent performance ($D^* \sim 2 \times 10^{14} \text{ cmHz}^{1/2}/\text{W}$ at 269 nm) with very low noise and strong rejection of wavelengths longer than 290 nm. [45] Typical responsivities at 280 nm were $\sim 0.12 \text{ A/W}$. GaN avalanche photodiodes (APDs) have been demonstrated [46]–[48], but the yields were very low due to defect-related micro-plasmas in the materials, and the devices were fragile and short-lived (typically a few minutes) [47], [48], which has precluded the development of APDs with acceptable performance.

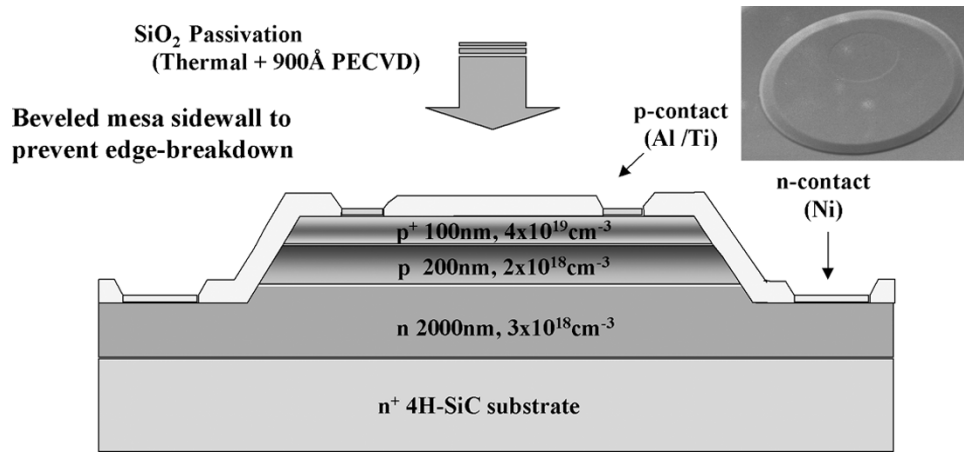


Fig. 14. Photocurrent, dark current, and gain of 100- μ m-diameter 4H-SiC APD.

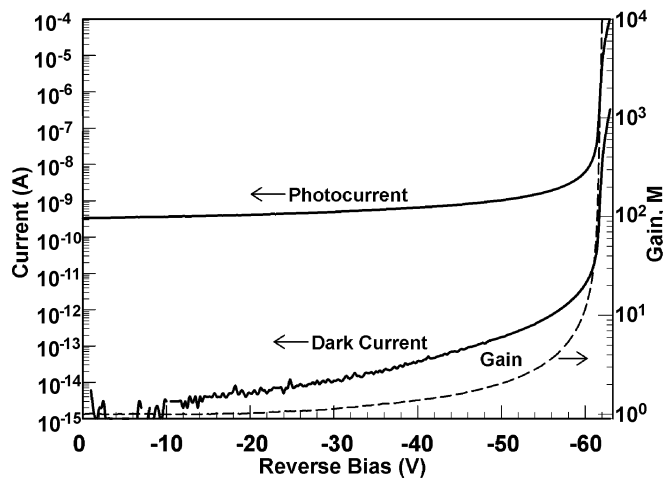


Fig. 15. Spectral response of 4H-SiC APD for a range of bias voltages.

Recently, 4H-SiC avalanche photodiodes with strong UV responsivities (comparable to photomultipliers), low multiplication noise, and moderate bias voltages (<70 V) have been demonstrated [49]–[53]. Benefiting from an indirect wide band gap and its material maturity and stability, 4H-SiC is an attractive candidate for avalanche photodiodes. Konstantinov *et al.* have shown that 4H-SiC exhibits widely disparate ionization coefficients [54]. The low k value for hole initiated impact ionization and resulting low noise are advantageous for applications such as missile detection, laser-induced fluorescence biological-agent warning systems, and nonline-of-sight UV communications, for which low noise and high gain are crucial.

Fig. 13 shows the structure of a SiC APD grown on n^+ 4H-SiC substrate. It consists of a 0.1- μ m p^+ cap layer, a 0.2- μ m p layer, and a 2- μ m n layer. Mesas were defined by reactive ion etching (RIE), with BCl_3 , to the underlying n layer. The sidewall passivation was achieved by 750 $^\circ$ C thermal oxidation in a wet oxidation furnace for 4 h. P-type (Al/Ti) contacts and n-type (Ni) contacts were patterned and deposited by a standard liftoff process. Both contacts were annealed in an RTA at 850 $^\circ$ C for 6 min in N_2 .

Fig. 14 shows the reverse current-voltage characteristics of a typical 100- μ m-diameter device. The devices exhibited an abrupt uniform breakdown near 61 V. In order to determine

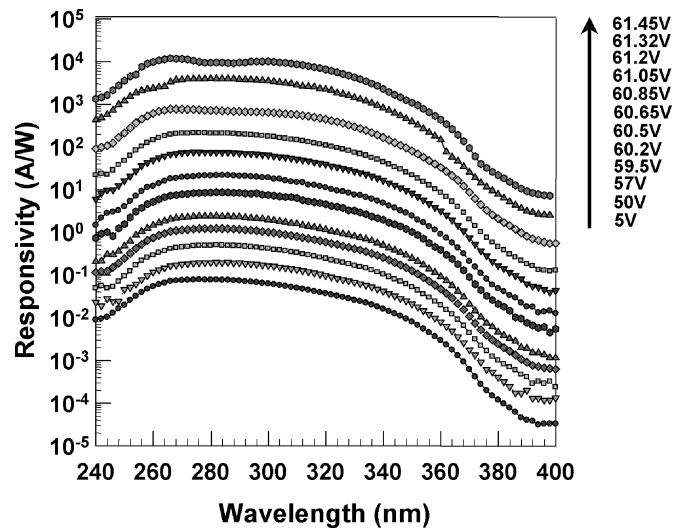


Fig. 16. Responsivity of 4H-SiC APD with and without a 266-nm “laser line” filter.

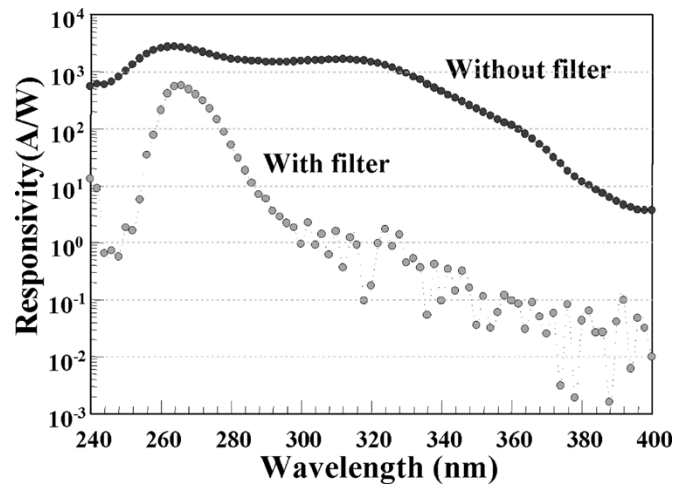


Fig. 17. Raster scans of the photocurrent of (a) nonbeveled and (b) beveled mesa-structure SiC APDs.

the gain, the photocurrent at -5 V was used as the unity gain reference point. Above this voltage, a slight linear increase in the photocurrent with bias is observed. It has been shown that

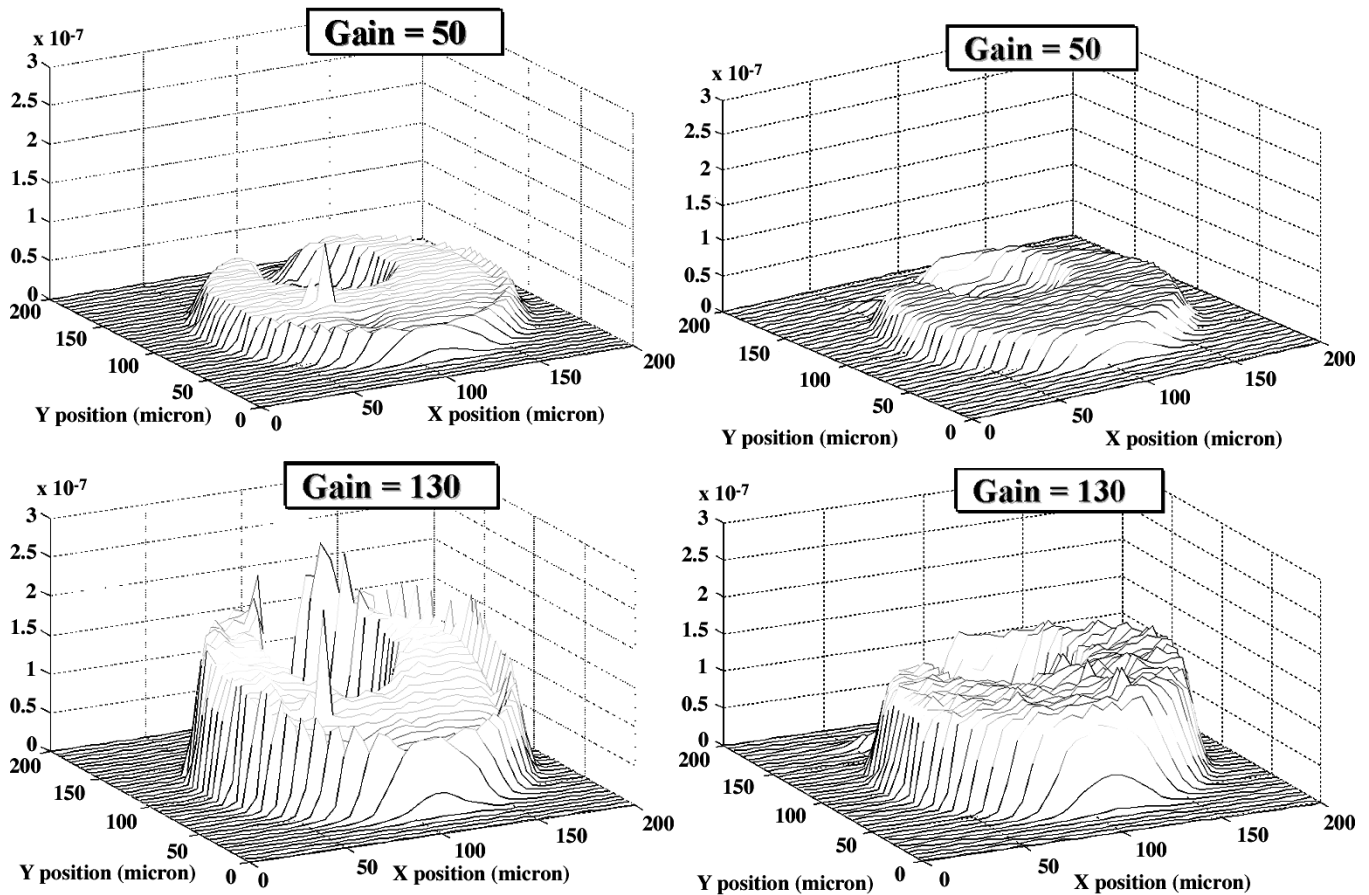


Fig. 18. Measured excess noise, $F(M)$, of a SiC APD versus gain, M . The excess noise corresponds to a k value of 0.15.

this slope in the photocurrent is due to slight widening of the depletion region [55]. A linear correction to account for this has been used for the gain determination. Below 30 V, the dark current was <10 fA and for photocurrent gain $\sim 10^3$, the dark current was <0.87 nA. The average dark current density at 95% of breakdown was 32 nA/cm².

The spectral response for a range of bias voltages is shown in Fig. 15. The response begins to cut off at 380 nm, corresponding to the 3.26-eV bandgap of 4H-SiC. The long-wavelength cutoff is not as sharp as that of direct bandgap semiconductors such as GaN. Nevertheless, the response drops by almost three orders of magnitude between 320 and 400 nm, providing a good visible blind response. At unity gain, the external quantum efficiency was $\sim 35\%$ at 276 nm (responsivity = 78 mA/W). As the bias increased toward breakdown, the responsivity increased by over five orders of magnitude; the peak responsivity was greater than 10 000 A/W at 266 nm. For applications that require a true solar-blind response, utilization of a SiC APD will require an external filter. Fig. 16 shows the responsivity with a "laser line" filter having a center wavelength of 266 nm. A sharp narrowband response with a peak responsivity of ~ 800 A/W was observed.

At very high gains, spatial uniformity of the photoresponse becomes a critical issue. Small variations in the electric field whether structural or materials in origin can result in large "gain spikes." For mesa structure SiC APDs, breakdown tends to occur at the mesa edge for negative bevel angles and steep

positive bevels [56]. This can be suppressed by fabricating very shallow ($\leq 7^\circ$) positive bevels. [57] This is illustrated by the two-dimensional raster scans of the photoresponse of nonbeveled and beveled SiC APDs in Fig. 17(a) and (b). The beveled sample had a bevel angle of approximately 7° while the nonbeveled device showed no discernible bevel angle, indicating $\sim 90^\circ$ sidewall. For both types of devices, the scans at unity gain (5-V reverse bias) exhibit a flat, uniform response. The circular gaps near the rear are the top p-type contacts, which shield the incident light. Fig. 17(a) shows photocurrent scans for a nonbeveled device at gains of 50 and 130. At a gain of 50, edge breakdown begins around the edges of the device. This becomes more pronounced at a gain of 130. The increased response occurring behind the contact, toward the device edge, results primarily from field crowding. The beveled device [Fig. 17(b)], on the other hand, shows no evidence of edge breakdown at gains of 50 and 130. The luminescence of the beveled device at breakdown (current density > 1.5 A/cm²) was uniform, and indication bulk breakdown.

It is well known that multiplication dominated by a single carrier type, either an electron or a hole, has better noise performance than devices with equal multiplication events of both carrier types. Fig. 18 shows the measured excess noise factors of a SiC APD as a function of gain. The excess noise of the device corresponds to a k value of 0.15.

An upper-bound of detectivity D^* can be estimated by assuming that the device is thermal noise limited at zero bias.

In that case, the spectral density of the noise current S_n is given by $S_n = 4k_B T / R_0$, where $R_0 = (dV/dI)_{V=0}$, k_B is Boltzman's constant, and T is temperature. Accordingly, D^* is given by $D^* = \Re \sqrt{R_0 A_D} / 4k_B T$, where \Re is the responsivity and A_D is the cross-sectional area of the photodetector. Curve fitting to the current-voltage characteristic of a 480- μm -diameter device yielded $R_0 = 3.7 \times 10^{15} \Omega$. Details of the curve-fitting procedure can be found in [58]. Consequently, an upper-bound of D^* was estimated to be $1.6 \times 10^{15} \text{ cm} \cdot \text{Hz}^{1/2} / \text{W}$ at 276 nm.

VI. CONCLUSION

Optical receivers for telecommunications has pushed the development of APDs with high bandwidth, low excess noise, and high gain bandwidth products. It has been shown that lower noise and higher gain bandwidth products can be achieved by submicron scaling of the multiplication region thickness and replacing InP in the multiplication layer with $\text{Al}_{0.48}\text{In}_{0.52}\text{As}$. We project that impact ionization engineering with beneficially designed heterostructures can reduce the noise even further. High-speed operation can be achieved with waveguide structures. We have described an evanescently-coupled APD structure with a short multimode input waveguide section that is easy to fabricate. These APDs have demonstrated bandwidths >30 GHz, responsivity of 0.6 A/W at 1.55 μm , and gain-bandwidth product of 160 GHz. For high-sensitivity infrared imaging applications, HgCdTe APDs have achieved extremely low noise consistent with single carrier multiplication. Through Monte Carlo modeling, we have shown that this can be explained to a great extent through consideration of the bandstructure of HgCdTe. SiC APDs appear to be promising candidates for UV sensing. We report gains of 10^4 , low dark current, and low excess noise ($k \sim 0.15$), however, spatial uniformity of the photoresponse at very high gains remains work in progress.

REFERENCES

- [1] R. J. McIntyre, "Multiplication noise in uniform avalanche diodes," *IEEE Trans. Electron Devices*, vol. ED-13, pp. 164–168, Jan. 1966.
- [2] —, "The distribution of gains in uniformly multiplying avalanche photodiodes: Theory," *IEEE Trans. Electron Devices*, vol. ED-19, pp. 703–713, 1972.
- [3] R. B. Emmons, "Avalanche-photodiode frequency response," *J. Appl. Phys.*, vol. 38, no. 9, pp. 3705–3714, 1967.
- [4] B. K. Ng, J. P. R. David, R. C. Tozer, M. Hopkinson, G. Hill, and G. J. Rees, "Excess noise characteristics of $\text{Al}_{0.8}\text{Ga}_{0.2}\text{As}$ avalanche photodiodes," *IEEE Photon. Tech. Lett.*, vol. 14, pp. 522–524, Apr. 2002.
- [5] X. G. Zheng, X. Sun, S. Wang, P. Yuan, G. S. Kinsey, A. L. Holmes, Jr., B. G. Streetman, and J. C. Campbell, "Multiplication noise of $\text{Al}_x\text{Ga}_{1-x}\text{As}$ avalanche photodiodes with high Al concentration and thin multiplication region," *Appl. Phys. Lett.*, vol. 78, pp. 3833–3835, 2001.
- [6] B. K. Ng, J. P. R. David, G. J. Rees, R. C. Tozer, M. Hopkinson, and R. J. Airey, "Avalanche multiplication and breakdown in $\text{Al}_x\text{Ga}_{1-x}\text{As}$ ($x < 0.9$)," *IEEE Trans. Electron Dev.*, vol. 49, pp. 2349–2351, Feb. 2002.
- [7] J. D. Beck, C. F. Wan, M. A. Kinch, and J. E. Robinson, "MWIR HgCdTe avalanche photodiodes," *Proc. SPIE, Materials for Infrared Detectors*, vol. 4454, pp. 188–197, 2001.
- [8] A. Chen and A. Sher, "CPA band calculation for (Hg, Cd)Te," *J. Vac. Sci. Technol.*, vol. 21, pp. 138–141, 1982.
- [9] R. W. Miles, C. L. Jones, J. C. Brice, and P. Capper, *Properties of Mercury Cadmium Telluride*, J. Brice and P. Capper, Eds. London, U.K.: INSPEC, 1987, p. 101.
- [10] L. V. Keldysh, *Sov. Phys.—JETP*, vol. 10, p. 509, 1960.
- [11] C. L. Anderson and C. R. Crowell, "Threshold energies of electron-hole pair production by impact ionization in semiconductors," *Phys. Rev. B, Condens. Matter*, vol. 5, pp. 2267–2272, 1972.
- [12] K. F. Li, S. A. Plimmer, J. P. R. David, R. C. Tozer, G. J. Rees, P. N. Robson, C. C. Button, and J. C. Clark, "Low avalanche noise characteristics in thin InP $p^+ - i - n^+$ diodes with electron initiated multiplication," *IEEE Photon. Tech. Lett.*, vol. 11, pp. 364–366, Mar. 1999.
- [13] J. C. Campbell, S. Chandrasekhar, W. T. Tsang, G. J. Qua, and B. C. Johnson, "Multiplication noise of wide-bandwidth InP/InGaAsP/InGaAs avalanche photodiodes," *J. Lightwave Technol.*, vol. 7, pp. 473–477, Mar. 1989.
- [14] P. Yuan, C. C. Hansing, K. A. Anselm, C. V. Lenox, H. Nie, A. L. Holmes, Jr., B. G. Streetman, and J. C. Campbell, "Impact ionization characteristics of III-V semiconductors for a wide range of multiplication region thicknesses," *IEEE J. Quantum Electron.*, vol. 36, pp. 198–204, Feb. 2000.
- [15] M. A. Saleh, M. M. Hayat, P. O. Sotirelis, A. L. Holmes, J. C. Campbell, B. Saleh, and M. Teich, "Impact-ionization and noise characteristics of thin III-V avalanche photodiodes," *IEEE Trans. Electron Devices*, vol. 48, pp. 2722–2731, Dec. 2001.
- [16] K. F. Li, D. S. Ong, J. P. R. David, R. C. Tozer, G. J. Rees, S. A. Plimmer, K. Y. Chang, and J. S. Roberts, "Avalanche noise characteristics of thin GaAs structures with distributed carrier generation," *IEEE Trans. Electron Devices*, vol. 47, pp. 910–914, May 2000.
- [17] K. F. Li, D. S. Ong, J. P. R. David, G. J. Rees, R. C. Tozer, P. N. Robson, and R. Grey, "Avalanche multiplication noise characteristics in thin GaAs $p^+ - i - n^+$ diodes," *IEEE Trans. Electron Dev.*, vol. 45, pp. 2102–2107, Oct. 1998.
- [18] C. Hu, K. A. Anselm, B. G. Streetman, and J. C. Campbell, "Noise characteristics of thin multiplication region GaAs avalanche photodiodes," *Appl. Phys. Lett.*, vol. 69, no. 24, pp. 3734–3736, 1996.
- [19] D. S. Ong, K. F. Li, G. J. Rees, G. M. Dunn, J. P. R. David, and P. N. Robson, "A Monte Carlo investigation of multiplication noise in thin $p^+ - i - n^+$ GaAs avalanche photodiodes," *IEEE Trans. Electron Dev.*, vol. 45, pp. 1804–1810, Aug. 1998.
- [20] S. A. Plimmer, J. P. R. David, D. C. Herbert, T.-W. Lee, G. J. Rees, P. A. Houston, R. Grey, P. N. Robson, A. W. Higgs, and D. R. Wight, "Investigation of impact ionization in thin GaAs diodes," *IEEE Trans. Electron Dev.*, vol. 43, pp. 1066–1072, July 1996.
- [21] C. Lenox, P. Yuan, H. Nie, O. Baklenov, C. Hansing, J. C. Campbell, and B. G. Streetman, "Thin multiplication region InAlAs homojunction avalanche photodiodes," *Appl. Phys. Lett.*, vol. 73, pp. 783–784, 1998.
- [22] C. H. Tan, J. C. Clark, J. P. R. David, G. J. Rees, S. A. Plimmer, R. C. Tozer, D. C. Herbert, D. J. Robbins, W. Y. Leong, and J. Newey, "Avalanche noise measurements in thin Si $p^+ - i - n^+$ diodes," *Appl. Phys. Lett.*, vol. 76, no. 26, pp. 3926–3928, 2000.
- [23] C. H. Tan, J. P. R. David, J. Clark, G. J. Rees, S. A. Plimmer, D. J. Robbins, D. C. Herbert, R. T. Carline, and W. Y. Leong, "Avalanche multiplication and noise in submicron Si $p - i - n$ diodes," *Proc. SPIE, Silicon-Based Optoelectronics II*, vol. 3953, pp. 95–102, 2000.
- [24] B. K. Ng, J. P. R. David, G. J. Rees, R. C. Tozer, M. Hopkinson, and R. J. Riley, "Avalanche multiplication and breakdown in $\text{Al}_x\text{Ga}_{1-x}\text{As}$ ($x < 0.9$)," *IEEE Trans. Electron Devices*, vol. 49, pp. 2349–2351, Dec. 2002.
- [25] B. K. Ng, J. P. R. David, R. C. Tozer, M. Hopkinson, G. Hill, and G. H. Rees, "Excess noise characteristics of $\text{Al}_{0.8}\text{Ga}_{0.2}\text{As}$ avalanche photodiodes," *IEEE Photon. Tech. Lett.*, vol. 14, pp. 522–524, Apr. 2002.
- [26] C. H. Tan, J. P. R. David, S. A. Plimmer, G. J. Rees, R. C. Tozer, and R. Grey, "Low multiplication noise thin $\text{Al}_{0.6}\text{Ga}_{0.4}\text{As}$ avalanche photodiodes," *IEEE Trans. Electron Devices*, vol. 48, pp. 1310–1317, July 2001.
- [27] B. K. Ng, J. P. R. David, R. C. Tozer, G. J. Rees, Y. Feng, J. H. Zhao, and M. Weiner, "Nonlocal effects in thin 4H-SiC UV avalanche photodiodes," *IEEE Trans. Electron Devices*, vol. 50, pp. 1724–1732, Aug. 2003.
- [28] C. H. Tan, R. Ghin, J. P. R. David, G. J. Rees, and M. Hopkinson, "The effect of dead space on gain and excess noise in $\text{In}_{0.48}\text{Ga}_{0.52}\text{P}$ $p^+ - i - n^+$ diodes," *Semicon. Sci. Technol.*, vol. 18, no. 8, pp. 803–806, 2003.
- [29] D. S. Ong, K. F. Li, G. J. Rees, G. M. Dunn, J. P. R. David, and P. N. Robson, "A Monte Carlo investigation of multiplication noise in thin $p^+ - i - n^+$ GaAs avalanche photodiodes," *IEEE Trans. Electron Devices*, vol. 45, pp. 1804–1809, Aug. 1998.
- [30] X. Li, X. Zheng, S. Wang, F. Ma, and J. C. Campbell, "Calculation of gain and noise with dead space for GaAs and $\text{Al}_x\text{Ga}_{1-x}\text{As}$ avalanche photodiodes," *IEEE Trans. Electron Devices*, vol. 49, pp. 1112–1117, July 2002.

- [31] P. Yuan, S. Wang, X. Sun, X. G. Zheng, A. L. Holmes, Jr., and J. C. Campbell, "Avalanche photodiodes with an impact-ionization-engineered multiplication region," *IEEE Photon. Technol. Lett.*, vol. 12, pp. 1370–1372, Oct. 2000.
- [32] S. Wang, R. Sidhu, X. G. Zheng, X. Li, X. Sun, A. L. Holmes, Jr., and J. C. Campbell, "Low-noise avalanche photodiodes with graded impact-ionization-engineered multiplication region," *IEEE Photon. Technol. Lett.*, vol. 13, pp. 1346–1348, Dec. 2001.
- [33] S. Wang, F. Ma, X. Li, R. Sidhu, X. G. Zheng, X. Sun, A. L. Holmes, Jr., and J. C. Campbell, "Ultra-low noise avalanche photodiodes with a "centered-well" multiplication region," *IEEE J. Quantum Electron.*, vol. 39, pp. 375–378, Feb. 2003.
- [34] O.-H. Kwon, M. M. Hayat, S. Wang, J. C. Campbell, A. L. Holmes, Jr., B. E. A. Saleh, and M. C. Teich, "Optimal excess noise reduction in thin heterojunction $\text{Al}_{0.6}\text{Ga}_{0.4}\text{As}$ –GaAs avalanche photodiodes," *IEEE J. Quantum Electron.*, vol. 39, pp. 1287–1296, Oct. 2003.
- [35] M. M. Hayat, O.-H. Kwon, S. Wang, J. C. Campbell, B. E. A. Saleh, and M. C. Teich, "Boundary effects on multiplication noise in thin heterostructure avalanche photodiodes: Theory and experiment," *IEEE Trans. Electron Dev.*, vol. 49, pp. 2114–2123, Dec. 2002.
- [36] S. Wang, J. B. Hurst, F. Ma, R. Sidhu, X. Sun, X. G. Zheng, A. L. Holmes, Jr., J. C. Campbell, A. Huntington, and L. A. Coldren, "Low-noise impact-ionization-engineered avalanche photodiodes grown on InP substrates," *IEEE Photon. Tech. Lett.*, vol. 14, pp. 1722–1724, Dec. 2002.
- [37] F. Capasso, W. T. Tsang, A. L. Hutchinson, and G. F. Williams, "Enhancement of electron impact ionization in a superlattice: A new avalanche photodiode with a large ionization rate ratio," *Appl. Phys. Lett.*, vol. 40, pp. 38–40, 1982.
- [38] R. Chin, N. Holonyak, Jr., G. E. Stillman, J. Y. Tang, and K. Hess, "Impact ionization in multilayered heterojunction structures," *Electron. Lett.*, vol. 16, pp. 467–469, 1980.
- [39] C. Cohen-Jonathan, L. Giraudet, A. Bonzo, and J. P. Praseuth, "Waveguide AlInAs/GaAlInAs avalanche photodiode with a gain-bandwidth product over 160 GHz," *Electron. Lett.*, vol. 33, pp. 1492–1493, 1997.
- [40] T. Nakata, T. Takeuchi, K. Makita, and T. Torikai, "High-speed and high-sensitivity waveguide InAlAs avalanche photodiode for 10–40 Gb/s receivers," in *Proc. Laser Electro-Optical Soc.*, 2001, paper ThN3.
- [41] G. S. Kinsey, J. C. Campbell, and A. G. Dentai, "Waveguide avalanche photodiode operating at 1.55 μm with a gain-bandwidth product of 320 GHz," *IEEE Photonics Tech. Lett.*, vol. 13, pp. 842–844, Aug. 2001.
- [42] J. Wei, F. Xia, and S. R. Forest, "A high-responsivity high-bandwidth asymmetric twin-waveguide coupled InGaAs-InP-InAlAs avalanche photodiode," *IEEE Photon. Technol. Lett.*, vol. 14, pp. 1590–1592, 2002.
- [43] S. Demiguel, N. Li, X. Li, X. Zheng, J. Kim, J. C. Campbell, H. Lu, and K. A. Anselm, "Very high-responsivity evanescently-coupled photodiodes integrating a short planar multimode waveguide for high-speed applications," *IEEE Photon. Technol. Lett.*, vol. 15, pp. 1761–1763, Dec. 2003.
- [44] M. J. Lange, J. C. Dries, and W. Huang, "Confocal SWIR and 3D range finding using InGaAs P-I-N and APD detector arrays," in *Proc. Laser Electro-Optical Soc. Annu. Meet.*, Tucson, AZ, 2003, pp. 688–689.
- [45] C. J. Collins, U. Chowdhury, M. M. Wong, B. Yang, A. L. Beck, R. D. Dupuis, and J. C. Campbell, "Improved solar-blind detectivity using an $\text{Al}_x\text{Ga}_{1-x}\text{N}$ heterojunction p-i-n photodiode," *Appl. Phys. Lett.*, vol. 80, pp. 3754–3756, 2002.
- [46] K. A. McIntosh, R. J. Molnar, L. J. Mahoney, A. Lightfoot, M. W. Geis, K. M. Molvar, I. McIngails, R. L. Aggarwal, W. D. Goodhue, S. S. Choi, D. L. Spears, and S. Verghese, "GaN avalanche photodiodes grown by hydride vapor-phase epitaxy," *Appl. Phys. Lett.*, vol. 75, pp. 3485–3487, 1999.
- [47] J. C. Carrano, D. J. H. Lambert, C. J. Eiting, C. J. Collins, T. Li, S. Wang, B. Yang, A. L. Beck, R. D. Dupuis, and J. C. Campbell, "GaN avalanche photodiodes," *Appl. Phys. Lett.*, vol. 76, pp. 924–926, 2000.
- [48] B. Yang, T. Li, K. Heng, C. Collins, S. Wang, J. C. Carrano, R. D. Dupuis, J. C. Campbell, M. J. Schurman, and I. T. Ferguson, "Low dark current GaN avalanche photodiodes," *IEEE J. Quantum Electron.*, vol. 36, pp. 1389–1391, Dec. 2000.
- [49] F. Yan, Y. Luo, J. H. Zhao, and G. H. Olsen, "4H-SiC visible blind UV avalanche photodiodes," *Electron Lett.*, vol. 35, pp. 929–930, 1999.
- [50] B. K. Ng, F. Yan, J. P. R. David, R. C. Tozer, G. J. Rees, C. Qin, and J. H. Zhao, "Multiplication and excess noise characteristics of thin 4H-SiC UV avalanche photodiodes," *IEEE Photon. Technol. Lett.*, vol. 14, pp. 1342–1344, Sept. 2002.
- [51] B. K. Ng, J. P. R. David, R. C. Tozer, G. J. Rees, F. Yan, and M. Weiner, "Nonlocal effects in thin 4H-SiC UV avalanche photodiodes," *IEEE Trans. Electron Devices*, vol. 50, pp. 1724–1732, Aug. 2003.
- [52] F. Yan, J. H. Zhao, and G. Olsen, "Demonstration of the first 4H-SiC avalanche photodiodes," *Solid State Electron.*, vol. 44, pp. 341–346, 2000.
- [53] X. Guo, A. Beck, B. Yang, and J. C. Campbell, "Low dark current 4H-SiC avalanche photodiodes," *Electron. Lett.*, vol. 39, no. 23, pp. 1673–1674, 2003.
- [54] A. O. Konstantinov, Q. Wahab, N. Nordell, and U. Lindefelt, "Ionization rates and critical fields in 4H silicon carbide," *Appl. Phys. Lett.*, vol. 71, pp. 90–92, 1997.
- [55] S. Wang, R. Sidhu, G. Karve, F. Ma, X. Li, X. Zheng, J. B. Hurst, X. Sun, N. Li, A. L. Holmes, Jr., and J. C. Campbell, "A study of low-bias photocurrent gradient of avalanche photodiodes," *IEEE Trans. Electron. Devices*, vol. 49, pp. 2107–2113, 2002.
- [56] B. J. Baliga, *Power Semiconductor Devices*. Boston, MA: PWS, 1995.
- [57] F. Yan, C. Qin, J. H. Zhao, M. Weiner, B. K. Ng, J. P. R. David, and R. C. Tozer, "Low-noise visible-blind UV avalanche photodiodes with edge terminated by 2° positive bevel," *Electron. Lett.*, vol. 38, pp. 335–336, 2002.
- [58] C. J. Collins, T. Li, D. J. H. Lambert, M. M. Wong, R. D. Dupuis, and J. C. Campbell, "Selective regrowth of $\text{Al}_{0.30}\text{Ga}_{0.70}\text{N}$ p-i-n photodiodes," *Appl. Phys. Lett.*, vol. 77, pp. 2810–2812, 2000.



Joe C. Campbell (S'73–M'74–SM'88–F'90) received the B.S. degree in physics from the University of Texas at Austin in 1969, and the M.S. and Ph.D. degrees in physics from the University of Illinois at Urbana-Champaign in 1971 and 1973, respectively.

From 1974 to 1976, he was with Texas Instruments, where he worked on integrated optics. In 1976, he joined the staff of AT&T Bell Laboratories, Holmdel, NJ. In the Crawford Hill Laboratory, he worked on a variety of optoelectronic devices including semiconductor lasers, optical modulators, waveguide switches, photonic integrated circuits, and photodetectors with emphasis on high-speed avalanche photodiodes for high-bit-rate lightwave systems. In January 1989, he joined the faculty of the University of Texas at Austin as Professor of Electrical and Computer Engineering and Cockrell Family Regents Chair in Engineering. At present, he is actively involved in Si-based optoelectronics, high-speed, low-noise avalanche photodiodes, high-power photodiodes, ultraviolet photodetectors, and quantum-dot IR imaging. He has coauthored six book chapters, more than 300 journal publications, and 200 conference presentations.

Prof. Campbell is a member of the National Academy of Engineering, a Fellow of the Optical Society of America, and a Fellow of the American Physical Society.

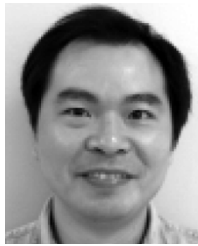


Stephane Demiguel was born in Gennevilliers, France, in 1971. He received the engineer degree in electrical engineering from Ecole Supérieure d'Ingenieurs en Génie Electrique (ESIGELEC), Rouen, France, in 1996, and the Ph.D. degree in optoelectronics from Rouen University, Rouen, France, in 2001. His Ph.D. dissertation was on high-speed photodiodes integrating spot size converter for 60-GHz radio over fiber links and 40-Gb/s optical transmissions.

In 2000, he worked on the design and measurements of high-speed photodiodes at Alcatel Opto+, Marcoussis, France. In particular, he was involved in optical and electrical modeling for optoelectronic devices. In 2002, he joined Prof. Joe Campbell's group at the University of Texas at Austin. He is currently working on high-speed PIN, APD, and high-power photodiodes utilizing an evanescently-coupled approach integrating a multimode waveguide.

Feng Ma was born in Beiyang, China, on April 18, 1973. He received the B.S. degree in applied physics from Beijing Institute of Technology, Beijing, China, in 1991, the M.S. degree in theoretical physics from Beijing Normal University, Beijing, in 1994, and the M.A. and Ph.D. degrees in astronomy and the Ph.D. degree in electrical engineering from the University of Texas at Austin in 1997, 2000, and 2001, respectively.

Ariane Beck received the B.S. and M.S. degrees in electrical and computer engineering from the University of Texas at Austin in 2000 and 2002, respectively. Currently, she is working toward the Ph.D. degree in electrical engineering at the Microelectronics Research Center at the University of Texas at Austin. Her research focuses on wide-bandgap ultraviolet photodetectors.



Xiangyi Guo received the B.S. and M.S. degrees from the Physics Department of East China Normal University, Shanghai, China, in 1991 and 1997, respectively. He is currently pursuing the Ph.D. degree in electrical engineering at the University of Texas at Austin.

He was with Shanghai Institute of Technical Physics, Chinese Academy of Sciences, from 1994 to 1996, working on solar radiation detection. From 1997 to 2001, he was with Philips Optical Storage, Shanghai, where he was engaged in the application

of optical storage devices. His research interests are wide-bandgap optoelectronic devices.



Shuling Wang received the B. S. degree in microelectronics from Beijing University, Beijing, China in 1995, the M.S.E.E. degree from the University of Notre Dame in 1999, and the Ph.D. degree in electrical engineering from the University of Texas at Austin in 2002.

She is currently a Research Scientist in the Microelectronics Research Center at the University of Texas working on high-speed, low-noise avalanche photodiodes.

Dr. Wang is a member of the IEEE Laser and Electro-Optics Society (LEOS).



Xiaoguang Zheng received the B.S.E.E. degree from the Beijing Institute of Technology, Beijing, China, in 1985, the M.S. degree in electrical engineering from the Hebei Semiconductor Research Institute in 1991, and the Ph.D. degree in electrical engineering from the University of Texas at Austin in 2003.

His major research interests are in optoelectronic devices: impact ionization properties of III-V compound materials, high-speed long-wavelength avalanche photodiodes and arrays, and heterogeneous material integration via direct wafer bonding.



Xiaowei Li was born in Beijing, China, in 1970. He received the B.S. and M.S. degrees from the Physics Department of Peking University, Beijing, China, in 1994 and 1997, respectively. He is currently pursuing the Ph.D. degree in electrical engineering from the Microelectronic Research Center at the University of Texas at Austin.

His research interests are avalanche process simulations and high saturation power photodetectors for 1.55- μm applications.

Jeffrey D. Beck (S'69–M'72) received the S.B and S.M. degrees in electrical engineering from the Massachusetts Institute of Technology, Cambridge, in 1972.

He is a Distinguished Member of the Technical Staff in the Research and Development group at DRS Infrared Technologies, Dallas, TX. He has over 35 years of experience in infrared technology. He began his career in the infrared in 1968 as an MIT Electrical Engineering intern working for Honeywell Radiation Center in Lexington, MA, where he was employed until 1978. In 1978, he relocated to Dallas to accept a position as Member of the Technical Staff at the Central Research Laboratories of Texas Instruments.

Michael A. Kinch, photograph and biography not available at the time of publication.



Andrew Huntington received the B.S. degree in chemistry from the California Institute of Technology, Pasadena, in 1997. He is currently a graduate student in the Materials Department of the University of California at Santa Barbara.

He specializes in growth of arsenide compounds lattice-matched to InP for optoelectronic applications, including long wavelength multiple-active region vertical-cavity lasers and avalanche photodiodes.



Larry A. Coldren (S'67–M'72–SM'77–F'82) received the Ph.D. degree in electrical engineering from Stanford University, Stanford, CA, in 1972.

After 13 years in the research area at Bell Laboratories, he was appointed Professor of Electrical and Computer Engineering at the University of California at Santa Barbara (UCSB) campus in 1984. In 1986, he assumed a joint appointment with Materials and ECE, and in 2000 the Fred Kavli Chair in Optoelectronics and Sensors. He is also Chairman and Chief Technology Officer of Agility Communications, Inc.

At UCSB, his efforts have included work on novel guided-wave and vertical-cavity modulators and lasers as well as the underlying materials growth and fabrication technology. He is now investigating the integration of various optoelectronic devices, including optical amplifiers and modulators, tunable lasers, wavelength-converters, and surface-emitting lasers. He has authored or coauthored over 500 papers, five book chapters, one textbook, and has been issued 32 patents.

Prof. Coldren is a Fellow of the Optical Society of America (OSA) and a past Vice-President of IEEE Laser and Electro-Optics Society (LEOS).



Jean Decobert was born in Lille, France, in 1964. He received the Ph.D. degree in microelectronics from Lille I University in 1993.

Since 1987, he has been working on semiconductor compounds epitaxial growth by MOVPE. He started working on the design of MOVPE reactors and he is particularly involved in aluminum containing semiconductor material for opto- and micro-electronic devices. He joined the National Center of Telecommunication Research (CNET) France Telecom, Bagneux, France, in 1993, where

his research focused on the MOVPE growth and fabrication of InP based HEMT and PIN-HEMT devices for OEICs. In 1998, he joined Opto+, Marcoussis, France, the research laboratory founded by Alcatel and France Telecom. Since 2001, he has worked at Alcatel Research and Innovation, Marcoussis, France, where he is in charge of III-V material growth for opto-electronic applications.

Nadine Tschertner was born in Le Coteau, France, in 1969.

She joined the Alcatel Research and Innovation laboratories, Marcoussis, France, in 1991, in the team of Dr. Eugene Duda where she has developed the process technology of InP devices. Since 2001, she has worked on the MOVPE growth and characterization of III-V semiconductor heterostructures for optoelectronic applications.



Relationship of growth mode to surface morphology and dark current in InAlAs/InGaAs avalanche photodiodes grown by MBE on InP

A.S. Huntington^{a,b}, C.S. Wang^{c,*}, X.G. Zheng^d, J.C. Campbell^d, L.A. Coldren^{a,c}

^a Department of Materials, University of California, Santa Barbara, Santa Barbara, CA 93106, USA

^b Voxtel, Inc., Beaverton, OR 97005, USA

^c Department of Electrical and Computer Engineering, University of California, Santa Barbara, Santa Barbara, CA 93106, USA

^d Department of Electrical and Computer Engineering, The University of Texas, Austin, TX 78712, USA

Received 24 November 2003; accepted 20 April 2004

Communicated by D.W. Shaw

Abstract

We present the relationship between surface roughness and dark current measured for avalanche photodiodes with InGaAs absorbers and thin InAlAs multiplication layers fabricated from material grown lattice-matched to InP by molecular beam epitaxy. In particular, the leakage current at unity gain measured for sets of 125 μm diameter devices was found to have an exponential dependence upon the peak-to-peak surface roughness of the material, and was characterized by an order of magnitude increase for every 15 nm of roughness. We also present the results of an atomic force microscope study of surface morphology and growth conditions, interpreting the results in the context of diffusional versus convective growth modes. The best material was obtained at a substrate temperature of 500°C and an arsenic beam pressure of 8×10^{-6} Torr; the smooth growth window was bounded on the high-arsenic/low-temperature side by roughness resulting from low adatom surface mobility, and on the low-arsenic/high-temperature side by nonstoichiometric arsenic deficient growth.

© 2004 Elsevier B.V. All rights reserved.

Keywords: A1. Surface roughness; A3. Molecular beam epitaxy; B2. Semiconducting quaternary alloys; B3. Avalanche photodiodes

1. Introduction

We have previously reported molecular beam epitaxy (MBE)-grown avalanche photodiodes

(APDs) with InGaAs absorbers and thin InAlAs multiplication layers fabricated in highly uniform 12×12 and 18×18 arrays [1,2]. We have also demonstrated individual devices which we believe to be the largest of their type yet reported (1 mm), and impact-ionization-engineered (I^2E) multiplication layers with extremely low excess noise [2,3]. Several growth attempts were necessary in each

*Corresponding author. Tel.: +1-805-893-7065; fax: +1-805-893-4500.

E-mail address: cswang@engineering.ucsb.edu (C.S. Wang).

case to produce wafers suitable for the studies in question because of variations in device performance that were traced to run-to-run variations in material quality. In particular, it was empirically found that APDs fabricated from wafers with moderately rough surfaces tended to exhibit high dark leakage currents. Similar observations have been reported in the past relating interface morphology in heterostructures to optical and electronic properties, such as photoluminescence (PL) line width, electron mobility, and transport lifetimes [4–6]. This paper examines the impact of growth conditions upon wafer morphology and presents an empirical relationship between surface roughness and APD dark current.

1.1. Epitaxially-grown SACM APDs

The control over layer composition, thickness, and dopant density afforded by epitaxial growth allows several refinements of APD design that are not possible to implement in homojunction APDs formed by standard dopant diffusion techniques. The low bandgap material necessary to receive the long-wavelength (1310–1550 nm) light relevant to fiberoptic telecommunications is susceptible to leakage via interband tunneling when placed under strong bias. This source of dark current can be suppressed by isolating the low-bandgap material in a dedicated absorption layer in which the electric field is moderated by an adjacent charge layer: the separate absorption, charge, and multiplication (SACM) design, as diagrammed in Fig. 1 [7]. SACM APDs can also be modulated faster than homojunction APDs because photogeneration of carriers is confined to a single layer, which shortens the impulse response of the detector [7,8]. A second advantage of epitaxial growth is the opportunity to engineer the multiplication layer so as to produce spatial correlations between impact ionization events, thereby suppressing multiplication noise [9,10]. However, these advanced designs typically involve multiplication layers on the order of 150–200 nm thick, supporting fields above 400 kV cm^{-1} . Consequently, small variations in film thickness caused by rough growth can have a large impact on device function. In particular, premature breakdown can occur at thin spots in

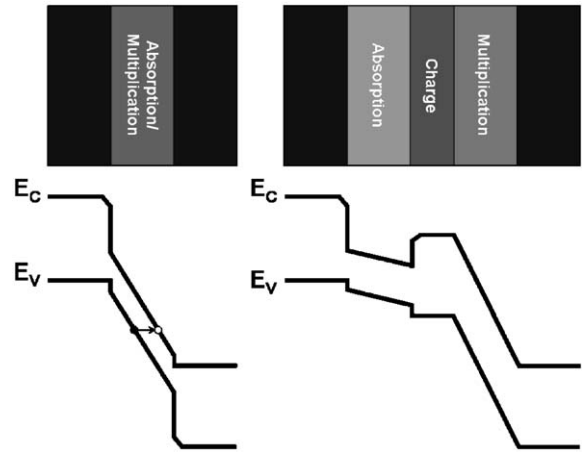


Fig. 1. Layer schematic and band edge diagram of how a SACM design (right) reduces tunneling leakage in long-wavelength APDs.

the multiplication layer, allowing dark current to pass through the conductive microplasmas that form. Growth of smooth layers of uniform thickness is therefore essential.

1.2. Growth mode and surface roughness

Surface morphology of unstrained thin films depends upon the relative balance between diffusive and convective mass flow during growth. Following the discussion of Tsao, growth mode can be categorized by a Peclet number expressing the ratio between step flow velocity driven by the arrival of new adatoms (convective mass flow) and the surface diffusion velocity of those adatoms [11]:

$$P = \frac{L^2 \times r}{D}, \quad (1.1)$$

where L is the average spacing between monolayer steps, r is the deposition rate in monolayers per second, and D is the surface diffusion constant.

When $P \ll 1$, diffusion dominates and growth proceeds by the step-flow mechanism in which group-III adatoms migrate to step edges, where they preferentially incorporate. Step-flow conditions produce very smooth surfaces since the adatoms tend to fill in depressions and erase irregularities. On the other hand, when $P > 1$

diffusion cannot keep pace with the arrival of new adatoms, and growth proceeds by a two-dimensional nucleation process in which the surface becomes segmented into island-like clusters which grow and coalesce. Depending upon the particulars, the islands may stay two-dimensional, periodically forming complete monolayers and preserving a smooth surface (small P), or they may pile up into three-dimensional mounds, forming a rough surface divided into a network of cells (large P). Growth mode can therefore be manipulated by controlling P : L varies with the vicinal angle of the substrate; r is controlled directly by the grower; D largely depends upon adatom lifetime and surface migration velocity (a function of substrate temperature, the bond strength of each chemical species, and arsenic overpressure).

It should be emphasized at this point that the materials in question are lattice-matched both to their substrate and to each other, so the well-known islanding mechanisms associated with growth of strained layers are not active. Except for the extreme case of arsenic deficiency, lattice-matching of AlGaInAs is insensitive to variation of arsenic overpressure and substrate temperature, as its stoichiometry is established by the group-III fluxes. Thus, it can be said with a fair degree of assurance that variations in surface morphology brought about by variations of temperature and excess arsenic pressure are dictated by the transport considerations outlined above, rather than strain effects.

1.3. The AlGaInAs material system

The AlGaInAs material system grown lattice-matched to InP bears some resemblance to the more conventional AlGaAs/GaAs material system. AlGaInAs grown by MBE is typically synthesized as a digital alloy of the two lattice-matched ternaries $\text{In}_{0.53}\text{Ga}_{0.47}\text{As}$ and $\text{In}_{0.52}\text{Al}_{0.48}\text{As}$, just as AlGaAs is commonly synthesized from the binaries GaAs and AlAs. As in the AlGaAs/GaAs material system, the aluminum-containing compound (InAlAs) forms stronger bonds and tends to grow by islanding and coalescence rather than step flow [12]. As shown

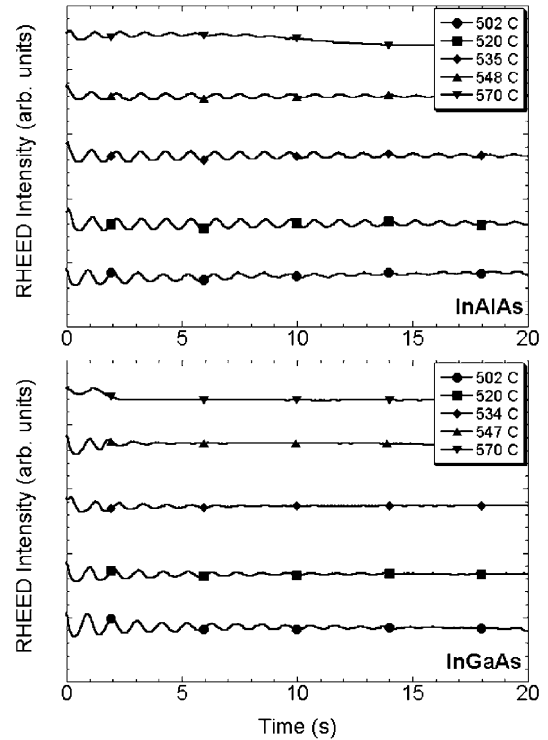


Fig. 2. RHEED intensity oscillations of InAlAs (top) and InGaAs (bottom) grown at different substrate temperatures. As the substrate temperature is raised, adatom diffusivity increases and diffusion-driven step flow growth becomes favored. The InGaAs RHEED oscillations disappear at a lower temperature than the InAlAs oscillations because InGaAs is less sticky and diffuses better at lower temperatures.

in Fig. 2, this is evident from observation of reflection high-energy electron diffraction (RHEED) intensity oscillations, which cannot be seen during pure step flow growth because they originate from cycles of partial and complete monolayer coverage on the growing surface. Therefore, low adatom surface mobility and consequent three-dimensional islanding is one possible source of surface roughness in this material system. Higher substrate temperature and lower arsenic overpressure both favor smooth diffusion-driven growth because they act to increase adatom lifetime and diffusional range. Thus, InAlAs can be grown hotter than InGaAs to improve material optical quality and reduce alloy clustering [12,13]. However, the substrate

temperature and arsenic beam flux conditions which allow smooth growth are bounded by regions of the system's phase diagram in which stoichiometric AlGaInAs is no longer stable, and the growing surface decomposes into metal droplets and arsenic vapor. Thus, smooth AlGaInAs growth can only be obtained within a narrow window bounded by rough three-dimensional islanding on one side, and arsenic deficiency on the other.

2. Experimental procedure and results

The experimental work reported on in this paper was conducted in two parts. The investigation of growth conditions, growth mode, and surface morphology was based upon a set of five samples grown under varying conditions and evaluated by AFM. The relationship between surface morphology and dark current was determined by measuring the I - V characteristics of identical devices fabricated from five SACM APD wafers of similar design but differing roughness.

2.1. Material growth

All samples discussed in this paper were grown in a Varian Gen-II solid source MBE chamber at a rate of 1 monolayer per second on InP substrates oriented 0.5° off the (100) plane towards the (111)A plane. Lattice-matching was verified to be better than 0.16% by X-ray diffraction and growth rates were calibrated to within 1–2% by optical cavity measurements; both calibrations were tied to group-III beam fluxes to allow reproducibility from run-to-run. Substrate temperature was monitored using optical pyrometry.

Prior to growth, removal of surface oxide from the virgin substrate was accomplished by rapid heating under vacuum. Substrate temperature was ramped from 500°C to 530°C in the span of 15 s, with a minimal (10^{-6} Torr) arsenic flux supplied once the substrate passed through 520°C . Growth was initiated immediately once the substrate reached 530°C in order to minimize exchange reactions between the supplied arsenic and the phosphorus in the substrate.

2.2. Growth conditions, growth mode and surface morphology

The vicinal angle of the miscut substrates used in this study was chosen to be compatible with the epitaxial growth of InP, which was optimized in a separate investigation. Further, production of thick structures becomes impractical for growth rates much below 1 monolayer per second, so the growth rate was held constant during this study. Substrate temperature and arsenic beam flux—the two remaining levers for controlling growth

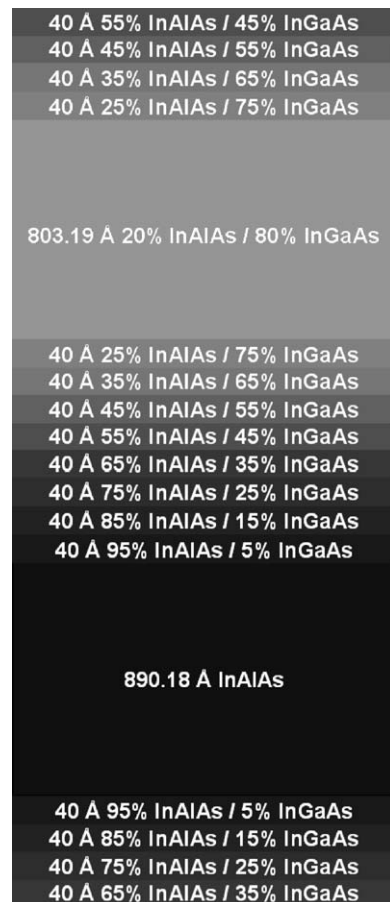


Fig. 3. Layer schematic of one DBR period appropriate for optoelectronic applications at 1550 nm. 45.5 periods were grown to make the $10.5\ \mu\text{m}$ structures used to investigate the relationship between growth conditions and surface morphology in very thick structures. The layers consist of pure InAlAs and $\text{In}_{0.53}\text{Ga}_{0.38}\text{Al}_{0.10}\text{As}$ with graded interfaces.

mode—were varied in order to find conditions for smooth AlGaInAs growth.

2.2.1. Sample set

Two structures were examined in this study. As shown in Fig. 3, graded 10.5 μm distributed Bragg reflectors (DBRs) of a type appropriate for optoelectronic applications at 1550 nm were grown to investigate the relationship between growth conditions and surface morphology in very thick structures. Although diffusion-driven growth tends to smooth out surface features as more material accumulates, surface roughness caused by low adatom surface mobility or arsenic deficiency tends to worsen with continued growth. Therefore, subtle differences in growth mode can more easily be detected by examining tall structures than thin ones. Past experience had indicated that optimal growth conditions for AlGaInAs on InP occur near 10^{-5} Torr of arsenic overpressure at a

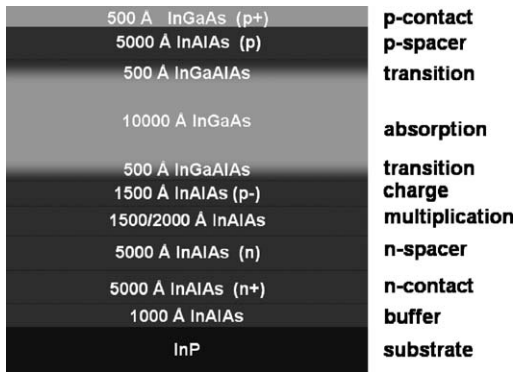


Fig. 4. APD layer schematic. The wafer grown for the growth mode study had a 2000 Å multiplication layer; the wafers grown for the dark current study had either a 1500 or 2000 Å thick multiplication layer.

substrate temperature of 500°C. In order to observe the predicted marginal improvement of surface morphology with increased adatom lifetime—up to the onset of arsenic deficiency, that is—three DBR structures were grown at 500°C under arsenic beam fluxes of 4×10^{-6} , 6×10^{-6} , and 8×10^{-6} Torr. The InAlAs portions of a fourth DBR were grown at 550°C under 8×10^{-6} Torr of arsenic to test for improved morphology resulting from higher Al adatom surface mobility. The fifth structure studied, as shown in Fig. 4, was a 3 μm SACM APD wafer grown at 500°C under 1.2×10^{-5} Torr of arsenic. This last sample was grown in order to find the onset of rough three-dimensional growth caused by low adatom lifetime, the severity of which makes it detectible in shorter structures.

2.2.2. Results

Surface roughness was extracted from AFM images of all five wafers; the results are tabulated in Table 1 and three AFM images are shown in Fig. 5a, b, and c. Optimal results were obtained from the sample grown at 500°C under 8×10^{-6} Torr of arsenic; a metal-rich polycrystalline surface was obtained from the lowest arsenic growth, whereas the highest arsenic growth gave rise to significant three-dimensional islanding.

These results illustrate two points. First, the variations of surface roughness in the structurally-identical DBR samples indicate that growth conditions—and not interfacial composition—are the origin of the observed roughness. Second, the range of observed behavior—*islanding at high arsenic overpressure and faceting at low arsenic overpressure*—is in keeping with what one would expect from a smooth growth window bounded by

Table 1
Growth conditions and RMS surface roughness of the samples grown to study growth mode and surface morphology

Sample	Thickness (μm)	Growth temperature ($^{\circ}\text{C}$)	Arsenic flux (Torr)	RMS roughness (nm)
DBR	10.5	500	8×10^{-6}	1.88
DBR	10.5	500	6×10^{-6}	5.38
DBR	10.5	500	4×10^{-6}	157.78
DBR	10.5	550 ^a	8×10^{-6}	9.15
APD	3	500	1.2×10^{-5}	7.06

^a Only the InAlAs was grown at this temperature; the $\text{In}_{0.53}\text{Ga}_{0.38}\text{Al}_{0.10}\text{As}$ was grown at 500°C.

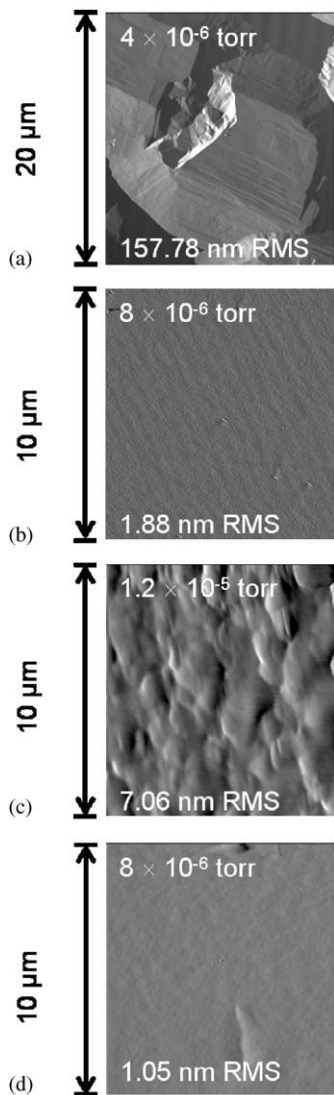


Fig. 5. AFM images of 4 samples grown at 500°C under an arsenic beam fluxes of (a) 4×10^{-6} Torr (DBR), (b) 8×10^{-6} Torr (DBR), and (c) 1.2×10^{-5} Torr (APD, sample C), and (d) 8×10^{-6} Torr (APD, sample A).

low adatom lifetime on one side and loss of stoichiometry on the other.

2.3. Surface morphology and dark current

The relationship between surface morphology and APD characteristics was investigated by studying devices fabricated from five SACM

APD wafers of similar design but varying roughness. These samples were selected from a set of wafers grown in support of previously published studies, and—except for the smoothest sample—represent “failed” growths in which equipment problems allowed substrate temperature to stray outside the optimal range for the arsenic pressure used in Refs. [1,2]. Surface roughness was extracted from AFM images of the wafers.

2.3.1. Sample set

All five wafers share the layer structure shown previously in Fig. 4. Surface roughness, expressed both as an RMS value and a peak-to-peak value, are tabulated in Table 2, and AFM images of two APD wafers are shown in Fig. 5c (sample C), and 5d (sample A). Sets of 125 μm diameter APDs were fabricated from each wafer using a process described elsewhere [1]. I – V characteristics were measured for 15 devices from each wafer, and dark current was measured at the unity gain bias point (15 V).

2.3.2. Results

The strong dependence of dark current upon surface roughness is evident when I – V characteristics representative of devices fabricated from different wafers are compared side-by-side, as shown in Fig. 6. Fig. 7 is a plot of unity gain dark current against peak-to-peak roughness and reveals an exponential relationship between the two quantities, amounting to an order-of-magnitude increase for every 15 nm of roughness.

We believe that this behavior can be understood in terms of inhomogeneous breakdown: formation of microplasmas at thin areas in the multiplication region. Just as an exponential rise in current results from a linear increase in bias (and therefore field strength) in the case of a healthy APD during controlled avalanche multiplication, the premature breakdown of a small region inside an APD results in something similar when dark current is considered. Surface roughness arising from large P (convective growth) accumulates as growth proceeds and so is indicative of variations in layer thickness throughout the structure. Accordingly, the peak-to-peak roughness of the wafer should reflect the scale of the multiplication layer’s

Table 2
Schedule of samples used in the dark current study

Sample	M-layer thickness (Å)	Peak-to-peak (nm); RMS roughness (nm)
A	2000	9.93 ; 1.05
B	2000	39.29 ; 4.86
C	2000	46.15 ; 7.06
D	1500	25.59 ; 4.40
E	1500	41.54 ; 5.19

The samples cover a broad range of roughness, and the dependence of unity gain dark current to peak-to-peak roughness is evident in Fig. 7, regardless of the difference in multiplication layer thickness.

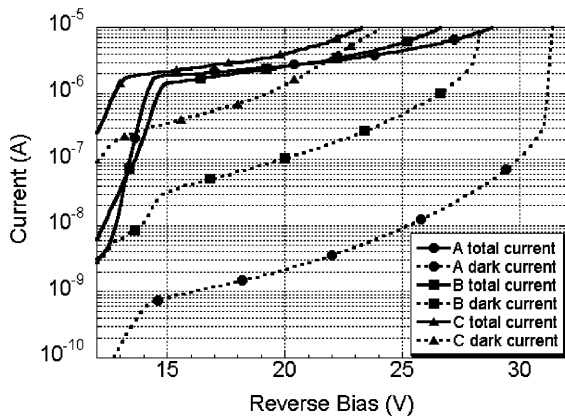


Fig. 6. I - V characteristics of APDs fabricated from samples A, B, and C, with differing amounts of surface roughness, as described in Table 2.

thickness variations, and in particular, its thinnest excursions. Since field strength is inversely proportional to the distance over which the potential drops inside an APD, it is sensible that dark current arising from premature breakdown should increase exponentially with a linear increase in peak-to-peak roughness.

One might object to this explanation on the grounds that surface roughness does not necessarily reflect the morphology of underlying layers. While it is true that surface roughness can arise suddenly with a change in layer composition and just as rapidly be obscured by succeeding layers, such phenomena respectively involve a sudden change in stoichiometry (lattice constant) and

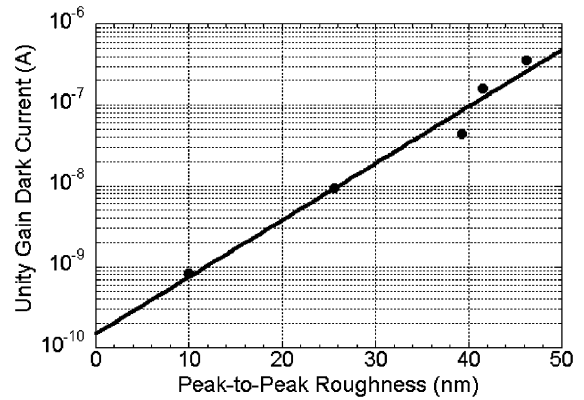


Fig. 7. Plot of unity gain dark current versus peak-to-peak roughness, revealing an exponential relationship between the two quantities. There is an order-of-magnitude increase in dark current for every 15 nm of roughness.

diffusion-dominated growth, neither of which apply in this instance. Moreover, having demonstrated control over surface roughness by means of arsenic pressure, we can be confident that the origin of the roughness lies in transport phenomena.

3. Conclusions

A narrow window for smooth AlGaInAs growth by MBE on InP has been identified and related to the mechanism of growth. Further, an empirical relationship between the surface roughness of an APD wafer as-grown and the dark current found for devices fabricated from that wafer has been discovered. Taken together, these findings constitute both a recipe for minimizing dark current in SACM APDs with thin multiplication regions, and a basis for evaluating the quality of SACM APD material prior to device fabrication and testing.

Acknowledgements

The authors wish to thank DARPA for supporting this work via CHIPS. We also want to thank the excellent laboratory support of Art Gossard, John English, and everyone else in the

UCSB MBE lab. This work made use of MRL Central Facilities supported by the MRSEC Program of the National Science Foundation under award No. DMR00-80034.

References

- [1] X.G. Zheng, J.S. Hsu, X. Sun, J.B. Hurst, X. Li, S. Wang, A.L. Holmes Jr., J.C. Campbell, A.S. Huntington, L.A. Coldren, *IEEE J. Quant. Electron.* 38 (2002) 1536.
- [2] X.G. Zheng, J.S. Hsu, J.B. Hurst, X. Li, S. Wang, X. Sun, A.L. Holmes Jr., J.C. Campbell, A.S. Huntington, L.A. Coldren, *IEEE J. Quant. Electron.* accepted for publication.
- [3] S. Wang, J.B. Hurst, F. Ma, R. Sidhu, X. Sun, X.G. Zheng, A.L. Holmes Jr., A. Huntington, L.A. Coldren, *J.C. Campbell, IEEE Photon. Technol. Lett.* 14 (2002) 1722.
- [4] C. Weisbuch, R. Dingle, A.C. Gossard, W. Wiegmann, *Solid State Commun.* 38 (1981) 709.
- [5] M. Kohl, D. Heitmann, S. Tarucha, K. Leo, K. Ploog, *Phys. Rev. B* 39 (1989) 7736.
- [6] L. Gottwaldt, K. Pierz, F.J. Ahlers, E.O. Göbel, S. Nau, T. Torunski, W. Stolz, *J. Appl. Phys.* 94 (2003) 2464.
- [7] J.N. Hollenhorst, *IEEE J. Light. Technol.* 8 (1990) 531.
- [8] C. Lenox, H. Nie, P. Yuan, G. Kinsey, A.L. Holmes Jr., B.G. Streetman, J.C. Campbell, *IEEE Photon. Technol. Lett.* 11 (1999) 1162.
- [9] F. Ma, S. Wang, X. Li, K.A. Anselm, X.G. Zheng, A.L. Holmes Jr., J.C. Campbell, *J. Appl. Phys.* 92 (2002) 4791.
- [10] M.A. Saleh, M.M. Hayat, P.P. Sotirelis, A.L. Holmes Jr., J.C. Campbell, B.E.A. Saleh, M.C. Teich, *IEEE Trans. Electron. Devices* 48 (2001) 2722.
- [11] J.Y. Tsao, *Materials Fundamentals of Molecular Beam Epitaxy*, Academic Press, San Diego, 1993.
- [12] T.M. Brennan, J.Y. Tsao, B.E. Hammons, J.F. Klem, E.D. Jones, *J. Vac. Sci. Technol. B* 7 (1989) 277.
- [13] D.F. Welch, G.W. Wicks, L.F. Eastman, *Appl. Phys. Lett.* 43 (1983) 762.

Long-Wavelength $\text{In}_{0.53}\text{Ga}_{0.47}\text{As}-\text{In}_{0.52}\text{Al}_{0.48}\text{As}$ Large-Area Avalanche Photodiodes and Arrays

X. G. Zheng, J. S. Hsu, J. B. Hurst, X. Li, S. Wang, X. Sun, Archie L. Holmes, Jr., *Member, IEEE*, Joe C. Campbell, *Fellow, IEEE*, Andrew S. Huntington, and Larry A. Coldren, *Fellow, IEEE*

Abstract—Large-area (500- μm diameter) mesa-structure $\text{In}_{0.53}\text{Ga}_{0.47}\text{As}-\text{In}_{0.52}\text{Al}_{0.48}\text{As}$ avalanche photodiodes (APDs) are reported. The dark current density was $\sim 2.5 \times 10^{-2} \text{ nA}/\mu\text{m}^2$ at 90% of breakdown; low surface leakage current density ($\sim 4.2 \text{ pA}/\mu\text{m}$) was achieved with wet chemical etching and SiO_2 passivation. An 18×18 APD array with uniform distributions of breakdown voltage, dark current, and multiplication gain has also been demonstrated. The APDs in the array achieved 3-dB bandwidth of $\sim 8 \text{ GHz}$ at low gain and a gain-bandwidth product of $\sim 120 \text{ GHz}$.

Index Terms—Avalanche multiplication, avalanche photodiodes, excess noise factor, impact ionization, ionization coefficient, photodetectors, photodiode.

I. INTRODUCTION

THE $\text{In}_{0.53}\text{Ga}_{0.47}\text{As}-\text{In}_{0.52}\text{Al}_{0.48}\text{As}$ avalanche photodiodes (APDs) have been widely studied for wide-band optical communication applications. Much of the research on these APDs has focused on achieving higher gain-bandwidth products to accommodate the ever-increasing bit rates of fiber-optic systems. For this application, small device size is preferred in order to reduce the RC time constant. On the other hand, emerging optical measurement systems that operate in the eye-safety wavelength range ($\sim 1.5 \mu\text{m}$) require long-wavelength, high-sensitivity photodiodes with large detection area. For many applications of this type an APD is preferable to a p-i-n photodiode since the internal gain of the APD affords higher sensitivity. Good material uniformity is required by three-dimensional infrared imaging systems, which utilize APD arrays that operate in the short-wavelength infrared (SWIR) range ($0.8 \mu\text{m} \leq \lambda \leq 2.2 \mu\text{m}$) and have gigahertz bandwidths [1]. Both applications present stringent challenges to the quality and uniformity of the epitaxial layers from which the APDs are fabricated. In addition, passivation of the InP-based material is critical. If large defect densities are created during material growth (MBE or MOCVD), the bulk leakage current will be high, severe microplasma-induced speed degradation will result

Manuscript received December 2, 2003; revised April 20, 2004. This work was supported by the Defense Advanced Research Projects Agency through the Heterogeneous Optoelectronics Technology Center and the 3-D Imaging Program.

X. G. Zheng, J. S. Hsu, J. B. Hurst, X. Li, S. Wang, X. Sun, A. L. Holmes, Jr., and J. C. Campbell are with the Department of Electrical and Computer Engineering, Microelectronics Research Center, University of Texas, Austin, TX 78712 USA (email: jcc@mail.utexas.edu).

A. S. Huntington and L. A. Coldren are with the Materials Department, Optoelectronics Technology Center, University of California, Santa Barbara, CA 93106 USA.

Digital Object Identifier 10.1109/JQE.2004.831637

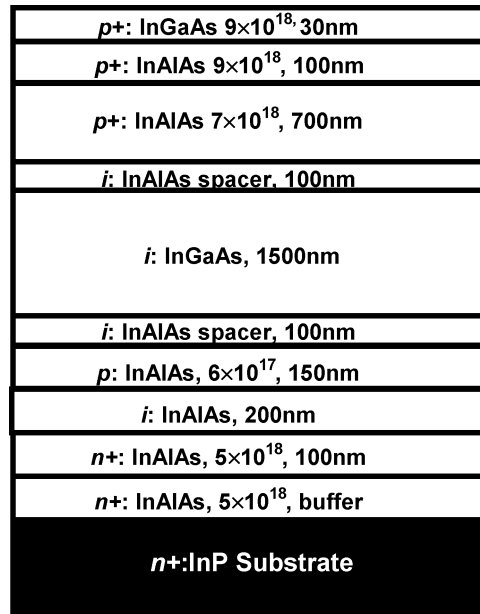


Fig. 1. Device structure for large-area APDs and arrays.

[2], and the device reliability for large-area APDs and arrays will suffer [3]. From a processing point of view, the quality of device passivation is critical if low dark currents are to be achieved [4]. Previously, a 100- μm -diameter InAlGaAs-InAlAs super-lattice APD integrated with a 200- μm diameter microlens has been reported for eye-safe optical measurements [5]. In this paper, we report $\text{In}_{0.53}\text{Ga}_{0.47}\text{As}-\text{In}_{0.52}\text{Al}_{0.48}\text{As}$ long-wavelength APDs with mesa diameter up to 500 μm . The multiplied dark current density was $\sim 2.5 \times 10^{-2} \text{ nA}/\mu\text{m}^2$ at 90% of breakdown. An 18×18 APD array has also been demonstrated with the same InP-based material. This APD array exhibited uniform distributions of breakdown voltage, dark current, and multiplication gain. The APDs in the array demonstrated bandwidth of $\sim 8 \text{ GHz}$ at low gains and a gain-bandwidth product of $\sim 120 \text{ GHz}$.

II. EXPERIMENT

The separate absorption, charge, and multiplication (SACM) structure that was utilized for the large-area APDs and APD arrays is shown in Fig. 1. This type of device structure typically exhibits low dark current, low multiplication noise, and broad bandwidth if the electric field profile in the entire depleted region is adequately optimized [6]–[10]. A previous report on an $\text{In}_{0.53}\text{Ga}_{0.47}\text{As}-\text{In}_{0.52}\text{Al}_{0.48}\text{As}$ 12×12 APD array has demonstrated that long-wavelength APD arrays are achievable based

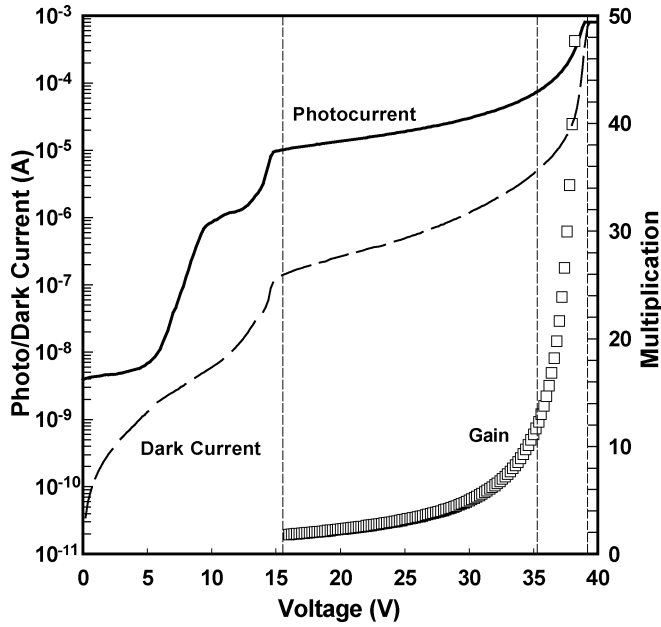


Fig. 2. I - V curves for a 500- μm -mesa-diameter APD.

on state-of-the-art MBE epitaxial technology, but the speed performance of the 12×12 APD array was not satisfactory due to carrier multiplication in the $\text{In}_{0.53}\text{Ga}_{0.47}\text{As}$ absorber [11]. This can be alleviated, to a great extent, by reducing the electric field in the $\text{In}_{0.53}\text{Ga}_{0.47}\text{As}$ absorber. This will also provide the added benefit of reducing the generation-recombination component of the dark current in the absorber, which is the dominant dark current mechanism. In this paper, the charge layer doping has been adjusted to reduce the field in the absorption layer to <150 kV/cm. The improved APD wafer structure, as shown in Fig. 1, was grown by molecular beam epitaxy on n-type InP substrates. Detailed material growth conditions and device processing procedures can be found in the previous paper [11].

III. RESULTS AND DISCUSSION

A. Large-Area InGaAs-InAlAs APDs

The typical photoresponse and dark current curves of a 500- μm -diameter APD are shown in Fig. 2. The punch-through voltage was ~ 15.0 V and the breakdown voltage was ~ 39.2 V. The photocurrent was not flat above the punch-through voltage, an indication that gain has been achieved prior to punch-through [2]. In order to estimate the gain, the external quantum efficiency was measured [11] at different biases above punch-through. Fig. 3 shows the quantum efficiency versus wavelength at bias voltages of $V = 16.0$ and 17.0 V. For bias voltage of 16.0 V, the APD is clearly beyond punch-through and the external quantum efficiency was $\sim 85\%$ at the wavelength of $1.55 \mu\text{m}$, which is much higher than that of previous APD array devices [11], where the unity-gain external quantum efficiency was $\sim 45\%$ at $1.55 \mu\text{m}$. The only difference between these device structures was the charge layer doping level; the large-area APD device has ~ 1.85 times higher Be doping concentration in the charge layer. This APD array result can be utilized as a reliable reference for unity-gain quantum efficiency since the APD array device in [11] exhibited very flat photoresponse

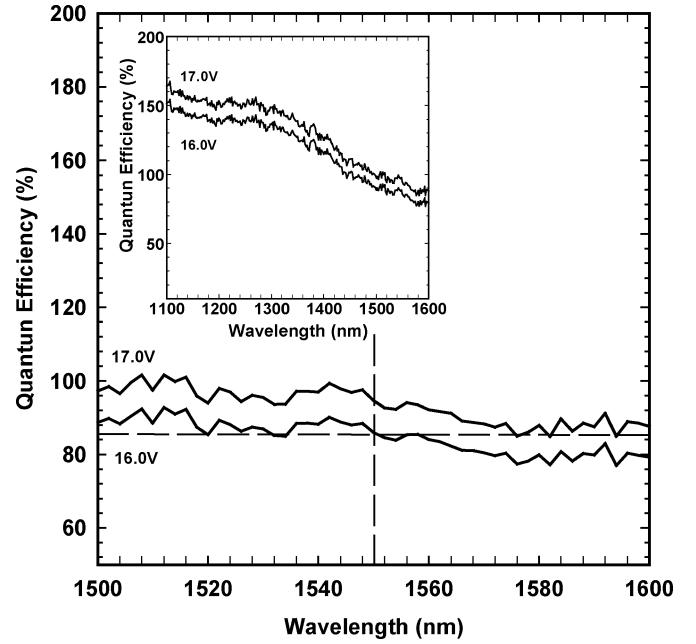


Fig. 3. External quantum efficiency versus wavelength at bias levels of 16.0 and 17.0 V.

after punch-through and no obvious gain-enhanced quantum efficiency was observed. Based on this reference the gain at bias voltage of 16.0 V can be estimated as ≥ 1.8 . The assertion of gain at punch-through can be also corroborated by an estimate of the electric field intensity. At a reverse bias of 16.0 V, the electric field in the $\text{In}_{0.52}\text{Al}_{0.48}\text{As}$ multiplication region is ~ 580 kV/cm, assuming a 200-nm $\text{In}_{0.52}\text{Al}_{0.48}\text{As}$ undoped multiplication region and a 150-nm p-type ($6 \times 10^{17} \text{ cm}^{-3}$) $\text{In}_{0.52}\text{Al}_{0.48}\text{As}$ charge region. This value of electric field is consistent with measurements on $\text{In}_{0.52}\text{Al}_{0.48}\text{As}$ homojunction APDs [12], from which it was found that the electric field in a 200-nm-thick multiplication region at gain of 1.8 was ~ 560 kV/cm.

The gain of the APD versus voltage was determined using the expression

$$M^* = \frac{I_p - I_d}{I_{pu} - I_{du}}, \quad M = M_0 \cdot M^* \quad (1)$$

where M_0 is the gain factor determined from the quantum efficiency measurement ($M_0 = 1.8$), I_p and I_d are the photocurrent and dark current for bias values above the reference voltage (16 V in this case), I_{pu} and I_{du} are the primary photocurrent and dark current at the reference voltage, M^* is the gain from the I - V measurement, and M is the estimated gain of the APD. The gain curve of a 500- μm -diameter APD is plotted in Fig. 2. APDs having a wide range of mesa diameter (from 20 to 500 μm) exhibited gain values above 40.

The dark current versus voltage curves for APDs with mesa diameters in the range from 20 to 500 μm are shown in Fig. 4. The dark current of the 30- μm -diameter APD was ~ 26.7 nA at bias voltage of 35.2 V (90% of the breakdown where gain >10). This compares favorably with SiN_x -passivated APDs: 0.7 $\mu\text{A}/30 \mu\text{m}$ by Kagawa *et al.* [13], 0.41 $\mu\text{A}/30 \mu\text{m}$ by Kim *et al.* [3], 0.4 $\mu\text{A}/80 \mu\text{m}$ by Makita *et al.* [14], and the polyimide-passivated APDs (67 nA/30 μm) and the

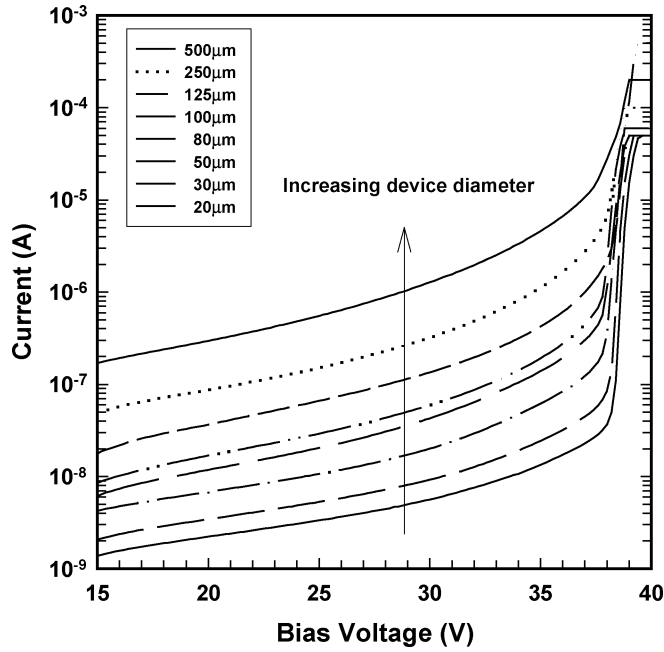


Fig. 4. Dark current versus voltage for APDs with mesa diameters in the range 20–500 μm .

BCB-passivated APDs (38 nA/30 μm) reported by Kim *et al.* [3].

The APD dark current consists of the bulk leakage current, which is proportional to the mesa area, and the sidewall leakage current, which is only proportional to the mesa perimeter. The total dark current can be expressed as

$$I_{\text{total}} = J_{\text{sidewall}} \cdot \pi \cdot d + \frac{J_{\text{bulk}} \cdot \pi \cdot d^2}{4} \quad (2)$$

where J_{sidewall} is the sidewall leakage current density (A/m) and J_{bulk} is the bulk leakage current density ($\text{A}/\mu\text{m}^2$). The measured dark currents at bias voltage of ~ 35.2 V (90% of breakdown) are plotted in Fig. 5(a) versus mesa diameter. The solid line is a quadratic fit, which shows that the bulk component of the dark current is dominant. From the fit, the surface dark current density, J_{sidewall} , was 0.19 nA/ μm and the bulk dark current density was 0.023 nA/ μm^2 . The total dark current can also be expressed in terms of the multiplied dark current and unmultiplied dark current using the relation

$$I_{\text{total}} = I_{\text{unmultiplied}} + I_{\text{multiplied}} \cdot M. \quad (3)$$

In Fig. 5(b), (3) was fitted to the dark current of a 100- μm -diameter APD. The unmultiplied dark current (density) was ~ 1.32 nA (4.2 pA/ μm) and the multiplied dark current was ~ 1.54 nA. The dependence of dark current on gain remains linear to gain values > 50 . The low value of the unmultiplied dark current (density) is an indication of good material quality and surface passivation; it can be neglected for APDs biased at high gains.

The spatial photoresponse profile of the large-mesa-area APD was measured by the raster-scanning technique. A 1.5- μm -wavelength He-Ne laser beam with a beam-waist < 5 - μm was scanned across a 500- μm -diameter APD at bias voltage of 36.8 V ($M \sim 20$). A flat, uniform photoresponse

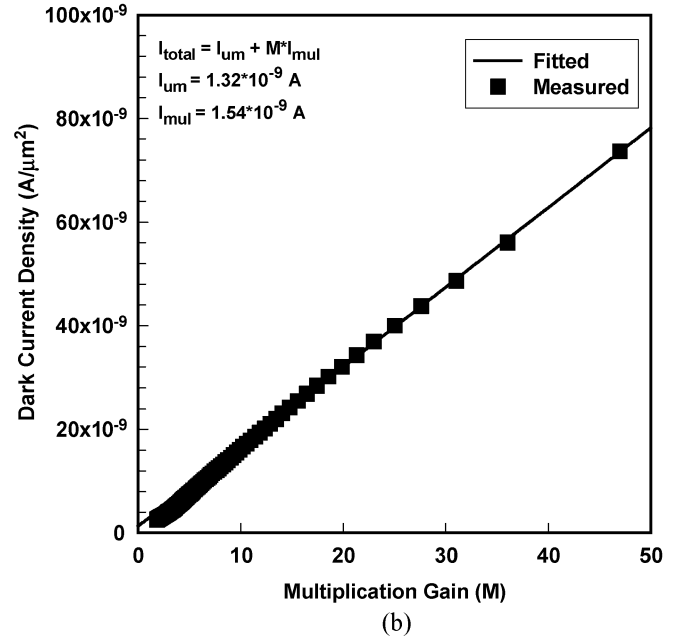
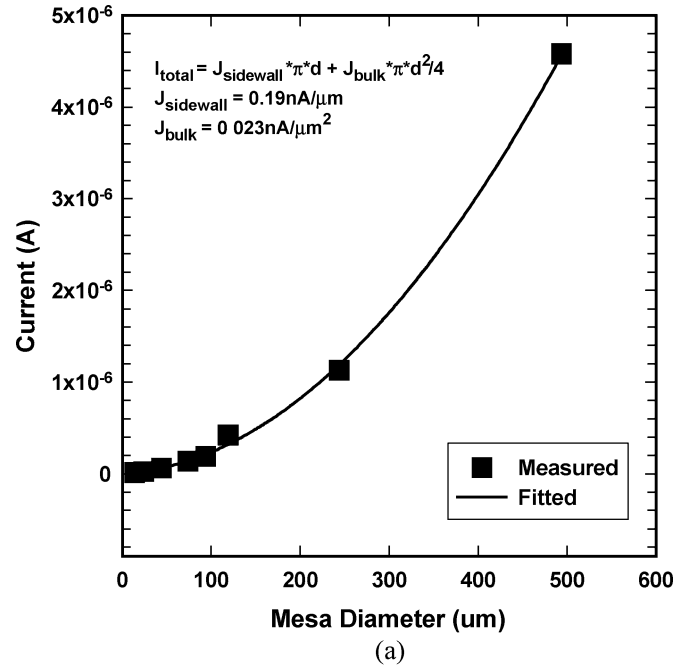


Fig. 5. (a) Dark current and quadratic fit as a function of mesa diameter. (b) Dark current and quadratic fit as a function of gain for a 100- μm device.

profile was obtained across the whole mesa area, as shown in Fig. 6. No spikes in the interior or edge peaks were observed.

B. InGaAs-InAlAs APD Arrays

The photocurrent, dark current, and gain of each device in an 18×18 array of 50- μm -diameter APDs were measured. Three devices on the array failed due to improper probing. Statistical analysis of the dark current for the other 321 devices exhibited a mean value of ~ 4.4 nA and a standard deviation of 1.5 nA at a bias voltage of 16.0 V (gain ~ 1.8). The dark current distribution at 90% of the breakdown exhibited a mean value of ~ 71 nA and a standard deviation of 13 nA. The higher fractional spread at higher bias was due to poor sidewall passivation on several devices. Uniform photocurrent was consistently observed across

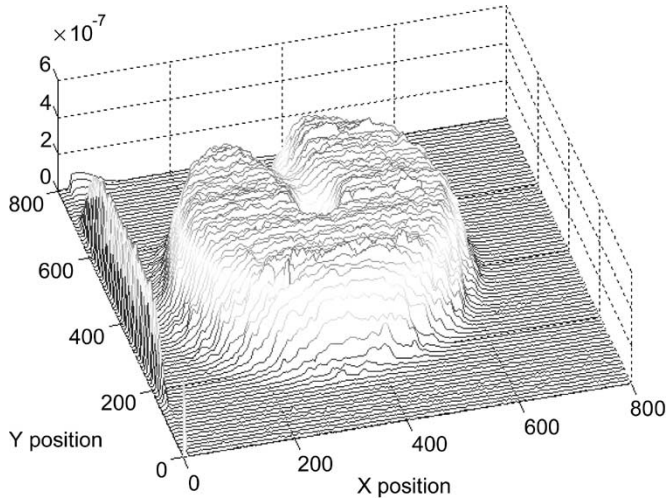


Fig. 6. Spatial photo-response of a 500- μm APD at bias voltage of 38.6 V ($M \geq 20$).

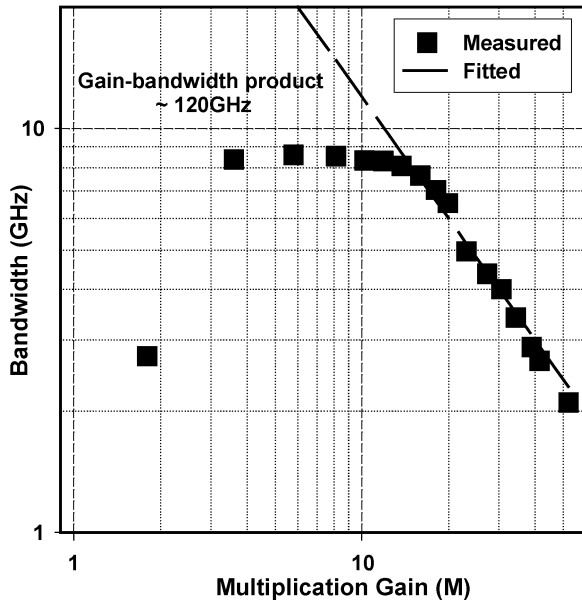


Fig. 7. $C-V$ characteristics of a 50- μm APD array device and a 500- μm large-area APD (shown in the inset).

the array. As described above, the gain was calculated using (1). The mean value of gain was 10.9, 16.1, 22.1, and 43.4 at reverse bias voltages of 35.0, 36.4, 37.2, and 38.2 V, respectively. The standard deviations of the gain distribution at each of the above reverse bias conditions were 0.9, 1.4, 2.1, and 5.6, respectively. These results agree very well with previous 12×12 APD array results [11], especially for the high-gain regime.

The bandwidth of the array devices was measured with a HP8703A lightwave component analyzer at the wavelength of 1.3 μm . The bandwidth versus gain is plotted in Fig. 7. The low-gain bandwidth of a typical 50- μm -diameter APD device was ~ 8 GHz. The bandwidth at low gain was limited by the transit time through the long carrier transport path ($\sim 3.9 \mu\text{m}$) associated with the depleted absorption, charge, and multiplication regions. To verify this, the capacitance of an APD array device was measured versus voltage. For a 50- μm -diameter APD, the measured capacitance was ~ 125

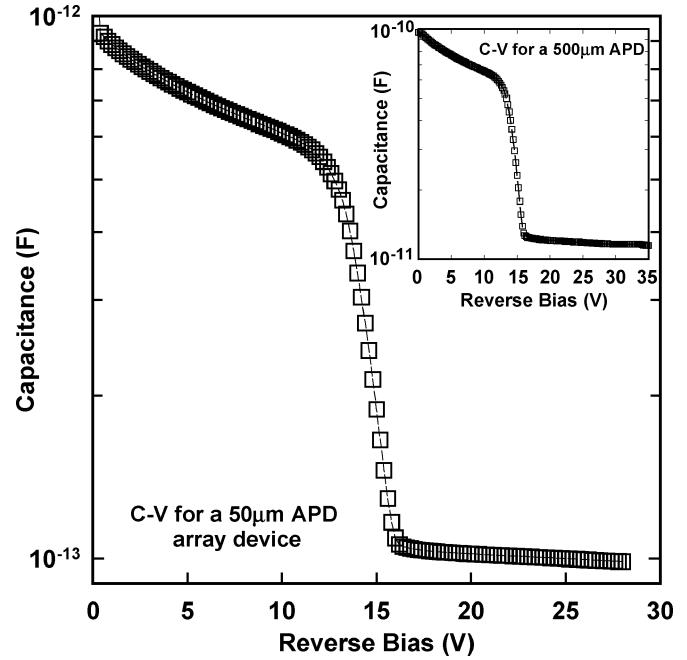


Fig. 8. Bandwidth versus gain for a 50- μm APD array device.

fF ($\sim 6.4 \times 10^{-2} \text{ fF}/\mu\text{m}^2$) at low frequency (1 MHz) and at bias voltage of 16.0 V, as plotted in Fig. 8. A capacitance of ~ 13 pF ($\sim 6.6 \times 10^{-2} \text{ fF}/\mu\text{m}^2$) at bias voltage of 16.0 V was also obtained for a 500- μm -diameter device, as shown in the inset of Fig. 8. These measured results are consistent with the calculated capacitance value ($6.3 \times 10^{-2} \text{ fF}/\mu\text{m}^2$), and the capacitance was found to be scalable to the mesa area for large-area APDs. The capacitance curve exhibited a sharp decrease before punch-through, but only a slight change was observed after punch-through owing to total depletion of the absorption, charge, and multiplication regions. The capacitance and resistance were also measured with a HP8703A network analyzer with RF calibration frequency up to 10 GHz. The measured capacitance was ~ 100 fF and total load resistance was $\sim 60 \Omega$ ($\sim 10 \Omega$ contact resistance + 50Ω terminal resistance). The 3-dB RC -bandwidth was estimated to be >20 GHz using these measured values. The slight discrepancy between the high frequency RF measurement and the low frequency $C-V$ measurement can, at least in part, be attributed to the frequency dependence of the dielectric constant. At higher gains a gain-bandwidth product of 120 GHz was observed. In comparison with previous results [11], the gain-bandwidth increased ≥ 5 times due to an improved electric field profile, which reduced the field intensity in the 1500 nm-thick $\text{In}_{0.53}\text{Ga}_{0.47}\text{As}$ absorption region. By increasing the charge layer doping, the electric field strength in the $\text{In}_{0.53}\text{Ga}_{0.47}\text{As}$ absorber decreased from >250 kV/cm to <150 kV/cm at bias voltages close to breakdown.

IV. CONCLUSION

Large-area mesa $\text{In}_{0.53}\text{Ga}_{0.47}\text{As}-\text{In}_{0.52}\text{Al}_{0.48}\text{As}$ APDs have been demonstrated. APDs with mesa diameter of 500 μm exhibited low dark current density of $\sim 2.5 \times 10^{-2} \text{ nA}/\mu\text{m}^2$ at 90% of the breakdown. Low surface leakage current density

(~ 4.2 pA/ μm) was achieved with wet chemical etching and SiO₂ passivation. An 18 \times 18 APD array has also been demonstrated based on the same material and device structure. This APD array exhibited uniform distributions of breakdown voltage, dark current, and multiplication gain. A bandwidth of ~ 8 GHz at low gains and a gain-bandwidth product of ~ 120 GHz were achieved.

REFERENCES

- [1] R. S. Balcerak, "Unattended imaging sensors," in *Proc. 3-D Imaging Receivers SPIE Conf.*, Apr. 2000, pp. 11–14.
- [2] G. S. Kinsey, J. C. Campbell, and A. G. Dentai, "Waveguide avalanche photodiode with a gain-bandwidth product of 320 GHz," *IEEE Photon. Technol. Lett.*, vol. 13, pp. 842–844, Aug. 2001.
- [3] H. S. Kim, J. H. Choi, H. M. Bang, Y. Jee, S. W. Yun, J. Burm, M. D. Kim, and A. G. Choo, "Dark current reduction in APD with BCB passivation," *Electron. Lett.*, vol. 37, no. 7, pp. 455–457, Mar. 2001.
- [4] D. Schmidt and D. Trommer, "Conservation of low dark current of InGaAs photodiodes after NH₃F/HF etch a BCB passivation layer," in *Proc. Indium Phosphide and Related Materials Conf.*, pp. 302–305.
- [5] M. Hayashi, I. Wantababe, T. Nakata, M. Tsuji, K. Makita, S. Yamakata, and K. Taguchi, "Microlens-integrated large-area InAlGaAs-InAlAs superlattice APDs for eye-safety 1.5- μm wavelength optical measurement use," *IEEE Photon. Technol. Lett.*, vol. 10, pp. 576–578, Apr. 1998.
- [6] I. Watanabe, M. Tsuji, M. Hayashi, K. Makita, and K. Taguchi, "Design and performance of InAlGaAs-InAlAs superlattice avalanche photodiodes," *J. Lightwave Technol.*, vol. 15, pp. 1012–1019, June 1997.
- [7] C. Cohen-Jonathan, L. Giraudet, A. Bonzo, and J. P. Praseuth, "Waveguide AlInAs/GaAlInAs avalanche photodiode with a gain-bandwidth product over 160 GHz," *Electron. Lett.*, vol. 33, no. 17, pp. 1492–1493, 1997.
- [8] H. Nie, K. A. Anselm, C. Lenox, P. Yuan, C. Hu, G. Kinsey, B. G. Streetman, and J. C. Campbell, "Resonant-cavity separate absorption, charge, and multiplication avalanche photodiodes with high speed and high gain-bandwidth product," *IEEE Photon. Technol. Lett.*, vol. 10, pp. 409–411, Mar. 1998.
- [9] C. Lenox, H. Nie, P. Yuan, G. Kinsey, A. L. Holmes Jr., B. G. Streetman, and J. C. Campbell, "Resonant-cavity InGaAs-InAlAs avalanche photodiodes with gain-bandwidth product of 290 GHz," *IEEE Photon. Technol. Lett.*, vol. 11, pp. 1162–1164, Sept. 1999.
- [10] K. Kato, "Ultrawide-band/high-frequency photodetectors," *IEEE Trans. Microwave Theory Tech.*, vol. 47, pp. 1265–1281, July 1999.
- [11] X. G. Zheng, J. Hsu, X. Sun, J. B. Hurst, X. Li, S. Wang, A. L. Holmes Jr., J. C. Campbell, A. S. Huntington, and L. A. Coldren, "A 12 \times 12 In_{0.53}Ga_{0.47}As-In_{0.52}Al_{0.48}As avalanche photodiode array," *IEEE J. Quantum Electron.*, vol. 38, pp. 1536–1540, Nov. 2002.
- [12] C. Lenox, P. Yuan, H. Nie, O. Baklenov, C. Hansing, J. C. Campbell, A. L. Holmes Jr., and B. G. Streetman, "Thin multiplication region InAlAs homojunction avalanche photodiodes," *Appl. Phys. Lett.*, vol. 73, no. 6, pp. 783–784, 1998.
- [13] T. Kagawa, Y. Kawamura, and H. Iwamura, "A wide-bandwidth low-noise InGaAsP-InAlAs superlattice avalanche photodiode with a flip-chip structure for wavelength of 1.3 μm and 1.55 μm ," *IEEE J. Quantum Electron.*, vol. 29, pp. 1387–1392, May 1993.
- [14] K. Makita, I. Watanabe, M. Tsuji, and K. Taguchi, "Dark current and breakdown analysis in In(Al)GaAs/InAlAs superlattice avalanche photodiodes," *Jpn. J. Appl. Phys.*, vol. 35, pp. 3440–3444, 1996.



X. G. Zheng received the B.S.E.E. degree from the Beijing Institute of Technology, Beijing, China, in 1985, and the M.S. degree in electrical engineering from the Hebei Semiconductor Research Institute in 1991. He is currently pursuing the Ph.D. degree in electrical engineering at the University of Texas at Austin.

His major research areas are in optoelectronic devices, such as impact ionization properties of III-V compound materials, high-speed long-wavelength avalanche photodiodes and arrays, and heterogeneous material integration via direct wafer bonding.

J. S. Hsu received the B.S.E.E. degree from the Pennsylvania State University, University Park, in 1996, and the M.S. Degree in electrical engineering from the University of Texas at Austin in 2002.

Her research includes compound semiconductor avalanche photodetectors operating in the near-infrared long-wavelength regime as well as characterization of avalanche photodetector arrays and large-area avalanche photodetectors.



J. B. Hurst received the B.S. degree in electrical engineering from the University of Oklahoma, Norman, in 1999, and the M.S. degree in electrical engineering from the University of Texas at Austin in 2001. He is currently pursuing the Ph.D. degree at the University of Texas.

His current research interests include molecular beam epitaxy growth of III-V semiconductors, direct wafer bonding, and long-wavelength avalanche photodetectors.



X. Li was born in Beijing, China, in 1970. He received the B.S. and M.S. degrees from the Physics Department, Peking University, Beijing, China, in 1994 and 1997, respectively. He is currently pursuing the Ph.D. degree in electrical engineering at the Microelectronic Research Center, University of Texas at Austin.

His research interests are avalanche process simulations and high-saturation power photodetectors for 1.55- μm applications.



S. Wang received the B.S. degree in microelectronics from Beijing University, Beijing, China, in 1995, and the M.S.E.E. degree from the University of Notre Dame, South Bend, IN, 1999. She is currently pursuing the Ph.D. degree at the Microelectronics Research Center, University of Texas at Austin, working on high-speed, low-noise avalanche photodiodes.

Ms. Wang is a student member of the IEEE Lasers and Electro-Optics Society (LEOS).



X. Sun received the B.S. and M.S. degrees in materials science and engineering from Tsinghua University, Beijing, China, in 1995 and 1997, respectively, and the M.S.E.E. degree from the University of Texas at Austin in 2000. He is currently pursuing the Ph.D. degree at the Microelectronics Research Center, University of Texas.

His research interests include molecular beam epitaxy growth of III-V compound semiconductors and characterization, and design and fabrication of high-speed near-infrared photodetectors.



Archie L. Holmes, Jr. (M'92) received the B.S.E.E. degree from the University of Texas at Austin in 1991, and the M.S. and Ph.D. degrees in electrical engineering from the University of California, Santa Barbara, in 1992 and 1997, respectively.

He joined the Department of Electrical and Computer Engineering, University of Texas as an Assistant Professor in 1997. His major research areas are in electronic materials and devices, growth of novel semiconductor alloys by molecular beam epitaxy, high-speed photodetectors, and heterogeneous materials integration via direct wafer bonding. He has published more than 80 journal and conference papers.

Dr. Holmes is a member of IEEE Lasers and Electro-Optics Society (LEOS) and the American Society for Engineering Education.



Joe C. Campbell (S'73–M'74–SM'88–F'90) received the B.S. degree in physics from the University of Texas at Austin in 1969, and the M.S. and Ph.D. degrees in physics from the University of Illinois at Urbana-Champaign, in 1971 and 1973, respectively.

From 1974 to 1976, he was employed by Texas Instruments Inc. where he worked on integrated optics. In 1976, he joined the staff of AT&T Bell Laboratories, Holmdel, NJ. In the Crawford Hill Laboratory, he worked on a variety of optoelectronic devices including semiconductor lasers, optical modulators, waveguide switches, photonic integrated circuits, and photodetectors with emphasis on high-speed avalanche photodiodes for high-bit-rate lightwave systems. In January 1989, he joined the faculty of the University of Texas as Professor of electrical and computer engineering and Cockrell Family Regents Chair in Engineering. At present, he is actively involved in Si-based optoelectronics, high-speed, low-noise avalanche photodiodes, high-power photodiodes, ultraviolet photodetectors, and quantum-dot IR imaging. He has coauthored six book chapters, more than 300 journal publications, and 200 conference presentations.

Dr. Campbell is a member of the National Academy of Engineering, a Fellow of the Optical Society of America, and a Fellow of the American Physical Society.



Larry A. Coldren (M'72–SM'77–F'82) received the Ph.D. degree in electrical engineering from Stanford University, Palo Alto, CA, in 1972.

After 13 years in the research area at Bell Laboratories, he was appointed Professor of electrical and computer engineering at the University of California at Santa Barbara (UCSB) in 1984. In 1986, he assumed a joint appointment with Materials and Electrical and Computer Engineering, and the Fred Kavli Chair in Optoelectronics and Sensors in 2000. He is also Chairman and Chief Technology Officer of Agility Communications, Inc., Santa Barbara. At UCSB his research efforts have included work on novel guided-wave and vertical-cavity modulators and lasers as well as the underlying materials growth and fabrication technology. He is now investigating the integration of various optoelectronic devices, including optical amplifiers and modulators, tunable lasers, wavelength-converters, and surface-emitting lasers. He has authored or coauthored over 500 papers, five book chapters, and one textbook, and has been issued 32 patents.

Prof. Coldren is a Fellow of the Optical Society of America, a former Vice-President of IEEE Lasers and Electro-Optics Society, and has been active in technical meetings.



Andrew S. Huntington received the B.S. degree in chemistry from the California Institute of Technology, Pasadena, in 1997. He is currently a graduate student at the Materials Department, University of California at Santa Barbara.

His current research interests are the growth of arsenide compounds lattice-matched to InP for optoelectronic applications, including long-wavelength multiple-active region vertical-cavity lasers and avalanche photodiodes.

IV. Terahertz Technology

Terahertz electro-optic wavelength conversion in GaAs quantum wells: Improved efficiency and room-temperature operation

S. G. Carter,^{a)} V. Ciulin, and M. S. Sherwin

Department of Physics and iQUEST, University of California, Santa Barbara, California 93106

M. Hanson, A. Huntington, L. A. Coldren, and A. C. Gossard

Materials Department, University of California, Santa Barbara, California 93106

(Received 3 July 2003; accepted 8 December 2003)

A 4- μm -thick sample containing 50 GaAs/AlGaAs asymmetric coupled quantum wells was driven with a strong terahertz (THz) electric field of frequency ω_{THz} and probed with a near-infrared (NIR) laser of frequency ω_{NIR} . The THz beam modulated the probe to generate sidebands at $\omega_{\text{NIR}} + n\omega_{\text{THz}}$, where n is an integer. Up to 0.2% of the NIR laser power was converted into the $n = +1$ sideband at 20 K, and sidebands were observed up to room temperature. The strong THz fields also induced changes in the NIR absorption of the sample. © 2004 American Institute of Physics. [DOI: 10.1063/1.1645662]

In an efficient wavelength division multiplexed (WDM) optical communication network, it is necessary to switch data from one near-infrared (NIR) wavelength to another.¹ Wavelength conversion has been performed all-optically in semiconductor optical amplifiers,^{1,2} semiconductor lasers,³ optical fibers,⁴ LiNbO₃,⁵ and in bulk GaAs.⁶ In previous work, we have demonstrated all-optical wavelength conversion by THz electro-optic (EO) modulation in GaAs quantum wells.^{7–12} This method is not limited in speed by gain and carrier dynamics, as are SOAs and lasers, and has the advantage of occurring in a system with strong nonlinearities¹³ and resonances that can be tuned by electric fields⁷ and band-gap engineering.

The THz EO modulation involves a NIR beam of frequency ω_{NIR} that mixes with a THz beam of frequency ω_{THz} in a GaAs/AlGaAs heterostructure. Sidebands are emitted at $\omega_{\text{sideband}} = \omega_{\text{NIR}} + n\omega_{\text{THz}}$, where $n = \pm 1, 2, 3$, etc. For low THz fields the resonant structure of sideband conversion can be well described by a resonant nonlinear susceptibility model, in which sidebands are strongest when ω_{NIR} is resonant with interband transitions and ω_{THz} is resonant with intersubband transitions.⁹ The resonances can be modified by changing the sample structure or by applying a dc voltage.⁷ For stronger THz fields, the sideband resonances change as the THz field “dresses” the exciton states.^{12,14}

This letter reports sideband conversion efficiencies more than 10 times higher than the best previous results using THz EO modulation.⁷ Sidebands are also observed at room temperature. Finally, the strong THz field influences the exciton states and the resonant structure of the sideband generation. The key to the improvements over previous work is sample design. The sample studied here has a much larger interaction length, and it was designed to transmit the NIR beam and sidebands instead of reflecting them from a distributed Bragg reflector (DBR). Since the frequencies of excitonic resonances shift strongly with temperature, the elimination of the fixed-bandwidth DBR greatly simplified the measure-

ment of sidebands for a wide range of temperatures (20–295 K).

The sample consists of 50 periods of double GaAs quantum wells, nominally 100 and 120 Å wide and separated by a 25 Å Al_{0.2}Ga_{0.8}As tunnel barrier (see inset of Fig. 1). Each pair of wells is separated by a 200 Å Al_{0.3}Ga_{0.7}As barrier. The difference between the widths of the GaAs wells breaks inversion symmetry in the growth direction, thus allowing the generation of sidebands with odd n .⁸ Furthermore, the tunnel splitting produces a spacing between electron subbands in the range of our THz source,⁷ the UCSB Free Electron Laser. The semi-insulating GaAs substrate absorbs NIR radiation resonant with excitonic transitions. In previous experiments on similar coupled quantum wells, NIR and side-

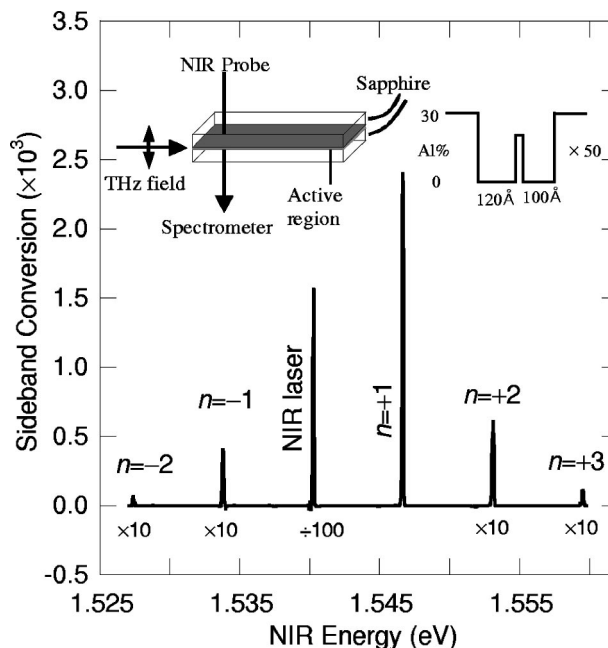


FIG. 1. Transmitted sideband spectrum taken at 20 K with a FEL frequency of 1.5 THz (6.4 meV). The transmitted beam at ω_{NIR} is divided by 100 and the $n = +3, +2, -1, -2$ sidebands are multiplied by 10 for clarity. The THz power was ~ 1 kW and the NIR power was 0.2 mW. The experimental geometry and the conduction band diagram of a sample well are inset in the figure.

^{a)}Electronic mail: scarcer@physics.ucsb.edu

bands have been reflected off a DBR placed between the QW and the substrate. To allow transmission of the NIR probe through the present sample, the sample was glued to a piece of sapphire and the semi-insulating GaAs substrate was etched away. This left a 4- μm -thick epitaxial layer glued to sapphire, which included a 2.2- μm -active region, 0.7 μm of buffer layers, two doped gate QWs (unused), and a 1- μm -etch stop layer. The sample was then glued to another piece of sapphire so that the active region was in the middle of a dielectric waveguide, maximizing the THz field.

The experimental geometry is shown in the inset of Fig. 1. The sample was placed in a closed-cycle He cryostat, where its temperature could be varied from room temperature down to 18 K. The THz beam was coupled into the edge of the sample with its polarization perpendicular to the plane of the QW. The THz beam was on for about 4 μs at a repetition rate of 1.5 Hz with a peak power of ~ 1 kW. It was focused onto the sample with an off-axis parabolic mirror ($f/4$) to a spot measured to be about 1.2 mm in diameter, yielding a maximum intensity of ~ 90 kW/cm² (~ 2 kV/cm in the sample).

The NIR beam came from a cw tunable Ti:sapphire laser which was chopped by an acousto-optic modulator into ~ 200 μs pulses that overlapped each THz pulse. The beam was incident perpendicular to the sample and typically focused to an intensity of roughly 5 W/cm², yielding an exciton density of about 10^9 cm⁻² when tuned in resonance with the exciton transition. It then passed through the sample and was sent to a 0.85 m double monochromator, where it was detected by a photomultiplier tube (PMT). For measurements of the change in transmission by the THz field, the transmitted laser beam was sent directly to a silicon photodiode.

Figure 1 shows a typical sideband spectrum. The transmitted laser line at 1.54 eV (attenuated by 100) had sidebands at multiples of 6.4 meV (1.5 THz), the THz frequency. The $n = +1$ sideband was far stronger than the others with an intensity of about 0.2% of the incident NIR beam. This sideband spectrum was measured with an incident NIR intensity of about 2.5 W/cm², so the sideband intensity was about 5 mW/cm². For higher incident intensity of about 40 W/cm², the sideband intensity saturated near 25 mW/cm². The conversion efficiency of 0.2% was an order of magnitude higher than in previous work.⁷ The increase is attributed to the five-fold increase in the interaction length of the sample, which is still only 2 μm .

The THz EO effect that gives rise to sidebands in our sample is different from the conventional EO effect in that both the THz and NIR frequencies are close to resonances of the sample. This resonant structure is shown in a sideband resonance spectrum in Fig. 2(b), taken by changing the incident NIR frequency while always moving the spectrometer to measure the $n = +1$ sideband. Figure 2(a) displays the exciton absorption lines in the transmission spectra for comparison. The lines have been assigned by comparison with theory.¹⁵ The exciton formed by an electron in the n th conduction subband and a hole in the m th heavy hole subband is called $E_n\text{HH}_m$. The strongest sideband resonance at 1.533 eV (which appears to be split for lower THz power) had the incident NIR frequency resonant with E1HH2 and the 1.3 THz frequency (5.5 meV) resonant with the E1HH2–E2HH1

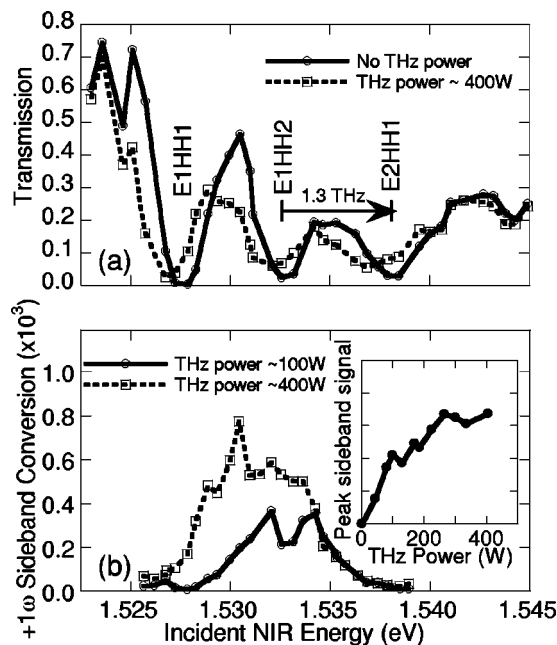


FIG. 2. (a) Sample transmission spectrum at 20 K taken when the FEL is off (open dots and solid lines) and at high power (open squares and dashed lines), indicating the effect of the strong THz field on the linear absorption. The absorption lines are labeled by theory (see Ref. 15). The arrow illustrates that the THz field is close to resonance with the E1HH2–E2HH1 transition. (b) Two $n = +1$ sideband resonance spectra at 20 K taken at low THz power (open dots and solid lines) and high THz power (open squares and dashed lines), indicating the change in resonant structure at high THz powers. Each point of the resonance spectra represents the $n = +1$ sideband signal when the NIR laser frequency is tuned to the value on the horizontal axis. The inset shows the $n = +1$ sideband peak intensity dependence on THz power. For each graph the FEL was at 1.3 THz (5.5 meV).

transition, a double resonance. (A more detailed discussion of this resonance can be found in Ref. 7.) The splitting was actually due to the strong absorption of both the incident NIR beam and the sideband when on resonance. This was confirmed by a coupled amplitude equation model¹⁶ that propagated the sideband and incident laser through the sample as a function of wavelength and thickness. The model includes the nonlinear susceptibility and absorption loss. The significant increase in sideband conversion compared to samples 5 times shorter is consistent with this model.

Changes in the absorption, due to the strong THz field, modified the sideband resonances. Figure 2(a) displays the NIR transmission with and without a strong THz field. The excitonic absorption features redshifted, broadened, and absorbed less strongly when the THz field was on. The effects decreased as the THz field decreased but were qualitatively similar. Driving with 1.5 THz produced similar results as well. These changes were also manifest in the sideband resonance spectra shown in Fig. 2(b). The resonance spectrum at high THz field was redshifted, broadened, and the dip due to absorption was essentially gone. This could be due to the peak broadening and the decrease in absorption when the THz field was on. The inset graph shows the peak sideband signal as a function of THz power, illustrating the saturation that occurred at high powers. Some of these effects were directly due to strong THz fields.^{12,14} However, some changes in the transmission persisted after the FEL pulse was turned off, indicating that the sample was heated during the FEL pulse. The heating effects could not be separated from

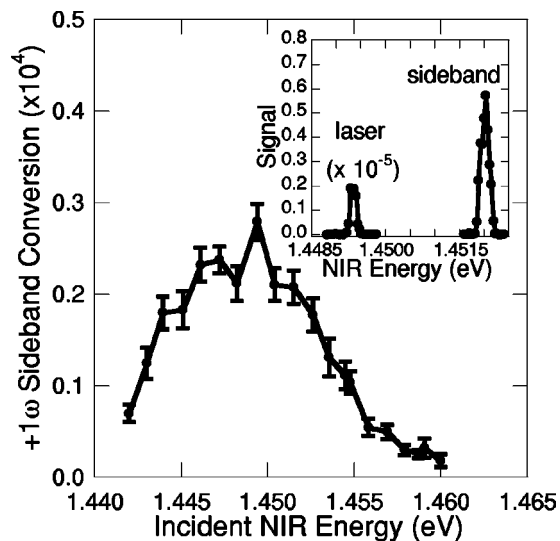


FIG. 3. Transmitted sideband spectrum (inset) and the $n = +1$ sideband resonance spectrum taken at 295 K with FEL frequency 0.66 THz (2.7 meV). Each point of the resonance spectrum represents the $n = +1$ sideband signal when the NIR laser frequency is tuned to the value on the horizontal axis. The THz power was ~ 6 kW and the NIR power was 3.2 mW.

the strong field effects, making a detailed understanding of changes in transmission impossible. The persistent heating effect did not come from photogenerated carrier heating as the effect has very little dependence on NIR power. Heating of carriers from residual extrinsic doping, or of the GaAs or sapphire lattice directly by the THz field could be the cause. This persistent effect was strong in samples with substrates removed, like the one studied here. A sample from the same wafer but with its substrate still attached exhibited changes in reflectivity during FEL pulses with very little persistent change, strongly supporting our conclusion that the changes in transmission reported here were not wholly due to heating. Further work in samples that do not exhibit persistent heating is being performed.

Sidebands were also generated at room temperature, as shown in Fig. 3. The figure displays the $n = +1$ sideband spectrum inset in a sideband resonance spectrum. At this temperature both the band gap and the intersubband spacing decreased, so ω_{THz} was reduced to 0.66 THz (2.7 meV). The fraction of the incident NIR beam converted to the sideband was about 3×10^{-5} , much smaller than at 20 K. A series of measurements were performed on the temperature dependence of the sideband generation. Thermal cycling produced irreversible changes in the optical spectra that were likely due to strain in the thinned sample. Thus the results varied from one cooldown to the next. However, compared to 20 K, the sideband conversion of this sample decreased by not more than a factor of 3 at 100 K and by not more than a factor of 10 at 200 K. The decrease in conversion came from at least two factors. First, the exciton linewidths broadened with increasing temperature, which decreased the peak non-linear susceptibility and indicated an increase in the dephasing rate. This is demonstrated by how broad the sideband resonance spectrum is in Fig. 3 compared to Fig. 2(b). Second, while the sapphire is transparent to THz frequencies at low temperatures, it is absorbing ($\alpha \sim 3 \text{ cm}^{-1}$) at high temperatures.¹⁷ This could have significantly decreased the THz field in the sample.

In summary, we performed terahertz EO experiments in a GaAs multi-quantum well sample that generated sidebands with an efficiency up to 0.2%. The sample also exhibited an interesting change in absorption that was partially due to strong THz field effects. The sideband conversion efficiency is not close to any fundamental limits of which we are aware, but is sufficient to be regenerated to full power by optical amplifiers. It is also comparable to efficiencies achieved in wavelength converters based on SOAs² or semiconductor lasers.³ By comparison, a 4- μm -thick LiNbO₃ sample in the same experimental conditions should have a conversion efficiency of $\sim 3 \times 10^{-8}$, assuming an EO coefficient of 9.6 pm/V.¹⁸ Our device operated from 20 K up to room temperature, but had significantly decreased conversion efficiency at higher temperatures. This could be overcome by coupling the NIR light into the quantum well plane, further increasing the interaction length. A device like the one measured could be made voltage tunable as in Refs. 7 and 12 and could be implemented in InGaAs wells on InP for operation at 1.55 μm . The extremely small thickness of our wavelength converter makes it suitable for insertion into microphotonic circuits. Recently developed THz quantum cascade lasers¹⁹ have, inside their cavities, THz electric fields comparable to the $\sim \text{kV/cm}$ fields used in this study.²⁰ Thus, all-semiconductor THz EO wavelength converters with integrated THz sources may be achieved in the future.

The authors thank David Citrin and Alex Maslov for helpful discussions. This research was funded by NSF-DMR 0070083 and SUN Microsystems. V.C. thanks the Swiss NSF for additional support.

- ¹D. Nasset, T. Kelly, and D. Marcenac, *IEEE Commun. Mag.* **36**, 56 (1998).
- ²M. L. Masanovic, V. Lal, J. S. Barton, E. J. Skogen, D. J. Blumenthal, and L. A. Coldren, *IEEE Photonics Technol. Lett.* **15**, 1117 (2003).
- ³A. Hsu and S. L. Chuang, *IEEE Photonics Technol. Lett.* **15**, 1120 (2003).
- ⁴K. Torri and S. Yamashita, *J. Lightwave Technol.* **21**, 1039 (2003).
- ⁵M. Asobe, O. Tadanaga, H. Miyazawa, Y. Nishida, and H. Suzuki, *Opt. Lett.* **28**, 558 (2003).
- ⁶M. A. Zudov, J. Kono, A. P. Mitchell, and A. H. Chin, *Phys. Rev. B* **64**, 121204 (2001).
- ⁷M. Y. Su, S. G. Carter, M. S. Sherwin, A. Huntington, and L. A. Coldren, *Appl. Phys. Lett.* **81**, 1564 (2002).
- ⁸C. Phillips, M. Y. Su, M. S. Sherwin, J. Ko, and L. Coldren, *Appl. Phys. Lett.* **75**, 2728 (1999).
- ⁹M. Y. Su, C. Phillips, J. Ko, L. Coldren, and M. S. Sherwin, *Physica B* **272**, 438 (1999).
- ¹⁰J. Kono, M. Y. Su, T. Inoshita, T. Noda, M. S. Sherwin, S. J. Allen, and H. Sakaki, *Phys. Rev. Lett.* **79**, 1758 (1997).
- ¹¹J. Cerne, J. Kono, T. Inoshita, M. Sherwin, M. Sundaram, and A. C. Gossard, *Appl. Phys. Lett.* **70**, 3543 (1997).
- ¹²M. Y. Su, S. G. Carter, M. S. Sherwin, A. Huntington, and L. A. Coldren, *Phys. Rev. B* **67**, 125307 (2003).
- ¹³F. Capasso, C. Sirtori, and A. Y. Cho, *IEEE J. Quantum Electron.* **30**, 1313 (1994).
- ¹⁴A. V. Maslov and D. S. Citrin, *Phys. Rev. B* **62**, 16686 (2000).
- ¹⁵M. Y. Su, Ph.D. thesis, University of California, Santa Barbara, 2002.
- ¹⁶R. W. Boyd, *Nonlinear Optics* (Academic, San Diego, 1992), Chap. 2, p. 69.
- ¹⁷E. V. Loewenstein, D. R. Smith, and R. L. Morgan, *Appl. Opt.* **12**, 398 (1973).
- ¹⁸R. W. Boyd, *Nonlinear Optics* (Academic, San Diego, 1992), Chap. 10, p. 404.
- ¹⁹R. Kohler, A. Tredicucci, F. Beltram, H. E. Beere, E. H. Linfield, A. G. Davies, D. A. Ritchie, R. C. Iotti, and F. Rossi, *Nature (London)* **417**, 156 (2002).
- ²⁰D. S. Citrin (private communication).

Terahertz-optical mixing in *n*-doped GaAs quantum wells

S. G. Carter, V. Ciulin, and M. S. Sherwin

Physics Department and iQUEST, Building 981, University of California, Santa Barbara, California 93106
scarter@physics.ucsb.edu

C. S. Wang, A. Huntington and L. A. Coldren

Materials Department, University of California, Santa Barbara, California, 93106

Abstract: Non-linear mixing of a strong Terahertz and a weak near-infrared beam is observed for the first time in an *n*-doped GaAs quantum well. Our results are compared to those for undoped wells.

© 2003 Optical Society of America

OCIS Codes: (230.2090) Electro-optical devices; (230.5590) Quantum-well devices; (190.5970) Semiconductor nonlinear optics including MQW;

The mixing of near-infrared (NIR) and terahertz (THz) lasers has been studied experimentally and theoretically as a way of achieving optical wavelength conversion [1] and of observing strong THz field effects [2]. The mixing results in sidebands at $\omega_{\text{sideband}} = \omega_{\text{NIR}} + n\omega_{\text{THz}}$, where $n = \pm 1, 2, 3, \dots$, as shown in Fig. 1a. The sideband signal has been shown to be strong primarily when ω_{NIR} and ω_{THz} are close to interband and intersubband resonances, respectively [3]. Previous studies dealt with undoped wells in which NIR and THz radiation coupled states which were well-described as excitons. In this paper, sideband generation in doped quantum wells is reported for the first time and compared to that in undoped wells. The presence of charge in the wells screens the excitons and dramatically changes both the resonant behavior of the sideband generation and the strength of the sidebands.

We studied a doped sample and an undoped sample. They consist of 10 periods of double GaAs quantum wells (QWs), nominally 100 and 120 Å wide and separated by a 25 Å $\text{Al}_{0.2}\text{Ga}_{0.8}\text{As}$ tunnel barrier (see inset of Fig. 2b). The doped sample has an electron concentration $n_e \sim 1.5 \times 10^{11} \text{ cm}^{-2}$ per QW. These active QWs are in between two doped gate QWs, used for applying a DC electric field to the sample, thus tuning the intersubband transitions. Behind these QWs is a distributed Bragg reflector (DBR), which reflects the NIR beam and prevents absorption by the GaAs substrate. The experimental geometry is illustrated in Fig. 1b.

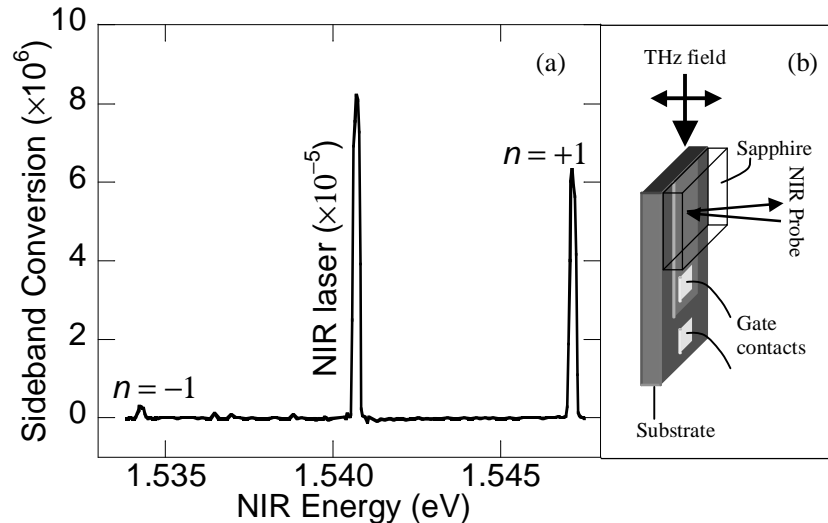


Fig. 1. (a) Sideband spectrum taken at 15 K with an FEL frequency of 1.5 THz (6.4 meV). The reflected beam at ω_{NIR} is multiplied by 10^5 . The THz power was approximately 500 W and the NIR power was 0.67 mW. (b) The experimental geometry.

The photoluminescence (PL) and reflectivity of the two samples are shown in Fig. 2. There are a number of absorption lines in both samples (Fig. 2a). A more detailed description of these transitions (in the undoped sample)

can be found in ref. 3, but the lowest energy line comes from the heavy hole 1 to electron 1 transition (E1HH1). The reflectivity and PL lines are significantly broader in the doped sample, and the doped sample displays an energy shift between the PL and reflectivity, indicating significant charge in the wells.

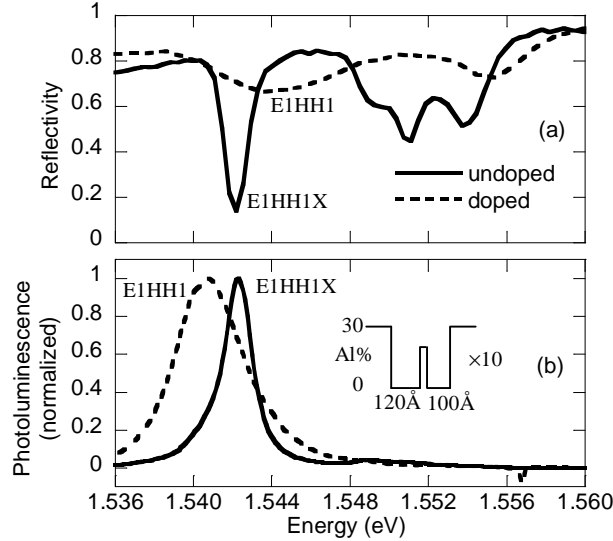


Fig. 2. (a) Reflectivity spectra of the undoped (solid) and doped (dashed) samples at ~ 20 K. The lowest lines come from transitions between the 1st heavy hole subband (HH1) and 1st electron subband (E1) but are excitonic (E1HH1X) in the undoped sample. (b) Photoluminescence spectra taken with excitation power less than 1 mW at ~ 1.6 eV. The spectrum of the undoped sample was taken at 21 K, while that of the doped one was recorded at 15 K. The peak PL of the doped sample is ~ 10 times weaker than that of the undoped sample. Conduction band profile of the QWs is inset in the figure.

The maps in Fig. 3 show the $+1\omega_{\text{THz}}$ sideband resonances of the two samples. For each point, the sideband intensity is measured at the NIR laser energy (varied on the vertical axis) plus ω_{THz} . The DC electric field is varied to bring the THz field into resonance with the intersubband transitions. The two maps look very different. The undoped sample (Fig. 3b) has a lower resonance involving only an electron transition and two upper resonances involving hole transitions (see ref. 3 for details). While sideband resonances involving hole transitions should still be possible in n -doped wells, they should be weaker. In the doped sample (Fig. 3a), however, only the E1HH1 \rightarrow E2HH1 resonance remains. The peak sideband signal is an order of magnitude weaker in the doped sample compared to the undoped one and much broader. These observations can be explained by the interband oscillator strength being more spread out in the doped wells. This study provides interesting new phenomena to explore and also opens the possibility of optically observing strong THz field effects such as period-doubling bifurcations [4].

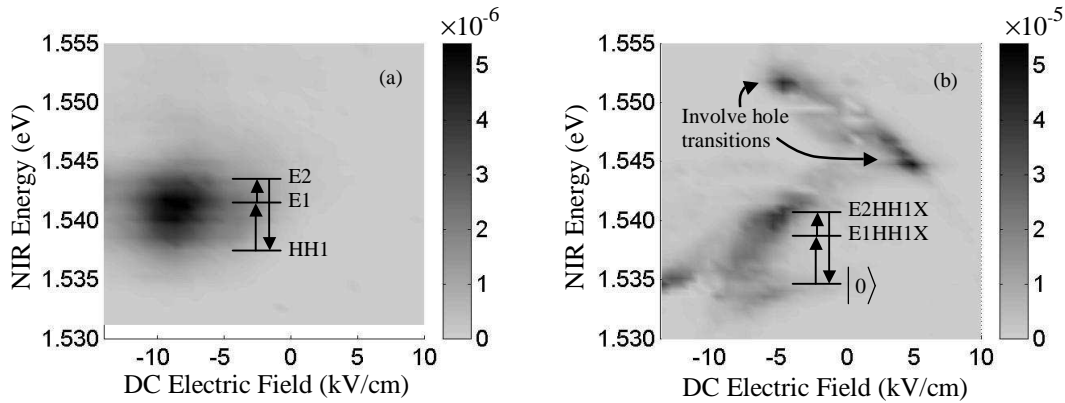


Fig. 3. Sideband maps taken with a NIR power less than 1 mW and THz power of about 300W. Each point represents the $n = +1$ sideband conversion efficiency when the NIR laser energy is tuned to the value on the vertical axis. (a) Map of the doped well sample at 15K with $\omega_{\text{THz}} = 1.5$ THz (6.4 meV). The resonance appears near where the E1 \rightarrow E2 intersubband transition is expected and near the E1HH1 energy. (b) Map of the undoped well sample at 21K with $\omega_{\text{THz}} = 2.0$ THz (8.2 meV). The resonances are excitonic and are labeled according to ref. 3.

- [1] S. G. Carter, V. Ciulin, M. S. Sherwin, M. Hanson, A. Huntington, L. A. Coldren, and A. C. Gossard, "THz electro-optic wavelength conversion in GaAs quantum wells: Improved efficiency and room-temperature operation," *Appl. Phys. Lett.* (to be published).
- [2] M. Y. Su, S. G. Carter, M. S. Sherwin, A. Huntington, and L. A. Coldren, "Strong-field terahertz optical mixing in excitons," *Phys. Rev. B* **67**, 125307(1-5) (2003).
- [3] M. Y. Su, S. G. Carter, M. S. Sherwin, A. Huntington, and L. A. Coldren, "Voltage-controlled wavelength conversion by terahertz electro-optic modulation in double quantum wells," *Appl. Phys. Lett.* **81**, 1564-1566 (2002).
- [4] B. Galdrikian and B. Birnir, "Period Doubling and Strange Attractors in Quantum Wells," *Phys. Rev. Lett.* **76**, 3308-3311 (1996).

Terahertz optical mixing in biased GaAs single quantum wells

V. Ciulin,* S. G. Carter, and M. S. Sherwin

iQUEST and Physics Department, University of California, Santa Barbara, California 93106, U.S.A

A. Huntington and L. A. Coldren

Materials Department, University of California, Santa Barbara, California 93106, U.S.A

(Received 23 February 2004; published 20 September 2004)

The nonlinear mixing of near-infrared (NIR) and terahertz (THz) laser beams is investigated experimentally in a square GaAs quantum well structure, where the symmetry of the sample can be controlled by applying an electric field along the growth direction. The mixing produces sidebands, which appear at $\omega_{\text{sideband}} = \omega_{\text{NIR}} + n\omega_{\text{THz}}$, where $n = \pm 1, 2, \dots$. For a given THz frequency, the intensity of the $n = \pm 1$ sidebands displays two main resonances as a function of the NIR frequency. These resonances are separated by the THz frequency. Their intensity is found to depend strongly on the electric bias and on THz frequency. The $n = \pm 1$ sideband intensity is zero when the sample is unbiased and increases significantly with bias. The sideband is strong when the THz laser frequency is tuned in resonance with an intersubband transition and also at low THz frequencies. The main features of our results are explained qualitatively, except at very high THz intensities, by a perturbative model of the nonlinear susceptibility $\chi^{(|n|+1)}$. At high THz intensities, the resonances are observed to red shift and broaden.

DOI: 10.1103/PhysRevB.70.115312

PACS number(s): 78.67.De, 42.65.-k, 78.20.Jq

I. INTRODUCTION

Electric fields affect the optical interband properties of semiconductors.¹ The effect is particularly strong in the quantum-confined Stark effect, when the field is applied along the growth direction of a quantum well (QW) sample. This allows efficient optical modulators and switches. Using high-frequency ac fields in the terahertz (THz) range is technologically interesting as demand grows for faster devices.^{2,3} Fields in this energy range can furthermore couple conduction or valence subbands, allowing resonant effects. ac Stark effects have been predicted at high ac fields.⁴⁻⁶

In undoped QW's, the THz field can couple different excitonic states and thus modulate the interband (optical) polarization. This leads to changes in the exciton optical absorption and to the emission of sidebands at $\omega_{\text{sideband}} = \omega_{\text{NIR}} + n\omega_{\text{THz}}$, where ω_{NIR} (ω_{THz}) is the frequency of the near infrared (THz) beam and $n = \pm 1, \pm 2, \dots$. There is a wealth of theoretical investigations predicting significant changes of the absorption under THz illumination and of sideband generation.^{5,7-10} Previous experimental studies, in which the THz field was oriented in the QW plane, have reported small changes in absorption under a strong THz field¹¹ and even ($n = 2, 4, \dots$) sideband generation.¹² To generate odd sidebands, especially the efficient $n = 1$, asymmetric coupled QW structures have been used with the ac electric field polarized in the growth direction of the QW.^{3,13} In these structures, the intersubband spacings can be tuned by a dc bias.¹⁴ For weak THz fields, some sideband properties were explained by a $\chi^{(|n|+1)}$ nonlinear susceptibility model.^{12,15} At high THz intensities nonperturbative theories have been found necessary.¹⁶ Odd and even sidebands have been also observed in bulk GaAs.¹⁷

Here, we present a detailed study of the nonlinear mixing of a near-infrared (NIR) and THz laser beam in a square QW

structure. The THz electric field is oriented along the growth direction of the QW. To enhance the nonlinear mixing, the sample symmetry can be broken by applying a dc electric field along the growth direction. This model system has the advantage that the level of asymmetry can be controlled and that the resonances are well defined and much less numerous than in coupled QW's. In the present case, we can consider a three-state system including two heavy-hole excitonic levels and the ground state. The oscillator strength of the exciton is stronger than for coupled wells and it has been predicted that this configuration leads to very efficient sideband generation.^{9,18} There are also several theoretical studies of THz electro-optic effects in square wells to which our results can be compared,^{5,19} although the THz fields used theoretically are stronger than the ones achieved experimentally. We observe and study sidebands resulting from a three-wave ($n = \pm 1$) and a four-wave ($n = \pm 2$) mixing process. The $n = 1$ sideband is zero in the absence of electric bias and grows approximately as the dc electric field squared. In contrast, the $n = 2$ sideband intensity changes little when a small dc bias is applied to the sample. For a given THz frequency, the $n = \pm 1$ sideband typically exhibits two main resonances as the NIR frequency is varied: the resonances occur when the NIR frequency or the sum of NIR and THz frequencies is tuned to the lowest heavy-hole excitonic transition. The $n = \pm 1$ sideband intensity is also found to depend on the THz frequency. It is strong when the THz pump is resonant with an intersubband transition and also at low THz frequencies when the THz pump is nonresonant. At medium THz field strength, our measurements can be qualitatively explained by a perturbative model of the nonlinear susceptibility $\chi^{(|n|+1)}$. This model is not adequate for stronger THz fields as the interband absorption strength and energy position are modified by the ac field.

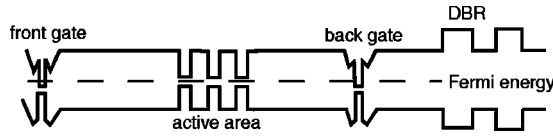


FIG. 1. Schematic diagram of the conduction band structure of the studied sample.

II. SAMPLE AND EXPERIMENT

The samples are GaAs/AlGaAs heterostructures that consist of an active area, two gate QW's, and a 30-period 600-Å $\text{Al}_{0.3}\text{Ga}_{0.7}\text{As}$ and 682-Å $\text{Al}_{0.99}\text{Ga}_{0.01}\text{As}$ $\lambda_{\text{NIR}}/4$ distributed Bragg reflector (DBR). A schematic band diagram of the studied structure is shown in Fig. 1. The active area contains either a single or three 150-Å GaAs QW's separated by 300-Å $\text{Al}_{0.3}\text{Ga}_{0.7}\text{As}$ barriers. Its center is situated close to a multiple of $\lambda_{\text{NIR}}/2$ from both the sample surface and the DBR. Therefore the incident and reflected NIR laser beams interfere constructively at the center of the active area and the effective electric field of the NIR laser is enhanced. This leads to a peak absorption of the heavy-hole exciton larger than 50%, which is consistent with transfer matrix calculations.²⁰ The two gates, one on each side of the active area, are separated by about 1 μm . They consist of 80-Å QW's with a δ -doping layer 100 Å away. The distance between the DBR and the closest gate is 1600 Å.

The gates were contacted ohmically to allow applying a dc bias to the sample. To minimize potential electrical heating effects, the bias was turned on only when taking measurements with the THz source, which is on for about 5 μs with a repetition rate of 1.5 Hz. The dc electric field was thus applied for 25 μs and synchronized with each THz pulse. A piece of sapphire was mechanically pressed on the sample surface to form a waveguide for the THz in which the active area is close to the waveguide center. The two studied samples showed similar behavior and we restrict the present discussion to the sample with three QW's, as its sideband signal is stronger.

The sample's reflectivity spectrum is plotted in Fig. 2(a). The two peaks are the heavy-(hh1X) and light-(lhX) hole excitons. We will use the notation $hhmX$ for the heavy-hole exciton formed by an electron in the first conduction level and a hole in the m th level. When applying a bias, the hh1X and lhX spectral lines redshift as expected for the quantum confined Stark effect.^{1,22} The change in energy with electric field, shown in Fig. 2(b), is strong for the hh1X. The graph is not totally symmetric around zero bias. An asymmetry is also observed in the current versus voltage curves not shown here. At negative bias, it appears that the maximum electric field achieved inside the sample is smaller than for positive bias: for $V_{\text{bias}} < -1.6$ V the hh1X energy no longer changes. A possible explanation for this observation is interface roughness, since the GaAs/AlGaAs interface is poorer than the AlGaAs/GaAs one.²³ In addition, the intensity of the integrated photoluminescence (PL) was not constant for $|V_{\text{bias}}| > \sim 2$ V, indicating the presence of disorder and/or charge transfer from the barrier or the gates into the QW. When an electric field is applied, the hh2X excitonic transi-

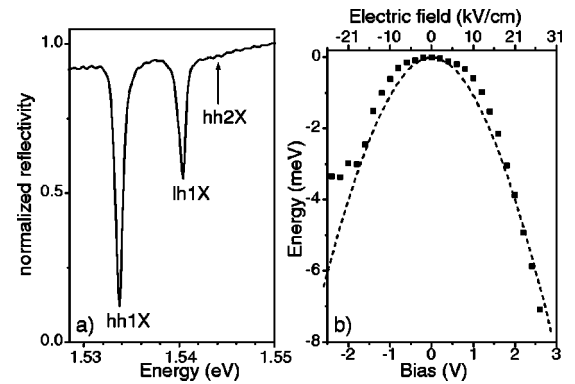


FIG. 2. (a) High-resolution normalized reflectivity spectra at 19 K and zero bias. The arrow indicates the spectral position of the hh2X transition that does not appear for unbiased structures. (b) Energy change of the hh1X reflectivity line as a function of bias and estimated electric field at 19 K, solid squares. The dashed line shows the result of our calculations (Ref. 21).

tion becomes possible and a peak appears at the energy indicated by the arrow in Fig. 2(a). The measured hh2X absorption was quite small (less than 1%) at around 0.5 V but was reliably measured using a differential technique that detects the change in the reflectivity when the bias is modulated.

Figure 3(a) shows the experimental configuration. For the measurements, the sample was held near 20 K in a closed-cycle helium cryostat. The THz beam was provided by the UCSB free electron laser²⁴ and was focused onto the cleaved edge of the sample by an off-axis parabolic mirror. The beam was on for 3–6 μs at a repetition rate of 1.5 Hz. The THz laser power was measured before the sample with an electrically calibrated photothermophone energy meter (Thomas Keating Ltd.). To obtain the THz intensity, the spot size was measured by scanning a small aperture across the THz laser focus. The maximum intensity was found to be $\sim 0.4 \text{ MW cm}^{-2}$ and the resulting estimated THz electric field inside the sample is $\sim 9 \text{ kV/cm}$. The polarization of the electric field of the THz laser was oriented along the growth direction of the sample, thus allowing coupling to intersubband transitions. The electron and light-hole intersubband

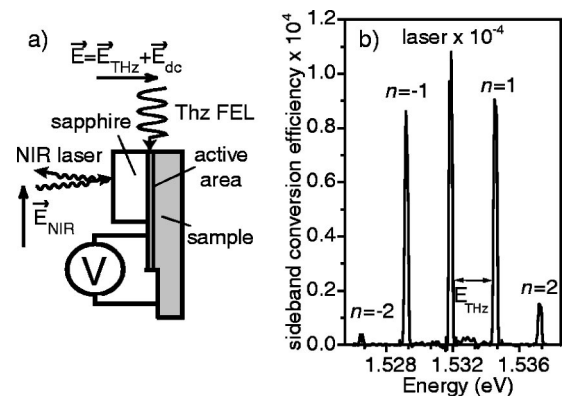


FIG. 3. (a) Schematic drawing of the experimental configuration. (b) Sideband spectra at 25 K for $\hbar\omega_{\text{THz}} = 2.7 \text{ meV}$ with a bias $V_{\text{bias}} = 1 \text{ V}$ and a THz laser intensity of $\sim 0.1 \text{ MW cm}^{-2}$.

transitions occur for energies larger than 40 meV and are out of reach of our THz source (0.5–20 meV). But the heavy-hole transition between the first two levels is around 10 meV and thus within the range of our source. The energy difference between the first heavy-hole and light-hole levels is around 6 meV. However, for small in-plane wave vectors, intersubband transitions between the heavy and light holes are weak.²⁵ Thus, in our model, we will consider only three levels: the ground state and the first and second heavy-hole excitons.

The NIR probe beam came from a tunable cw Ti-sapphire laser, which was chopped by an acousto-optic modulator into approximately 200 μ s pulses that overlapped each THz pulse. The NIR beam was reflected off the sample close to normal incidence and sent to a 0.85-m double monochromator, where it was detected by a photomultiplier tube. The NIR intensity on the sample was ~ 7 W cm⁻², yielding a total exciton density $n_X \sim 10^{10}$ cm⁻² when the frequency is tuned in resonance with the hh1X transition. This excitation density is relatively high. Note, however, that the excitation density is lower when the NIR laser frequency is tuned away from the hh1X resonance. To verify that the high excitation density does not influence our observations significantly, measurements were also taken with an order-of-magnitude lower NIR intensity. The sideband resonances associated with the hh1X transition were narrower, but all trends were the same as those presented herein.

III. EXPERIMENTAL OBSERVATIONS

Figure 3(b) shows a typical sideband spectrum. The central line is the NIR laser and the four surrounding peaks are the THz optical sidebands. They are separated from the main laser line by multiples of the THz frequency. The conversion efficiency from the NIR laser into the sidebands is here $\sim 10^{-4}$. This is comparable to the maximum conversion efficiency achieved in coupled QW samples with a similar number of QW's.¹⁴ The intensity of the sideband in a given sample depends on several factors: (a) the NIR and THz laser frequencies with respect to the resonances, (b) the value of the dc electric field, and (c) the NIR and THz power. First, we will explore points (a) and (b) in the linear regime of THz power—i. e., where the $n=1$ sideband intensity increases linearly with the THz intensity and the $n=2$ increases quadratically.¹⁷

As the active region of the sample is very thin (< 150 nm), the intensity of the sidebands is significant only close to the resonances of our system and the bulk contribution is not observable. Figure 4(a) presents sideband resonance scans obtained by measuring the sideband signal at $\omega_{\text{NIR}} + n\omega_{\text{THz}}$ for $n=-1$, while scanning the NIR frequency. The spectra display a peak when the NIR frequency is close to the hh1X exciton transition. A second peak, higher in energy, appears when the sum of the NIR and THz frequencies is resonant with the hh1X. Therefore, the two peaks in the $n=-1$ sideband resonance spectra are separated by ω_{THz} as shown in the inset of Fig. 4(a). Schematic drawings of the transitions are shown in Fig. 4(b). Other resonances can occur that involve the hh2X level but they were not clearly

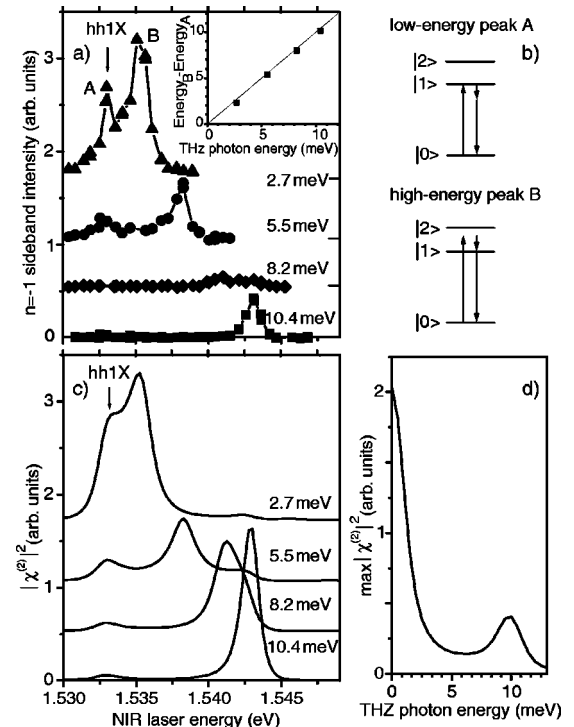


FIG. 4. (a) Sideband resonance spectra, showing the $n=-1$ sideband intensity as a function of the NIR laser energy. The measurements were taken at 25 K and $V_{\text{bias}}=1$ V ($E_{\text{dc}}=10$ kV/cm) for $\hbar\omega_{\text{THz}}=2.7$ (triangles), 5.5 (circles), 8.2 (diamonds), and 10.4 (squares) meV and THz laser intensities of $\sim 25, 30, 40,$ and 55 kW cm⁻², respectively (Ref. 26). The spectra have been offset for clarity. For each curve the offset is shown by a small line on the right side of the panel. Inset: energy difference between the two resonances labeled A and B as a function of $\hbar\omega_{\text{THz}}$. The line shows the predicted one-to-one-correspondence. (b) Schematic level model of the different transitions. (c) $|\chi^{(2)}|^2$ calculated using Eq. (1) for the $\hbar\omega_{\text{THz}}$ and E_{dc} used experimentally (Ref. 21). For the numerical evaluation of the plotted curves, we used $\gamma=1$ meV and a GaAs band gap of 1.52 eV. (d) Calculated maximum of $|\chi^{(2)}|^2(\omega_{\text{NIR}})$ as a function of ω_{THz} .

seen experimentally. The $n=1$ sideband spectra also show two peaks, as seen in Fig. 5(a), which arise from transitions similar to those presented in Fig. 4(b). For $n=2$, the sideband is weak under the present experimental conditions and we observed only one resonance when $\hbar\omega_{\text{NIR}}$ is close to the hh1X energy.

We were able to observe sidebands at all THz frequencies explored, which ranged from $\hbar\omega_{\text{THz}}=2.7$ to 14.1 meV. As shown in Fig. 4(a), the maximum intensity of the $n=\pm 1$ sideband spectra varied nonmonotonically as a function of ω_{THz} . A peak in intensity is found for $\hbar\omega_{\text{THz}} \cong 10$ meV, which is close to resonance with the hh1 to hh2 transition. However, stronger sidebands were observed at small THz frequencies, even though the THz excitation intensities were smaller. It should be noted that it is difficult to quantitatively compare the sideband intensities for different THz frequencies. Indeed, the sideband intensity depends not only on the intensity of the THz beam before it hits the sample, which is the value that we can measure, but also on the efficiency of the coupling into the edge of the sample. In a first approxi-

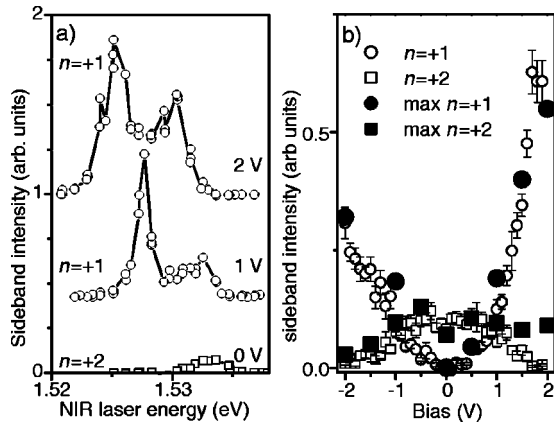


FIG. 5. (a) Sideband resonance spectra at 19 K with $\hbar\omega_{\text{THz}} = 5.5$ meV and a THz laser intensity of ~ 30 kW cm^{-2} . The signal is detected at ω_{sideband} as a function of the NIR laser energy. The $n=2$ sideband intensity at $V_{\text{bias}} = 0$ V is shown with open squares and the $n=1$ sideband with open circles at $V_{\text{bias}} = 1$ and 2 V. The spectra have been offset for clarity. (b) Intensity of the $n=1$ (circles) and $n=2$ (squares) sideband as a function of bias, V_{bias} , at $\hbar\omega_{\text{NIR}} = 1.530$ and 1.5325 eV, respectively. The solid symbols show the peak intensity of the sideband resonance spectra when ω_{NIR} is tuned to the hh1X energy.

mation, we neglect the effect of the waveguide as the NIR probe was close to the edge of the sample.

Figure 5 shows the intensity of the $n=1$ and $n=2$ sideband as a function of bias. The peaks are observed, Fig. 5(a), to shift towards the red with increasing bias. This is due mainly to the quantum confined Stark effect shown in Fig. 2(b). As the sideband resonance is broad around the hh1X energy, we were able to measure the sideband intensity faithfully as a function of bias by sitting at a given NIR frequency, as seen in Fig. 5(b). The measurement at fixed NIR frequency is not as good for the $n=2$ sideband, as shown by the deviation between the open and solid square symbols at positive bias. The $n=1$ sideband intensity is zero for a square well and increases, roughly proportionally with E_{dc}^2 , when the QW is biased and its symmetry is broken. The $n=2$ sideband intensity is almost independent of bias for positive bias and decreases at negative bias. Figure 5(b) shows that the curves for the $n=1$ and $n=2$ are not symmetric around zero. An asymmetry between the positive and negative biases was also observed in the spectral properties without THz illumination in Fig. 2(b). We believe that these effects are linked and that the sideband properties are altered by interface roughness, disorder, and/or charge transfer. The measured dependence of the $n=1$ and $n=2$ sidebands with bias was qualitatively similar for all the THz frequencies used. However, from cool-down to cool-down, variations were observed for $|V_{\text{bias}}| > 1.5$ V, and we also have measurements where the sidebands peak intensity decreases between 1.5 and 2 V. These changes are attributed to a degradation of the optical properties of the sample under strong dc electric field.

At high THz intensities, resonant coupling between subbands leading to the Autler-Townes splitting of the exciton absorption spectrum has been predicted.⁴ Numerical calculations have been performed for a single quantum well, where

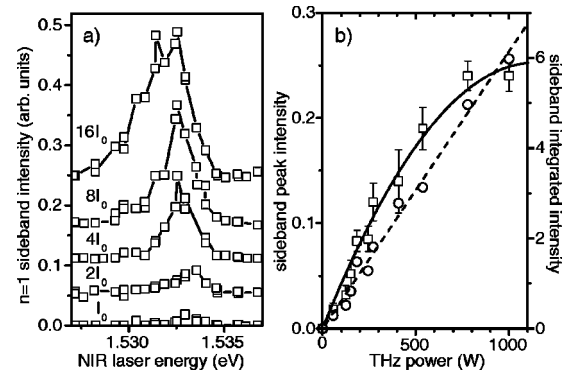


FIG. 6. (a) $n=1$ sideband resonance spectra at 19 K with $\hbar\omega_{\text{THz}} = 10.4$ meV and $V_{\text{bias}} = 1$ V for different THz laser intensities. The max THz power is ~ 1 kW. (b) $n=1$ sideband peak (open squares) and integrated (open circles) intensity as a function of THz laser power. The lines are guides to the eyes.

the terahertz couples to the heavy-hole intersubband transition.^{5,19,27} Experimentally, nonperturbative effects showing a saturation of the sideband intensity with the THz intensity have been reported in coupled QW's and in bulk GaAs.^{16,17} Intense THz fields can dress the exciton states, and effects such as the Autler-Townes splitting are predicted to appear when the Rabi frequency $\mu E_{\text{THz}}/\hbar$, with μ being the intersubband dipole moment, is larger than the dephasing rate. The necessary THz fields should be within our reach at the highest THz intensities. Figure 6 shows our experimental observations of the sideband resonance as a function of THz power. The maximum estimated THz intensity was ~ 0.2 MW cm^{-2} and the THz photon energy was 10.4 meV. The sideband resonance is observed to shift to the red and to broaden with increasing THz power. At higher THz intensity, the peak intensity of the $n=1$ sidebands saturates. When plotting the integrated intensity of the $n=1$ sideband, a linear power dependence is recovered. Thus the observed saturation in the sideband peak intensity comes here from broadening of the resonance under the THz field. A broadening of the resonance could be the first sign of the Autler-Townes splitting, when the THz pump is tuned to the heavy-hole transition as is the case experimentally. When the THz pump is out of resonance with the heavy-hole transition, theoretical calculations predict that the optical spectrum is affected in a different way.⁵ Broadening of the sideband resonances was also observed with $\hbar\omega_{\text{THz}} = 6.3$ meV, making an assignment of our observations to the Autler-Townes splitting possible but unlikely. Lattice heating by the THz beam can be in part responsible for the observed sideband broadening and redshift. However, this cannot be the only effect as the value of the redshift implies a much smaller increase in the lattice temperature than the broadening. A small in-plane component of the THz field could also contribute to a part of the observed redshift and broadening. Such a component may arise because of focusing and coupling into the modes of the dielectric waveguide of which the sample is a part. It would not contribute directly to the $n = \pm 1$ sideband generation but can affect the absorption spectra.¹¹ Further experimental and theoretical studies are needed to elucidate the exact origin of our observations at high THz fields.

IV. MODEL AND DISCUSSION

With the exception of the observed saturation at high THz intensities, our results can be qualitatively explained by calculating the nonlinear optical susceptibility $\chi^{(n+1)}$. We consider only three levels: the ground state, hh1X, and hh2X. The intensity of the $n=1$ sideband is proportional to $|\chi^{(2)}|^2 |E_{\text{NIR}}^x|^2 |E_{\text{THz}}^z|^2$ with²⁸

$$\chi^{(2)}(\omega_{\text{NIR}} + \omega_{\text{THz}}, \omega_{\text{NIR}}, \omega_{\text{THz}}) \propto \sum_{m\nu} \frac{\mu_{0m}^x \mu_{m\nu}^z \mu_{\nu 0}^x}{(\omega_{m0} - \omega_{\text{NIR}} - \omega_{\text{THz}} - i\gamma_{m0})(\omega_{\nu 0} - \omega_{\text{NIR}} - i\gamma_{\nu 0})}, \quad (1)$$

where 0 is the ground state and $m, \nu=1, 2$ are indices of the two heavy-hole exciton states considered, the hh1X and hh2X, respectively. In Eq. (1), some nonresonant terms that are very small have been ignored. γ is a measure of the linewidth of the transition. In the numerical evaluation of Eq. (1), a fixed value of 1 meV was used. μ^x and μ^z are the interband and intersubband matrix elements, respectively. μ^x is proportional to the overlap of the electron and hole wave function of the transition. μ^z is evaluated as

$$\mu_{m\nu}^z \propto \langle \Psi_{h\nu} | z | \Psi_{h_m} \rangle - \langle \Psi_{e_1} | z | \Psi_{e_1} \rangle \delta_{mm}. \quad (2)$$

The $n=-1$ sideband intensity is proportional to Eq. (1) using a negative value for ω_{THz} . The intensity of the $n=\pm 2$ sideband is proportional to $|\chi^{(3)}|^2 |E_{\text{NIR}}^x|^2 |E_{\text{THz}}^z|^4$. The expression of $\chi^{(3)}$ can be written analogously to Eq. (1).

The wave functions necessary to calculate the matrix elements in Eq. (1) are obtained by solving the Schrödinger equation numerically for electrons and holes in our QW as a function of the applied electric field.²¹ To test our parameters, we have also variationally calculated the exciton binding energy:²⁹ the energy difference between the hh1X and hh2X of ~ 9.5 meV and the change in hh1X exciton energy with electric bias agree fairly well with the measurements, as shown in Fig. 2. Using Eq. (1), $|\chi^{(2)}|^2$ can be evaluated as a function of ω_{NIR} for a given ω_{THz} . The calculated curve has at least two peaks that correspond to the transitions described in Fig. 4. The energy position of these peaks matches the measurements well.

The intensity of the calculated $n=-1$ sideband resonant spectra depends strongly on ω_{THz} as shown in Fig. 4(c). It follows a nonmonotonic behavior similarly to the experimental spectra in Fig. 4(a). Our calculations do not fully reproduce the relative intensity of the peaks in the measured sideband resonance spectra. Some of the calculated peaks appear broader than in the measured spectra. The calculated spectra were normalized so that for the lowest used THz frequency, the intensities of the calculated and measured spectrum are comparable. Under these conditions, the calculated spectra at the two largest THz frequencies show a stronger signal than the one observed experimentally. There are several differences between measurements and calculations that can explain this. In the model, we have considered a fixed value of γ when evaluating Eq. (1), but γ_{10} and γ_{20} are not necessarily equal. This can change the relative intensity of the two peaks in each sideband resonance spectra. Also, the matrix

elements used to evaluate $|\chi^{(2)}|^2$ are calculated for a bare QW and do not take into account that the cavity formed by the DBR and the sample surface enhances the strength of the optical transitions selectively. This can modify the relative intensity of the sideband resonances as a function of ω_{THz} . Using Eq. (1), we have calculated the maximum value of $|\chi^{(2)}(\omega_{\text{NIR}})|^2$ as a function of ω_{THz} . Figure 4(d) shows the result of these calculations as a function of ω_{THz} . The predicted $|\chi^{(2)}|^2$ displays a peak when ω_{THz} is close to the hh1X to hh2X intersubband transition and a larger maximum when ω_{THz} tends towards zero. Thus, the model reproduces our data qualitatively. In our calculations, the large maximum at small ω_{THz} arises from the term in which $m=\nu=1$. This term involves only the hh1X and ground states and is small for large ω_{THz} . It takes advantage of the large interband matrix element of hh1X, while the interband matrix element of hh2X is quite small. The sideband signal can be thought of as arising from the optical transition being quasistatically modulated. This effect can be stronger when the hh1X transition strength is enhanced by a cavity. Several studies have theoretically addressed the issue of nonresonant modulation with low THz frequencies.^{4,5,30}

The model also predicts that the intensity of both peaks of the $n=\pm 1$ sideband is zero for a square well and increases as the electric field breaks the sample symmetry. The calculated dependence of the intensity of the high-energy peak of $n=1$ sideband has the shape of a parabola, centered at zero, but it saturates around $|V_{\text{bias}}|=1.5$ V. At this voltage, the calculated overlap between the electron and hole wave functions decreased significantly with respect to the zero-bias value. In a similar way, we have calculated $|\chi^{(3)}|^2$ to model the behavior of the $n=2$ sideband. The peak intensity around the hh1X transition is predicted to stay almost constant until 1 V and then increase a little before decreasing at 1.5 V. Our calculations reproduce most of the experimentally observed features shown in Fig. 5. The $n=1$ sideband intensity increases significantly for small applied biases while the $n=2$ sideband intensity stays rather constant. Discrepancies between experiment and calculations occur at larger biases and the decrease in the sideband intensity predicted for $|V_{\text{bias}}|>1.5$ V is not clearly observed experimentally. The latter could be masked by disorder and/or charge transfer related effects that modify the sample optical properties at large biases.

V. CONCLUSION

In conclusion, we have studied nonlinear THz electro-optical effects in single GaAs QW's, where the symmetry can be broken by applying a bias. We find that we can control the intensity of the $n=\pm 1$ sideband by changing the applied bias and the frequency of the THz beam. At zero bias, the $n=\pm 1$ sideband intensity is zero and it increases roughly quadratically with the applied dc electric field. The $n=\pm 1$ sideband intensity also varies nonmonotonically with the frequency of the THz beam. It becomes particularly strong at low THz frequencies. With a careful sample design, this effect could be exploited for efficient wavelength

conversion. Our results are explained qualitatively, except at very high THz intensities, by a perturbative model of the nonlinear susceptibility. The model also predicts that the sideband intensity can saturate at finite dc electric fields due to the decrease in overlap between the electron and hole wave functions. At high THz intensities, where strong changes to the absorption spectrum had been predicted,⁵ the resonances are observed to shift in energy and broaden.

ACKNOWLEDGMENTS

We are grateful for fruitful discussions with A. V. Maslov and D. S. Citrin. We thank A. V. Maslov for encouraging us in this study and for sharing unpublished high-THz-field calculations with us. We acknowledge support from NSF Grant No. DMR 0244390 and Sun Microsystems. V. C. thanks the Swiss NSF for additional support.

*Present address: V. Birkedal née Ciulin, Department of Chemistry, University of Aarhus, Langelandsgade 140, DK-8000 Århus C, Denmark.

- ¹S. Schmitt-Rink, D. S. Chemla, and D. A. B. Miller, *Adv. Phys.* **38**, 89 (1989).
- ²D. S. Citrin and S. Hughes, *Appl. Phys. Lett.* **78**, 1805 (2001).
- ³S. G. Carter, V. Ciulin, M. S. Sherwin, M. Hanson, A. Huntington, L. C. Coldren, and A. C. Gossard, *Appl. Phys. Lett.* **84**, 840 (2004).
- ⁴S. Autler and C. H. Townes, *Phys. Rev.* **100**, 703 (1955).
- ⁵A. V. Maslov and D. S. Citrin, *Phys. Rev. B* **62**, 16 686 (2000).
- ⁶A. Liu and C. Z. Ning, *J. Opt. Soc. Am. B* **17**, 433 (2000).
- ⁷A. P. Jauho, and K. Johnsen, *Phys. Rev. Lett.* **76**, 4576 (1996).
- ⁸D. S. Citrin, *Phys. Rev. B* **60**, 13695 (1999).
- ⁹A. Shimizu, M. Kuwata-Gonokami, and H. Sakaki, *Appl. Phys. Lett.* **61**, 399 (1992).
- ¹⁰C. J. Dent, B. N. Murdin, and I. Galbraith, *Phys. Rev. B* **67**, 165312 (2003).
- ¹¹K. B. Nordstrom, K. Johnsen, S. J. Allen, A.-P. Jauho, B. Birnir, J. Kono, T. Noda, H. Akiyama, and H. Sakaki, *Phys. Rev. Lett.* **81**, 457 (1998).
- ¹²J. Cerne, J. Kono, T. Inoshita, M. Sherwin, M. Sundaram, and A. C. Gossard, *Appl. Phys. Lett.* **70**, 3543 (1997).
- ¹³C. Phillips, M. Su, M. Sherwin, J. Ko, and L. Coldren, *Appl. Phys. Lett.* **75**, 2728 (1999).
- ¹⁴M. Y. Su, S. G. Carter, M. S. Sherwin, A. Huntington, and L. A. Coldren, *Appl. Phys. Lett.* **81**, 1564 (2002).
- ¹⁵M. Y. Su, C. Phillips, J. Ko, L. Coldren, and M. S. Sherwin, *Physica B* **272**, 438 (1999).
- ¹⁶M. Y. Su, S. G. Carter, M. S. Sherwin, A. Huntington, and L. A. Coldren, *Phys. Rev. B* **67**, 125307 (2003).
- ¹⁷M. A. Zudov, J. Kono, A. P. Mitchell, and A. H. Chin, *Phys. Rev. B* **64**, 121204(R) (2001).
- ¹⁸A. V. Maslov and D. S. Citrin, *Solid State Commun.* **120**, 123 (2001).
- ¹⁹A. V. Maslov and D. S. Citrin, *Phys. Rev. B* **64**, 155309 (2001).
- ²⁰V. Savona, L. Andreati, P. Schwendimann, and A. Quattropani, *Solid State Commun.* **93**, 733 (1995).
- ²¹Calculation parameters for the numerical solution of Schrödinger's equation: electron mass, $m_e=0.067$; hole mass, $m_{h(z)}=0.48$; in-plane hole mass, $m_{h(R)}=0.082$. The band gap was split 60:40 between the conduction and valence bands.
- ²²E. E. Mendez, G. Bastard, L. L. Chang, L. Esaki, H. Morkoc, and R. Fischer, *Phys. Rev. B* **26**, 7101 (1982).
- ²³M. Naganuma, T. Ishibashi, and Y. Horikoshi, *J. Appl. Phys.* **62**, 644 (1987).
- ²⁴G. Ramian, *Nucl. Instrum. Methods Phys. Res. A* **318**, 225 (1992).
- ²⁵F. Szmulowicz and G. J. Brown, *Phys. Rev. B* **51**, 13 203 (1995).
- ²⁶The sideband spectra shown are not corrected for the fact that the THz pulse length is not the same at all ω_{THz} . The shortest pulse occurred at $\hbar\omega_{\text{THz}}=2.7$ meV. Correcting for this effect would increase the sideband intensity at the lowest ω_{THz} by less than a factor 2.
- ²⁷A. V. Maslov and D. S. Citrin, *IEEE J. Sel. Top. Quantum Electron.* **8**, 457 (2002).
- ²⁸R. W. Boyd, *Nonlinear Optics* (Academic Press, San Diego, 1992).
- ²⁹D. A. B. Miller, D. S. Chemla, T. C. Damen, A. C. Gossard, W. Wiegmann, T. H. Wood, and C. A. Burrus, *Phys. Rev. B* **32**, 1043 (1985).
- ³⁰D. S. Citrin and W. Harshawardhan, *Phys. Rev. B* **60**, 1759 (1999).